HIGH PRESSURE COAL COMBUSTION KINETICS PROJECT

COOPERATIVE AGREEMENT NO DE-FC26-01NT40777
PERIOD OF PERFORMANCE: JUNE 2000 – DECEMBER 2004

FINAL REPORT

FOR

NETL AAD Document Control Bldg. 921
U.S. Department of Energy
National Energy Technology Laboratory
P.O. Box 10940
626 Cocharans Mill Road
Pittsburgh, PA 15236-0940

BY

Stefano Orsino
Fluent Inc.
Primary Recipient
10 Cavendish Court, Lebanon, NH 03766
Point of Contact: Kristi C. Fenner (Business and Financial)
Point of Contact: Stefano Orsino (Technical)

Foster Wheeler Development Corporation
12 Peach Tree Hill Rd., Livingston, NJ 07039

SRI International
333 Ravenswood Ave., Menlo Park, CA 94025

American Air Liquide
5230 S. East Ave., Countryside, IL 60525

University of Connecticut
Department of Chemical Engineering, University of Connecticut, 191 Auditorium Rd., Unit 3222, Storrs, CT 06269-3222

Brown University
Division of Engineering, Box D, 182 Hope St., Brown University, Providence RI 02912

Niksa Energy Associates
Niksa Energy Associates, 1745 Terrace Dr., Belmont, CA 94002

Report issued: March 30, 2005

DISCLAIMER

1. Abstract

As part of the U.S. Department of Energy (DoE) initiative to improve the efficiency of coal-fired power plants and reduce the pollution generated by these facilities, DOE has funded the High-Pressure Coal Combustion Kinetics (HPCCK) Projects. A series of laboratory experiments were conducted on selected pulverized coals at elevated pressures with the specific goals to provide new data for pressurized coal combustion that will help extend to high pressure and validate models for burnout, pollutant formation, and generate samples of solid combustion products for analyses to fill crucial gaps in knowledge of char morphology and fly ash formation. Two series of high-pressure coal combustion experiments were performed using SRI's pressurized radiant coal flow reactor. The first series of tests characterized the near burner flame zone (NBFZ). Three coals were tested, two high volatile bituminous (Pittsburgh #8 and Illinois #6), and one sub-bituminous (Powder River Basin), at pressures of 1, 2, and 3 MPa (10, 20, and 30 atm). The second series of experiments, which covered high-pressure burnout (HPBO) conditions, utilized a range of substantially longer combustion residence times to produce char burnout levels from 50% to 100%. The same three coals were tested at 1, 2, and 3 MPa, as well as at 0.2 MPa. Tests were also conducted on Pittsburgh #8 coal in CO_2 entrainment gas at 0.2, 1, and 2 MPa to begin establishing a database of experiments relevant to carbon sequestration techniques. The HPBO test series included use of an impactor-type particle sampler to measure the particle size distribution of fly ash produced under complete burnout conditions.

The collected data have been interpreted with the help of CFD and detailed kinetics simulation to extend and validate devolatilization, char combustion and pollutant model at elevated pressure. A global NO_X production sub-model has been proposed. The sub-model reproduces the performance of the detailed chemical reaction mechanism for the NBFZ tests.

Char morphologies of the NFBZ chars were extensively characterized to provide information on the char formation process and the properties of newly formed chars, which serve as important inputs into char combustion and burnout models. Many young char properties were similar to those measured previously at atmospheric conditions, but coal fluidity and swelling factors were significantly higher for the two bituminous coals studied at pressures of 10 atm and above. Electron microscopy and pore structure characterization by vapor adsorption techniques were applied to HPBO chars. A large presence of very low density, thin-walled chars from the two bituminous coals was observed at 10 atm pressure and above that led to extensive fragmentation in the late stages of burnout for these coals.

A systematic theoretical analysis of char combustion rate forms was undertaken with the particular goal of determining whether the common and convenient power-law form has enough fundamental justification to make it a reliable approach over the wider range of pressures and temperature expected in future coal technologies.

Coal chars were characterized using scanning electron microscopy (SEM) to identify the important parameters in ash formation under elevated pressure. Pressure was seen to affect the number distribution of char subtypes obtained for each of these coals. Ash particles obtained during complete burnout conditions were examined by SEM and then were also analyzed in more detail by computer controlled scanning electron microscopy (CCSEM). Results from the CCSEM analysis were also compared to information extracted from experiments conducted using the low pressure cascade impactor. These results therefore provide strong indication that pressure effects that change char pore structure and wall structure have a direct and predictable effect on the resulting ash particle size distributions.

The results of the char characterization and ash particle size distribution measurements were incorporated into an ash particle formation model to predict ash particle size distributions at elevated pressures under conditions of complete char burnout. Particle size distributions calculated with this model showed qualitative agreement with the trends identified in the experimental portion of this effort.

Advanced coal combustion sub-models have been deployed into Aspen and FLUENT. The CBK/E char combustion model has been implemented in FLUENT. An interface between FLUENT and PC Coal Lab® has been developed. The interface will allow to specify in FLUENT all the parameters related to devolatilization calculated in PC coal Lab. PC coal Lab has been has been deployed as a USER Block in Aspen Plus.

The Foster Wheeler integrated Vision 21 power plant has been analyzed. An Aspen Plus flow sheet model was set up and the system analysis and optimization on the conceptual plant were performed. It was shown that an overall plant efficiency of 61.9% can be achieved for the conceptual plant. A conceptual design and CFD analysis of the Pressurized Pulverized Coal Combustor (PPCC) has been performed. Several PPCC designs have been evaluated using FLUENT CFD modeling. The final design was a cylindrical furnace with a down-firing burner. In this design the pressure vessel and the waterwalls were combined to make a more compact simpler design. Furnace volume and residence time is similar to the previous design, but flame shape and stability are improved due to firing axially rather than wall-firing across a short depth. The FLUENT-Aspen controller was tested simulating the FW Vision 21 power plant providing suggestion for future development of the Controller.

TABLE OF CONTENTS

2. Experimental Overview

The experimental program plan called for the testing of three coals: two high volatile bituminous coals and a sub-bituminous coal, at up to four pressures, namely, 0.2,1, 2, and 3 MPa (2, 10, 20, and 30 atm). The test conditions were divided into two ranges: (a) near burner flame zone (NBFZ) conditions, which covered a range of burnout conditions from secondary pyrolysis through volatiles burnout, substantial soot burnout, and partial char burnout; and (b) high-pressure burnout (HPBO), where the residence time in the furnace was extended so that complete char burnout was achieved and ash was the only solid product. It was intended that pulverized coal particles be suspended in oxygen/nitrogen entrainment gases, but for technical reasons the majority of tests were conducted in oxygen/argon mixtures. Under AAL sponsorship, SRI also performed HPBO tests of one coal at three elevated pressures using oxygen/CO_2 entrainment. These tests were done to address the feasibility of CO_2 sequestration schemes. SRI's experimental facilities and the measurements techniques are described in Appendix A.

2.1 Near Burner Flame Zone (NBFZ) Experiments

After upgrading the pressurized radiant cold-flow reactor (p-RCFR) for operation at pressures up to 30 atm, SRI performed three sets of experiments on the sub-bituminous (PRB) coal at pressures of 10, 20, and 30 atm. These results were transmitted to NEA, where careful evaluation showed that the combustion conditions did not meet the requirements of the NBFZ study because complete secondary pyrolysis was not achieved. That is, conversion of tar to soot was not occurring for tests without oxygen present. As a consequence, modeling of the combustion of volatiles, soot, and char was confused by the simultaneous conversion of residual tar.

The solution to this experimental shortcoming was a slight redesign of the p-RCFR to accommodate a longer furnace. In the redesign, the furnace length was increased from 7 cm to 15 cm, and other minor changes were made to improve the accuracy of combustion product analyses.

The modified short-residence-time reactor (SRT-RCFR) was used to perform all the NBFZ experiments, as described in Appendix A. However, the "preliminary" PRB experiments, while not conducted under full secondary pyrolysis conditions, are nevertheless valid measurements, albeit under their more restrictive test conditions. For completeness, these results are also presented in Appendix A.

Addition of existing furnace extension sections to the upgraded SRT-RCFR created the long-residence-time reactor (LRT-RCFR). The HPBO experiments performed in this facility are reported in the Appendix A.

In spite of the challenges of measuring complete gaseous and solid product yields at elevated pressures and temperatures, it was possible to cover the entire NBFZ operating

domain by running the SRT-RCFR facility at a fixed coal feed rate with variable inlet oxygen concentrations to impose the same range of stoichiometric ratios at all test pressures. This strategy yielded datasets for the three subject coals at 1.0, 2.0 and 3.0 MPa. These data represent a major advance in the fundamental characterization of near-burner pulverized fuel combustion at elevated pressures.

The measurements are of such quality that only relatively small adjustments to the raw data were needed to close the balances on mass and C/H/N within ± 5 % in individual runs. The adjusted datasets show the expected tendency in the burnout of gaseous and solid fuels to increase steadily for progressively more oxidizing conditions. They also show that formation of NO_x increases rapidly at stoichiometric ratio (SR) values above 0.5. These data are well suited to serve as benchmarks for development of kinetic models for pyrolysis, gaseous and solid product production and burnout, and pollutant formation, as well as for characterizing char and ash properties. The data have also been used to tune chemical sub-models that describe evolution of the different species in a manner that can be incorporated into full-scale CFD process simulators [Liu and Niksa, 2003].

2.2 High-Pressure Burnout (HPBO) Experiments

The NBFZ tests described in Section 2.1 were designed to study combustion processes during the early stages (nominal hot zone residence times of 517 ms, but actual times of 200 ms or less) for a broad range of stoichiometric ratios. In the second stage of the program, the HPBO tests imposed much longer residence times to monitor the final stages of char burnout at elevated pressure. The experimental facility used for the HPBO experiments is described in Appendix A.

One of the primary objectives of these tests was the preparation of char samples for these conditions, which are used to guide the development of fly ash formation models at UConn and the development of char oxidation mechanisms at Brown University. In addition, NEA has used the results as a benchmark to evaluate the CBK/E model of char burnout using parameters derived from the NBFZ data (Niksa, 2004).

Although the majority of HPBO tests were conducted using argon as the entrainment gas, three series of tests of Pittsburgh #8 coal were also conducted using CO_2 entrainment. These tests were performed under sponsorship of AAL in support of their interest in carbon sequestration techniques. The test conditions and collected data are reported in Appendix A.

The collected data reveal a complex interplay of pressure, gas composition, thermal history, coal type, and oxygen concentration in determining the extent of char burnout. The datasets have been modeled to evaluate the CBK/E model. The burnout rates are somewhat slower with CO_2 as the entrainment gas primarily because of the increased heat capacity. This result has implications for oxygen-fired combustors with exhaust gas recirculation to aid CO_2 capture and sequestration. Combusting pulverized coal particles release ash and carbon at comparable rates until both materials reach about 50% level.

The remaining ash tends to stay as heavy particles through the final stages of carbon burnout.

2.3 Impactor Tests

An objective of the HPCCK program at UConn was to characterize the ash properties of the different coals, and in particular to establish the effects of high-pressure combustion on the ash properties. In addition to using optical and electron microscopy to analyze "char" samples from the NBFZ and HPBO tests, UConn was interested in "macroscopic" measurements of ash particle size distributions. In an effort to achieve these measurements, UConn furnished SRI with its 11-stage low-pressure impactor and auxiliary components. The experimental details and test results are described in Appendix A.

3. Analysis of the NBFZ Tests

NEA provided computational support for the laboratory testing at SRI, in both the design of the facilities and the interpretation of results. All the tests were run in a novel coal flow reactor called the pressurized radiant coal flow reactor (p-RCFR). Unlike conventional drop-tube furnaces that heat the fuel particles with a preheated gas stream, the p-RCFR uses radiant heating to better control the particle heating process, thereby expediting the detailed kinetic interpretation of data. The NBFZ configuration characterizes flame phenomena, particularly NO_X production, under the operating conditions in near-burner regions of large pulverized coal flames.
A 2D FLUENT simulator for the p-RCFR for all the NBFZ tests was developed. The tests and CFD simulations represent three coals of sub-bituminous through high volatile (hv) bituminous rank, three pressures from 1.0 to 3.0 MPa, and a wide range of stoichiometric ratios (S. R.).

The simulator accounts for the intense radiant flux from this flow reactor by incorporating axial profiles of tube wall temperature and radiant heat flux from stand-alone heat transfer calculations. Turbulent dispersion of particles is modeled with the stochastic discrete-particle approach, based on the standard κ-ε model and the two-layer zonal model for near-wall effects. The chemistry sub-model includes five reactions: coal devolatilization, partial volatiles combustion to form CO and H_2, soot oxidation to form CO, char oxidation to produce CO, and CO and H_2 oxidation in the gas phase. Nearly all the adjustable parameters in the associated rate expressions were evaluated from the results of PC Coal Lab® simulations or from an empirical correlation for the activation energy of char oxidation. The results of all CFD simulations are reported in Appendix B.

During the facility development stage of the project, NEA's CFD simulator was instrumental in guiding the testing team at SRI toward a longer furnace hot zone to alleviate the problems that had plagued the initial test series. Once the furnace was lengthened, most of the problems with plugging and deposition, softening of the flow tube, and incomplete secondary volatiles pyrolysis at low furnace stoichiometric ratio

became manageable. The CFD simulations also showed that particles would inevitably accumulate near the walls of the flow tube in the transitional and turbulent flows at all the elevated pressures in NBFZ tests, thereby explaining the basis for particle deposition and reactor plugging.

Ultimately, the SRI testing team was able to cover the entire NBFZ operating domain by running the p-RCFR at a fixed coal feed rate with variable inlet O_2 concentrations to impose the same range of S. R. at all test pressures. This strategy yielded datasets that represent a major advance in the fundamental characterization of near-burner pulverized fuel combustion at elevated pressures. Only relatively small adjustments to the raw data – mostly for the omission of S-species in the product analysis and for intermittent equipment malfunctions – were needed to close the balances on mass and C/H/N in individual runs. Indeed, the ultimate datasets exhibit closures within ± 5 % on all four balances in nearly every test case.

These datasets clearly resolve the stages of pressurized pulverized fuel combustion according to the consumption of the major fuel groups: gaseous volatiles, soot, and char. The fuel that wins the competition for the available O_2 at different stages of the combustion process is apparent in the burnout profiles – extents of burnout versus stoichiometric ratio - assigned for each fuel group from the test data. All the burnout profiles increase for progressively greater stoichiometric ratio, as expected. Those for both gaseous fuels and soot were insensitive to variations in both pressure and coal rank, albeit with exceptions. Soot effectively competes for the available O_2 at low stoichiometric ratio, but gases win the competition under more oxidizing conditions. The char burnout profiles are very sensitive to variations in both pressure and coal rank. The extents of char burnout uniformly diminished for progressively higher pressures, due to the cooler gas temperatures that inhibited char ignition at elevated test pressures. The chars from coals of lower rank also burned faster, as expected.

Once the datasets were qualified and accepted, they were used to tune-in the CFD simulations. Four of the pre-exponential factors in the chemistry sub-model were adjusted to match the reported extents of burnout for gaseous volatiles, soot, and char and the total O_2 utilization assigned for each individual test. This matching ensured that the simulated heat release rates were accurate which, in principle, ensures that the simulated thermal fields would satisfy useful quantitative tolerances. The qualified CFD simulator was used to predict the detailed operating conditions and flame structure in all 45 of the NBFZ tests, which covered three coal types, pressures from 1.0 to 3.0 MPa, and S. R. values from 0 to 1.8.

The simulations revealed that the structures of flames in the p-RCFR were surprisingly complex. At a superficial level, the flame structure shares elements in common with both premixed Bunsen flames and laminar diffusion flames. The main similarity is that gaseous volatiles are always ignited on the wall at the inlet to the furnace hot zone, and this flame propagates toward the flow axis to form a 2D parabolic flame surface. But fuel consumption is not restricted to this flame zone at all. Within the core, char particles are continuously heated by the radiant flux and by turbulent convection from the near-wall

region. Provided that the heat transfer rates are sufficient, all the residual fuel compounds in the core surpass the ignition threshold and burn at their fully ignited burning rates. This stage of the combustion is premixed. Within the near-wall region, the volatiles flame propagates away from the wall but does not consume all the O_2 in the near-wall region. Consequently, char particles dispersed into the sheath burn beyond the radial position of the volatiles flame, closer to the wall. This stage of the combustion consumes residual CO and H_2 and char and is also premixed. Note that the volatiles flame segregates the flow according to the following three stages of combustion: (1) within the core, residual gaseous fuels, soot, and char may eventually reach their ignition threshold and burn in a premixed mode; (2) outward transport of gaseous volatile fuels, soot, and O_2 sustains the volatiles flame as it propagates from the near-wall region toward the flow axis; and (3) residual CO, H_2, and char burns in the near-wall region after the volatiles flame has propagated deeper into the core as long as O_2 is available.

Whether or not the flame closes on the centerline in the available residence time will be mainly determined by pressure and stoichiometric ratio, although there are also coal quality effects. The thermal capacitance of the gas flow is proportional to the gas density and, therefore, increases for progressively higher pressures. Since the radiant heat flux to the suspension is insensitive to pressure, the core gas temperature diminishes at higher pressures. Consequently, inlet conditions that form closed flames at a lower test pressure will eventually sustain open flames at progressively higher pressures. The impact of decreasing stoichiometric ratio is qualitatively similar. For lower stoichiometric ratio, the volatiles flame ignited in the near-wall region releases less heat, because its burning rate is slower at the lower O_2 level. Moreover, two related factors inhibit combustion in the core: First, the slower heat release in the near-wall region directly slows the convective transfer rate into the core, which delays the ignition of combustibles in the core flow. Second, the lower O_2 level diminishes the heat release after the core finally ignites. Since the joint effect of all three factors is to lower core gas temperatures, conditions that sustain a closed flame at a higher stoichiometric ratio will eventually sustain open flames at progressively lower stoichiometric ratio.

At 1.0 MPa, the threshold stoichiometric ratio value for closed flames is roughly 0.20 with Pit. #8; 0.5 with PRB; and 0.8 with Ill. #6. None of the flames were closed with any coal at 2.0 and 3.0 MPa for stoichiometric ratio values near unity.

These characteristics have important implications for the near-burner performance of pulverized-fuel burners at elevated pressures. As the pressure is increased, flame ignition and, by association, flame stability will become much more problematic. There is no way to circumvent the greater thermal capacitance of air streams at progressively higher pressures, and this relation is the root cause of slower gas heating. Without proper remediation, gas temperature profiles across near-burner zones will be significantly cooler than necessary for rapid ignition and stable flame attachment. The most direct remedy would be to simply increase the suspension loading to compensate for the higher thermal capacitance with proportionate increases in the heat release rates. But the severe agglomeration characteristics of pulverized coal at elevated pressures render this approach infeasible. For example, to re-scale the suspension loading for operation at 3.0

MPa, the loading must be increased by a factor of thirty. Given the dramatically enhanced plasticity at elevated pressures of bituminous coals, in particular, burner deposits, abrasion, erosion, agglomeration, and plugging will almost certainly prevent stable operation at such high suspension loadings. These factors only become more intractable in oxy-blown systems, which are frequently proposed for pressurized combustors as a means to facilitate CO_2 sequestration.

4. Sub-Models for Pollutant Formation

The NBFZ test were analyzed using the ChemNet™ Post-Processing (CNPP) approach which incorporates realistic reaction mechanisms into an equivalent network of idealized reaction elements that was fully specified from CFD simulations. The CNPP approach is described in details in Appendix B. First, dynamic operating conditions were assigned for each test from CFD simulations in which rate parameters in the chemistry sub-models were adjusted to match the measured product distributions at the reactor exit. Matching the product distribution ensures that the simulated heat release rates are accurate which, in principle, ensures that the simulated thermal fields satisfy useful quantitative tolerances. Then the flows were subdivided into two regions, a wall layer containing most of the particles surrounding a central core flow with a very dilute coal suspension. Finally, the CFD flow and temperature fields were used to quantitatively specify thermal histories, residence time distributions, and entrainment rates into CSTR-series for every NBFZ test. NEA's FLASHCHAIN® determined the complete distribution of volatiles, including gaseous fuels and soot, and all char properties from each coal's proximate and ultimate analyses. The reaction mechanism for chemistry in the gas phase contains 444 elementary reactions among 66 species, including all relevant radicals and N-species. All rate parameters were assigned independently, so there are also no adjustable parameters in the sub-model for gas phase chemistry. The soot chemistry sub-model depicts oxidation by O_2, O-atoms, and OH; recombinations of H-atoms and OH; and NO reduction into N_2. Char burning rates were evaluated from CBK/E to account for thermal annealing, ash encapsulation, and a transition among all three char oxidation regimes. In total, there are only two adjustable parameters in this analysis: (1) The initial char oxidation reactivity was specified in a one-point calibration with the extent of char burnout for near-stoichiometric flames at 1.0 MPa; and (2) The fraction of char-N converted to NO during char oxidation was assigned to fit the NO_X emissions from the flame series at 1.0 MPa.

The CNPP simulations accurately depict all the important trends in the NBFZ database with both coal quality and for increasing pressure. The yields of char, soot, CO_2, H_2, and H_2O were generally within experimental uncertainty for all coals for the full range of stoichiometric ratio. The most serious quantitative flaw is that CO yields were under predicted by roughly a factor of two throughout, although the predictions correctly indicate higher CO levels for coals of progressively lower rank. Most important, the reaction mechanisms correctly predict less conversion of coal-N into NO and persistence of HCN for higher stoichiometric ratio values, for progressively higher pressures. For atmospheric coal flames, one expects less NO from coals of lower rank but this tendency was not evident in the predictions or data for the three coals in this test series. Coals of

lower rank generate more NH_3, but this species is negligible except for intermediate stoichiometric ratio, where it is a minor intermediate. The results of the CNPP simulations are reported in Appendix B.

Based on this performance, a global NO_X production sub-model was developed to reproduce the performance of the detailed chemical reaction mechanism in interpreting the NBFZ datasets. Sensitivity studies of the CNPP simulations for Pittsburgh #8 at all three test pressures identified a global NO_X production scheme like the one in the v.6.1 FLUENT NO_X sub-model, except for two additional features: (1) The intermediate decomposition products of HCN (HCNO and amines) are explicitly represented as pseudo-HNCO; and (2) The additional concentration dependences on O_2 and NO are also explicit in the global reactions. The v.6.1 FLUENT sub-model could not interpret the NBFZ database within useful quantitative tolerances even when applied to CFD simulations that had been fit to predict all the major reaction products, and even when the NO_X sub-model parameters were freely adjusted. Predicted NO emissions were too high, because the sub-model overestimates the conversion of coal-N into NO. NEA's NO_X sub-model quantitatively depicted all the important trends with Pit. #8 over the full pressure range from 1.0 to 3.0 MPa. Flaws surfaced when the sub-model was applied to different coals without re-adjusting rate parameters, which probably reflects a generic limitation of global NO_X production sub-models for coal combustion.

Finally, the impact of pressure on NO emissions was resolved more finely in a series of CNPP simulations that imposed standardized thermal histories and extents of char burnout at all three test pressures. These results verify the apparent trend in the NO emissions with pressure from the NBFZ tests, and establish that pressure variations, alone, shift N-species conversion chemistry toward the production of N_2 at the expense of NO. The pressure dependence on NO emissions was slightly under predicted, and HCN levels were over predicted. But the satisfactory extrapolation from NBFZ test temperatures to flame temperatures represents a major hurdle that has been sustained. NEA's NO_X sub-model predicts NO emissions for broad ranges of temperature and pressure within useful quantitative tolerances.

5. Characterization of NBFZ and HPBO Chars

NFBZ and HPBO chars have been characterized to determine the key properties that are needed as sub-model inputs (swelling properties, intrinsic reactivity, char morphology and surface area). The experimental techniques used in the char characterization are described in the Appendix C together with a detailed discussion of the results.

5.1 NFBZ Chars

Based on the NBFZ char characterization, the intrinsic reactivities and total physical surfaces areas of the high-pressure p-RCFR chars are similar to those of atmospheric pressure chars in the literature database. For the two bituminous coals, however, fluidity and swelling appear to be significantly enhanced at the 10 atm and 20 atm conditions, and incorporation of swelling factors from 1.4-1.5 (compared to 1.1-1.2 under conventional

atmospheric conditions) will lead to model predictions of significantly accelerated burnout. A reasonable modeling approach at this time would be to use the existing correlations for reactivity, but for bituminous steam coals to enhance the swelling factors currently used as model inputs to 1.45. Future work should address higher-rank, low volatile bituminous coals (though these are a less important class of steam coals) and should examine the effects of heating rate, which along with pressure can also determine the swelling behavior in flames.

5.2 HPBO Chars

HPBO samples have experienced significant extents of char oxidation. Many are essentially ash samples with residual unburned carbon similar to that found in current coal-fired boiler ash samples, while others have higher carbon levels. The goal of the HPBO char characterization was to examine the morphology and porosity of these chars, or residual carbon samples, for comparison to the known properties of residual carbons from current units and laboratory reactors operating at atmospheric pressure. The detailed results are reported in Appendix C.

Overall, the HPBO chars show similar surface area to other highly reacted chars and unburned carbon samples (50-100 m2/g for bituminous coals and 200-400 m^2/gm for sub-bituminous coals). The 2 atm chars show lower surface areas for reasons that are not fully understood. In terms of morphology, the HPBO sub-bituminous chars are similar to their atmospheric pressure relatives, which is consistent with their lack of fluidity at all pressures examined. The bituminous chars from high-pressure combustion, however, are distinctly different. They contain an abundance of plate-like shards that are clearly fragments of larger particles. This structure is consistent with the predominance of low-density foam structures with ultra-thin membranes observed in the NBFZ chars. This structure with its high macroporosity and tendency to fragment will make these high-pressure chars easier to burnout that their atmospheric pressure counterparts that have been widely studied due to their relevance to current pulverized coal fired practice.

5.3 Evaluation of Power-Law Kinetics for Char Oxidation

Power-law kinetics used in CBK8 char reaction model and more complex rate laws have been evaluated to identify the best modeling approach for high pressure char oxidation. The details of this evaluation are reported in Appendix C.

Simple models of surface heterogeneity, whether intrinsic or induced, predict power-law behavior over wide ranges of partial pressure if the breadth of the activation energy distribution for adsorption and/or desorption is large. The available measurements of desorption activation energy distributions show more than enough breadth for this power-law behavior to be generally expected for non-graphitic carbons, in accordance with experimental observations.

The heterogeneous surface model of Haynes is a promising framework for describing the major features in the low-temperature carbon oxidation database. The Haynes model with

minor perturbations to the original parameters determined experimentally for spherocarb is capable of describing the rates, reaction orders, and pressure dependence of reaction order for several literature datasets on polymer and coal chars, along with the known existence of stable oxide. The Haynes model is also capable of predicting the lower orders and the gradual change in reaction order with pressure for graphitized carbon black, a behavior that is intermediate between power-law and Langmuirian kinetics. The model predicts these features as the direct consequence of the narrower distribution of site energies for the more homogeneous highly annealed carbon forms.

5.4 Char Combustion Modeling

Although the available data on high-pressure combustion is still quite limited, the experimental and theoretical results described in this report provide a useful basis for making estimates that extend present models of char combustion to high pressure. Intrinsic reactivity is affected little by the formation of chars under pressure and existing data and correlations should be used unless and until more extensive data becomes available. Swelling factors are important parameters in char burnout, and there is evidence in this study that bituminous coals swell markedly more at elevated pressure. It is recommended to increase swelling factors for high-volatile bituminous coals from the values used in current codes (1.0-1.2) to the range 1.4-1.5 to model high-pressure char combustion and burnout. No change is recommended for low-rank coals (sub-bituminous and lignite) and more data is needed to make an assessment for the fluid, medium, and low-volatile coals.

Because of the enhanced swelling of bituminous coals, it is possible that particle fragmentation will be more extensive at pressure leading to accelerated burnout and to finer ash distributions. The data in the present project suggests this trend but does not provide sufficient quantitative data to allow the postulation of a model. Most atmospheric pulverized-coal combustion models do not currently consider fragmentation when attempting to predict carbon burnout.

Finally the surface areas of the highly reacted chars from high-pressure operation are similar to those from atmospheric pulverized-coal combustion, so it can be expected that their activity toward concrete surfactants will be similar. Thus the ash utilization problems associated with unburned carbon from pressurized operation may be similar to those from current units achieving the same overall burnout or loss-on-ignition values. Since particle size also plays a role in surfactant uptake, it is possible that unburned carbon from high-pressure operation will show somewhat elevated activities if higher extents of fragmentation are realized in the large scale systems.

The theoretical work in the previous section provides badly needed fundamental scientific underpinning for the power-law kinetic form. Although more work is needed to extend this analysis to high temperature, the work to date suggests that the power-law form in CBK8 with its intrinsic reaction order of 0.5 is a reasonable approach for near term applications. Based on the current state of understanding, there is insufficient data to justify the additional complexity of the three-step rate form incorporated in CBK/E.

6. Simulation of HPBO Tests

SRI's HPBO database covers the last quarter of coal burnout for three coals at pressures from 0.2 to 3.0 MPa. Tests with Illinois #6 and Wyodak PRB imposed similar inlet conditions to the corresponding NBFZ runs, which enabled in-furnace operating conditions to be assigned from previous CFD simulations. Nearly the entire database with Illinois #6 and PRB were interpreted this way, but only half the Pittsburgh #8 data could be analyzed, because many runs had much higher suspension loadings than in any of the NBFZ tests with this coal.

Where possible, histories of gas and wall temperature and O_2 partial pressure throughout the furnace were assigned from the NBFZ simulations, or else they were re-scaled for different inlet O_2 concentrations and pressures. The assigned O_2 consumption in simultaneous volatiles combustion and char oxidation within the radiant furnace section decreased for progressively higher pressures. Estimated gas temperatures within the radiant section were much hotter than the 1400°C isothermal sections downstream for 0.2 and 1.0 MPa, but not for the higher test pressures, which reflects higher sensible enthalpy requirements at elevated pressure.

All qualified HPBO datasets were interpreted with CBK/E simulations based on the initial char reactivities assigned in previous interpretations of the NBFZ datasets. Hence, no model parameters were tuned to improve the quantitative agreement in the HPBO evaluations. The simulation results are reported in details in Appendix C.

The data for Pittsburgh #8 cover the broadest range of coal burnout, for which the predictions are uniformly accurate throughout. The extents of burnout for the Illinois #6 were over predicted by up to 7% for extents of burnout under 90%, but there are only two measured values in this range. The worst performance was for PRB for extents of burnout under 90%, which is not surprising because no NBFZ CFD simulations were available for either pressure in these HPBO tests. Even so, the predictions for the last 10% of coal conversion are reasonably accurate for PRB and for both other coals.

Each predicted particle thermal history exhibits two initial surges before it relaxes to an ultimate temperature of 1400°C: one due to ignition under the very high inlet O_2 concentrations and another due to the increasing gas temperatures in the radiant section. The second surge dissipates as soon as the char burning rate relaxes to some saturation limit for each of the different pressures, around the time where the extent of char burnout approaches 80 % for the higher test pressures. This near-extinction phenomenon is associated with a transition in the burning mechanism, either back to kinetic control or to ash layer transport control during the latest stages.

The predicted char burnout histories exhibit a complex dependence on pressure because the inlet O_2 mass fractions for 2.0 and 3.0 MPa were significantly lower than for the lower test pressures. For the same inlet O_2 concentration, chars burned out much faster at higher pressure, because the O_2 partial pressure was higher. The trend was apparent in the predictions for pressures from 0.2 to 2.0 MPa with Pittsburgh #8. But at 3.0 MPa, the

increase in pressure was almost compensated for by the reduction in inlet O_2 mass fraction. Chars burned slower at 3.0 MPa because the gas temperatures, and hence particle temperatures, were cooler throughout.

To assist in the interpretation of char characterization data from the HPBO tests, the maximum predicted char particle temperatures were compiled and found to vary with pressure as well as inlet O_2 level. The maximum is hotter at 1.0 MPa despite hotter gas temperatures at 0.2 MPa because the O_2 partial pressure is much higher. But for higher pressures, the cooler gas temperatures partially compensate for the higher O_2 pressures. For similar operating conditions, PRB generates the hottest chars because it burns fastest, followed by the next-fastest burning char, Illinois #6, followed by Pittsburgh #8.

7. Flyash and Fumes Formation

Ash particles formed during combustion are derived from the inorganic minerals in the coal. Such minerals can be present either as excluded minerals (discrete minerals separate from the coal's carbonaceous material) or included minerals that are associated with the organic portion of the coal (Benson et al., 1993, Rusell et al., 2002, Yan et al., 2002). Because of this association with the coal, during the exothermic process of char oxidation, included minerals will reach higher temperatures compared to excluded minerals (Benson et al., 1993), and thus contribute differently to the resulting ash formed from combustion.

During char combustion, the two types of minerals identified above will undergo different pathways leading to ash formation. Excluded minerals may fragment or melt, with the extent of each process depending on their composition and the local gas temperature (Tomeczek and Palugniok, 2002). Included minerals may also fragment or melt, but an important distinction is that Included minerals can coalesce when brought into contact with other minerals in the char if conditions are favorable, thus altering both the size and the chemical composition of individual ash particles. Excluded minerals will not coalesce with other minerals during combustion. The basis for the ash particle formation model was a model developed under prior DOE funding by Physical Sciences Inc.

7.1 Preliminary Ash Formation Modeling Calculation

The ash particle formation model requires as an input mineral size and composition data from computer controlled scanning electron microscopy (CCSEM) for the minerals present in the coal. Basic coal property data (ultimate and proximate analyses) are also required. The basic model then follows the processes outlined in the PSI model; char is allowed to react, and as the carbon is removed, minerals coalesce when they come in contact with one another. Excluded minerals, which are identified in CCSEM analysis and then binned separately, are not permitted to coalesce. The model was then used first to systematically address the effects of excluded minerals on ash particle size and composition distributions as described in Appendix D.

These results showed the importance of approaching ash formation through different pathways of formation for different types of minerals: excluded and included minerals. As the amount of excluded mineral matter increased, an increase in the amount of the smallest ash particles was observed. This was attributed to a decrease in the extent of coalescence of the smallest included minerals. As excluded mineral matter amounts increased, larger concentrations of silicates, and potassium and iron aluminosilicates were observed as a result of their lack of transformation ("dilution") into aluminosilicate particles.

In order to account for the broader coal particle size distribution used in the experimental tasks of this project, preliminary calculation of the effect of differences on coal particle size distribution on the fly ash composition and size distributions was conducted. Following the idea to evaluate the effect of different coal size distributions on the calculated fly ash particle composition and size distributions, another parametric study allowing for different but narrow coal particle size ranges was conducted. The results are reported in Appendix D.

As the results of these calculations indicate, there were no major differences in the ash particle composition distribution resulting from changes in coal particle size among the 76/108, 76/92 and 92/108 μm size distributions.

7.2 CCSEM Analysis of Coals

In order to obtain the necessary input information for the ash particle formation model, Computer Controlled Scanning Electron Microscopy (CCSEM) was conducted for the three studied coals to obtain mineralogical information. Analyses were conducted on a purchase order basis by an external laboratory associated with the University of North Dakota Energy and Environmental Research Center. The results of the CCSEM are reported in Appendix D.

In summary, the CCSEM analysis appears to have provided a good indication of the presence of non-iron minerals but is biased in this case toward iron such that higher iron contents than expected, and higher pyrrhotite contents, are obtained.
As excluded and included minerals may follow different ash formation pathwyas, an analysis of the different mineral types considering particle size and composition distributions was done, based on the CCSEM results.

7.3 Char Characterization (Near-burner Flame Zone Experiments)

In order to obtain the parameters needed for the modeling prediction of ash formation from included minerals, characterization of pyrolyzed char samples obtained from near-burner flame zone experiments (NBFZ) conducted at SRI was undertaken. The main parameters needed for this purpose were morphology parameters including wall thickness, swelling properties and porosity. The samples chosen for this characterization were obtained under combustion conditions with a stoichiometric ratio close to 1.1 and an

oxygen/coal ratio close to 200%. The results of the NBFZ char characterization are reported in Appendix D.

Pressure significantly influences the formation of char particles during pulverized coal combustion. For Pittsburgh #8 coal and the pressure range considered, a maximum in the formation of cenospheric char particles occurred at 10 atm. For the high vitrinite content coal examined, pressures up to 20 atm did not change the amount of cenospheric char particles formed significantly. A correlation based on the operating pressure and the vitrinite content of the parent coal, which will be helpful in estimating the amount of cenospheric chars, was then proposed. This correlation works up to 30 atm pressure and was based on the data of three bituminous coals available from a previous study as well as this present study.

This correlation is the first approach in order to model the effects of pressure on ash formation mechanisms. Each type of char evolves differently, resulting in different sizes of ash particles. Solid char particles favor the coalescence of included mineral, while cenospheric char chars favor the formation of finer ash particles.

7.3.1. Mercury Porosimetry Analysis

Char porosity is also an important parameter in understanding ash formation under pressurized conditions. Mercury porosimetry analyses of selected NBFZ char samples were conducted. The results are reported in Appendix D.

Macroporosity (300-5000 nm assumed) in the two types of coals analyzed increases with increasing operating pressure. This increase is significant when compared to the parent coal macroporosity for Pittsburgh #8 (3.43% porosity at 30 atm. v. 0.89% porosity for the parent coal). Assuming that the microporous region consists of pores between 5 and 30 nm, porosimetry suggests that this region only exists for the parent coal. It must be noted that the total porosity does not change significantly with pressure.

Macroporosity increases as a result of pyrolysis. For the bituminous coal, a maximum is reached at 30 atm operating pressure. For the subbituminous coal, a maximum is reached at 10 atm. This behavior agrees with results found by Tomezcek and Gil, 1997 and it can be explained as the parental coal microporosity being reduced by pyrolysis, with these pores increasing in size, leading to enhancing the macroporosity.

7.4 Ash Characterization (HPBO experiments)

Scanning Electron Microscopy of SRI high pressure burnout experiments (HPBO) samples generated with argon as a carrier gas was performed to determine characteristics of the char particles and to ascertain if complete burnout was reached at operating conditions.

Computer Controlled Scanning Electron Microscopy analysis was done for selected HPBO samples from Pittsburgh #8. Based on the ash particle size data that were collected

and analyzed, it was concluded that the ash formation mechanism that most affects ash size and composition distributions under elevated pressure conditions is char fragmentation. Char fragmentation is the key factor in the formation of fine ash particles (<20 μm), and it is found to occur at early stages during combustion. This agrees with the conclusions of Wu et al. 2000 as a proposed mechanism for ash formation at earlier and middle stages of burnout.

7.4.1. Analysis of Mercury Retention in Solid Residue

Mercury retention levels on char (expressed as a weight percentage of the total Hg in the system) have been measured for tests with Pit. #8. The Hg-retention level were higher for the HPBO tests than for NBFZ tests at the same pressure. The primary cause of lower Hg retentions in the NBFZ data is thought to be the much greater soot yields in these tests. Due to the small size of soot agglomerates, soot is expected to effectively compete for Hg vapor with the much larger char particles, so measured char-Hg levels are lower for progressively higher soot loadings. Contributing to the analysis of mercury retention for Pittsburgh #8 in solid residue, analysis of the BET surface measurements provided by Brown University was done. The results of the Hg-retention level are reported in the Appendix.

7.5 Ash Formation Model

The starting point for the ash formation model was a modified version of the Engineering Model for Ash Formation (EMAF) developed at Physical Sciences Inc. under Department of Energy funding in earlier programs. EMAF predicts the size and composition of fly ash generated during combustion under fuel lean conditions, but was not developed to consider high pressure conditions.

The modified model requires the particle size distribution for the coal and the minerals, coal proximate and ultimate analysis, mineral composition, combustion stoichiometric ratio, gas and particle temperature, pressure and oxygen concentration as input data. Necessary mineral information can be derived from CCSEM coal and mineral characterizations and include the size and composition distributions of the minerals.

Given the different ways that included and excluded minerals evolve in the formation of ash, the first part of the modified algorithm included the option for inputs of different information for the particle size distribution and composition of excluded and included minerals. If the specific information for both excluded and included minerals, is not available, the existing algorithm utilizes a random Monte Carlo distribution for the different minerals.

A significant contribution from this study is the correlation of bituminous coals with the included mineral transformational pathway. Determined by a parent coal property (vitrinite content, %) and operation conditions, a percentage number can be calculated to predict the char morphology or structure type distribution. Different char types, either cenospheric or solid, follow different ash formation pathways. For cenospheric chars, char fragmentation is the most important pathway to consider, and leads to formation of a finer ash particle size distribution. For the solid type of char, coalescence of included

minerals attached to the char will be the dominant pathway to form ash particles in the medium and larger size ranges.

The data provided by the model are useful for calculating the ash particle size and composition distributions needed for further applications in modeling potential deposition in boilers and designing efficient particulate emission controls

8. Deployment of Sub-Models in Design Codes

8.1 Deployment of PC Coal Lab in Aspen Plus

PC Coal Lab was deployed as a USER Block in Aspen Plus. The implementation of PC Coal Lab in Aspen Plus was carried out with the following two objectives:

- The use of PC Coal Lab as a stand-alone block from Aspen Plus.
- The use of PC Coal Lab as an integrated block in Aspen Plus.

The details of the installation procedure and the use of the PC Coal Lab module in Aspen Plus are reported in Appendix E.

8.2 Sub-Models Incorporated in Aspen Plus

The sub-models being developed under the "High Pressure Coal Combustion Kinetics" project were supposed to be implemented in Aspen Plus. In particular, the sub-models included the Char Burnout Kinetics (CBK) sub-model from Brown University and the Ash Transformation sub-model from UConn. After extensive discussion within the project team, it was mutually agreed that the Char Burnout Kinetics sub-model, being a single particle model, was not appropriate to be implemented in Aspen Plus. With the approval of DOE, it was decided that these sub-models were not to be implemented in Aspen Plus. Instead, the Aspen-FLUENT coupling/integrator, newly developed by Fluent Inc. under a separate DOE project, was tested as will be discussed further in the report.

8.3 Coupling PC Coal and FLUENT

The objective of the PC Coal-FLUENT coupling was to specify all CFD input related to devolatilization from PC Coal Lab®, including the total weight loss, a global devolatilization rate, the elemental compositions of char and volatiles, the heat of volatiles combustion, and the volatile-N expressed as a percentage of the coal-N.

Preliminary CFD runs are used to specify a particle size distribution, the standard coal properties, and a particle thermal history. A user defined function was developed in FLUENT to generate an input files containing this information. A PC coal interface to FLUENT was developed to read and process the FLUENT input file, execute the PC Coal Lab simulation, retrieve the results and prepare a one-page output report. The

FLUENT user then manually enters the input parameters into the FLUENT case file. The development and performance of the interface are described in Appendix E.

8.4 Sub-Models Incorporated into FLUENT

The original plan to develop a stream-lined version of Char burnout Kinetics (CBK) for deployment in FLUENT was reviewed in favor of full implementation. The CBK8

model had been implemented into FLUENT. The model includes effects of thermal annealing and ash inhibition on the char combustion. In the Appendix are reported detailed of the model and its implementation into FLUENT.

9. Process Design Analysis

The Vision 21 program is a strategic plan for the development of advanced fossil fuel-based technologies for the production of electricity, liquid transportation fuels and high-value chemicals. The conceptual design of the integrated Vision 21 power plant is reported in the next section together with the results of the system analysis using the Aspen Plus code and a conceptual design and CFD analysis of the pressurized pulverized coal combustor (PPCC).

9.1 Vision 21 System Specification

Foster Wheeler's (FWDC) Vision 21 plant configuration is shown in Figure 1 and it includes a Partial Gasification Module (PGM) and a PPCC module.

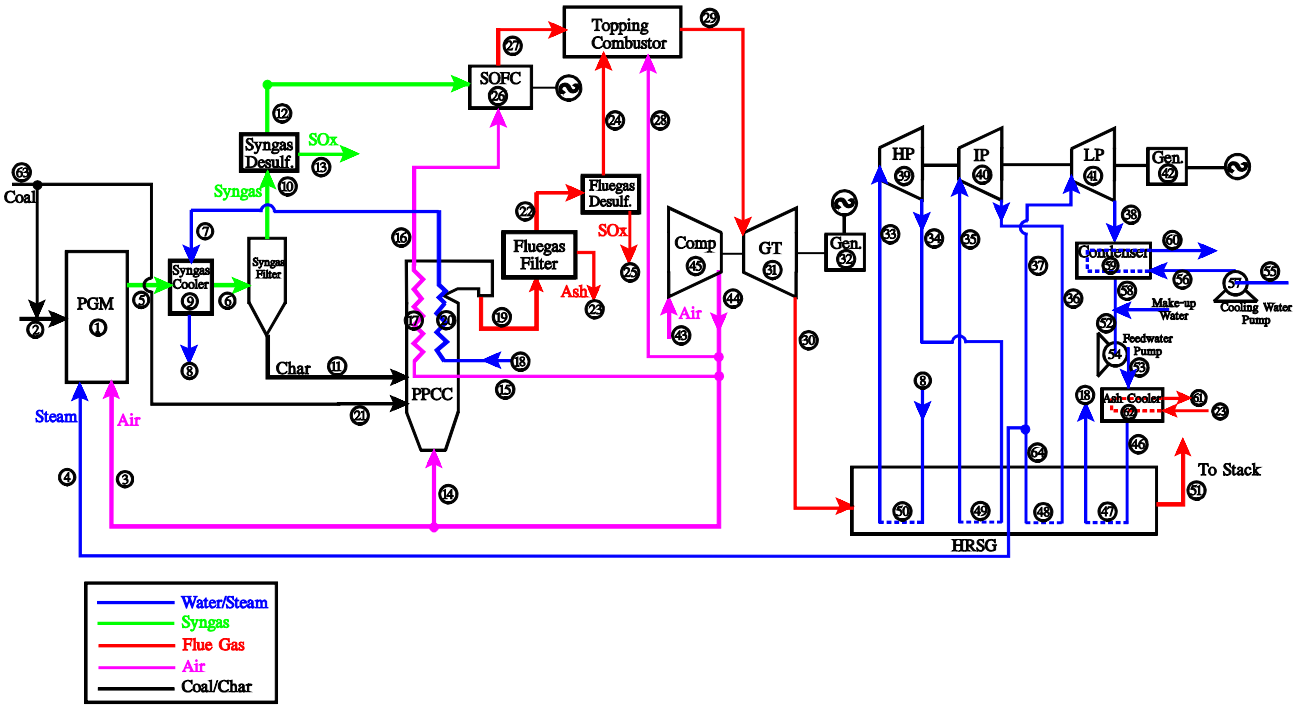

Figure 1 Vision 21 Plant Layout with PPCC

This specific design has been modeled using the Aspen Plus computer code. According to the Aspen Plus calculations, this process satisfies all of the following specific performance targets of the Vision 21 program:

- Net efficiency (electrical generation) greater than 60% with coal (on HHV basis).
- Near zero emissions of smog and acid rain forming species.
- Greater than 40% reductions in CO_2 emissions by efficiency improvement; 100% reduction with sequestration.

In addition to these specific targets, other characteristics of this Vision 21 plant configuration are as follows:

- Conversion of the energy from coal to electricity or production of liquid transportation fuels from coal if the syngas from PGM is further processed.
- Generation of greater than 30 MWe or equivalent energy output if other products are produced.
- Use of fossil-fuel-based feedstocks, either alone or in combination with biomass and/or other opportunity fuels. The alternative fuels can be fired either in the PGM or the PPCC.
- Emphasis on market flexibility, including multiple feedstocks and products.
- Ability to concentrate CO_2 stream for sequestration purposes if the air is replaced by oxygen gas as the oxidizer.

9.1.1. Description of Vision 21 Plant Layout

The integrated power plant consists mainly of a partial gasification module (PGM), a pressurized pulverized coal and char combustor with steam generation and high-temperature air heating (PPCC), a solid oxide fuel cell (SOFC) unit, a topping combustor, an air compressor, an advanced gas turbine, a supercritical steam turbine, and a heat recovery steam generator (HRSG). The plant uses coal as the only fuel, air as the oxidizer, and steam as reactant for gasification. The details of the plant are discussed in Appendix E together with the results of the system analysis
An Aspen Plus flow sheet model was set up and the system analysis and optimization on the conceptual plant were performed. The key analysis results for the system and its components are summarized below.

<u>PGM</u>
Operating Temperature = 1800^{o}F (982^{o}C)
Operating Pressure = 500 psia (3.45 MPa)

<u>Syngas Cooler</u>
Inlet/Outlet Syngas Temperature = 1800^{o}F/1200 ^{o}F (982^{o}C/649^{o}C)
Thermal Duty = 275 MM Btu/hr (80.6 MW)

PPCC
Inlet/Outlet Preheat Air Temperature = 987°F/1509 °F (531°C/821°C)
Inlet/Outlet Steam Temperature = 717°F/982 °F (381°C/528°C)
Thermal Duty = 785 MM Btu/hr (230 MW)

SOFC
Operating Temperature = 2000°F (1093°C)
Electricity Generation = 159.8 MW

TC/GT
Combustion Temperature = 3000°F (1649°C)
Outlet Flue Gas Temperature = 260°F (127°C)
Electricity Generation = 621.2 MW

HRSG/ST
ST Steam Inlet Conditions = 6500 psia/1300°F/1300°F/1300°F
(44.8 MPa/704°C/704°C/704°C)

HRSG Thermal Duty = 1351 MM Btu/hr (396 MW)
Electricity Generation = 283.7 MW

Overall Cycle
Gross Electricity Generation = 915.9 MW
Net Electricity Generation = 796 MW
Net Plant Efficiency = 61.9%

As presented above, an overall plant efficiency of 61.9% can be achieved for the conceptual plant if the advancements can be made on some key components such as SOFC, ATS (advanced gas turbine system), barrier filters and supercritical steam turbines. Operating parameters of individual components and detailed stream properties from the Aspen simulation are presented in the Appendix and can be used as the basis for the development of those advanced components.

9.2 FLUENT-Aspen Coupled Simulation

The FLUENT-Aspen controller was tested simulating the vision 21 conceptual power plant design proposed by Foster Wheeler. The FLUENT-Aspen Controller is a Cape-Open add-in that allows run-time interaction between Aspen Plus and FLUENT. It is a promising software and its use has been demonstrated in a number of applications including pulverized fuel based power plants and fuel cells. The FLUENT and Aspen simulation have been modified to run the coupled simulation (detailed are reported in Appendix E). Several issues have been encountered while setting up and running this simulation and the simulation was not completed by the end of the project. A useful feedback has been provided to the developers containing suggestion on improving the code, the documentation and usability of the controller.

9.3 PPCC Performance Description

The PPCC technology has been identified as an enabling technology within the Vision 21 advanced combustion systems program. The PC combustor designed herein performs both steam generation and air heating duties.
The solid char that is generated in the PGM gasifier is fired in the pressurized PC combustion furnace. Hot char enters the furnace at 1200°F (649°C) after being cooled in a syngas/char cooler. To aid in combustion initiation and stabilization, 10% of the raw coal fed to the plant is burned with the char in the furnace to achieve a high char burnout. Air pressurized to 450 psia (3.10 MPa) and 1006°F (541°C) is introduced into the furnace as the fuel oxidizer. Flue gas containing 3.0% O_2 exits the PPCC at 1300°F (704°C) and is sent to a filter where the fly ash is separated from the gas.

High-pressure supercritical water flowing at 1.22 MM lb/hr (154 kg/sec) enters the furnace waterwalls (from the HRSG economizer) at 6850 psia (47.2 MPa) and 717°F (381°C) and exits at 982°F (528°C) to the syngas/char cooler. Air flowing at 1.09 MM lb/hr (137 kg/sec) from the gas turbine air compressor at 430 psia (2.96 MPa) is heated in the PPCC from 987°F (531°C) to 1509°F (821°C) and is sent to the fuel cell. The thermal duty of the furnace is 785 MM Btu/hr (230 MW) consisting of 154 MM Btu/hr (45 MW) of air heating and 631 MM Btu/hr (185 MW) of water/steam heating.

Several PPCC designs were evaluated using FLUENT CFD modeling. Initial designs were based on Foster Wheeler furnace and burner design guidelines (for atmospheric PC boilers) and on past FW CFD modeling experience. Each subsequent PPCC design was improved based upon the lessons learned from the modeling of the previous PPCC FLUENT modeling (these initial designs are documented in Appendix E).

The final design is a cylindrical furnace with a down-firing burner. In the previous designs, the furnace was rectangular in shape and required a large cylindrical pressure vessel. In the new design the pressure vessel and the waterwalls are combined to make a more compact simpler design. Furnace volume and residence time is similar to the previous rectangular design, but flame shape and stability are improved due to firing axially rather than wall-firing across a short depth.

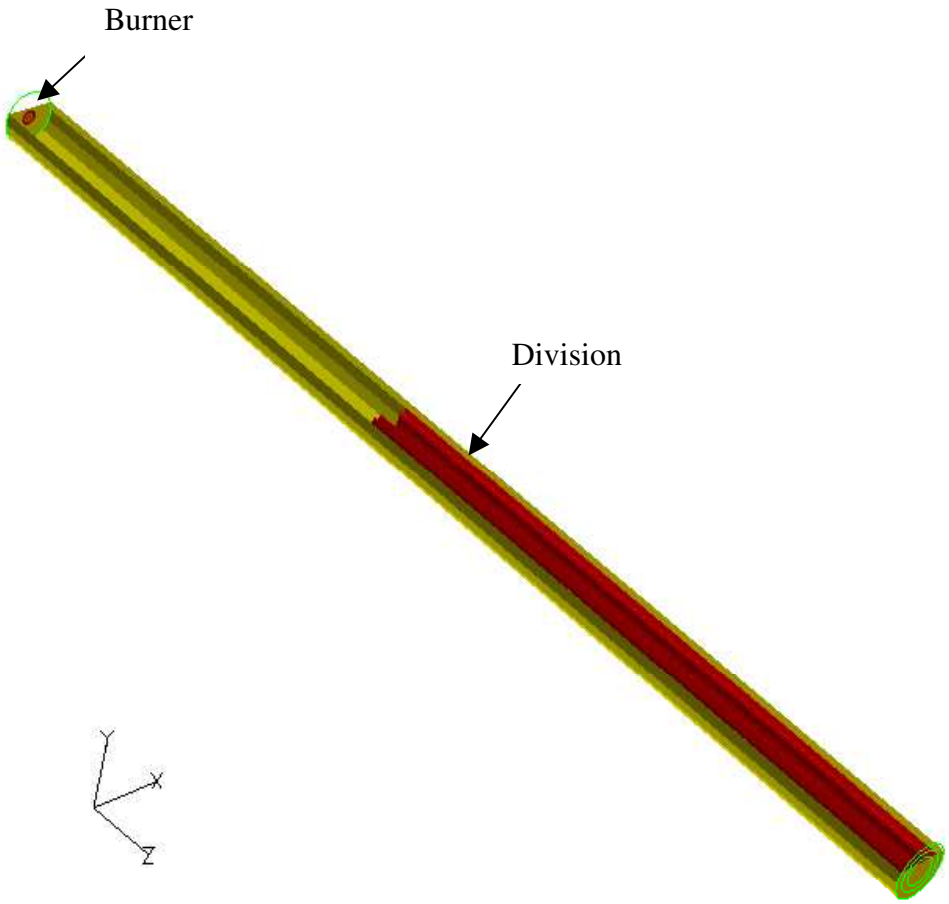

Figure 2. PPCC Furnace Model: Final Model

The PPCC furnace is a 167' (50.9 m) long, 7.5' (22.9 m) diameter cylindrical vessel with a single down-firing burner. To reduce NOx formation, the burner separates the secondary air into two zones: a low velocity inner zone and a high velocity swirled outer zone. Over-fire air ports are provided for combustion staging to further reduce NOx production. To simplify the modeling and improve convergence, OFA ports are modeled as a continuous ring on the vessel outer wall. Two cylindrical division walls are included in the furnace to achieve the required heat transfer absorbance. The model contains 33,120 cells and is shown in Figure 2.

The following fluent sub-models were utilized in the fluent simulation

Turbulence: standard two-equation k-ε model.
Radiation: discrete ordinates model

Species Transport: eddy dissipation with volumetric reactions
Gaseous radiation emissivity: domain based
Char devolatilization: two competing rates
Char oxidation: CBK-8 model
NOx: UDF from NEA (fuel NOx)

Boundary conditions are based on the Vision 21 Plant Concept Specification. The input data required by FLUENT include fuel analysis, coal/char particle size distribution, waterwall temperatures, and the velocities, flow rates and temperatures of primary and secondary air streams. Boundary conditions are detailed in Table 1

Table 1. PPCC Boundary Conditions: Final Model

Coal		asr	dry	daf	Size		
Ultimate Analysis					Distribution		
Ash	%	10.58%	10.74%		7.0 micron	%	57.2
S	%	1.49%	1.51%	1.69%	32.5 micron	%	22.2
H	%	5.14%	5.22%	5.85%	70.2 micron	%	12.6
C	%	74.75%	75.89%	85.02%	121.2 micron	%	4.4
H2O	%	1.50%			175.3 micron	%	3.6
N	%	1.63%	1.65%	1.85%	Total	%	100.0
O	%	4.91%	4.98%	5.58%			
Total	%	100.00%	100.00%	100.00%	< 200 Mesh	%	87.33
					< 50 Mesh	%	99.50
Volatile Matter	%	33.33%	33.84%	37.91%			
HHV, as received	Btu/lb	13,742	13,951	15,630			

	lb/hr	F
Coal Flow	32,000	
Moisture in Coal	522	
Dry Coal Flow	31,478	60
Char Flow	31,500	1200
Ash Flow	30,410	1200

TCA	lb/hr	806,688
Excess O2	%	16.5
OFA	%	25.0

	Flow Rate		Temperature	Density	Inner Diam.	Outer Diam.	Area per Port	No. of Ports	Axial Velocity	Tan./Axial	Solids Flow
	lb/hr	%	F	lb/ft3	in	in	ft2		ft/sec	Velocity	lb/hr
Primary	201,672	25.0	200	1.849	3.000	8.700	0.364	1	83.3	0.00	93,910
Outer Secondary Air	342,842	42.5	1100	0.782	15.600	22.600	1.458	1	83.5	0.40	
Inner Secondary Air	60,502	7.5	1100	0.782	8.700	15.600	0.914	1	23.5		
OFA	201,672	25.0	1100	0.782			0.384	1	186.5	0.00	
	806,688	100.0									93,910

The waterwalls of the furnace are assumed to be gray and diffusive. A uniform emissivity of 0.7 was applied to the walls. Average wall temperature was assumed to be 1000ºF (538ºC).

The coal devolatilization kinetic properties were obtained from NEA for Pittsburgh #8 and 30 atm. as follows:

y1= 0.38; A1= 1.4e05; E1= 17.6 kcal/mole
y2= 1.00; A2= 3.2e06; E2= 30.0 kcal/mole

The default FLUENT Pittsburgh #8 CBK parameters were applied for char oxidation. Volatile reaction stoichiometric coefficients were calculated from coal ultimate and proximate analysis by a scheme developed by FLUENT (see Appendix E for details).

9.3.1. Furnace Modeling Results

A summary of the FLUENT results is shown in Table 2.

Table 2 – Summary of FLUENT Results: Final Model

Results at Outlet		Fluent	ASPEN
Burnout	%	98.4	99.5
FEGT	F	1936	1905
Heat absorption	MM Btu/hr	632	631
NOx	ppm	373	
O2	%	3.29	3.00

The ASPEN column specifies the results of the system analysis, which are approximate design requirements. The predicted heat absorption of the design predicted by FLUENT is 632 MM Btu/hr (185.2 MW), which exceeds the 631 MM Btu/hr (184.9 MW) requirement. This heat transfer is based on a conservative particle emissivity of 0.15. Since the actual particle emissivity is expected to be 0.5 or greater, the actual heat transfer is expected to be greater than 632 MM Btu/hr (185.2 MW).
The detailed results of the final furnace modeling are reported in Appendix E.

9.4 Benefits and Feasibility

The pressurized pulverized coal combustor is a key component of the high-efficiency combined cycle plant. Operating the combustor at high pressure allows the furnace outlet to be expanded through a gas turbine and to maximize the system efficiency. Conventional coal-fired power plants with only a steam cycle are limited to an efficiency of about 40%, whereas efficiencies of over 60% can be achieved in combined cycle technology.

Pressurized combustion has been applied in large-scale commercial combined cycle power plants utilizing pressurized fluidized and bubbling bed combustors in worldwide operation for the past 15 years.

A 1 MW pressurized pulverized coal test facility has been operating in Germany for 15 years at a pressure of 18 bar and a furnace temperature up to 1750°C. This test furnace is similar to the final design of the PPCC furnace in that it uses a cylindrical vessel with a single down-fired burner.

The main challenges in the PPCC design are material selection in the furnace where the heat flux is about three times higher than conventional furnaces and material selection in the air heater due to the high air temperature and relatively low gas-to-gas heat transfer coefficient.

10. References

Bailey JG, Tate A, Diessel CFK, Wall TF. (1990). *Fuel*, 69; 225-239.

Benedetto, D., S. Pasini, M. Falcitelli, C. La Marca, and L. Tognotti (2000). "NO_X emission prediction from 3-D complete modeling to reactor network analysis." *Combust. Sci. and Technol.* 153: 279-294.

Benfell KE. Assessment of char morphology in high pressure pyrolysis and combustion. PhD thesis, Department of Geology, The University of Newcastle, NSW, Australia, 2001.

Benson, S. Jones, M. Harb, J. (1993). In Fundamentals of coal combustion: for clean and efficient use. Elsevier.

Brunauer, S., *The Adsorption of Gases and Vapors*, Vol 1, Princeton University Press, Princeton, NJ, 1945.

Charon, O. Sarofim, A. Beer, J. (1990). Distribution of mineral matter in pulverized coal. Prog. Energy Combust. Sci., 16; 319-326.

S.G. Chen, R.T. Yang, F. Kapteijn, J.A. Moulijn, *Ind. Eng. Chem. Res.* 32 (1993) 2835-2840.

Chen, J. C., and Niksa, S., "A radiant flow reactor for high-temperature reactivity studies of pulverized solids", *Rev. Sci. Instrum.*, 63, 2073 (1992)

Cho, S., "Experimental and numerical study on combustion of secondary pyrolysis products from various coals". PhD Dissertation, Stanford University, CA (1993)

Cor, J., N. Manton, G. Mul, D. Eckstrom, W. Olson, and R. Malhotra, "An Experimental Facility for the Study of Coal Pyrolysis at 10 Atmospheres," Energy and Fuels, 14, 692-700, 2000.

De Soete, C. G., (1975). "Overall Reaction Rates of NO and N_2 Formation from Fuel Nitrogen." *Proceedings of the Combustion Institute*, 15: 1093.

Z. Du, A.F. Sarofim, J.P. Longwell, *Energy and Fuels*, 4 (1990) 296-302

Falcitelli, M., L. Tognotti, and S. Pasini (2002). "An algorithm for extracting chemical reaction network network models from CFD simulation of industrial combustion systems." *Combust. Sci. and Technol.* 174(11-12): 27-42.

Froberg, R.W., Essenhigh, R., *Proc. Comb. Inst.* 17 (1979) 179-187.

Glarborg, P., Alzueta, M. U., Dam-Johansen, K., and Miller, J. A. (1998), "Kinetic modeling of hydrocarbon/nitric oxide interactions in a flow reactor." Combust. Flame, 115:1-27.

Gupta, R. Wall, T. Kajifaya, I. Miyamae, S. Tsumita, Y. (1998). *Prog. Energy Combust. Sci*., 24; 523-543.

B.S. Haynes, *Combust. Flame* 126 (2001) 1421-1432.

B.S. Haynes, T.G. Newbury, *Proc. Combust. Inst.* 28 (2000) 2197-2203.

W.C. Hecker P.M. Madsen, M.R. Sherman, J.W. Allen, R.J. Sawaya, T.H. Fletcher, *Energy and Fuels*, 17(2) (2003) 427-432.

Hong J-H, Modeling char oxidation as a function of pressure using an intrinsic Langmuir rate equation. PhD Dissertation, Department of Chemical Engineering, Brigham Young University, Utah, 2000.

Hurt, RH, Haynes, BS., On the origin of power-law kinetics in carbon oxidation, Proceedings of the Combustion Institute, Vol. 30, 2005, in press.

Hurt, R. H., J.-K. Sun, and M. Lunden (1997), "A Kinetic Model of Carbon Burnout in Pulverized Coal Combustion." *Combust. Flame* 113(1/2): 181.

Hurt RH and Calo JM. Semi-global intrinsic kinetics for char combustion modeling. Combust. Flame 2001; 125:1138-1149.
Hurt RH, Lunden MM, Brehob EG, and Maloney DJ. Statistical kinetics for pulverized coal combustion. Proc. Combust. Inst. 1996; 26:3169.
Külaots, I., *Structure, properties and surfactant adsorption behavior of fly ash carbon*, PhD Thesis, Brown University 2001
Lang, T., Hurt RH, Char combustion reactivities for a suite of diverse solid fuels and char-forming organic model compounds, Proceeding of the Combustion Institute, 2002; 29:423-431.
Lau, C.-W., and Niksa, S., "The impact of soot on the combustion characteristics of particles of different coal types", *Combustion and Flame*, 95, 1-21 (1993)
A. E. Lear, Ph.D. Thesis, Department of Chemical Engineering, University of Sydney, 1992.
Lee CW, Scaroni AW and Jenkins RG, Effect of pressure on the devolatilization and swelling behavior of a softening coal during rapid heating, Fuel, 1991;70:957-965.
Lee CW, Jenkins RG, Schobert HH, Structure and reactivity of char from elevated pressure pyrolysis of Illinois No. 6 bituminous coal, Energy and Fuels, 1992; 6: 40-47.
J. M. Levy, L. K. Chen, A. F. Sarofim, and J. M. Beer. "NO/Char Reactions at Pulverized Coal Flame Conditions." *Proceedings of the Combustion Institute,* 18: 111.
Y.-L. Liu, J. Cor, D. Eckstrom, R. Malhotra, S. Niksa, "The Impact of Pressure Variations on Coal Devolatilization Products, Part 1. Detailed Product Distributions from 0.1 MPa," Energy & Fuels, 18, 508 (2004).
M.C. Ma, B.S. Haynes, *Proc. Combust. Inst.* 26 (1996) 3119-3125.
P.M. Madsen, T.H. Fletcher, W.C. Hecker, *ACS Division of Fuel Chemistry Preprints*, 1, (2001) 318-320.
Manton, N., J. Cor, G. Mul, D. Eckstrom, R. Malhotra, S. Niksa, "The Impact of Pressure Variations on Coal Devolatilization Products, Part 2. Detailed Product Distributions from 1.0 MPa," Energy & Fuels, 18, 520 (2004).
R.I. Masel, *Principles of Adsorption and Reaction on Solid Surfaces,* (1996) J. Wiley and Sons., New York.
McLenan, A. Bryant, G. Stanmore, B. and Wall, T. (2000). *Energy & Fuels,* 14; 150-159.
Mitchell, R. E., Hurt, R. H., Baxter, L. L. and Hardesty, D. R., "Compilation of Sandia coal char combustion data and kinetic analysis", Milestone Report, SAN92-8208, Sandia National Laboratory, CA, USA (1995)
Niksa, S., Liu, G.-S., Hurt, R. "Coal conversion submodels for design applications at elevated pressures". Prog. Energy Combust. Sci. 2003, 29: 425-477.
Niksa, S., "Predicting the devolatilization behavior of any coal from its ultimate analysis". *Combust. Flame*. 100, 384-394 (1995)
Niksa, S., Cho, S. "Assigning meaningful stoichiometric ratios for pulverized coal flames". *Proc. Comb. Inst.* 27, 2905-2913 (1998)
Niksa, S., Liu, G., Bush, P.V., and Boylan, D.M. (2003). "Predicting the Emissions from Biomass Cofiring." The 28th International Technical Conference on Coal Utilization & Fuel Systems, March 10 - 13, 2003 Clearwater, Florida, USA
Park, C., and Appleton, J. P., "Shock-tube measurements of soot oxidation rates." *Combust. Flame*, 20, 369-379 (1973)

Pedersen, L. S., P. Glarborg, et al. (1998a). "A chemical engineering model for predicting NO emissions and burnout from pulverized coal flames." *Combust. Sci. and Technol.* 132: 251-314.
Pedersen, L. S., P. Glarborg, et al. (1998b). "A reduced reaction scheme for volatile nitrogen conversion in coal combustion." *Combust. Sci. and Technol.* 131: 193-223.
Reist, P. (1993). Aerosol Science and Technology. New York, Mc Graw Hill.
Robertson, A., Y. Tsuo, and R. McKinsey, "Vision 21 Plants Utilizing Foster Wheeler's Partial Gasification Module," 2001 Clearwater Conference. (2001).
Roberts DG and Harris DJ, Char gasification with O_2, CO_2 and H_2O: Effects of pressure on intrinsic reaction kinetics, Energy & Fuels, 2000; 14:483-489.
Roberts DG, Harris DJ and Wall TF, On the effects of high pressure and heating rate during coal pyrolysis on char gasification reactivity, Energy & Fuels, 2003, 17:887-895.
Rusell, N. Mendez, L. Wigley, F. Williamson, J. (2002). *Fuel*, 81; 657-663.
Shim H-S, Hurt RH, Thermal annealing of chars from diverse organic precursors under combustion-like conditions, Energy and Fuels, 2000; 14:340-348.
Speight J. (1983). The Chemistry and Technology of Coal. New York, Marcel Dekker
Sun J-K and Hurt RH. A numerical study of the origin of unburned carbon, Ninth International Conference on Coal Science, Essen, Germany, DGMK Tagungsberichte 9703, 927-930, 1997.
Suuberg EM, Wojtowicz M and Calo JM, Reaction order for low temperature oxidation of carbons, Proceeding of Combustion Institute, 1988; 22:79-87.
Tognotti, L., Longwell, J. P. and Sarofim, A. F., "The products of the high temperature oxidation of the a single char particle in an electrodynamic balance", *Proceedings of the Combustion Institute*, 23, 1400 (1990)
Tomeczek, J. Palugniok, H. (2002). *Fuel*, 81; 1251-1258.
Tomeczek, J. and Gil, S. (1997). *Proceedings ICCS;* 545-548.
Tomeczek, J. and Gil, S. (2003). *Fuel*, 82; 285-292.
Touloukian, Y. S., "Thermal Properties of Matter. Volume 9: Thermal Radiative Properties – Nonmetallic Solids.", IFI/Plenum, New York, 1972
R.J. Tyler, H.J. Wouterlood, F.R. Mulcahy, *Carbon* 14 (1976) 271-278
Uijttewaal, W. S. J., and Oliemans, R. V. A., "Particle dispersion and deposition in direct numercal and large eddy simulations of vertical pipe flows." *Phys. Fluids*, 8(10), 2590-2604 (1996)
Wigley, F. Williamson, J. Gibb, W. (1997). *Fuel,* 76; 1283-*1288.*
Wilemski, G. Srinivasachar, S. (1993). *Proc of Eng Foundation Conference*; 151-164.
Wall TF, Liu G, Wu H, Roberts D, Benfell K, Gupta S, Lucas J, Harris D. (2002). *Progress in Energy and Combustion Science,* 28; 405-433.
Wu H, Bryant G, Benfell K and Wall T. An experimental study on the effect of system pressure on char structure of an Australian bituminous coal. Energy & Fuels, 2000; 14:282-290.
Wu H. (2000) Ash formation during pulverized coal combustion and gasification at pressure. PhD thesis, Department of Chemical Engineering, University of Newcastle.
Wu H, Bryant G, Wall TF. (2000). *Energy & Fuels*,14;745-750.
Wu H, Wall TF, Liu G, Bryant G. (1999). *Energy & Fuels*, 13;1197-1202.
Yan, L. (2000) CCSEM analysis of minerals in pulverized coal and ash formation modeling. Thesis. University of Newcastle.

Yan, L. Gupta, R. Wall, T. (2002). *Fuel,* 81; 337-344.
Q. Zhuang, T. Kyotani, A. Tomita, *Energy and Fuels* 9 (1995) 630-634.

The following files were posted on the HPCCK website:

NBFZ CFD Simulations

Part_Temp_His.xls

NBFZ Tests

PRB_10atm.xls
PRB_20atm.xls

HPBO Tests

HPBO_ILL_2_atm.xls
HPBO_ILL_20_atm.xls
HPBO_Pitt_2_atm.xls
HPBO_Pitt_10_atm.xls
HPBO_Pitt_30atm.xls
HPBO_PRB_2_atm.xls
HPBO_PRB_20_atm.xls
HPBO_Pitt_CO2_2_atm.xls
HPBO_Pitt_CO2_10_atm.xls
HPBO_Pitt_CO2_20atm.xls

11. Bibliography

Niksa, S., and Liu, G.-S. “Detailed reaction mechanisms for coal-nitrogen conversion in p.f. flames.” *Proceedings of the Combustion Institute*, **29**: 2259-2265.

Niksa, S., and Liu, G.-S. “Incorporating detailed reaction mechanisms into simulations of coal-nitrogen conversion in p.f. flames.” *Fuel*, **81**: 2371-2385.

High Pressure Coal Combustion Experiments
Eckstrom,D.J., Hirschon,A.S. Malhotra, R. and Niksa,S
12th International Conference on Coal Science, 2003

Hurt, RH, Haynes, BS., On the origin of power-law kinetics in carbon oxidation, Proceedings of the Combustion Institute, Vol. 30, 2005, in press

G.-S. Liu and S. Niksa, "Pulverized coal flame structures at elevated pressures. Part 1. Detailed operating conditions," Fuel, submitted (2004).

S. Niksa and G.-S. Liu, "Pulverized coal flame structures at elevated pressures. Part 2. Interpreting NOX production with detailed reaction mechanisms," Fuel, submitted (2004).

G.-S. Liu and S. Niksa, "A global NOX submodel for pulverized coal flames at elevated pressures," Combust. Sci. Technol., submitted (2004).

12. List of Acronyms and Abbreviations

Name	Description
AAL	American Air Liquide
BU	Brown University
CBK	Carbon Burnout Kinetics
CCSEM	Computer controlled scanning electron microscopy
CNPP	NEA's ChemNet Post Processing
CFD	Computational Fluid Dynamics
CSTR	Continuously Stirred Tank Reactors
ECT	Electric Charge Transfer Device
FWC	Foster Wheeler Corporation
HPBO	High Pressure Burnout
HPCCK	High Pressure Coal Combustion Kinetics
LRT-RCFR	long-residence-time reactor
NBFZ	Near-Burner Flame Zone
NEA	Niksa Energy Associates
NETL	National Energy Technology Laboratory
NOX	(NO_x) oxides of nitrogen
PC	pulverized coal
PGM	Partial Gasification Module
PPCC	pressurized pulverized coal combustor
PRB	Powder River Basin
p-RCFR	pressurized radiant cold-flow reactor
SEM	scanning electron microscopy
S. R.	stoichiometric ratio
SRI	SRI International
SRT-RCFR	short-residence-time reactor
UConn	University of Connecticut
UDF	user-defined function

HIGH PRESSURE COAL COMBUSTION KINETICS PROJECT
Appendix A – Experimental Details

A.1 NBFZ Experiments

A.1.1 The SRT-RCFR Experimental Facility

The NBFZ experiments were performed in a slightly modified version of SRI's pressurized-radiant coal flow reactor (p-RCFR) [Cor et al., 2000] shown schematically in Figure A.1. The pulverized coal path began in the pressure vessel on the left, in which a positive displacement feeder released coal into the drop tube, where it was entrained by gases fed into the pressure vessel from below. The entrained coal passed through a U-tube and was fed into the central tube ("core") of the injector. Upward flow through the reactor was chosen to minimize buoyancy effects that were predicted to cause recirculation in downward flows at high pressures. A sheath flow of the same gas composition (consisting of the inert carrier gas plus a variable fraction of oxygen) was fed into an annulus that surrounds the core flow. The average velocities of the sheath flow and core flow were set to equal values to minimize turbulence, and therefore mixing, across the interface, in an effort to keep coal particles from impinging on the flow tube walls in the hot zone. Since the areas of the sheath and core are equal, the flow rates of the entrainment and sheath flows were also equal. However, modeling studies show that at the high pressures of these experiments, turbulence rapidly mixed the particles throughout the tube cross section, and in fact tended to concentrate them near the walls [Liu and Niksa, 2003].

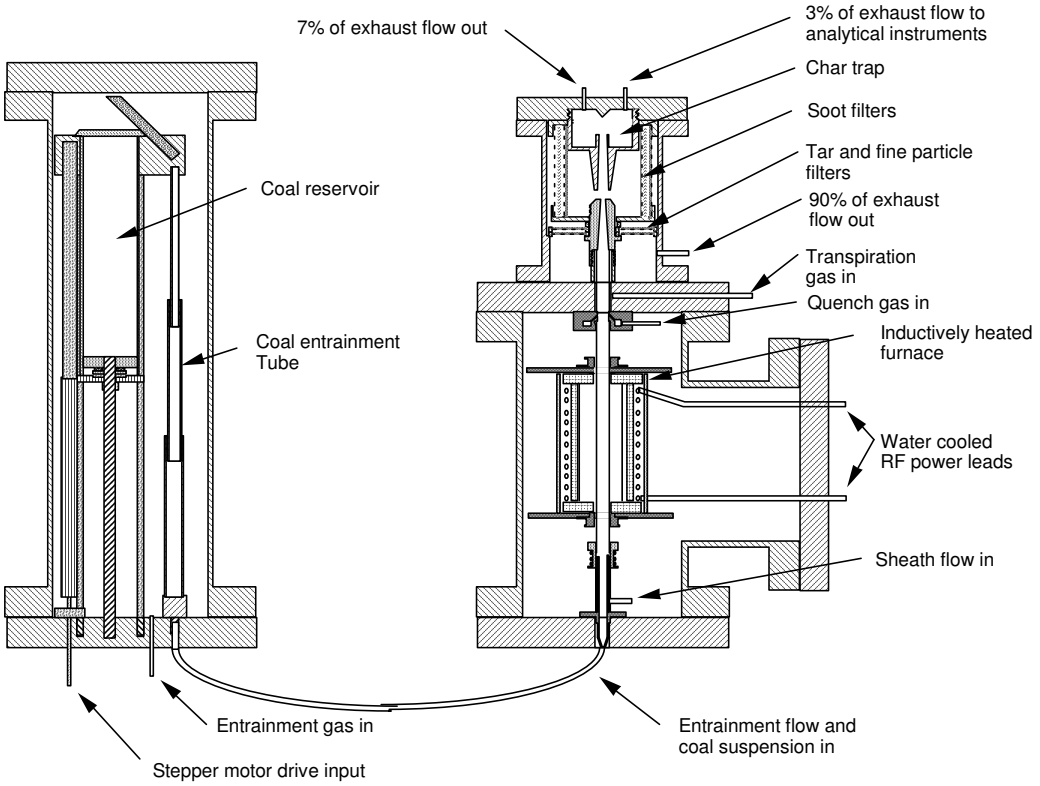

Figure A.1. SRI's Short-Residence-Time Radiant Coal Flow Reactor (SRT-RCFR)

The flow tube in these experiments was made of mullite and was 16 mm OD × 12 mm ID. This 27-cm long tube passed through a furnace consisting of an RF-induction heated graphite sleeve of 5 cm outer diameter, 6 mm wall thickness, and 15.8 cm length. The graphite temperature was maintained in the range of 1560 – 1620°C during the experiments, resulting in a radiant flux on the mullite tube of approximately 60 W/cm^2. The mullite tube was in near radiative equilibrium with the graphite, leading to a comparable mullite wall temperature as well as a comparable radiative flux on the particles within the tube. Details of the calculations of radiant flux distributions and resulting wall temperature distributions are given in NEA's Third Interim Report [Liu and Niksa, 2003].

The entrainment gas was argon with a varying percentage of oxygen. Because these gases are transparent to infrared radiation, the gas within the furnace was heated by a combination of conduction from the walls and convection from the radiatively superheated particles. Wall temperatures and radiative rates were relatively insensitive to the test pressure, so the heating rates were also similar. However, because the heat capacity of the carrier gas increases linearly with pressure, the gas temperature rise varies inversely with pressure. In the absence of combustion, the centerline argon gas temperatures at the end of the flow tube (at 27 cm from the inlet) were calculated to be approximately 1050°C, 850°C, and 650°C at 1, 2, and 3 MPa, respectively, while the gas temperatures at the wall were in near equilibrium with the wall temperature, i.e., near 1600°C within the furnace region [Liu and Niksa, 2003]. The lower gas temperatures at higher pressures caused increased convective cooling of the coal particles, resulting in lower peak particle temperatures. Calculations indicate that the peak particle

temperatures decreased from approximately 1400°C at 1 MPa to 1230°C at 2 MPa and to approximately 1100°C at 3 MPa [Liu and Niksa, 2003]. More details of the temperature distributions, and the resulting flame structures, are given by Liu and Niksa [2003].

At 4 cm downstream of the end of the flow tube, cold N_2 gas was injected into the flow stream at a rate of approximately 75% of the combined entrainment and sheath flow rates to drop the gas temperature to below 1000°C, thereby quenching the process chemistry and nucleating any residual tar into an aerosol. The mixed flow was then transported through a sintered wall "transpiration" tube where another 25% of N_2 flow was added to reduce deposition on the tube walls. The flow was finally accelerated through a slightly converging nozzle into a virtual impactor called a centripeter. Approximately 10% of the flow was exhausted through the centripeter basket to assist in char capture. Particles with sufficient mass and momentum penetrated the quasi-stagnation flow at the tip of the char trap and were collected as "char." Lighter particles, characterized as tar and soot, followed the gas streamlines and were trapped on a series of filters. Calculations indicate that the division between "heavy" and "light" particles occurs at around 15 – 20 μm. Since partially burned char particles were always larger than this and tar or soot particles were much smaller, the division between types of solid products was well defined.

Since the fraction of exhaust gas exiting through the centripeter basket also carries fine particles, a quartz paper filter (not shown in Figure 1) was placed at the top of the basket to capture these particles. The majority of fine particles were trapped either on cylindrical soot filters or on a series of two annular tar and fine particle filters, as indicated in Figure 1. The soot filter was a sandwich consisting of a quartz wool blanket between two quartz paper filters, while the tar filters were annular quartz paper discs. The fraction of soot and tar captured on the soot filter ranged from 35% to 90%, with an average value of approximately 63%. The higher percentages occurred for low-oxygen runs where soot was more abundant.

A.1.2 Product Analysis Techniques

After passing through the fine particle filters, the majority of the exhaust stream passed through a throttling valve that dropped the pressure to atmospheric. In addition to the small fraction of gases bled off through the char trap to assist in char capture, additional high-pressure gas was drawn from the same area for product analysis by the battery of instruments listed in Table A.1. This analytical gas stream was partitioned between (a) a California Analytics Model 300 multi-sensor that measured CO and CO_2 by non-dispersive infrared spectroscopy and O_2 by paramagnetic resonance; (b) a Rosemount Model 880A NDIR that measured H_2O, followed by a Nicolet Model 730 Fourier transform infrared spectrometer fitted with a 6.5 m multipass gas cell held at 335 K and calibrated to measure HCN, NH_3, and NO; (c) a heated multiport valve sampling loop system that can store up to 16 samples, typically at 20-s intervals; and (d) two flasks fitted with bubblers and filled with solutions that captured HCN and NH_3 for subsequent analysis by colorometric techniques.

Table A.1. Analytical Equipment for Determining Various Gases

Analytical Equipment	Gases
Gas chromatograph	CH_4, C_2H_x, C_3H_x, oils, H_2
FTIR	CO*, CO_2*, HCN*, NH_3, NO
Non-dispersive IR	CO, CO_2, H_2O
Paramagnetic resonance	O_2
Wet chemistry	HCN, NH_3*

* Redundant determination

Following completion of each run, the contents of each sampling loop were analyzed in turn by injection into an SRI Instruments Model 8610C gas chromatograph. This instrument was fitted with an internal 10-port valve for column switching and sample injection, and with three detectors in series. Two columns were used: a molecular sieve column to separate light gases (H_2, CO, and CH_4), and a Hayesep D column to separate the CO_2 and higher hydrocarbons (C_2H_2+C_2H_4, C_2H_6, C_3H_6, C_3H_8, C_4's). A portion of the injected sample was diverted into an empty capillary column that led directly into the FID for total hydrocarbon analysis. Yields of oils, defined as hydrocarbons with carbon numbers of 5 and higher that remained in the gas phase, were based on the integrated total hydrocarbon signal from the FID reduced by the amounts of the C_1-C_4 hydrocarbons determined for the same sample injection.

Although redundant measurements of several species were possible, reliance was placed on the NDIR measurements of CO, CO_2, and H_2O, on FTIR measurements of NO and NH_3, and on wet chemistry determination of HCN. Major products (CO, CO_2, H_2O) as well as O_2 were characterized to the 0.01% level, while hydrocarbons and nitrogen-containing species were measured to the ppm level. The analytical gas line was heated to minimize condensation of H_2O and oils. Nevertheless, there was consistent evidence that condensation of H_2O occurred when moisture levels in the exhaust stream exceeded 2 – 3 % by volume, and corrections to this parameter were made as required to improve hydrogen, oxygen, and mass balances.

Solid product yields were determined gravimetrically. The char component was primarily the material captured in the centripeter basket, plus small quantities of heavy particles that could be easily shaken from the filters as well as material recovered from the walls of the quench nozzle. In preliminary tests (described in section A4), complete secondary pyrolysis was not achieved, and so the fine aerosol products captured on the quartz paper filters consisted of both tar and soot. In those tests, aerosol products were extracted from the filters with tetrahydrofuran (THF). The solution/suspensions were filtered through a millipore filter. The solids captured on the membrane were denoted as soot, while the dissolved material was recovered by evaporative drying and denoted as tar. It was the persistence of tar that motivated the modification of the furnace to increase the length of the hot zone. After that change was made, tests of the filters in THF showed that tar was no longer present, and from that point forward (i.e., throughout these NBFZ tests), all the material captured on the filters was assigned as soot. The soot samples were then recovered directly from the filter surfaces. Char and soot samples were submitted to an outside laboratory for elemental analysis.

The coal feed rate was determined by pre- and post-test calibration, and consistency of the measurements was confirmed by determining that the mass balance between fed coal and solid +

gaseous products closed to within 5%. Furthermore, the elemental balance on C, H, and O typically also closed to 5%, with some excursions to 10%. Elemental nitrogen does not balance because N_2 was not measured, although at low oxygen levels N_2 is not a major product, and other species then close the N balance to about 20%. No sensors were deployed to measure sulfur-containing products such as H_2S and SO_2.

A.1.3 Test Conditions

Three coals were tested, including two high volatile bituminous (Pittsburgh No. 8 and Illinois No. 6) and one western sub-bituminous (Powder River Basin). The coal samples were obtained from the Penn State coal bank; their specific identifications and properties are given in Table A.2. Pitt #8 coal was tested at 1, 2, and 3 MPa (10, 20, and 30 bar), Illinois #6 was tested at 1 and 2 MPa, and PRB was tested at 1 MPa. The coal was ground, pre-classified by aerodynamic vortexing, and sieved to the double cut range of –140 + 200 (75 – 105 μm). Test samples were dried in a vacuum oven at 90°C overnight to moisture levels < 1% before being placed in the coal feeder reservoir.

Table A.2. Composition of Coals Studied

Coal Name	Proximate Analysis, ad wt.%				Ultimate Analysis, daf wt.%				
	M	Ash	VM	FC	C	H	O	N	S
Pit. #8 DECS 23	0.7	12.3	37.9	49.1	80.8	5.4	5.8	1.7	6.3
Ill. #6 DECS 24	0.2	17.3	35.8	46.7	74.1	5.5	8.2	1.4	10.8
PRB DECS 26	0.1	5.0	39.4	55.5	73.7	5.6	19.0	1.1	0.6

The entrainment and sheath flow rates were adjusted to give an average velocity at the inlet to the furnace of 30 cm/s at all pressures. The nominal residence time in the furnace was then 500 ms, while actual residence times were substantially less because of expansion of the gas due to heating. The nominal coal feed rate was 1.5 g/min, resulting in suspension loadings of approximately 0.05 g_{coal}/g_{gas} at 1 MPa, 0.025 g_{coal}/g_{gas} at 2 MPa, and 0.017 g_{coal}/g_{gas} at 3 MPa. Higher coal feed rates led to problems of clogging or of overheating the flow tube. Even at the reduced coal loadings, clogging of the inlet section of the flow tube or of the centripeter nozzles occurred at the lowest oxygen levels for Pitt #8 at 30 atm, for Ill #6 at 10 and 20 atm, and for PRB at 10 atm, thus limiting the minimum oxygen levels used for those coals. Oxygen concentrations in the entrainment and sheath flows ranged from nearly zero (when possible) to approximately stoichiometric values. Absence of feed oxygen gave secondary pyrolysis conditions, wherein tars and aerosols were converted to soot within the available residence times, while under stoichiometric oxygen/coal ratios burnout of hydrocarbons was nearly always complete, soot burnout was nearly complete, and substantial char burnout also occurred. Seven to ten ratios of oxygen/coal were tested for each coal and pressure condition in order to map the transition between the two operating conditions. The operating conditions for the six test series are listed in Table A.3, as tabulated by NEA [Liu and Niksa, 2003].

Table A.3(a). Operating Conditions for NBFZ Tests in the SRT-RCFR.

Run No.	Coal Name	Pressure (MPa)	Inlet Velocity (cm/s)	Susp. Loading (%)	O_2 Mass Fr. (%)	S.R.
50C	Pit. #8	1	29.3	4.75	0.01	0.001
56C	Pit. #8	1	29.1	4.70	1.40	0.147
55C	Pit. #8	1	29.1	4.74	2.36	0.245
54C	Pit. #8	1	29.2	4.43	3.34	0.372
53C	Pit. #8	1	29.1	4.70	4.82	0.506
52C	Pit. #8	1	29.2	4.95	7.22	0.719
51C	Pit. #8	1	29.3	5.12	9.89	0.953
64C	Pit. #8	2	29.2	2.49	0.10	0.020
63B	Pit. #8	2	29.2	2.57	0.45	0.086
62B	Pit. #8	2	29.2	2.51	1.17	0.230
61B	Pit. #8	2	29.1	2.46	1.91	0.382
60B	Pit. #8	2	29.2	2.53	3.44	0.670
59B	Pit. #8	2	29.1	2.47	4.07	0.812
58B	Pit. #8	2	29.2	2.37	4.85	1.008
77B	Pit. #8	3	29.7	1.46	0.29	0.087
74B	Pit. #8	3	29.7	1.53	0.74	0.212
73B	Pit. #8	3	29.4	1.50	1.19	0.350
71B	Pit. #8	3	29.2	1.65	1.67	0.447
72B	Pit. #8	3	29.4	1.59	1.92	0.533
70B	Pit. #8	3	29.3	1.61	2.32	0.635
69B	Pit. #8	3	30.0	1.57	2.83	0.795
67B	Pit. #8	3	29.3	1.66	3.01	0.799

Table A.3(b). Operating Conditions for NBFZ Tests in the SRT-RCFR (Continued)

Run No.	Coal Name	Pressure (MPa)	Inlet Velocity (cm/s)	Susp. Loading (%)	O_2 Mass Fr. (%)	S.R.
68B	Pit. #8	3	29.2	1.63	3.28	0.887
79B	Pit. #8	3	29.8	1.51	3.74	1.088
88C	Ill. #6	1	29.6	4.71	0.41	0.043
87C	Ill. #6	1	29.4	4.74	1.60	0.167
86C	Ill. #6	1	29.5	4.66	2.16	0.229
85C	Ill. #6	1	29.7	4.64	4.81	0.511
84C	Ill. #6	1	29.5	4.49	6.97	0.765
83C	Ill. #6	1	29.7	4.44	9.45	1.049
82C	Ill. #6	1	29.6	4.88	11.45	1.156
97C	Ill. #6	2	29.6	2.27	1.28	0.279
95C	Ill. #6	2	29.5	2.24	2.28	0.502
94C	Ill. #6	2	29.6	2.25	3.45	0.756
93C	Ill. #6	2	29.5	2.28	4.85	1.046
99C	Ill. #6	2	29.6	2.53	6.08	1.187
89C	Ill. #6	2	29.5	2.31	6.49	1.384
91C	Ill. #6	2	29.6	2.37	8.51	1.769
110C	PRB	1	29.5	4.50	0.27	0.028
109C	PRB	1	29.3	4.57	1.18	0.121
108C	PRB	1	29.4	4.52	2.32	0.241
107C	PRB	1	29.4	4.44	3.81	0.404
105C	PRB	1	29.3	4.78	5.88	0.578
104C	PRB	1	29.4	4.79	7.65	0.751
103C	PRB	1	29.5	4.88	9.70	0.934
102C	PRB	1	29.4	4.87	11.31	1.092
101C	PRB	1	29.1	4.88	13.21	1.272

A.1.4 Results

The six series of NBFZ tests consist of measurements of Pittsburgh #8 coal at 1, 2, and 3 MPa, of Illinois #6 coal at 1 and 2 MPa, and of PRB coal at 1 MPa. The results for these six series are summarized in Tables A.4-A.9. Each table lists the runs for that series in order of increasing O_2/coal ratio, beginning with the minimum oxygen run on the left and progressing to approximately stoichiometric O_2/coal ratio on the right. It will be noted that each table contains two columns for each individual run, labeled "M" and "C" for measured and corrected values, respectively. The corrections made by NEA primarily account for the following problems:

As noted above, there was consistent evidence of water vapor condensation in the gas analysis line. As a result, it was necessary to increase the H_2O product levels above measured values for cases of medium to high O_2/coal ratio (i.e., the tests on the right-hand side of the tables).

Because sulfur-containing products were not measured, the assumption was made that all sulfur in the coal was converted to gas-phase product. The product was assumed to be H_2S when

combustion conditions were sufficiently reducing to retain gaseous fuel compounds, and to be SO_2 under conditions where essentially all the gaseous fuel compounds had burned.

Corrections to various other product yields were made in isolated cases throughout the data sets as required to close mass and elemental balances. These corrections were guided by NEA's Flashchain model. With these limited corrections, the results provide a remarkably self-consistent database of product yields as a function of combustion conditions under these difficult experimental conditions. For example, the rows in the lower quarter of each table that list the mass and elemental balances show that the mass balances typically close to better than 5%, with rare excursions to 10%. Similar closures are demonstrated for C, H, and O.

Tables A.6-A.9 contain an additional column on the left-hand side labeled "2^{nd} PY." These values, which represent conditions where no external oxygen is present, were generated by NEA using a combination of extrapolation from our lowest oxygen runs and calculations using PC Coal Lab®. These additions to the data sets were required in those cases where clogging problems precluded tests at low oxygen/coal ratios, as mentioned above. Finally, the bottom three rows of the tables present the extent of burnout values for hydrocarbons, soot, and char. In each case, the DAF values of each product were normalized by the yield of that product under secondary pyrolysis conditions [$X_i = 100 \times (Y_{2nd\ Py} - Y_i)/Y_{2nd\ Py}$]. These values form the basis for the comment made above, namely, that stoichiometric ratios of O_2/coal lead to burnout levels of hydrocarbons ranging from 95% to 100%, of soot from 76% to 93%, and of char from 27% to 92%

Table A.4. Pittsburgh. #8, 1.0 MPa NBFZ Datasets, with Corrected Values, in DAF wt. %.

					55C		54C		53C		52C		51C	
	M	C	M	C	M	C	M	C	M	C	M	C	M	C
CO_2	0.4		29.4		52.2		70.9		94.3		142.6		197.7	
H_2O	1.2		14.2		22.0		23.7		29.3	33.4	29.2	42.5	28.4	45.8
CO	7.8		35.9		45.1		43.3		41.3		20.1		15.5	
CH_4	1.0		0.7		0.5		0.3		0.1		0.0		0.0	
C_2	1.4		0.5		0.4		0.2		0.0		0.0		0.0	
C_3	0.1		0.1		0.1		0.0		0.0		0.0		0.0	
Oils	0.3		0.3		0.1		0.0		0.0		0.0		0.0	
H_2	2.4	3.8	2.5		2.7		2.2		1.3		0.43		0.17	
HCN	1.04		0.89		0.54		0.29		0.06		0.00		0.00	
NH_3	0.03		0.06		0.05		0.03		0.02		0.00		0.00	
NO	0		0.01		0.01		0.00		0.01		0.02		0.19	
Tar	0		0		0		0		0		0		0	
H_2S	Nm	7.4	Nm	7.4	Nm	7.4	Nm	7.4	Nm		Nm		Nm	
SO_2	Nm		Nm		Nm		Nm		Nm	13.8	Nm	13.8	Nm	13.8
Soot	21.1	29.1	19.5		8.0		9.6		13.9		7.6		2.0	
Char	40.3	48.5	36.9		38.4		35.7		35.6		26.1		20.4	
ΣMass		1.020		1.095		1.063		1.042		1.081		1.027		1.076
ΣC		1.018		0.994		0.991		1.027		1.091		0.999		1.021
ΣH		1.008		0.966		1.135		1.062		0.999		1.000		1.004
ΣO		1.011		1.363		1.243		1.132		1.111		1.092		1.147
X_{HC}		0		39.5		53.1		68.5		87.4		100.0		100.0
X_{Soot}		0		32.7		72.5		67.0		52.7		74.2		93.2
X_{Char}		0		23.9		20.8		26.4		27.6		46.2		57.9

Note: M: measured; C: corrected; Nm: not measured. Notations are the same in Tables A.5-A.9.

Table A.5. Pittsburgh #8, 2.0 MPa NBFZ Datasets, with Corrected Values, in DAF wt. %.

	64B		63B		62B		61B		60B		59B		58B	
	M	C	M	C	M	C	M	C	M	C	M	C	M	C
Product Distribution														
CO_2	1.6		4.4		36.4		46.7		119.0		142.0		179.3	
H_2O	1.5		6.9		15.3		18.7		27.7	34.9	27.1	39.0	30.7	41.7
CO	12.0		21.8		30.1		33.3		35.5		29.9		22.0	
CH_4	2.7		2.1		1.0		0.7		0.3		0.2		0.1	
C_2	1.9		1.4		0.6		0.4		0.2		0.1		0.1	
C_3	0.3		0.3		0.1		0.1		0.0		0.0		0.0	
Oils	0.8		0.6		0.2		0.1		0.0		0.0		0.0	
H_2	3.5		3.1		3.0		2.3		1.1		0.7		0.33	
HCN	1.51		1.39		0.95		0.45		0.23		0.02		0.01	
NH3	0.08		0.07		0.08		0.08		0.05		0.03		0.00	
NO	0		0.05		0		0.03		0.01		0.02		0.11	
Tar	0		0		0		0		0		0		0	
H_2S	Nm	7.4	Nm	7.4	Nm	7.4	Nm	7.4	Nm		Nm		Nm	
SO_2	Nm		Nm		Nm		Nm		Nm	13.8	Nm	13.8	Nm	13.8
Soot	21.2	25.1	15.3	25.1	15.6		9.5		4.4		4.6		3.3	
Char	45.1		43.5		42.4		39.8		32.3		35.5	25.3	37.7	19.8
Mass Balances														
ΣMass		0.964		1.008		1.023		0.981		1.006		1.104		1.028
ΣC		0.956		1.000		0.992		0.936		1.036		1.000		1.000
ΣH		1.101		0.979		1.057		1.024		1.000		1.000		1.000
ΣO		0.955		1.034		1.070		1.027		1.045		1.143		1.050
Burnout														
X_{HC}		0.0		21.4		60.8		75.3		90.1		93.8		96.9
X_{Soot}		0.0		0.8		39.8		63.3		83.0		82.2		87.3
X_{Char}		0.0		2.9		6.0		11.8		23.7		43.9		56.1

Table A.6. Pittsburgh #8, 3.0 MPa NBFZ Datasets, with Corrected Values, in DAF wt. %.

	2nd Py	77B		74B		73B		72B		67B		71B		70B		68B		69B		79B	
		M	C	M	C	M	C	M	C	M	C	M	C	M	C	M	C	M	C	M	C
										1.1.1.1.1.1 Product Distribution											
)2	0.8	12.5		23.9		58.1		78.8		85.2		86.2		116		141		130		170	
O	1.6	11.5		15.9		18.8		23.3		24.2		31.5		31.4		27.8	30.4	28.4	38.3	32.3	36.0
)	5.6	20.9		32.8		31.6		32.0		27.9		26.5		29.4		21.6		27.2		21.7	
H4	5.0	4.64		3.54		2.36		1.27		0.75		0.71		0.08		0.33		0.60		0.38	
	4.5	2.94		1.85		1.25		0.53		0.31		0.31		0.41		0.16		0.27		0.19	
	1.6	0.48		0.16		0.17		0.14		0.06		-		0.15		0.04		0.10		0.05	
ls	-	1.71		0.78		0.34		0.21		0.05		0.08		0.77		0.17		0.11		-	
	2.1	3.36	0.36	2.54	0.50	1.85	0.65	1.86		1.80		0.65		0.80		1.16		0.65		1.01	
CN	1.5	1.29		0.74		0.66		0.17		0.30		0.40		0.13		0.03		0.05		0.06	
H3	0.18	0.14		0.17		0.18		0.06		0.09		0.11		0.11		0.06		0.02		0.02	
)	-	-		-		-		-		-		-		-		0.07		-		0.08	
r	-	-		-		-		-		-		-		-		-		-		-	
S	7.4	-	7.4	-	7.4	-	7.4	-	7.4	-	7.4	-	7.4	-	7.4	-	7.4	-	-	-	-
)2	-	-		-		-		-		-		-		-		-		-	13.8	-	13.8
ot	22.9	16.5		7.4	13.0	9.5		5.3		7.4		3.8		5.2		7.8		4.6		3.6	
ar	46.8	55.2	46.8	51.3	45.4	53.7	44.0	42.5		38.8		43.9		44.2		33.3		34.1		34.3	
ass Balances																					
	0.98		1.03		1.03		1.06		1.04		1.01		1.02		1.16		1.09		1.06		1.15
[	1.00		1.00		1.00		1.00		1.05		1.02		0.96		0.97		1.00		1.00		1.00
)	1.01		1.12		1.01		1.00		1.07		1.00		0.97		1.01		1.07		1.00		1.00
urnout																					
C	0.0		12.5		44.2		63.0		81.5		89.1		89.2		87.0		94.0		90.8		94.8
oot	0.0		28.0		43.2		58.5		76.9		67.7		83.4		77.3		65.9		79.9		84.3
har	0.0		0.0		3.0		6.0		9.2		17.1		-		-		28.9		27.1		26.7

Table A.7. Illinois #6, 1.0 MPa NBFZ Datasets, with Corrected Values, in DAF wt. %

	2nd Py	88C		87C		86C		85C		84C		83C		82C	
		M	C	M	C	M	C	M	C	M	C	M	C	M	C
Product Distribution															
O_2	1.3	1.3		19.3		28.6		82.4		133.9		184.3		192.7	
$_2O$	2.4	2.4		19.5	13.2	23.4	18.0	32.4		41.6		42.7		44.4	
O	9.0	16.2	12.3	36.7		38.2		43.2		28.8		15.3		15.0	
H_4	2.0	1.1		0.5		0.5		0.1		0.0		0.0		0.0	
$_2$	2.4	2.0		0.4		0.4		0.0		0.0		0.0		0.0	
$_3$	0.4	0.1		0.0		0.1		0.0		0.0		0.0		0.0	
l	-	0.3		0.2		0.2		0.0		0.0		0.0		0.0	
$_2$	2.60	3.77	3.00	2.57		2.13		1.40		0.63		0.37		0.34	
CN	1.00	1.02		1.06		0.24		0.04		0.00		0.00		0.00	
H_3	0.00	0.02		0.04		0.04		0.03		0.02		0.01		0.02	
O	0.00	0.00		0.00		0.00		0.00		0.00		0.21		0.26	
ur	-	-		-		-		-		-		-		-	
$_2S$	11.4	-	11.4	-	11.4	-	11.4	-		-		-		-	
O_2	-								21.6		21.6		21.6		21.(
ot	21.0	22.5		12.1		10.8		9.2		4.6		3.9		3.7	
ar	47.6	47.6		41.7		38.5		28.1		22.7		15.8		13.1	
Mass Balances															
Mass	1.011		1.029		1.000		0.990		0.952		1.002		1.003		1.00
C	1.027		1.044		1.013		0.991		1.049		1.023		1.028		1.01
H	0.993		0.993		1.007		1.009		0.985		1.015		0.947		1.00
il O_2,%	0	1.9	18.0	80.0	95.0	75.0	89.5	81.1	92.2	71.5	81.5	64.8	71.0	60.3	67.(
O	1.003		1.000		0.990		1.000		1.000		1.000		1.091		1.00(
urnout															
HC	0		28.2		71.8		80.1		97.2		99.2		99.6		100.(
oot	0		-0.1		42.4		48.6		56.2		78.1		81.4		82.4
har	0		0.0		12.4		19.1		41.0		52.3		66.8		72.3

Table A.8. Illinois #6, 2.0 MPa NBFZ Datasets, with Corrected Values, in DAF wt. %

	2nd Py	97C		95C		94C		93C		99C		89C		91C	
		M	C	M	C	M	C	M	C	M	C	M	C	M	C
roduct Distribution															
$)_2$	1.3	31.9		67.1		109.6		165.1		180.8		200.1		224.0	
O	2.4	23.3	17.7	30.8	25.6	42.5	39.4	44.3		44.8		45.6		46.3	
)	9.0	37.8		42.6		31.8		20.8		16.1		10.1		5.9	
I_4	2.0	1.0		0.7		0.3		0.1		0.1		0.1		0.0	
	2.4	0.6		0.4		0.2		0.1		0.1		0.1		0.0	
	0.4	0.1		0.2		0.1		0.0		0.0		0.0		0.0	
	-	0.3		0.2		0.1		0.0		0.0		0.0		0.0	
	2.60	1.94		1.28		0.64		0.31		0.16		0.13		0.09	
:N	1.00	0.79		0.08		0.01		0.00		0.03		0.01		0.00	
I_3	0.00	0.09		0.05		0.02		0.00		0.00		0.01		0.01	
)	0.00	0.02		0.00		0.00		0.02		0.09		0.00		0.16	
r	-	-		-		-		-		-		-		-	
S	11.4	-	11.4	-	11.4	-		-		-		-		-	
$)_2$		-		-		-	21.6	-	21.6	-	21.6	-	21.6	-	21.6
ot	21.0	12.3		7.1		3.5		2.9		3.4		2.8		2.5	
ar	47.6	40.1		34.5		28.9		20.6		17.8		15.2		9.3	
lass Balances															
lass	1.011		1.029		0.966		0.986		1.007		1.006		1.004		1.000
	1.027		1.044		1.061		1.024		1.042		1.041		1.034		1.016
[	0.993		0.993		1.000		1.000		1.011		0.988		0.993		0.990
O_2,%	0	77.1		68.4		65.9	73.0	61.6	68.0	58.1	63.0	50.9	57.0	43.8	48.3
)	1.003		1.000		1.037		1.000		1.000		1.000		1.000		1.000
urnout															
C	0		61.0		76.6		89.5		96.2		96.8		97.7		98.8
oot	0		41.4		66.2		83.3		86.2		83.8		86.7		88.1
har	0		15.8		27.5		39.3		56.7		62.6		68.1		80.5

Table A.9. PRB, 1.0 MPa NBFZ Datasets, in DAF wt. % (No Corrections Necessary).

	2^{nd} Py	110C	109C	108C	107C	105C	104C	103C	102C	101C
		M	M	M	M	M	M	M	M	M
Product Distribution										
CO_2	6.6	6.6	18.9	36.9	61.1	90.4	126.1	166.4	192.6	203.1
H_2O	8.1	8.1	15.9	23.6	27.5	32.0	36.1	39.4	43.8	45.9
CO	12.3	17.1	30.6	41.5	50.8	49.8	43.3	37.4	31.3	26.4
CH_4	2.9	2.9	2.4	1.5	0.6	0.1	0.0	0.0	0.0	0.0
C_2	4.0	4.0	2.2	1.0	0.3	0.0	0.0	0.0	0.0	0.0
C_3	0.4	0.3	0.1	0.0	0.0	0.0	0.0	0.0	0.0	0.0
Oils	-	1.8	0.9	0.1	0.0	0.0	0.0	0.0	0.0	0.0
H_2	2.75	2.75	2.41	2.06	1.92	1.56	1.20	0.82	0.57	0.34
HCN	0.69	0.69	.61	0.57	0.45	0.19	0.05	0.05	0.00	0.00
NH_3	0.07	0.07	0.09	0.13	0.17	0.11	0.06	0.05	0.02	0.01
NO	0.00	0.00	0.00	0.00	0.00	0.00	0.00	0.00	0.08	0.11
Tar	-	-	-	-	-	-	-	-	-	-
H_2S	0.64	0.64	0.64	0.64	0.64	-	-	-	-	-
SO_2	-	-	-	-	-	1.20	1.20	1.20	1.20	1.20
Soot	9.1	9.1	3.8	1.5	1.6	3.1	3.3	4.1	1.7	2.2
Char	52.4	52.4	49.9	42.8	34.7	24.0	18.3	11.5	6.9	4.4
Mass Balances										
ΣMass	1.000	1.016	1.015	1.002	1.001	0.996	1.003	1.001	0.992	1.003
ΣC	1.000	1.021	1.028	0.998	1.016	0.985	1.004	1.039	1.007	0.991
ΣH	0.975	0.997	1.002	0.961	0.991	0.962	0.964	0.954	0.984	0.981
ΣO	1.002	1.000	0.995	1.009	0.992	1.009	1.008	0.991	0.991	1.012
Burnout										
X_{HC}	0	2.0	35.6	64.5	85.0	97.3	99.2	99.5	99.9	100.0
X_{Soot}	0	0	58.2	83.5	82.4	65.9	63.7	55.0	81.3	75.8
X_{Char}	0	0	4.8	18.3	33.8	54.2	65.1	78.1	86.8	91.6

Figures A.2-A.6 give examples of the results of measurements for Pittsburgh #8 coal at 1 MPa. Figure A.2 shows that secondary pyrolysis gives a char yield of 53% (char product/coal fed = 0.53 on a DAF basis for the lowest oxygen test), while the tar + soot yield was 23% (all product yields are given on a DAF basis). For this coal, an O_2/coal ratio of 2.1 corresponds to a stoichiometric ratio of 1. At S.R. = 1, 60% of the char and 90% of the soot have been consumed. Hydrogen is 95% consumed (Figure A.6), while the volatile hydrocarbon products are essentially totally consumed at oxygen levels well below stoichiometric (Figure A.4). The volatile nitrogen species HCN and NH_3 decrease by >99% and 90%, respectively, as the oxygen level increases, while NO increases (Figure A.5). These opposing trends result in a minimum in the nitrogen pollutants at an oxygen level of about 75% of stoichiometric. Note that the experiments were conducted in Ar/O_2 mixtures rather than N_2/O_2 mixtures, so that the thermal NO_x mechanism was not operative. Analogous sets of data were collected at other pressures and for the other coals to study the effect of pressure and coal type on the combustion.

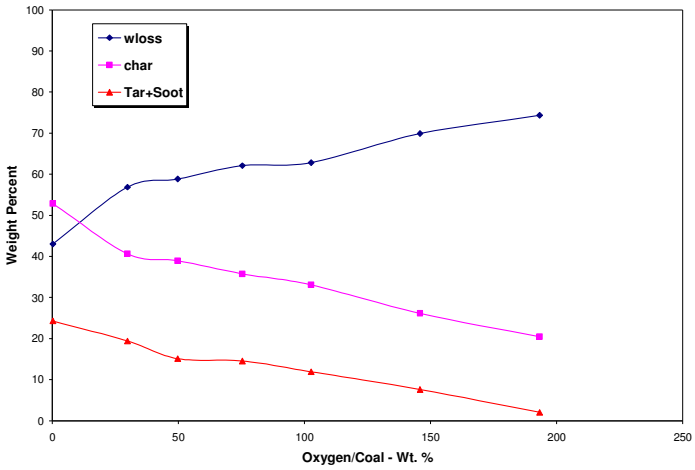

Figure A.2. Yield of major products during combustion of Pittsburgh coal at 1.0 MPa.

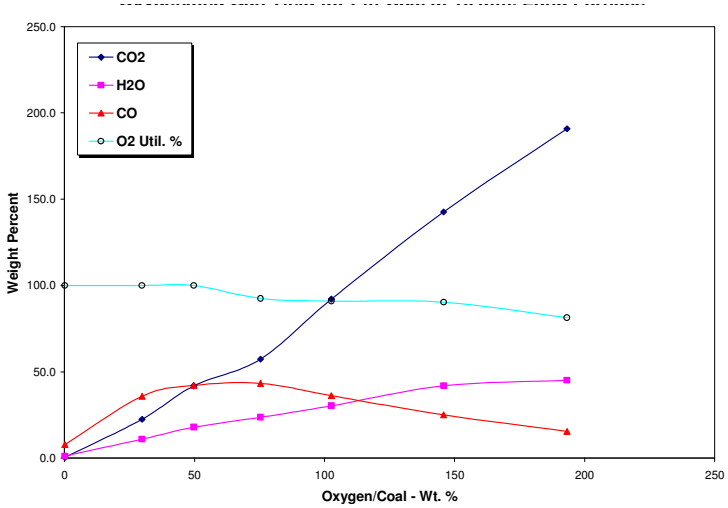

Figure A.3. Yield of oxygenated gases during combustion of Pittsburgh coal at 1.0 MPa.

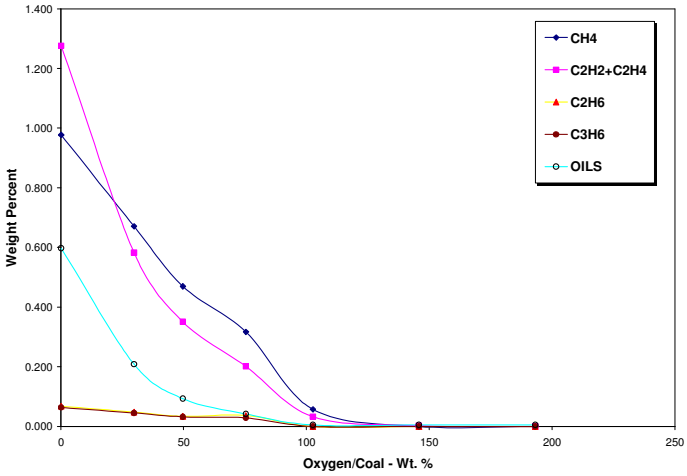

Figure A.4. Yield of hydrocarbon gases during combustion of Pittsburgh coal at 1.0 MPa.

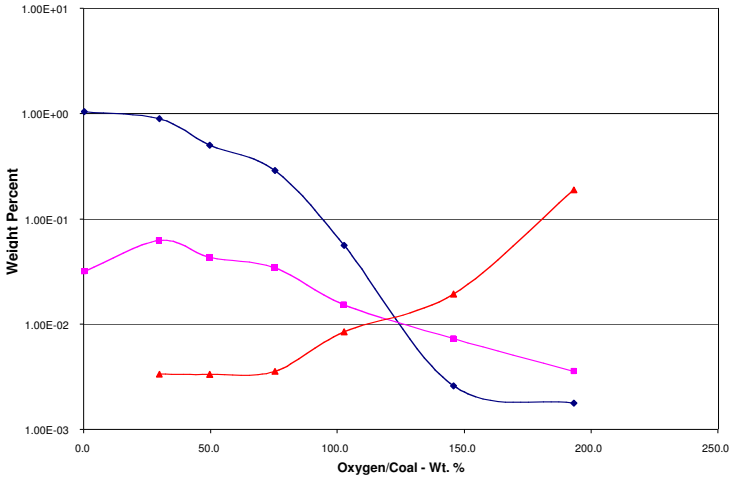

Figure A.5. Yield of nitrogen gases during combustion of Pittsburgh coal at 1.0 MPa.

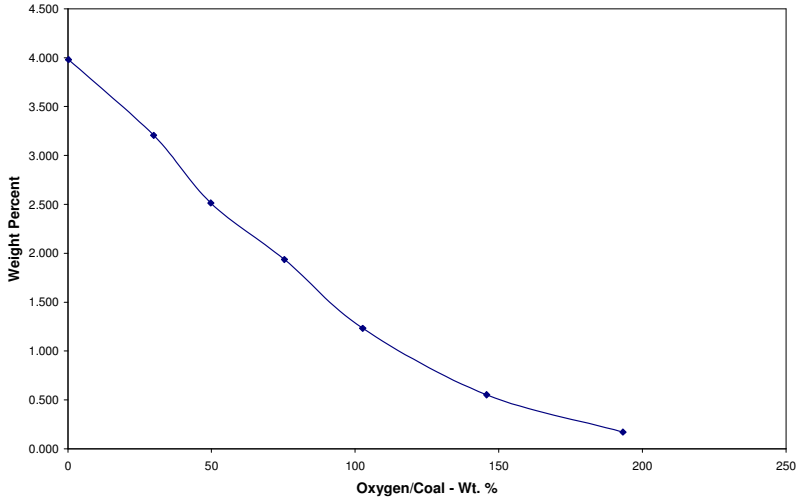

Figure A.6. Yield of hydrogen during combustion of Pittsburgh coal at 1.0 MPa.

The effects of pressure on these burnout histories for Pittsburgh #8 coal are summarized in Figures A.7-A.9. The increasing thermal capacity of the entrainment gas with increasing pressure results in lower gas temperatures, and thus delayed flame ignition, and it is this effect that dominates the reduced char burnout with increasing pressure seen in Figure A.7. However, the same effect is not apparent in the soot and hydrocarbon burnout histories. This may reflect the fact that in regions where ignition does not take place (e.g., on the flow centerline for "open flames" [Liu and Niksa, 2003], char will persist but no soot or hydrocarbons are generated).

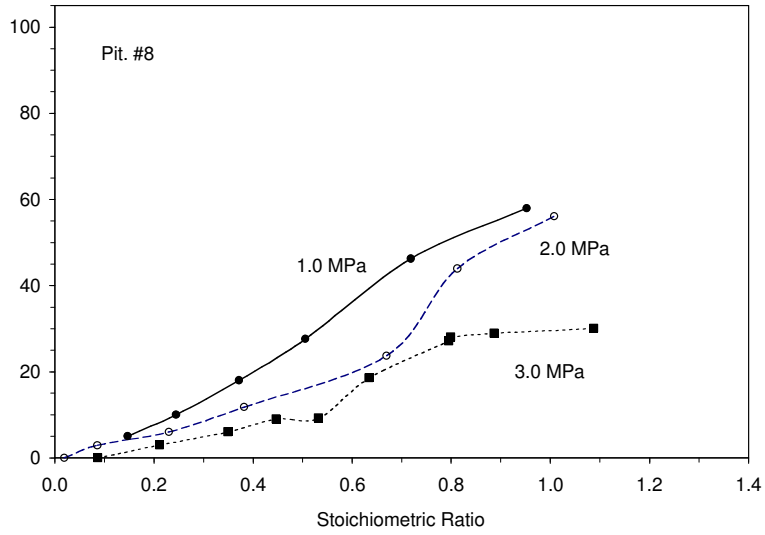

Figure A.7. Char burnout at various pressures for Pittsburgh coal.

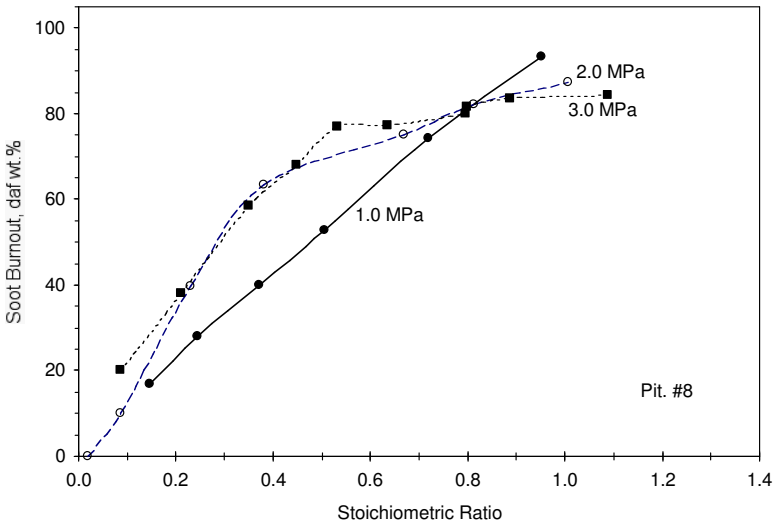

Figure A.8. Soot burnout at various pressures for Pittsburgh coal.

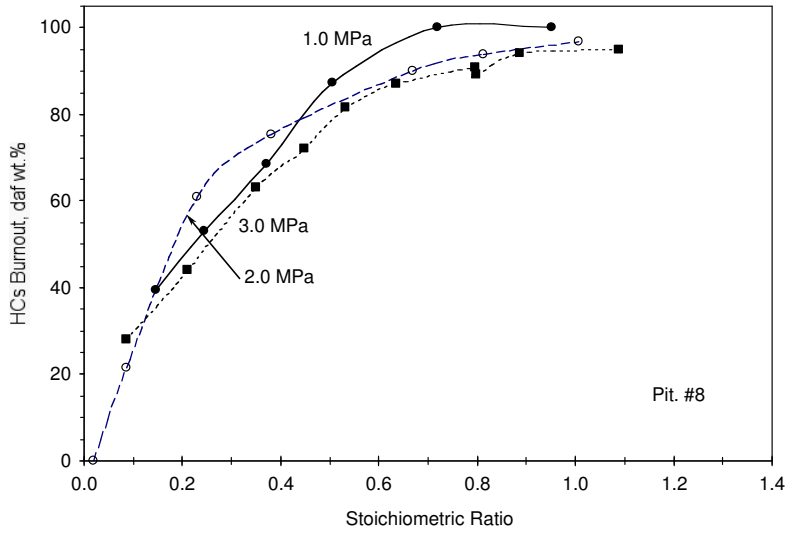

Figure A.9. Hydrocarbon burnout at various pressures for Pittsburgh coal

The effect of coal type at a pressure of 1 MPa is summarized in Figures A.10-A.12. Figure A.10 shows that char burnout is much more extensive for the sub-bituminous PRB coal than for the bituminous Illinois #6 or Pittsburgh #8 coals, consistent with expectations based on coal rank. Similar trends hold for soot burnout shown in Figure A.11, although this may be a thermal effect (i.e., somewhat higher flame temperatures and more extensive flames because of enhanced char burnout) since the soot compositions were found to be nearly independent of coal type.

Frequent reference has been made here to NEA's Third Interim Report [Liu and Niksa, 2003]. That report describes the extensive modeling that NEA has done in support of these NBFZ experiments, both regarding the fluid mechanics of the flows and the implications of the results with respect to the effects of pressure on combustion for these coal types. That report should be consulted for a complete interpretation of these experiments.

In addition to the combustion results described here, the NBFZ tests provided char samples for conditions ranging from secondary pyrolysis to complete volatiles burnout and substantial soot burnout. These samples were provided to UConn and to Brown for their use in developing models of ash formation and char burnout at high pressures.

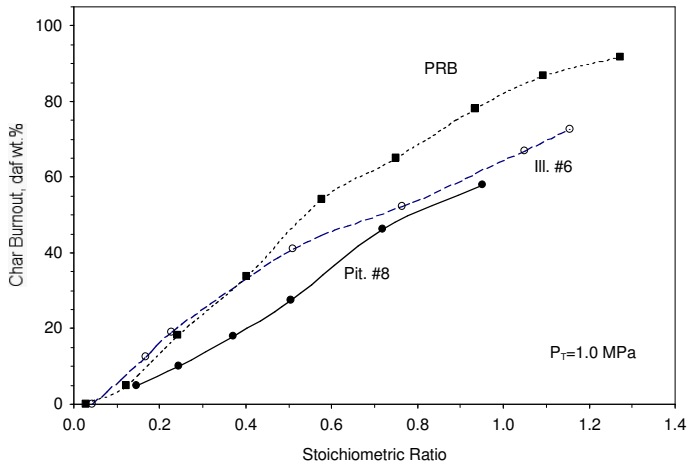

Figure A.10. Char burnout for PRB, Pittsburgh, and Illinois coals at 1.0 MPa.

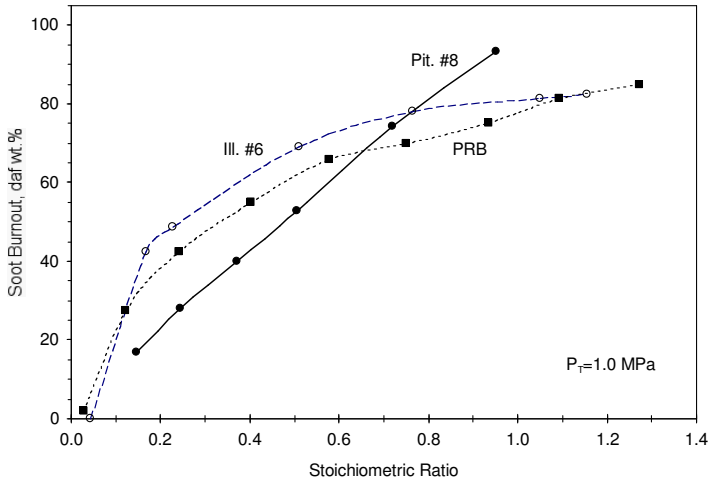

Figure A.11. Soot burnout for PRB, Pittsburgh, and Illinois coals at 1.0 MPa.

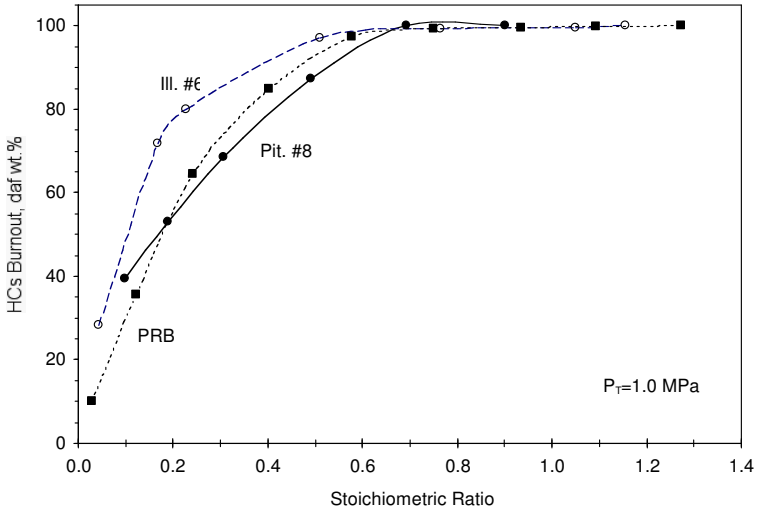

Figure A.12. Hydrocarbon burnout for PRB, Pittsburgh, and Illinois coals at 1.0 MPa.

A.2 HPBO Experiments

A.2.1 The LRT-RCFR Experimental Facility

The objective of the HPBO experiments was to systematically vary the degree of char burnout from nominally 50% to essentially 100% while maintaining O_2/coal ratios near stoichiometric levels. As indicated in Tables A.4-A.9 above, the maximum char burnout levels under NBFZ test conditions varied from 27% to 92%. Thus, achievement of complete burnout required modification of the test facility to permit longer particle residence times. We also found it necessary in most cases to increase the O_2/coal ratios to well above stoichiometric levels in order to achieve the maximum extent of burnout.

To increase the residence times, additional sections of radiantly heated furnaces were inserted between the RF-heated furnace of the SRT-RCFR and the quench/transpiration/centripeter/filter section of the reactor. Figure A.13 schematically shows the addition of two such sections. Each 30-cm-long section contains four $MoSi_2$ heater elements (Kanthal Super 1800-3/6) configured in a U shape. The 3-mm-diameter elements are 27 cm long and the legs are separated by 4 cm. The 6-mm-diameter leads are bent at 90° and exit the high-pressure reactor radially through high-temperature feedthroughs. The elements are positioned within cylindrical high-temperature insulation of 10 cm ID and 20 cm OD (Zircar alumina Type SALI and Type ALC-AA). The temperature within each central cavity was monitored with a Type W5 thermocouple mounted within a closed titanium sheath. The high-current, low-voltage power supplies for the Kanthal heaters were controlled automatically based on the thermocouple outputs to maintain furnace temperatures near the set point of 1400°C.

In the NBFZ tests, it had been observed that flow meters and pressure gauges exhibited fluctuations during the higher pressure runs. These fluctuations might be attributed to turbulence in the flow and combustion, although turbulence frequencies are usually too high to observe on digital instruments, and so the fluctuations might more properly be assigned to unsteady combustion. In any case, during the series of HPBO tests on Pittsburgh #8 coal with argon carrier gas, this phenomenon became more apparent. In fact, in the 10 atm tests the flow became so unsteady as to exhibit complete reversal. This can be concluded from the fact that in several tests the coal in the feeder hopper began burning after being ignited by burning coal particles from the reactor that were swept back into the feeder. Since the feeder was filled to high pressure by an argon/oxygen mixture, the ignited coal in the hopper continued to burn for several minutes until the oxygen in the feeder was consumed.

The solution to this problem was to switch from premixed entrainment and sheath flows to a pure argon entrainment flow, with all oxygen introduced through the sheath. This approach was first used near the end of the series for Pittsburgh #8 coal with argon entrainment gas, and was implemented by simply turning off the entrainment O_2 flow and increasing the sheath O_2 flow. Tests Pitt-223 and Pitt-224 in that series were conducted in this manner, while all other tests in the series used premixed entrainment flows.

Because the sheath and entrainment flows joined only 5 cm below the furnace in the original flow system design shown in Figure A.13, we were concerned that lack of mixing of oxygen within the core flow would delay onset of combustion and retard burnout. To mitigate this

problem, the injector was redesigned so that mixing began 15 cm below the furnace. This new injector was installed at run Pitt-236, and all subsequent HPBO experiments were conducted using inert entrainment gas, with 100% of the oxygen injected through the sheath flow.

Other aspects of the reactor remained the same as for the NBFZ tests. The RF-heated furnace section was pre-heated to 1570°C. The graphite wall temperature increased during the run, but the RF power was manually adjusted to limit the temperature rise to approximately 1600°C. Because of the more extensive soot burnout during these HPBO tests, it was not necessary to use the cylindrical "soot filter".

A test series for each coal and pressure consisted of five to nine runs made to cover a range of residence times. Tests were conducted with no furnace extensions, so as to reproduce the NBFZ conditions, and with one, two, and in one case three, extensions in place. The typical inlet flow velocity was 30 cm/s, which gave nominal residence times of 517, 1867, 2967, and 4000 ms for 0, 1, 2, and 3 extensions. However, higher velocities were also used to give nominal residence times as short as 172 ms, as well as to provide residence times intermediate between the nominal values. Little difference was found in the extent of burnout with two versus three extensions, and so only the first set of experiments conducted with Pitt #8 coal in argon carrier gas used the third extension.

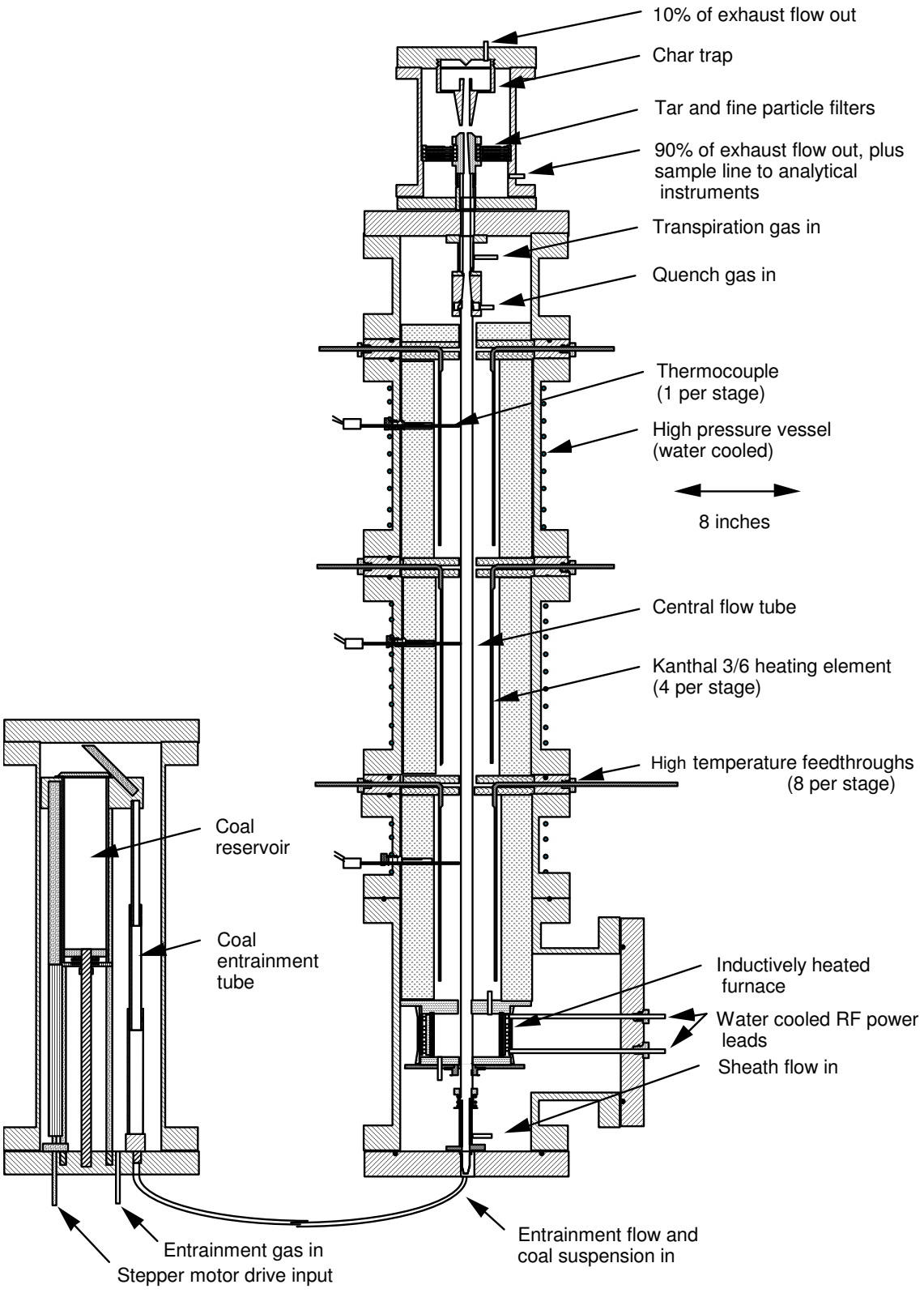

Figure A.13. SRI's Long Residence Time Radiant Coal Flow Reactor (LRT-RCFR)

A.2.2 Product Analysis Techniques

Analysis techniques for the HPBO experiments were generally the same as for the NBFZ experiments, with one exception. Because of the perceived importance of making accurate measurements of NO production, we added a California Analytical Instruments Model 600-CLD sensor to the analytical suite. This sensor uses chemiluminescent detection to achieve accurate NO and NO_x measurements from <1 ppm to 1,000 ppm. A pump within this instrument drew the sample gas from the main exhaust gas stream after its pressure had been dropped to 1 atm.

A second small difference from the NBFZ experiments concerns the analyses of the fine particles trapped on the quartz paper filters. The NBFZ experiments showed that these fines contained little or no tar. In those experiments, the fines were generated in sufficient quantity that they could be submitted for analysis, which showed that they consisted of a combination of soot and ash. It was also noted above that when oxygen/coal ratios approached stoichiometric, the soot burnout ratio varied from 76% to 93%. In the HPBO experiments, which involved extended residence times, the quantity of fines continued to diminish to the point where there was no longer enough material available to permit its analysis. Thus it was necessary to estimate the compositions of fines, which entered the calculations of the carbon elemental balances as well as the ash balances. Accordingly, it was assumed that they consisted of 40% carbon/60% ash for the shorter residence time tests, increasing to 100% ash for longer residence times. Although this assignment was somewhat arbitrary, the percentage of fines was always small enough that little uncertainty was introduced into the balance calculations.

The extensive burnout conditions of the HPBO tests caused the yields of hydrocarbons, H_2, NH_3, and HCN to be very small. In fact, in all but a few cases the hydrocarbon and H_2 yields were too small to measure, and the accuracies of the NH_3 and HCN yield measurements were often limited.

A.2.3 Test Conditions

The same three coals were tested as in the NBFZ tests. The test conditions were extended, however, to include low-pressure tests (p = 0.2 MPa) and three series of Pitt coal using CO_2 as the carrier gas instead of argon. The original intent was to use N_2 as the primary carrier gas, and a number of tests with PRB coal were also conducted using N_2.

The complete HPBO program consisted of eleven test series. Pitt #8 coal was tested at 0.2, 1, 2, and 3 MPa using argon carrier gas, and at 0.2, 1, and 2 MPa using CO_2 carrier gas. The Illinois #6 and PRB coals were tested at 0.2 and 2 MPa using argon carrier. Specific test conditions, and some characterizations for the solid product yields, are presented in Tables A.10-A.13.

A.2.4 Data Analyses

Data collection and analyses proceeded in the same way as for the NBFZ tests, with two exceptions. The first difference is in the graphical data presentation. Whereas in each NBFZ test series the nominal residence time was held constant and results were plotted versus the varying O_2/coal ratio, in the HPBO tests the residence time was the primary variable and results were

plotted versus residence time. In each of the test series, most of the tests were conducted at approximately the same O_2/coal ratio that provided a stoichiometric ratio near 1.15, but in some tests a higher ratio was used, particularly to achieve the maximum burnout. Attention should be paid to that parameter when evaluating the results.

Table A.10(a). HPBO Run Data for Pittsburgh #8 Coal with Argon Entrainment Gas

Run No.	Pressure (atm)	Furnace Length (cm)	Res. Time (ms)	Coal Feed Rate (g/min)	Coal Susp'n Loading (Wt %)	O_2 Conc. (Wt %)	O_2/ Coal (Wt. %)	Wt. Loss (%AR)	Retained Ash (Wt%)	Primary Char Yield (Wt%)[a]	C Yield In Char (Wt%)[b]	Max-imum Ash (Wt%)[c]	Carbon Content of Char (%)[d]	Ash Content of Char (%)[e]
180	2	120	2676	0.74	7.6	23.5	309	89	64	11	4.0	77	26	72.8
183	2	88	1956	0.66	6.8	19.1	282	91	66	9.0	1.1	83	8.5	90.9
197	2	56	1244	0.62	6.4	20.3	319	89.4	59	10.6	4.45	77	29.6	69.1
198	2	15.5	344	0.68	7.0	19.8	282	82.8	43	17.2	17.0	55	68.6	30.4
199	2	15.5	172	1.44	7.5	19.8	264	74.9	64	25.1	24.1	77	67.8	31.4
200	2	15.5	115	2.25	7.9	22.9	290	72.2	90	27.8	23.3	>100	59.1	40.0
206	2	15.5	86	2.83	7.4	20.3	275	64.9	63	35.1	38.2	67	76.7	22.1
226	2	88	1977	0.75	7.6	20.3	266	90.0	42	10.0	6.6	57	46.3	51.6
173	10	120	4000	1.72	5.4	19.5	365	96.7	20	3.3	1.3	28	26.6	72.9
190	10	89	2967	1.52	4.7	17.0	361	88.9	67	11.1	3.8	92	24.4	75.1
204	10	15.5	129	5.97	4.7	20.0	431	86.4	33	13.6	13.3	47	13.3	30.0
207	10	15.5	129	9.75	7.6	22.8	300	74.5	70	25.5	23.4	81	64.8	34.1
208	10	15.5	172	7.86	8.2	17.8	217	68.2	69	31.8	32.5	90	72.0	26.9
209	10	15.5	258	5.14	8.0	19.9	247	77.8	84	22.2	16.7	93	52.8	46.4
210	10	15.5	517	2.53	7.9	21.6	275	78.1	53	21.9	21.6	67	69.2	29.6
221	10	56	1867	2.52	8.0	24.2	303	88.2	68	11.8	4.9	79	29.1	70.4
223	10	89	2967	2.53	7.9	21.4	271	89.4	36	10.6	8.6	46	57.4	41.6

Table continues on next page.

Table A.10(b). HPBO Run Data for Pittsburgh #8 Coal with Argon Entrainment Gas (Continued)

Run No.	Pressure (atm)	Furnace Length (cm)	Res. Time (ms)	Coal Feed Rate (g/min)	Coal Susp'n Loading (Wt %)	O_2 Conc. (Wt %)	O_2/ Coal (Wt. %)	Wt. Loss (%AR)	Retained Ash (Wt%)	Primary Char Yield (Wt%)[a]	C Yield In Char (Wt%)[b]	Max-imum Ash (Wt%)[c]	Carbon Content of Char (%)[d]	Ash Content of Char (%)[e]
169	20	120	4000	1.76	2.72	14.6	538	92.0	49	8.0	2.8	59	24.6	74.9
191	20	89	2967	1.59	2.45	13.4	548	91.6	67	8.4	0.2	92	1.6	98.3
205	20	15.5	517	1.63	2.51	16.1	643	93.7	49	6.3	0.4	67	4.2	95.4
211	20	15.5	517	3.29	5.07	14.0	276	81.6	57	18.4	Na	na	Na	Na
212	20	15.5	259	6.39	4.92	16.1	326	81.7	42	18.3	na	na	na	na
213	20	15.5	259	6.17	4.73	9.9	209	68.0	75	32.0	34.3	90	71.2	27.2
214	20	15.5	518	3.24	4.97	14.2	286	81.1	66	18.9	15.1	78	56.3	42.9
218	20	56	1867	1.55	2.32	5.53	239	82.7	66	17.3	12.8	70	52.3	46.9
225	20	89	2967	1.52	2.28	5.54	243	87.7	48	12.3	9.0	54	51.5	47.8
193	30	89	2967	1.61	1.63	8.26	506	93.1	55	6.9	0.1	72	1.0	98.9
194	30	56	1867	1.65	1.67	9.38	562	90.6	73	9.4	0.3	86	2.4	95.7
215	30	15.5	517	5.04	5.14	10.7	208	75.0	88	25.0	19.6	99	55.3	43.6
217	30	56	1867	1.53	1.52	3.44	226	82.9	47	17.1	15.8	50	65.0	34.2
224	30	89	2967	1.50	1.50	3.32	222	80.2	55	19.8	18.2	61	64.6	34.3

Notes:

[a] Primary char yield on an as-received basis. Equals total char weight divided by total coal sample weight. Equals 1 – Wt. Loss

[b] Percent of carbon in coal sample retained in char.

[c] Max. ash equals ash in char plus assumption that all fine particles are ash. This typically overestimates recovered ash.

[d] Percent of char that is carbon (from Huffman analysis).

[e] Percent of char that is ash (from Huffman analysis).

Table A.11. HPBO Run Data for Pittsburgh # 8 Coal with CO_2 Entrainment Gas

Run No.	Pressure (atm)	Furnace Length (cm)	Res. Time (ms)	Coal Susp'n Loading (Wt %)	O_2 Conc. (Vol %)	O_2/ Coal (Wt. %)	Wt. Loss (%AR)	Retained Ash (Wt%)	Primary Char Yield (Wt%)[a]	C Yield In Char (Wt%)[b]	Maximum Ash (Wt%)[c]	Carbon Content of Char (%)[d]	Ash Content of Char (%)[e]
242	2	89	1977	9.37	36	410	88.9	35	11.1	9.3	49	59.0	39.2
249	2	89	1977	7.3	20	214	86.1	70	13.9	7.4	73	37.4	62.1
250	2	56	1244	7.0	26	226	85.9	53	14.1	10.7	54	53.3	46.1
257	2	15.5	344	7.8	18	214	79.2	51	20.8	20.4	55	69.2	30.4
258	2	15.5	172	7.1	21	267	75.1	53	24.9	25.8	55	72.9	26.0
259	2	15.5	115	7.4	21	225	70.4	48	29.6	33.1	51	78.8	20.0
263	2	56	700	7.7	21	215	84.3	43	15.7	14.5	46	65.1	33.9
239	10	89	2967	4.9	21	311	92.4	48	7.6	2.5	55	22.7	77.0
246	10	89	2967	7.1	27	415	93.8	55	6.2	8.9	65	47.5	51.7
252	10	56	1867	7.7	27	196	88.5	50	11.5	7.5	54	45.9	49.8
256	10	15.5	517	7.9	27	214	81.7	55	18.3	16.0	61	61.5	37.2
260	10	15.5	258	7.5	29	214	68.9	48	30.1	35.0	60	79.3	18.9
262	10	56	1100	8.0	21	218	87.5	45	12.5	9.8	52	54.9	44.0
243	20	89	2967	2.2	12.3	349	91.5	68	8.5	0.2	76	1.8	98.2
244	20	89	2967	2.0	7.6	239	89.6	63	10.4	3.6	73	24.8	74.7
253	20	56	1867	2.4	7.6	154	73.8	75.8	26.2	23.5	81	63.1	35.7
254	20	15.5	517	2.4	7.6	153	48.9	86.1	51.1	58.6	92	77.7	20.0
261	20	56	1100	2.1	6.7	189	62.3	80.2	37.7	38.1	89	71.1	26.2

See footnotes to Table A.10.

Table A.12. HPBO Run Data for PRB Coal with Argon Entrainment Gas

Run No.	Pressure (atm)	Furnace Length (cm)	Res. Time (ms)	Coal Feed Rate (g/min)	Coal Susp'n Loading (Wt %)	O_2 Conc. (Wt %)	O_2/ Coal (Wt. %)	Wt. Loss (%AR)	Retained Ash (Wt%)	Primary Char Yield (Wt%)[a]	C Yield In Char (Wt%)[b]	Maximum Ash (Wt%)[c]	Carbon Content of Char (%)[d]	Ash Content of Char (%)[e]
264	2	15.5	115	2.49	9.62	19.1	198	83.4	64	16.6	18.9	64	80	19.3
265	2	15.5	172	1.67	8.7	17.4	199	86.5	60	13.5	14.9	69	77	22.3
266	2	15.5	344	0.83	9.7	23.1	237	97.3	20	2.7	2.4	29	62	37
272	2	56	622	1.66	8.2	17.8	218	96.4	34	3.6	2.6	56	51	47
271	2	56	1244	0.83	7.9	17.4	220	98.4	24	1.6	0.5	43	21	78
273	2	88	1956	0.83	8.3	19.5	235	98.6	26	1.4	0.1	40	7	93
267	20	15.5	517	1.5	2.15	5.0	232	81.2	83	18.8	20.3	89	76	22
270	20	56	1244	2.25	2.2	4.5	204	90.8	54	9.2	9.0	75	69	29
269	20	56	1867	1.5	2.18	4.16	191	94.6	46	5.4	4.2	71	55	43
275	20	88	2933	1.5	2.25	8.0	355	94.2	75	5.8	2.6	94	32	65
276	20	88	2933	1.5	2.17	17.1	790	98.1	37	1.9	0.02	64	0.9	99

See footnotes to Table A.10.

Table A.13. HPBO Run Data for Illinois #6 Coal with Argon Entrainment Gas

Run No.	Pressure (atm)	Furnace Length (cm)	Res. Time (ms)	Coal Feed Rate (g/min)	Coal Susp'n Loading (Wt %)	O_2 Conc. (Wt %)	O_2/ Coal (Wt. %)	Wt. Loss (%AR)	Retained Ash (Wt%)	Primary Char Yield (Wt%)[a]	C Yield In Char (Wt%)[b]	Maximum Ash (Wt%)[c]	Carbon Content of Char (%)[d]	Ash Content of Char (%)[e]
298	2	15.5	172	1.73	8.27	25.7	311	90.8	25.9	9.2	7.44	34	50.2	49.1
297	2	15.5	344	0.87	9.01	23.9	265	89.6	25.2	10.4	9.55	31	56.9	42.3
290	2	56	622	1.73	8.01	20.9	261	90.4	49.1	9.6	1.51	60	9.8	89.5
288	2	56	1244	0.86	8.30	23.3	281	87.9	44.4	12.1	6.60	53	33.6	63.7
296	2	88	1600	1.06	8.94	24.3	272	91.1	48.0	8.9	0.81	60	5.6	93.9
286	2	88	1956	0.87	8.37	21.2	254	91.1	50.1	8.9	0.27	62	1.9	97.9
287	2	88	1956	0.88	8.69	25.9	298	92.9	36.1	7.1	1.11	45	9.7	89.2
299	20	15.5	517	1.50	2.17	5.22	241	78.5	43.7	21.5	22.0	53	63.3	35.5
292	20	56	1244	2.25	2.18	5.94	273	86.3	54.6	13.7	6.6	62	29.8	69.4
291	20	56	1867	1.50	2.17	5.51	254	89.3	54.3	10.7	2.01	62	11.6	88.0
295	20	88	2400	1.83	2.22	5.44	245	87.6	67.8	12.4	0.88	78	4.4	95.4
294	20	88	2933	1.50	2.16	5.72	264	93.1	39.6	6.9	0.03	43	0.23	99.6
285	20	88	2933	1.47	2.00	15.48	774	91.8	47.0	8.2	0.06	47	0.45	99.5

See footnotes to Table A.10.

The second difference was in the accounting of unmeasured or undermeasured species. As noted for the NBFZ tests, no measurements of sulfur-containing species were made. For those tests, NEA assumed the complete conversion of coal sulfur to H_2S or SO_2 depending on the stoichiometric ratio, as indicated in Tables A.4-A.9. The direct treatment of sulfur in the HPBO data analysis was omitted until the final two test series on Illinois #6 coal. The level of sulfur in this coal (10.74% DAF) was so high that it was difficult to assess the quality of mass and elemental balances in individual tests without accounting for the sulfur product. Therefore, since all the HPBO tests used oxygen in excess, it was assumed that 100% of the sulfur in coal was converted to SO_2. This assumed product species contributed to mass balance, and also to the oxygen elemental balance.

The spreadsheet revised to include SO_2 formation was used to analyze all the Illinois #6 HPBO tests. Since Pittsburgh #8 coal also has a relatively high sulfur content (6.37% DAF), we also went back and re-analyzed the Pittsburgh #8 HPBO tests with both argon and CO_2 carrier gas. PRB coal has very low sulfur (0.56% DAF), and so sulfur was ignored in the PRB HPBO tests.

In addition to performing elemental analyses and calculation of elemental balances, we also calculated an ash balance. The main component of ash was found in char, and its magnitude was determined from the analysis of ash in each char sample by Huffman Laboratories, coupled with the char yield. It was also assumed that some fraction of the fine particles trapped on the filters was ash. This fraction ranged from 60% to 100%, as described above. The total ash recovery was the sum of the char ash and the fine particle ash. These ash balance values are listed in Tables A.10-A.13 as “maximum ash”; they range from 28% to 100%, but average about 60%. “Missing ash” must be assumed to have deposited on the flow tube walls either within the reactor or in the short sections that include the quench nozzle, the tubing, and the converging centripeter nozzle.

A.2.5 Results

Combustion Products

The key results in terms of product yields as a function of O_2/coal ratio and residence time are presented in Tables A.14– A.24. The results in each table are separated into groups with similar O_2/coal ratios, to call attention to the use of significantly different stoichiometries, as noted above.

In contrast to the NBFZ results of Tables A.4–A.9, no distinction is made between measured and corrected results. Rather, all results have undergone minor correction as follows:

- The concentrations of CO_2 in the exhaust gas stream, as measured by the California Avionics NDIR sensor, were modified as required to achieve a carbon elemental balance close to unity. The other significant components of the carbon balance were from CO in the exhaust gas stream and from carbon in char and soot.
- The concentrations of water vapor in the exhaust gas stream, as measured by the Rosemount Engineering NDIR, were modified as required to achieve a hydrogen elemental balance close to unity. Water vapor was the major source of hydrogen, with small contributions coming from the hydrogen in char and, occasionally, from hydrogen in hydrocarbons, H_2, NH_3, and HCN.

- The oxygen concentration in the exhaust gas stream, as measured by the California Analytics paramagnetic sensor, was modified slightly as required to achieve an O balance near unity. This consumption of oxygen from the inlet gas stream was balanced against oxygen found in CO, CO_2, and H_2O. The O balance was adjusted after the C and H balances had been achieved.

As noted in Tables A.14–A.24, these refinements typically led to achievement of C/H/O balances to within 1%. After this process was completed, one final adjustment to the results was made by adding into the mass balance the "missing ash" described above. This correction could be quite substantial, since the proximate ash concentrations in the tested coals were 12.34% for Pitt, 17.42% for Ill #6, and 5.01% for PRB. However, upon adding these missing ash masses to the product masses, the mass balance closed to within 2% in every case, as shown in Tables A.14–A.24 (in fact, in most cases the closures are to 99±1%). Thus, we were able to achieve excellent mass and elemental balances for the entire HPBO series of tests. In fact, the mass balances were very sensitive to the adjustments in CO_2, H_2O, and O_2, and the remarkable accuracy of all the mass closures justifies the corrections.

Table A.14. Results for HPBO Tests of Pittsburgh #8 Coal with Argon Entrainment Gas at 0.2 MPa[a]

Run No.	206	200	199	198	197	183	226	180
Res. Time (ms)	86	115	172	344	1244	1956	1977	2676
O_2/Coal (Wt%)	275	290	264	282	319	282	266	309
CO_2	175	221	224	244	283	293	277	285
CO	5.5	4.3	1.7	0.3	0.1	0.1	0.6	0.1
H_2O	47.8	47.5	48.2	48.2	47.5	48.0	47.2	47.6
CH_4	0	0	0	0	0	0	0	0
C_2	0	0	0	0	0	0	0	0
C_3	0	0	0	0	0	0	0	0
Oils	0	5E-3	0	0	0	0	0	0
H_2	0	4E-2	0	0	0	0	0	0
HCN	9.1E-6	9.3E-6	2.3E-5	1.3E-5	0	2.5E-5	0	1.1E-5
NH_3	0	0	0	0	0.096	0.047	0	0.076
NO	0.42	0	0	0	0.52	0.46	1.09	1.53
Char+Ash	31.3	19.1	19.7	13.9	3.8	0.9	5.6	3.4
Soot+Ash	2.9	3.6	4.0	2.1	2.5	2.3	2.2	1.8
SO_2[b]	12.7	12.7	12.7	12.7	12.7	12.7	12.7	12.7
ΣMass[c]	0.95	0.99	0.96	0.92	0.96	0.96	0.93	0.96
ΣC	1.00	1.00	1.00	1.00	1.00	1.00	1.00	1.00
ΣH	1.00	1.00	1.00	1.00	1.00	1.00	1.00	1.00
ΣO	1.00	1.00	1.00	1.00	1.00	1.00	1.00	1.00
X_{Char} (%)	18	50	48	63	90	96	86	91

[a] All yields reported as Wt% DAF

[b] Assumption based on complete conversion of coal S to SO_2

[c] Accounting for missing ash brings mass balances to 0.99±0.01

Table A.15. Results for HPBO Tests of Pittsburgh #8 Coal with Argon Entrainment Gas at 1 MPa[a]

Run No.	207	204	208	209	210	221	223	109	173
Res. Time (ms)	129	140	172	258	517	1867	2967	2975	4000
O_2/Coal (Wt%)	273	431	217	247	275	303	271	361	365
CO_2	195	242	165	211	205	269	249	281	293
CO	16.4	4.9	16.2	19.9	12.1	7.1	11.0	2.6	0.6
H_2O	45.7	47.7	45.0	44.5	45.7	47.7	48.1	48.2	48.5
CH_4	7.2E-3	5.9E-3	4.9E-3	0	0	0	0	0	0
C_2	5.4E-3	2.1E-3	3.1E-3	0	0	0	0	0	0
C_3	0	0	0	0	0	0	0	0	0
Oils	8.4E-3	1.2E-2	3.7E-3	0	0	0	0	0	0
H_2	0.18	0	0.27	0.37	0.24	0.07	0.01	0	0
HCN	1.5E-3	0	2.7E-4	4.1E-4	1.4E-3	1.7E-3	6.6E-4	6.6E-4	0
NH_3	0	0	0	0	0	0	0	0	0
NO	0	0.70	0	0	0	0.32	0.25	1.01	0
Char+Ash	19.3	11.0	26.7	13.7	17.7	4.0	7.1	3.2	1.0
Soot+Ash	3.0	4.0	5.8	2.6	4.0	2.0	3.0	3.5	1.1
SO_2[b]	12.7	12.7	12.7	12.7	12.7	12.7	12.7	12.7	12.7
ΣMass[c]	.95	.93	.98	.97	.94	.96	.92	.98	.89
ΣC	1.00	1.00	1.00	1.00	1.00	1.00	1.00	1.00	1.00
ΣH	1.00	1.00	1.00	1.00	1.00	1.00	1.00	1.00	1.00
ΣO	1.00	1.00	1.00	1.00	1.00	1.00	1.00	1.00	1.00
X_{Char} (%)	49	72	32	65	55	90	82	92	97

[a] All yields reported as Wt% DAF
[b] Assumption based on complete conversion of coal S to SO_2
[c] Accounting for missing ash brings mass balances to 0.99±0.01

Table A.16. Results for HPBO Tests of Pittsburgh #8 Coal with Argon Entrainment Gas at 2 MPa[a]

Run No.	213	212	211	214	218	225	205	191	169
Res. Time (ms)	270	259	517	525	1867	2967	525	1867	2967
O_2/Coal (Wt%)	209	350	276	285	239	243	643	548	538
CO_2	164	222	213	213	236	250	293	296	285
CO	13.9	9.4	20.3	22.5	13.8	12.8	1.0	0.2	2.1
H_2O	42.7	46.8	46.6	45.9	48.1	47.3	46.7	48.6	48.3
CH_4	6.7E-2	0	0	0	0	0	1.9E-3	0	0
C_2	3.1E-2	0	0	0	0	0	1.82E-2	0	0
C_3	0	0	0	0	0	0	0	0	0
Oils	0.12	0	0	0	0	0	0.06	0	0
H_2	0.35	0	0	0.24	0	0.14	0.18	0	0
HCN	0	1.0E-3	1.7E-3	0	1.1E-3	5.5E-3	0	1.6E-3	0
NH_3	0	0	0	0	0	0	0	1.2E-2	0
NO	0	0	0	0	0.25	0.26	0	0.90	0
Char+Ash	28.4	15.1	13.1	12.3	10.5	7.3	0.3	0.2	2.3
Soot+Ash	4.2	2.8	2.8	3.0	0.7	1.1	2.5	3.5	1.5
SO_2[b]	12.7	12.7	12.7	12.7	12.7	12.7	12.7	12.7	12.7
ΣMass[c]	0.97	0.93	0.95	0.96	0.95	0.94	0.96	0.98	0.94
ΣC	1.00	1.00	1.00	1.00	1.00	1.00	1.00	1.00	1.00
ΣH	1.00	1.00	1.00	1.00	1.00	1.00	1.00	1.00	1.00
ΣO	1.00	1.00	1.00	1.00	1.00	1.00	1.00	1.00	1.00
X_{Char} (%)	64			71	75	83	99.2	99.6	94.6

[a] All yields reported as Wt% DAF
[b] Assumption based on complete conversion of coal S to SO_2
[c] Accounting for missing ash brings mass balances to 0.99±0.01

Table A.17. Results for HPBO Tests of Pittsburgh #8 Coal with Argon Entrainment Gas at 3 MPa[a]

Run No.	**215**	**217**	**224**	**194**	**194**
Res. Time (ms)	517	1867	2967	1867	2967
O_2/Coal (Wt%)	208	226	222	562	506
CO_2	182	216	220	296	296
CO	32.2	20.5	13.8	0	0.2
H_2O	42.5	44.1	47.0	48.2	48.2
CH_4	0.012	0	0	0	0
C_2	0	0	0	0	0
C_3	0	0	0	0	0
Oils	9.1E-3	0	0	0	0
H_2	0.56	0.43	0.10	0	0
HCN	1.7E-3	1.2E-3	1.4E-3	2.2E-3	2.2E-3
NH_3	0	0	0	2.4E-2	4.9E-2
NO	0	0	0.16	0.85	0.95
Char+Ash	16.2	12.9	15.0	0.5	0.1
Soot+Ash	3.0	0.8	1.0	1.7	2.4
SO_2[b]	12.7	12.7	12.7	12.7	12.7
ΣMass[c]	0.98	0.93	0.94	0.98	0.97
ΣC	1.00	1.00	1.00	1.00	1.00
ΣH	1.00	1.00	1.00	1.00	1.00
ΣO	1.00	1.00	1.00	1.00	1.00
X_{Char} (%)	70	76	72	99.5	99.8

[a] All yields reported as Wt% DAF
[b] Assumption based on complete conversion of coal S to SO_2
[c] Accounting for missing ash brings mass balances to 0.99±0.01

Table A.18. Results for HPBO Tests of Pittsburgh #8 Coal with CO_2 Entrainment Gas at 0.2 MPa[a]

Run No.	**259**	**258**	**257**	**263**	**250**	**249**	**242**
Res. Time (ms)	115	172	344	700	1244	1977	2050
O_2/Coal (Wt%)	225	236	214	215	226	214	410
CO_2	192	215	222	245	238	246	264
CO	2.7	2.1	7.8	4.6	16.7	17.7	0.1
H_2O	48.3	47.9	18.2	48.2	48.4	48.0	47.8
CH_4	0	0	0	0	0	0	0
C_2	0	0	0	0	0	0	0
C_3	0	0	0	0	0	0	0
Oils	8.1E-3	1.8E-3	2.2E-3	1.8E-3	8.9E-3	0	0
H_2	0	0	3.0E-2	1.6E-3	2.4E-2	5.2E-2	0
HCN	0	0	0	2.0E-4	1.2E-3	3.7E-4	0
NH_3	0	0	0	0	0	0	0
NO	1.12	1.14	0.96	0.91	0.53	0.52	1.13
Char+Ash	27.2	21.2	16.6	11.9	8.7	6.1	7.8
Soot+Ash	1.2	1.0	1.0	0.7	0.3	0.5	3.3
SO_2[b]	12.7	12.7	12.7	12.7	12.7	12.7	12.7
ΣMass[c]	0.93	0.94	0.93	0.92	0.94	0.95	0.93
ΣC	1.00	1.00	1.00	1.00	1.00	1.00	1.00
ΣH	1.00	1.00	1.00	1.00	1.00	1.00	1.00
ΣO	1.00	1.00	1.00	1.00	1.00	1.00	1.00
X_{Char} (%)	28	44	56	69	77	84	80

[a] All yields reported as Wt% DAF
[b] Assumption based on complete conversion of coal S to SO_2
[c] Accounting for missing ash brings mass balances to 0.99±0.01

Table A.19. Results for HPBO Tests of Pittsburgh #8 Coal with CO_2 Entrainment Gas at 1 MPa[a]

Run No.	260	256	262	252	246	239
Res. Time (ms)	259	517	1100	1867	2967	3000
O_2/Coal (Wt%)	214	214	218	196	228	311
CO_2	149	199	206	206	249	279
CO	27.4	30.0	37.9	43.0	13.1	6.6
H_2O	46.1	46.9	47.8	47.4	46.5	48.4
CH_4	0	0	0	0	0	0
C_2	0	0	0	0	0	0
C_3	0	0	0	0	0	0
Oils	2.49E-3	5.3E-3	0	1.8E-3	0	1.1E-2
H_2	0.030	0.114	0.042	0.078	0.023	0
HCN	0	1.8E-3	1.5E-3	4.3E-4	7.7E-4	2.6E-3
NH_3	0	0	0	0	0	0
NO	0.26	0.20	0.32	0.18	0.13	0.26
Char+Ash	29.0	13.2	8.0	6.2	7.3	2.0
Soot+Ash	4.2	1.6	1.4	0.7	1.4	1.0
SO_2[b]	12.7	12.7	12.7	12.7	12.7	12.7
ΣMass[c]	0.94	0.94	0.93	0.92	0.94	0.93
ΣC	1.00	1.00	1.00	1.00	1.00	1.00
ΣH	1.00	1.00	1.00	1.00	1.00	1.00
ΣO	1.00	1.00	1.00	1.00	1.00	1.00
X_{Char} (%)	27	66	80	84	91	95

[a] All yields reported as Wt% DAF
[b] Assumption based on complete conversion of coal S to SO_2
[c] Accounting for missing ash brings mass balances to 0.99±0.01

Table A.20. Results for HPBO Tests of Pittsburgh #8 Coal with CO_2 Entrainment Gas at 2 MPa[a]

Run No.	**254**	**261**	**253**	**244**	**243**
Res. Time (ms)	517	1100	1867	2967	3000
O_2/Coal (Wt%)	153	189	154	239	349
CO_2	58	166	141	254	292
CO	36	8.9	54	19	2.1
H_2O	41.3	43.2	47.8	48.1	48.7
CH_4	0.245	0.144	0	0	0
C_2	0.16	0.011	0	0	0
C_3	0.031	0.021	0	0	0
Oils	0.147	0.012	0	0	0
H_2	0.106	0	0.030	0	0
HCN	1.2E-3	0	1.2E-3	1.2E-3	1.3E-3
NH_3	0	0	0	0	0
NO	0.092	0.162	0.093	0.146	0.241
Char+Ash	48.8	31.9	19.4	3.0	0.2
Soot+Ash	2.7	1.7	1.0	1.7	1.1
SO_2[b]	12.7	12.7	12.7	12.7	12.7
ΣMass[c]	0.98	0.98	0.96	0.95	0.96
ΣC	1.00	1.00	1.00	1.00	1.00
ΣH	1.00	1.00	1.00	1.00	1.00
ΣO	1.00	1.00	1.00	1.00	1.00
X_{Char} (%)	0	35	60	94	99.7

[a] All yields reported as Wt% DAF
[b] Assumption based on complete conversion of coal S to SO_2
[c] Accounting for missing ash brings mass balances to 0.99±0.01

Table A.21. Results for HPBO Tests of PRB Coal with N_2 and Argon Entrainment Gases at 0.2 MPa[a]

Run No.	115[d]	114[d]	116[d]	264	265	266	272	271	273
Res. Time (ms)	1190	1850	1890	115	172	344	622	1244	1956
O_2/Coal (Wt%)	207	308	227	198	199	237	218	220	235
CO_2	235	218	261	204	216	256	246	252	264
CO	18.7	24.1	5.9	6.2	6.2	4.8	11.3	10.8	4.3
H_2O	47.7	41.2	49.8	49.6	49.5	49.6	48.9	49.1	49.8
CH_4	0	0.042	0	0	0	0	0	0	0
C_2	0	0.020	0	0	0	0	0	0	0
C_3	0	0	0	0	0	0	0	0	0
Oils	3E-3	5E-3	7E-4	3E-4	0	0	0	0	0
H_2	0.23	0.96	0.05	0.03	0.03	0.05	0.12	0.11	0.05
HCN	3E-3	0.101	0	0	0	9E-5	7E-4	0	0
NH_3	4E-3	6E-3	1E-3	2E-3	9E-3	3E-2	2E-2	5E-3	0
NO	0.423	0.528	1.245	0.784	0.949	0.781	0.848	0.923	1.081
Char+Ash	2.0	3.5	0.2	14.1	11.12	1.8	2.0	0.4	0.1
Soot+Ash	1.3	2.4	1.3	2.1	1.8	0.7	1.3	1.0	0.7
SO_2[b]	1.12	1.12	1.12	1.12	1.12	1.12	1.12	1.12	1.12
ΣMass[c]	0.97	0.97	0.98	0.97	0.97	0.95	0.97	0.96	0.96
ΣC	1.00	1.00	1.00	1.00	1.00	1.00	1.00	1.00	1.00
ΣH	1.00	1.00	1.00	1.00	1.00	1.00	1.00	1.00	1.00
ΣO	1.00	1.00	1.00	1.00	1.00	1.00	1.00	1.00	1.00
X_{Char} (%)				71	77	96	96	99.2	99.8

[a] All yields reported as Wt% DAF
[b] Assumption based on complete conversion of coal S to SO_2. Not included in mass balance.
[c] Accounting for missing ash brings mass balances to 1.00±0.01
[d] N_2 entrainment gas.

Table A.22. Results for HPBO Tests of PRB Coal with N_2 and Argon Entrainment Gases at 2 MPa[a]

Run No.	**111[d]**	**113[d]**	**112[d]**	**119[d]**	**267**	**270**	**269**	**275**	**276**
Res. Time (ms)	517	1190	1867	2967	517	1244	1867	2933	2980
O_2/Coal (Wt%)	240	189	208	211	232	204	191	355	790
CO_2	147	168	170	202	195	227	201	260	271
CO	29.2	40.7	46.8	40.7	10.1	12.5	37.6	2.3	0.2
H_2O	40.9	41.3	40.5	45.8	47.2	48.9	47.4	48.9	50.3
CH_4	0.146	0.026	0.068	0	0	0.008	0	0	0
C_2	0.083	0.002	0.004	0	0	0.007	0	0	0
C_3	0.019	0	0	0	0	0	0	0	0
Oils	3.2E-2	7.1E-3	0	0	3.1E-1	6.2E-3	0	0	0
H_2	0.66	0.81	0.94	0.45	0.11	0.087	0.26	0	0
HCN	9.1E-2	1.8E-2	1.3E-1	0	1.5E-3	0	4.2E-3	0	0
NH_3	0.088	0.151	0.091	0.091	0.036	0.013	0.016	0.021	0.036
NO	0.076	0	0.007	0	0.200	0.206	0.170	0.317	0.422
Char+Ash	21.3	10.4	7.2	1.5	15.4	6.8	3.2	2.1	0
Soot+Ash	0.8	1.2	0.8	0.6	1.2	1.1	1.3	1.0	1.4
SO_2[b]	1.12	1.12	1.12	1.12	1.12	1.12	1.12	1.12	1.12
ΣMass[c]	0.99	1.00	1.00	0.99	0.98	0.98	0.97	0.98	0.97
ΣC	1.00	1.00	1.00	1.00	1.00	1.00	1.00	1.00	1.00
ΣH	1.00	1.00	1.00	1.00	1.00	1.00	1.00	1.00	1.00
ΣO	1.00	1.00	1.00	1.00	1.00	1.00	1.00	1.00	1.00
X_{Char} (%)					70	87	94	96	100

[a] All yields reported as Wt% DAF
[b] Assumption based on complete conversion of coal S to SO_2. Not included in mass balance.
[c] Accounting for missing ash brings mass balances to 0.99±0.01
[d] N_2 entrainment gas.

Table A.23. Results for HPBO Tests of Illinois #6 Coal with Argon Entrainment Gas at 0.2 MPa[a]

Run No.	**298**	**297**	**290**	**293**	**288**	**296**	**286**	**287**
Res. Time (ms)	172	344	622	933	1244	1600	1956	1956
O_2/Coal (Wt%)	311	265	260	282	283	258	254	298
CO_2	248	246	269	256	256	271	268	272
CO	1.9	1.5	0.7	0.9	0.1	0.5	3.9	0
H_2O	48.0	48.0	48.0	48.2	45.8	48.2	48.3	48.0
CH_4	0	0	0	0	0	0	0	0
C_2	0	0	0	0	0	0	0	0
C_3	0	0	0	0	0	0	0	0
Oils	0	4.7E-3	0	5.7E-3	0	6.7E-3	8.9E-4	0
H_2	3.1E-2	1.3E-2	0	0	0	1.8E-2	7.9E-3	0
HCN	4.4E-5	3.2E-4	4.9E-4	0	1.2E-3	4.5E-4	0	1.1E-4
NH_3	0	1.8E-2	3.8E-3	1.8E-2	4.2E-3	5.8E-3	2.7E-2	9.5E-3
NO	0.93	1.17	1.08	0.89	1.12	1.13	1.07	1.02
Char+Ash	5.7	7.3	1.2	3.6	5.3	0.7	0.2	0.9
Soot+Ash	2.8	1.7	2.6	3.7	2.0	2.8	2.6	1.8
SO_2[b]	20.94	20.94	20.94	20.94	20.94	20.94	20.94	20.94
ΣMass[c]	0.88	0.87	0.92	0.89	0.91	0.92	0.93	0.89
ΣC	1.00	1.00	1.00	1.00	1.00	1.00	1.00	1.00
ΣH	1.00	1.00	1.00	1.00	1.00	1.00	1.00	1.00
ΣO	1.00	1.00	1.00	1.00	1.00	1.00	1.00	1.00
X_{Char} (%)	88	84	98	92	69	99	99.6	98

[a] All yields reported as Wt% DAF
[b] Assumption based on complete conversion of coal S to SO_2
[c] Accounting for missing ash brings mass balances to 0.99±0.01

Table A.24. Results for HPBO Tests of Illinois #6 Coal with Argon Entrainment Gas at 2 MPa[a]

Run No.	299	292	291	295	294	285
Res. Time (ms)	517	1244	1867	2400	2933	2933
O_2/Coal (Wt%)	241	273	254	245	264	774
CO_2	192	252	260	266	273	275
CO	7.6	2.4	5.9	4.1	0.8	0
H_2O	47.3	47.5	48.3	48.1	48.4	48.3
CH_4	0.085	0	0	0	0	0
C_2	0.064	0	0	0	0	0
C_3	0.016	0	0	0	0	0
Oils	0.072	0	0	0	0	0
H_2	5.9E-3	5.5E-3	0	1.9E-2	0	0
HCN	1.2E-3	4.8E-4	1.4E-3	0	4.0E-3	0
NH_3	1.3E-3	6.0E-2	8.8E-3	2.4E-2	4.4E-3	1.3E-1
NO	0.30	0.33	0.30	0.32	0.21	0.51
Char+Ash	16.8	5.1	1.6	0.7	0	0.1
Soot+Ash	4.8	1.9	1.6	2.1	0.8	0
SO_2[b]	20.94	20.94	20.94	20.94	20.94	20.94
ΣMass[c]	0.91	0.92	0.92	0.95	0.89	0.90
ΣC	1.00	1.00	1.00	1.00	1.00	1.00
ΣH	1.00	1.00	1.00	1.00	1.00	1.00
ΣO	1.00	1.00	1.00	1.00	1.00	1.00
X_{Char} (%)	65	90	97	99	100	99.9

[a] All yields reported as Wt% DAF
[b] Assumption based on complete conversion of coal S to SO_2
[c] Accounting for missing ash brings mass balances to 0.99±0.01

The extent of char burnout achieved in these HPBO tests is illustrated by the graphs of Figure A.14. The four panels of this figure present the extent of char burnout versus the nominal test residence times for Pitt coal in argon entrainment gas, Pitt coal in CO_2 entrainment gas, PRB coal in argon, and Illinois coal in argon, respectively. The percent of char burnout, X_{char}, is based on the carbon yield in the char compared to the carbon yield in char under secondary pyrolysis conditions as determined in the NBFZ tests, as follows:

$$X_{char} = (1 - C_{char}/C_{char\text{-}2nd\ pyrolysis}) \times 100$$

Since no NBFZ runs were made at 0.2 MPa, nor were such runs made using CO_2 entrainment gas, estimates of the secondary pyrolysis yields were made for these cases. The resulting set of carbon yields in char under secondary pyrolysis conditions used to calculate the X_{char} values are summarized in Table A.25.

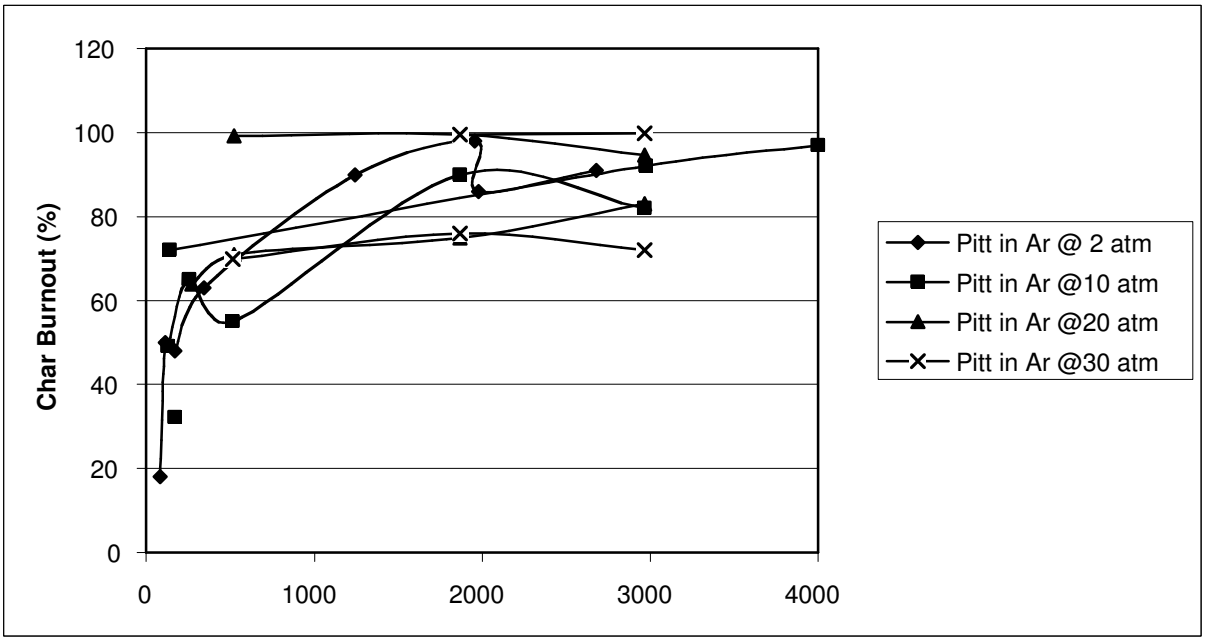

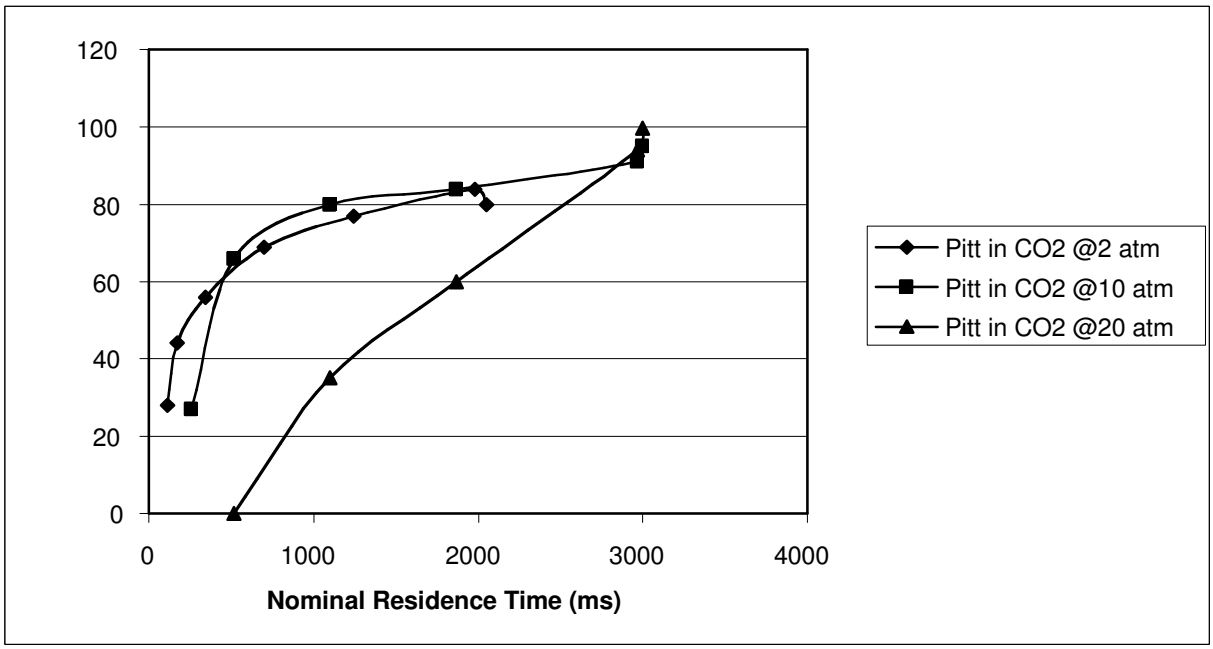

Figure A.14(a). Variation of Char Burnout with Nominal Residence Time

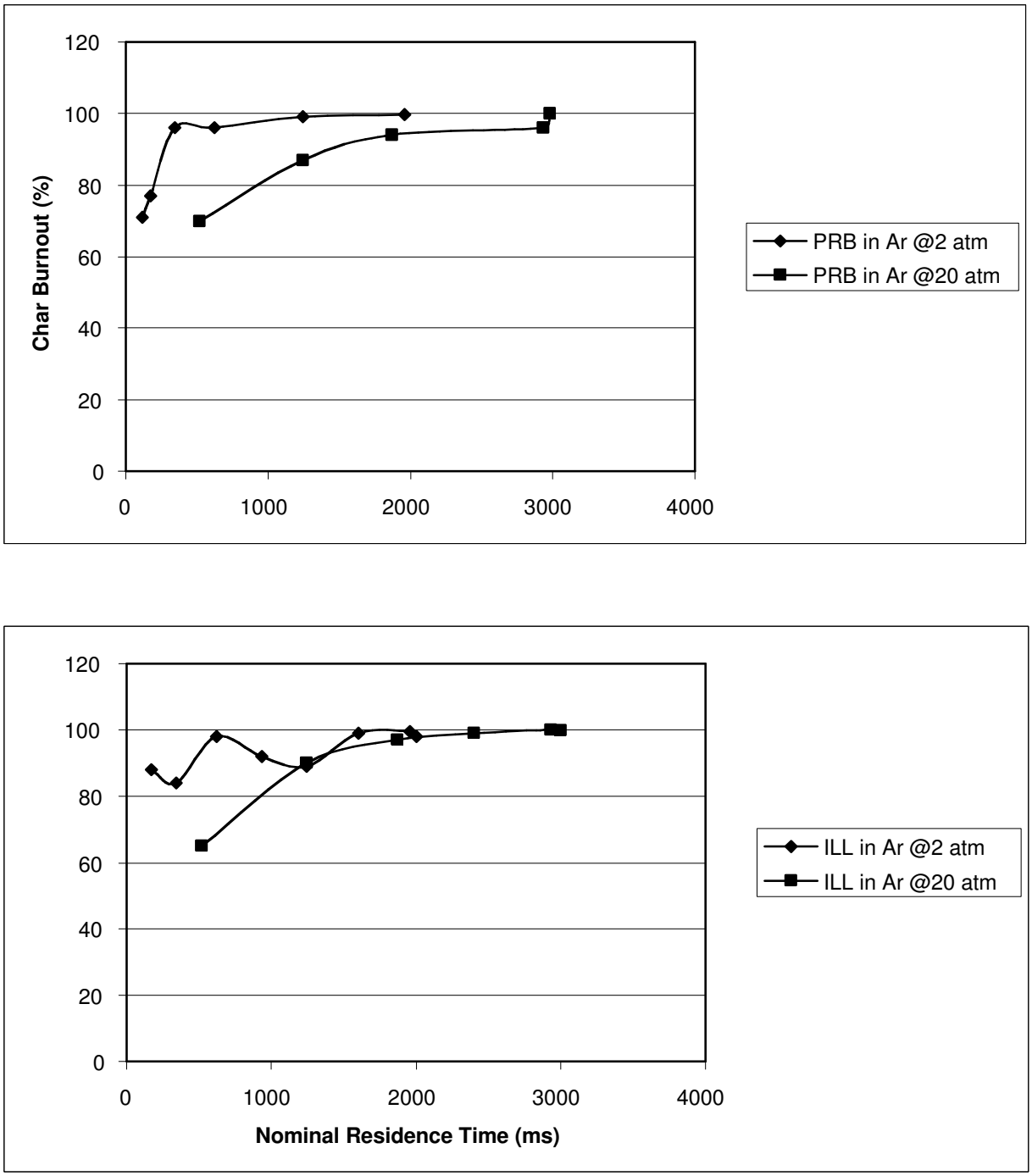

Figure A.14(b). Variation of Char Burnout with Nominal Residence Time (Continued)

Table A.25. Carbon Yields in Char Under Secondary Pyrolysis Conditions

Coal	Entrain Gas	Pressure (atm)	$C_{char\text{-}2nd\ pyrolysis}$	C_{coal}
Pittsburgh #8	Ar	2	46.3*	70.5
"	"	10	47.8	"
"	"	20	52.0	"
"	"	30	65.0	"
Pittsburgh #8	CO_2	2	46.3*	"
"	"	10	47.8*	"
"	"	20	58.6*	"
PRB	Ar	2	65*	70.1
"	"	20	68	"
Illinois #6	Ar	2	61*	69.2
"	"	20	63	"“

* Estimated

Because of the necessity of estimating some of the $C_{char\text{-}2nd\ pyrolysis}$ values, Niksa has calculated a coal burnout, which is defined in the same way as the char burnout except that the carbon content of coal, C_{coal} is used instead of $C_{char\text{-}2nd\ pyrolysis}$. The values of C_{coal} for our test coals are also given in Table 25. They are not much different than the values of $C_{char\text{-}2nd\ pyrolysis}$, and so values of X_{coal} will also not be much different from those of X_{char}.

The variations of char burnout with residence times in Figure A.14 show some irregularities and in some cases are double-valued, because the stoichiometry of the runs in any given series was not constant. With the effects of stoichiometry taken into account, the graphs show a consistent trend of increasing burnout with increasing residence time. The greatest variation in extent of burnout occurs for Pittsburgh #8 coal, where that parameter ranges from approximately 25% to >99%. The effect of pressure is not readily apparent for this coal except for the case of entrainment in CO_2 at 20 atm, where it appears that the high thermal capacity of this gas at high pressures suppressed the gas temperature significantly, and thus retarded the flame.

The extents of char burnout for both PRB and Illinois #6 coals were consistently higher than for Pittsburgh #8, and for both of these coals a modest effect of pressure can be seen. On the basis of these graphs alone, one would conclude that Illinois #6 coal burns most readily of the three coals tested, which is somewhat surprising since PRB is the lowest rank coal. However, for a more careful evaluation of the results, reference should be made to the analysis by Niksa [Niksa, 2004].

Char Samples

A major objective of this portion of the program was the production of char and ash samples for analysis by UConn and Brown. In keeping with this objective, the heavy particle samples collected from the char trap in each test were divided into three parts. One portion was sent to Huffman Laboratories for C/H/N and ash analyses. The other two portions were distributed to the two universities.

The carbon and ash fractions of each "char" sample are listed in Tables A.10–A.13 under the headings "carbon content of char" and "ash content of char." Scrutiny of the pairs of values will show that these two components typically constituted ~ 99% of the samples, indicating that H and N constituted < 1% in almost every case. The heavy particle products from the highest burnout cases had ash concentrations of ≥ 99%, but such high burnouts were rare, and, as noted above, were generally achieved only by addition of oxygen to well above stoichiometric levels.

Ash Retention and Release from Char

It is frequently assumed that the ash in pulverized coal is retained in the char until a substantial fraction of the carbon has been burned out from the char [Niksa, private communication]. Since all of our char samples were analyzed for ash content, it is straightforward to examine this assumption. Figure A.15 presents the results from the eleven HPBO test series in the form of plots of retained ash in the char versus retained carbon in the char. There is substantial scatter in the results, but it is clear that only a fraction of the ash, typically around 50%, is retained over the range of char burnout values the samples were subjected to in these tests. There is slight evidence that more ash is retained in the higher pressure tests than in those at low pressure, as shown most clearly for the 20 atm tests of Pittsburgh #8 coal in CO2 entrainment gas. There is also some evidence that ash release increases monotonically with carbon release, as shown again clearly for the 20 atm tests of Pitt in CO_2 and to a lesser extent in the PRB tests at 2 atm.

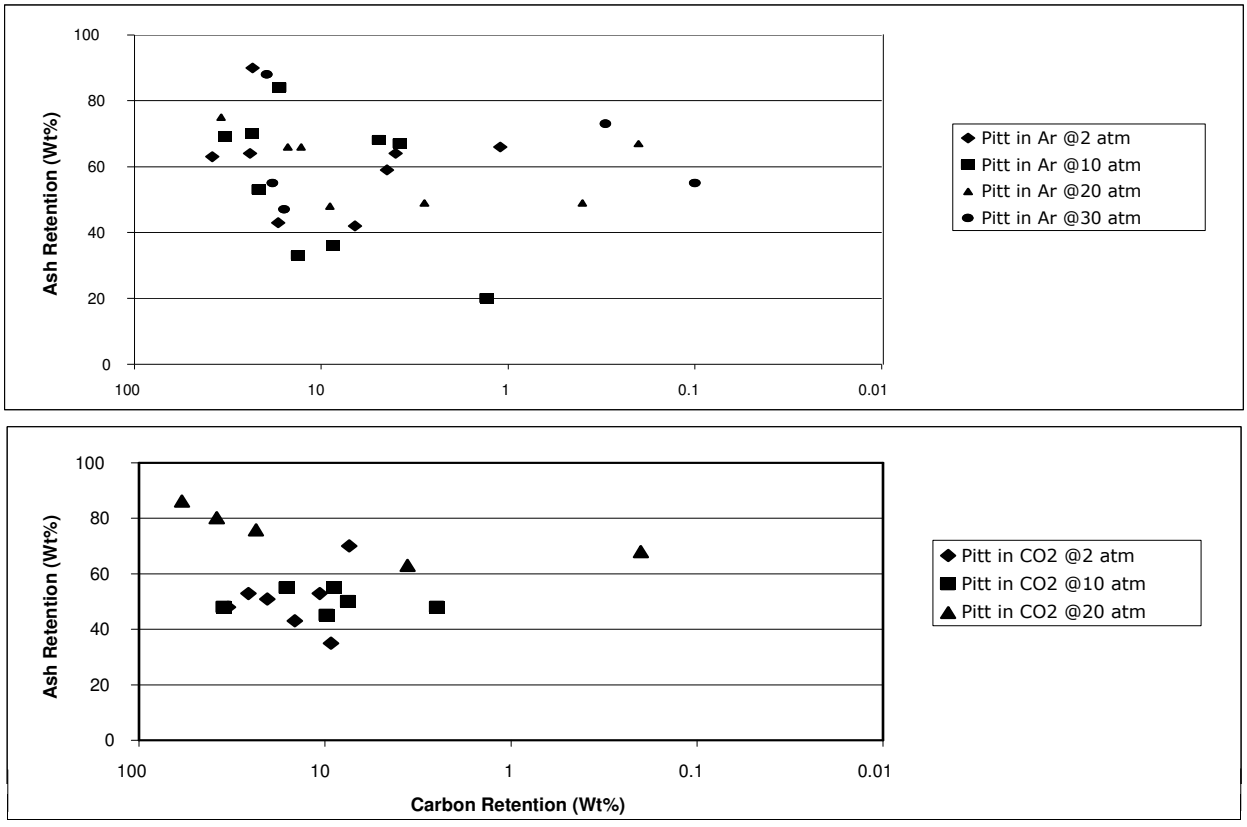

Figure A.15(a). Retention of Ash in Char Versus Retention of Carbon in Char from HPBO Tests

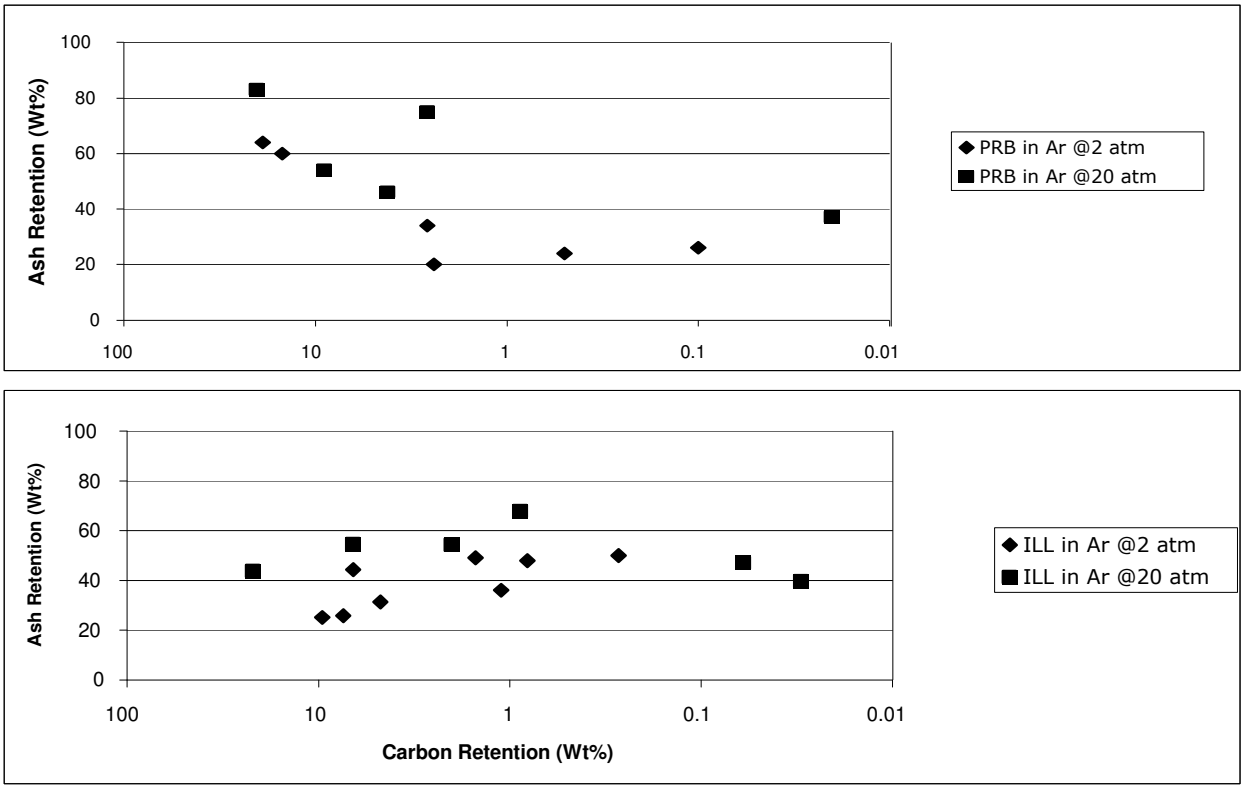

Figure A.15(b). Retention of Ash in Char Versus Retention of Carbon in Char from HPBO Tests (Continued)

Because the HPBO results already exhibit significant ash release from the chars, it is of interest to examine similar data from the NBFZ tests, which cover the range from secondary pyrolysis to partial char burnout. These results are shown in Figure A.16. The PRB result at 10 atm is unique in indicating total ash retention over the NBFZ combustion range of 20%-90% carbon burnout. By contrast, the Pittsburgh #8 and Illinois #6 NBFZ results show a rapid transition from 80% - 100% ash retention at secondary pyrolysis conditions to 50%-60% retention at carbon burnout levels of 30%-50%. Thus for these two coals, the NBFZ and HPBO results taken together show that significant ash release occurs early in the burnout process, but that the ash retention level then seems to plateau at around the 50% level until late in the burnout process. In fact, Pitt coal tests show ash retention levels of 50% to 70% at carbon burnout levels of >99%, while Illinois tests show ash retention levels >40% at carbon burnout levels of >99.9%.

It should be pointed out that only the NBFZ tests on Pitt coal at 10 and 20 atm could be conducted with low enough oxygen levels to constitute truly secondary pyrolysis conditions. In all other cases, the lowest carbon burnout points were for cases where some combustion had already occurred. This may account for the fact that ash retention levels near 100% do not appear for most NBFZ test series.

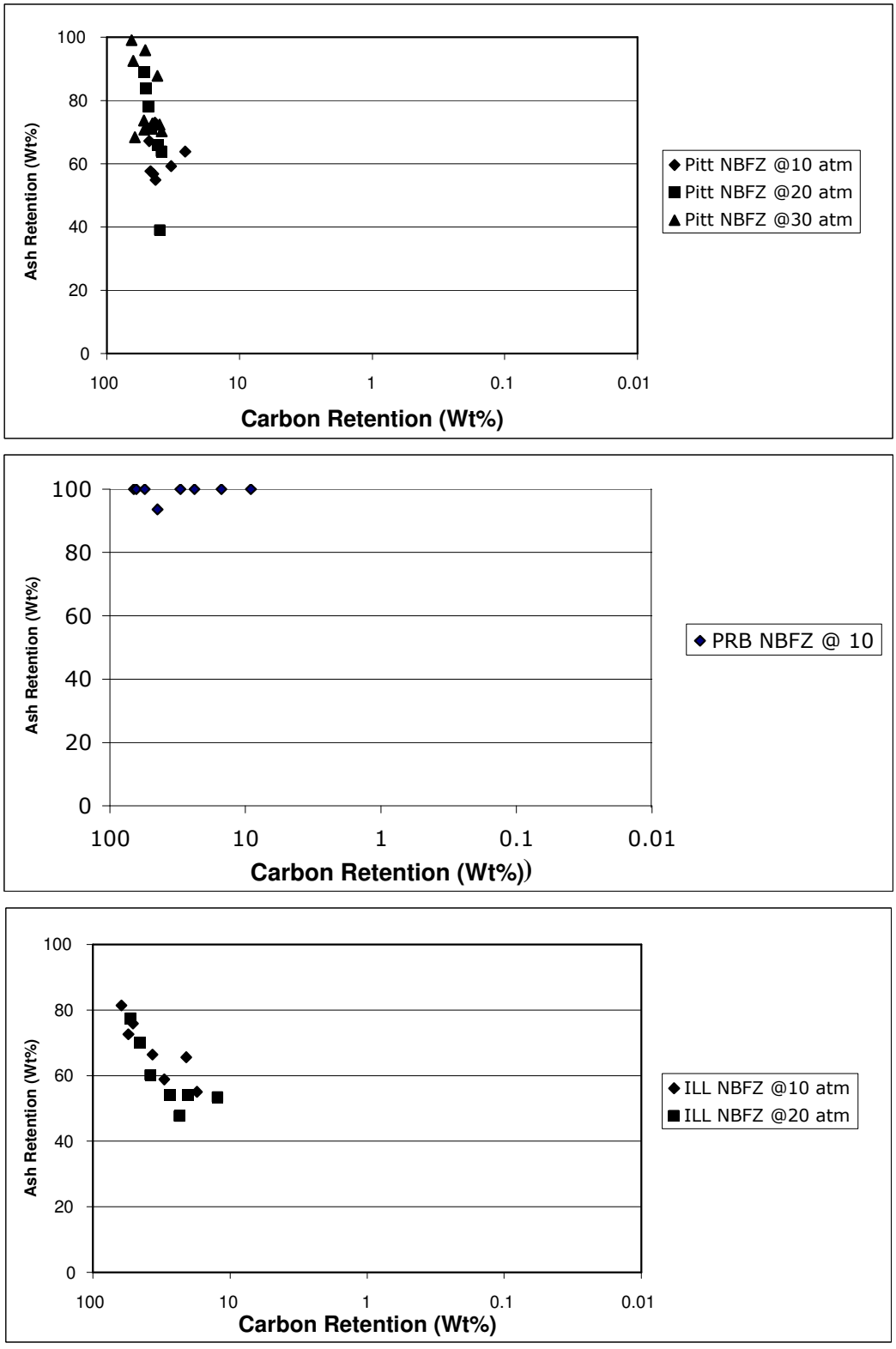

Figure A.16. Retention of Ash in Char Versus Retention of Carbon in Char from NBFZ Tests

Ash retention at carbon burnout levels as high as 99% and above must indicate that the ash agglomerates into particles that are heavy enough to be captured in the centripeter basket. These tests do not establish the ultimate fate of these heavy particles, i.e., whether they ultimately break up into fly ash or fall out as clinkers.

The apparently anomalous behavior of the PRB results from the NBFZ test series at 10 atm leads us to examine the similar results from the early PRB tests at 10, 20, and 30 atm conducted using a short furnace (see Appendix A). Because of the limited reaction times in these tests, complete secondary pyrolysis conditions were not achieved, and one series of NBFZ tests of PRB coal at 10 atm was repeated as indicated above. However, these "pre-NBFZ" tests do provide additional data on the relation between ash release and carbon burnout. These results are presented in Figure A.17. As do the NBFZ tests of Pitt and Illinois coals, these PRB tests show a rapid transition from 100% ash retention to values approaching 60% retention. These results are quite consistent with the PRB results from HPBO tests shown in Figure A.15.

Taken all together, these results suggest that ash is released from combusting pulverized coal at approximately the same rate as carbon until both materials reach their 50% levels, and that the remaining 50% of ash remains in heavy particles throughout subsequent high levels of carbon burnout.

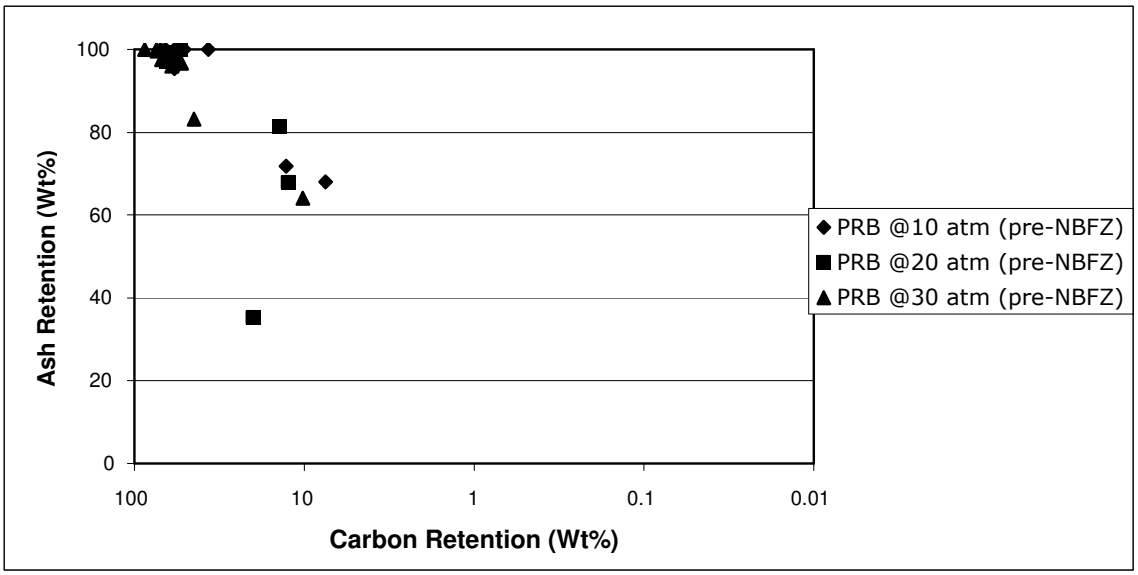

Figure A.17. Retention of Ash in Char Versus Retention of Carbon in Char from Short Furnace Tests

Analysis of Mercury in Char

The disposition of the mercury content of coal during and following the combustion process is an important environmental issue. In an effort to determine whether the NBFZ and/or HPBO experiments might address this question, we submitted six char samples from tests of Pittsburgh #8 coal in argon entrainment gas, as well as one sample of the raw coal, to Frontier Geosciences Laboratory in Seattle, WA, for mercury analysis. This lab was chosen because they are unique in being able to use the cold vapor atomic fluorescence spectroscopy technique, which gives a

sensitivity of 5 ppb for samples of less than 1 gram, improving to 0,5 ppb for multi-gram samples. Two of the samples were from the NBFZ series, and were cases of low oxygen/coal ratio, so that they represent primary pyrolysis conditions. The four samples from the HPBO series were from the four different test pressures; the 2 atm case was from a short residence time test, so the sample was representative of secondary pyrolysis conditions, while the 10, 20, and 30 atm cases were from long residence time tests, representing nearly complete burnout conditions. In all four HPBO tests, the oxygen/coal ratio was near stoichiometric.

The results of the mercury analyses for these samples are presented in Table A.26. They show that the Hg concentration in the raw coal was 355 ppb, while that in the char samples ranged from 13.5 ppb to 262 ppb. Because the char weights were only a small fraction of the original fed coal weights, the fraction of initial mercury remaining in the chars, presented in the right-hand column, was very small, ranging from 2.3 Wt% to 15.2 Wt%.

It was the consensus of opinion by research partners at NEA, UConn, and Brown that the mercury found in the chars had not been retained throughout the combustion process, but rather that it had re-condensed on the chars downstream of the furnace. Furthermore, the partitioning of condensation between the larger char and finer ash particles is expected to depend on their respective surface areas, which were not determined. Finally, the retention of re-condensed mercury on particles depends on temperature histories of the particles, which were largely uncertain. Therefore, the measured values were not considered very meaningful, and no further analyses of char samples were performed.

Table A.26. Mercury Analysis Results for Pittsburgh #8 Coal

Sample	Pressure (atm)	Residence Time (msec)	O_2/Coal (Wt%)	Char Yield (Wt% AR)	Hg in Char (ng/g)	Retained Hg (Wt%)
Virgin Coal	--	--	--	--	355	--
Pitt-56	10	400	29.8	39.2	51.4	5.7
Pitt-77	30	400	19.8	60.3	13.5	2.3
Pitt-206	2	86	275	35.1	89.8	8.9
Pitt-218	20	1867	239	17.3	311	15.2
Pitt-223	10	2967	271	10.6	262	7.8
Pitt-224	30	2967	222	19.8	212	11.8

A.3. Impactor Tests

A.3.1 Experimental Details

Since the objective of these experiments was to study pure ash, they were conducted using the same furnace and flow conditions as the maximum burnout runs in the HPBO test series. That is, two furnace extensions were used, and the oxygen/coal ratio was well above stoichiometric. Those parameters for all the impactor runs are given in Table A.27.

Table A.27. Test Conditions for Impactor Runs

Coal	Run	Carrier Gas	Stages Greased	Furnace Length (cm)	Press (atm)	Res. Time (ms)	Coal Feed Rate (g/min)	Coal Susp'n Loading (Wt%)	O_2 Conc. (Wt%)	Total Solids Recov. (Wt%)
Pitt	227	Ar	Alt	89	20	2967	1.41	2.3	9.2	3.6
"	229	"	"	"	2	1977	0.73	7.8	31.2	1.8
"	231	"	"	"	30	2967	1.55	1.68	10	1.2
"	238	"	"	"	10	"	1.52	5.3	21	2.7
Pitt	232	CO_2	Alt	89	20	2967	1.67	2.3	9.2	7.1
"	233	"	"	"	2	1977	0.73	7.8	31.2	4.8
"	236	"	"	"	10	2967	1.63	5	21	1.3
PRB	277	Ar	Alt	89	20	2967	1.44	2.25	14	1.9
"	278	"	"	"	2	1977	0.82	8.64	21	1.5
Ill	279	Ar	Alt	89	2	1977	0.80	9.0	21	2.7
"	281	"	All	"	2	"	0.86	8.6	28	2.4
"	282	"	All	"	20	2967	1.394	2.25	14	3.2
"	284	"	Alt	"	20	"	1.32	2.25	14	2.6

The impactor uses the balance between aerodynamic drag and particle inertia to separate particles by size. Each stage consists of a plate that forces the flow to turn radially outward, then turn again and transit longitudinally through a series of holes, and finally to turn radially inward toward the impactor centerline. The impaction surfaces are placed behind the holes, and particles with too much momentum to follow the flow as it turns radially inward impact the surface and are trapped. As the flow progresses through the impactor, the hole diameters and the gaps between plates become smaller, so that progressively smaller particles are trapped.

The stages of the impactor were numbered from the outlet end toward the inlet as Stages 1 – 11. The entrance impaction surface, Stage 11, was a 3.1-cm-diameter disc that directly faced the 1.5-cm-diameter flow inlet. The impaction surfaces for Stages 2 – 10 were annular discs of 3.0-cm inside diameter (I.D.) and 6.4-cm outside diameter (O.D.). At the 2.5-cm-diameter outlet of the impactor, quartz paper filter was installed (called Stage 0), which captured any particles and fumes that transited through all the impactor stages. The presence of any black material on this filter indicated that complete burnout was not achieved, and results from tests were only reported when the filter appeared light beige in color.

All impaction surfaces were covered with aluminum foil, which was used either "as is" or "greased" with a dilute solution of halocarbon vacuum grease. It was assumed that greased foils would capture all particles incident on the surface, thus overcoming any potential loss of particles from each stage because of the negative effects of gravity. These tests thus provided an accurate particle size distribution through weighing of the foils before and after each test.

However, presence of the grease on the surfaces also complicated the use of scanning electron microscopy to characterize particle morphology and size distribution. Therefore, repetitive tests were run using bare foils, where the capture of particles on the surfaces was due to impaction alone. In fact, it was often found very small differences between the weight distributions on the foils with and without grease, and so for most of the cases reported here only a single test using was done alternating greased and ungreased foils.

Although the impactor was originally intended for use at atmospheric pressure, its mechanical housing was sufficiently rugged that it could withstand the highest pressures of our tests. Only the bolts intended to hold the unit together were deemed inadequate for high-pressure use. Therefore, an auxiliary jig suitable for containing the components at high pressures was designed.

The impactor was intended to be oriented so that the particle-laden exhaust stream flowed downward through the unit, in case gravity played a role in retaining particles on the various impaction surfaces. Therefore, in initial tests the filters and centripeter were removed from the centripeter housing, and a 2.5-cm I.D. pipe bent 90° on a 37-cm radius was fitted on a port in the housing sidewall. The impactor was attached at the bottom of this pipe, and the entire gas flow was exhausted through the pipe and impactor. However, limited experience with this arrangement indicated that there was some settling of particles in the centripeter housing, and that there may have been deposition on the housing and pipe walls as well. These observations led to the conviction that it was essential to couple the impactor more closely to the exhaust point of the flow tube.

After discussions with Professor Helble at UConn, we decided that more accurate impactor measurements could be made by inverting the impactor and attaching it immediately above the top flange of the reactor pressure vessel. Accordingly, the cylindrical chamber shown at the top of Figure A.13 was removed, as were the char trap, tar/fine particle filters, and the converging centripeter nozzle. In their place we fabricated and installed a fitting that enclosed the top of the transpiration tube and provided a flange for directly attaching the impactor. With this configuration the distance from the quench nozzle to the inlet of the impactor could be reduced to as little as 10 cm of straight flow.

In addition to dealing with the use of the impactor at high pressure, it was necessary to accommodate the fact that the exhaust gases were at high temperature, perhaps 700°C or above. At pressures of 0.2 and 1 MPa, the heat capacities of the exhaust gases were small enough that the impactor temperature remained within tolerable levels. But at 2 MPa and 3 MPa, temperatures rose to the point where the Buna-N O-rings within the impactor degraded, and, in some cases it appeared that the halocarbon grease on some foils baked off, resulting in a net weight loss on those foils during the test. A partial solution to the temperature problem was to procure and install viton O-rings in place of the Buna-N units. However, we also found it necessary to fabricate and install a water-cooled flow tube extension of 30-cm length and 2.2-cm I.D. between the transpiration tube flange and the impactor. This extension tube was used for the later 2-MPa and 3-MPa tests.

In most of these tests, we found some particles lying loose in the entrance section of the impactor, indicating that they were too large to be captured on the foil of Stage 11. These particles were weighed and designated as Stage 12. There was also evidence that some particles were deposited along the flow tube walls, particularly when the cooled extension tube was used. We cannot accurately estimate the mass or size range of those particles.

A.3.2 Results

The mass distributions measured for the impactor runs listed in Table A.27 are presented in Tables A.28–A.31. In each case, values are tabulated for the raw weights of material on each stage and then for the weights normalized by the total weight of material recovered from the impactor. Note that the normalization weight includes the loose material collected from the initial stages of the impactor and assigned as Stage 12. Note also that the balance used to weigh the foils had a resolution of 0.1 mg, and in those few cases where the weight change was zero or negative, we still assigned a weight gain of 0.1 mg in order to permit the results to be plotted on a logarithmic scale. Examination of the results in these tables indicates that in some cases there is a systematic reduction in captured weight on ungreased stages compared to adjacent greased stages. This is particularly true for Pitt-232 and PRB-277, where the variations approach a factor of 10. For Pitt-231, the variation is less than a factor of 2. The other runs show no significant differences between greased and ungreased stages. The tables also show a large variation in the ratio of weight of loose particles to fine particles (i.e., the ratio of weight on Stage 12 to the sum of weights on Stages 0 – 11) for the various runs. It appears that this is a function of the efficiency of transport of the larger particles upward through the quench nozzle, transpiration tube, and cooling tube. We have compared the absolute and relative masses collected in the char trap and on the filters in the centripeter runs with those collected in Stage 12 and Stages 0 – 11. For all cases, the absolute yields of fine particle mass in Stages 0 – 11 agreed quite well with the absolute yields of fine particles captured on the filters. However, the yields of heavy particles captured in the char trap were always larger, and usually significantly larger, than the yields of material in Stage 12.

Table A.28. Mass Distributions for Impactor Tests on Pittsburgh #8 Coal with Argon Carrier Gas

Stage No.	Pitt-229		Pitt-238		Pitt-227		Pitt-231	
	P = 2 atm		P = 10 atm		P = 20 atm		P = 30 atm	
	M (mg)	Normal-ized	M (mg)	Normal-ized	M (mg)	Normal-ized	M (mg)	Normal-ized
0	2.5	0.092	5.6	0.069	6.8	0.156	4.0	0.206
1-U	0.1	0.004	0.5	0.006	0.8	0.018	0.1	0.005
2-G	0.5	0.018	0.9	0.011	1.0	0.023	0.4	0.021
3-U	0.9	0.033	1.1	0.014	1.3	0.030	0.3	0.015
4-G	0.3	0.011	1.3	0.016	3.7	0.085	0.9	0.046
5-U	0.6	0.022	1.6	0.020	3.5	0.080	1.0	0.052
6-G	1.0	0.037	3.9	0.048	4.8	0.110	1.6	0.082
7-U	3.9	0.143	6.0	0.074	4.9	0.113	1.3	0.067
8-G	4.1	0.151	7.3	0.091	5.5	0.126	1.9	0.098
9-U	3.2	0.118	7.2	0.089	4.2	0.097	1.4	0.072
10-G	2.5	0.092	3.9	0.048	2.9	0.067	3.6	0.186
11-U	7.1	0.261	2.4	0.030	2.6	0.060	2.4	0.124
12	0.5	0.018	38.9	0.483	1.5	0.034	0.5	0.026
Sum	27.2	1.00	80.6	1.00	43.5	1.00	19.4	1.00

Table A.29. Mass Distributions for Impactor Tests on Pittsburgh #8 Coal with CO_2 Carrier Gas

Stage No.	Pitt-233		Pitt-236		Pitt-232	
	P = 2 atm		P = 10 atm		P = 20 atm	
	M (mg)	Normal-ized	M (mg)	Normal-ized	M (mg)	Normal-ized
0	1.5	0.021	7.7	0.175	1.3	0.011
1-U	0.1	0.001	0.8	0.018	0.1	0.001
2-G	0.3	0.004	0.9	0.020	0.1	0.001
3-U	0.1	0.001	1.1	0.025	0.1	0.001
4-G	0.1	0.001	1.5	0.034	0.1	0.001
5-U	0.3	0.004	2.3	0.052	0.1	0.001
6-G	0.5	0.007	2.2	0.050	0.4	0.003
7-U	1.6	0.023	2.7	0.061	0.4	0.001
8-G	2.9	0.041	3.4	0.077	0.6	0.005
9-U	2.3	0.032	2.4	0.055	0.1	0.001
10-G	10.5	0.148	3.3	0.075	0.9	0.008
11-U	6.3	0.089	1.3	0.030	0.3	0.003
12-G	44.3	0.626	14.4	0.327	114.8	0.965
Sum	70.8	1.000	44.0	1.000	119.0	1.000

Table A.30. Mass Distributions for Impactor Tests on PRB Coal with Ar Carrier Gas

Stage No.	PRB-278		PRB-277	
	P = 2 atm		P = 20 atm	
	M (mg)	Normal-ized	M (mg)	Normal-ized
0	2.9	0.079	4.1	0.089
1-U	0.1	0.003	0.4	0.009
2-G	0.2	0.005	1.0	0.022
3-U	0.3	0.008	0.7	0.015
4-G	0.2	0.005	1.3	0.028
5-U	0.1	0.003	0.6	0.013
6-G	0.3	0.008	2.4	0.052
7-U	1.0	0.027	0.5	0.011
8-G	2.6	0.071	4.4	0.095
9-U	3.1	0.085	0.9	0.019
10-G	2.3	0.063	5.5	0.119
11-U	2.8	0.077	0.8	0.017
12	20.7	0.566	23.7	0.512
Sum	36.6	1.000	46.3	1.000

Table A.31. Mass Distributions for Impactor Tests on Illinois #6 Coal with Ar Carrier Gas

Stage No.	ILL-279		ILL-281*		ILL-284**		ILL-282*	
	P = 2 atm		P = 2 atm		P = 20 atm		P = 20 atm	
	M (mg)	Normal-ized	M (mg)	Normal-ized	M (mg)	Normal-ized	M (mg)	Normal-ized
0	2.5	0.039	2.3	0.037	3.6	0.053	3.6	0.027
1-U	0.1	0.002	0.1	0.002	0.6	0.009	0.9	0.007
2-G	0.2	0.003	0.1	0.002	0.8	0.012	1.0	0.008
3-U	1.5	0.023	2.6	0.042	1.5	0.022	6.2	0.047
4-G	0.1	0.002	1.5	0.024	2.2	0.032	12.3	0.093
5-U	0.1	0.002	0.7	0.011	2.9	0.043	8.0	0.061
6-G	0.1	0.002	0.8	0.013	4.6	0.068	7.1	0.054
7-U	0.9	0.014	2.3	0.037	5.5	0.081	4.1	0.031
8-G	2.7	0.042	4.0	0.064	4.1	0.060	1.9	0.014
9-U	2.7	0.042	4.8	0.077	4.3	0.063	2.9	0.022
10-G	3.4	0.052	2.8	0.045	5.2	0.076	10.6	0.080
11-U	1.9	0.029	16.4	0.264	4.8	0.070	11.5	0.087
12	48.6	0.750	23.7	0.382	28	0.411	61.7	0.468
Sum	64.8	1.000	62.1	1.000	68.1	1.000	131.8	1.000

*In Runs 281 and 282 all stages were greased.
** Run 284 was 2 minutes long, while other runs were 3 minutes long.

The inconsistency of transport and capture of large particles in the impactor tests suggests that the weights for Stages 0 – 11 in Tables A.27–A.30 should have been normalized by neglecting the weights on Stage 12. The results determined in this way are shown graphically in Figure A.18. These charts show vividly the differences between greased and ungreased stages for the runs indicated above. They also show a tendency for a local maximum in the mass distributions around stages 7 – 9. According to calculations performed at UConn, the cutoff diameters for these stages range from 2 to 7 μm. There is also a significant fraction of the mass captured on the final outlet filter, indicating that from 5% to 25% of the fine particles are smaller than 1 μm in diameter.

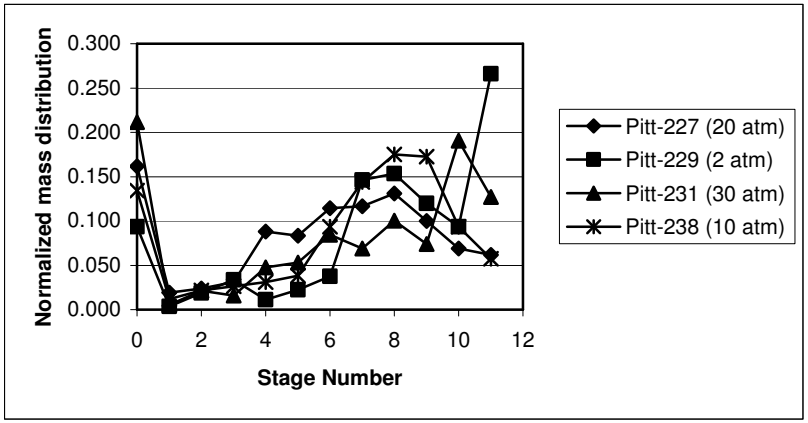

a. Pittsburgh #8 Coal in Argon Entrainment Gas

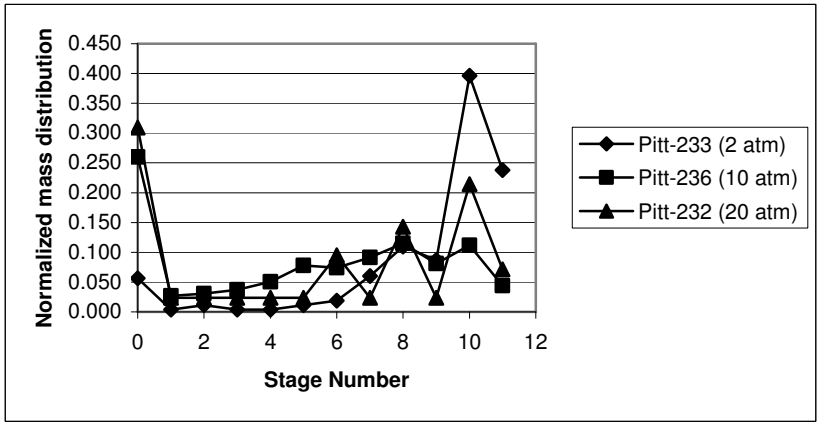

b. Pittsburgh #8 Coal in CO_2 Entrainment Gas

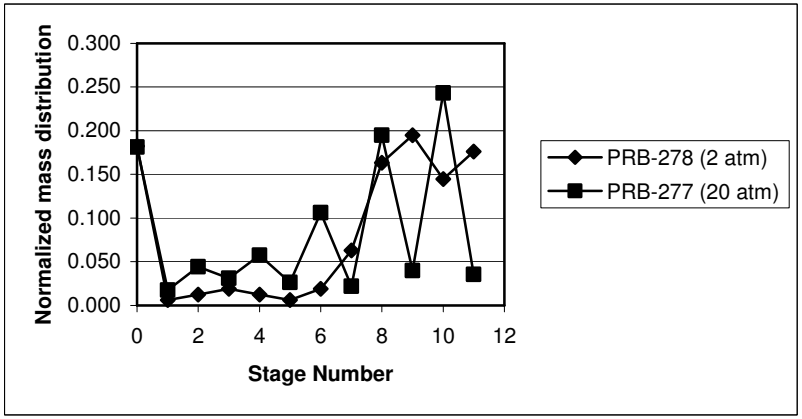

c. PRB Coal in Argon Entrainment Gas

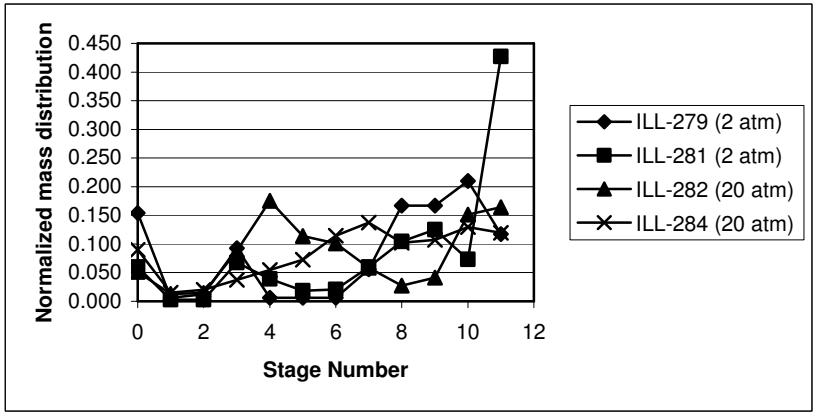

d. Illinois #6 Coal in Argon Entrainment Gas

Figure A.18. Mass distributions on impactor stages for maximum burnout experiments

A.4 Short Furnace Experiments

When this experimental program began, it was anticipated that the NBFZ experiments could be conducted using SRI's existing pressurized radiant coal flow reactor (p-RCFR). This reactor had been used previously for an extensive series of pressurized combustion experiments emphasizing primary pyrolysis of pulverized coals [Manton et al., 2004 and Liu et al., 2004]. Accordingly, we began the NBFZ studies by performing three series of tests in the p-RCFR using PRB coal at pressures of 1, 2, and 3 MPa.

When NEA began modeling these PRB experiments, they realized that the experimental conditions under which the tests were performed did not lead to the extent of reactive processing desired. Specifically, they recognized that the persistence of tar among the reaction products in the oxygen-free tests indicated that secondary pyrolysis was not being achieved. This complicated the modeling by forcing consideration of the tar oxidation and tar conversion to soot as competitive processes to the oxidation of gaseous products, soot, and char. Once this shortcoming was identified, we modified the reactor to provide a furnace length that was 2.5 times longer than the one in the p-RCFR, as described in Section 2.1, and all subsequent NBFZ tests were performed using that modified SRT-RCFR facility.

Although these "pre-NBFZ" tests performed in the short-furnace reactor were conducted under other than planned reaction conditions, they nevertheless were conducted with the same care and attention to detail as the successful NBFZ and HPBO series, and are equally valid, albeit for their unique test conditions. Therefore, the results of these experiments are presented here for future reference.

A.4.1 The p-RCFR Reactor

The p-RCFR reactor is shown schematically in Figure A.19. The radiant heat source in this system was a graphite cylinder of 10 cm O.D., 0.625 cm wall thickness, and 7 cm length. The flow tube in initial experiments was a quartz tube of 16 mm O.D. x 14 mm I.D.; beginning with Run 13 this was changed to a mullite tube of 16 mm O.D. x 12 mm I.D.. Although quartz is transparent over the range from 0.3 μm to 2.7 μm while mullite is opaque at all wavelengths, calculations showed that the change in tube material had little effect on the radiation intensity incident on the pulverized coal, and therefore little effect on the temperature histories of either the coal particles or the entrainment gases [Liu and Niksa, 2003]. Heating of the top flange to minimize water vapor condensation in the analytical gas stream line began at Run 24.

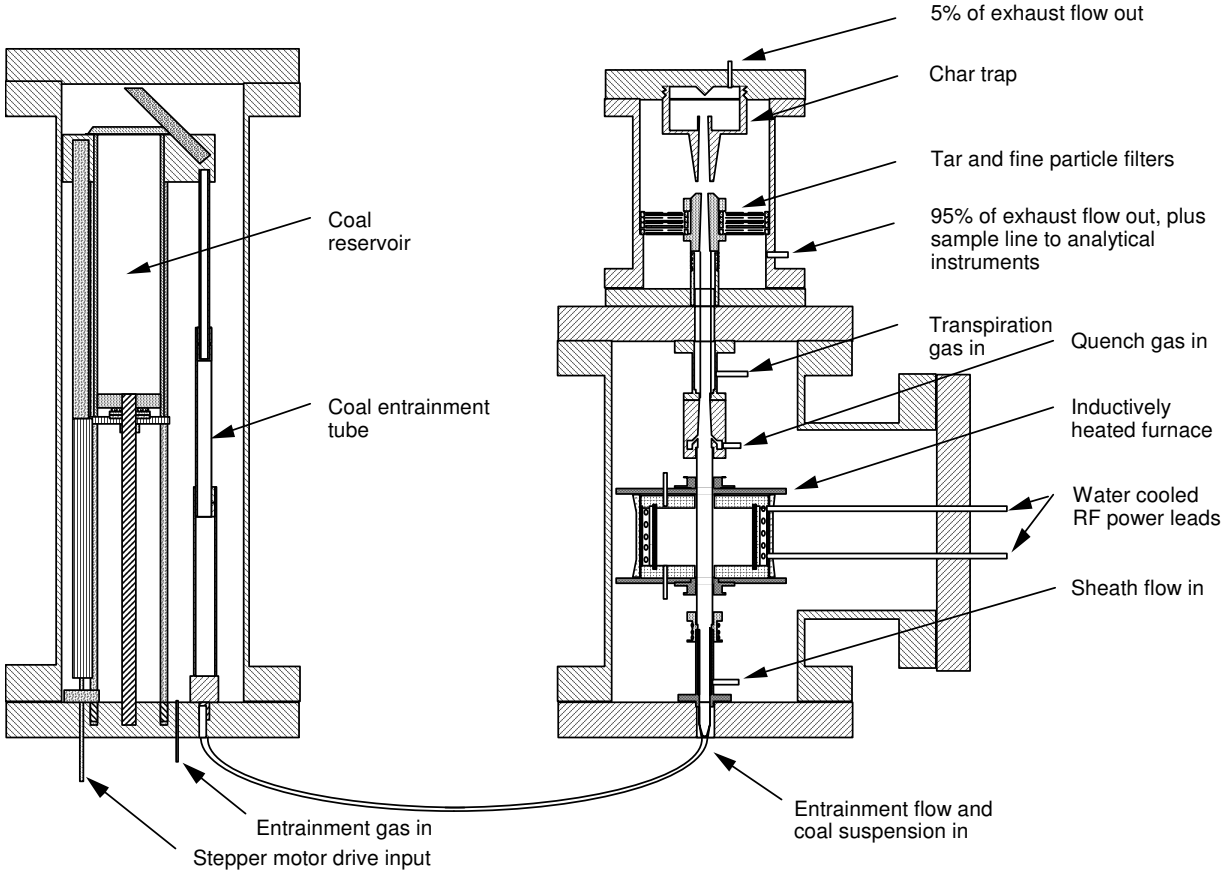

Figure A.19. SRI's Short Residence Time Radiant Coal Flow Reactor (p-RCFR)

Product Analysis Techniques

The analytical detection system was identical to that described in Section A.1.2, with the exception of the treatment of solid products. As in the later NBFZ tests, the solid product yields were determined gravimetrically. Aerosol products were extracted from the quartz paper filters with tetrahydrofuran (THF). The solution/suspensions were filtered through a millipore filter. The solids captured on the membrane were denoted as soot, while the dissolved material was recovered by evaporative drying and denoted as tar. The soot fraction was calculated as the weight of material captured on the membrane divided by the total aerosol weight. Char, tar, and soot samples were submitted to an outside laboratory for elemental analysis.

Test Conditions

These initial series of tests were conducted using PRB coal. The operating conditions are given in Table A-1. Note that a range of coal suspension loadings was used in each series to examine the effect of coal loading on the extent of char burnout, and it demonstrated the expected result that higher loadings led to more intense flames within the short furnace region and consequently to more complete product burnout. However, frequent flow tube failures due to overheating ultimately established upper limits on the suspension loadings at

each pressure, and these limiting loadings were used in the long-furnace NBFZ tests reported above.

Data Analysis Techniques

The data were analyzed in the same manner as described for the NBFZ tests, with the exception of how the oxygen elemental balance was calculated. In the present tests, the oxygen in the coal itself was considered the "input" and the oxygen in the CO_2, CO, H_2O, and char products minus the oxygen consumed from the entrainment gas stream was the "output." Since there was very little oxygen in the coal itself (the 19% DAF content for PRB being the highest of all the coals), the oxygen in the CO_2, CO, and H_2O came predominantly from the entrainment stream, and small inaccuracies in measuring the yields of these products or in measuring the change in concentration of O_2 in the entrainment gas stream gave larger deviations in the oxygen balances based on comparison with the oxygen content of the coal. Therefore, in the NBFZ and HPBO test results presented above, the "total" oxygen elemental balance was calculated by taking the oxygen in the coal plus the oxygen in the incoming entrainment stream as the input and the sum of the oxygen content of the products plus the oxygen remaining in the exhaust gas stream as the output.

Because the oxygen balance results presented below were calculated using the earlier definition, the values presented below typically constitute small differences between large numbers, and so the deviations from 100% do not accurately reflect the overall accuracy of the results.

A.4.2 Results

The results for the three "pre-NBFZ" tests are summarized in Tables A.33-A.35. Each table is separated into groups of tests with similar suspension loadings, with each group ordered in increasing oxygen/coal ratio. No corrections have been applied to these results. They show the expected trends of increasing CO_2 yields and decreasing char, tar, and hydrocarbon yields with increasing stoichiometric ratio. However, the H_2O yields do not increase with stoichiometry as they should, a problem we attributed to condensation of water vapor in the analytical gas flow line. As a result, the H-atom balances shown near the bottom of each table depart increasingly from 100% with increasing O_2/coal ratio. The same effect was noted in the NBFZ results, where the H_2O yields were adjusted to correct for it. When H_2O yields were too low, the O-atom elemental balances were also usually too low because the oxygen in H_2O can be a significant part of the oxygen yield. In the worst cases, even the mass balance was suppressed by the missing water vapor.

The hydrocarbon yields show the expected burnout with increasing O_2/coal ratio, but the H_2 and HCN yields do not necessarily decrease in the same way, suggesting that these species continue to be formed as the char and tar are burned out. Since both species decrease monotonically with O_2/coal ratio in the NBFZ experiments where tar is no longer present after secondary pyrolysis is complete, one might conclude that tar conversion is the source of H_2 and HCN in the present experiments. NO increases with

O_2/coal ratio in the tests at 1 MPa and 2 MPa as expected, but the yields decreased with increasing pressure, and were immeasurably small at 3 MPa. This result suggests that high-pressure combustion may be an effective technique for reducing NOx emissions. These data provide a good opportunity to study ash retention during the early stages of coal pyrolysis and combustion. These results were presented and discussed in conjunction with the ash retention results for the HPBO and NBFZ tests in Section A2.5 above.

Table A.32. Operating Conditions for Tests of PRB Coal in the Short Furnace Reactor

Run No.	Pressure (MPa)	Suspension Loading (Wt%)	O_2 Mass Fraction (Wt%)	S.R.
14C	1	5.00	0.06	0.006
11C	1	4.77	0.15	0.015
10C	1	4.82	2.07	0.203
9C	1	4.97	3.64	0.347
8C	1	4.65	5.56	0.569
13C	1	6.44	10.75	0.791
16C	1	6.96	16.11	1.10
15C	1	7.01	19.39	1.31
20C	2	3.42	0.06	0.009
18C	2	3.35	2.71	0.384
17C	2	3.37	4.65	0.654
19C	2	3.42	9.17	1.30
24C	2	6.77	1.47	0.104
23C	2	6.79	4.56	0.318
21C	2	7.39	9.83	0.630
22C	2	7.19	14.89	0.981
32C	3	4.46	0.11	0.011
29C	3	4.39	0.24	0.027
33C	3	4.46	1.26	0.134
26C	3	4.39	2.63	0.284
34C	3	4.48	4.96	0.526
27C	3	3.23	4.99	0.730
28C	3	4.51	9.93	1.04
30C	3	2.26	0.20	0.041
31C	3	2.25	0.60	0.127
35C	3	1.41	0.01	0.004

Table A.33. Results for Short-Furnace Tests of PRB Coal at 1 MPa[a]

Run No.	**14C**	**11C**	**10C**	**9C**	**8C**	**13C**	**16C**	**15C**
Susp. Load (Wt%)	5.00	4.77	4.82	4.97	4.65	6.44	6.96	7.01
O_2/Coal (Wt%)	1.2	3.1	42.9	73.3	120	167	232	276
CO_2	10.4	6.8	23.8	67.9	139	159	228	280
CO	10.1	12.5	19.7	42.4	27.9	32.3	34.5	25.5
H_2O	5.1	5.1	6.8	8.4	6.6	5.6	5.5	5.3
CH_4	2.43	2.12	0.77	2.15	0.39	0.21	0.038	0.038
C_2	2.80	3.01	0.81	1.57	0.34	0.11	0.010	0.014
C_3	0.69	0.51	0.17	0.08	0.006	0.018	0	0.007
Oils	0.44	0.37	0.12	0.08	0.024	0.008	0	0
H_2	0.76	1.06	0.64	0.96	0.74	0.69	0.52	0.35
HCN	0.26	0.54	0.36	0.48	0.24	0.17	0.034	0.027
NH_3	0.013	0.010	0.005	0.012	0.002	0.001	0.001	0.001
NO	0	0	0.003	0.021	0.120	0.035	0.149	0.166
Char+Ash	57.3	54.4	50.1	46.9	41.9	29.3	10.5	6.1
Tar	13.5	7.7	3.45	2.49	1.2	3.78	0.82	0.27
Soot+Ash	0.90	0.82	1.04	1.97	1.1	1.13	0.99	0.86
ΣMass[c]	103.5	94.6	90.3	104.5	101.4	88.3	86.3	Na
ΣC	92.0	87.4	84.3	116.3	121.3	118	118	Na
ΣH	91.4	83.3	58.4	60.4	39.1	37	24	Na
ΣO	153	123	119	73.1	45.2	---	---	Na

[a] All yields reported as Wt% DAF

Table A.34. Results for Short-Furnace Tests of PRB Coal at 2 MPa[a]

Run No.	**20C**	**18C**	**17C**	**19C**	**24C**	**23C**	**21C**	**22C**
Susp. Load (Wt%)	3.42	3.35	4.27	3.42	6.77	6.79	7.39	7.19
O_2/Coal (Wt%)	1.9	80.9	138	275	21.7	67.2	133	207
CO_2	7.3	64.9	115	231	13.5	47.1	123	193
CO	6.3	24.6	21.4	25.6	10.8	33.7	46.4	39.3
H_2O	4.2	6.4	7.7	6.8	5.9	7.0	5.6	5.3
CH_4	1.08	1.35	0.25	0.030	1.66	1.27	0.22	0.12
C_2	1.23	1.07	0.20	0.02	1.14	0.59	0.06	0.02
C_3	0	0.23	0.02	0.01	0	0	0	0
Oils	0.265	0.096	0.015	0	0.25	0.08	0.014	0
H_2	0.075	0.65	0.48	0.44	0.54	0.79	1.23	0.96
HCN	0.220	0.20	0.33	0.047	0.092	0.33	0.12	0.054
NH_3	0.023	0.010	0.012	0.005	0.081	0.06	0.038	0.005
NO	0	0.004	0.055	0.059	0	0	0.033	0.055
Char+Ash	58.4	52.2	44.0	11.1	55.6	48.8	17.9	9.8
Tar	8.39	1.97	2.80	3.38	7.11	2.49	6.99	3.10
Soot+Ash	0.57	0.50	0.58	0.12	0.71	1.15	0.94	0.68
ΣMass[c]	88	92	98	85	83	86	80	81
ΣC	81	104	111	117	85	101	99	111
ΣH	75	57	42	29	66	57	46	34
ΣO	120	53	63	---	76	31	16	---

[a] All yields reported as Wt% DAF

Table A.35. Results for Short-Furnace Tests of PRB Coal at 3 MPa[a]

Run No.	**32C**	**29C**	**33C**	**26C**	**34C**	**27C**	**28C**	**30C**	**31C**	**35C**
Susp. Load (Wt%)	4.46	4.39	4.46	4.39	4.48	3.23	4.51	2.26	2.25	1.41
O_2/Coal (Wt%)	2.4	5.6	28.2	59.9	111	154	220	8.7	26.7	0.9
CO_2	6.5	4.5	17.3	36.8	71.2	88.7	202	7.6	11.2	9.5
CO	5.3	3.6	10.7	19.0	43.2	24.3	26.6	7.1	10.0	9.0
H_2O	---	2.3	21.2	10.5	64.2	14.7	22.6	1.4	6.7	10.5
CH_4	1.19	0.67	1.01	1.16	0.60	0.23	0.071	1.15	1.44	1.61
C_2	0.97	0.60	0.70	0.64	0.26	0.17	0.011	1.10	1.07	1.48
C_3	0.29	0.18	0.23	0.04	0.04	0	0	0.31	0.34	0.44
Oils	0.87	0.51	0.66	0.40	0.07	0.12	0.001	0.86	1.00	2.23
H_2	0.49	0.41	0.35	0.31	1.06	0.57	0.58	0.50	0.70	0.91
HCN	0.12	0.082	0.062	0.091	0.117	0.085	0.013	0.171	0.10	0.30
NH_3	0.056	0.017	0.067	0.107	0.183	0.086	0.070	0.066	0.070	0.083
NO	0.003	0	0	0	0	0	0	0	0	0
Char+Ash	69.1	82.8	66.5	54.2	45.2	40.9	8.6	72.0	63.9	62.2
Tar	11.0	3.55	4.00	2.41	2.75	3.77	5.63	7.17	6.52	4.83
Soot+Ash	0.33	0.47	1.19	0.33	1.42	0.44	1.56	2.19	2.34	1.24
ΣMass[c]	95	99	108	92	142	95	90	100	96	104
ΣC	95	96	91	89	110	96	105	96	91	89
ΣH	81	87	102	65	174	69	67	76	83	90
ΣO	100	114	174	109	275	100	36	116	109	167

[a] All yields reported as Wt% DAF

HIGH PRESSURE COAL COMBUSTION KINETICS PROJECT
Appendix B – Analysis of the NBFZ Tests and Sub-Models for Pollutant Formation

B.1 Analysis of the NBFZ Tests

B.1.1 Improvements to the p-RCFR for NBFZ Combustion Tests

SRI's p-RCFR was initially designed for pyrolysis tests at elevated pressures. Combustion test conditions are more severe than pyrolysis in several ways, as follows:

- The coal particles and gas stream experience more severe thermal histories, coal particles reach a maximum temperature of 900°C during pyrolysis in Ar at 1.0 MPa. They reach temperatures as high as 1300-1500°C during combustion at 1.0 MPa and the highest stoichiometric ratio values. The gas temperatures during combustion tests depend on the ignition characteristics, but are always much hotter than in any pyrolysis cases. The mullite flow tube also operates at much hotter temperatures in combustion tests.

- For the same inlet gas velocities, the suspensions have shorter residence times in combustion tests than in pyrolysis tests, due to the hotter gas flow. Preliminary combustion tests with a 6 cm quartz tube - the same length used in pyrolysis tests – indicated that the residence times were too short to complete secondary volatiles pyrolysis. Also, the design calculations showed that a 6 cm hot zone is not long enough to ignite the char particles in combustion tests, particularly at pressures above 1.0 MPa. Higher particle loadings and longer tube lengths were recommended to circumvent these difficulties.

Based on these recommendations, SRI extended the graphite heating element from 6 to 15.8 cm, and changed the flow tube material from quartz to mullite, which softens at about 1750°C, which is about 200°C higher than quartz. The mullite tube has an internal diameter of 1.2 cm, slightly smaller than that of quartz tube.

B.1.2 Coal Properties

Table B.1 lists the proximate and ultimate analyses of the Pittsburgh #8, Illinois #6, and Wyodak (PRB) sub-bituminous used in the tests. Their properties are typical of raw coals, but not of the cleaned coals exclusively fired at power stations. Note the extremely high sulfur contents of the Illinois #6 and Pittsburgh #8 samples, and the high ash content of the Illinois #6. These coals were obtained from the Penn State Database, then aerodynamically classified by Vortec Corp. Coal samples are a "double cut" or mixture of two sieve sizes, which range from 75 to 90 μm and from 90 to 105 μm, so the mean size was about 90 μm.

Table B.1. Coal Properties in NBFZ Combustion Tests

Coal Name	Proximate Analysis, ad wt.%				Ultimate Analysis, DAF wt.%				
	M	Ash	VM	FC	C	H	O	N	S
Pittsburgh #8	0.7	12.3	37.9	49.1	80.8	5.4	5.8	1.7	6.3
Illinois #6	0.2	17.3	35.8	46.7	74.1	5.5	8.2	1.4	10.8
PRB	0.1	5.0	39.4	55.5	73.7	5.6	19.0	1.1	0.6

B.1.3 NBFZ Test Conditions

Tests in the NBFZ test configuration simulate near-burner pulverized-fuel flame conditions without the complications of turbulent, rotational, swirling flow fields. For tests with a particular fuel-type, particle size, and pressure, the p-RCFR furnace temperature, suspension loading, and nominal residence time are fixed while the inlet O_2 concentration is varied from 0 to 50 %, to progressively increase the stoichiometric ratio values. A case without O_2 determines the total volatiles yield and distributions of so-called secondary volatiles pyrolysis products. Secondary volatiles pyrolysis products are the volatiles and soot remaining after the primary volatiles from the coal are pyrolyzed further in hot gases. They consist of soot, oils, CH_4, C_2H_2, CO, CO_2, H_2O, H_2, H_2S and N-species. As the inlet O_2 level is progressively increased in succeeding tests, the process chemistry will be moved through oxidative pyrolysis, volatiles combustion, soot oxidation, and char oxidation. Of course, these stages exhibit considerable overlap, depending on the relative burning rates of the various fuels in the reaction system. They are resolved by depletion of the available O_2; i.e., flows with higher inlet O_2 levels progress deeper into the sequence of chemical reaction stages before the flames are extinguished by the consumption of O_2.

The test plan comprised six test series that characterized Pittsburgh #8 at 1.0, 2.0, and 3.0 MPa, Illinois #6 at 1.0 and 2.0 MPa, and Wyodak (PRB) at 1.0 MPa only. Each test series contains from seven to ten individual tests with progressively higher inlet O_2 levels, hence, stoichiometric ratio values. Table B.2 lists the operating conditions of all tests. Seven columns are included in the table. The first column gives the run number recorded by SRI staff, followed by the coal name, total pressure, mean inlet velocity, suspension loading by mass, inlet O_2 mass fraction, and stoichiometric ratio The test series in the table begin with Pittsburgh #8 at 1.0, 2.0 and 3.0 MPa, followed by Illinois #6 at 1.0 MPa and 2.0 MPa, and PRB at 1.0 MPa. In each test series, the tests appear in order of increasing stoichiometric ratio value. The inlet gas velocities were about 29.5 cm/s in all tests, although residence times were significantly variable due to different extents of heat release among the various test conditions.

Table B.2. Operating Conditions for NBFZ Tests in the p-RCFR.

Run No.	Coal Name	Pressure (MPa)	Inlet Velocity (cm/s)	Susp. Loading (%)	O_2 Mass Fr. (%)	stoichiometric ratio
50C	Pittsburgh #8	1	29.3	4.75	0.01	0.001
56C	Pittsburgh #8	1	29.1	4.70	1.40	0.147
55C	Pittsburgh #8	1	29.1	4.74	2.36	0.245
54C	Pittsburgh #8	1	29.2	4.43	3.34	0.372
53C	Pittsburgh #8	1	29.1	4.70	4.82	0.506
52C	Pittsburgh #8	1	29.2	4.95	7.22	0.719
51C	Pittsburgh #8	1	29.3	5.12	9.89	0.953
64C	Pittsburgh #8	2	29.2	2.49	0.10	0.020
63B	Pittsburgh #8	2	29.2	2.57	0.45	0.086
62B	Pittsburgh #8	2	29.2	2.51	1.17	0.230
61B	Pittsburgh #8	2	29.1	2.46	1.91	0.382
60B	Pittsburgh #8	2	29.2	2.53	3.44	0.670
59B	Pittsburgh #8	2	29.1	2.47	4.07	0.812
58B	Pittsburgh #8	2	29.2	2.37	4.85	1.008
77B	Pittsburgh #8	3	29.7	1.46	0.29	0.087
74B	Pittsburgh #8	3	29.7	1.53	0.74	0.212
73B	Pittsburgh #8	3	29.4	1.50	1.19	0.350
71B	Pittsburgh #8	3	29.2	1.65	1.67	0.447
72B	Pittsburgh #8	3	29.4	1.59	1.92	0.533
70B	Pittsburgh #8	3	29.3	1.61	2.32	0.635
69B	Pittsburgh #8	3	30.0	1.57	2.83	0.795
67B	Pittsburgh #8	3	29.3	1.66	3.01	0.799
68B	Pittsburgh #8	3	29.2	1.63	3.28	0.887
79B	Pittsburgh #8	3	29.8	1.51	3.74	1.088
88C	Illinois #6	1	29.6	4.71	0.41	0.043
87C	Illinois #6	1	29.4	4.74	1.60	0.167
86C	Illinois #6	1	29.5	4.66	2.16	0.229
85C	Illinois #6	1	29.7	4.64	4.81	0.511
84C	Illinois #6	1	29.5	4.49	6.97	0.765
83C	Illinois #6	1	29.7	4.44	9.45	1.049
82C	Illinois #6	1	29.6	4.88	11.45	1.156
97C	Illinois #6	2	29.6	2.27	1.28	0.279
95C	Illinois #6	2	29.5	2.24	2.28	0.502
94C	Illinois #6	2	29.6	2.25	3.45	0.756
93C	Illinois #6	2	29.5	2.28	4.85	1.046
99C	Illinois #6	2	29.6	2.53	6.08	1.187
89C	Illinois #6	2	29.5	2.31	6.49	1.384
91C	Illinois #6	2	29.6	2.37	8.51	1.769
110C	PRB	1	29.5	4.50	0.27	0.028
109C	PRB	1	29.3	4.57	1.18	0.121
108C	PRB	1	29.4	4.52	2.32	0.241
107C	PRB	1	29.4	4.44	3.81	0.404
105C	PRB	1	29.3	4.78	5.88	0.578
104C	PRB	1	29.4	4.79	7.65	0.751
103C	PRB	1	29.5	4.88	9.70	0.934
102C	PRB	1	29.4	4.87	11.31	1.092
101C	PRB	1	29.1	4.88	13.21	1.272

In the seven tests with Pittsburgh #8 at 1.0 MPa, suspension loadings were nearly uniform at 4.7 wt. %, whereas the O_2 mass fraction was varied from zero for the secondary pyrolysis case to 9.9 %. Consequently, stoichiometric ratio varied from 0 to 0.953 in fairly uniform increments. There are seven and ten tests in the series at 2.0 MPa and 3.0 MPa, respectively. For progressively higher pressures, the suspension loadings were decreased from 4.7 % at 1.0 MPa, to 2.5 % at 2.0 MPa, to 1.55 % at 3.0 MPa; in other words, coal feed rates were essentially the same at all test pressures. This arrangement was found to be the best way to manage deposition and plugging of the furnace flow tube. Inlet O_2 mass fractions were regulated at the higher pressures to impose similar ranges of stoichiometric ratio values in all test series. The maximum stoichiometric ratio values were 1.0 at 2.0 MPa and 1.09 at 3.0 MPa.

Illinois #6 was characterized with seven individual tests each at 1.0 and 2.0 MPa. The suspension loadings were 4.6 and 2.3 % at 1.0 and 2.0 MPa, respectively, which are almost the same as those for Pittsburgh #8. The stoichiometric ratio was increased to 1.16 at 1.0 MPa and to 1.77 at 2.0 MPa. Wyodak was only tested at 1.0 MPa with nine individual tests. The stoichiometric ratio values were varied from 0.03 to 1.27.

The operating conditions in Table B.2 are those for the final, accepted NBFZ test runs. Preliminary tests with a 6 cm quartz tube verified the problems with insufficient residence times and softening furnace flow tubes described in Sec. B.2. Product distributions in these tests indicated that secondary volatiles pyrolysis was not complete. Attempts to alleviate this condition by increasing the suspension loadings were unsuccessful, due to frequent plugging and furnace tube melting.

B.1.4 Test Results

NBFZ tests represent very significant challenges, due to the elevated pressures, high operating temperatures, the very complex distributions of products from the early stages of pulverized-fuel combustion, and variable ignition characteristics that yielded significant heat release rates under some, but not all, conditions. Our primary standards for quality control on the testing procedures and interpretations are the balances on mass and elemental recovery. Indeed, SRI's test facilities are unique in this research area for their recovery of all condensed materials in every run, along with representative sampling of major portions of the gas stream. This arrangement enables closures on the balances for total mass and C/H/N to be directly assigned from the suite of measurements in each individual test.

Ultimately, the testing team achieved the same balance closures for NBFZ tests as for the much simpler tests on pressurized pyrolysis in earlier research projects, which constitutes a significant research milestone. But many of the earlier NBFZ tests were run while the protocol was still developing; others were affected by intermittent equipment failures; all were affected by the omission of sulfur species from the gas analyses. The data were adjusted as explained in this section to minimize the impact of such flaws, so that the

most accurate characteristics of pressurized combustion would be available for the validation of a NO_X production sub-model.

Pittsburgh #8 Tests

Three datasets for Pittsburgh #8 at 1.0, 2.0, and 3.0 MPa appear in Tables B.3-B.5, respectively. There are two columns under each run number of the tabulated datasets. The left column reports the measured values of each species in the complete product distribution, and the right column shows any adjustments made to improve the closure of any of the mass or elemental balances. For example, in the second and third columns in the 1.0 MPa dataset, the H_2 yield was adjusted from its measured value of 2.4 DAF wt. % to 3.8 % to close the H-balance. The closures on the balances for total mass, C, H, and O appear below the block of product yields. The mass balance is based on the DAF coal mass plus the amount of oxygen that was actually incorporated into gaseous products, which is typically 60 to 80 % of the O_2 fed into the furnace. The percentage O_2 utilization was assigned from the measured values of residual O_2 in the exhaust. The burnout percentages assigned to gaseous fuels (evaluated for hydrocarbons plus HCN), soot, and char appear below the block of balance closures.

Two adjustments were made uniformly to all these datasets: (1) estimates for the volatile S-species; and (2) corrected H_2O yields at high moisture levels. Since the Pittsburgh #8 contains 6.3 DAF. wt. % sulfur, volatile S-species are not negligible. But they were not monitored in the tests either. We arbitrarily expressed the volatile-S species as H_2S under conditions that were sufficiently reducing to retain gaseous fuel compounds, and as SO_2 under conditions where essentially all the gaseous fuel compounds had burned. This procedure would be expected to overestimate the volatile-S species under the most reducing conditions, because we have no evidence that all the coal-S had actually been released into the gas phase under the relatively moderate temperatures in these tests. The procedure probably overestimates the amount of SO_2 as well, because we have not yet considered the equilibrium product distributions for the test conditions. When the equilibrium analysis has been completed, the estimated volatile-S species will be refined.

SRI staff believes that all water levels over 27 to 30 DAF wt. % recorded with Pittsburgh #8 were affected by condensation in the transfer lines to the detectors. Corrected values were estimated by adding a sufficient amount of H_2O to close the H-balances. This procedure is probably as accurate as a direct determination because H_2O is the only significant repository for hydrogen whenever moisture condensed in the transfer lines. Such H_2O yields were corrected for all three pressures.

The only other adjustments made to the 1.0 MPa dataset were for the secondary pyrolysis case (50C) without O_2, in which the decomposition products plugged the reactor flow tube and the aerosol particle separator. In addition to the upward adjustment to the H_2 yield, the soot yield was increased to the value predicted by PC Coal Lab® for the thermal histories imposed in this test, then the char yield was increased to close the mass balance.

Table B.3. Pittsburgh #8, 1.0 MPa Datasets, with Corrected Values, in DAF wt. %

	50C		56C		55C		54C		53C		52C		51C	
	M	C	M	C	M	C	M	C	M	C	M	C	M	C
CO_2	0.4		29.4		52.2		70.9		94.3		142.6		197.7	
H_2O	1.2		14.2		22.0		23.7		29.3	33.4	29.2	42.5	28.4	45.8
CO	7.8		35.9		45.1		43.3		41.3		20.1		15.5	
CH_4	1.0		0.7		0.5		0.3		0.1		0.0		0.0	
C_2	1.4		0.5		0.4		0.2		0.0		0.0		0.0	
C_3	0.1		0.1		0.1		0.0		0.0		0.0		0.0	
Oils	0.3		0.3		0.1		0.0		0.0		0.0		0.0	
H_2	2.4	3.8	2.5		2.7		2.2		1.3		0.43		0.17	
HCN	1.04		0.89		0.54		0.29		0.06		0.00		0.00	
NH_3	0.03		0.06		0.05		0.03		0.02		0.00		0.00	
NO	0		0.01		0.01		0.00		0.01		0.02		0.19	
Tar	0		0		0		0		0		0		0	
H_2S	Nm	7.4	Nm	7.4	Nm	7.4	Nm	7.4	Nm		Nm		Nm	
SO_2	Nm		Nm		Nm		Nm		Nm	13.8	Nm	13.8	Nm	13.8
Soot	21.1	29.1	19.5		8.0		9.6		13.9		7.6		2.0	
Char	40.3	48.5	36.9		38.4		35.7		35.6		26.1		20.4	
ΣMass		1.020		1.095		1.063		1.042		1.081		1.027		1.076
ΣC		1.018		0.994		0.991		1.027		1.091		0.999		1.021
ΣH		1.008		0.966		1.135		1.062		0.999		1.000		1.004
ΣO		1.011		1.363		1.243		1.132		1.111		1.092		1.147
X_{HC}		0		39.5		53.1		68.5		87.4		100.0		100.0
X_{Soot}		0		32.7		72.5		67.0		52.7		74.2		93.2
X_{Char}		0		23.9		20.8		26.4		27.6		46.2		57.9

Note: M: measured; C: corrected; Nm: not measured. Notations are the same in Tables B.4-B.8.

Table B.4. Pittsburgh #8, 2.0 MPa Datasets, with Corrected Values, in DAF wt. %

	64B		63B		62B		61B		60B		59B		58B	
	M	C	M	C	M	C	M	C	M	C	M	C	M	C
Product Distribution														
CO_2	1.6		4.4		36.4		46.7		119.0		142.0		179.3	
H_2O	1.5		6.9		15.3		18.7		27.7	34.9	27.1	39.0	30.7	41.7
CO	12.0		21.8		30.1		33.3		35.5		29.9		22.0	
CH_4	2.7		2.1		1.0		0.7		0.3		0.2		0.1	
C_2	1.9		1.4		0.6		0.4		0.2		0.1		0.1	
C_3	0.3		0.3		0.1		0.1		0.0		0.0		0.0	
Oils	0.8		0.6		0.2		0.1		0.0		0.0		0.0	
H_2	3.5		3.1		3.0		2.3		1.1		0.7		0.33	
HCN	1.51		1.39		0.95		0.45		0.23		0.02		0.01	
NH3	0.08		0.07		0.08		0.08		0.05		0.03		0.00	
NO	0		0.05		0		0.03		0.01		0.02		0.11	
Tar	0		0		0		0		0		0		0	
H_2S	Nm	7.4	Nm	7.4	Nm	7.4	Nm	7.4	Nm		Nm		Nm	
SO_2	Nm		Nm		Nm		Nm		Nm	13.8	Nm	13.8	Nm	13.8
Soot	21.2	25.1	15.3	25.1	15.6		9.5		4.4		4.6		3.3	
Char	45.1		43.5		42.4		39.8		32.3		35.5	25.3	37.7	19.8
Mass Balances														
ΣMass		0.964		1.008		1.023		0.981		1.006		1.104		1.028
ΣC		0.956		1.000		0.992		0.936		1.036		1.000		1.000
ΣH		1.101		0.979		1.057		1.024		1.000		1.000		1.000
ΣO		0.955		1.034		1.070		1.027		1.045		1.143		1.050
Burnout														
X_{HC}		0.0		21.4		60.8		75.3		90.1		93.8		96.9
X_{Soot}		0.0		0.8		39.8		63.3		83.0		82.2		87.3
X_{Char}		0.0		2.9		6.0		11.8		23.7		43.9		56.1

Table B.5. Pittsburgh #8, 3.0 MPa Datasets, with Corrected Values, in DAF wt. %

	2nd Py	77B		74B		73B		72B		67B		71B		70B		68B		69B		79B	
		M	C	M	C	M	C	M	C	M	C	M	C	M	C	M	C	M	C	M	C
Product Distribution																					
CO_2	0.8	12.5		23.9		58.1		78.8		85.2		86.2		116		141		130		170	
H_2O	1.6	11.5		15.9		18.8		23.3		24.2		31.5		31.4		27.8	30.4	28.4	38.3	32.3	36.0
CO	5.6	20.9		32.8		31.6		32.0		27.9		26.5		29.4		21.6		27.2		21.7	
CH_4	5.0	4.64		3.54		2.36		1.27		0.75		0.71		0.08		0.33		0.60		0.38	
C_2	4.5	2.94		1.85		1.25		0.53		0.31		0.31		0.41		0.16		0.27		0.19	
C_3	1.6	0.48		0.16		0.17		0.14		0.06		-		0.15		0.04		0.10		0.05	
Oils	-	1.71		0.78		0.34		0.21		0.05		0.08		0.77		0.17		0.11		-	
H_2	2.1	3.36	0.36	2.54	0.50	1.85	0.65	1.86		1.80		0.65		0.80		1.16		0.65		1.01	
HCN	1.5	1.29		0.74		0.66		0.17		0.30		0.40		0.13		0.03		0.05		0.06	
NH_3	0.18	0.14		0.17		0.18		0.06		0.09		0.11		0.11		0.06		0.02		0.02	
NO	-	-		-		-		-		-		-		-		0.07		-		0.08	
Tar	-	-		-		-		-		-		-		-		-		-		-	
H_2S	7.4	-	7.4	-	7.4	-	7.4	-	7.4	-	7.4	-	7.4	-	7.4	-	7.4	-	-	-	-
SO_2	-	-		-		-		-		-		-		-		-		-	13.8	-	13.8
Soot	22.9	16.5		7.4	13.0	9.5		5.3		7.4		3.8		5.2		7.8		4.6		3.6	
Char	46.8	55.2	46.8	51.3	45.4	53.7	44.0	42.5		38.8		43.9		44.2		33.3		34.1		34.3	
Mass Balances																					
ΣMass	1.00		0.99		1.01		1.03		1.02		0.97		0.99		1.06		1.07		1.02		1.04
ΣC	0.98		1.03		1.03		1.06		1.04		1.01		1.02		1.16		1.09		1.06		1.15
ΣH	1.00		1.00		1.00		1.00		1.05		1.02		0.96		0.97		1.00		1.00		1.00
ΣO	1.01		1.12		1.01		1.00		1.07		1.00		0.97		1.01		1.07		1.00		1.00
Burnout																					
X_{HC}	0.0		12.5		44.2		63.0		81.5		89.1		89.2		87.0		94.0		90.8		94.8
X_{Soot}	0.0		28.0		43.2		58.5		76.9		67.7		83.4		77.3		65.9		79.9		84.3
X_{Char}	0.0		0.0		3.0		6.0		9.2		17.1		-		-		28.9		27.1		26.7

Note that all four balances were closed to within 2 % by these adjustments. Whereas no additional adjustments were made for any of the other test results, the balances on C and H generally close to within ± 5 %. Breaches in the mass balances are only slightly higher. The O_2 balances are generally oversubscribed by over 10 %, and by more than one-third in 56C. Hence, in this dataset, the closures are fine except for the O-balances on runs 56C and 55C. Only one of these runs (55C) was affected by plugging, and all the fed O_2 was utilized in both of them, which is highly unusual. Adjusting the O_2 utilization factors downward would improve the O-balance closures and probably improve the mass balance closures as well.

The assigned extents of burnout for the gaseous fuel compounds exhibit the expected tendency to increase monotonically for progressively more oxidizing conditions. But only the final three extents of soot burnout are as systematic. The other three non-zero values are much more erratic. The initial extents of char burnout may also seem peculiar, in that they immediately increase to 24 %, then stay the same while the gases and soot burn away. However, as shown in CFD simulations, particles are very rapidly dispersed into the sheath in this turbulent flow, and these particles may be responsible for the immediate increase in burnout.

Additional adjustments to the 2.0 MPa dataset were made for the two most reducing cases and the two most oxidizing cases. In both of the most reducing tests, the soot yields were increased to 25.1 %, consistent with the PC Coal Lab® prediction. Following these adjustments, all four balances closed to within the target tolerance except for the H-balance on 64B. No adjustments whatsoever were made to the results of 62B, 61B, and 60B, yet nearly all the associated balances close to within ± 5 %. In the two most oxidizing runs, the char yields were adjusted downward to close the C-balances. These adjustments are large. It is hard to understand how the extent of char burnout could remain the same after substantial additions of O_2, as indicated by the data. In addition, data collected in runs 65B and 66B were completely rejected, due to very poor closures on the C-, H-, and O-balances. Both these cases imposed similar conditions to 63B, so no information was lost by their omission.

It is gratifying to see the expected tendencies in the extents of burnout for gases, soot, and char in the 20 atm dataset. Gases burn faster than soot which, in turn, burns faster than char. And each burnout profile develops with little or no scatter in the assigned values.

In 3.0 MPa dataset, the H_2O data in runs 68B, 69B, and 79B were corrected, and the two general adjustments made for 1.0 and 2.0 MPa were also made to runs 72B, 67B, 71B, 70B, and 68B. Consequently, it is especially significant that all four balances close to well within the target uncertainty of ± 5% in run 71B. The situation is essentially the same for run 67B, except that the O_2 utilization into products was increased from 42.6 % to 47.5 % to close the O-balance. The uncertainties on the O-balances on runs 72B and 68B slightly exceed the target, and those in the H-balances on runs 70B and 68B have more substantial breaches. In both the latter two runs, the defects must be associated with the determinations of H_2O and H_2, because the hydrocarbon yields are low and there is too little hydrogen in soot and char to explain the discrepancy.

The O_2 utilization percentages were also increased in runs 77B and 73B of the 3.0 MPa dataset, although increasing the percentage to 100 % was still insufficient to close the O-balance in run 77B. But this is the only flaw in the O-balances for this dataset. There were two additional adjustments to runs 77B, 74B, and 73B. The H_2 yields were significantly reduced to close H-balances. This adjustment is more arbitrary than the others, because the problems could be in the relatively very high hydrocarbon yields. However, the analytical uncertainties are generally much lower for hydrocarbons, because they are detected with a flame ionization detector versus a thermal conductivity cell for H_2. The second adjustment is the reduction in char yields, from 50 – 55 DAF wt. % to 44 - 47 %. The assigned values for runs 74B and 73B were interpolated from the value assigned for run 77B and the measured value for run 72B. Finally, the corrected soot yield for run 74B is an interpolated value based on the soot yields measured in runs 77B and 73B. This dataset did not include a case for pure secondary volatiles pyrolysis. The estimated product distribution is largely based on the measured yields of hydrocarbons and N-species for run 77B and the yields of oxygenated gases and soot predicted with PC Coal Lab®. Of course, all four balances are essentially closed for the estimated products.

The assigned extents of burnout for the gaseous fuel compounds exhibit the expected tendency to increase monotonically for progressively more oxidizing conditions, except for runs 70B and 69B where burnout is nearly complete. The extents of soot burnout are almost as systematic, except that there is more scatter in the values for the final four runs. The extents of char burnout increase very gradually for progressively higher O_2 utilization, then reach an asymptotic value of 27 to 29 % for runs 68B, 69B, and 79B. Values for runs 71B and 70B were omitted because they are clearly at odds with the tendency for more burnout for higher O_2 utilization.

Illinois #6 Tests

The datasets with Illinois #6 at 1.0 and 2.0 MPa appear in Tables B.6 and B.7. The only difference in the labeling from Tables B.3-B.5 is the second column labeled “2nd Py”, which represents the estimated product distribution for complete secondary volatiles pyrolysis, in which the coal provided the only source of oxygen. Run 88C with Illinois #6 at 1.0 MPa had only small amounts of supplemental O_2, so the estimated secondary pyrolysis distributions are very similar to the measured ones, except that the partial oxidation of hydrocarbons into CO and H_2 has been reversed by adding additional hydrocarbons and reducing the CO yields. The distribution collected under run 97C with Illinois #6 at 2.0 MPa represents a much higher O_2 flowrate, even though it is the lowest in this test series. The distribution for secondary pyrolysis from the 1.0 MPa test was therefore applied to 2.0 MPa, because pressure effects are asymptotic at roughly 0.5 MPa. The actual differences in product composition for these two pressures should be negligible.

The S-species adjustments made to the Pittsburgh #8 datasets were applied uniformly to the Illinois #6 datasets, and were especially significant for the Illinois #6 because its sulfur content is 10.8 DAF wt. %. Also, the O_2 utilization percentages had to be

increased from the levels assigned from the measured exhaust O_2 concentrations for all tests at 1.0 MPa, but only for the cases with higher O_2 levels at 2.0 MPa. These adjustments identically closed the O-balances, and they also brought the closures on the mass balances essentially to unity. In addition, at 1.0 MPa, the measured H_2 and CO yields from run 88C were reduced to close the H- and C-balances, and the H_2O yields from runs 87C and 86C were reduced to close the H-balances. Similarly, at 2.0 MPa, the H-balances for runs 97C, 95C, and 94C could only be closed by lowering the H_2O yields. Note that all the adjustments to H_2O, CO, and H_2 yields are relatively small. Most important, the burnout indices on hydrocarbons gases, soot and char increase smoothly across almost the entire range of conversion. Whereas higher pressure accelerates the combustion of gases and soot, char burnout is retarded. This effect is probably due to O_2 depletion rather than a mechanistic shift.

Table B.6. Illinois #6, 1.0 MPa Datasets, with Corrected Values, in DAF wt.%

	2nd Py	88C		87C		86C		85C		84C		83C		82C	
		M	C	M	C	M	C	M	C	M	C	M	C	M	C
Product Distribution															
CO_2	1.3	1.3		19.3		28.6		82.4		133.9		184.3		192.7	
H_2O	2.4	2.4		19.5	13.2	23.4	18.0	32.4		41.6		42.7		44.4	
CO	9.0	16.2	12.3	36.7		38.2		43.2		28.8		15.3		15.0	
CH_4	2.0	1.1		0.5		0.5		0.1		0.0		0.0		0.0	
C_2	2.4	2.0		0.4		0.4		0.0		0.0		0.0		0.0	
C_3	0.4	0.1		0.0		0.1		0.0		0.0		0.0		0.0	
Oil	-	0.3		0.2		0.2		0.0		0.0		0.0		0.0	
H_2	2.60	3.77	3.00	2.57		2.13		1.40		0.63		0.37		0.34	
HCN	1.00	1.02		1.06		0.24		0.04		0.00		0.00		0.00	
NH_3	0.00	0.02		0.04		0.04		0.03		0.02		0.01		0.02	
NO	0.00	0.00		0.00		0.00		0.00		0.00		0.21		0.26	
Tar	-	-		-		-		-		-		-		-	
H_2S	11.4	-	11.4	-	11.4	-	11.4	-		-		-		-	
SO_2	-								21.6		21.6		21.6		21.6
Soot	21.0	22.5		12.1		10.8		9.2		4.6		3.9		3.7	
char	47.6	47.6		41.7		38.5		28.1		22.7		15.8		13.1	
Mass Balances															
ΣMass	1.011		1.029		1.000		0.990		0.952		1.002		1.003		1.001
ΣC	1.027		1.044		1.013		0.991		1.049		1.023		1.028		1.019
ΣH	0.993		0.993		1.007		1.009		0.985		1.015		0.947		1.003
Util O_2,%	0	1.9	18.0	80.0	95.0	75.0	89.5	81.1	92.2	71.5	81.5	64.8	71.0	60.3	67.0
ΣO	1.003		1.000		0.990		1.000		1.000		1.000		1.091		1.000
Burnout															
X_{HC}	0		28.2		71.8		80.1		97.2		99.2		99.6		100.0
X_{Soot}	0		-0.1		42.4		48.6		56.2		78.1		81.4		82.4
X_{Char}	0		0.0		12.4		19.1		41.0		52.3		66.8		72.5

Table B.7. Illinois #6, 2.0 MPa Datasets, with Corrected Values, in DAF wt.%

	2nd Py	97C		95C		94C		93C		99C		89C		91C	
		M	C	M	C	M	C	M	C	M	C	M	C	M	C
Product Distribution															
CO_2	1.3	31.9		67.1		109.6		165.1		180.8		200.1		224.0	
H_2O	2.4	23.3	17.7	30.8	25.6	42.5	39.4	44.3		44.8		45.6		46.3	
CO	9.0	37.8		42.6		31.8		20.8		16.1		10.1		5.9	
CH_4	2.0	1.0		0.7		0.3		0.1		0.1		0.1		0.0	
C_2	2.4	0.6		0.4		0.2		0.1		0.1		0.1		0.0	
C_3	0.4	0.1		0.2		0.1		0.0		0.0		0.0		0.0	
Oil	-	0.3		0.2		0.1		0.0		0.0		0.0		0.0	
H_2	2.60	1.94		1.28		0.64		0.31		0.16		0.13		0.09	
HCN	1.00	0.79		0.08		0.01		0.00		0.03		0.01		0.00	
NH_3	0.00	0.09		0.05		0.02		0.00		0.00		0.01		0.01	
NO	0.00	0.02		0.00		0.00		0.02		0.09		0.00		0.16	
Tar	-	-		-		-		-		-		-		-	
H_2S	11.4	-	11.4	-	11.4	-		-		-		-		-	
SO_2		-		-		-	21.6	-	21.6	-	21.6	-	21.6	-	21.6
Soot	21.0	12.3		7.1		3.5		2.9		3.4		2.8		2.5	
Char	47.6	40.1		34.5		28.9		20.6		17.8		15.2		9.3	
Mass Balances															
ΣMass	1.011		1.029		0.966		0.986		1.007		1.006		1.004		1.000
ΣC	1.027		1.044		1.061		1.024		1.042		1.041		1.034		1.016
ΣH	0.993		0.993		1.000		1.000		1.011		0.988		0.993		0.990
Util O_2,%	0	77.1		68.4		65.9	73.0	61.6	68.0	58.1	63.0	50.9	57.0	43.8	48.3
ΣO	1.003		1.000		1.037		1.000		1.000		1.000		1.000		1.000
Burnout															
X_{HC}	0		61.0		76.6		89.5		96.2		96.8		97.7		98.8
X_{Soot}	0		41.4		66.2		83.3		86.2		83.8		86.7		88.1
X_{Char}	0		15.8		27.5		39.3		56.7		62.6		68.1		80.5

Wyodak Tests

The Wyodak (PRB) coal was only tested at 1.0 MPa, and the dataset is summarized in Table B.8. The second column in the table labeled "2nd Py" is the estimated product distribution for complete secondary volatiles pyrolysis. Run 110C had only small amounts of supplemental O_2, so the estimated distributions are very similar to the measured ones, except that the partial oxidation of hydrocarbons into CO and H_2 has been reversed by adding additional hydrocarbons and reducing the CO yields.

In the PRB dataset, the S-species estimation is the only adjustment to the entire dataset. The closures on all the mass and elemental balances for every test are within the target uncertainty of ± 5%. The assigned burnout indices for hydrocarbon gases and char increase for progressively higher O_2 levels, as expected, and the gases burn much faster than char, as expected. It is also noteworthy that the extents of char burnout are significantly greater than for the Pittsburgh #8 and Illinois #6 at the same pressure and stoichiometic ratio, as they should be. The only flaw in this dataset is the scatter in the burnout indices for soot combustion. This is not very serious, because soot from all coal types has similar burning rates, so the burnout profile for PRB-derived soot can be estimated from the profiles for the other coals.

B.1.5 Burnout Profiles

The burnout indices assigned to all tests in Tables B.3-B.8 appear in Figures B.1-B.3. The index for gaseous fuel compounds is based on conversion of hydrocarbons, including HCN. The curves in the figures have been "smoothed" to eliminate most of the unphysical scatter seen in the tabulated assignments, which remains evident in the data points. The smoothed values were matched in the CFD simulations to properly estimate heat release and conversion rates. In this section, they are used to illustrate the impacts of stoichiometric ratio, pressure, and coal rank on the burnout of three classes of combustibles: gases, soot, and char.

Table B.8. PRB Sub-bituminous, 1.0 MPa Datasets, in DAF wt. % (No Corrections Necessary)

	2^{nd} Py	110C M	109C M	108C M	107C M	105C M	104C M	103C M	102C M	101C M
Product Distribution										
CO_2	6.6	6.6	18.9	36.9	61.1	90.4	126.1	166.4	192.6	203.1
H_2O	8.1	8.1	15.9	23.6	27.5	32.0	36.1	39.4	43.8	45.9
CO	12.3	17.1	30.6	41.5	50.8	49.8	43.3	37.4	31.3	26.4
CH_4	2.9	2.9	2.4	1.5	0.6	0.1	0.0	0.0	0.0	0.0
C_2	4.0	4.0	2.2	1.0	0.3	0.0	0.0	0.0	0.0	0.0
C_3	0.4	0.3	0.1	0.0	0.0	0.0	0.0	0.0	0.0	0.0
Oils	-	1.8	0.9	0.1	0.0	0.0	0.0	0.0	0.0	0.0
H_2	2.75	2.75	2.41	2.06	1.92	1.56	1.20	0.82	0.57	0.34
HCN	0.69	0.69	.61	0.57	0.45	0.19	0.05	0.05	0.00	0.00
NH_3	0.07	0.07	0.09	0.13	0.17	0.11	0.06	0.05	0.02	0.01
NO	0.00	0.00	0.00	0.00	0.00	0.00	0.00	0.00	0.08	0.11
Tar	-	-	-	-	-	-	-	-	-	-
H_2S	0.64	0.64	0.64	0.64	0.64	-	-	-	-	-
SO_2	-	-	-	-	-	1.20	1.20	1.20	1.20	1.20
Soot	9.1	9.1	3.8	1.5	1.6	3.1	3.3	4.1	1.7	2.2
Char	52.4	52.4	49.9	42.8	34.7	24.0	18.3	11.5	6.9	4.4
Mass Balances										
ΣMass	1.000	1.016	1.015	1.002	1.001	0.996	1.003	1.001	0.992	1.003
ΣC	1.000	1.021	1.028	0.998	1.016	0.985	1.004	1.039	1.007	0.991
ΣH	0.975	0.997	1.002	0.961	0.991	0.962	0.964	0.954	0.984	0.981
ΣO	1.002	1.000	0.995	1.009	0.992	1.009	1.008	0.991	0.991	1.012
Burnout										
X_{HC}	0	2.0	35.6	64.5	85.0	97.3	99.2	99.5	99.9	100.0
X_{Soot}	0	0	58.2	83.5	82.4	65.9	63.7	55.0	81.3	75.8
X_{Char}	0	0	4.8	18.3	33.8	54.2	65.1	78.1	86.8	91.6

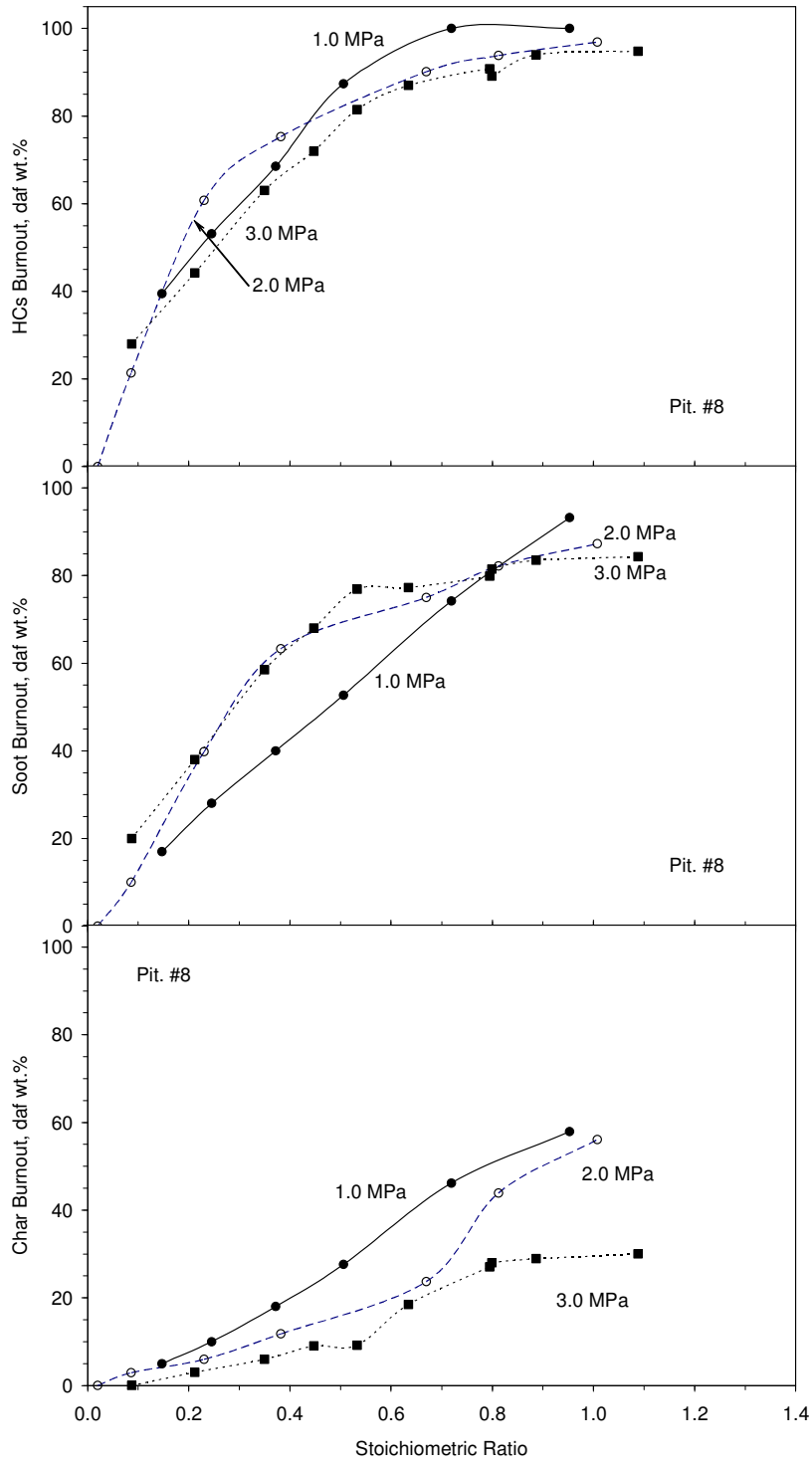

Figure B.1. Measured burnout of hydrocarbons (upper), soot (middle), and char (lower) from Pittsburgh #8 at 1.0 MPa (● and solid line), 2.0 MPa (○ and dashed line) and 3.0 MPa (■ and dotted line).

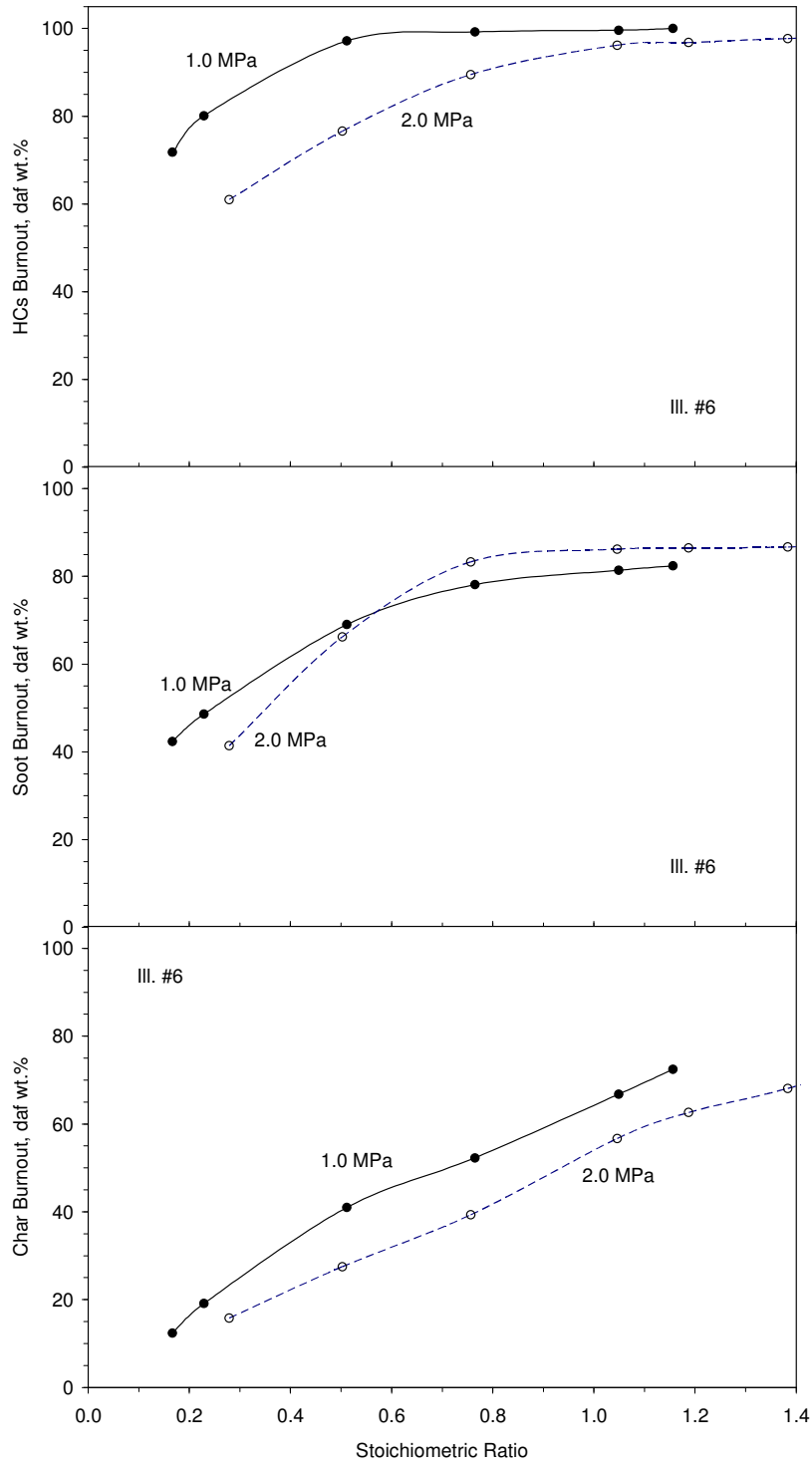

Figure B.2. Measured burnout of hydrocarbons (upper), soot (middle), and char (lower) from Illinois #6 at 1.0 MPa (● and solid line), and 2.0 MPa (○ and dashed line).

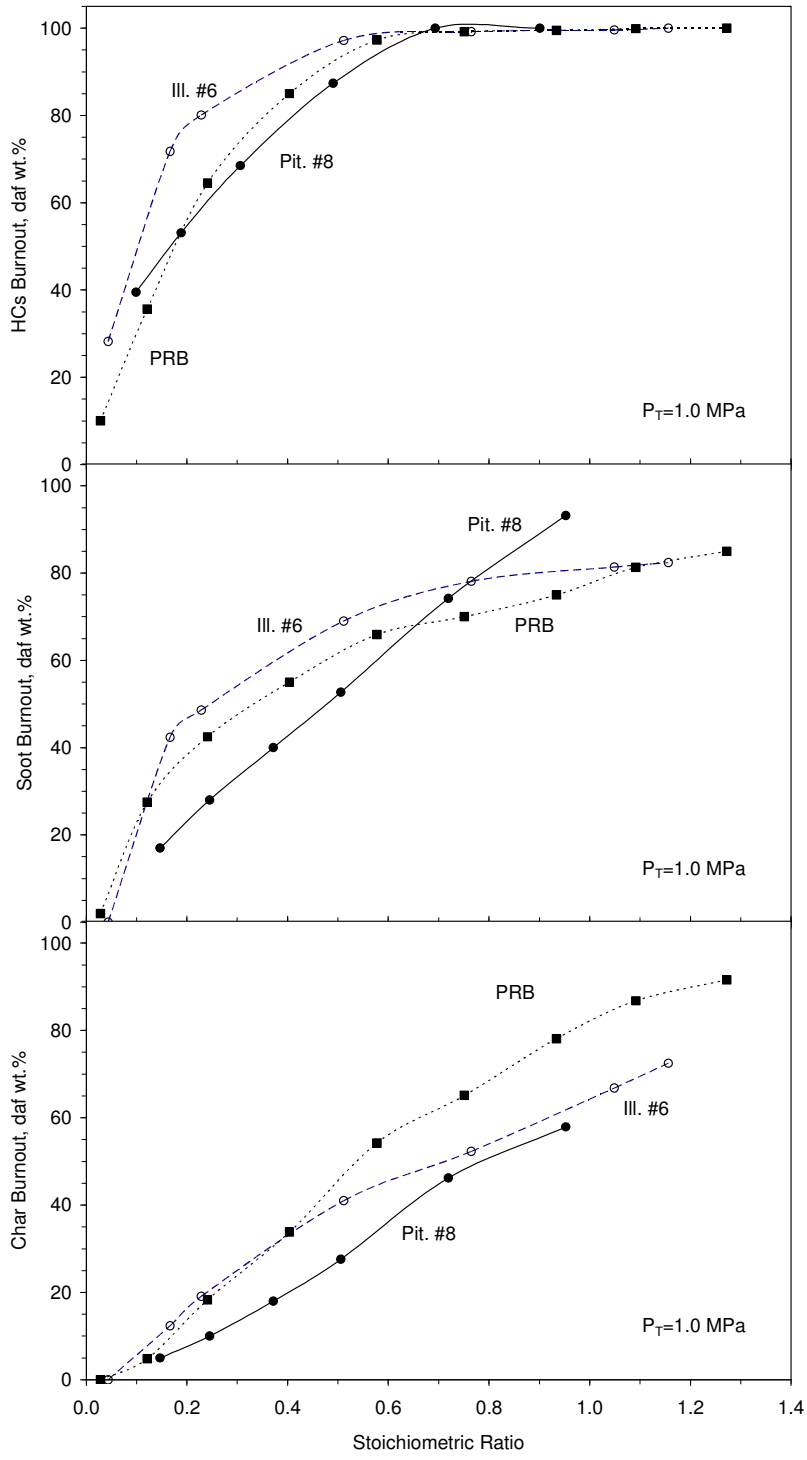

Figure B.3. Measured burnout of hydrocarbons (upper), soot (middle), and char (lower) from Pittsburgh #8 (● and solid line), Illinois #6 (○ and dashed line) and PRB (■ and dotted line) at 1.0 MPa.

In the upper panel of Figure B.1, the extents of burnout for gaseous fuels from Pittsburgh #8 at 1.0 MPa increase monotonically from 40 % at an stoichiometric ratio of 0.1 to 95 % at stoichiometric ratio of 0.6, then approach the asymptotic value of 100 % for further increases in stoichiometric ratio Extents of soot burnout at 1.0 MPa increase in direct proportion to stoichiometric ratio, but to lower values than the extents of gas burnout for a specified stoichiometric ratio The extents of char burnout at 1.0 MPa in the lower panel increase from 25 % to 56 % as stoichiometric ratio progressively increases from 0.1 to 0.95. As expected, gaseous fuels burn out first and char burns last.

The burnout profiles for gaseous volatiles at 2.0 and 3.0 MPa are within experimental uncertainty of the profile for 1.0 MPa, indicating that the total pressure has little impact on the burnout profiles for gaseous volatiles combustion. This does not imply that the burning rate and combustion mechanisms were independent of pressure, because the profiles are plotted versus stoichiometric ratio rather than a time-based coordinate. Moreover, the gas temperature history reaches progressively cooler maxima at higher pressures, as discussed after the gas temperature is characterized from the CFD simulations. The soot burnout profiles for 2.0 and 3.0 MPa are essentially the same, but have higher extents of burnout than the profile for 1.0 MPa at stoichiometric ratio values between 0.2 and 0.7.

The strongest impact of pressure is seen in the char burnout profiles. At a stoichiometric ratio value of 0.95, the extents of char burnout of Pittsburgh #8 decrease from 57.5 DAF wt. % at 1.0 MPa to 52.5 % at 2.0 MPa to 27 % at 3.0 MPa. The impact of pressure is also apparent at all lower stoichiometric ratio values in these datasets. In fact, the O_2 partial pressures in these three datasets were almost the same for progressively higher pressures because the same coal feed rate was used at all pressures and the O_2 flow rates were the same to maintain the same stoichiometric ratio Oxygen partial pressures were fixed by reducing the O_2 inlet concentrations for progressively higher pressures. The diminished char burnout is mostly due to the lower particle temperatures at higher pressures, which will be further discussed.

The burnout profiles for Illinois #6 appear in Figure B.2. Unlike those for Pittsburgh #8, the gas burnout profile at 1.0 MPa is slightly higher than that at 2.0 MPa. Soot burnout, however, is similar at both pressures. In the lower panel of Figure B.4, the char burnout at 1.0 MPa is about 10 % higher than that at 2.0 MPa across the entire stoichiometric ratio range, consistent with the Pittsburgh #8 char burnout profiles. In fact, the soot burnout profiles at both pressures and the gas burnout profile at 2.0 MPa for Illinois #6 are quantitatively consistent with the soot and gas burnout profiles for Pittsburgh #8. Only the gas burnout profile at 1.0 MPa is different.

Since the products from PRB were only monitored at 1.0 MPa, the burnout profiles are directly compared with the profiles from both other coals at this pressure in Figure B.3. Illinois #6 has higher extents of burnout of gaseous volatiles than Pittsburgh #8 and PRB at 1.0 MPa for all stoichiometric ratio below 0.6. Among the gas burnout profiles for all test pressures, only the one for Illinois #6 at 1.0 MPa is distinctive. Similarly, the soot burnout profiles for all fuels are essentially the same, except for the one for Pittsburgh #8

at 1.0 MPa. The dominant soot burnout profile is similar to the gas burnout profile for stoichiometric ratio less than 0.2, but shows substantially less conversion under leaner conditions. Soot probably burns at a rate that is independent of coal rank, because it contains mostly carbon (>98.5%) with small amounts of hydrogen and nitrogen. The soot compositions are nearly the same for all coal types.

Unlike gaseous volatiles and soot, char burnout is strongly affected by coal rank, as expected. At 1.0 MPa and a stoichiometric ratio value of 0.95, the char burnout for Pittsburgh #8 is 57.5 DAF wt.%, 60 % for Illinois #8, and 77 % for PRB. PRB has the fastest char burning rate, in so far as this char is the most effective competitor for O_2 with the gaseous fuels and soot. The extent of PRB char burnout even overtakes soot burnout at a stoichiometric ratio value of 0.85. The impact of coal rank is consistent with extensive databases on char oxidation at both atmospheric pressure (Mitchell et al., 1995) and elevated pressures (Niksa et al., 2003).

Regardless of the pressure and coal type, gaseous volatiles combustion consumes most of the available O_2 at low stoichiometric ratio. Soot effectively competes for O_2 at low stoichiometric ratio, but burnout of the chars of the lowest rank eventually overtakes soot burnout at stoichiometric ratio over 0.8. This is probably a reflection of disparate deactivation rates for these two condensed fuels. There are master burnout profiles for the gaseous volatiles and soot from all fuels and all pressures, albeit, each has an exception at one operating condition. But char burnout profiles are strong functions of coal quality and pressure. Char burnout diminishes for chars of progressively higher rank and for progressively higher pressures. Whereas this rank dependence has already been established with large databases, the apparent impact of rank and pressure are significantly mitigated by thermal effects in the p-RCFR tests/

B.2 P-RCFR NBFZ Simulations

The following sessions report simulations performed for NBFZ combustion tests in the p-RCFR furnace. In total, 45 CFD simulations were performed for the three coals and three pressures in the six test series.

B.2.1 Model Parameters

The input data for the FLUENT simulator for NBFZ tests comprise the reaction rate parameters, various p-RCFR configuration parameters, and the operating conditions. Reaction rate parameters and stoichiometric coefficients appear in Table B.9. The coal properties and operating conditions are also given in Tables B.9. In Table B.9, the coal density, devolatilization rate parameters and ultimate yield, and the stoichiometric coefficients for volatiles combustion were specified with NEA's PC Coal Lab® (PC Coal Lab Manual). This program simulates the complete distribution of products from the devolatilization of any coal at any operating conditions. Thermal histories were assigned from NEA's previous estimates with a 2D FLUENT simulator; e. g., particles were heated to 1050°C at 10^4 °C/s at 1.0 MPa but the ultimate temperature and heating rate were less severe for the higher pressures. The molar stoichiometric coefficients for

volatiles combustion were assigned for combustion of the complete distribution of gaseous volatiles into CO and H_2. The activation energies for char oxidation were assigned from the correlation based on the burning rate database from Sandia National Laboratories, Livermore (Mitchell et al. 1995).

The furnace specifications are collected in Table B.10. These are the dimensions of the furnace and the flow tube actually used in NBFZ tests. Note that coal particles are uniformly injected into the tube over the core region, and that the inlet gas compositions in the core and sheath are the same.

In the FLUENT simulator, the input operating conditions include coal feed rate, inlet gas velocity, O_2 mass fraction, and pressure, were directly taken from Table B.9. A mean particle size of 90 μm was used in all simulations.

Table B.9. Reaction Parameters Assigned for the p-RCFR Simulations.

Parameter	Units	Values					
Coal Name	-	Pittsburgh #8	Pittsburgh #8	Pittsburgh #8	Illinois #6	Illinois #6	PRB
Pressure	MPa	1.0	2.0	3.0	1.0	2.0	1.0
Coal Density	g/cm^3	1.23	1.23	1.23	1.18	1.18	0.96
Coal Swelling Ratio	-	1.4	1.3	1.16	1.11	1.09	1.11
Devolatilization rate parameters							
A-factor	1/s	1631	2.73×10^5	9.97×10^5	4.82×10^4	1.73×10^5	3200
E_a	kJ/mole	28.55	74.15	84.56	61.45	70.47	33.65
Coal Volatility							
Total Volatiles Yield	dry wt%	45.95	51.11	46.68	44.24	44.24	45.15
Gaseous Volatile Fraction	-	0.45	0.57	0.58	0.62	0.62	0.81
Gas Volatiles Molecule Weight	g/mole	8.6	11.2	13.5	13.2	13.2	13.6
Combustible Material (i.e. FC)	dry wt%	41.75	36.59	41.22	38.46	38.46	49.85
Stoichiometric Coefficients for Gaseous Volatiles Combustion							
Volatiles	-	1.0	1.0	1.0	1.0	1.0	1.0
O_2	mole/mole vol	0.093	0.12	0.253	0.177	0.177	0.448
H_2	mole/mole vol	0.94	0.94	1.15	0.96	0.96	0.927
CO	mole/mole vol	0.18	0.29	0.457	0.29	0.29	0.39
N_2	mole/mole vol	0.01	0.012	0.015	0.01	0.01	0.005
SO_2	mole/mole vol	0.069	0.074	0.096	0.135	0.135	0.0066
Mass-Based Stoichiometric Coefficients for Char Combustion (C→CO)							
Char		1.0	1.0	1.0	1.0	1.0	1.0
O_2	g/g-chra	1.35	1.35	1.35	1.37	1.37	1.37
Char Intrinsic Reactivity							
E	kJ/mole	95.07	95.07	95.07	85.13	85.13	84.53

Table B.10. p-RCFR Reactor Configuration Used in FLUENT Simulations.

Parameter	Value, cm
Furnace length	15.8
Inner radius of graphite heating element	5.08
Tube length	27.3
Tube radius	1.2
Radius of core flow, with particles	0.424
Thickness of sheath flow	0.176

B.2.2 Assignments of Extents of Conversion

The application strategy for the CFD simulations is to match the heat release in the actual p-RCFR tests for specified operating conditions, so that the predicted flow and thermal fields are accurate enough to use with detailed chemistry through NEA's ChemNet™ post-processing method. The heat release was matched by adjusting rate parameters to match the reported extents of conversion of the gaseous fuels, soot and char, and the oxygen utilization in the combustion system.

As seen in Figures B.4-B.5, the extents of burnout of all fuels increase as the inlet O_2 level progressively increases. This tendency is observed for all three coals and all test pressures. In addition, coal rank and pressure exert little impact on the burnout profiles of gaseous volatiles and soot. As discussed, some burnout profiles, particularly the soot profiles, are subject to inordinate scatter. Before matching the heat release with the CFD simulations, the discontinuities were eliminated by adjusting the reported burnout data. The smoothing was also based on the most consistent gas and soot burnout profiles for coals and test pressures that may have been different than the ones in the dataset being smoothed.

The burnout profiles fit with the CFD simulations are compared to the smoothed data in Figures B.4 and B.5. Clearly, the CFD simulations accurately reproduce the smoothed extents of fuel consumption. The CFD simulations closely matched the independent fuel consumption profiles for all three coals and all test pressures across the complete range of O_2 levels in the tests.

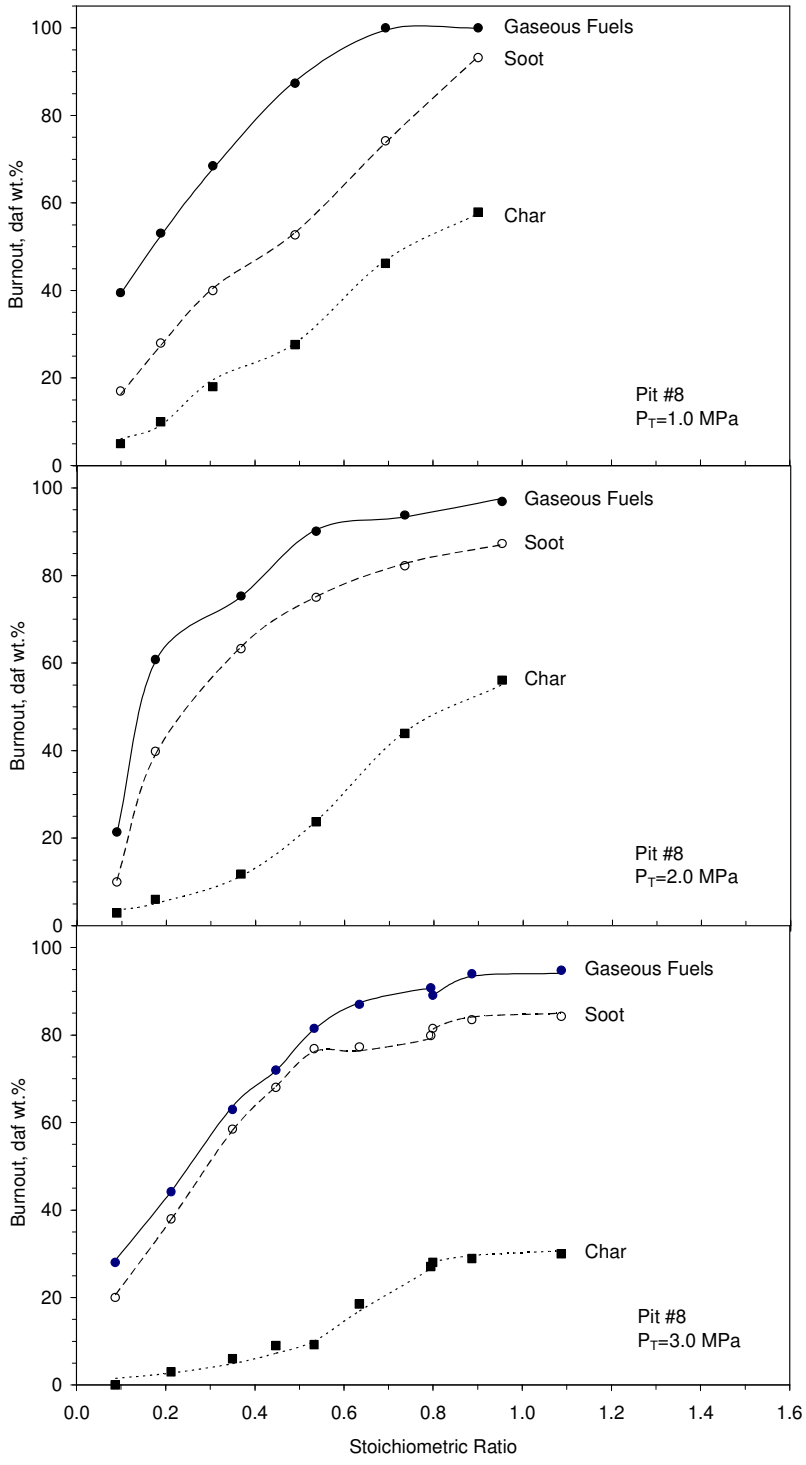

Figure B.4. Burnout profiles imposed in the CFD simulations for gaseous fuels (● and solid curve), soot (O and dashed curve), and char (■ and dotted curve) for Pittsburgh #8 at 1.0 (upper), 2.0 (middle), and 3.0 MPa (lower).

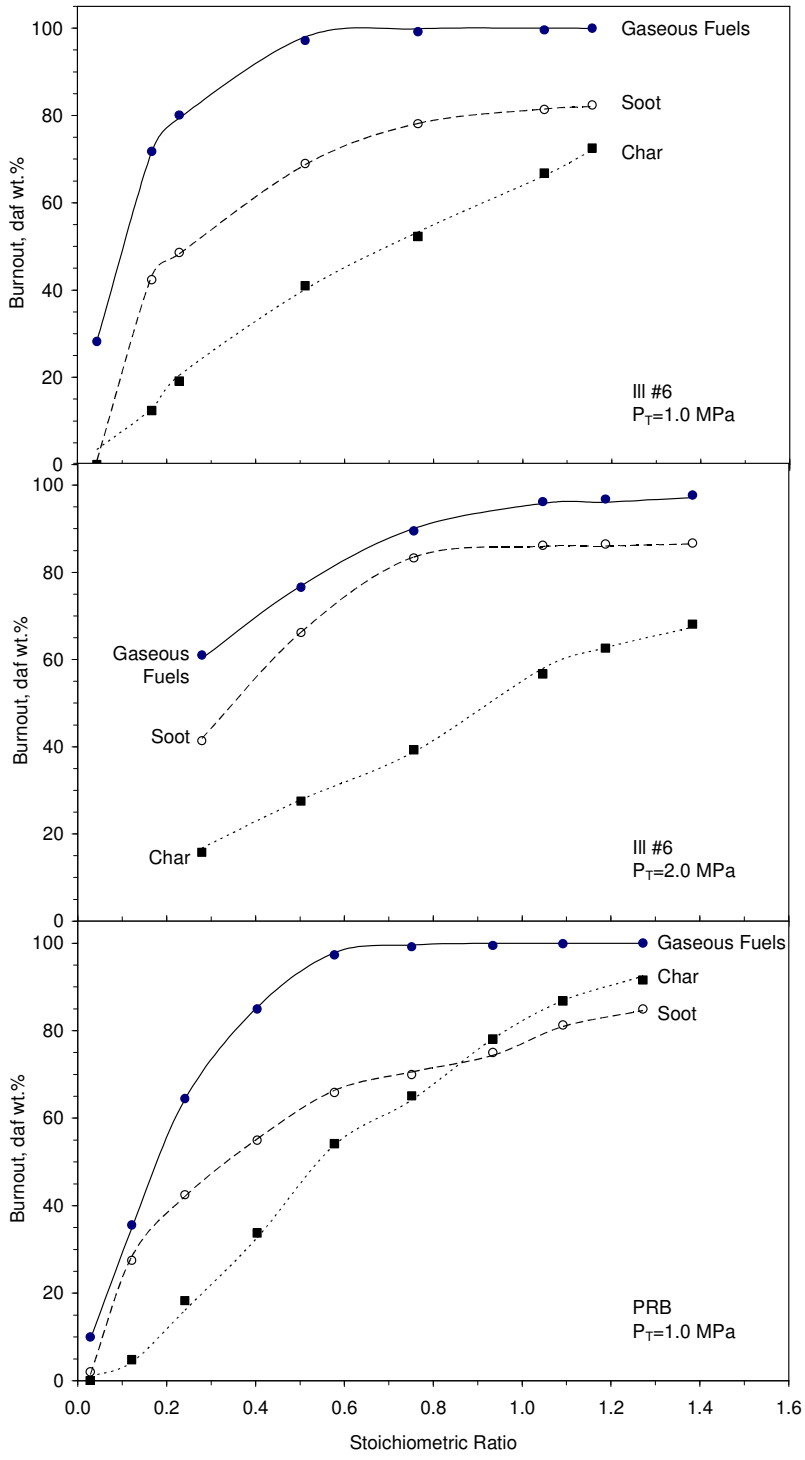

Figure B.5. Burnout profiles imposed in the CFD simulations for gaseous fuels (● and solid curve), soot (O and dashed curve), and char (■ and dotted curve) for Illinois #6 at 1.0 (upper) and 2.0 MPa (middle), and for PRB at 1.0 MPa (lower).

B.2.3 Assigned Rate Parameters

Pre-exponential factors for gaseous volatiles combustion, soot oxidation, CO and H_2 oxidation, and char combustion were adjusted to match the extents of burnout of these fuels for each individual test. The assigned values are collected in Table B.11. The global activation energy for gaseous volatiles, soot, and CO and H_2 were the same in all simulations, and only the pre-exponential factors were adjusted. For Pittsburgh #8 at 1.0 MPa, the A_V value for volatiles combustion varies from 3.3×10^8 to 5.0×10^8 without a consistent trend across the tested range of stoichiometric ratio The A_S value for soot oxidation varies from 3.5×10^5 to 4.3×10^6, almost an order of magnitude. It increases monotonically for progressively higher stoichiometric ratio The value for CO and H_2 combustion varies between 5.5×10^7 and 7.02×10^9, more than two orders of magnitude. Generally, A_{CO} is higher at lower stoichiometric ratio The large variations in A_S and A_{CO} probably reflect compensations for inappropriate activation energies. As discussed in the next section, the gas temperature is much hotter for progressively higher stoichiometric ratio A slight increase in activation energy for soot oxidation, and a slight decrease in the activation energy for CO and H_2 oxidation would reduce the variations in the assigned frequency factors for these reactions. The A value for char oxidation varies between 3.93 to 8.93, which is much smaller than those for soot and CO and H_2 oxidation.

The assigned frequency factors also vary for different pressures, which is not surprising because the thermal fields at different pressures are substantially different. The A_V values for volatiles from Pittsburgh #8 vary between 7.1×10^8 and 1.91×10^9 at 2.0 MPa, and between 1.2×10^9 and 5.2×10^9 at 3.0 MPa. The assigned A_V values increase for progressively higher pressures. The A_S values for soot oxidation of Pittsburgh #8 vary between 5.0×10^7 and 9.8×10^7 at 2.0 MPa, and between 3.0×10^6 and 9.2×10^8 at 3.0 MPa. Similarly, these values increase for higher pressures. The A_{CO} values for CO and H_2 oxidation vary between 2.5×10^8 and 2.4×10^9 at 2.0 MPa, and between 2.5×10^7 and 8.4×10^9 at 3.0 MPa. However, the mean A_{CO} value is almost the same for both pressures. The A for char oxidation is also seen to increase for higher pressures, but not monotonically. At 2.0 MPa, the A value varies between 4.93 and 15.93 and, at 3.0 MPa, it varies between 2.93 and 20.93. There are no systematic tendencies with stoichiometric ratio in the assigned A values for 2.0 and 3.0 MPa for this coal.

The Illinois #6 dataset at 1.0 MPa exhibits relatively constant frequency factors for gaseous fuels, soot, and CO and H_2 oxidation. Except for a much lower value of 4.0×10^8 assigned for run 88C, all A_V values for gaseous fuels vary between 1.2×10^9 and 2.1×10^9, a range smaller than that for the volatiles from Pittsburgh #8. The mean A_V value, however, is higher than that for Pittsburgh #8 at 1.0 MPa. The frequency factors assigned for soot oxidation and CO and H_2 oxidation are much lower for run 88C; however, the values for the rest of the runs are within 3.05×10^6 to 7.5×10^6, and 1.2×10^7 to 8.0×10^7, respectively. These ranges are much narrower than those for Pittsburgh #8. The A value assigned for char oxidation ranges from 7.31 to 25.01 for all runs except 88C. The much lower A-factors assigned for run 88C match the near-zero extents of soot and char burnout reported for this test.

Table B.11(a). Assigned Rate Parameters for CFD Simulations.

Run No.	stoichiometric ratio	A_V for Gaseous Fuels Oxidation, m^3/kg-s	A_S for Soot Oxidation, 1/s	A_{CO} for CO and H_2 Oxidation, m^3/kg-s	A for Char Oxidation, $g/cm^2/s/atm^{0.5}$
PIT. #8 at 1.0 MPa					
56C	0.147	4.00E+08	3.50E+05	1.07E+09	3.93
55C	0.245	4.10E+08	6.20E+05	2.00E+09	5.03
54C	0.372	3.30E+08	9.00E+05	7.02E+09	8.93
53C	0.506	3.40E+08	1.20E+06	3.32E+08	7.93
52C	0.719	5.00E+08	1.60E+06	1.32E+08	8.93
51C	0.953	5.00E+08	4.30E+06	5.50E+07	4.03
PIT. #8 at 2.0 MPa					
63B	0.089	7.10E+08	5.00E+05	1.40E+09	4.93
62B	0.175	3.01E+09	9.00E+06	2.40E+09	4.93
61B	0.367	2.01E+09	5.50E+07	2.50E+08	4.93
60B	0.536	1.21E+09	2.80E+07	1.55E+09	8.93
59B	0.735	1.91E+09	9.80E+07	2.50E+08	15.93
58B	0.953	1.57E+09	6.40E+07	4.50E+08	15.93
PIT. #8 at 3.0 MPa					
77B	0.09	1.20E+09	3.00E+06	2.50E+07	2.93
74B	0.21	4.10E+09	2.00E+07	8.04E+09	8.93
73B	0.35	3.30E+09	9.00E+07	1.70E+09	8.93
71B	0.45	3.00E+09	2.00E+08	7.50E+08	20.93
72B	0.53	4.70E+09	5.00E+08	4.00E+08	6.93
70B	0.63	3.40E+09	1.20E+08	4.40E+09	19.93
69B	0.79	4.80E+09	3.50E+08	5.50E+08	19.93
67B	0.8	5.20E+09	9.20E+08	4.50E+07	6.03
68B	0.89	4.80E+09	5.70E+08	4.30E+08	13.03
79B	1.09	4.00E+09	4.90E+08	6.00E+08	6.03
ILL. #6 at1.0 MPa					
88C	0.04	4.00E+08	1.50E+04	1.00E+04	1.91
87C	0.17	1.40E+09	3.05E+06	1.30E+07	20.91
86C	0.23	1.20E+09	4.45E+06	1.20E+07	10.01
85C	0.51	1.80E+09	6.55E+06	8.00E+07	25.01
84C	0.76	2.10E+09	7.50E+06	5.20E+07	8.51
83C	1.05	2.10E+09	6.30E+06	4.00E+07	7.31
82C	1.16	2.10E+09	5.35E+06	2.60E+07	7.61
ILL. #6 at 2.0 MPa					
97C	0.28	2.00E+09	1.14E+07	9.00E+08	15.51
95C	0.5	1.70E+09	6.85E+07	3.00E+08	5.01
94C	0.76	1.85E+09	1.65E+08	4.00E+08	2.61
93C	1.05	1.65E+09	1.10E+08	3.50E+08	3.01
99C	1.19	9.50E+08	7.00E+07	3.10E+08	2.51
89C	1.38	1.25E+09	9.50E+07	2.50E+08	2.6
91C	1.77	1.10E+09	1.10E+08	1.40E+08	3.7

Table B.11(b). Assigned Rate Parameters in CFD Simulations (Continued)

Run No.	stoichiometric ratio	A_V for Gaseous Fuels Oxidation, m^3/kg-s	A_S for Soot Oxidation, 1/s	A_{CO} for CO and H_2 Oxidation, m^3/kg-s	A for Char Oxidation, $g/cm^2/s/atm^{0.5}$
PRB Subbit. at 1.0 MPa					
110C	0.03	3.00E+08	1.00E+04	3.20E+07	0.68
109C	0.12	1.20E+09	1.30E+06	3.12E+09	5.68
108C	0.24	1.10E+09	1.45E+06	5.00E+08	52.68
107C	0.4	6.50E+08	2.50E+06	9.00E+07	30.08
105C	0.58	7.00E+08	3.20E+06	2.30E+07	16.08
104C	0.75	6.00E+08	2.30E+06	3.00E+07	13.08
103C	0.93	6.00E+08	1.60E+06	3.00E+07	15.08
102C	1.09	6.00E+08	1.60E+06	3.00E+07	45.08
101C	1.27	6.00E+08	2.10E+06	1.80E+07	14.08

Similarly, variations among the assigned frequency factors for Illinois #6 at 2.0 MPa were small. Except for run 97C, which had the lowest stoichiometric ratio, the frequency factors for the rest of the runs varied only between 9.5×10^8 and 1.85×10^9 for gaseous fuels combustion; between 6.85×10^7 and 1.65×10^8 for soot oxidation, and between 1.40×10^8 and 4.0×10^8 for CO and H_2 oxidation. The A value for char oxidation is between 2.6 and 5.0, except for run 97C. Pressure variations affected the assigned frequency factors for soot oxidation and CO and H_2 oxidation, but not for gaseous volatiles oxidation.

Except for run 110C, the assigned frequency factors for PRB at 1.0 MPa are within 6.0×10^8 to 1.2×10^9 for gaseous fuels combustion; 1.3×10^6 to 3.2×10^6 for soot oxidation; and 1.8×10^7 to 3.12×10^9 for CO and H_2 oxidation. The same value of A_V of 6.0×10^8 was assigned for gaseous volatiles combustion for runs 104C-101C, because the reported extents of volatiles burnout were essentially complete and, therefore, insensitive to the kinetics. Frequency factors assigned for run 110C are much lower than those for the rest of the runs, again, because the extents of burnout nearly vanished at the very low stoichiometric ratio imposed in the test. The A values assigned for char oxidation are between 5.69 and 52.69.

Generally, frequency factors assigned for Pittsburgh #8 have larger variations than those for the other two coals. There are fairly consistent trends in the values with variations in stoichiometric ratio, pressure, and coal rank, albeit, with some deviations. A clear trend with stoichiometric ratio on the rates of burnout of soot and CO and H_2 is apparent for Pittsburgh #8, but not for the other two coals. The pressure effect is evident in the rate parameters of all reactions, except for CO and H_2 oxidation for Pittsburgh #8. The pressure effect is weak on gaseous volatiles combustion for Illinois #6, but similar on the other reactions for all three coals. The rate parameters for PRB are similar to those of Illinois #6, consistent with their similar coal properties.

B.2.4 Simulation Results

In this section, the CFD simulations are described in detail for runs 51C and 56C with Pittsburgh #8 at 1.0 MPa. Since these runs have the highest and lowest stoichiometric ratio in this test series, at 0.95 and 0.147, respectively, they clearly illustrate the range of ignition behavior in the simulations for all other test conditions. After these cases, the impact of stoichiometric ratio, pressure, and coal rank on the CFD simulations of other tests will then be discussed.

Simulations for Run 51C

Flow Field

Figure B.6 shows the main simulation results including axial gas velocity, gas temperature, and mass fractions of gaseous fuels, soot and oxygen. The results appear as radial profiles at six axial positions: 0, 6, 12, 18, 24, and 27 cm from the inlet. The furnace hot zone begins at 5.8 cm, and ends at about 20.6 cm.
In the profiles of axial velocity, the profile at the inlet has a fully developed segment across the core and a uniform segment across the sheath. The discontinuity between these segments disappears within 6 cm from the inlet. The gas accelerates continuously as it moves through the tube, reaching a maximum velocity of 240 cm/s at the outlet. Due to buoyancy effects, the gas velocity reaches local maximum values near the tube wall as long as the flow is within the furnace hot zone. The velocity profile becomes parabolic at 24 and 27 cm.

A thermal boundary layer propagates into the flow from the wall temperature of about 1600°C. The centerline gas temperature rises continuously throughout the furnace even while, downstream of the hot zone, the temperature profiles are inverted by convective cooling through a cooler tube wall. For this most oxidizing case in the Pittsburgh #8 test series, the maximum gas temperature exceeds 1500°C. The rapid gas heating is primarily responsible for the rapid acceleration of the axial gas velocity.

Species Distributions

The mass fractions of gaseous volatiles and soot also appear in Figure B.6. Gaseous volatiles and soot are released within 6 cm of the inlet. Note their very high concentrations near the wall, where the gas temperature is hottest over this portion of the flow reactor. Particles are heated mainly by the radiant flux from the tube, but they are also heated by convection from the hotter gases near the wall. Consequently, the

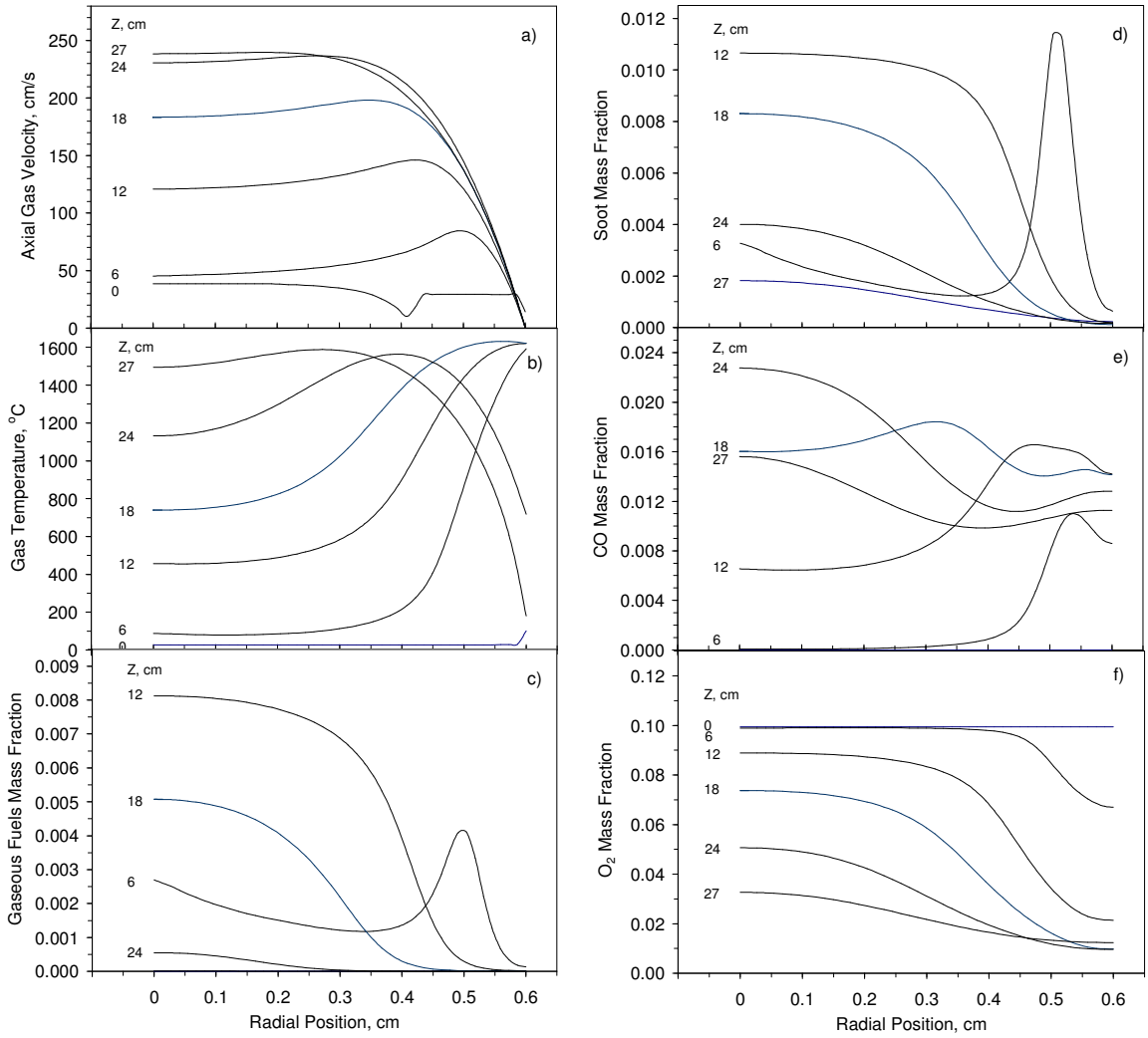

Figure B.6. Simulations of (a) axial gas velocity, (b) gas temperature, (c) gaseous volatiles mass fraction, (d) soot mass fraction, (e) CO mass fraction, and (f) O_2 mass fraction for Pittsburgh #8 at 1.0 MPa and a stoichiometric ratio of 0.95 (run 51C).

particles dispersed into the near-wall region devolatilize before those that remain in the core, and the gaseous fuel concentrations are correspondingly higher near the walls. By 12 cm, the concentration spikes have been eliminated by combustion, and the highest gaseous fuel concentrations are within the core. The fuel inventory is then depleted by a flame front propagating from the near-wall region toward the flow axis. The flame is fed by diffusion of both fuel compounds and O_2 from the core into the sheath flow. Since the gas temperature at 18 cm was well below the threshold for ignition, the core fuel concentration is reduced by transport at this axial position. But by 24 cm, the core is fully ignited and the fuel is depleted much faster. Almost all the gaseous fuels and soot were consumed before the reactor outlet in this particular run.

The CO profiles are considerably more complex than those for the volatiles-derived fuels, because CO is generated as a product of primary devolatilization and secondary volatiles pyrolysis, as well as by partial oxidation of gaseous fuels, soot, and char. At 6 cm, there is no CO in the core, where the gases remain below the onset temperature for devolatilization. But in the near-wall region, the CO profile exhibits the spike seen in the gaseous fuel profile. Further downstream, the CO level in the core grows mostly through contributions from char oxidation through 24 cm, before it finally diminishes at the reactor outlet. But within the near-wall region, CO accumulates at roughly 1.2 wt. % over the entire reactor, due to depletion of near-wall O_2 and diffusion of CO from the higher concentration in the core beyond 18 cm. The final oxidation of CO and H_2 is relatively slow to begin with, and decelerated further by O_2 depletion in this test case. Moreover, our chemistry submodel does not account for water-gas shift equilibrium, as actually occurs at the high temperatures in this test case. The substantial level of unburnt CO in the exhaust really reflects the shift equilibrium, rather than insufficient reaction time for complete combustion of CO, based on the finite-rate kinetics in the CFD simulation.

The O_2 profiles in Figure B.6 begin with a uniform mass fraction at the inlet of 0.10 for this run. The profiles then fall continuously from this level, beginning at 6 cm in the near-wall region. Diffusion of O_2 from the core into the sheath reduces the core O_2 level by 12 cm. By 18 cm, the near-wall O_2 level is below the threshold for gaseous volatiles combustion. Further downstream, the core O_2 levels diminish more rapidly once the char suspension has ignited. Overall, 81.4% of the O_2 was consumed during this run. Not all the O_2 was consumed in the near-wall region, but nearly all the residual O_2 in the exhaust was in the core flow.

Particle Trajectories

In each simulation, 500 particles were injected into the core flow at the inlet. Figure B-7 shows a few of the particle trajectories from the simulation of run 51C with Pittsburgh #8 at 1.0 MPa. There are a significant fluctuations in the particle motion, as expected. Almost immediately after injection, the particles acquire significant radial velocity components due to the turbulence and the wall collisions. All particles eventually penetrate the sheath, and almost all of them contact the wall as some point. Once the particles move into the boundary layer, they are unlikely to escape back into the core flow, so there is a higher particle concentration in the boundary layer than in the core.

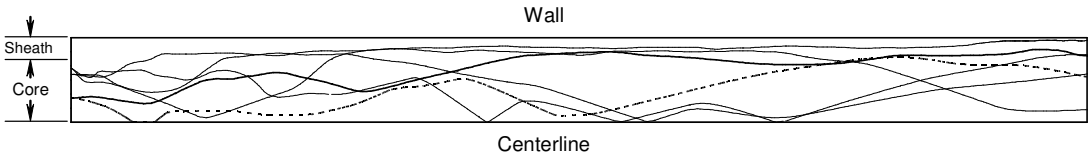

Figure B.7. Representation of particle trajectories of Pittsburgh #8 at 1.0 MPa and stoichiometric ratio of 0.95.

Figure B.8 shows the radial profiles of normalized particle number concentration at 6 cross sections. At the inlet, the particle level is uniform across the sheath, which extends to 0.707 of the tube radius (or 0.00424 cm). After 1 cm downstream of the inlet, particles are still concentrated in the core, and almost none have penetrated into the near-wall region, although a concentration gradient has been established across the sheath. After only 4 cm, the particle concentration profile has been inverted by dispersion into the sheath, and by accumulation within the boundary layer on the tube wall. Particle concentrations in the near-wall region continuously increase throughout the remainder of the furnace, while the concentrations in the core diminish. Hardly any particles remain on the flow axis at the reactor outlet.

This result bears two important implications for the performance of the p-RCFR. First, particle agglomeration near and on the walls will likely cause operational problems, due to the combination of slow particle velocities, high particle temperatures, and high particle concentrations in the near-wall region. Second, complete conversion will be difficult to achieve, because of the strong propensity for accumulation of all fuels in the near-wall region versus substantial amounts of O_2 that remain on the flow axis.

Particle Temperature and Mass Loss Histories

The mean histories for particle temperature and weight loss from the CFD simulation appear in Figure B.9. These histories represent mass-weighted average values based on statistics compiled for the full population of particle trajectories in the CFD simulation. As discussed earlier, particles are heated by radiation from the furnace wall and cooled by convection from the gas flow. During the initial 100 ms, the particles remain in the tube well upstream of the furnace hot zone, where both gas temperature and the radiation flux are low. Rapid heating begins at 150 ms, and the radiant flux drives the particles to a maximum temperature of 1410°C at 380 ms. Thereafter, the particles cool at nearly the same nominal rate as they were heated, which is about 7300°C/s. The maximum heating rate of 8500°C/s also represents substantial heat release from the combustion chemistry.

The weight loss history in Figure B.9 develops in two distinct stages, one each for devolatilization and char oxidation. Devolatilization begins at roughly 200 ms when the particles are heated beyond about 400°C. It is completed after roughly 110 ms, at a residence time of 310 ms. Char oxidation begins immediately thereafter, but proceeds with a much slower weight loss rate than devolatilization. The mean particle residence time in the tube is about 480 ms. The predicted total mass loss is 78.3 DAF wt. %, which compares well with the measured value of 80 %.

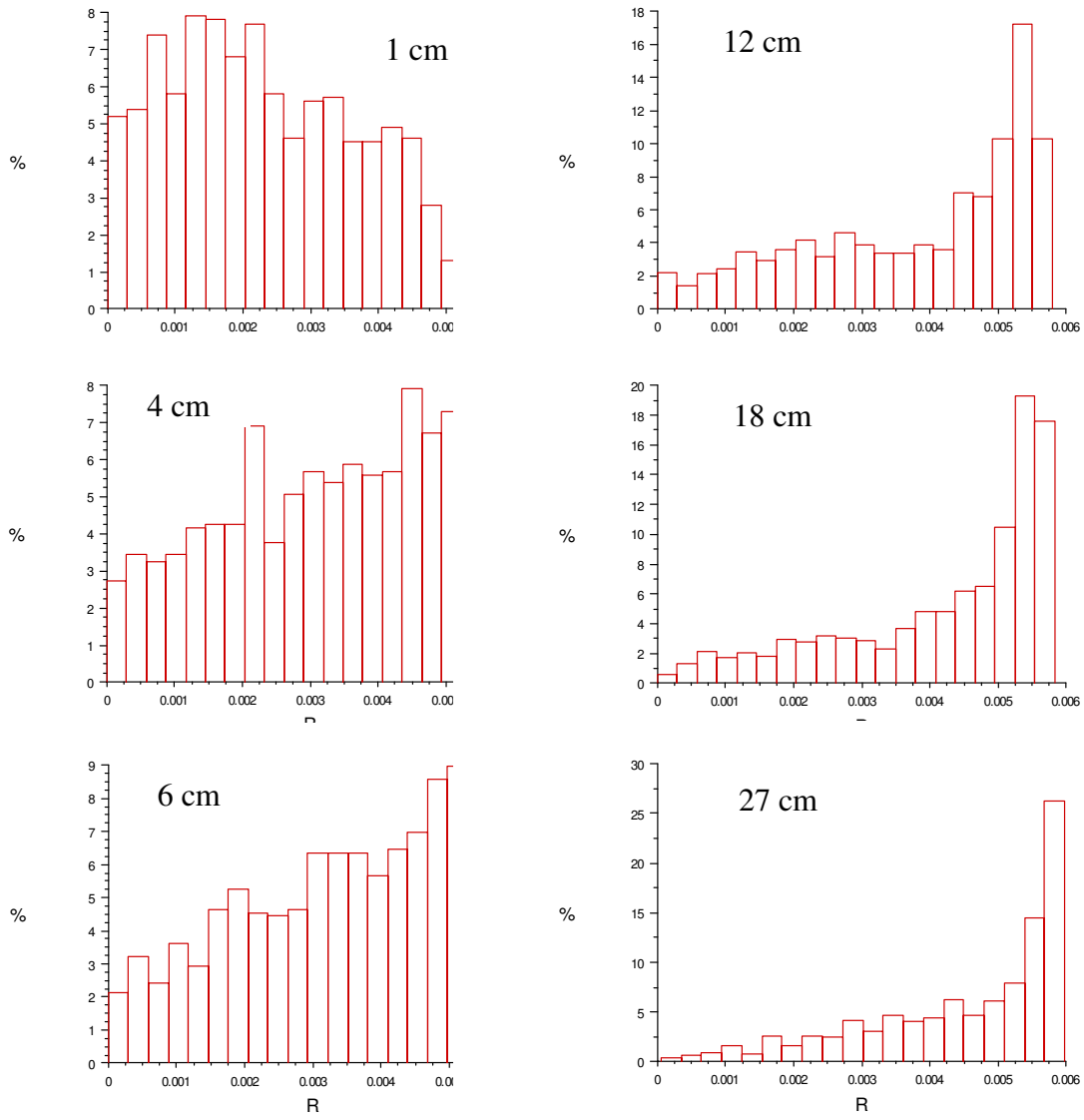

Figure B.8. Radial profiles of particle number concentration of Pittsburgh #8 at 1.0 MPa and stoichiometric ratio of 0.95 at axial positions of 1, 4, 6, 12, 18 and 27 cm.

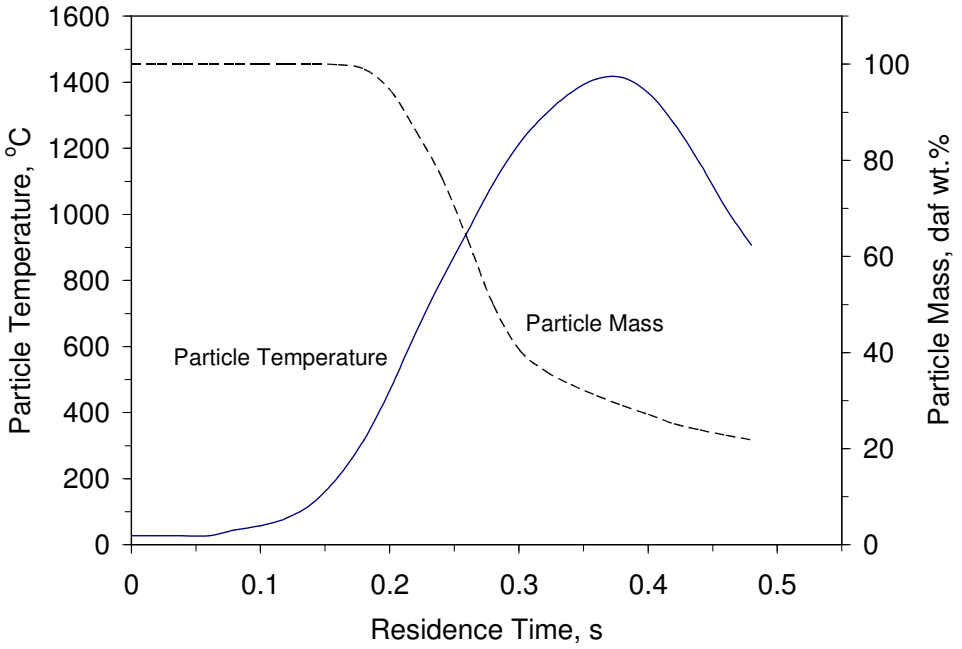

Figure B.9. Particle temperature (solid line) and weight loss (dashed line) of Pittsburgh #8 combustion at 1.0 MPa and a stoichiometric ratio of 0.95.

Particle Residence Time and Burnout Distributions

In addition to the kinetic data, the NBFZ tests are being used as a source of char samples for detailed characterization at Brown Univ. In light of the steep gradients in temperature, O_2 concentration, and particle concentration in the CFD simulation, we prepared distribution functions on the char characteristics to qualify the samples and the interpretations of the analytical data. The particle residence time distribution (RTD) in the tube in Figure B.10 is directly related to the burnout distribution of char particles collected at the tube outlet. This RTD was obtained from the simulation for Pittsburgh #8 at 1.0 MPa and a stoichiometric ratio of 0.95.

Almost 80 % of the particles have residence times between 330 and 480 ms, but the maximum time is 790 ms. The RTD is not normally distributed; rather, it has the form of a gamma distribution and resembles the RTDs for one or a few stirred tanks in series. Whereas there are no short-circuits in this flow field, the relatively few particles that become trapped in the near-wall region have significantly longer residence times than those remaining in the bulk flow. Progressively fewer particles are subjected to progressively longer residence times, as expected. The mean residence time determined from the RTD is 450 ms with a standard deviation of 70 ms.

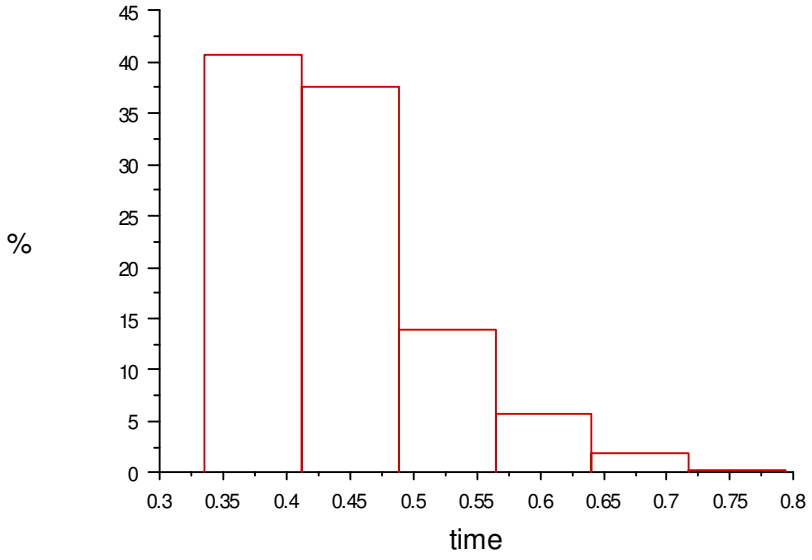

Figure B.10. Particle RTD for Pittsburgh #8 combustion at 1.0 MPa and a stoichiometric ratio of 0.95.

The RTD is only one of the factors responsible for the distributions of char burnout in Figure B.11. These panels show the number distributions for the extents of char burnout at the furnace outlet for the range of stoichiometric ratio values in the test series with Pittsburgh #8 at 1.0 MPa. For the lowest four stoichiometric ratio values, the burnout distributions are normal distributions with higher dispersions for progressively higher stoichiometric ratio values. The mean values also shift toward higher values, as expected. But at stoichiometric ratio values of 0.72 and 0.95, the burnout distributions become much more dispersed, and lose their Gaussian form.

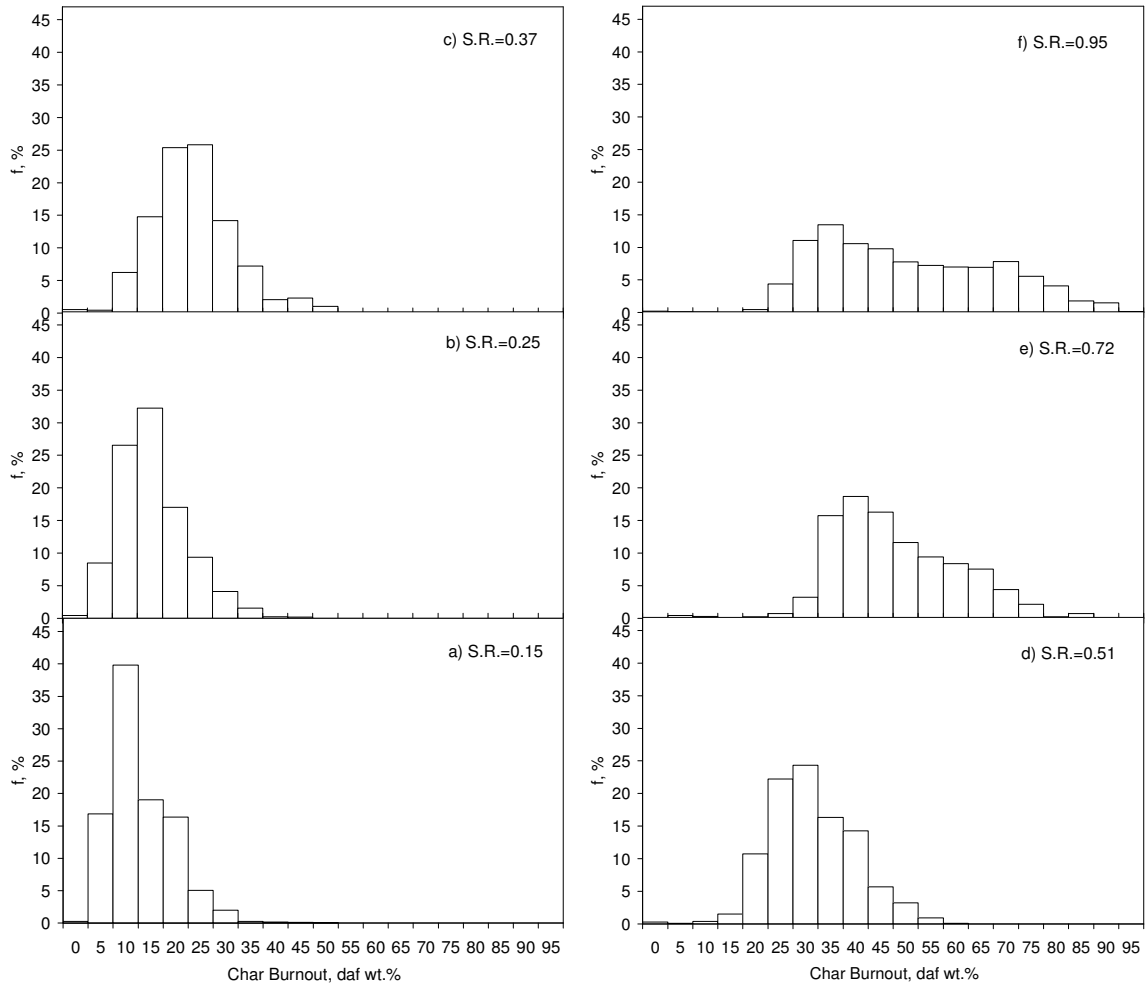

Figure B.11. Char burnout distributions at the furnace outlet for the test series with Pittsburgh #8 at 1.0 MPa and at stoichiometric ratio of (a) 0.15, (b) 0.25, (c) 0.37, (d) 0.51, (e) 0.72 and (f) 0.95.

Two mechanisms are apparently responsible for this abrupt change of form. First, the particles in the core flow continue to burn, which contributes to the portions of the burnout distribution in Figure B.11 that grow into the highest levels. Second, burning particles in the sheath are extinguished by O_2 depletion, so about half the population stays at the same extents of burnout. The O_2 depletion starts near the wall and propagates further toward the flow axis, as seen in Figure B.6 for the case with stoichiometric ratio = 0.95. Any residual char in these regions after the O_2 has been depleted will be extinguished and contribute to the lower extents in the burnout distributions.

Clearly, the non-uniform extents of burnout in Figure B.11 must be factored into interpretations of all analytical data on the recovered char samples, especially from tests with the highest stoichiometric ratio values. The data on chars from the four lowest stoichiometric ratio values should exhibit fairly typical tendencies. But data from both other tests should show much more dispersion than expected.

A Closed Flame Structure

The simulation results presented in the previous subsections of the case history for run 51C can now be synthesized into a flame structure, which directly pertains to the analysis with detailed chemistry in future work assigned for this project. Figure B.12 depicts the flame structure of Pittsburgh #8 combustion during run 51C at 1.0 MPa and at a stoichiometric ratio of 0.95. Even though the coal suspension was injected into only the core, almost all the particles are rapidly dispersed by turbulence into the sheath flow immediately downstream of the inlet. At the inlet, the sheath and core flows had the same gas composition. Whereas the radiant heat flux on the suspension is independent of radial position, convection from and to the gases is determined by the local gas temperature, which is subject to strong radial gradients. Since the gases are much hotter along the wall than in the core, particles in the near-wall region are the first to devolatilize and these first volatiles are quickly ignited by the hot local gases. Hence, the suspension is ignited by the combustion of gaseous volatiles and soot near the wall. The thin flame layer is visible in Figure B.12 immediately upstream of the furnace hot zone.

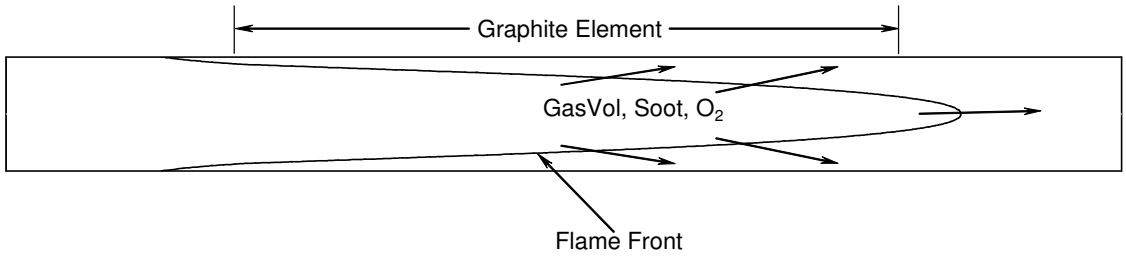

Figure B.12. Flame structure of Pittsburgh #8 combustion in the p-RCFR at 1.0 MPa and stoichiometric ratio of 0.95. The position of the flame front is the locus of positions where the gas temperature is 1050°C.

As the flow moves through the tube, the flame front propagates toward the flow axis, driven by convective heat transfer from the wall and by the heat release from combustion of gaseous volatiles and soot. Hence, the flame is sustained by outward diffusion of volatiles and O_2 toward the wall, and by inward heat transfer toward the center. Eventually, the annular flame front closes to a point on the flow axis which, for this particular case, occurs beyond the downstream edge of the furnace hot zone.

The sketch of this flame structure shares elements in common with both premixed Bunsen flames and laminar diffusion flames. But it really is different from both of these archetypes. The main reason is that fuel consumption is not restricted to the flame zone at all. Within the core, char particles are continuously heated by the radiant flux and by turbulent convection from the near-wall region. Eventually, all the residual fuel compounds in the core surpass the ignition threshold and burn at their fully ignited

burning rates. This stage of the combustion is premixed. Within the near-wall region, the volatiles flame propagates away from the wall but does not consume all the O_2 in the near-wall region. Consequently, char particles dispersed into the sheath burn beyond the radial position of the volatiles flame, closer to the wall. This stage of the combustion consumes residual CO and H_2 and char and is also premixed. Note that the volatiles flame segregates the flow according to the following three stages of combustion: (1) Within the core, residual gaseous fuels, soot, and char eventually reach their ignition threshold and burn in a premixed mode; (2) Gaseous volatile fuels and soot sustain the volatiles flame as it propagates from the near-wall region toward the flow axis; and (3) Residual CO, H_2, and char burns in the near-wall region after the volatiles flame has propagated deeper into the core.

Whether or not the flame closes on the centerline in the available residence time will be mainly determined by pressure and stoichiometric ratio The thermal capacitance of the gas flow is proportional to the gas density and, therefore, increases for progressively higher pressures. Since the radiant heat flux to the suspension is insensitive to pressure, the core gas temperature diminishes at higher pressures. Consequently, inlet conditions that form closed flames at a lower test pressure will eventually sustain open flames at progressively higher pressures. The impact of decreasing stoichiometric ratio is qualitatively similar. For lower stoichiometric ratio, the volatiles flame ignited in the near-wall region releases less heat, because its burning rate is slower at the lower O_2 level. Moreover, two related factors inhibit combustion in the core: First, the slower heat release in the near-wall region directly slows the convection rate into the core, which delays the ignition of combustibles in the core flow. Second, the lower O_2 level diminishes the heat release after the core finally ignites. Since the joint effect of all three factors is to lower core gas temperatures, conditions that sustain a closed flame at a higher stoichiometric ratio will eventually sustain open flames at progressively lower stoichiometric ratio. These shifts will become more apparent in the case study with a lower stoichiometric ratio in the next section.

Simulations for Run 56C

The simulation profiles for the least oxidizing run with Pittsburgh #8 at 1.0 MPa appear in Figure B.13. The gas velocity profiles are very similar to those of the most oxidizing run in Figure B.6, except that the maximum centerline velocity at the outlet is only 190 cm/s versus 240 cm/s in the most oxidizing test. The gas temperature profiles exhibit similar deviations. The temperature profiles through the first 18 cm are essentially independent of stoichiometric ratio, but the profiles further downstream are much cooler. The maximum gas temperature in the sheath flow is only 1200°C, versus 1500°C for run 51C, and the maximum on the flow axis is under 1000°C, versus 1500°C for run 51C.

Whereas the profile of gaseous volatile mass fraction at 6 cm is independent of stoichiometric ratio, the downstream concentrations never fall below 0.006 in the near-wall zone, and remain above this level in the core throughout the entire reactor. Beyond 12 cm, the fuel concentrations in the core diminish due to their slow oxidation but never burn at their fully ignited rates. The ultimate extent of burnout for the gaseous volatiles

is only 40 %. The tendencies in the profiles of soot fraction are similar but compounded by the even-slower burning rate of soot. Indeed the soot concentration hardly diminishes beyond 12 cm, and displays a minimal radial dependence.

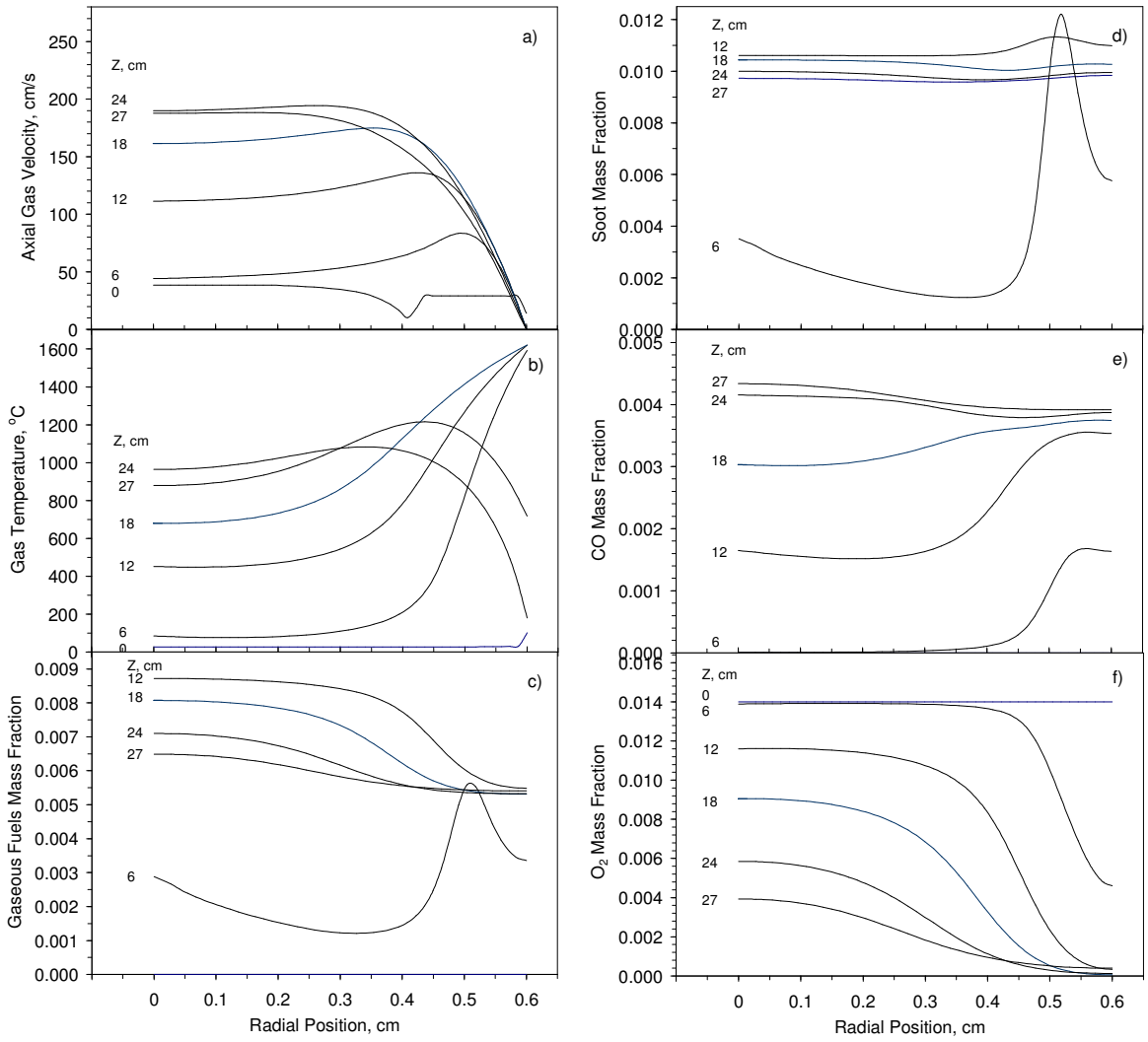

Figure B.13. Simulations of (a) axial gas velocity, (b) gas temperature, (c) gaseous volatile mass fraction, (d) soot mass fraction, (e) CO mass fraction, and (f) O_2 mass fraction for Pittsburgh #8 at 1.0 MPa and a stoichiometric ratio of 0.147 (run 56C).

The profiles of CO mass fraction have similar qualitative forms at the extreme stoichiometric ratio cases, but CO concentrations are substantially lower throughout the reactor at the lower stoichiometric ratio. Indeed the profiles through 18 cm have very similar shapes to those in Figure B.6, but have magnitudes that are lower by a factor of five. Further downstream, the profiles flatten as they grow to 0.0042, reflecting the very slow oxidation rates in this test. Similarly, the O_2 profiles are qualitatively the same for

both extreme stoichiometric ratio cases. But quantitatively, they remain below the threshold for fast-burning along the entire reactor core. Oxygen is only fully consumed near the walls, where the temperature is externally heated above the ignition threshold.

Impacts of Operating Conditions

The simulation results for other test conditions and with other coals have qualitatively similar profiles of velocity and species, and similar particle dispersion characteristics and RTDs. This section presents the most important and distinctive trends for variations in stoichiometric ratio, pressure, and coal rank.

Effect of stoichiometric ratio

The impact of stoichiometric ratio on gas temperature profiles appears in Figure B.14, based on six CFD simulations of the test series for Pittsburgh #8 at 1.0 MPa (runs 51C-56C). The results at the inlet and 6 cm downstream are omitted because they are independent of stoichiometric ratio At 12 cm, the core temperatures were the same in all runs, and the near-wall profiles became only slightly steeper for progressively higher stoichiometric ratio. At 18 cm, the profiles retained the same form, and the core temperatures became hotter for higher stoichiometric ratio while the near-wall profiles became hotter by almost 400°C.

At 24 cm, all the core temperatures are significantly hotter, yet they vary by about 300°C over the range of stoichiometric ratio in the test series. The spread is even greater at the outer edge of the core, reaching 400°C, and the maximum gas temperature exceeds 1500°C at the highest stoichiometric ratio. At the outlet; i.e., at 27 cm, the spread in the core temperature increases to 550°C. Note that the outlet gas temperature in the core at a stoichiometric ratio of 0.15 is only 950°C, which is not hot enough to sustain the rapid combustion of gaseous volatiles and soot. Consequently, this flame is open.

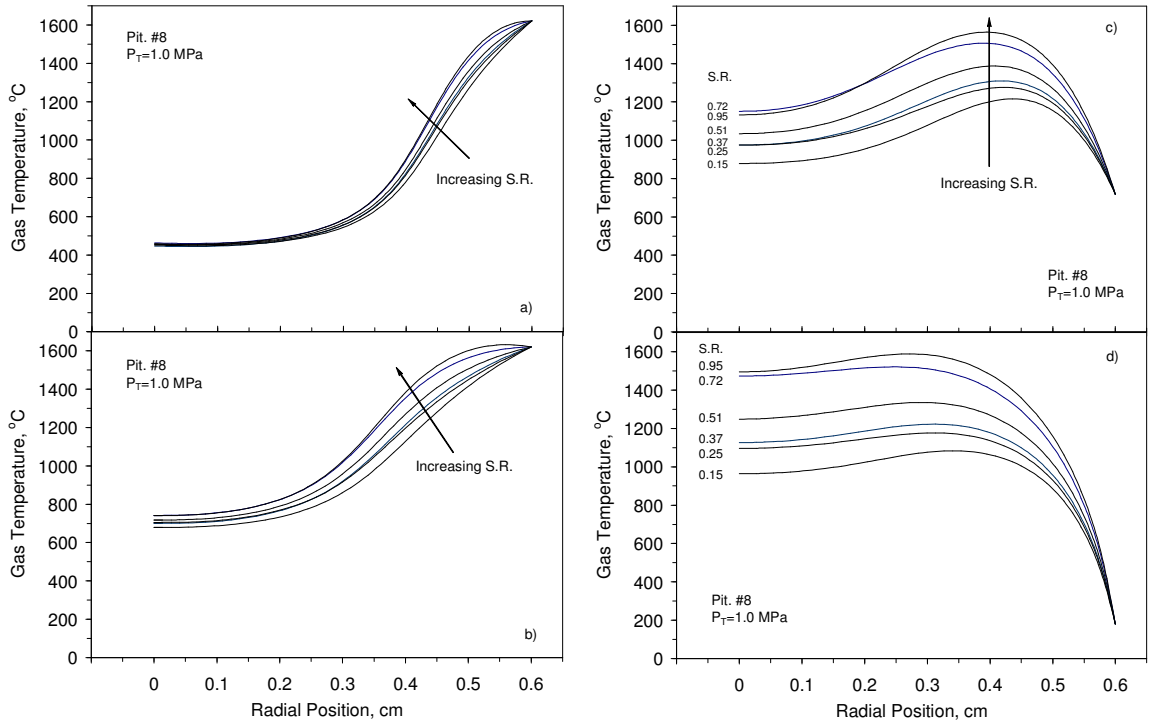

Figure B.14. Gas temperature profiles at axial positions of (a) 12 cm; (b) 18 cm; (c) 24 cm; and (d) 27 cm for Pittsburgh #8 combustion at 1.0 MPa at the stoichiometric ratio values in tests 51C – 56C. The unlabeled stoichiometric ratio values in (a) and (b) are referenced to the legend in (c).

The impacts of stoichiometric ratio on the histories of mean particle temperature and weight loss appear in Figure B.15. The particle temperature histories are almost independent of stoichiometric ratio, except for the spread of 100°C in the maximum particle temperature. As described earlier, the particle heating rate is insensitive to stoichiometric ratio variations because it is primarily determined by the radiant flux from the walls. The different maximum temperatures are due to the faster char burning rates at progressively higher stoichiometric ratio This is apparent in the lower panel of Figure B.15, which indicates greater ultimate extents of burnout for higher stoichiometric ratio The extents of char burnout vary from 5% to 57.9% over this range of stoichiometric ratio. The coal devolatilization behavior is essentially independent of stoichiometric ratio, as seen in the weight loss histories through 300 ms.

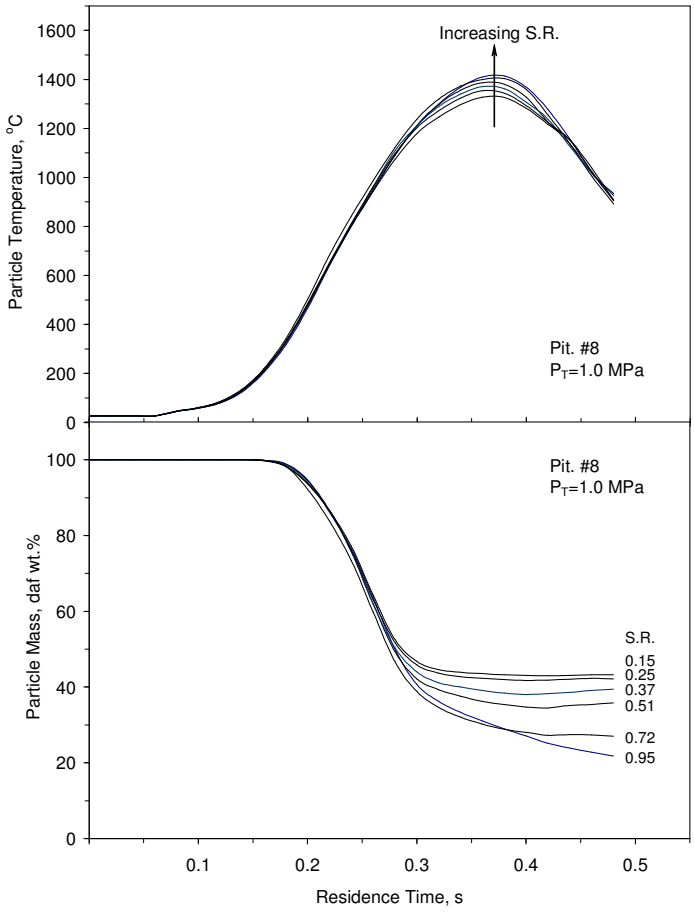

Figure B.15. Histories of (upper) mean particle temperature and (lower) weight loss for Pittsburgh #8 combustion at 1.0 MPa at various stoichiometric ratio

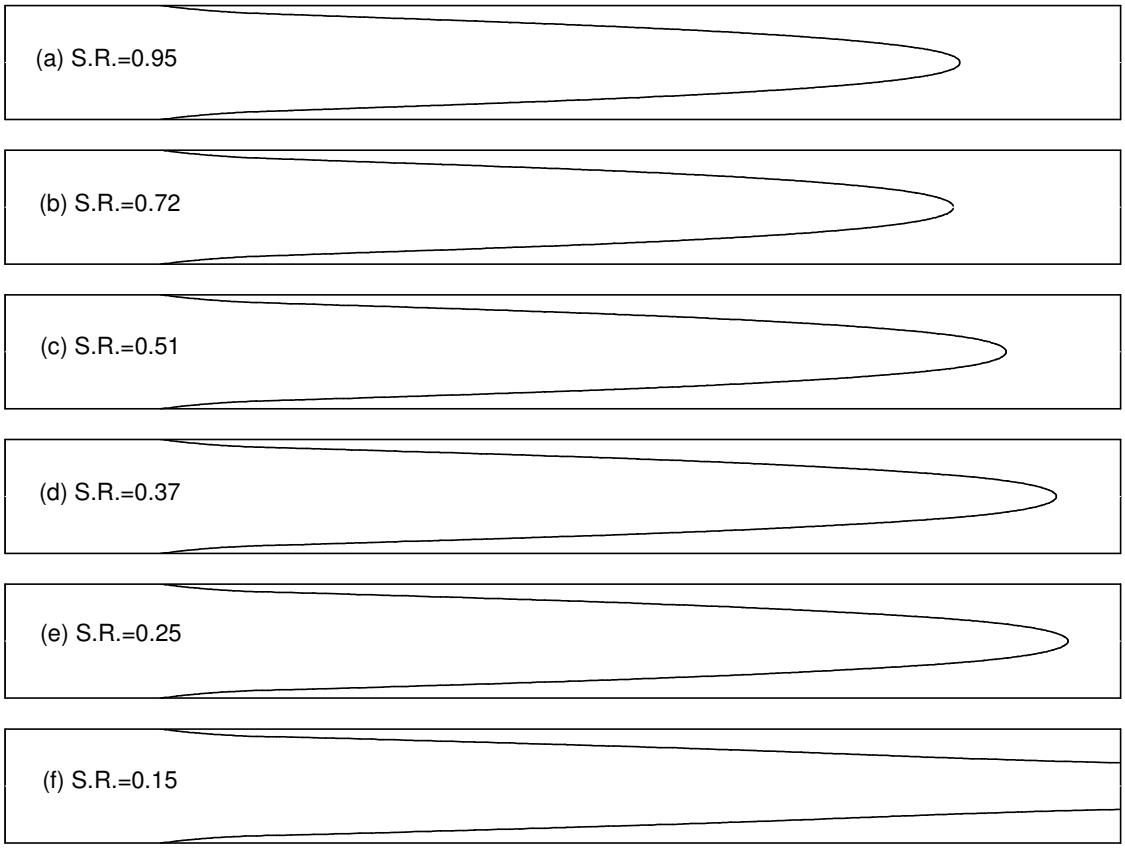

Figure B.16. Flame structures for Pittsburgh #8 combustion at 1.0 MPa and at stoichiometric ratio of (a) 0.95; (b) 0.72; (c); 0.51; (d) 0.37; (e); 0.25; and (f) 0.15. The position of flame front is the locus of positions where the gas temperature is 1050°C.

The flame structures of the six runs are shown in Figure B.16 in order of increasing stoichiometric ratio from bottom to top. The flames are closed for stoichiometric ratio values of 0.25 and higher, and the identical structures for stoichiometric ratio values of 0.72 and 0.95 appear to be asymptotic. The flame opens for an stoichiometric ratio value of 0.15. In the open flame, there is less penetration of the volatiles flame toward the core for progressively lower stoichiometric ratio, but gaseous volatiles always ignite on the wall at the same axial position, just upstream of the furnace hot zone.

Effect of Pressure Variations

We use the test series for Pittsburgh #8 to evaluate the impact of pressure, because it covers the widest range. This study should also be made at uniform stoichiometric ratio; in fact, no runs were performed at the exactly the same stoichiometric ratio for different pressures. The most uniform group includes run 51C at a stoichiometric ratio of 0.95 for 1.0 MPa, run 58B at a stoichiometric ratio of 1.01 for 2.0 MPa, and run 68B at a stoichiometric ratio of 0.89 for 3.0 MPa. The basis to illustrate the pressure effect is the

gas temperature profile which, as we have already demonstrated, undergoes a dramatic change of magnitude for closed and open flames.

The gas temperature profiles along the tube for the three test pressures appear in Figure B.17. The gas temperature profiles are substantially different at every axial position for these three test pressures. Indeed, at every axial location, the gas temperature profiles are uniformly cooler at every radial position for progressively higher pressures. The spread in the temperatures becomes broader as the flow moves through the furnace flow tube, reaching almost 900°C at the reactor outlet. Since the gas temperature profile determines whether or not the fuel compounds in the core will become fully ignited, the differences between the profiles for 1.0 and 2.0 MPa in Figure B.17 are substantially greater than between those for 2.0 and 3.0 MPa. The reason is that, as seen below in Figure B.19, the volatiles flame is closed at 1.0 MPa but open at both higher pressures. In addition, the high temperature layer near the wall becomes thinner for higher pressures, and never penetrates into the core for both higher pressures. This feature is another reflection of the open flame structure.

The cooler gas temperatures at higher pressures are due to the greater thermal capacitances of the gas flow for progressively higher pressures. Since thermal capacitance is proportional to gas density, the thermal capacitance of the gas flow at 3.0 MPa is three times that at 1.0 MPa. The gas in the tube is primarily heated by convection from the wall and particles, and by the heat release due to gaseous volatiles combustion. For similar wall temperatures with the same coal feedrate, the heat transfer rate into the gas flow where the volatiles flame ignites remains the same at the three test pressures. But the heating rate of the gas diminishes in inverse proportion to the greater thermal capacitance, so the gas temperature profiles become cooler for progressively higher pressures. This variation is disproportionate from 1.0 to 2.0 MPa because the gas heating rate is sufficiently fast to ignite the fuel compounds in the core only at 1.0 MPa. So this comparison reflects the difference in thermal capacitance compounded by the substantial heat release in the core at 1.0 MPa. The comparison between 2.0 and 3.0 MPa reflects only the difference in thermal capacitance. The heat release in the core is obviously negligible at 3.0 MPa because the maximum centerline temperature is only 630°C. At 2.0 MPa this maximum reaches 875°C, which is still too cool for full ignition. But ignition is hardly problematic at 1.0 MPa because the maximum gas temperature reaches 1500°C.

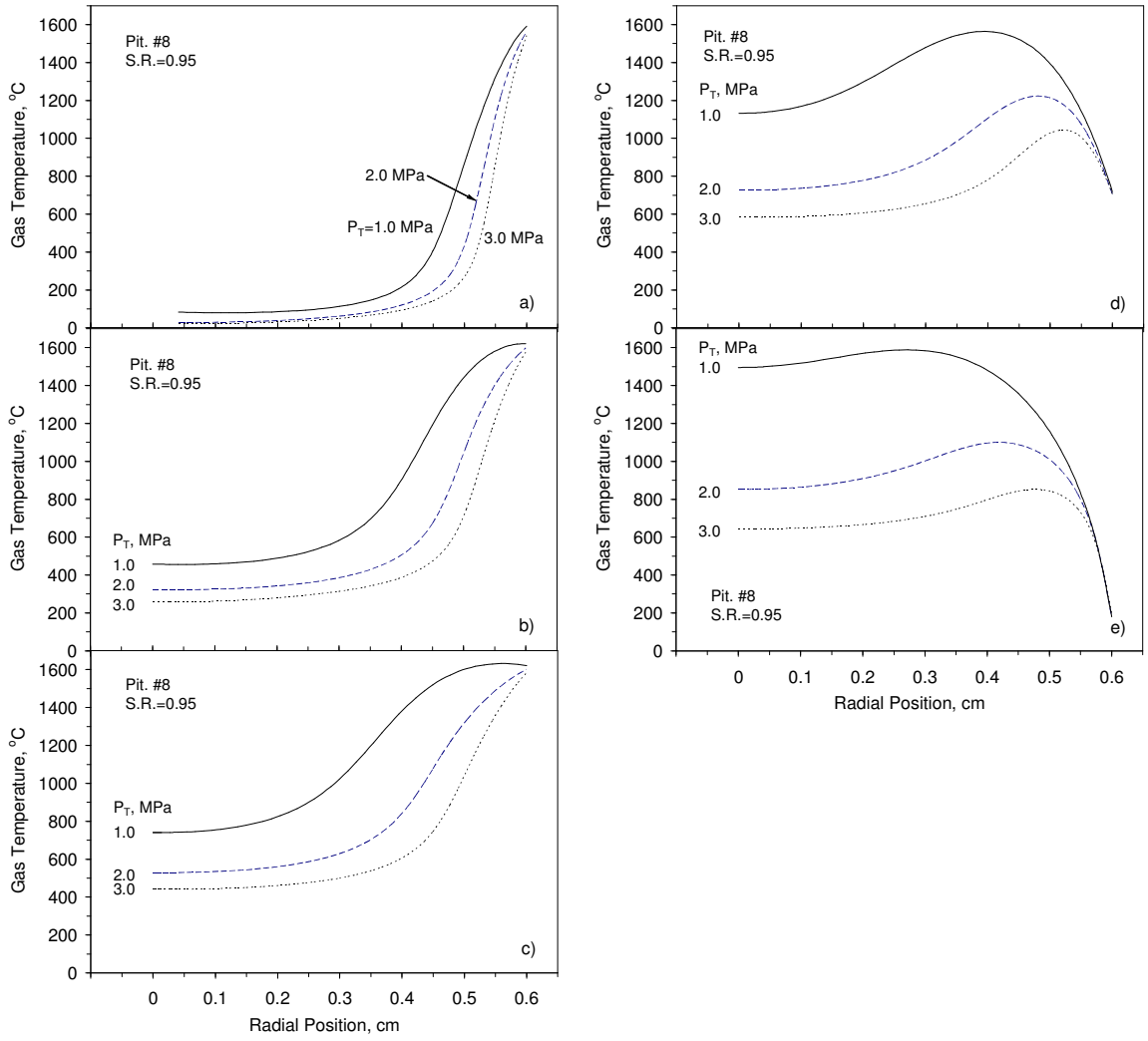

Figure B.17. Gas temperature profiles at axial positions of (a) 6; (b) 12; (c) 18; (d) 24 and (e) 27 cm for Pittsburgh #8 combustion at a stoichiometric ratio near unity at 1.0 MPa (solid curve), 2.0 MPa (dashed curve) and 3.0 MPa (dotted curve).

The pressure variations also significantly affect particle heating and mass loss, as shown in Figure B.18. The maximum heating rates of the coal particles are 8500°C/s at 1.0 MPa, 6070°C/s at 2.0 MPa, and 4860°C/s at 3.0 MPa. Heating rates diminish for progressively higher pressures, due to the faster convective losses to the cooler gas flows. The maximum particle temperature is also significantly cooler, decreasing from 1414°C at 1.0 MPa, to 1227°C at 2.0 MPa, to 1094°C at 3.0 MPa. Two factors are responsible for the slow heating at higher pressures: First, the gas temperatures throughout the tube decrease for higher pressures, so convective losses are greater. Second and less importantly, the radiant flux imposed on the particles slightly decreases at higher pressures; the calculated maximum radiant fluxes using were 66 W/cm^2 at 1.0 MPa, 63 W/cm^2 at 2.0 MPa, and 61 W/cm^2 at 3.0 MPa. Both factors contribute to the particle

energy balance that determines the particle heating rate and, therefore, the particle temperature.

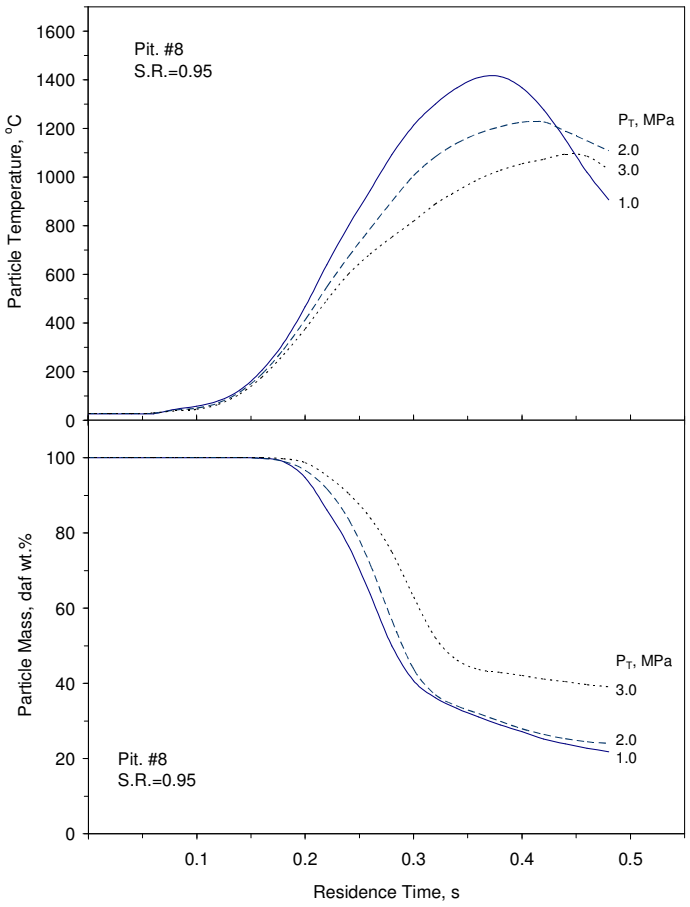

Figure B.18. Histories of (Upper) mean particle temperature and (lower) weight loss for Pittsburgh #8 combustion at a stoichiometric ratio near unity at 1.0 (solid curve), 2.0 (dashed curve) and 3.0 MPa (dotted curve).

The heating rate variations are large enough to significantly affect the devolatilization rate, as seen in the weight loss histories in Figure B.18. In fact, nominal devolatilization rates increase in direct proportion to increases in heating rate. So it is not surprising that the devolatilization time at 3.0 MPa is significantly longer than at 1.0 MPa. The ultimate total weight losses from devolatilization would be constant for the range of test pressures, provided that the same thermal histories were imposed in every test series. Actually, we have already seen that the maximum particle temperatures diminish for progressively higher pressures. But this effect is negligible because even the coolest maximum particle temperature (at 3.0 MPa) exceeds 1000°C, which is the threshold for asymptotic ultimate devolatilization yields. Hence, the devolatilization yields should be at the asymptotic limit for pressures above 0.5 MPa for all three test pressures. In actuality, the assigned weight loss values were 51.5, 54.9, and 53.2 DAF wt. % for pressures of 1.0, 2.0, and 3.0 MPa, respectively. The small differences reflect the imperative to match the measured

values as closely as possible, although the measured values show an even greater spread. In Tables B-3 to B-5, the soot yield decreased from 29.4 DAF wt. % at 1.0 MPa to 22.9 % at 3.0 MPa; the gaseous volatiles yield increases from 23.0 % at 1.0 MPa to 30.1 % at 3.0 MPa.

Char oxidation is indirectly retarded by the lower gas temperatures at progressively higher test pressures. Consequently, the ultimate extents of char burnout were 57.9, 56.1 and 32.5 % at pressures of 1.0, 2.0, and 3.0 MPa, respectively.

The flame structures for Pittsburgh #8 combustion at three pressures are depicted in Figure B.19. There is a closed flame at 1.0 MPa, but the flames were open at both higher pressures. Only thin flames attached to the wall are present at 2.0 and 3.0 MPa, with slightly more penetration into the core at 2.0 MPa. Whenever the fuel compounds in the core fail to ignite, the p-RCFR sustains only open flame structures.

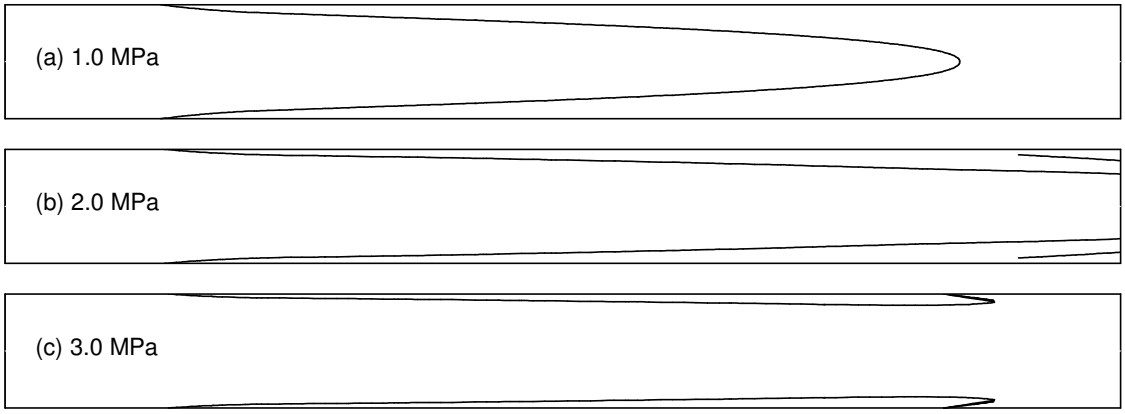

Figure B-19. Flame structures for Pittsburgh #8 combustion at a stoichiometric ratio near unity at (a) 1.0; (b) 2.0 and (c) 3.0 MPa. The position of the flame front is the locus of positions where the gas temperature is 1050°C.

Effect of Coal Rank

We use run 51C of Pittsburgh #8 at a stoichiometric ratio of 0.95, run 83C of Illinois #6 at a stoichiometric ratio of 1.05 and run 103C of PRB at a stoichiometric ratio of 0.93 to characterize the effect of coal rank. All these runs were performed at 1.0 MPa.

Figure B.20 shows the gas temperature profiles for three coals at various axial positions. At the inlet and 6 cm downstream, the gas temperature profiles for these coals are the same, and were omitted from Figure B.20. After 12 cm, there are only slight temperature spreads of about 50°C in the core and of 100°C in the near-wall region. After 18 cm, these respective spreads have grown to 100 and 200°C. At this stage, Illinois #6 generates the coolest gas temperature profile, and PRB and Pittsburgh #8 generate hotter and very similar profiles. These differences have expanded further by 24 cm, and the gas temperature at the outer edge of the core with PRB is more than 100°C hotter than with

Pittsburgh #8. But the most important difference is that the core remains below the ignition threshold with Illinois #6. At the reactor outlet, the cores have ignited with Pittsburgh #8 and PRB, but not with Illinois #6. The Pittsburgh #8 core burns hottest, at 1500°C; the PRB core burns at 1310°C; and the Illinois #6 core burns much more slowly at 1080°C.

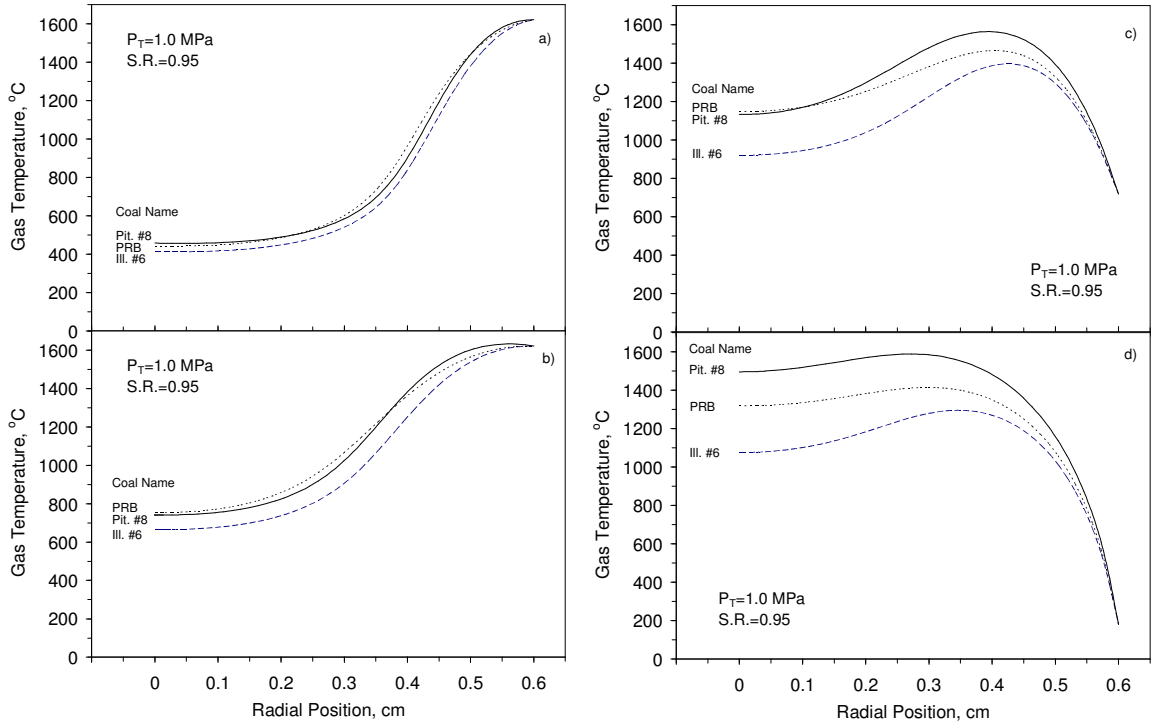

Figure B.20. Gas temperature profiles at axial positions of (a) 12; (b) 18; (c) 24; and (d) 27 cm for Pittsburgh #8 (solid line), Illinois #6 (dashed line) and PRB (dotted line) combustion at a stoichiometric ratio of 0.95 and 1.0 MPa.

Histories of mean particle temperature and weight loss appear in Figure B.21. Both the hv bituminous have essentially the same thermal histories, whereas the PRB has a shorter lag before the onset of rapid heating, by 30 ms. This feature reflects the significantly faster devolatilization rate of sub-bituminous coals, compounded by the associated volatiles combustion and heat transfer in the p-RCFR. During rapid heating, the nominal heating rates for these coals are very similar, although the maximum values are about 8500°C/s for both bituminous coals and 9440°C/s for the PRB. Such variations are inconsequential. The maximum particle temperature of Illinois #6 is about 60°C cooler than those with Pittsburgh #8 and PRB. PRB char has the fastest intrinsic oxidation reactivity, so it ignites at the lowest temperature and burns the fastest among these three coals. Consequently, the ultimate extents of burnout for these tests are 57.9 DAF wt.%, 66.8 % and 78.1 % for Pittsburgh #8, Illinois #6 and PRB, respectively.

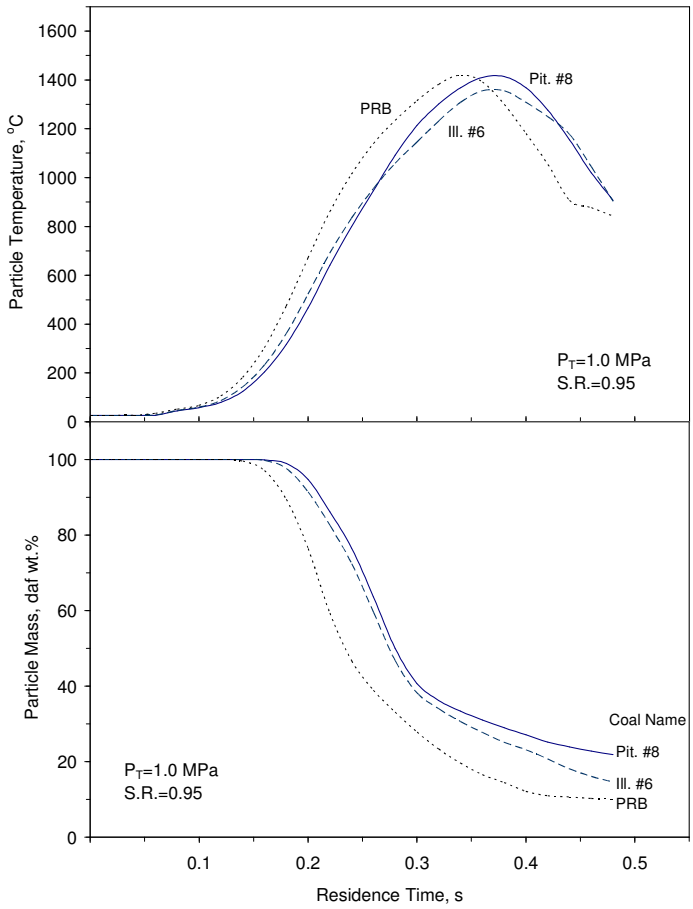

Figure B.21. Histories of (Upper) mean particle temperature and (lower) weight loss for combustion of Pittsburgh #8 (solid line), Illinois #6 (dashed line) and PRB (dotted line) at a stoichiometric ratio near unity and 1.0 MPa..

The flame structures of these coals at 1.0 MPa in Figure B.22 express all the distinctive differences in a concise diagram. These three coals sustain closed flames, although the Illinois #6 flame is nearly open, as expected from the gas temperature profiles.

It may seem surprising that a coal with an intermediate char oxidation reactivity is the one closest to an open flame structure in this comparison. This is probably due to the lost heat release associated with a large portion of unburned CO and H_2 in the Illinois #6 exhaust. In the CFD simulations, only 50% of total weight loss from the Illinois #6 was converted to the ultimate combustion products, CO_2 and H_2O, and most of the residual fuel components were present as unburnt CO and H_2 in the exhaust. The comparable percentages were 67 % for Pittsburgh #8 and 73 % for PRB. Consequently, the total heat release within the flow tube was lowest with Illinois #6, which degraded this coal's ignition characteristics.

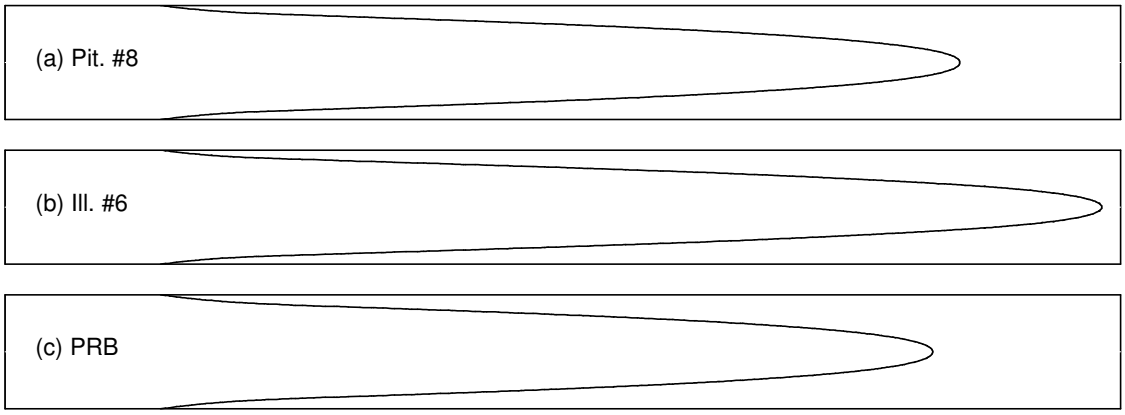

Figure B.22. Flame structures for combustion of (a) Pittsburgh #8, (b) Illinois #6 and (c) PRB at a stoichiometric ratio near unity and 1.0 MPa.

B.3 Sub-Models for Pollutant Formation

B.3.1 Overview of CNPP

NEA's CNPP method generates an equivalent network of idealized reactor elements from a conventional CFD simulation. The reactor network is a computational environment that accommodates realistic chemical reaction mechanisms; indeed, mechanisms with a few thousand elementary chemical reactions can now be simulated on ordinary personal computers, provided that the flow structures are restricted to the limiting cases of plug flow or perfectly stirred tanks. The network is "equivalent" to the CFD flow field in so far as it represents the bulk flow patterns in the flow. Such equivalence is actually implemented in terms of the following set of operating conditions: The residence time distributions (RTDs) in the major flow structures are the same in the CFD flow field and in the section of the reactor network that represents the flow region under consideration. Mean gas temperature histories and the effective ambient temperature for radiant heat transfer are also the same. The entrainment rates of surrounding fluid into a particular flow region are evaluated directly from the CFD simulation. To the extent that the RTD, thermal history, and entrainment rates are similar in the CFD flow field and reactor network, the chemical kinetics evaluated in the network represents the chemistry in the CFD flow field.

The information flow is sketched and compared with conventional CFD post-processing in Figure B.23. In conventional CFD post-processing, a first-pass calculation imposes a rudimentary reaction scheme involving a radically reduced set of chemical species to predict the heat release and its impact on the flow field, but not the emissions. Then the converged solutions for the flow field, temperature field, and major species concentration fields are re-analyzed with additional species and more global reaction processes to predict emissions. In contrast, CNPP utilizes the flow and temperature fields but not the species concentration fields from the first pass, because these reflect deficiencies in the

rudimentary reaction scheme. In addition, CNPP uses fields of the turbulent diffusivity and selected conserved scalar variables, which are always computed in CFD but not normally reported to the user. The CNPP method then specifies an equivalent reactor network directly from the CFD flow and temperature fields. Finally, realistic elementary reaction mechanisms are used to determine the concentrations of all major and various minor species across the reactor network, including any emissions of particular interest.

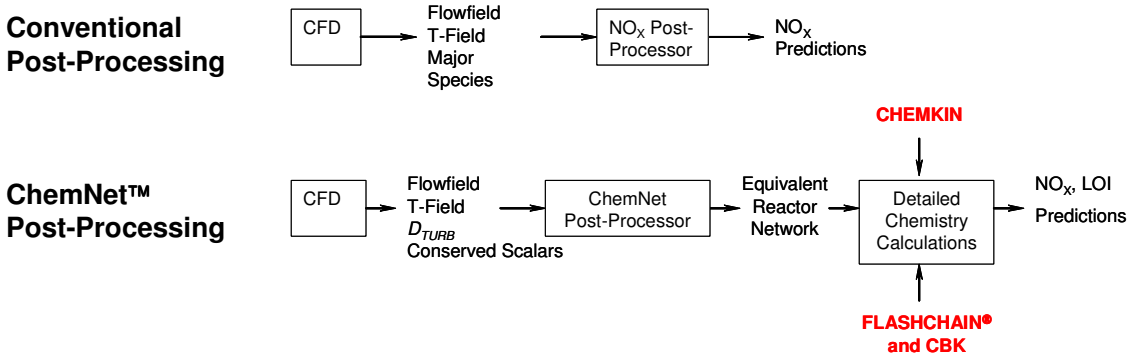

Figure B.23. Schematic of the information flow in conventional and ChemNet™ post-processing.

From a practical perspective, it is only possible to implement CNPP after the CFD flow field has first been subdivided into regions. The regions are the rudimental elements of the chemical structure of the flow field. As such, each region sustains a collection of chemical reaction mechanisms that are distinctive. Regions are usually much more extensive than any distinct flow structures. For example, the core formed by the primary jet within a dual register burner is a region, because the very high loadings of particles and soot in this region will significantly perturb the chemical reaction rates in the gas phase, especially the N-conversion mechanisms. Mixing layers formed by simultaneous entrainment of fuel-rich fluid into secondary or tertiary air streams are also regions, because the temperature profiles along the direction of mixing exhibit similar maximum values across the entire layer. The portion of an OFA jet remaining to be mixed with a process stream is another region, because the absence of fuel essentially eliminates all chemistry.

B.3.2 CFD Simulations of NBFZ Combustion Tests

Basis for an Equivalent Reactor Network

A coal-fired furnace cannot be analyzed as a homogeneous reaction system like other chemical processes. One reason is that coal flames comprise several separate regions, each with its own distinctive chemical reaction and transport mechanisms. These distinctive mechanisms determine the most important species concentrations, especially the species associated with NO_X emissions. Another reason is that the flowfield near coal burners governs the mixing rates between fuel and oxidizer streams which, in turn,

govern the combustion intensity. Interactions and entrainment among these flows directly affect emissions.

So the first step in developing an equivalent reactor network is to subdivide the CFD flow field into its distinctive regions. These regions are distinctive in terms of their chemical reaction mechanisms, rather than their fluid dynamic structure. In addition to distinctive chemistry, regions must have operating conditions that can be expressed as functions of time only because, by definition, a network of idealized reactors reduces all spatial variations to a time dependence. This condition imposes several constraints on how regions are defined, as follows.

The flow field determines the residence times of all fluid elements moving across a particular region. Since regions are generally fed by multiple streams of grossly different compositions, the flow fields within regions are rarely one-dimensional. Multi-dimensional flow fields determine RTDs, rather than a nominal residence time. For example, suppose that a region was defined as a round turbulent jet emanating from a cylindrical injector. Most of the fluid remains near the jet axis and travels far downstream from the injector within this region. This fluid has the longest residence times. But some of the fluid has a sufficiently fast radial velocity component to quickly move off axis and cross the boundary into another region. Such fluid has much shorter residence times. By tracking many fluid elements over the injector cross section, we can formulate an RTD for the region that accounts for the multi-dimensional character of the flow field, without reducing the flow field to a single spatial coordinate. The RTDs for all regions in the CFD simulation must be matched in the equivalent reactor network to depict the impact of the multi-dimensional flow character on the chemical kinetics.

The most versatile way to match the RTDs is to represent the operating conditions in each region by an assembly of idealized reactor elements, either continuously stirred tank reactors (CSTRs) or plug flow reactors (PFRs). These two reactors represent the extreme extents of backmixing of products with reactants, in that CSTRs are completely backmixed whereas PFRs have no backmixing. This feature is responsible for their characteristic RTDs as well. A CSTR RTD is an exponential decay, and therefore as broad as possible. The PFR RTD is a Dirac delta function with no dispersion whatsoever. Most important, the RTDs of CSTRs-in-series can be varied continuously between these limiting forms simply by varying the number of CSTRs in the series. In CNPP practice, only series of CSTRs are used because the RTD of a PFR equals that of a CSTR-series in the limit of a large number of reactors. We have encountered regions whose RTDs did not fall within this range, but were nevertheless able to represent the RTD with a more complicated reactor assembly, such as a CSTR-series in parallel with a PFR.

The multi-dimensional flow through a particular region can be reduced to a single function of time by evaluating the RTD with particle tracking. Hence, we are committed to re-casting the CFD flowfield into a Lagrangian field of individual trajectories in time for both fluid elements and actual fuel particles. In other words, all the operating conditions that affect chemical kinetics must be re-cast into functions of a common time coordinate.

The gas temperature field within each region must be reducible to a thermal history; i.e., an average temperature as a function of time. In principle, the profile could be expressed in terms of one spatial coordinate or in terms of a time coordinate. We always use the time coordinate because a thermal history maps directly onto the average residence time profile along a series of CSTRs. This stipulation is potentially confusing to implement because it certainly does not imply that the gas temperature field within each region must be one-dimensional. Rather, it means that the gas temperature field must be amenable to meaningful averaging, whereby each fluid element is subjected to a similar thermal history, regardless of its particular residence time in the RTD.

To illustrate this point further, consider a 2D, axisymmetric, laminar diffusion (Burke-Schumann) flame. This flame consists of a relatively cool core of fuel, surrounded by air at ambient temperature. The interface between these two regions is a reacting surface fed by fuel from one side and by air from the other. The interface also determines the locus of maximum temperatures for the entire flame, so the gas temperature field is definitely not one-dimensional. Nevertheless, each fluid element that moves from the fuel core into the flame surface is rapidly heated to the flame temperature, then cooled as it penetrates into the air stream. The crucial point is that the imposed thermal history is essentially independent of position on the flame surface. Whether the fluid leaves the fuel core immediately after leaving the burner or from the streamline on the flame axis into the flame tip, essentially the same thermal history is imposed: it rapidly increases from the low value in the fuel core, passes through the maximum value at the flame surface, then diminishes to the low value in the air stream.

We use fluid element tracking to compile a population of thermal histories for all trajectories represented by the RTD. We then average the temperatures of the population in time to assign an average gas temperature history for the region under consideration. Once the average temperature history has been specified, it is rendered in a discretized version to each of the reactors in the CSTR-series for this particular region. Note that each individual CSTR is isothermal. Provided that many CSTRs are used to represent the region, there is little uncertainty introduced by rendering the average thermal history into a discrete form.

In addition to the gas temperature history, two additional thermal histories must be specified. Both pertain to the particulate phase. First, an effective ambient (wall) temperature for radiation transfer must be specified. During char oxidation, the instantaneous particle temperature represents the interplay among numerous heat transfer mechanisms, including thermal inertia, convection, radiation, and the heat release due to char oxidation. So, in our char oxidation simulations, we simultaneously assign particle temperature histories and burnout histories from coupled balances on particle mass, size, and enthalpy. The radiation flux in the enthalpy balance contains the effective ambient temperature, which must be specified as a function of the mean residence time throughout the region under consideration. We certainly do not want to apply the particle histories from the CFD simulation in the calculations with detailed chemistry, because that would compromise the benefits of the advanced reaction mechanisms for char oxidation in the detailed calculations.

In principle, the radiation analysis in the CFD simulation was already used to evaluate the radiation flux to the particle along each particle trajectory in the CFD simulation. This flux could be used to directly evaluate an effective ambient temperature. In practice, this would entail a deep interrogation of the CFD simulation that is hard to justify, because the effective ambient temperature is usually much lower than the particle temperature (after ignition), which often renders it negligible. In practice, we specify effective ambient temperatures as average values over various sections of the surroundings. Effective ambient temperature histories are also implemented in discrete forms across CSTR-series.

The second required thermal history for the particulate phase is only needed at fuel injectors. To evaluate our devolatilization mechanism, a representative thermal history must be specified for the entire suspension. Usually, this is not ambiguous because, for the relatively high mass loadings in commercial burners, the suspension and primary air streams have very similar temperature histories prior to ignition, and these histories are insensitive to particle size. We assign a thermal history for devolatilization as an average of the histories for all the available particle trajectories from each injector. It usually extends from 80 to 100 ms, although devolatilization is usually complete in significantly shorter periods.

The thermal history for devolatilization is not implemented in discrete form. Rather, it is used in a separate devolatilization simulation with PC Coal Lab® to determine the time-resolved yields of all the important volatile species. The product yield histories are then subdivided into increments for the mean residence time of each CSTR in a series for the near-injector region under consideration. In other words, the fuel fed into a near-injector CSTR-series is a mixture of char and volatiles, where the volatiles are added in increments assigned for the residence times of individual reactors from a separate devolatilization simulation.

The final operating conditions to be specified are the entrainment rates into all regions. When the region under consideration is an injector, the flow rates of fuel and air into the region are unambiguous. However, for mixing layers, relatively thin zones for char burnout, OFA injection elevations, and other regions in which two or more streams mix, all flow rates into the region must be specified. In particular, all inlet flow rates must be specified as an entrainment rate in terms of the mean residence time across the region, because we have already mapped the flow and thermal fields from the CFD simulation into an average Lagrangian history on this time coordinate. For regions of simpler, axisymmetric shapes, the entrainment rates may be evaluated from the analytical definition for the turbulent flux across the boundary of the region. More generally, we use fluid element tracking from the surrounding flows that cover the entire surface of the region under consideration. The tracking directly indicates the flow rate entering the region, which is interpreted as the entrainment rate. The total entrainment flow rate is then distributed in time, based on the flow rates through particular locations on the regional boundary compiled in the particle tracking. This procedure bases the entrainment rate on the multi-dimensional gradients and turbulent transport rates in the CFD simulation, yet remains compatible with the Lagrangian trajectory in the reactor

network calculations. Note, however, that the entrained fluid is assumed to be instantaneously dispersed over the cross section of the region in the directions transverse to the nominal flow (time) coordinate, as implemented in the governing equations for CSTRs and PFRs.

To summarize the definition of an equivalent reactor network will proceed through the following sequence of steps:

(1) The CFD flowfield is delineated into regions whose chemistry is distinctive. The actual basis for the delineation may be the local concentrations of combustibles, especially soot and fuel particles, or a temperature field that can specify a meaningful average thermal history, or by an abundance of oxidizer and no fuel, which essentially suppresses the chemistry.

(2) The RTDs of each region are determined from the CFD simulations by fluid element tracking. Each RTD is then assigned a sequence of reactors, usually by fitting the analytical RTD for a CSTR-series to specify the number of CSTRs for the RTD under consideration.

(3) An average gas temperature history for each region is evaluated from the CFD gas temperature field by fluid element tracking. The average history in then implemented in discrete form across the CSTR-series under consideration.

(4) An effective ambient (wall) temperature for radiation transfer is evaluated as an average over the surrounding sections around the region under consideration. It is also implemented in discrete form across the CSTR-series.

(5) If the region is a fuel injector, an average particle temperature history is assigned as the average of the thermal histories over all particle trajectories from the injector, so that the fuel's devolatilization behavior can be evaluated. The predicted volatiles yields are implemented as discrete injections into all CSTRs whose residence times include a portion of the predicted devolatilization period.

(6) Entrainment rates into all regions are evaluated as functions of the nominal time coordinate through the region under consideration. These rates are specified from the definition of the total mass flux into the boundary of the region, for simple shapes, or from fluid element tracking from the surroundings into the region, in the more general situation.

Delineating Regions

Subdivision of the CFD flow field into regions with distinctive chemistry is the first step in CNPP. This section first introduces a conserved scalar variable that delineates regions near the fuel injectors, then discusses other criteria to specify regions for the bulk of the furnace volume.

Combustibles Mass Fraction

Regions near the fuel injectors should be identified on the basis of the extents of mixing between the fuel suspension and any secondary air streams (since the primary fuel jets are premixed with primary air). To quantitatively characterize the mixing near fuel injectors, we introduce the mass fraction of all combustible material (C, H, O, N, S) in both the particle and gas phases, normalized by the inlet value, which is defined as:

$$\psi(x, y, z) = \frac{m_{chons}(x, y, z)}{m_{chons,0}} \tag{B.1}$$

where ψ is the local combustibles mass fraction; m_{chons} is the mass fraction of combustibles at any position; and $m_{chons,0}$ is the combustible mass fraction at the inlet plane of the injector. The mass fraction of combustibles is calculated from the mass fractions of volatiles, CO_2, CO, H_2O, SO_2 and DAF mass concentration of particles, as follows:

$$m_{chons} = \frac{\rho_{daf} + \rho\left(m_{vol} + \frac{12}{44} m_{CO_2} + \frac{12}{28} m_{CO} + \frac{2}{18}(F_O) m_{H_2O} + \frac{32}{64} m_{SO_2} \right)}{\rho_{daf} + \rho} \tag{B.2}$$

where ρ_{daf} is the DAF concentration of char particles (kg/m^3) calculated as $\rho_{daf} = \left(\sum_{i=1}^{n_p} (m_i - m_{i0} f_{ash}) \right) / V_{cell}$; ρ is the local gas density (kg/m^3); m_{vol}, m_{CO_2}, m_{CO}, m_{H_2O}, m_{SO_2} are mass fractions of volatiles, CO_2, CO, H_2O and SO_2, respectively. The factor F_O in the H_2O-term is one plus the ratio of the percentages of oxygen to hydrogen in the fuel, and it accounts for the contribution of fuel-O to the combustibles mass fraction. Coal-N was omitted from the CFD simulations, so it could not be included in the evaluation of combustibles mass fraction. This omission is inconsequential because nitrogen is a minor contributor to the combustibles mass fraction. Note that the combustibles mass fraction includes the combustible elements, *regardless of phase and regardless of whether they appear in reactants, intermediates, or products*.

The field of the combustibles mass fraction was evaluated by incorporating Equations B.1 and B.2 into FIELDVIEW to process the CFD output files. Since this variable is a conserved scalar, its local value is determined entirely by the convective and diffusive transport mechanisms in the CFD simulation. Sources and sinks, such as chemical reactions, do not affect its value. As such, the value of the combustibles mass fraction diminishes in proportion to the entrainment of surrounding fluid into the primary fuel stream and the dispersion of combustibles away from the primary fuel stream.

Regions of NBFZ Flames

In NBFZ combustion tests, the coal particle injector has only half the cross section of the reactor flow tube. Due to turbulence characteristics discussed in NEA's Third Interim Report, particles are quickly dispersed after injection, and move radially toward the wall. Once particles reach the near-wall momentum boundary layer, they rarely escape due to momentum loss in this region. The particle concentration in the near-wall region is always much higher than in the core. Consequently, the combustibles mass fraction defined by Equations B.1 and B.2 is higher in the near-wall region than in the core. This variable is evaluated across the tube for axial positions of 10, 15, 20, 27.3 cm in the upper panel of Figure B.24. The combustibles mass fraction is uniform across a central core at all positions, except for a diminishing spike on the centerline that reflects the inlet condition. Near the inlet, coal particles and gas accelerate into the core in order to develop a momentum boundary layer. This spike is not resolved in the analysis because coal particles are still heating as they traverse this zone, and chemistry is negligible. In the boundary layer, the combustibles mass fraction passes through a maximum with radial position, due to the accumulation of particles and the near-zero value at the wall. These portions of the profiles are very similar for all axial positions.

Pressure significantly affects the turbulence characteristics, as explained in NEA's Third Interim Report. Turbulence becomes stronger at higher pressures, simply because the Reynolds Number is proportional to density and, in turn, to pressure. As a consequence, the thickness of the region of higher combustibles mass fraction near the wall diminishes for progressively higher pressures, as seen in the middle and lower panels of Figure B.24.

Since profiles of combustibles mass fraction are similar for all axial positions, we assigned a single radius to delineate the core region (CR) and near-wall boundary layer region (BL) along the entire length of the tube, as shown in Figure B.25. This radius was evaluated as the location of the intersection of lines through the variable toward the boundary, as indicated in Figure B.24. At 1.0 MPa, this radius is 0.45 cm; it slightly increases to 0.51 and 0.53 cm as pressure increases from 2.0 to 3.0 MPa. This radius is a function of pressure alone, and is independent of stoichiometric ratio and coal type, because the turbulent dispersion of suspensions is very insensitive to variations in stoichiometric ratio and coal type.

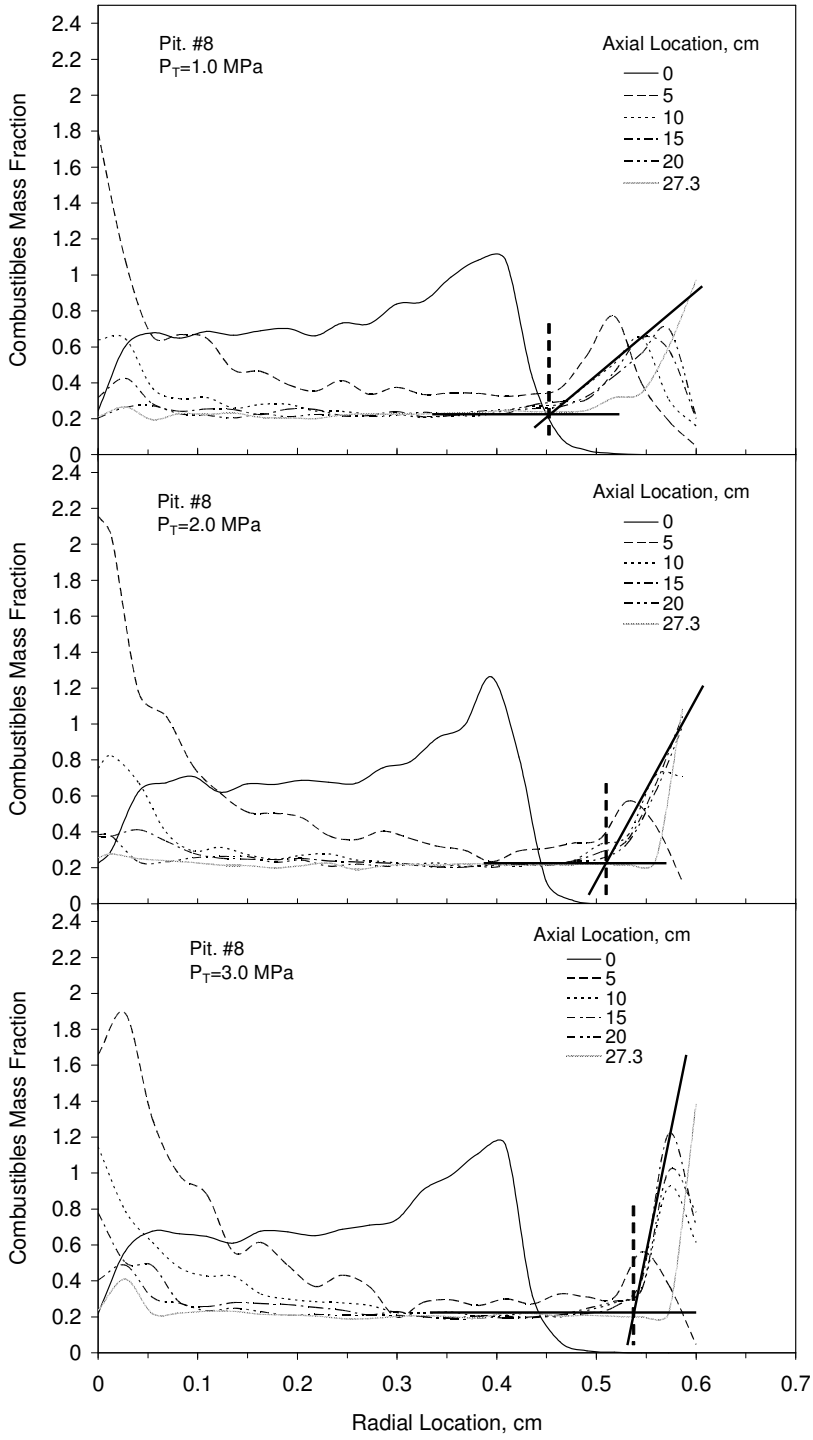

Figure B.24. Profiles of combustibles mass fraction (ψ) for Pittsburgh #8 at (upper) 1.0, (middle) 2.0, and (lower) 3.0 MPa. The bold solid and dashed lines indicate how the radius that delineates the core and sheath regions is determined.

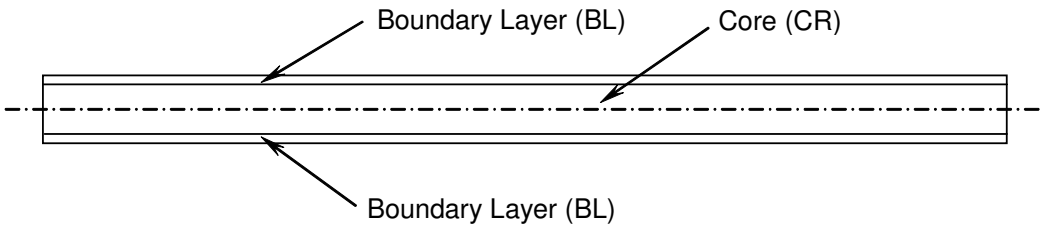

Figure B.25. CNPP regions for NBFZ flames delineated from the CFD simulation.

RTDs and Equivalent Reactor Assemblies

As explained once a boundary for a region has been assigned, the residence time of a single fluid element is easily evaluated with fluid element tracking, based on the difference between the initial time that a fluid enters the region and the elapsed time to its departure. Then a statistical analysis compiles an RTD from the residence times for the population of individual trajectories.

Such CFD-based RTDs are then used to specify the number of CSTRs in a series that will represent the region under consideration in the equivalent reactor network. The section of the network for a specific region is called an "equivalent reactor assembly." We try to exclusively use CSTR-series for all reactor assemblies but, occasionally, more complicated configurations are necessary. CSTR-series are emphasized because the CSTR-number in the series is easily determined from a least-squares fit of the following analytical expression to the CFD-based RTD:

$$RTD(t) = \frac{1}{(N-1)!\bar{t}_i}\left(\frac{t}{\bar{t}_i}\right)^{N-1}\exp\left(-\frac{t}{\bar{t}_i}\right) \qquad \text{(B.3)}$$

where *RTD(t)* is the exit age distribution of fluid in the region as a function of time, *t*; *N* is the number of CSTRs in the series; and t_i-bar is the mean residence time of an individual CSTR. All reactors in the series have the same nominal residence time. The assignment of *N* in the least-squares fit to the CFD-based RTD is particularly efficient because only integer values are acceptable. Cases which have *N* greater than 125 during the analysis are aborted to avoid overflows and interpreted as plug flow systems.

An Equivalent Reactor Network for the NBFZ Flow Field

The CSTR network from a CNPP analysis of the baseline case of Pittsburgh #8 at 1.0 MPa with an stoichiometric ratio of 0.953 appears in Figure B.26. The networks for all other NBFZ flames have similar branches and feed streams but appreciably different quantitative specifications. Both the boundary layer and core regions contain fuel

particles. Due to the significantly hotter temperature in the wall layer, the residence time of 157 ms in this layer is shorter than the mean time of 185 ms in the core. Each core and boundary layer is subdivided into two regions. The devolatilization zone covers the upstream portion of the core where volatiles are being released from fuel particles and burned with primary air. The devolatilization times of 134 and 180 ms for the wall layer and core, respectively, were determined from stand-alone devolatilization simulations for the average thermal histories of particles from the CFD simulation. Devolatilization is complete within these residence times. Devolatilization is represented as a series of discrete additions of volatiles to the CSTR-series for both flows, based on the corresponding yield increments and gas compositions in the stand-alone devolatilization simulations. Burnout zones appear downstream, where gas chemistry is minimal but char continues to burn, although the time available for char burn out in the core is negligible. Note that core fluid is entrained into the CSTR-series for the boundary layer region. The entrainment is represented as a series of discrete additions over several reactors in the series. The specific additions of core fluid are specified from the continuous entrainment profiles evaluated from the CFD simulation.

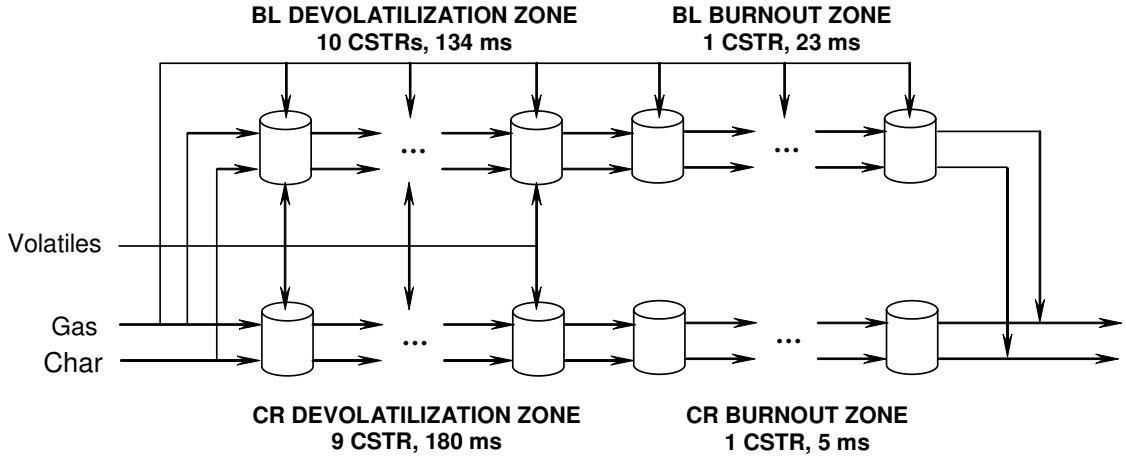

Figure B.26. Equivalent reactor network for Pittsburgh #8 flame at 1.0 MPa and a stoichiometric ratio of 0.953.

Operating Conditions in Regions

Mean Gas Temperature Histories

Due to their dissimilar suspension loadings, the core and boundary layer regions sustain distinctive temperature profiles. As reported in NEA's Third Interim Report, gases and particles in the boundary layer are much hotter than in the core region due to fast heat transfer from the hot reactor wall. Flames always form first in the boundary layer, then propagate into the core, which compounds the temperature difference. These differences are responsible for the distinctive chemistry in these regions, as discussed in Ch. 3.

The mean gas temperature histories are simultaneously assigned with the RTDs. The time scale for the temperature history is evaluated as 50 equal increments of the longest populated residence time in the RTD. The longest populated time is evaluated as the time in the RTD which is longer than the residence times of 95 % of the individual fluid elements residence times. Then the temperatures along the trajectories of individual fluid elements are recorded in the same time increments. This operation puts the individual temperature histories on a consistent time scale for averaging. The gas temperatures for all fluid elements in the region are averaged at each time increment, according to:

$$\overline{T}_{gi} = \frac{\sum_{j=1}^{N_f} \left(u_{0j} \cdot T_{gi,j} \right)}{\sum_{j=1}^{N_f} u_{0j}} \tag{B.4}$$

where subscript i represents the i th time increment in the time scale and j represents the j th fluid trajectory; N_f is the total number of fluid tracks in the region; and u_0 is the fluid velocity at the injector, which is used to mass-weight the average, since the gas density at the injection plane is uniform because the temperatures are uniform.

The time increments were adjusted to eliminate an attachment length of about 6 cm between the end of the coal injection tube and the beginning of the heated reactor wall. While the suspension moves through this length, gas is heated very slowly and no radiation flux is imposed on the particles. Since no significant chemistry occurs in this region, the transit time is eliminated from the time scale for the detailed chemistry calculations. This attachment length corresponds to a mean gas residence time of 137 ms for the baseline case of Pittsburgh #8 at 1.0 MPa and a stoichiometric ratio of 0.953. This time is subtracted from the original temperature histories from the CFD simulation. Since the same inlet velocity of 30 cm/s was imposed in all NBFZ tests, the same transit time was eliminated for all tests.

Figures B.27 and B.28, respectively, show the mean gas temperature histories and wall temperature histories in the boundary layer and core regions. These temperature histories have already been shortened by the transit time through the attachment length. The gas temperature in the boundary layer increases from 800°C to a maximum of 1550°C at 105 ms, then cools to about 1000°C at the tube exit. The discrete gas temperatures assigned for CSTR series appear as data points in Figure B.27, and are fairly consistent with the history from the CFD simulation.

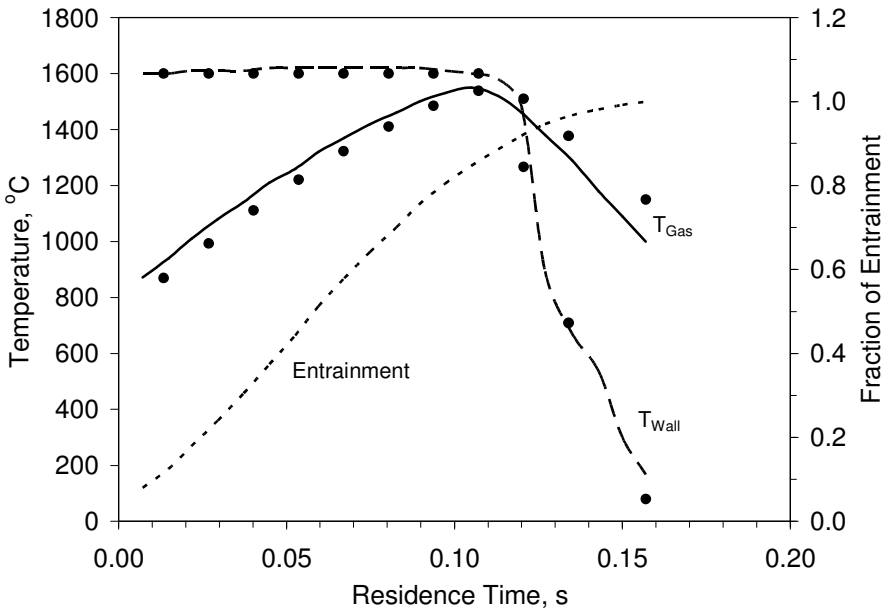

Figure B.27. Histories of gas temperature (solid), wall temperature (dashed), and O_2 entrainment (dotted) from the CFD simulation and discrete values for the CSTR series (●) for the boundary layer with Pittsburgh #8 at 1.0 MPa and an stoichiometric ratio of 0.953.

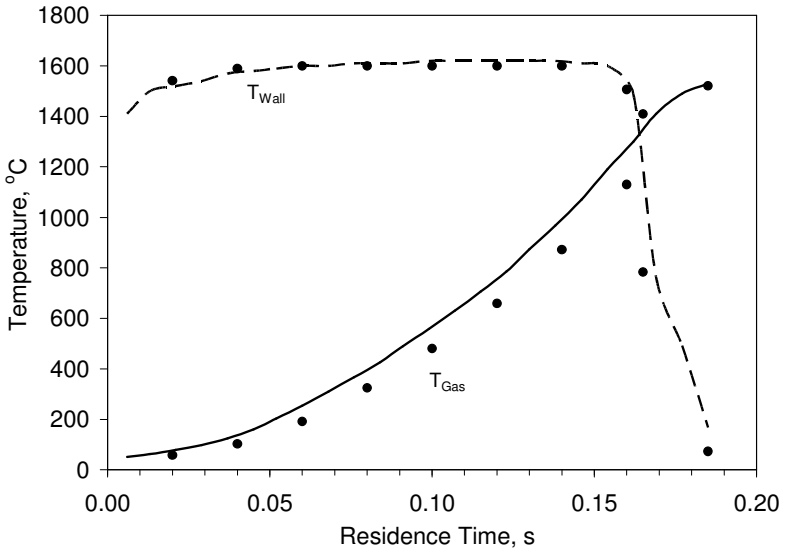

Figure B.28. Histories of gas temperature (solid), wall temperature (dashed), and O_2 entrainment (dotted) for the core for the case in Figure B.27.

The gas temperature history in Figure B.28 for the core is much cooler over almost the entire reactor length. It gradually increases to 1530°C at the tube exit. The volatiles

flame for this baseline case is closed, in tests in which the flame does not close across the centerline, the gas temperature history for the core remains much cooler even at the tube exit. Again, the discrete gas temperatures assigned for CSTR series for the core region are also consistent with the history from the CFD simulation.

Mean Particle Temperature Histories

Particle temperature histories are only used to assign a thermal history for the devolatilization simulations, and separate histories for the wall layer and core are evaluated from the particle trajectories assigned in the CFD simulation. These particle trajectory data files are structured like the fluid tracking files, so the same analytical procedure is implemented. One important difference is that the boundaries for regions cannot be identified with particle trajectories, because the combustibles mass fractions that define the extents of cores were not included in the particle trajectory data files. In the analysis, we imported the regional boundaries from the fluid trajectories into the analysis of particle tracks. Mass-weighting was also applied in the averaging of particle temperature histories, based on the initial masses of particles.

Figure B.29 shows the particle temperature histories for the boundary layer and core regions for the baseline case of Pittsburgh #8 at 1.0 MPa and a stoichiometric ratio of 0.953. Although the same radiation flux is imposed onto all particles, coal particles in the boundary layer are heated at a higher rate than those in the core, simply because the gas temperature in the boundary layer is hotter. The heating rates calculated from these temperature histories are 7600 and 5500°C/s for the boundary layer and core regions, respectively. The same thermal histories are imposed in the devolatilization simulations with PC Coal Lab® by freely adjusting the ambient conditions simply to match the thermal histories. For the baseline case of Pittsburgh #8 at 1.0 MPa and a 0.953 stoichiometric ratio, for example, the initial particle temperature was 25°C, gas and wall temperatures were 1120 and 1700°C, respectively, and particle size was 470 μm in the PC Coal Lab® runs. Although these were not the real operating conditions, the thermal histories were the same, which is all that matters in evaluating the correct devolatilization rates and yields. The pseudo-conditions for all tests are presented in Sec. 3.2.

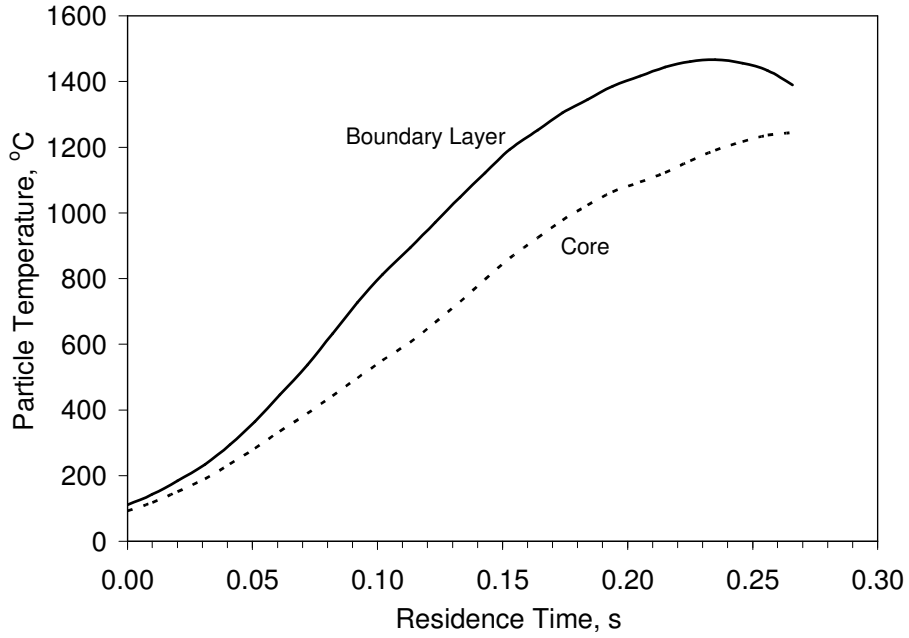

Figure B.29. Particle temperature histories from the CFD simulation for boundary layer (solid line) and core (dashed line) with Pittsburgh #8 at 1.0 MPa and a stoichiometric ratio of 0.953.

Effective Radiation (Wall) Temperature

An effective ambient temperature is required by our char oxidation sub-model to evaluate the incident radiation flux in an energy balance for a burning char particle. In the energy balance, wall temperature only appears in the definition of the radiation flux between a particle and its environment. In principle, it should be evaluated as an effective ambient temperature for radiant transfer; i.e., one that delivers the same flux as the actual collection of non-isothermal sources surrounding the particle. A legitimate implementation of this definition requires a comprehensive radiation analysis like the one in the CFD simulation. Such an effort cannot be justified by the impact of the assigned value on the char burnout predictions, which is fairly weak. Consequently, the effective wall temperature histories were assigned from mean wall temperatures.

The wall temperature histories of the boundary layer and core regions for the baseline case are also shown in Figures B.27 and B.28. In fact, these wall temperature histories are based on the wall temperature profile imposed in the CFD simulation. The tube wall remains at 1600°C as long as it is exposed to the graphite heating element, then rapidly cools to room temperature. Discrete wall temperatures for the CSTR series for the boundary layer and core are consistent with those from CFD simulation.

Entrainment Rates in Regions

The entrainment of oxidizing streams into fuel-rich streams is obviously crucial to accurate predictions of furnace exhaust compositions. In furnaces where the regions have simple shapes and regular boundaries, entrainment rates can be directly specified from the entrainment flux across the boundary of a region. This flux, Q_{O_2} in kg/m^2-s of O_2, is defined as follows:

$$Q_{O_2}(s) = -\rho D_{eff,O_2}\left(\vec{n}\cdot\nabla m_{O_2}\right) + \rho m_{O_2}(\vec{v}\cdot\vec{n}) \qquad \text{(B.5)}$$

where m_{O_2} is O_2 mass fraction; D_{eff,O_2} is the effective (turbulent) diffusivity of O_2; $\vec{n}$ is the unit vector normal to the boundary; and $\vec{v}$ is the velocity vector. The two terms on the right hand side of Equation B.5 represent diffusion and convection of O_2, respectively.

The entrainment rate $\dot{m}_{O_2}$ (kg/s) is evaluated by integrating the entrainment flux over the entire boundary, according to

$$\dot{m}_{O_2} = \iint_s Q_{O_2}(s)\,ds \qquad \text{(B.6)}$$

where s is the boundary of the region.
These expressions can be evaluated in FIELDVIEW, and then the assigned entrainment rates can be transformed onto the mean residence time coordinate used for the temperature histories. The entrainment of O_2 is mainly driven by the diffusion from the core into the boundary layer. The entrainment history is also discretized to assign entrainment increments for each reactor in the CSTR-series. Only boundary layer simulations involve O_2 entrainment. In the core simulations, the total entrained flow rate of O_2 is deducted from the total O_2 flow rate at the core inlet.

Detailed Chemical Reaction Mechanisms

Once the equivalent reactor network has been specified, the chemistry in each reactor in the network is sequentially evaluated from the species balances based on elementary reactions for the gas phase and on soot. All chemical reaction mechanisms incorporated into our simulations, and how they were used in CNPP, have been presented in detail elsewhere (Niksa et al, 2002a; 2002b). This section briefly reviews the reaction mechanisms.

A multitude of fuel species – CO, H_2, CH_4, C_2H_2, HCN, soot, and char – compete for the available O_2 in a pulverized-fuelflame. This competition determines local heat release rates, which govern flame stability, combustion efficiency and UBC, and the local oxidizing potential of the gas phase, which governs N-species conversion. The central premise behind our modeling approach is that the crucial outcome of this competition cannot be forecast from the burning rates of the individual fuels determined in isolation.

Instead, realistic chemical kinetics for each distinctive combustion process must be incorporated into a comprehensive analysis. Our analysis incorporates the most comprehensive chemical reaction sub-models available, and imposes no *a priori* assumptions whatsoever regarding the apportioning of O_2.

The devolatilization sub-model, called FLASHCHAIN®, distinguishes primary devolatilization, which relates fuel properties to the composition of volatiles, from secondary volatiles pyrolysis, which generates the volatiles that actually burn in pulverized-fuel flames. FLASHCHAIN® determines the complete distribution of primary products from almost any p. f., and also predicts the yield and elemental composition of char (Niksa 1995). When combined with a swelling factor correlation and a correlation for the initial carbon density in char, it specifies all the necessary char properties for a char oxidation simulation. Hence, the complete distribution of volatiles, including gaseous fuels and soot, and all char properties are completely determined from the fuel's proximate and ultimate analyses.

The reaction mechanism for chemistry in the gas phase must describe the ignition and combustion of all secondary volatiles pyrolysis products, as well as the conversion of all N-species across the full range of stoichiometric ratio values in pulverized-fuel flames. Our homogeneous reaction mechanism contains 448 elementary reactions among 66 species, including all relevant radicals and N-species (Glarborg et al. 1998). It is implemented in the simulations without any approximations whatsoever. All rate parameters were assigned independently, so there are also no adjustable parameters in the sub-model for gas phase chemistry.

Soot plays several important roles. As it burns, it directly competes for the available O_2 and also consumes O-atoms and OH that would otherwise sustain homogeneous chemistry. Soot also promotes recombinations of H-atoms and OH that could also sustain homogeneous chemistry (Pedersen et al. 1998b). And soot reduces NO directly into N_2. Our soot chemistry sub-model depicts all these effects in the form of a collection of elementary reactions that can be coupled to the homogeneous reaction mechanism within the CHEMKIN/SURFACE CHEMKIN framework.

Char burning rates are determined by thermal annealing, ash encapsulation (of low-rank chars), and a transition to chemical kinetic control. The Char Burnout Kinetics (CBK) Model includes all these effects, and depicts the impact of variation in gas temperature, O_2 level, and char particle size within useful quantitative tolerances (Hurt et al. 1997). However, it is not yet possible to specify the initial char reactivity within useful tolerances from the standard coal properties. We must calibrate this value with a single extent of char conversion or some other suitable index on combustion efficiency. The sub-model for char-N conversion is subject to a similar calibration requirement (with NO emissions), compounded by its simplistic mechanistic premise; viz., that a fixed fraction of char-N is converted into NO at the overall burning rate throughout all stages of char oxidation.

To summarize the status of our reaction mechanisms, we believe that the sub-models for devolatilization, homogeneous chemistry, and char burnout are complete, whereas those for soot/radical chemistry and for char-N conversion will probably be subject to revisions in the near term. Neither of these latter two situations introduces significant uncertainties into NEA's simulations of the p-RCFR. Since these reaction mechanisms have already been independently validated across an enormous domain of conditions, what matters most is the degree to which all model parameters can be specified from the available information on the furnace operating conditions. The initial char reactivity and the fraction of char-N converted to NO can only be specified from calibration procedures, whereby these parameters are adjusted to match the predicted extent of char conversion and NO_X emissions to reported values for a single set of operating conditions. Then the same values should be imposed for all other operating conditions. Except for these two parameters, all other model parameters can be assigned from the fuel's proximate and ultimate analyses within useful quantitative tolerances, or directly adopted from literature.

Implementation

A diagram of the information flow in the computerized version of the CNPP calculations appears in Figure B.30. A custom FORTRAN program sequences through the reactor network region-by-region, and element-by-element within each region. All the chemical sub-models were implemented in the conservation equations for each CSTR in the network, as follows: The jth CSTR is fed by an inlet char flow, F^C_j, an inlet flow of gaseous fuels and combustion products plus soot, F^P_j, and an entrainment flow, F^E_j, which consists of volatiles or secondary air or OFA in the CRF. In the analysis, the key organizational principle is the competition for O_2 among chemistry in the gas phase versus the oxidation of soot and char, which is apparent in the following O_2 balance for a CSTR in the network:

$$F^E_j y^E_{O_2,j} + F^P_j y^P_{O_2,j} - F^P_{j+1} y^P_{O_2,j+1} = \frac{\Delta X^C_j F^C_0 (1 - x^A_0) \nu_C}{M'_C} - M_{O_2} V_j \omega_{O_2} \qquad \text{(B.7)}$$

where subscript j denotes the index on the CSTR under consideration; superscripts E, P, and C denote entrainment, gaseous product, and char flows, respectively; and y^I denotes the O_2 mass fraction in stream I. The terms on the left of the balance represent the net efflux of O_2 from the jth CSTR. The two terms on the right represent the O_2 consumed by char oxidation and by oxidation of gaseous fuels and soot, respectively. The consumption term for char oxidation is written in terms of the burnout predicted by CBK for the residence time increment of the jth CSTR, ΔX^C_j, and the flowrate of ash-free combustibles into the furnace, $F^C_0(1-x_0^A)$. The stoichiometric O_2 requirement, ν_C, and the char molecular weight, M_C', account for the presence of heteroatoms in the char combustibles. The consumption term for oxidation of gaseous fuels and soot incorporates the molar rate of O_2 consumption per unit volume, ω_{O2}.

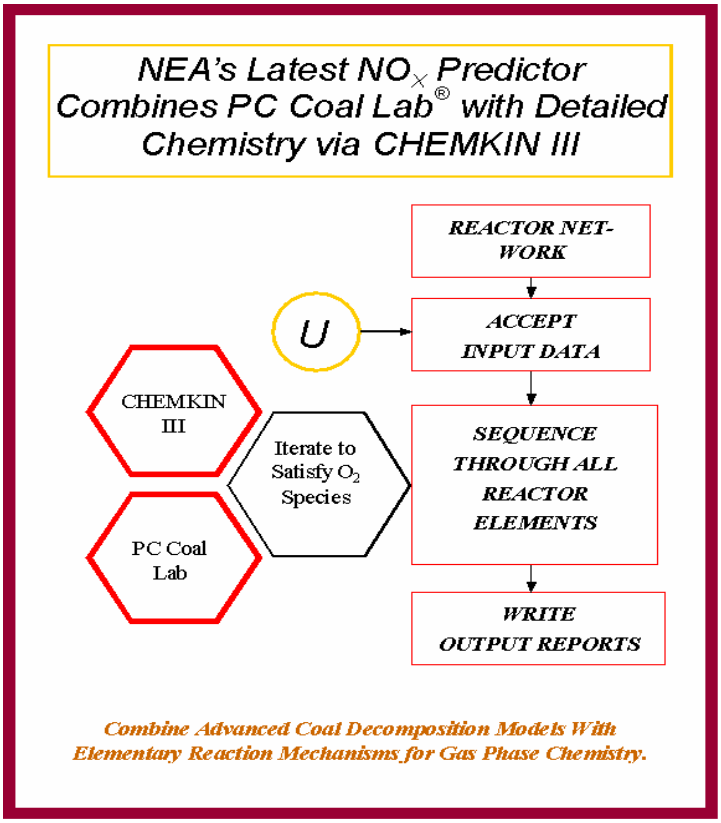

Figure B.30. Information flow in the computerized CNPP analysis for NBFZ flames.

These rates were determined with CHEMKIN and SURFACE CHEMKIN software, then incorporated into the iteration routine that satisfied the O_2 balance. Rates were converted to a mass basis by multiplying by the molecular weight of O_2, M_{O2}, and the CSTR volume, V_j.

Note that the analysis does not determine the apportioning of O_2 among the various fuels in this reaction system in advance, or through any imposed constraints. The kinetics for oxidation of soot, char, and gaseous fuels govern O_2 apportioning, as in actual pulverized-fuel flames.

On a Pentium 4 microprocessor operated at 1.5 GHz, each simulation of a CRF reactor network takes from 15 to 50 min, depending on the fuel combination and network specifications.

B.4 Predicting Major Products and Emissions of NBFZ Tests with Detailed Reaction Mechanisms

B.4.1 Adjustable Parameters in CNPP Simulations

All rate parameters, except two, involved in the detailed reaction mechanisms are fixed in all our CNPP simulations. The only fuel-dependent adjustable parameters are *the initial char oxidation reactivity* and *the fraction of char-N converted into NO*. Although both char oxidation reactivity and fraction of char-N conversion are adjustable, they only depend on fuel properties. In other words, in our simulations, once these parameters were specified for the baseline case with a particular coal sample, they remained the same throughout all other simulation conditions with this fuel. In order to match the measured char burnout data, we had to decrease the default char reactivity parameter in CBK/E, A_{30}, by a factor of six for Pittsburgh #8; decrease it by a factor of two for Illinois #6; and increase it by a factor of 2 for PRB. These adjustments are consistent with the uncertainties associated with our interpretations of a large database on pressurized char oxidation with CBK/E (Niksa et al. 2003). By coincidence, the fraction of char-N converted into NO is 0.2 for both Pittsburgh #8 and PRB, and 0.7 for Illinois #6.

Also, after the first sweep of simulations for all NBFZ tests, the predicted soot burnout was found to be systematically low. This flaw was rectified by increasing the pre-exponential factor of the elementary step $S_A+O_2(g)=>O(g)+S_O$ by a factor of four from the default values used in other CNPP applications (Niksa et al., 2002a; 2002b). Once adjusted, this parameter was fixed throughout all NBFZ test simulations.

B.4.2 Predicted Devolatilization Behavior

Devolatilization is one of the most important processes affecting the chemistry of fuel-N conversion. A stand-alone PC Coal Lab® simulation was used to specify a volatiles release rate and volatiles product distribution into each reactor in a CSTR-series whose residence time is shorter than the devolatilization time. A fictitious set of operating conditions must be assigned for the PC Coal Lab® simulation to match the particle temperature history to that evaluated from the CFD simulation. These conditions comprise an initial particle temperature, gas and wall temperatures, particle size, and devolatilization time. The O_2 mole fraction was set as 0.1 % for all cases because only cases with O_2 tabulate the char particle density and swollen particle sizes. Once assigned, the same set of conditions was applied to the entire test series with a particular coal at a particular pressure. Different conditions had to be specified for the boundary layer and core regions, because they have different particle temperature histories. The upper part of Table B.12 shows these devolatilization conditions for boundary layer and core regions for all NBFZ test series. The devolatilization times vary between 0.14 and 0.28 s; gas temperatures vary between 920 and 1100°C; wall temperatures are between 1430 and 1700°C; and the particle sizes vary from 430 to 490 μm. Note that these conditions are fictitious and only used in the devolatilization simulations, and do not represent the actual operating conditions in the CNPP simulations.

The predicted distributions of secondary pyrolysis products are collected in the middle of Table B.12. Under the specified operating conditions, the total volatiles yields vary between 48 and 53 DAF wt. % for Pittsburgh #8, decreasing for progressively higher pressures, as expected. The yield in the boundary layer are also slightly higher than that in the core for all three pressures, due to a higher particle heating rate. Similar impacts of pressure and region are apparent for Illinois #6 and PRB. Pittsburgh #8 has the highest soot yield of 28.8 DAF wt. %, whereas PRB has the lowest of 10 %. As expected for sub-bituminous, PRB produces much more CO, CO_2 and H_2O than both Illinois #6 and Pittsburgh #8. The yields of hydrogen and hydrocarbons are comparable among these three coals. HCN is the only volatile-N species with all three coals, and is most abundant for Pittsburgh #8 and least abundant for PRB.

The char composition, char ash content and char particle size are shown in the lower part of Table B.12. Char compositions are very similar among all three coals at all pressures, except that char-O is highest in PRB chars and char-N is highest in Pittsburgh #8 chars. The impacts of pressure and region on char-N are negligible for all coals.

B.4.3 Flame Structures

The chemical structures of the boundary layer and core regions of the flowfield are developed in terms of two zones: a devolatilization zone and a burnout zone. The chemical structures of the devolatilization zone are determined by volatiles combustion and NO production followed by NO reduction, whereas char oxidation is the only chemical reaction in the burnout zone. The first predictions in this section are for the baseline case of Run 51C for Pittsburgh #8 at 1.0 MPa and the highest stoichiometric ratio of 0.953, followed by predictions for Run 56C, which has the same coal and same pressure but the lowest stoichiometric ratio of 0.147. Qualitative structures for other NBFZ flames are similar, and will not presented.

Baseline Run 51C for the Highest Stoichiometric Ratio

Boundary Layer

The predicted structure of the boundary layer for the baseline Run 51C flame appears in Figure B.31. In counterclockwise order from the upper left, the four panels of this figure display the variation in gas temperature and stoichiometric ratio values for the gas phase only; the mass fractions of O_2 and CO; the extent of burnout of char and soot; and the mass concentrations of the major N-species. The stoichiometric ratio values do not include the combustibles in either soot or char and therefore indicate the oxidation potential for the gas phase chemistry. Each parameter is plotted versus the mean residence time. For this particular test, devolatilization is completed within 134 ms, and the flow leaves the reactor at 158 ms.

Table B.12. Fictitious Devolatilization Conditions and Distributions of Secondary Pyrolysis Products and Char Properties for the NBFZ Test Series.

Test Series	PIT10	PIT10	PIT20	PIT20	PIT30	PIT30	ILL10	ILL10	ILL20	ILL20	PRB10	PRB10
Region	BL	CR	BL	CR	BL	CR	BL	CR	BL	CR	BL	CR
Devolatilization Parameters												
T_{P0}, °C	25	25	75	25	75	25	85	25	75	25	75	25
T_G, °C	1120	920	1120	950	1120	950	1100	950	1050	950	1100	900
T_W, °C	1700	1520	1660	1460	1660	1460	1700	1440	1650	1430	1700	1440
t_{DVOL}, s	0.134	0.180	0.190	0.220	0.220	0.280	0.140	0.180	0.140	0.180	0.134	0.180
D_P, µm	470	430	460	450	460	450	490	450	490	450	480	450
Volatiles, DAF wt. %												
Weight Loss	52.9	52.0	50.3	49.1	48.4	47.8	51.3	50.2	49.3	48.1	48.0	46.1
C-Soot	28.8	28.1	25.3	24.8	23.3	22.9	19.5	19.0	17.3	16.9	9.9	9.5
H_2	3.7	3.6	4.1	3.6	4.0	4.0	3.8	3.4	3.7	3.2	3.5	3.0
CH_4	0.4	0.4	0.5	0.5	0.5	0.5	0.4	0.4	0.4	0.4	0.7	0.7
C_2H_2	3.3	3.4	3.8	3.8	4.0	4.0	2.7	2.7	2.9	3.0	5.1	5.2
CO	3.2	3.2	3.1	3.0	3.0	3.0	8.3	8.3	8.2	8.2	14.0	13.1
CO_2	2.6	2.6	2.7	2.7	2.8	2.8	1.0	1.0	1.0	1.0	5.9	5.9
H_2O	2.2	2.2	2.3	2.3	2.4	2.4	3.1	3.1	3.2	3.2	7.4	7.4
HCN	1.3	1.3	1.3	1.2	1.3	1.2	1.0	0.9	1.1	0.8	0.9	0.7
H_2S	7.2	7.2	7.3	7.3	7.3	7.3	11.5	11.5	11.5	11.5	0.6	0.6
Char Comp., DAF wt. %												
C	96.3	96.0	97.6	96.5	97.4	97.3	97.9	96.9	97.7	96.5	97.3	95.3
H	1.2	1.4	0.4	1.3	0.4	0.5	0.4	1.3	0.7	1.6	1.2	2.1
O	0.1	0.3	0.0	0.0	0.0	0.0	0.0	0.0	0.0	0.0	0.2	1.2
N	2.1	2.1	2.1	2.1	2.1	2.0	1.9	1.9	1.6	1.8	1.2	1.4
S	0.1	0.3	0.0	0.0	0.0	0.0	0.0	0.0	0.0	0.0	0.0	0.0
Char Ash, wt. %	23.4	23.1	22.5	22.1	21.8	21.6	30.3	29.8	29.4	28.9	9.2	8.9
Char size, µm	102	102	102	102	102	102	102	102	102	102	91	91

The gas temperature increases gradually and approaches a maximum of 1540°C at 105 ms, then decreases to 1150°C at the exit of the reactor. The stoichiometric ratio value for the gas phase begins at infinity (because no fuel vapor is present at the inlet), then falls quickly while volatiles are released into the flow, making it less oxidizing. But it does not ever cross the threshold for reducing conditions despite the abundant yield of volatiles from this coal, because a very large portion of volatiles are converted into soot, which does not factor into the stoichiometric ratio value for the gas phase. Even at the end of devolatilization, the stoichiometric ratio value is 1.24, which is still larger than the whole-coal-based value (i.e. 0.953). Clearly, the chemical environment in the boundary layer is much more oxidizing than expected from the nominal stoichiometric ratio value. Significant amounts of volatiles are released when the gas temperature is roughly 1300°C, based on the decay in the O_2 concentration. All accumulated hydrocarbons are consumed at ignition, and neither H_2 nor any of the hydrocarbon fuels are present in the boundary layer in significant amounts. Gaseous hydrocarbons ignite the flow, but are otherwise unimportant. They are certainly not effective NO_X reductants, because NO forms well after they have been eliminated.

The O_2 concentration decays sharply during volatiles combustion and is depleted at about 120 ms. The CO concentration starts to increase sharply until all O_2 is depleted, then reaches a maximum at 130 ms, and decays during cooling. Its ultimate value reflects water gas shifting once all the O_2 has been consumed.

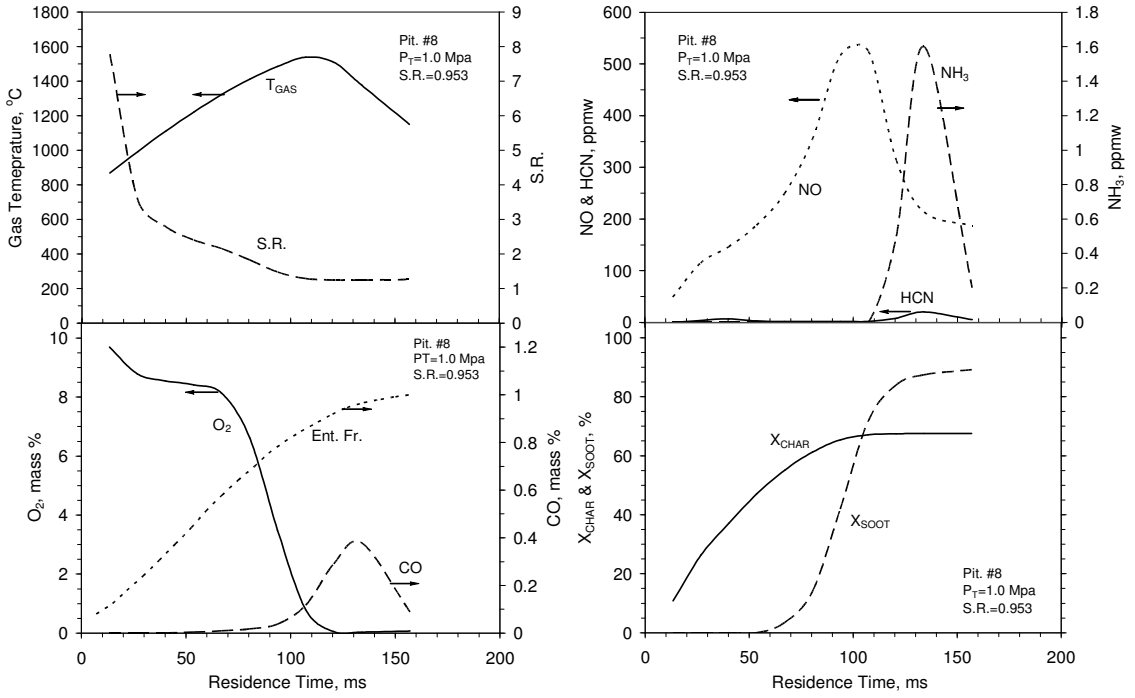

Figure B-31. Structure of the boundary layer of the baseline Run 51C for a Pittsburgh #8 flame at 1.0 MPa showing, in counterclockwise order from the upper left, the operating conditions, major species, char and soot burnout, and N-species.

Char competes very effectively with the gaseous fuel compounds for the available O_2 at the beginning, due to the very rapid burning rates of the smallest char particles in the PSD. The char ignites even in the first reactor of the CSTR-series, where the gas temperature is 870°C. An ultimate char burnout of 67.1 % is achieved at 110 ms when O_2 is depleted. Despite its very small size, soot does not ignite until the gas temperature exceeds 1300°C, because of its low intrinsic oxidation reactivity. Soot oxidation soon competes with char oxidation for O_2, because thermal annealing has come into play for char oxidation. Consequently, almost 90 % of the soot burns out in the boundary layer.
The NO concentration initially surges to 524 ppmw due to the rapid conversion of HCN, the primary volatile-N species, in the boundary layer, while the stoichiometric ratio value falls from 8 to 1.3. But once the available O_2 falls below 2 %, the NO concentration diminishes. The HCN concentration is much lower than that of NO, and never exceeds 20 ppmw. Even so, the HCN concentration exhibits two peaks at 40 and 134 ms. It is surprising that the HCN concentration does not increase while NO decays. The relatively high level of CO may be responsible for NO reduction in this stage. Ammonia appears as soon as NO reduction begins, but its concentration never exceeds 1.6 ppmw in the boundary layer. At the reactor outlet, there is 187 ppmw NO, but only 5 ppmw HCN and 0.2 ppmw NH_3.

Core

The predicted structure of the core for the baseline Run 51C flame appears in Figure B.32, including four panels in the same order as Figure B.31. In this flame core, the devolatilization time is 180 ms, and the flow leaves the reactor at 185 ms. Similar to the boundary layer, neither H_2 nor any of the hydrocarbon fuels are present in the core in significant amounts. The gas temperature increases gradually from 50°C to a flame temperature of about 1500°C at the exit of the reactor. The stoichiometric ratio value for the gas phase begins at infinity, and then falls sharply to 5 followed by a slow decrease. The stoichiometric ratio at the outlet of the reactor is 2.5, more than double the whole-coal-based value.

The O_2 concentration starts to decay at 100 ms when char particles ignite, but does not vanish because there is insufficient fuel in the core. The exhaust O_2 mass fraction is 1.5 %. CO increases rapidly at 100 ms when char ignites. It approaches a maximum at 135 ms, and then decays through 160 ms. The CO concentration remains below 0.01 % in the rest of the flow domain.

The char ignites at 100 ms when the gas temperature is only 470°C, and continues to burn until the reactor outlet, achieving an ultimate extent of char burnout of 36 DAF wt. %. Soot again does not ignite until the gas temperature is much hotter, exceeding 800°C. The soot oxidation rate then exceeds the char burning rate, and the extent of soot burnout at the outlet is 86 %.

HCN is released as the primary volatile N-species at 40 ms, and the HCN concentration continues to increase to a maximum value of 85 ppmw at 120 ms. Although the O_2

concentration during volatiles release is high enough for HCN oxidation to NO, the temperature is too cool. Ammonia appears as soon as HCN begins to decay, but its concentration remains well below 1 ppmw. HCN diminishes at 160 ms. NO does not form until 120 ms, when the gas temperature is 670°C. Since the core flow is always oxidizing, the NO concentration continues to increase to 66 ppmw at the outlet. NO is the only gaseous N-species at the reactor outlet. Note that the ultimate NO level in the core is lower than that in the boundary layer by a factor of 3. This is because only 15 % of the coal suspension flows through the core. The rest of the fuel is concentrated in the boundary layer region, due to the turbulent particle dispersion presented in NEA's Third Interim Report.

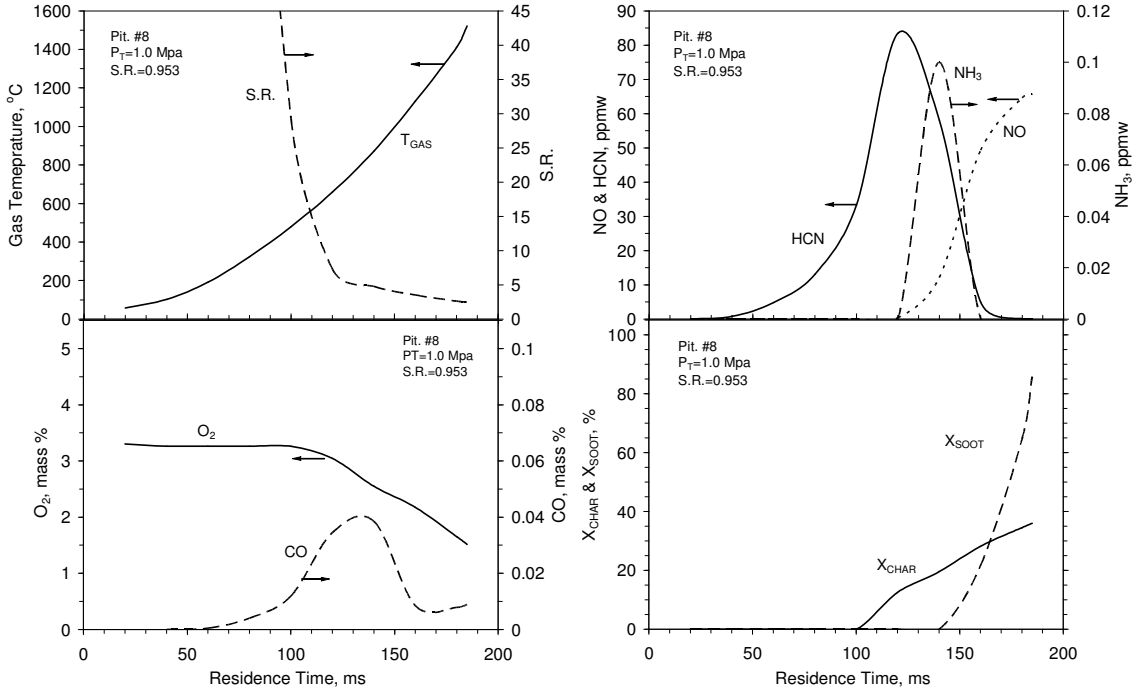

FigureB-32. Structure of the core of the baseline Run 51C for a Pittsburgh #8 flame at 1.0 MPa showing, in counterclockwise order from the upper left, the operating conditions, major species, char and soot burnout, and N-species.

Run 56C for the Lowest Stoichiometric Ratio

The structure of the boundary layer for Run 56C for the lowest stoichiometric ratio appears in Figure B.33. The total flow time is 185 ms, about 27 ms longer than that in the baseline case, due to a much cooler thermal history. However, the same devolatilization time of 134 ms was assigned for coal particles in the boundary layer. The gas temperature increases gradually from 860°C to a maximum of 1380°C at 120 ms, then decreases to 1030°C at the reactor exit. The gas temperature is about 150°C lower than that for the baseline case. The stoichiometric ratio value for the gas phase begins at

a very high value, then falls quickly before it slowly relaxes to 0.5 when the O_2 is depleted. The gas phase remains reducing until the reactor exit. The O_2 concentration decays sharply during volatiles combustion and is depleted at about 75 ms. The CO concentration starts to increase sharply at 60 ms and reaches a maximum value at 135 ms. It then remains constant through the rest of the flow domain. Since the gas phase remains reducing after the depletion of O_2, H_2, CH_4, and C_2H_2 are present in gas phase, and reach ultimate mass fractions of 0.3 %, 0.08 % and 0.12 %, respectively. It is not evident, however, that these reducing agents are NO_X reductants, because NO is eliminated well before these gases appear. Char and soot also compete with the gaseous fuel compounds for the available O_2 at the beginning. Since temperature is much lower in the baseline case, char annealing is much less important so that char ignites much sooner than soot. The ultimate burnouts of char and soot are 13.8 and 4.9 DAF wt. %. The NO concentration initially surges to 73 ppmw due to the rapid conversion of HCN from the primary volatiles while stoichiometric ratio exceeds 1.0. Once the available O_2 falls below 0.5 %, the NO concentration diminishes. The HCN concentration surges as NO diminishes, approaching a maximum value of 1200 ppmw at 120 ms that persists in the effluent. Ammonia appears simultaneously with HCN, but its ultimate concentration is only 29 ppmw in the boundary layer. At the reactor exit, there is 1210 ppmw HCN, 29 ppmw NH_3, but only 5 ppmw NO.

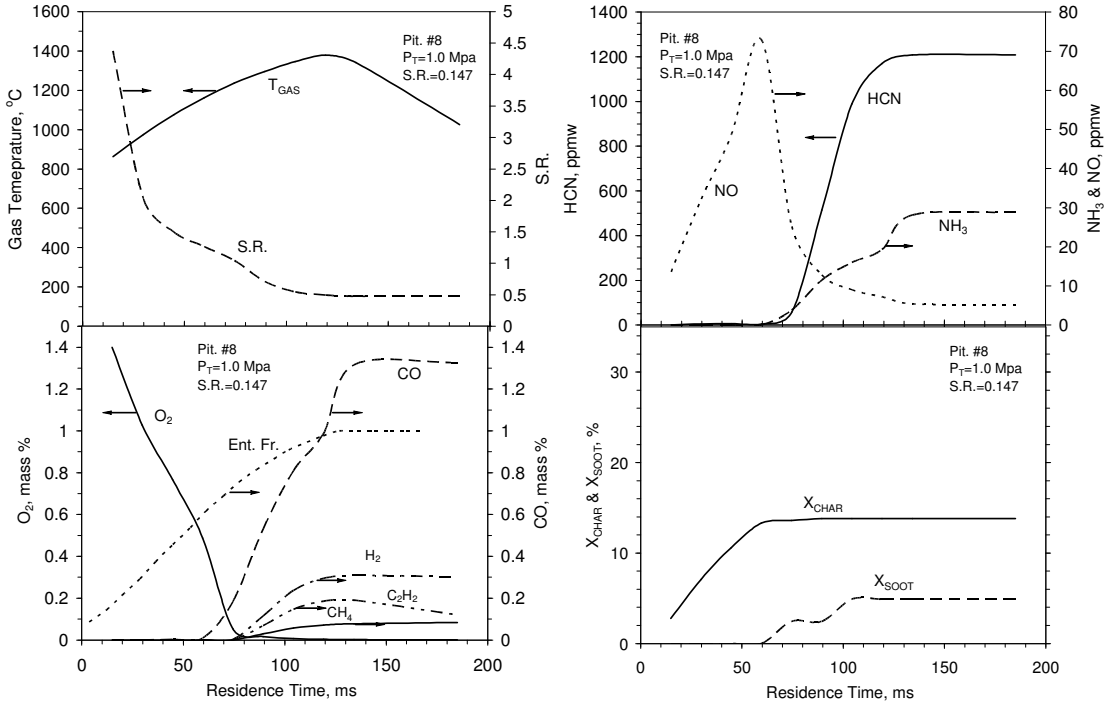

Figure B.33. Structure of the boundary layer of Run 56C for a Pittsburgh #8 flame at 1.0 MPa showing, in counterclockwise order from the upper left, the operating conditions, major species, char and soot burnout, and N-species.

Figure B.34 shows the structure of the core for Run 56C at the lowest stoichiometric ratio The total flow time is 200 ms, and the same devolatilization time of 180 ms was assigned for coal particles in the core. The gas temperature increases gradually from 120°C to a maximum of 1060°C at the reactor exit, which is much cooler than in the core region of the baseline case, so that this flame is not closed. The stoichiometric ratio value for the gas phase begins at infinity, and then falls sharply to a value below 1.0. Due to the low gas temperature, O_2 is depleted much slower than in the boundary layer, while the ultimate CO concentration is much higher. Char and soot burn much slower to ultimate extents of burnout of 5.6 and 4.5 DAF wt. %, respectively. HCN is the major N-species in the core region. Its concentration increases to a maximum value of 72 ppmw, followed by a rapid decrease. Ammonia appears at 120 ms, simultaneously with the appearance of NO. The NO concentration increases to 6.6 ppmw at the outlet of the reactor. Again only 14 % of the coal suspension flows through the core region, so the ultimate HCN level is much lower than in the boundary layer.

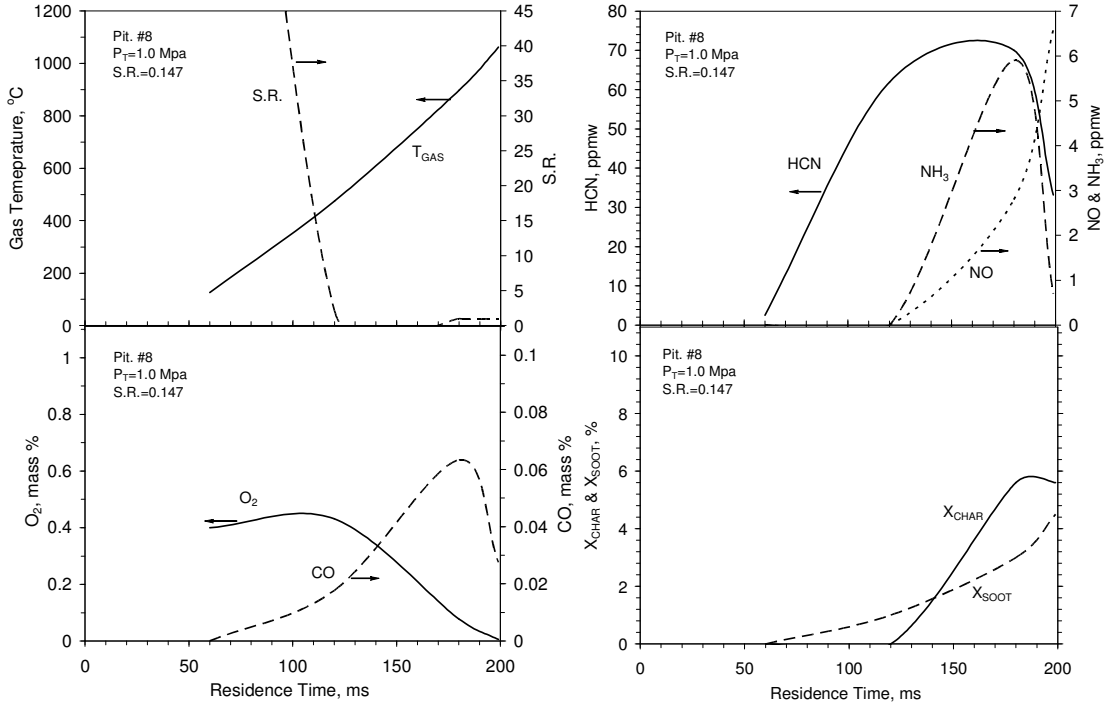

Figure B.34. Structure of the core of Run 56C for a Pittsburgh #8 flame at 1.0 MPa showing, in counterclockwise order from the upper left, the operating conditions, major species, char and soot burnout, and N-species.

B.4.4 Predictions for NO_X and the Major Product in the Exhaust

The predictions for the boundary layer and the core regions at the reactor exit were combined using mass-weighting to obtain the exhaust product distribution. Gas compositions for all NBFZ test series appear in Figures B.35-B.40.

Test Series With Pittsburgh #8

Figure B.35 shows the major products, CO and H_2 yields, and the coal-N conversion for the NBFZ test series with Pittsburgh #8 at 1.0 MPa. This test series includes baseline Run 51C with the highest stoichiometric ratio and Run 56C with the lowest stoichiometric ratio. All the major products and the CO and H_2 are expressed as weight percentages of coal on a DAF basis, and the N-speciation is expressed as percentages of total coal-N. As stoichiometric ratio was increased from 0.147 to 0.953, the measured weight loss due to devolatilization and char oxidation increased monotonically from 64 to 80 DAF wt. % in the upper panel of Figure B.35. The CO_2 yield increased from 30 to 200 DAF wt. %. The H_2O yield is much lower than CO_2 because there is so little coal-H, increasing from 14 to 46 DAF wt. % as stoichiometric ratio increases. The soot yield diminishes from 20 % to 2 % as it is burned out at the higher stoichiometric ratio conditions. The CO yield is much higher than H_2 on a mass basis in the middle panel of Figure B.35. As stoichiometric ratio was increased, the CO yields passed through a maximum at 45.1 DAF wt. % at stoichiometric ratio equal to 0.245. The H_2 yield decreased monotonically from 2.7 to 0.2 DAF wt. %. The conversion level of coal-N to HCN decreased for progressively higher stoichiometric ratio values, starting from conversion of 27.5 % of coal-N at the lowest stoichiometric ratio The coal-N conversion to NO much lower than expected for this coal during stoichiometric combustion at atmospheric pressure, reaching only 5.2 %.

The CNPP simulations quantitatively depict the impact of stoichiometric ratio on all major products and coal-N conversion, except one, within experimental uncertainty. The weight loss, CO_2, H_2O and H_2 yields are accurately predicted across the entire range of stoichiometric ratio. The soot yield is accurately predicted for stoichiometric ratio from 0.506 to 0.953, but over-predicted for runs with lower stoichiometric ratios. The predicted CO yields are well under measured values across the entire stoichiometric ratio range. As seen later for other test series, this under-prediction is systematic for all coals and also for all cases that were previously interpreted for atmospheric pressure. On this basis, it is probably due to a flaw in the gas phase reaction mechanism. Notwithstanding, the predicted CO yields exhibit a maximum value and the correct qualitative dependence on stoichiometric ratio. The measured CO approaches a maximum at stoichiometric ratio of 0.245, whereas the predicted CO reaches the maximum at 0.506.

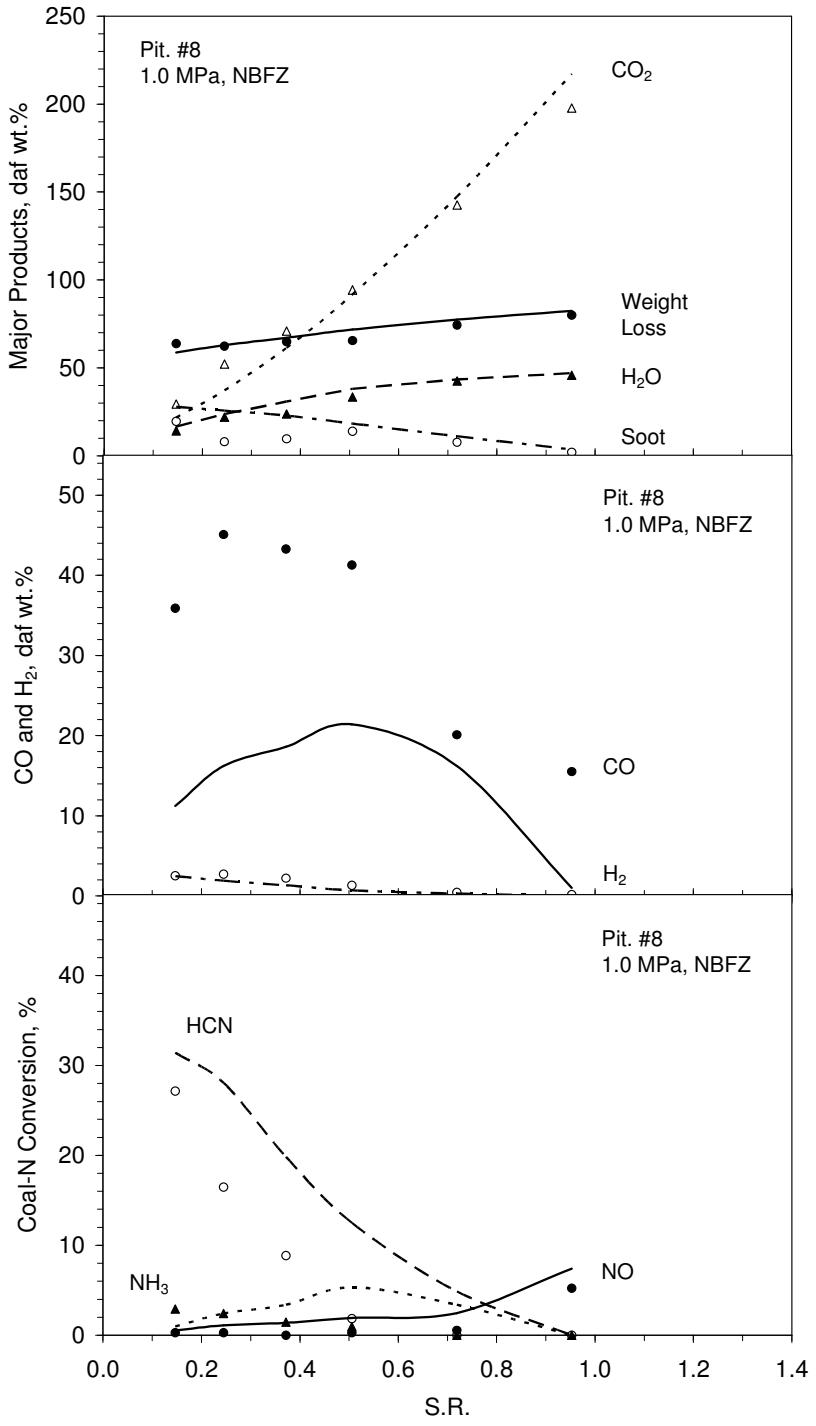

Figure B.35. Evaluations of predicted (Upper) major products, (middle) CO and H_2 yields, and (lower) coal-N conversion for NBFZ test series with Pittsburgh #8 at 1.0 MPa.

The coal-N conversion to HCN is over-predicted through the entire stoichiometric ratio range, but is qualitatively correct throughout. The NO conversion is only slightly over predicted, such that the emissions for the cases with the highest stoichiometric ratio are predicted to be 7.4 %, vs. a measured value of 5.2 %. Ammonia is predicted and observed to be a minor intermediate, although the predicted maximum value at a stoichiometric ratio of about 0.5 is not apparent in the measured values. This maximum is consistent with the results for atmospheric N-conversion in which ammonia acts as an intermediate N-species under reducing atmospheres.

The major product distributions and the N-species conversion for Pittsburgh #8 at 2.0 and 3.0 MPa appear in Figures B.36 and B.37, respectively. The predicted major products for 2.0 MPa are as accurate as for 1.0 MPa, but the discrepancies worsen for all the major species except weight loss at 3.0 MPa. In particular, the CO_2 yields and weight loss are all under-predicted, whereas the H_2O and soot yields are over-predicted throughout. The biggest flaw, again, is that CO yields are well under-predicted at both 2.0 MPa and 3.0 MPa. The H_2 yield is accurately predicted at both 2.0 and 3.0 MPa.

Predicted coal-N conversions are much better at both elevated pressures than at 1.0 MPa. At 2.0 MPa, the conversion to HCN is accurately predicted across the entire range of stoichiometric ratio. The NO is also accurately predicted throughout, with a discrepancy of less than 1.0 % for the run at the highest stoichiometric ratio. The predicted maximum in the NH_3 levels is more pronounced than the trend in the data, but most predictions are within experimental uncertainty. At 3.0 MPa, the predicted HCN levels are generally within experimental uncertainty, except that the persistence of HCN for stoichiometric ratio values over unity cannot be verified due to large scatter in the data for these conditions. Again, the maximum in the NH_3 levels is more pronounced in the predictions than in the data. Most important, there is less conversion to NO over the full range of stoichiometric ratio.

Perhaps the most important finding is that the conversion of coal-N into NO diminishes for progressively higher pressures. For stoichiometric ratio values from 0.95 to 1.1, the coal-N conversion to NO decreases from 5.2 % to 3.0 % to 2.2 % as pressure increases from 1.0 to 2.0 to 3.0 MPa. The trend is clearly evident in the predictions based on the detailed reaction mechanisms in the CNPP simulations. However, the variations in the flow fields, particle dynamics, and flame characteristics are substantial over this pressure range. They must factor in to any interpretations for the trend, in conjunction with shifts in the process chemistry.

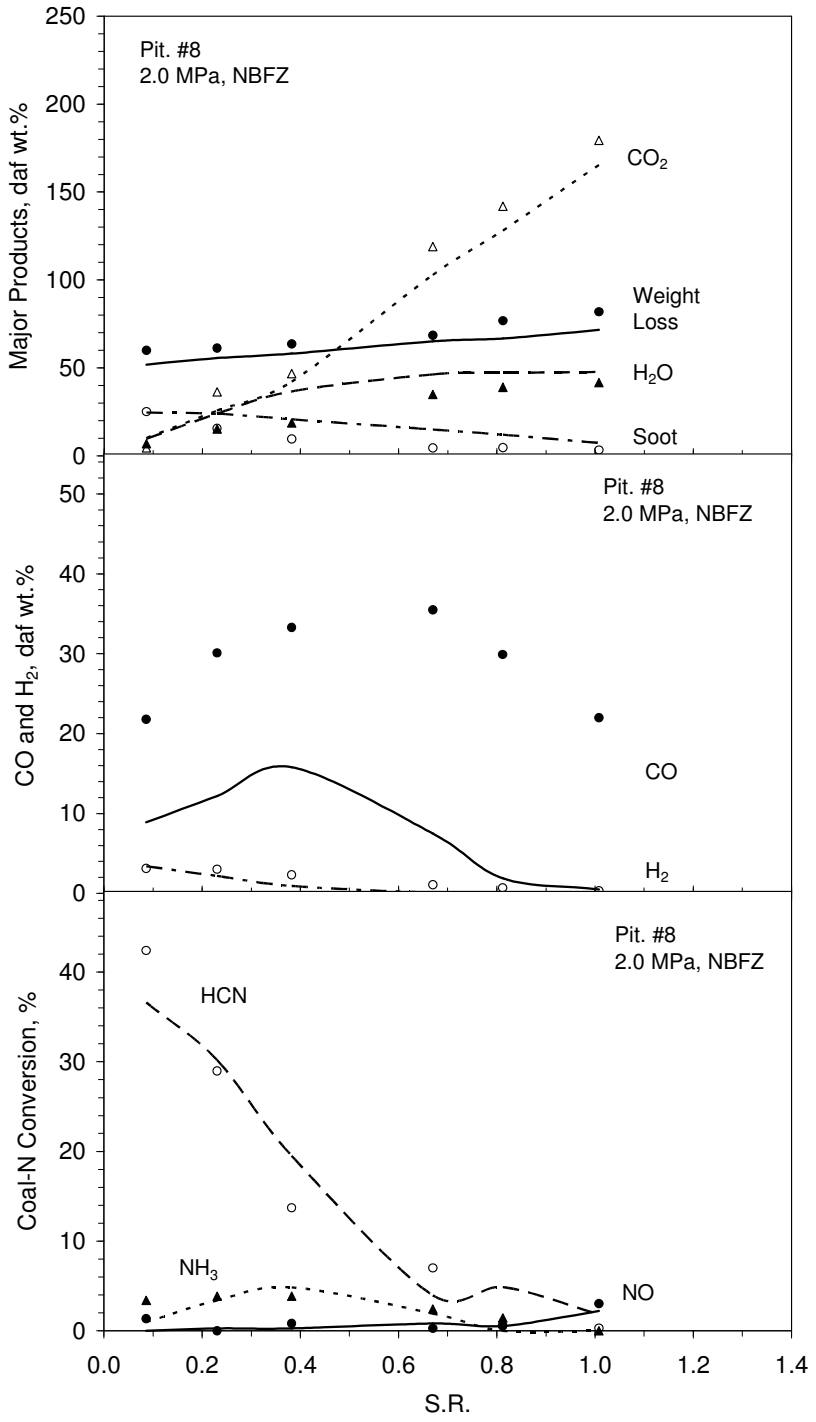

Figure B.36. Evaluations of predicted (Upper) major products, (middle) CO and H_2 yields, and (lower) coal-N conversion for NBFZ test series with Pittsburgh #8 at 2.0 MPa.

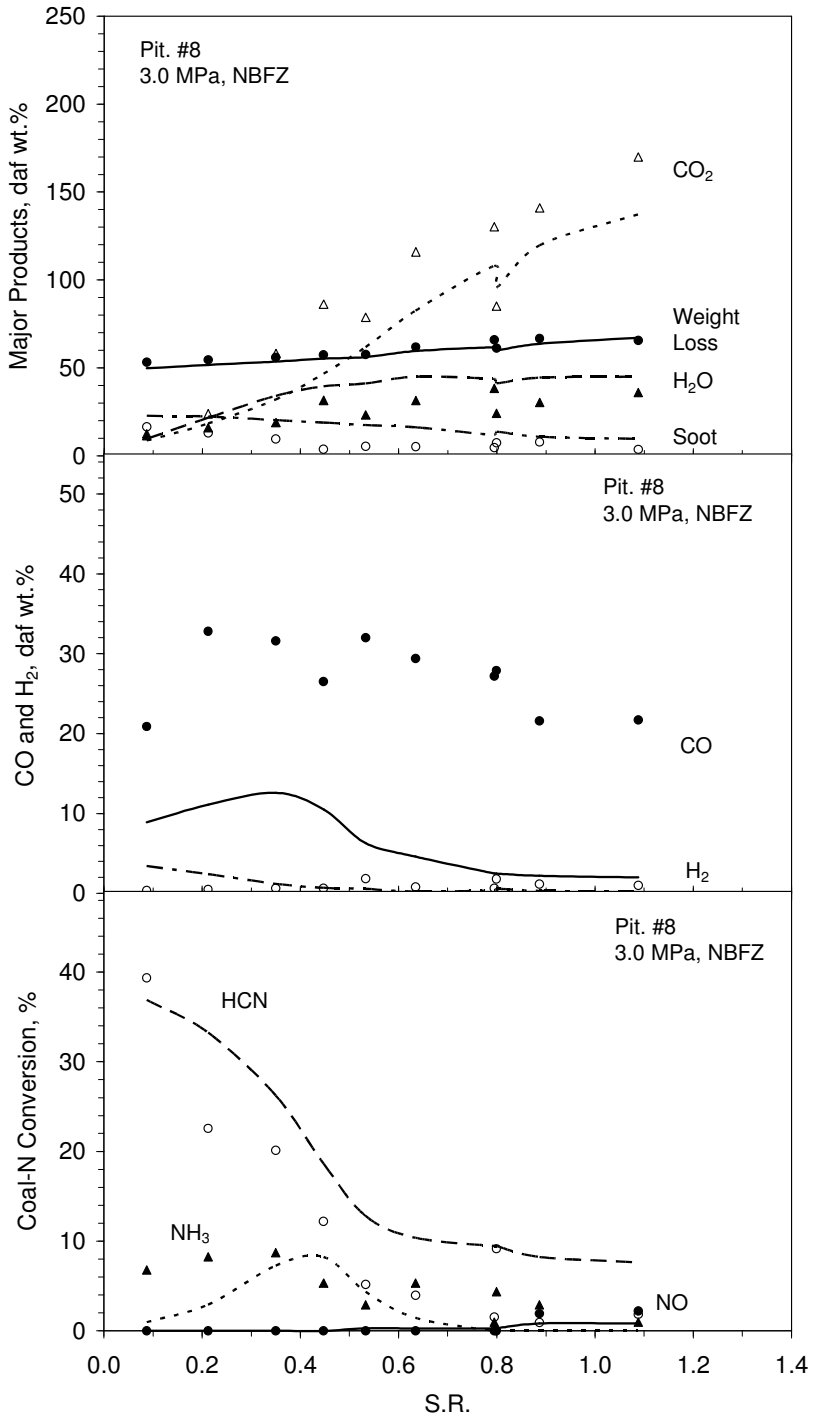

Figure B.37. Evaluations of predicted (Upper) major products, (middle) CO and H_2 yields, and (lower) coal-N conversion for NBFZ test series with Pittsburgh #8 at 3.0 MPa.

Test Series With Illinois #6

The major products for Illinois #6 at both 1.0 and 2.0 MPa are accurately predicted in the upper panels of Figs. B.38 and B.39. The predictions for all major products are within experimental uncertainty throughout and, in particular, the soot predictions are much more accurate than for Pittsburgh #8. Whereas the CO levels are still seriously under predicted, they are predicted and observed to be higher than with Pittsburgh #8. The stoichiometric ratio value at which the maximum CO level is achieved is accurately predicted for both 1.0 and 2.0 MPa. The H_2 levels are accurately predicted throughout.

The coal-N conversion to HCN at the lowest and the highest stoichiometric ratio is predicted within experimental uncertainty for both 1.0 and 2.0 MPa. Unfortunately, measured HCN levels for intermediate stoichiometric ratio values were either not recorded or are badly scattered, so a quantitative evaluation is not possible. For example, in the test series at 1.0 MPa, the coal-N conversions to HCN are 38 % and 39 % at stoichiometric ratio of 0.043 and 0.167, but only 9 % at a stoichiometric ratio of 0.229. Ammonia levels are over predicted throughout, and exhibit maxima that are not apparent in the data. Nevertheless, the predicted NO levels are accurate across the full range of stoichiometric ratio, and again indicate that coal-N conversion to NO diminishes for progressively higher pressures.

Test Series With PRB

PRB was only tested at 1.0 MPa. The major products are predicted within experimental uncertainty across the entire range stoichiometric ratio spectrum in Figure B.40, except that the CO_2 and H_2O levels are slightly over-predicted. The substantial reduction in the soot yields from this coal is evident in the predictions. Although the CO levels are again under-predicted, there is more CO from PRB than from both other coals in both the predictions and the data. The H_2 levels are accurately predicted, as for both other coals.

The coal-N conversion to HCN is slightly over-predicted for stoichiometric ratio values below 0.85, but exhibits the correct qualitative form. The predicted NH_3 levels are qualitatively correct but shifted toward higher stoichiometric ratio by 0.30. For the first time, the NO predictions are only qualitatively correct; in particular, the predicted NO level is double the measured value at the highest stoichiometric ratio of 1.27.

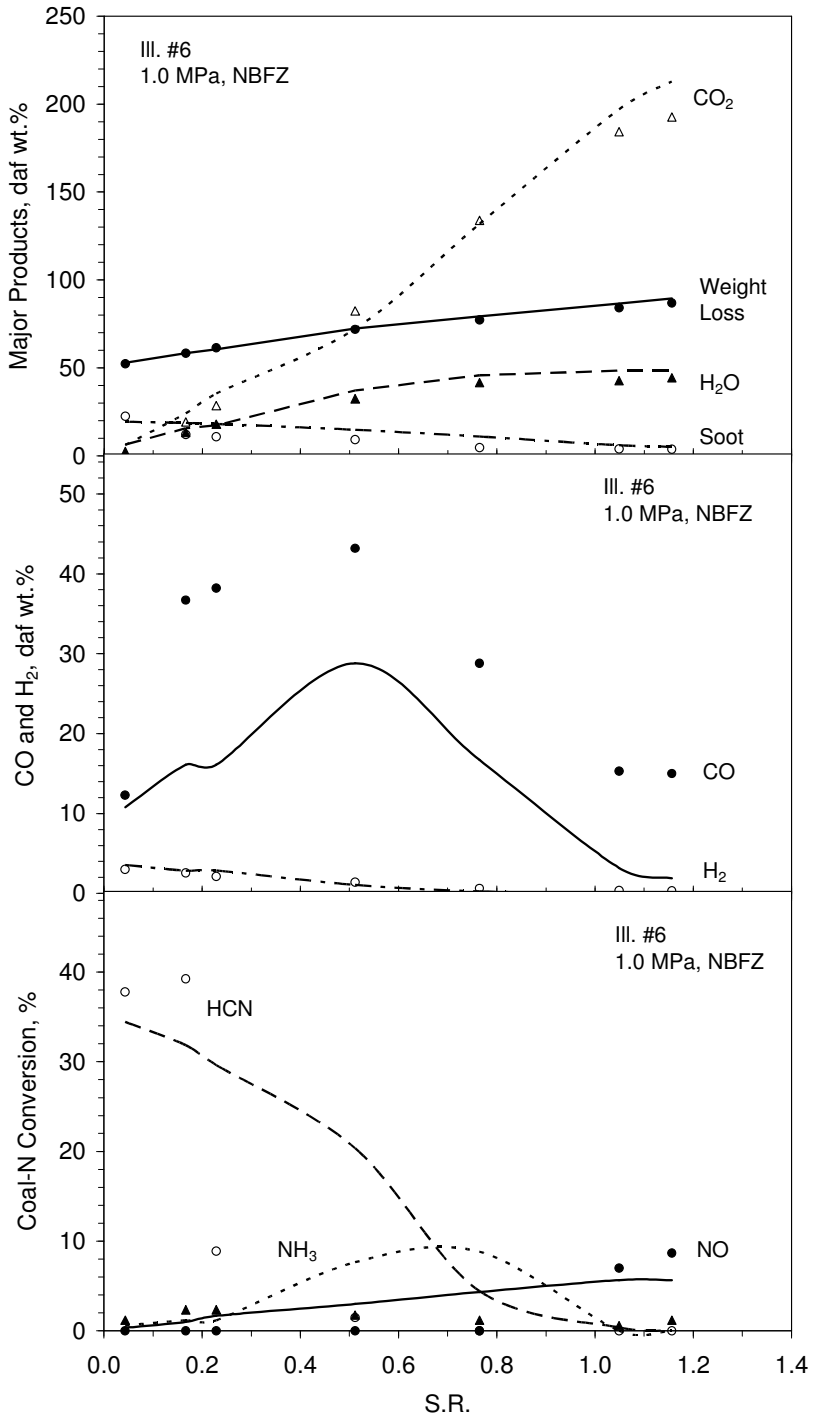

Figure B.38. Evaluations of predicted (Upper) major products, (middle) CO and H_2 yields, and (lower) coal-N conversion for NBFZ test series with Illinois #6 at 1.0 MPa.

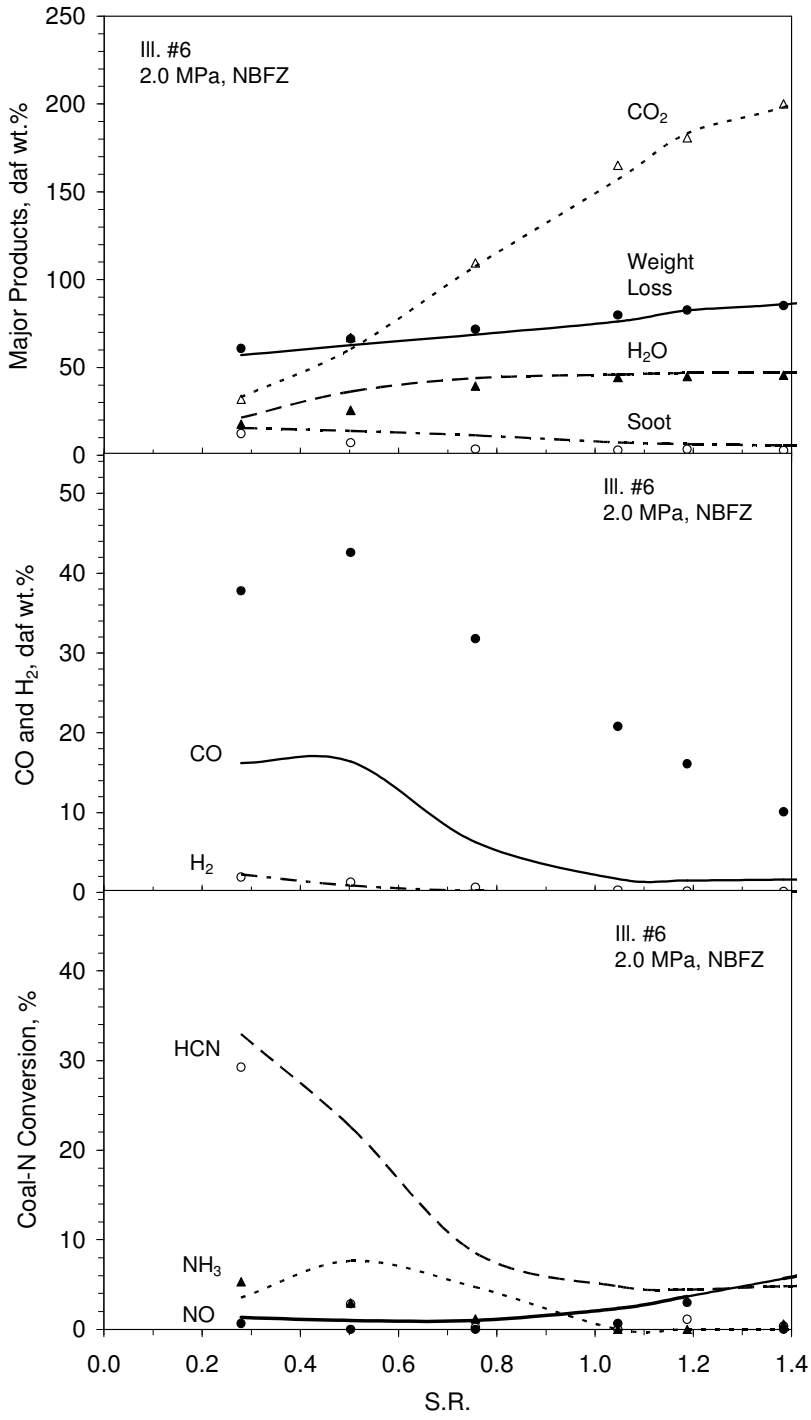

Figure B.39. Evaluations of predicted (Upper) major products, (middle) CO and H_2 yields, and (lower) coal-N conversion for NBFZ test series with Illinois #6 at 2.0 MPa.

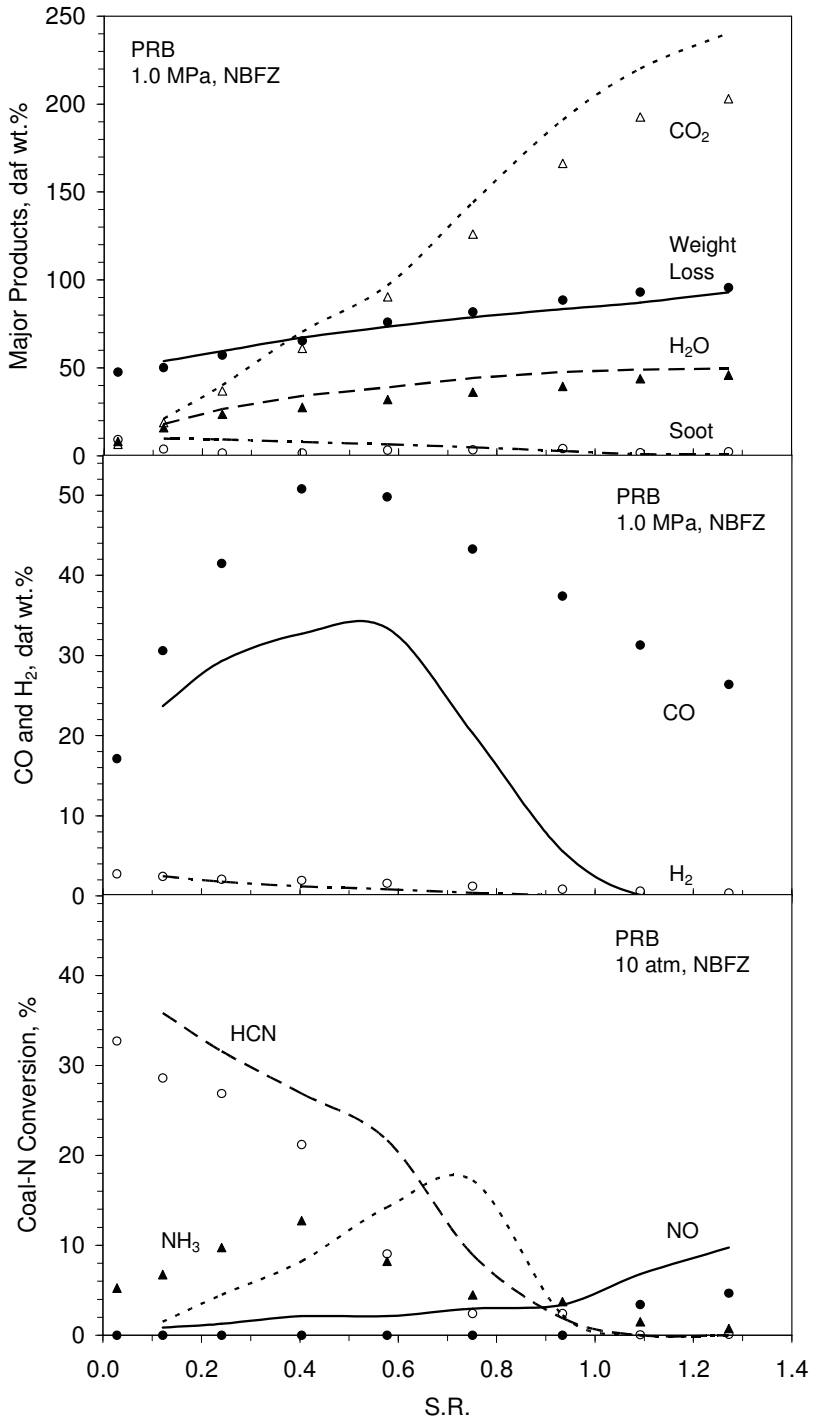

Figure B.40. Evaluations of predicted (Upper) major products, (middle) CO and H_2 yields, and (lower) coal-N conversion for NBFZ test series with PRB at 1.0 MPa.

Summary of Interpretations Based on Detailed Reaction Mechanisms

The detailed reaction mechanisms in the CNPP simulations depict all the important trends in the NBFZ database with both coal quality and for increasing pressure. The main differences in the major products are that soot yields diminish while total weight loss increases due to the faster char oxidation reactivity for coals of progressively lower rank The most serious quantitative flaw is that CO yields are under predicted by roughly a factor of two throughout, although the predictions correctly indicate higher CO levels for coals of progressively lower rank. Predicted H_2 yields were accurate for all cases. Most important, the reaction mechanisms correctly predict less conversion of coal-N into NO, and persistence of HCN for higher stoichiometric ratio values, for progressively higher pressures. For atmospheric coal flames, one expects less NO from coals of lower rank but this tendency was not evident in the predictions or data for the three coals in this test series. Coals of lower rank generate more NH_3, but this species is negligible except for intermediate stoichiometric ratio, where it is a minor intermediate.

Description of FLUENT NO_X Sub-Model

The NO_X sub-model in v.6.1 provides the capability to model thermal, prompt, and fuel NO_X formation as well as NO_X consumption due to reburning. To predict NO_X emissions, FLUENT solves a transport equation for NO concentration. For fuel-N conversion, FLUENT solves an additional transport equation for an intermediate N-species, which may be either HCN or NH_3. The NO_X species transport equations are solved over a previously specified flowfield and combustion solution. In other words, NO_X concentrations are post-processed from the major species fields from a combustion simulation. Clearly, an accurate combustion solution becomes a prerequisite for accurate NO_X predictions.

Since all NBFZ tests used an Ar carrier gas, thermal NO and prompt NO from N_2 in inlet gas are negligible, and these mechanisms are omitted from our simulations. Only fuel-derived NO is accounted for in all NBFZ simulations. The conversion pathways for coal-N in FLUENT appear in Figure B.41. After coal devolatilization, coal-N is partitioned into volatile-N and char-N. The volatile-N from all coals is HCN. The mass fractions of coal-N which is volatile-N and char-N are input specifications which, on our NBFZ simulations, were specified from stand-alone PC Coal Lab® simulations for coal devolatilization. Char-N is released into the gas phase at a same rate as carbon during char oxidation. FLUENT allows users to choose conversion of *all* char-N into *either* HCN *or* NO; none of the char-N is directly converted to N_2 in FLUENT.

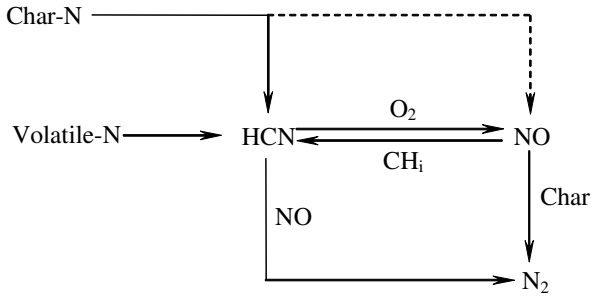

Figure B.41. Diagram of coal-N reaction pathways in FLUENT NO_X Sub-Model.

De Soete's two-step global model is used for N-conversion between HCN and NO in FLUENT:

$$HCN + O_2 \rightarrow NO + ... \quad \text{(B.8)}$$

$$HCN + NO \rightarrow N_2 + ... \quad \text{(B.9)}$$

Default parameter values for the pre-exponential factors, activation energies and O_2 reaction orders for these two reactions were reported by De Soete (1975), although the rate parameters can be adjusted through a user-defined function (UDF) in FLUENT v. 6.1. Heterogeneous NO reduction on char is based on the model of Sarofim and co-workers (1981), which requires a BET char surface area. FLUENT provides a default value of 2.5×10^4 m^2/kg.

NO reburning is also included in FLUENT. The reburning NO mechanism is a pathway whereby NO is reduced by hydrocarbons (CH, CH_2, CH_3) into HCN for temperatures from 1327 to 1827°C. As seen in the NBFZ datasets, NO and hydrocarbons never co-exist in the NBFZ tests, so NO reburning is deemed to be negligible.

NO_X Predictions of NBFZ Tests Based on the FLUENT NO_X Sub-Model

Predictions for Default Rate Parameters

The predicted HCN and NO levels for tests with Pittsburgh #8 from the FLUENT NO_X sub-model with default parameters are evaluated in Figure B.42. Although the default NO_X sub-model qualitatively depicts the impact of stoichiometric ratio on HCN and NO levels, there are huge quantitative discrepancies for all test conditions. The HCN levels are over predicted for all stoichiometric ratios, and HCN is predicted to persist for stoichiometric ratio values near-unity, at odds with the data. This flaw in the predictions worsens for progressively higher pressures, so that 40 % of coal-N is predicted for the highest stoichiometric ratio at 3.0 MPa, but none was measured. Moreover, the conversion of coal-N to NO is predicted to approach 25 % at 1.0 MPa, which is a typical value for atmospheric combustion for this coal type. Whereas the NO predictions

diminish for progressively higher pressures, they are always three to five times higher than the measured values. All char-N was converted into NO in the simulations, which may be partly responsible for the over-prediction of NO. However, if the only other option of converting all char-N into HCN was applied, then the HCN predictions would be even worse.

For the Illinois #6 test series in Figure B.43, the default NO_X sub-model predicts the HCN levels within experimental uncertainty for the two runs at 1.0 MPa with the lowest stoichiometric ratio The model, however, seriously over predicts the HCN levels for all other conditions in this test series. The predicted NO levels are over predicted throughout, and double the measured values at the highest stoichiometric ratio Both HCN and NO are overpredicted across the entire stoichiometric ratio range for this coal.

Surprisingly, the FLUENT sub-model with default parameters only slightly over predicts HCN levels over the entire range of stoichiometric ratio for the PRB test series in Figure B.44. But the extent of the over predictions in the NO levels is even worse than for both other coals.

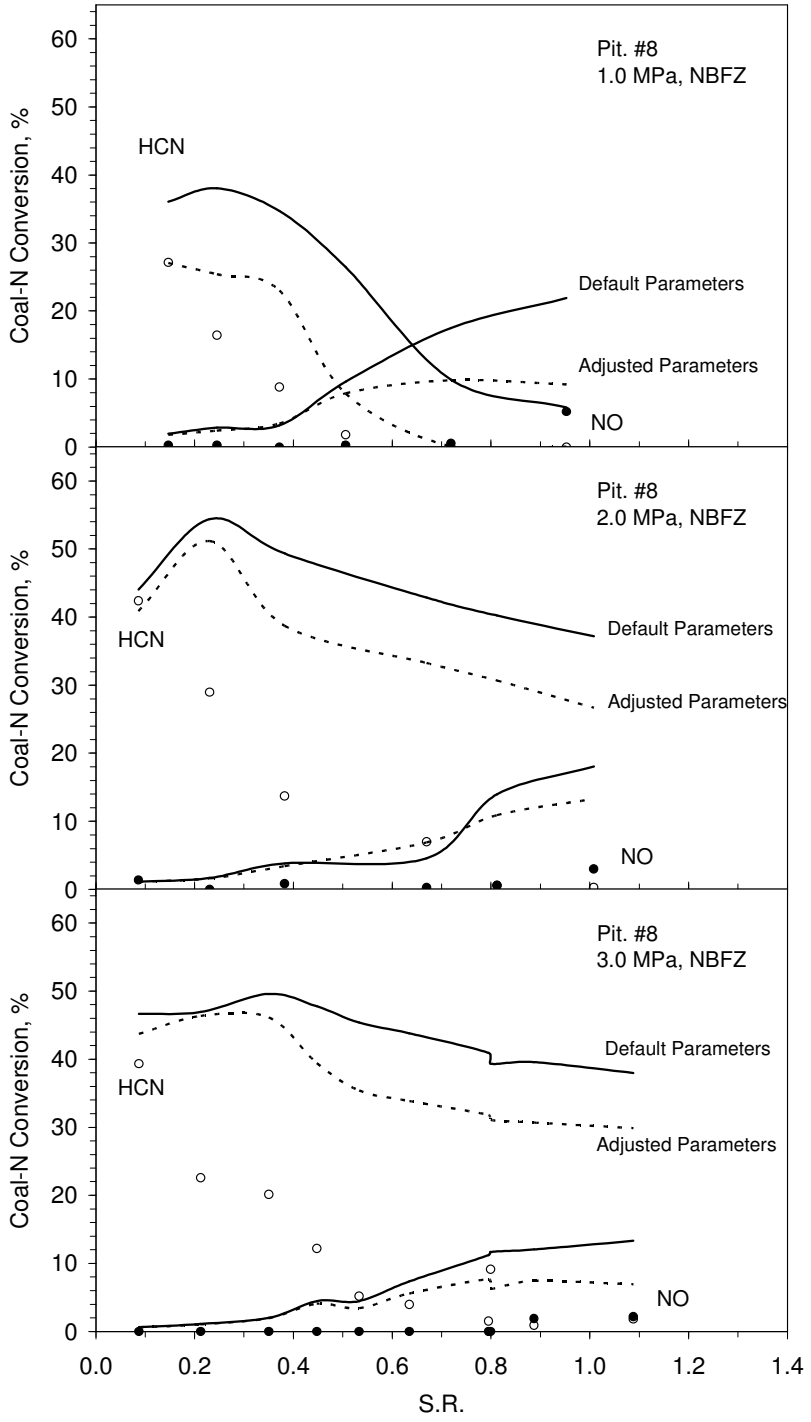

Figure B.42. Evaluation of predictions from v.6.1 FLUENT NO_X submodel with default parameters (solid line) and with adjusted parameters (dashed line) for Pittsburgh #8 at 1.0 (upper), 2.0 (middle) and 3.0 MPa (lower) with the measured HCN (○) and NO (●) levels.

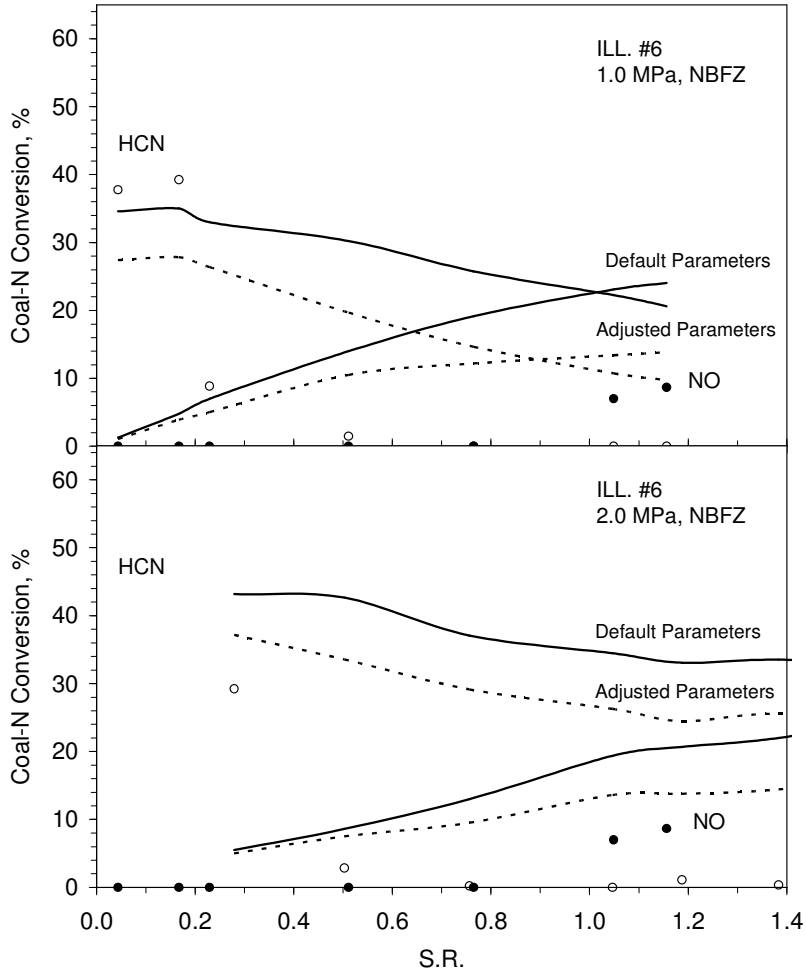

Figure B.43. Evaluation of predictions from v.6.1 FLUENT NO_X submodel with default parameters (solid line) and with adjusted parameters (dashed line) for Illinois #6 at 1.0 (upper) and 2.0 MPa (lower) with the measured HCN (○) and NO (●) levels.

Predictions With Adjusted Rate Parameters

The overpredicted HCN and NO levels for all NBFZ tests imply that reaction rates for both Equations B.8 and B.9 are too slow. In this section, predictions are reported for faster rates. The default pre-exponential factors were first increased by a factor of 10 to see if the earlier flaws could be attributed to default parameters, but not the proposed reaction scheme. Subsequent attempts to use even faster rates yielded essentially the same predictions, because NO and HCN were no longer simultaneously present in the same regions, so the impact of Equation B.9 reached a saturation limit. We also increased the char BET surface area from 2.5×10^4 to 5.0×10^5 m^2/kg, and noted very little improvement in the predicted NO levels.

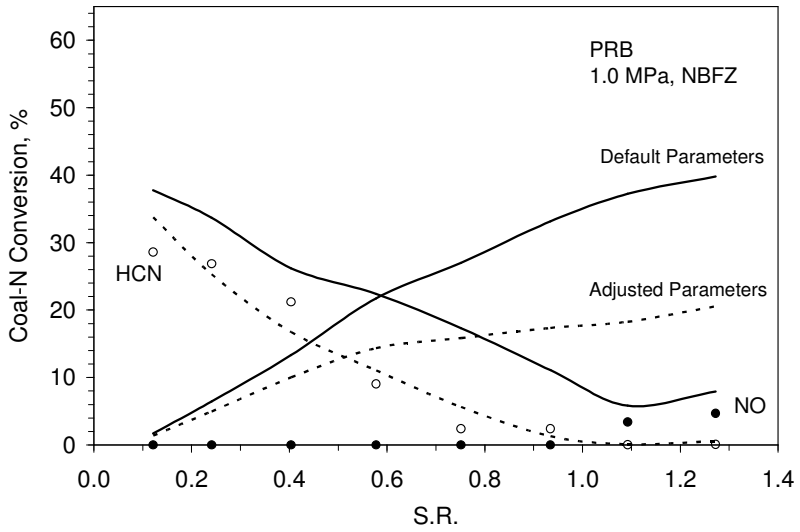

Figure B.44. Evaluation of predictions from v.6.1 FLUENT NO_X sub-model with default parameters (solid line) and with adjusted parameters (dashed line) for PRB at 1.0 MPa with the measured HCN (○) and NO (●) levels.

The predictions for the adjusted rate parameters for NBFZ tests appear in Figures B.42-B.44 as dashed lines. In general, both HCN and NO predictions are improved, but only marginally. For Pittsburgh #8 at 1.0 MPa, HCN is predicted to persist over the observed range of stoichiometric ratio, but the levels are over-predicted for intermediate stoichiometric ratio The HCN levels at both higher pressures are seriously over predicted, and HCN is still incorrectly predicted to persist for the highest stoichiometric ratio values. The NO predictions are significantly improved for 1.0 MPa, but not for both of the higher pressures; in fact, NO levels are still over predicted over the entire stoichiometric ratio range at all pressures.

Similarly marginal improvements are observed for Illinois #6 at 1.0 and 2.0 MPa. Again, both HCN and NO are significantly over-predicted for all but the lowest stoichiometric ratio values. But the HCN levels for the PRB are within experimental uncertainty over the full range of stoichiometric ratio; however, the NO levels remain seriously over-predicted.

In conclusion, the predicted HCN and NO levels from FLUENT NO_X submodel can be improved by adjusting rate parameters, but serious flaws associated with the proposed reaction scheme persist throughout the NBFZ test domain. In particular, the conversion of coal-N into NO is always seriously over predicted, whereas HCN is predicted to persist at much higher stoichiometric ratio values than recorded in the tests.

B.4.5 Development of Global NO_X Sub-Model

Strategy for Developing a Global NO_X Sub-Model

The global NO_X production sub-model was developed to reproduce the performance of the detailed chemical reaction mechanism in interpreting the NBFZ datasets. Obviously, the global scheme must be radically simpler than the full reaction mechanism involved in the NBFZ tests, and should preferably be developed with only those species in FLUENT's current NO_X sub-model. It was developed in the following sequence of steps:

1) Sensitivity analysis of selected CNPP simulations with detailed chemistry identified the major channels for fuel-N conversion, and to evaluate specific reaction rates and intermediate species concentrations. All such cases were for Pittsburgh #8 in order to cover the widest possible ranges of pressure, temperature, and stoichiometric ratio
2) The N-species pools in the CNPP simulations were examined to map out the main reaction pathways from HCN to NO and N_2.
3) The N-species conversion pathways with the full reaction mechanism were reduced to only the most important steps involving a minimum number of N-species.

Sensitivity Analysis of Full Chemistry Mechanism

Table B.13 lists the contributions from each elementary reaction to the overall rate of NO production (or destruction) in each of the CSTRs in the CNPP simulation for the boundary layer of the baseline flame. Only those reactions involving NO are included. The first row lists labels for all reactors in this CSTR-series, which comprise 10 CSTRs for the devolatilization zone, labeled DV01 to DV10, and one CSTR for char burnout, labeled CR01. The second row reports the overall NO conversion rate, which is positive for production and negative for consumption. These conversion rates only represent gas phase chemistry, and do not account for the direct conversion of char-N into NO and NO reduction by soot. The main body of the table lists each elementary reaction involving NO labeled as one of the 448 elementary reactions in the mechanism. The numbers in the body of the table indicate the percentage contribution of each step to the total NO conversion rate, which identifies the major channels at each stage of the test. Positive values contribute to the tendency in the overall NO conversion rate, either production or consumption. Negative values oppose the overall tendency.

Only those reactions that contribute over 20 % of the total NO conversion rate are regarded as main reaction pathways. The reactants in these steps were allocated to the N-species pool for the full reaction mechanism. Note that the composition of the pool shifts over different CSTRs; i. e., the main pathways and their associated species change during a single test. For this particular simulation, the N-species pool contains HNO, NO_2, HONO, HNO, NH_2, NH, N_2O, N, HCNO, NCO, HCN, which appear in Table B.13 in boldface type.

Table B.13. Contributions From Each Reaction Involving NO in Each CSTR of the Boundary Layer Region with Pittsburgh #8 at 1.0 MPa and a stoichiometric ratio of 0.953.

NO.	Reaction	DV01	DV02	DV03	DV04	DV05	DV06	DV07	DV08	DV09	DV10	CR01
		-8.79E-11	-1.94E-08	-1.20E-07	1.83E-08	2.28E-07	5.9E-07	1.04E-06	1.01E-07	-1.26E-06	-6.67E-07	-1.17E-07
238	H+NO+M=**HNO**+M	0.00	0.00	-0.03	0.11	-0.20	-0.60	-1.96	-52.11	0.63	0.39	8.26
239	H+NO+N2=HNO+N2	0.00	0.00	0.00	0.00	0.00	0.00	0.00	-0.01	0.00	0.00	0.00
240	NO+O+M=**NO2**+M	0.81	0.50	5.05	-135.31	-34.27	-29.50	-30.76	-233.31	0.72	0.10	3.22
241	OH+NO+M=**HONO**+M	-1.32	0.01	0.08	-1.73	-0.48	-0.55	-0.70	-5.30	0.02	0.00	0.31
242	HO2+NO=**NO2**+OH	0.13	0.50	2.80	-1.18	5.03	6.60	5.45	-0.56	0.31	0.59	11.01
243	**NO2**+H=NO+OH	0.00	-0.01	-0.87	20.77	7.38	9.76	17.18	211.84	-1.02	-0.67	-14.32
244	**NO2**+O=NO+O2	1.34	-0.07	-6.45	117.87	22.27	13.59	8.70	25.83	-0.01	0.00	-0.15
246	NO2+NO2=NO+NO+O2	0.04	0.00	0.00	0.02	0.00	0.00	0.00	0.00	0.00	0.00	0.00
247	NO2+NO2=NO3+NO	0.00	0.00	0.03	-0.23	-0.02	-0.01	0.00	-0.01	0.00	0.00	0.00
252	NO3+NO2=NO+NO2+O2	0.00	0.00	0.00	0.00	0.00	0.00	0.00	0.00	0.00	0.00	0.00
253	**HNO**+H=H2+NO	0.00	0.00	0.00	0.00	0.00	0.01	0.06	4.01	-0.13	-0.12	-1.23
254	**HNO**+O=NO+OH	0.00	0.00	0.00	0.06	0.02	0.04	0.07	1.19	0.00	0.00	-0.04
255	**HNO**+OH=NO+H2O	0.00	0.00	-0.04	1.06	0.44	0.81	2.19	50.85	-0.63	-0.29	-6.99
256	**HNO**+O2=HO2+NO	0.00	0.00	-0.01	0.14	0.03	0.03	0.03	0.16	0.00	0.00	-0.01
257	HNO+NO2=HONO+NO	0.00	0.00	0.00	0.00	0.00	0.00	0.00	0.00	0.00	0.00	0.00
259	HNO+NH2=NH3+NO	0.00	0.00	0.00	0.00	0.00	0.00	0.00	0.00	0.00	0.00	0.00
266	H2NO+NO=HNO+HNO	0.00	0.00	0.00	0.00	0.00	0.00	0.00	0.00	0.00	0.00	0.00
282	**NH2**+NO=NNH+OH	0.00	0.00	0.00	-0.01	0.00	0.00	-0.01	-0.30	0.07	0.10	0.12
283	**NH2**+NO=N2+H2O	0.00	0.00	0.00	-0.02	0.00	-0.01	-0.02	-0.51	0.12	0.18	0.25
284	**NH2**+NO=N2+H2O	0.00	0.00	0.00	-0.01	0.00	0.00	-0.01	-0.30	0.07	0.10	0.12
286	NH2+NO2=H2NO+NO	0.00	0.00	0.00	0.00	0.00	0.00	0.00	0.01	0.00	0.00	0.00
293	**NH**+O=NO+H	0.00	0.00	0.00	0.06	0.03	0.05	0.09	1.13	-0.01	0.00	0.00
297	**NH**+O2=NO+OH	0.00	0.00	-0.05	0.63	0.11	0.07	0.06	0.23	0.00	0.00	0.00
298	**NH**+NO=**N2O**+H	0.00	0.00	0.02	-0.32	-0.07	-0.07	-0.14	-2.28	0.21	0.11	0.13
299	**NH**+NO=N2O+H	0.00	0.00	0.01	-0.08	-0.02	-0.02	-0.04	-0.62	0.06	0.03	0.03
300	**NH**+NO=N2+OH	0.00	0.00	0.01	-0.09	-0.02	-0.02	-0.04	-0.67	0.06	0.03	0.04
304	**N**+OH=NO+H	0.00	0.00	0.00	0.01	0.01	0.02	0.07	1.49	-0.03	0.00	0.00
305	**N**+O2=NO+O	0.00	0.00	-0.02	0.65	0.18	0.20	0.26	1.31	-0.01	0.00	0.00
306	**N**+NO=N2+O	0.00	0.00	0.00	-0.04	-0.01	-0.02	-0.07	-1.53	0.08	0.02	0.01
309	N2H2+O=NH2+NO	0.00	0.00	0.00	0.00	0.00	0.00	0.00	0.00	0.00	0.00	0.00
312	N2H2+NO=N2O+NH2	0.00	0.00	0.00	0.00	0.00	0.00	0.00	0.00	0.00	0.00	0.00
319	NNH+O=**NH**+NO	0.00	0.00	0.00	-0.01	0.00	0.00	-0.01	-0.19	0.02	0.01	0.00
323	NNH+NO=N2+HNO	0.00	0.00	0.00	0.00	0.00	0.00	0.00	-0.01	0.01	0.01	0.00
329	**N2O**+O=NO+NO	0.00	0.00	0.00	0.17	0.03	0.02	0.02	0.10	0.00	0.00	0.00
332	N2O+OH=HNO+NO	0.00	0.00	0.00	0.00	0.00	0.00	0.00	0.00	0.00	0.00	0.00
333	N2O+NO=NO2+N2	0.00	0.00	0.00	0.00	0.00	0.00	0.00	0.00	0.00	0.00	0.00
347	CN+NO2=NCO+NO	0.00	0.00	0.00	0.00	0.00	0.00	0.00	0.00	0.00	0.00	0.00
350	CN+HNO=HCN+NO	0.00	0.00	0.00	0.00	0.00	0.00	0.00	0.00	0.00	0.00	0.00
352	CN+N2O=NCN+NO	0.00	0.00	0.00	0.00	0.00	0.00	0.00	0.00	0.00	0.00	0.00
369	**HCNO**+O=HCO+NO	0.00	0.00	0.00	0.00	0.00	0.02	0.02	0.39	-0.02	-0.01	0.00
370	**HCNO**+OH=CH2O+NO	0.00	0.00	0.00	0.00	0.00	0.02	0.03	0.94	-0.18	-0.17	-0.02
373	**NCO**+O=NO+CO	0.00	0.00	-0.09	3.36	1.06	1.02	1.15	5.52	-0.02	0.00	-0.01
374	NCO+OH=NO+HCO	0.00	0.00	0.00	0.01	0.00	0.01	0.01	0.11	0.00	0.00	0.00
375	**NCO**+O2=NO+CO2	0.00	-0.01	-0.14	2.13	0.32	0.19	0.10	0.18	0.00	0.00	0.00
378	**NCO**+NO=N2O+CO	0.00	0.03	0.33	-3.32	-0.41	-0.27	-0.31	-1.89	0.06	0.03	0.10
379	**NCO**+NO=N2+CO2	0.00	0.04	0.41	-4.17	-0.51	-0.34	-0.39	-2.38	0.07	0.03	0.13
380	NCO+NO2=CO+NO+NO	0.00	0.00	-0.01	0.05	0.00	0.00	0.00	0.00	0.00	0.00	0.00
382	NCO+HNO=HNCO+NO	0.00	0.00	0.00	0.00	0.00	0.00	0.00	0.00	0.00	0.00	0.00
388	NCN+O=CN+NO	0.00	0.00	0.00	0.00	0.00	0.00	0.00	0.00	0.00	0.00	0.00
389	NCN+OH=HCN+NO	0.00	0.00	0.00	0.00	0.00	0.00	0.00	0.00	0.00	0.00	0.00
391	NCN+O2=NO+NCO	0.00	0.00	0.00	0.00	0.00	0.00	0.00	0.00	0.00	0.00	0.00
399	CO+**NO2**=CO2+NO	0.00	0.00	0.00	0.21	0.06	0.06	0.10	1.57	-0.02	-0.02	-0.04
401	CO2+**N**=NO+CO	0.00	0.00	0.00	0.02	0.01	0.01	0.03	0.80	-0.07	-0.02	-0.01
404	HCO+NO=HNO+CO	0.00	0.00	0.00	0.00	0.00	-0.01	-0.01	-0.10	0.00	0.00	0.00
406	HCO+NO2=H+CO2+NO	0.00	0.00	0.00	0.00	0.00	0.00	0.00	0.00	0.00	0.00	0.00
407	HCO+HNO=CH2O+NO	0.00	0.00	0.00	0.00	0.00	0.00	0.00	0.00	0.00	0.00	0.00
410	CH3+NO=HCN+H2O	0.00	0.00	0.00	0.00	0.00	0.00	0.00	-0.01	0.00	0.00	0.00
411	CH3+NO=H2CN+OH	0.00	0.00	0.00	0.00	0.00	0.00	0.00	-0.01	0.00	0.00	0.00
412	CH3+**NO2**=CH3O+NO	0.00	0.00	-0.01	0.19	0.03	0.02	0.01	0.05	0.00	0.00	0.00
416	CH2+NO=**HCN**+OH	0.00	0.00	0.00	0.00	0.00	-0.02	-0.02	-0.27	0.01	0.01	0.00
417	CH2+NO=**HCNO**+H	0.00	0.00	0.00	0.00	0.00	-0.01	-0.01	-0.16	0.01	0.00	0.00
418	CH2+NO2=CH2O+NO	0.00	0.00	0.00	0.00	0.00	0.01	0.01	0.03	0.00	0.00	0.00
422	CH2(S)+NO=HCN+OH	0.00	0.00	0.00	0.00	0.00	0.00	0.00	-0.07	0.00	0.00	0.00
425	CH+NO2=HCO+NO	0.00	0.00	0.00	0.00	0.00	0.00	0.00	0.00	0.00	0.00	0.00
426	CH+NO=HCN+O	0.00	0.00	0.00	0.00	0.00	0.00	0.00	-0.04	0.00	0.00	0.00
427	CH+NO=HCO+N	0.00	0.00	0.00	0.00	0.00	0.00	0.00	-0.03	0.00	0.00	0.00
428	CH+NO=NCO+H	0.00	0.00	0.00	0.00	0.00	0.00	0.00	-0.01	0.00	0.00	0.00
431	CH+N2O=HCN+NO	0.00	0.00	0.00	0.00	0.00	0.00	0.00	0.00	0.00	0.00	0.00
432	C+NO=CN+O	0.00	0.00	0.00	0.00	0.00	0.00	0.00	0.00	0.00	0.00	0.00
433	C+NO=CO+N	0.00	0.00	0.00	0.00	0.00	0.00	0.00	0.00	0.00	0.00	0.00
435	C+N2O=CN+NO	0.00	0.00	0.00	0.00	0.00	0.00	0.00	0.00	0.00	0.00	0.00
439	C2H3+NO=C2H2+HNO	0.00	0.00	0.00	0.00	0.00	0.00	0.00	0.00	0.00	0.00	0.00
442	C2H+NO=CN+HCO	0.00	0.00	0.00	0.00	0.00	-0.01	-0.02	-0.33	0.03	0.02	0.00
444	HCCO+NO=**HCNO**+CO	0.00	0.00	0.00	0.00	0.00	-0.02	-0.04	-1.16	0.19	0.18	0.03
445	HCCO+NO=**HCN**+CO2	0.00	0.00	0.00	0.00	0.00	-0.05	-0.08	-2.59	0.43	0.39	0.06

Similar sensitivity analyses for the boundary layer and core regions of all test series with Pittsburgh #8 yielded 14 participating N-species, which are HCN, CN, HOCN, HNCO, NH_i, HNO, N, NCO, N_2, N_2O, NO, NO_2, HCNO, HONO.

Developing A Global N-Conversion Scheme

Reaction Paths from HCN to NO and N_2

The main reaction pathways for HCN conversion to NO and N_2 in the full reaction mechanism for NBFZ tests appear in Figure B.45. These reaction pathways include major N-products - HCN, NH_i, NO and N_2 – as well as intermediates present in very small concentrations - CN, N, NCO, HNO, HNCO, HOCN, HCNO, HONO, N_2O, NO_2. The bold lines indicate the reaction paths with higher rates, which are therefore regarded as the major reaction channels.

Other radicals and molecules that participate in these elementary reactions also appear in the diagram. The most important species are H, O, OH, O_2 and M (a third-body collision partner). The concentrations of these species depend on the stoichiometric ratio and temperature in the gas phase. Generally, they increase as temperature increases. O-atoms are abundant in fuel-lean flames, whereas H-atoms are abundant in fuel-rich flames. The OH concentration is highest in a flame with intermediate stoichiometric ratio

Simplification of the Full Reaction Path

We found that NCO and NH_i are the two major intermediates in the conversion of HCN into NO and N_2. Their paths from HCN are parallel. CN, HOCN, HNCO only appear as intermediates in these two major paths, and do not participate in other channels. N_2 and NO are the major ultimate products of N-conversion, whose relative yields depend on the gas environment. N_2O and NO_2 are minor products of NBFZ test conditions, and generally do not participate in other reactions. Therefore these species and associated reactions were neglected in the global mechanism.

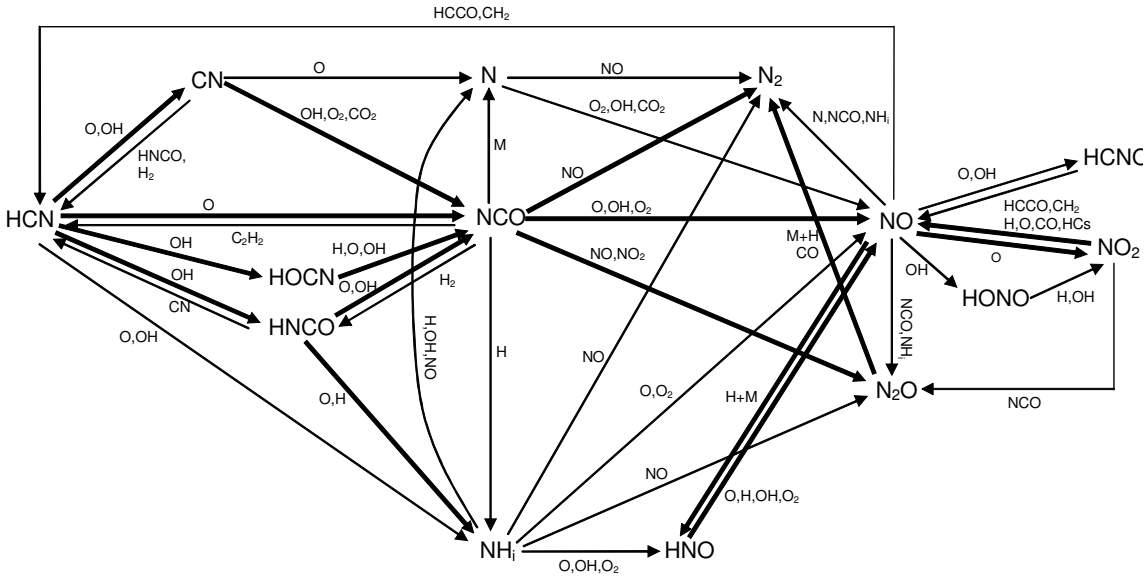

Figure B.45. Reaction pathways for HCN conversion into NO and N_2 in the CNPP simulations for NBFZ tests with Pittsburgh #8. Bold lines indicate the major reaction pathways.

The global scheme in Figure B.46 contains only the most important channels in the elementary reaction mechanism, with are the following three steps:

$$HCN + 0.5\ O_2 = HNCO \quad \text{(B.10)}$$

$$2\ HNCO + 1.5\ O_2 = 2\ NO + 2\ CO + H_2O \quad \text{(B.11)}$$

$$2\ HNCO + NO = 1.5\ N_2 + 2\ CO + H_2O \quad \text{(B.12)}$$

The scheme is the same as the v.6.1 FLUENT NO_X sub-model except for the addition of two features: (1) The intermediate decomposition products of HCN, HCNO and amines, are explicitly represented as pseudo-HNCO; and (2) The additional concentration dependences on O_2 and NO are also explicit in each of the three steps. The first addition is required to depict the high levels of residual HCN in the NBFZ tests at moderate temperatures even for stoichiometric ratio values greater than unity. For progressively higher pressures at moderate temperatures, the oxyhydroxyl radical pool (O, OH, and H) shrinks, which decelerates the rate of HCN conversion into HNCO and amines. The second addition is needed to depict less NO production for progressively higher pressures in the NBFZ tests. While the oxyhydroxyl radical pool shrinks at elevated pressures, the conversion of HNCO shifts toward N_2 production, so the predicted NO levels are lower, consistent with the data.

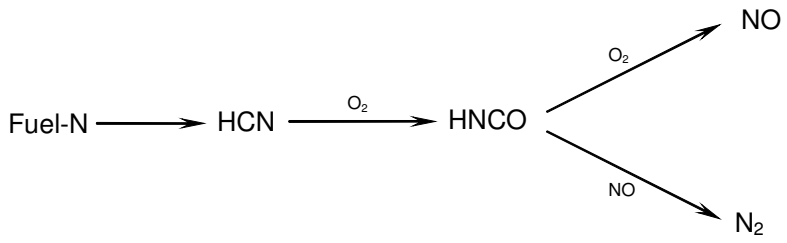

Figure B.46. Global scheme for HCN conversion into NO and N_2 simplified from full reaction mechanism for NBFZ Tests with Pittsburgh #8.

B.4.6 NO_X Predictions for NBFZ Tests from NEA's Global NO_X Sub-Model

Implementing NEA's Global NO_X Sub-Model in FLUENT

A global NO_X sub-model was developed trough UDF. User defined scalar are solved for NO, HCN and for pseudo-HNCO as an intermediate species. The source term for HNCO is calculated the same way as for HCN and NO, based on the following global rate expressions for reactions B.10, B.11 and B.12, respectively:

$$R_1 = A_1 X_{HCN} X_{O_2}^{n_1} e^{-E_1/RT} \quad \text{(B.10)}$$

$$R_2 = A_2 X_{HNCO} X_{O_2}^{n_2} e^{-E_2/RT} \quad \text{(B.11)}$$

$$R_3 = A_3 X_{HNCO} X_{NO} e^{-E_3/RT} \quad \text{(B.12)}$$

where R_1, R_2 and R_3 denote the conversion rate (s^{-1}) of HCN in reaction 4.3, of HNCO in reaction 4.4, and of HNCO in reaction 4.5. X denotes the mole fraction of each species.

All volatile-N is converted to HCN, so the total HCN yield from secondary pyrolysis appears in the source term for the HCN transport equation. We ignored NO reduction on char and the NO reburning mechanism that are included in the v.6.1 FLUENT NO_X sub-model. For consistency with our full-chemistry mechanism, we include a fractional char-N into NO conversion factor in the global sub-model. For NBFZ tests, this fraction is 0.2 for Pittsburgh #8 and PRB, and 0.7 for Illinois #6, as specified in the CNPP simulations. In this way, the rate of char-N conversion to NO contributes to the production rate in the NO source term. NO reduction on soot was omitted from the global sub-model, because it was found to make a small contribution to N-species conversion in the CNPP simulations.

Assigning Rate Parameters

Rate parameters in Equations B.13-B.15 are required to evaluate the source terms for HCN, HNCO and NO. These parameters include pre-exponential factors A_1, A_2 and A_3,

activation energies E_1, E_2 and E_3, and the reaction orders n_1 and n_2 with respect to the O_2 mole fraction. These parameters are determined by fitting the FLUENT predictions to the measured HCN and NO values for all test series with Pittsburgh #8. The adjustment continued until the predicted values best matched the measured values.

Table B.14 lists all the assigned rate parameters for the global NO_X submodel. Although a value of between 0 and 1 is expected for pressure orders n_1 and n_2, we found that an order of unity for both n_1 and n_2 gave the best fit over the full range of stoichiometric ratio In addition, the assigned activation energies E_1, E_2 and E_3 are very small, which is not surprising considering the multitude of elementary reactions lumped into each process in the global scheme.

Table B.14. Reaction Rate Parameters in NEA's Global NO_X Sub-Model.

Reaction	A, s^{-1}	E, kcal/mol	n
R_1	6.0×10^2	0.625	1
R_2	9.0×10^2	1.421	1
R_3	2.0×10^6	1.174	-

NO_X Predictions for NBFZ Tests From NEA's Global NO_X Sub-Model

FLUENT simulations were performed for all NBFZ tests with the global NO_X sub-model to prepare the evaluations with data and with predictions from the full reaction mechanism in Figures B.47-B.49. In the upper panel of Figure B.47 for the Pittsburgh #8 test series at 1.0 MPa, the HCN predictions from the global sub-model are in better agreement than the CNPP predictions, whereas the NO predictions are the same. For 2 MPa, the predictions for both species from the global sub-model and CNPP are very similar, except that the NO predictions from the sub-model are higher at the highest stoichiometric ratio values. Note that the global sub-model predicts that HCN persists in the flue gas for stoichiometric ratio values greater than unity. The performance for 3.0 MPa is similar, except that the over prediction of NO for high stoichiometric ratio is somewhat worse. Nevertheless, the global sub-model correctly depicts the impact of pressure on NO levels for the highest stoichiometric ratio cases.

The predictions for Illinois #6 are evaluated in Figure B.48. As noted earlier, the rate parameters in this global scheme were determined by fitting the test series with Pittsburgh #8.

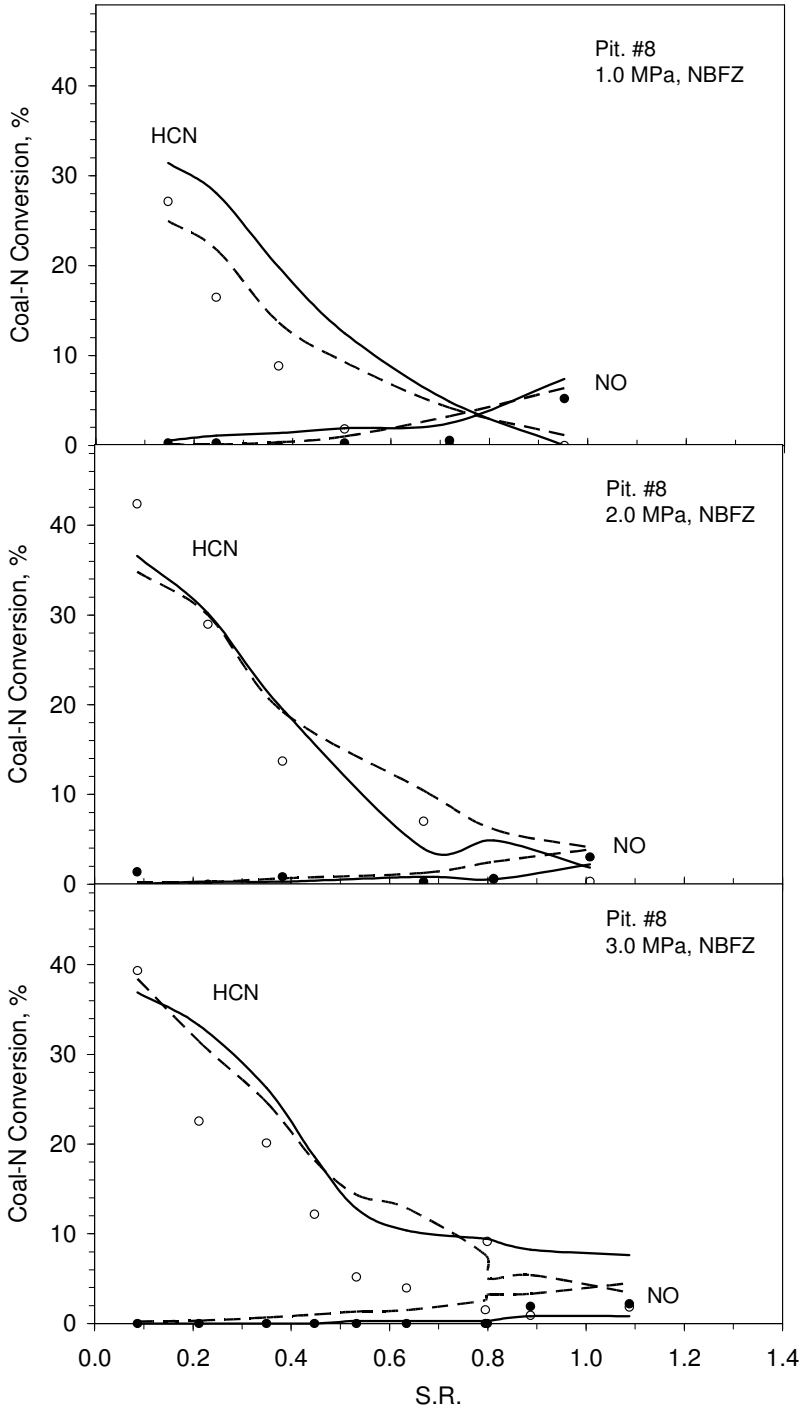

Figure B.47. Evaluation of predictions from NEA's NO_X sub-model (dashed curves) for Pittsburgh #8 at 1.0 (upper), 2.0 (middle) and 3.0 MPa (lower) with the measured HCN (○) and NO (●) levels and the CNPP predictions (solid curves).

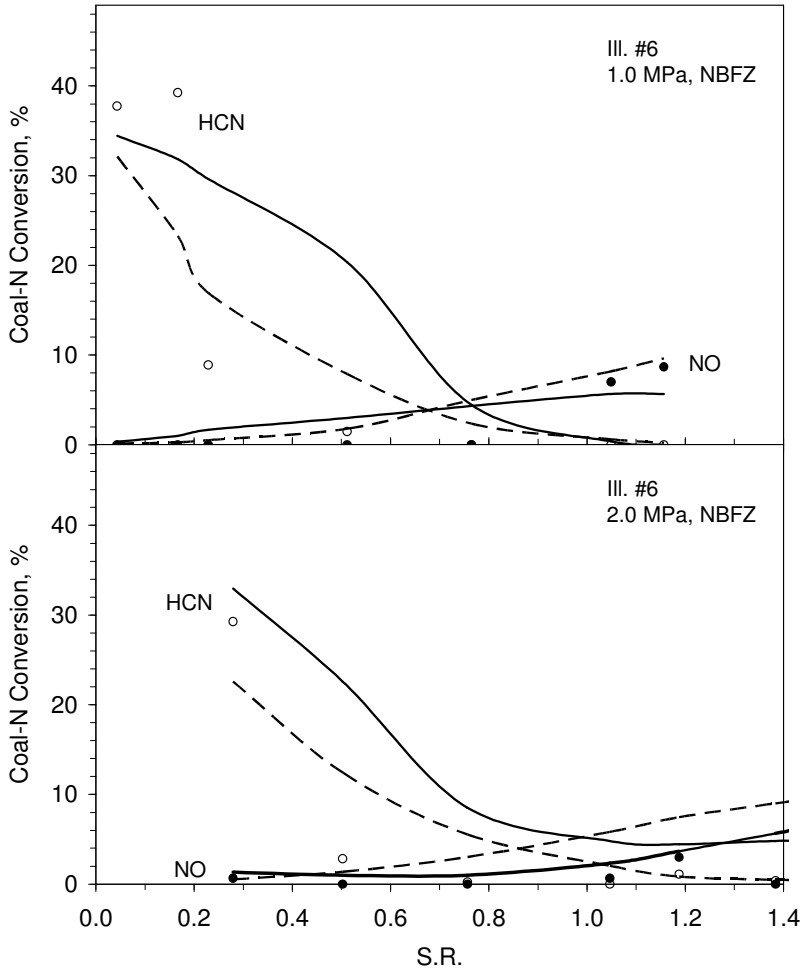

Figure B.48. Evaluation of predictions from NEA's NO_X sub-model (dashed curves) for Illinois #6 at 1.0 (upper) and 2.0 MPa (lower) with the measured HCN (○) and NO (●) levels and the CNPP predictions (solid curves).

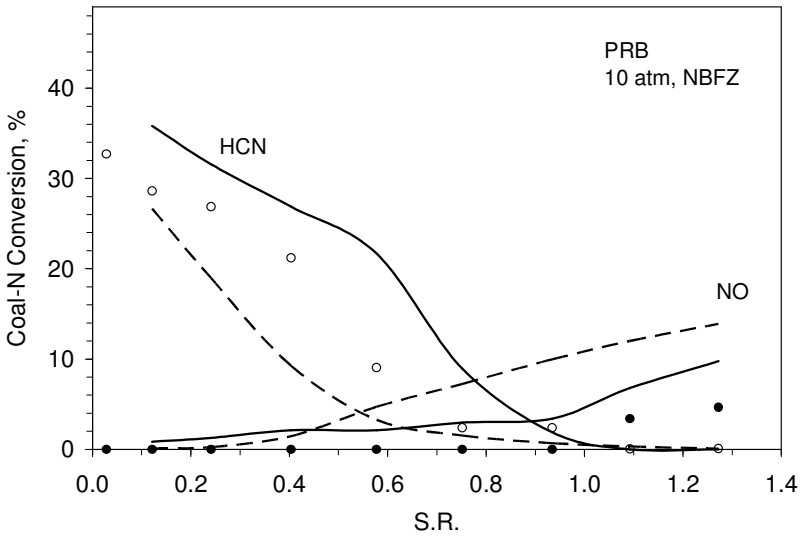

Figure B.49. Evaluation of predictions from NEA's NO_X submodel (dashed curves) for PRB at 1.0 MPa with the measured HCN (○) and NO (●) levels and the CNPP predictions (solid curves).

The same parameters were used to predict the test series with Illinois #6. As seen in Figure B.49, HCN levels from the global sub-model for 1.0 and 2.0 MPa are more accurate than the CNPP predictions, particularly for intermediate stoichiometric ratio values. The predicted NO levels are accurate throughout the test series at 1.0 MPa. But for 2.0 MPa, the predicted NO levels are almost double the measured values. Consequently, the global sub-model does not depict the reduction in fuel-N conversion to NO for higher pressure with this coal.

The evaluation with data for PRB coal is similar, as seen in Figure B.49. The predicted HCN levels are lower than those from CNPP, but not necessarily in better agreement with the data. Most important, the NO prediction is even worse, being about triple the measured value for the run with the highest stoichiometric ratio. For this condition, the CNPP prediction is twice as large as the measured NO.

In summary, the global scheme developed from the CNPP simulation with full chemistry faithfully represents the CNPP predictions over broad ranges of pressure, temperature, and stoichiometric ratio for the Pittsburgh #8. It is especially noteworthy that the sub-model depicted the tendency for lower conversion of coal-N into NO for progressively higher pressures for this coal, although the magnitude of the shift was under predicted. However, this performance was only apparent for the datasets that were used to specify the rate parameters. When the sub-model was extrapolated to the datasets for Illinois #6 and PRB, the predicted HCN levels were at least as accurate as the CNPP predictions. But predicted NO levels were only accurate at 1.0 MPa with Illinois #6. For the higher pressure with this coal and for PRB at 1.0 MPa, the predicted NO levels were much too high, so that the tendency for less NO at higher pressures was not depicted for Illinois #6, at odds with the data.

B.4.7 The Impact of Pressure on NO Production

As clearly seen in the NBFZ datasets and in their interpretation with CNPP simulations both measured and predicted conversion of coal-N into NO diminishes for progressively higher pressures, especially for the highest stoichiometric ratio values. In this session, additional CNPP simulations and CFD simulations with NEA's global NO_X submodel are discussed to interpret this tendency in more detail.

Observed Impact of Pressure on NO Production

The conversion fractions for coal-N to NO are much lower at elevated pressures than they are at atmospheric high pressures, and become progressively lower at higher pressures. For Pittsburgh #8 with stoichiometric ratios between 0.95 to 1.1, this fraction decreases from 5.2 % to 3.0 % to 2.2 % as pressure increases from 1.0 to 2.0 to 3.0 MPa. This pressure effect is accurately predicted by the elementary reaction mechanisms in the CNPP simulations.

Both the flow characteristics and the flame structures in NBFZ tests significantly changed as pressure was increased from 1.0 to 2.0 to 3.0 MPa. The important variations are as follows:

1) **Turbulence.** The Reynolds number of a turbulent flow is proportional to fluid density and, in turn, proportional to pressure. As pressure increases, the turbulence becomes stronger which has two important consequences: (i) Turbulent gas diffusivity increases proportionally; and (ii) Particle dispersion is primarily a consequence of turbulence, which tends to concentrate the particles in a boundary layer along the wall. As turbulence becomes stronger, the particles become more concentrated in this region.
2) **Gas temperature.** The gas temperature histories in both core and boundary layer regions become cooler for progressively higher pressures. For example, the centerline gas temperatures at the reactor exit are 1500°C, 850°C and 650°C, respectively, as pressure increases from 1.0 to 2.0 to 3.0 MPa. Although very similar wall temperature profiles were imposed in the simulations for all pressures, the mean gas temperature in the boundary layer also decreased for higher pressures, but not nearly as much as in the core region. Two reasons are responsible for this tendency. First, the suspension loading were inversely proportional to pressure, to minimize agglomeration and tube blockage. But lowering the suspension loading also lowers the convective heat transfer rate from the radiantly heated coal particles to the gas flow. Second, the sensible enthalpy requirement of the gas flow is proportional to fluid density and, in turn, to pressure. Consequently, the gas flow requires progressively more energy to achieve the same gas temperature. Since gas temperature is the main driving force for gas phase chemistry, lower gas temperatures decelerate chemistry in the gas phase, including N-species conversion.

3) **Char burnout.** For the cooler gas temperatures at the higher pressures, char particles burn at a slower rate and reach lower extents of burnout for progressively higher pressures. In NEA's Third Interim Report, we reported that the extents of char burnout for Pittsburgh #8 for the runs at near-unity stoichiometric ratio at 1.0, 2.0, and 3.0 MPs are 57.9, 56.1 and 26.7 DAF wt. %, respectively. Since the conversion fraction for char-N into NO is fixed in the CNPP simulations, the total NO production rate from char-N is proportional to the char burnout. So the decreased NO production from char-N also likely to reduce the NO level at the exhaust.

All these factors affect the NO emissions at the reactor exit. In order to determine the most important ones, CFD simulations similar to NBFZ tests were performed, except that similar thermal histories were imposed at all pressures. Predicted NO levels are standardized for consistent extents of char burnout. In this way, the impact of gas temperature and char burnout on the NO emissions was minimized, to clearly resolve the tendency for progressively higher pressure.

B.4.8 CFD Simulations for Tests with Similar Thermal Histories

The objective is to obtain flow and temperature fields that are similar to those in practical flames and are similar for different pressures. The baseline CFD simulation for 1.0 MPa is based on Run 51C of the NBFZ tests, except for the following changes:

1) The overall stoichiometric ratio is set to 1.15, a typical value in practical coal flames. We modified the coal particle flow rate and the O_2 mass fraction at the inlet accordingly. The suspension loading is 3 % in this baseline CFD simulation.
2) A Rosin-Rammler particle size distribution was applied to the coal particles. Two parameters, the mean particle diameter and the spread parameter, are needed in FLUENT to represent Rosin-Rammler distribution, which were 55 μm and 1.14, respectively. This size distribution is adapted from standard utility coal grinds (Niksa et al., 2003)
3) Particles were forced to remain in the core of the tube so that the O_2 in the boundary layer is able to gradually entrain into the core. This is the typical situation immediately downstream of the fuel injectors for tangential firing. It was obtained by switching off the stochastic dispersion sub-model in FLUENT.

The CFD simulations for 2.0 and 3.0 MPa were developed directly from the baseline simulation for 1.0 MPa. To impose similar temperature fields at these higher pressures, we imposed the baseline temperature field onto the solutions for higher pressures. This was done by applying the converged baseline case file to the simulations for 2.0 and 3.0 MPa, and then performing the simulations without an energy balance for the gas phase. In this way, the baseline temperature field was retained in the cases for 2.0 and 3.0 MPa, while the other transport equations for flow, species, and the mass and energy balance for the particles were solved. In the cases for 2.0 and 3.0 MPa, the suspension loadings are

set to the baseline value. However, the rate parameters for volatiles oxidation, soot oxidation, char and gaseous volatiles combustion are different. In these simulations, we use the rate parameters assigned to match the NBFZ data for different pressures for the highest stoichiometric ratio values.

The predicted extents of char burnout at the reactor exit are 64.2, 75.2, and 67.6 DAF wt. % for pressures of 1.0, 2.0, and 3.0 MPa, respectively. The predicted NO levels will be compared at the fixed char burnout of 64.2 % for the baseline case by using the product distributions for different axial positions at the other pressures. These axial positions are 27.3, 19.7, and 24.9 cm at 1.0, 2.0 and 3.0 MPa, respectively. Only flow characteristics upstream of this position were factored into the NO predictions.

B.4.9 CNPP of CFD Simulations

CNPP were applied to the three CFD simulations described in the previous section in order to predict the NO and HCN levels with full chemistry. Since all coal particles are forced to flow in the core, the delineated regions are much different than those for NBFZ tests, but are very similar to the regions assigned for laboratory coal flames at atmospheric pressure reported previously (Niksa and Liu, 2002a and 2002b). There are still two regions in co-flow: a core containing all coal particles, and a sheath along the wall that provides a source of entrained O_2. In fact, insignificant chemistry occurs in the sheath, so this region may be omitted from the full chemistry simulation.

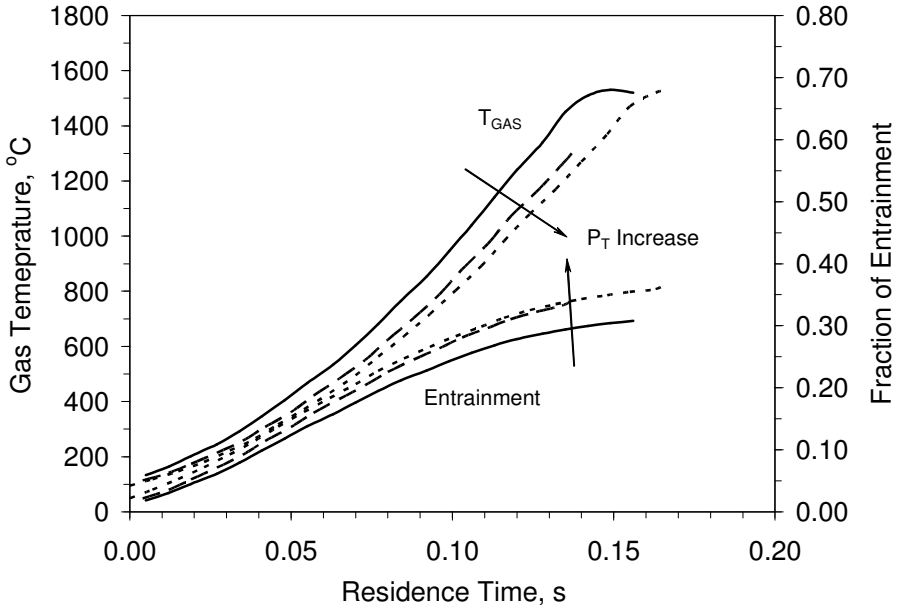

Figure B.50. Gas temperature and O_2 entrainment histories from CFD simulation for the core region at 1.0 (solid line), 2.0 (dashed line) and 3.0 MPa (dotted line).

The mean gas temperature histories in the core regions for 1.0, 2.0 and 3.0 MPa appear in Figure B.50. Only conditions up to the axial position where the char burnout is 64.2 % are included in the chemistry simulations. The gas residence times up to the corresponding positions are 156, 137, and 167 ms at 1.0, 2.0 and 3.0 MPa, respectively. The maximum flame temperature for the baseline 1.0MPa case is about 1500°C. Although the same temperature field was imposed in all three CFD simulations, the maximum gas temperature differ by about 200°C at 130 ms between the cases for 1.0 and 3.0 MPa. This difference is due to the more intense turbulence at a higher pressure, which decreases the thickness of the momentum boundary layer in the reactor. As a consequence, the axial velocity from which the residence time is determined decreases as pressure increases. Therefore, for a specified residence time, the gas temperature is lower at higher pressures. The O_2 entrainment fraction at 130 ms at 3.0 MPa is slightly higher than that at 1.0 MPa, but the entrainment histories at 2.0 and 3.0 MPa are very similar.

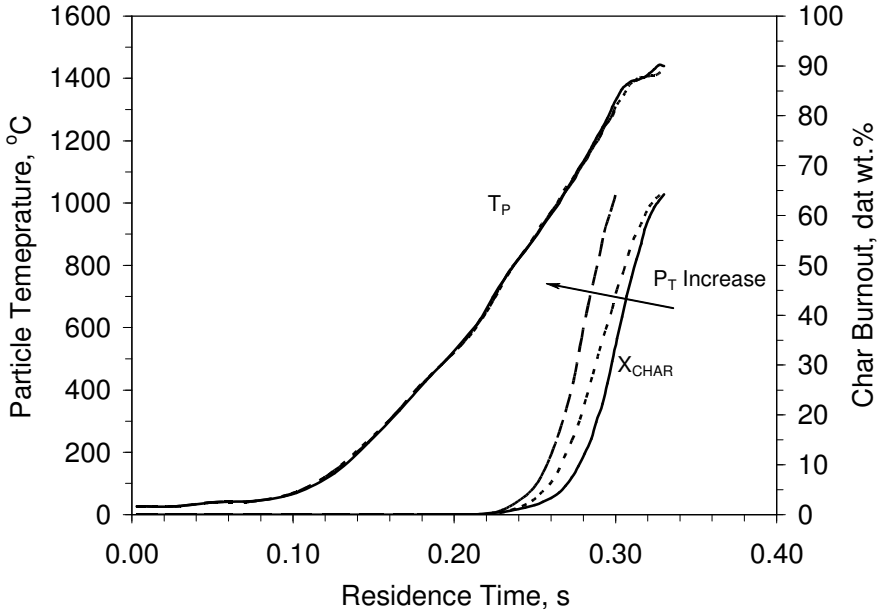

Figure B.51. Particle temperature and char burnout histories from CFD simulation for the core region at 1.0 (solid line), 2.0 (dashed line) and 3.0 MPa (dotted line).

Figure B.51 shows the mean particle temperature histories and burnout histories from the simulations. The particle temperature histories are exactly the same throughout the entire history, as expected. Nevertheless the char particles burn at progressively faster rates as pressure increases from 1.0 to 3.0 MPa. The S.R and suspension loading are fixed in these simulations, but O_2 concentration is proportional to pressure. Char particles burn faster at higher O_2 concentrations, thereby increasing the extent of burnout at a specified residence time.

B.4.10 Comparison of NO Emissions For Variable Pressures

As before, only two parameters needed to be specified for the CNPP simulations. The initial char oxidation reactivity was decreased by a factor of two from the default value in order to obtain similar extents of char burnout, which were 61.2, 64.2 and 63.0 DAF wt. % at 1.0, 2.0, and 3.0 MPa, respectively. The fractional conversion of char-N to NO of 0.2 was used at all pressures.

The predicted HCN and NO levels at three pressures from the full reaction mechanism appear as points in Figure B.52. Surprisingly, full chemistry predicts very low conversion of coal-N into NO at typical flame temperatures for elevated pressures. The fractional coal-N conversion to NO progressively decreases from 6.3 to 3.0 to 1.4 % as pressure increases from 1.0 to 2.0 and 3.0 MPa. No coal-N is converted to HCN at 1.0 and 3.0 MPa, whereas only 1.2 % is converted at 2.0 MPa. The low HCN level is expected for these flames, because the overall stoichiometric ratio is 1.15. This is also consistent with the simulations for NBFZ tests with the highest stoichiometric ratios. Hence, the CNPP simulations establish that coal-N conversion to NO diminishes for progressively higher pressures under typical burner operating conditions. This tendency is clearly evident, because the potentially confounding variations in turbulent particle dispersion, gas temperature, and char burnout were eliminated. It also appears that HCN does not persist in flue gas prepared at stoichiometric ratio of 1.15 or greater.

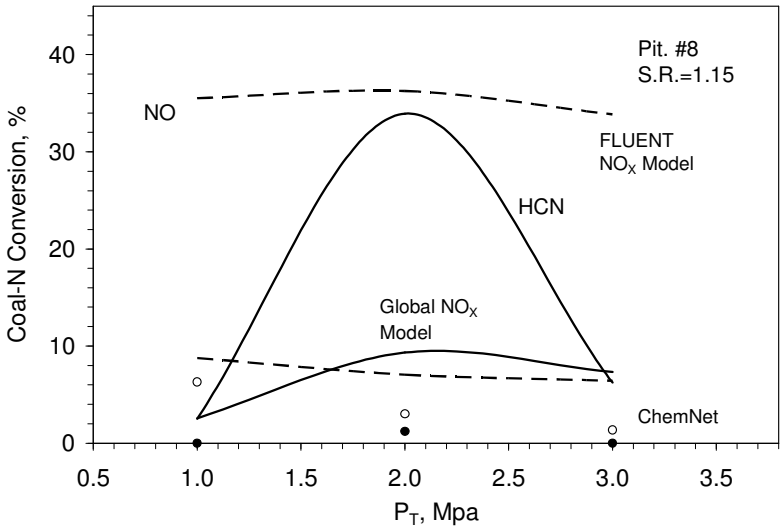

Figure B.52. CNPP predicted HCN (●) and NO (○) compared with predicted HCN (solid line) and NO (dashed line) by FLUENT NO_X submodel and global NO_X submodel for coal flames at different pressures.

The emissions predicted with the v.6.1 FLUENT NO_X sub-model and NEA's NO_X sub-model also appear in Figure B.52. The predicted conversion of coal-N into NO from the FLUENT NO_X sub-model is approximately 35% at all three pressures, which is several times larger than that predicted with full chemistry. The predicted HCN levels are comparable with full chemistry at 1.0 and 3.0 MPa, but the prediction for 2.0 MPa is poor. NEA's NO_X sub-model also over predicts HCN and NO emissions, but by much

smaller amounts. It also correctly depicts the impact of pressure on NO, whereby NO emissions decrease for progressively higher pressures. But the quantitative impact is much weaker than seen in the predictions for full chemistry. HCN is predicted to persist in the flue gas at all pressures, clearly at odds with the full chemistry predictions. The predicted conversion of coal-N into HCN is 2.6, 9.3, and 7.3 % at 1.0, 2.0, and 3.0 MPa, respectively.

Discussion

For similar temperature histories, O_2 entrainment rates, and extents of char burnout, the full reaction mechanism verifies the apparent trend in the NO emissions with pressure from the NBFZ tests. Whereas the measured trend was obscured by inadvertent variations in gas temperature, turbulence, and char burnout, the CNPP simulations isolate the impact of pressure alone. Hence, we have established that pressure variations, alone, shift N-species conversion chemistry toward the production of N_2 at the expense of NO. Some shift is inevitable because, for fixed suspension loading, the species concentrations are proportional to the pressure. As pressure increases, the reaction rates increase simply because the species concentrations are higher but, of course, not all channels are equally affected. Apparently, the mechanism shifts toward N_2 production, so the conversion of coal-N into NO diminishes.

Our simulations were focused on near-burner conditions, where the coupling between chemistry in the gas phase and heterogeneous chemistry is strongest due to the availability of extensive soot surface area. Even so, NO levels were primarily governed by gas phase chemistry. It is unlikely that subsequent char conversion could alter the tendency for lower NO emissions at elevated pressure. Once the gas phase becomes strongly oxidizing, which coincides with the disappearance of HCN, gas phase chemistry becomes unimportant. Thereafter, a fixed fraction of char-N is converted into NO at the char burning rate. The NBFZ datasets were successfully interpreted by applying the same fractional char-N conversion for all pressures, so we have no indications that the contributions to NO emissions from char-N conversion vary with pressure. Consequently, the stage of char burnout that was omitted from the CNPP simulations will probably make similar contributions to total NO emissions at all three pressures. In other words, the predicted NO emissions for complete burnout would be those in Figure B.52 supplemented by the amount associated with conversion of the last third of the char, which is the same for all three pressures. This displaces the curve of NO vs. pressure upward, but would not change its slope.

The NO predictions from NEA's NO_X sub-model were much better than those from the v.6.1 FLUENT sub-model. Even though the pressure dependence was under predicted, and HCN levels were over predicted, the evaluation in Figure B.52 demonstrates reasonable accuracy for realistic coal flame temperatures. By itself, the satisfactory extrapolation from NBFZ test temperatures to flame temperatures represents a major hurdle that has been sustained. NEA's NO_X submodel predicts NO emissions for broad ranges of temperature and pressure within useful quantitative tolerances. It's only major flaw is the over prediction of HCN levels, which should be ignored whenever flue gases are strongly oxidizing, as they are in practical applications with furnaces.

HIGH PRESSURE COAL COMBUSTION KINETICS PROJECT
Appendix C - Characterization of NBFZ and HPBO Chars

C.1 Materials and Experimental Techniques

C.1.1 Materials

All analyses were performed on chars sampled from the p-RCFR at SRI. The techniques below were applied to selected samples from two separate sample sets: (1) the NBFZ experiments designed to study the char formation process, and (2) HPBO experiments designed to understand the char combustion process at high pressure and its influence on char morphology, fragmentation, and residual carbon in ash.

C.1.2 Experimental Techniques

BET Surface Area Measurement

A standard nitrogen gas adsorption technique was applied to determine the porosities and surface areas of coal char samples. The apparatus used in this research was an Autosorb-1 system provided by Quantachrome Corp.

The principle of the instrument operation is that certain amount of known quantity of adsorbate gas [nitrogen] is added or removed into the sample cell containing pre-weight amount of solid adsorbent [char] at a constant liquid nitrogen boiling temperature (77 K). The adsorbed volumes per mass of solid char as a function of relative pressures of adsorbate are the data points that constitute the adsorption isotherm. The isotherm data are used in order to calculate char surface areas, pore volumes and pores size distributions.

The experimental procedure to measure the surface area and porosity requires the removal of the sample surface contaminants by outgasing coal char samples at 573 K about 24 hours prior the analysis. A full 84 data point isotherm is needed to obtain to perform porosity and surface area analysis.

A reference material, 8571 Alumina, distributed by U.S. Department of Commerce National Institute of Standards and Technology [NIST], Gaithersburgh, MD is used in order to check the performance of the Autosorb-1 apparatus before the analysis. NIST reports the mean BET specific surface area for 8571 Alumina to be 158 m^2/g, but with a variation from 150 to 165 m^2/g. The BET surface area of the Alumina 8571 measured on the Autosorb-1 instrument used in this research was 152 m^2/g of sample. The difference between mean NIST reported BET surface area and our value is not fully understood, but it should be kept in mind that our value is in full accord with the range of values that NIST considers reliable.

In some cases with NBFZ chars, tar deposition on the wall of the testing glass cell was observed during the de-gas process. Since the 300 ^oC de-gas temperature is too low to

make any tar from char samples due to the thermal decomposition. One explanation is that this tar may come from the pyrolysis process and condense on the char surface when the gas stream was cool down. During the heat treatment this tar was released. Since tar contamination will affect the physical and chemical properties of char samples, the surface area of these samples is not reported here.

Scanning Electron Microscopy

The scanning Electron microscopy (SEM) was used to investigate the morphology of the char samples. SEM is a powerful tool to examine surface features at size scale above 10 nanometers. LEO 1530 VP microscope is applied to obtain SEM images of char samples. For some samples, SEM energy disperse spectroscopy (EDS) was used to get the qualitative and quantitative data about elemental composition of the char particles.

Reactivity Measurement by Non-Isothermal TGA

A non-isothermal thermogravimetric method [1,2] was employed for char reactivity measurement in the present study. 5 ~ 7 mg char sample is placed in the TGA pan and stays for 30 min in dry air stream with flow rate 34 mL/min. Then the sample is heated up to 950 ^{o}C under heating rate 7 ^{o}C/min and hold for 10 min at the peak temperature. All the experiments were finished under atmospheric pressure. It is confirmed that the reaction is under chemical kinetic control. The sample weight and reaction temperature were monitored and recorded continuously during the experimental process. The standard reactivity index of char oxidation, R, is defined as a standard burning rate in air at 500 C and is calculated from:

$$R = -(1/m)(dm/dt)\exp\{-E/R(1/T_{ref} - 1/T)\} \qquad (C.1)$$

where m, dm/dt and T are the mass of carbon remaining in the char at time t, the mass loss rate and the particle temperature measured at 20% conversion (daf). T_{ref} is the standard reference temperature, which is set as 773K. The activation energy E of char oxidation reaction is normalized to 146 kJ/mol, a typical value for char oxidation in zone I [3,4], in which activation energies vary only modestly. The reactivity index A with unit (g-carbon/g-carbon remaining-second) is used to evaluate the reactivity of char oxidation. In cases where there was evidence of tar deposition on the NBFZ char samples (see section on surface area above), reactivity measurements were deemed unreliable and were not reported.

C.2 Results: Characterization of NBFZ Chars

This session presents experimental results on the characterization of NBFZ chars produced in the radiant coal flow reactor and supplied to Brown by SRI. The samples arise from three coals: Powder River Basin (PRB), Pittsburgh #8 and Illinois #6, which were milled and sieved as raw materials for the following tests. The proximate and ultimate analysis of these samples is listed in Table C.1.

Table C.1. Proximate and ultimate analyses of the test coals.

	PRB	Illinois #6	Pittsburgh #8
Proximate analysis wt.% (As received)			
Moisture	29.2	11.1	2.3
Volatile matter	30.8	35	37.9
Fixed carbon	34.4	44.2	53
Ash	5.5	9.7	6.9
Ultimate anaylsis wt.% (As received)			
Moisture	29.2	11.2	2.3
Carbon	48.9	63.8	72.9
Hydrogen	3.5	4.5	5.1
Nirtogen	0.9	1.3	1.2
Sulfur	0.3	0.3	2.5
Oxygen (by diff.)	11.7	6.9	9.2
Ash	5.5	9.7	6.9

A detailed description of the radiant coal flow reactor is given by Cor et al. [1]. Briefly, coal particles are entrained by a gas flow through a quartz tube. An outer gas stream surrounded the entrained flow in order to prevent the particles attaching to the wall of the tube. The particle density inside the gas stream was maintained relatively low, so that individual particles could be heated directly and uniformly by radiant heat flux. A quench nozzle was mounted at the outlet of the quartz tube to cool the char particles and nucleate tar into aerosol. An aerodynamic classifier segregated the products into solid particles and aerosol from non-condensable gases. The pressure inside the p-RCFR and the composition of the entraining gas flow are adjustable.

The experimental conditions are listed in Tables C.2-C.4. The ratio of O/C means the actual input amount of O_2 versus the stoichiometric O_2 required under the actual fuel input amount, which was calculated based on the coal analysis.

Table C.2. Reaction conditions for NBFZ char preparation from PRB coal

Run No.	Pressure (atm)	Oxygen/Coal ratio (%)	Wt. Loss (%AR)
PRB-101	10	271	92
PRB-102	10	232	87
PRB-103	10	199	83
PRB-104	10	160	77
PRB-105	10	123	73
PRB-106	10	90	46
PRB-107	10	86	62
PRB-108	10	51	53
PRB-109	10	26	40
PRB-110	10	6	45
PRB-14	10	4	41
PRB-10	10	30	47
PRB-8	10	100	55
PRB-13	10	200	70
PRB-15	10	400	89
PRB-20	20	2	40
PRB-23	20	67	49
PRB-21	20	133	78
PRB-19	20	275	85
PRB-35	30	1	36
PRB-26	30	60	44
PRB-27	30	154	60
PRB-28	30	220	87

Table C.3. Reaction conditions for NBFZ char preparation from Illinois #6 coal

Run No	Pressure (atm)	Oxygen/Coal ratio (%)	Wt. Loss (%AR)
ILL-80	10	243	70
ILL-81	10	173	39
ILL-82	10	234	80
ILL-83	10	203	77
ILL-84	10	155	71
ILL-85	10	99	65
ILL-86	10	40	56
ILL-87	10	24	53
ILL-88	10	5	46
ILL-89	20	284	78
ILL-90	20	258	64
ILL-91	20	364	83
ILL-92	20	257	67
ILL-93	20	216	70
ILL-94	20	156	64
ILL-95	20	104	58
ILL-96	20	68	43
ILL-97	20	58	53
ILL-98	20	22	N/A
ILL-99	20	245	77
ILL-100	2	160	75

Table C.4. Reaction conditions for NBFZ char preparation from Pittsburgh #8 coal

Run No.	Pressure (atm)	Oxygen/Coal ratio (%)	Wt. Loss (%AR)
Pitts-50	10	0.2	56.6
Pitts-56	10	29.8	60.8
Pitts-55	10	53.2	59.4
Pitts-54	10	75.4	62.1
Pitts-53	10	105.1	59.9
Pitts-52	10	145.8	69.39
Pitts-51	10	193.2	74.3
Pitts-64	20	5.8	49.7
Pitts-66	20	17.4	53.5
Pitts-63	20	17.5	54.8
Pitts-65	20	25.3	58.9
Pitts-62	20	46.7	52.7
Pitts-61	20	77.5	56.5
Pitts-60	20	135.8	59.5
Pitts-59	20	164.7	60.9
Pitts-58	20	204.4	62.3
Pitts-75	30	9.5	58.2
Pitts-77	30	20	39.7
Pitts-76	30	45	17.6
Pitts-74	30	48.6	46.9
Pitts-73	30	80.5	41.8
Pitts-72	30	122.7	51.1
Pitts-71	30	103.5	53
Pitts-70	30	146.6	52.4
Pitts-69	30	180.6	58
Pitts-68	30	210	62.3
Pitts-78	30	234	33.1
Pitts-79	30	248.8	59.2

C.2.1 Char Reactivity Measurements

Figure C.1 shows the standard oxidation reactivity for char samples prepared under various reaction pressures and O/C ratios. Similar to atmospheric pressure chars, the sub-bituminous PRB chars are much more reactive than chars from the two bituminous coals. There is a uniform trend of modest decreases in char reactivity with increasing O/C ratio. This effect could be due to partial oxidation of the chars, or more likely to annealing. The higher O/C ratios give higher particle and suspension temperatures, which are known to decrease char reactivity substantially even over the very short time periods in flames [2]. Pressure shows no consistent effect on char reactivity. The effects range from modest increases to modest decreases depending on coal and combustion conditions. Reactivity data for high pressure chars is scarce in the literature. Recently Roberts et al. [3,4] studied the reaction rates of high-pressure chars obtained in a pressurized entrained-

flow reactor or a pressurized drop-tube furnace. The reaction rates of chars were measured using a pressurized TGA under O_2/N_2 atmosphere. The char apparent reaction rate of one type of coal increases as the pyrolysis pressure increases, but the value of the other two coals does not show an obvious effect of pressure. Overall, the effect of pressure on char reactivity was a secondary effect for pressures up to 30 atm.

This data set, together with the limited literature data, suggests that current reactivity correlations may be adequate for new applications at high-pressure conditions. Note that these results deal only with the mass-specific intrinsic reactivity of the char, which is a function of the surface area and the chemistry of the char surface. As will be seen later in the chapter, pressure does have an effect on overall particle morphology, which can affect burning rates through porosity and char density.

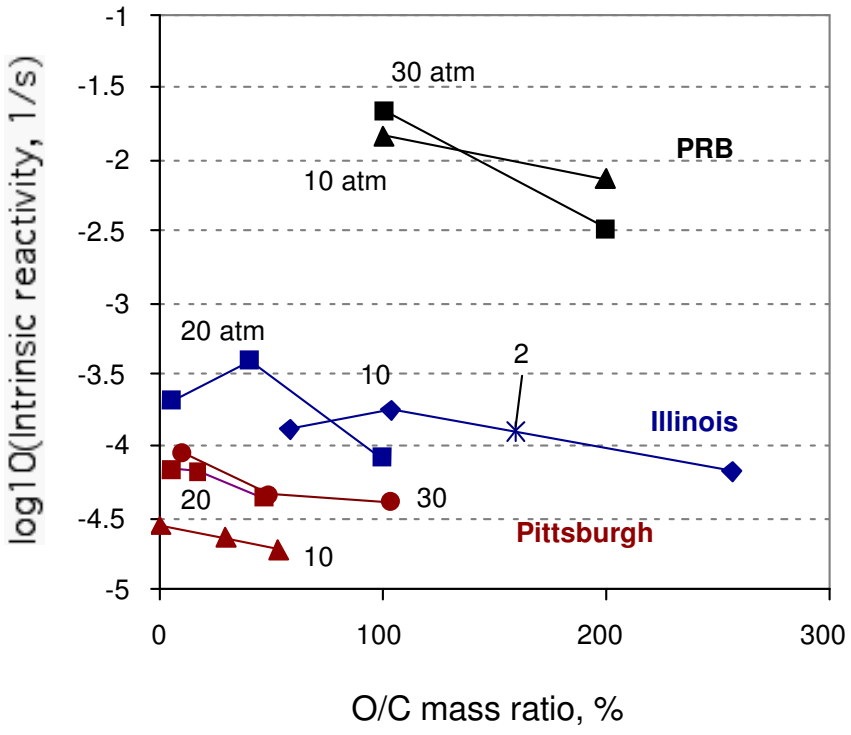

Figure C.1 Reactivity of NBFZ char samples.

C.2.2 Surface Area Measurements

Char surface areas as a function of gasification pressure and O/C ratio are shown in Figure C.2. There is a strong increase in surface area with increasing O/C across the data set. This trend likely reflects the opening of blocked pores by increased volatilization or oxidation at the higher temperatures and higher oxygen levels present in the high O/C tests. It is interesting that the increased surface areas in Figure C.2 correspond to

decreasing reactivities in Figure C.1. This trend has been seen before and is due at least in part to the poor correlation between total physical surface area and intrinsic char reactivity.

As with reactivity, there is no large and consistent effect of pressure on total surface area. The complete set of NBFZ char reactivity and surface area data is given in tabulated form in Table C.5.

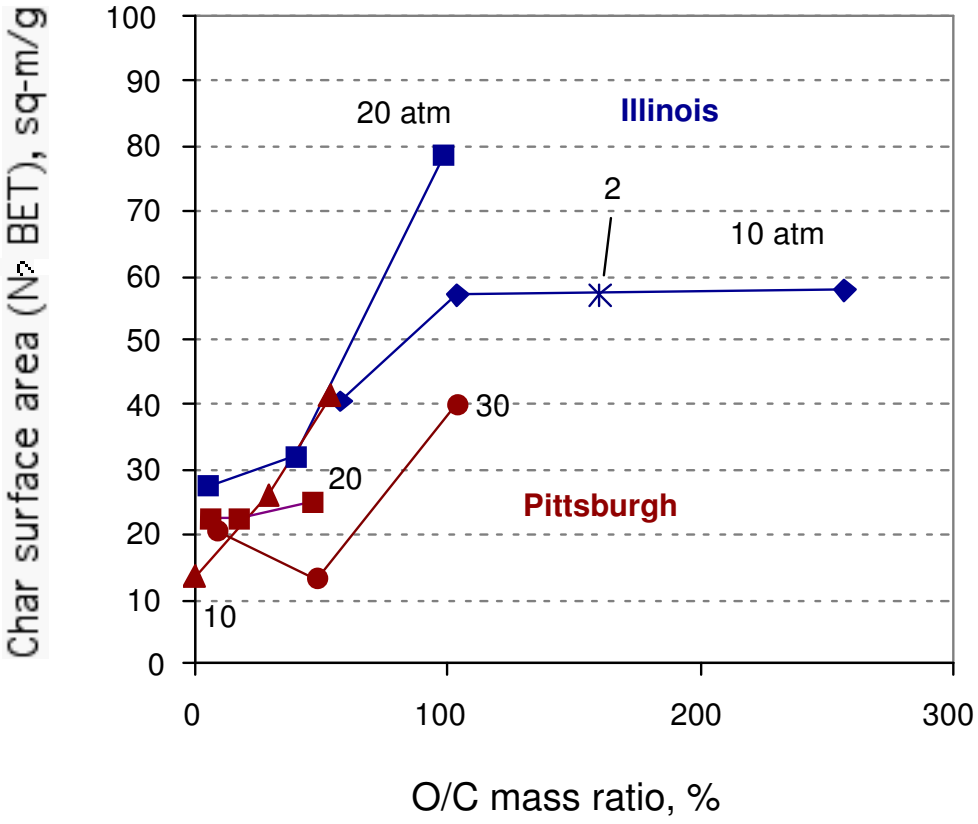

Figure C.2 Surface areas of various NBFZ chars.

C.2.3 Char Morphology

Figures C.3-C.13 are representative SEM images of char particle morphologies seen in the NBFZ samples. All the samples consisted primarily of whole particles with relatively few fragments. The 10 and 20 atm samples of the Pittsburgh and Illinois coals show evidence of high fluidity compared to atmospheric chars studied previously in our laboratory. The high-pressure conditions produce very low-density foam structures often covered with ultra-thin outer membranes. The 2 atm samples show signs of lower fluidity and also possess fewer visible macropores on their surfaces. The 30 atm. Pittsburgh and Illinois samples are generally similar to the 10 and 20 atm. samples, but there is some evidence for fewer ultra-low density particles with thin membranes. As seen in Figure C.5, the highest pressure led to many particles with thicker walls, irregular

globular shape, and smaller numbers of surface cavities in the form of what appear to be blowholes. Overall it is clear that fluidity increased significantly from the 2 atm to the 10 atm condition, but then remained nearly constant perhaps showing a modest decrease at the highest pressure of 30 atm. The PRB sub-bituminous coal produces irregular particle shapes at all pressures that indicate low fluidity (see Figure C.13 for example). This coal is non-softening and its atmospheric pressure chars are typically irregular in shape as the result of an essentially solid-state carbonization process. The results here show that elevated pressure, though it helps keep volatile products in the condensed phase longer during pyrolysis, does not change the physical mechanism of PRB coal devolatilization to that of a softening coal.

Some images show significant particle agglomeration, (see Figures C.10-C.12), especially for Ill-100 char (2 atm sample in Figure C.10). Since some of the particle clusters are closely fused and have extended overlap or neck regions, the agglomeration must occurred at elevated temperature. Some of the particle agglomeration may be the result of high particle-volume-fraction in some regions of the p-RCFR, which increases the probability of particle-particle collisions.

Table C.5. Reactivity and surface area of pressurized char samples.

Run No.	$\log_{10}$R (g/g-sec)	Surface area (m^2/g)
ILL-100	-3.89	57
ILL-85	-4.17	58
ILL-86	-3.74	57
ILL-88	-3.88	40
ILL-92	-4.08	79
ILL-95	-3.40	32
ILL-97	-3.69	27
Pitt-50	-4.55	14
Pitt-56	-4.64	26
Pitt-55	-4.72	41
Pitt-64	-4.17	23
Pitt-66	-4.17	23
Pitt-62	-4.36	25
Pitt-75	-4.05	20
Pitt-74	-4.35	13
Pitt-71	-4.40	40
PRB 8	-1.85	N/A
PRB 13	-2.13	N/A
PRB 27	-1.65	20
PRB 28	-2.50	315

Pitt. #8, 30 bar, O/Coal 48.6%

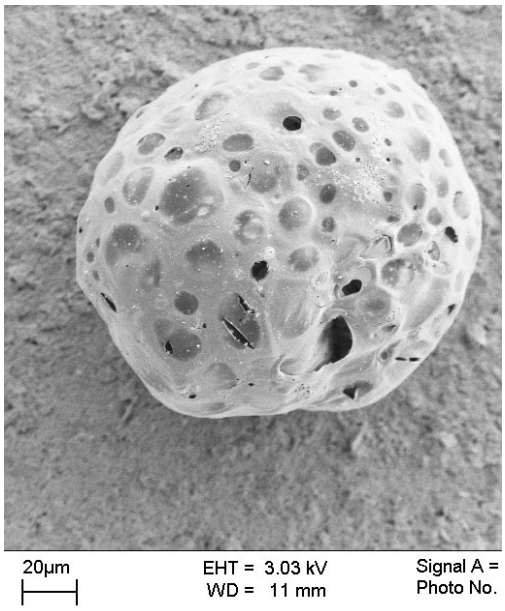

Pitt. #8, 30 bar, O/Coal 103%

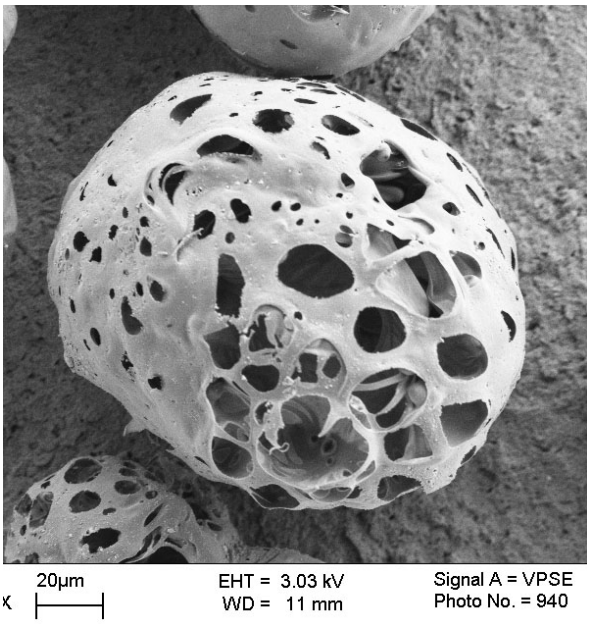

Figure C.3. High-resolution field emission SEM images of NBFZ chars

Pittsburgh #8, 10 atm. O/C: 29.8%

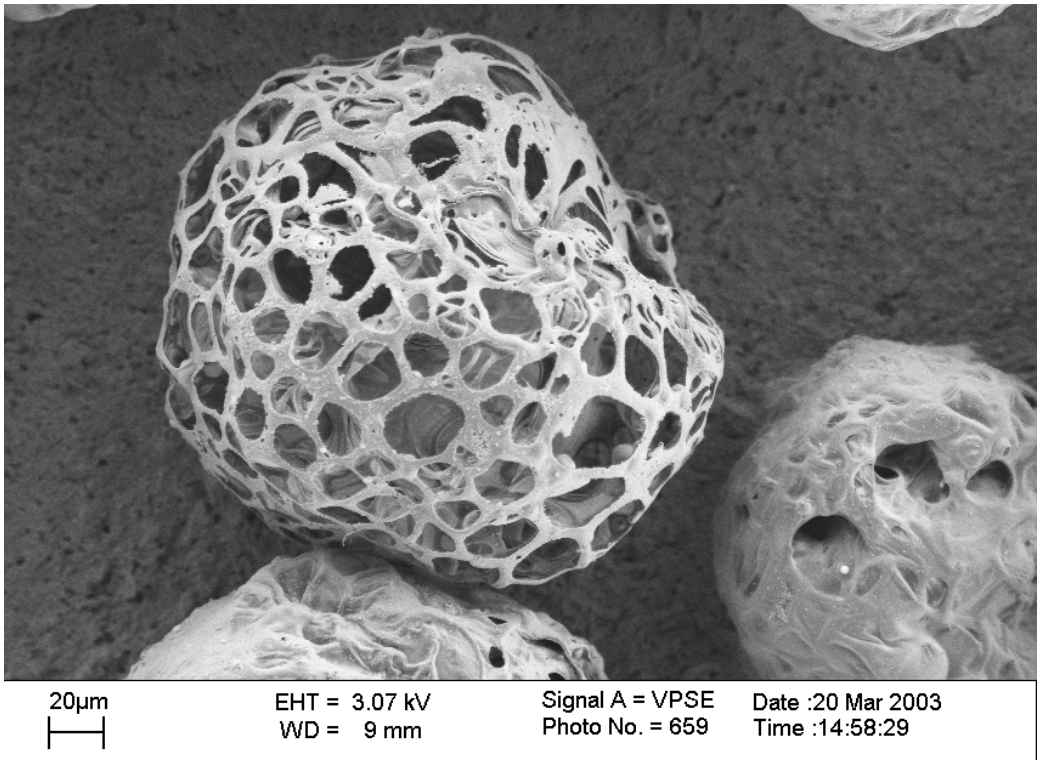

Figure C.4. High-resolution field emission SEM images of NBFZ chars

Pittsburgh,
30 atm.
O/C: 9.5%

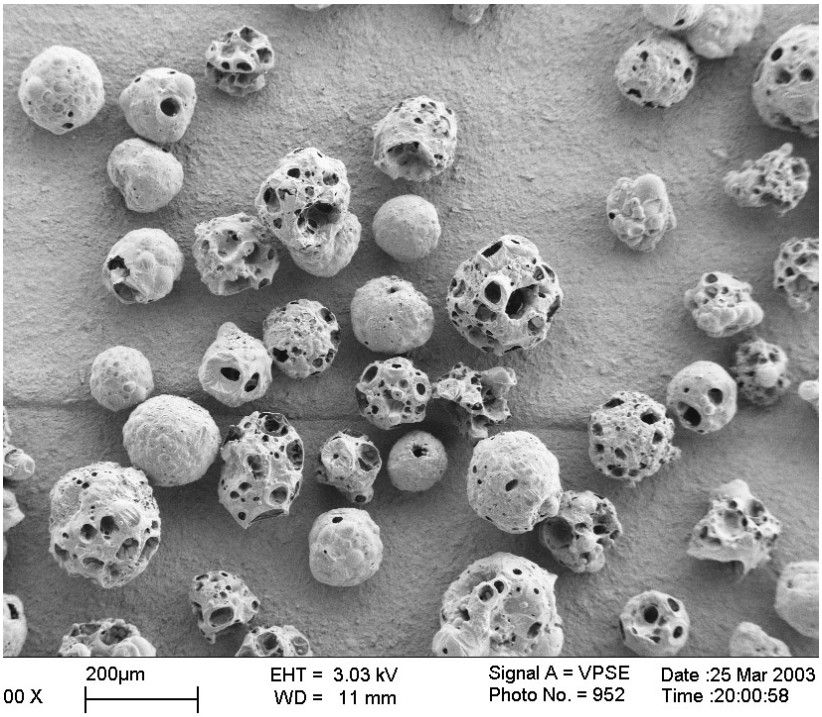

Figure C.5. High-resolution field emission SEM images of NBFZ chars

Pittsburgh, 30 atm., O/C: 9.5%

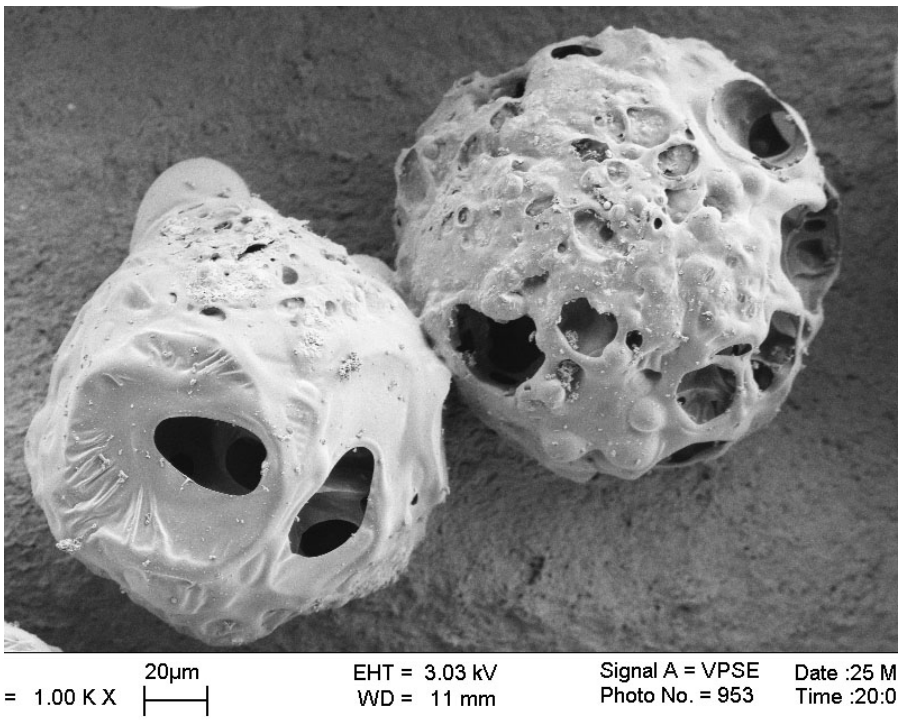

Figure C.6. High-resolution field emission SEM images of NBFZ chars

Pittsburgh,
30 atm.
O/C: 48.6%

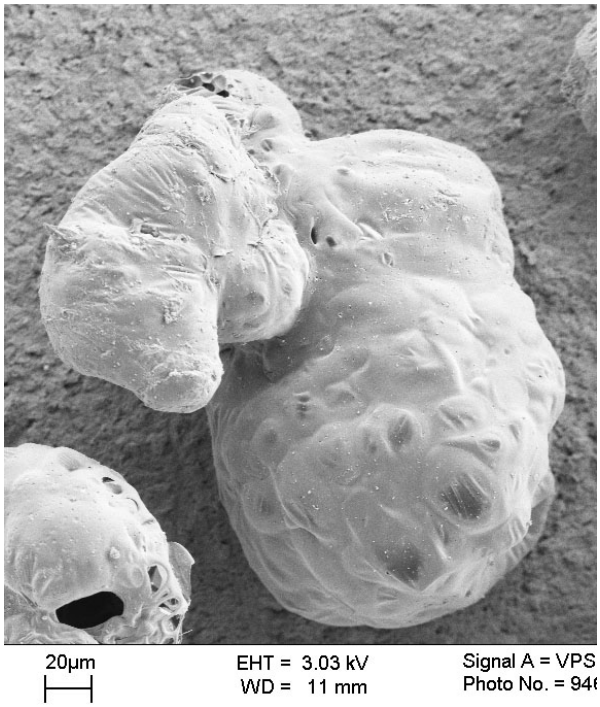

Figure C.7. High-resolution field emission SEM images of NBFZ chars.

Illinios#6, 20 atm. O/C: 58%

3 kV e-beam ***20 kV e-beam***

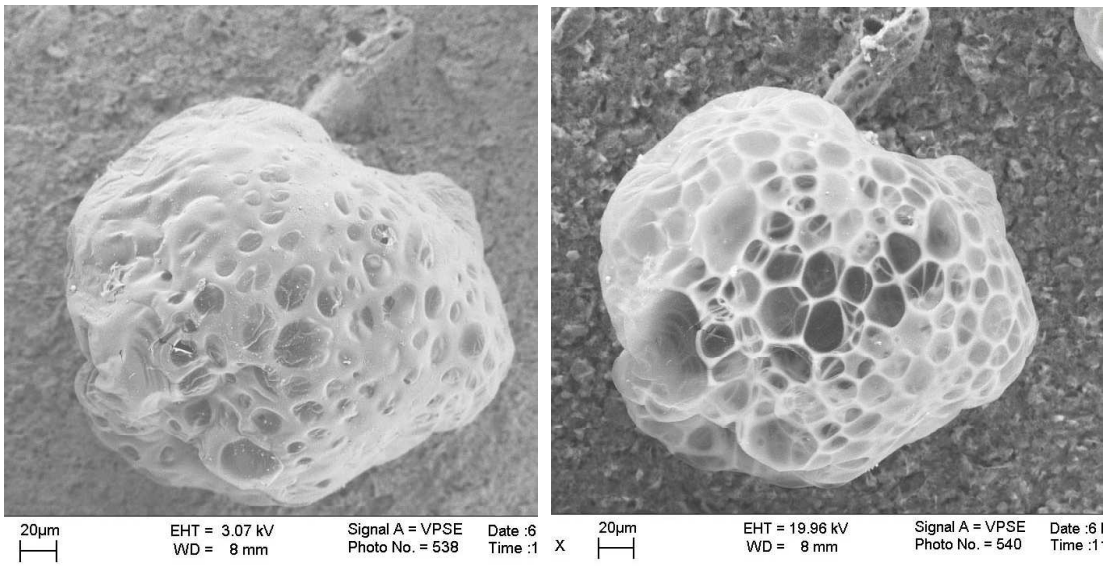

Figure C.8. High-resolution field emission SEM images of NBFZ chars

Illinois #6, 10 atm., O/C 99%

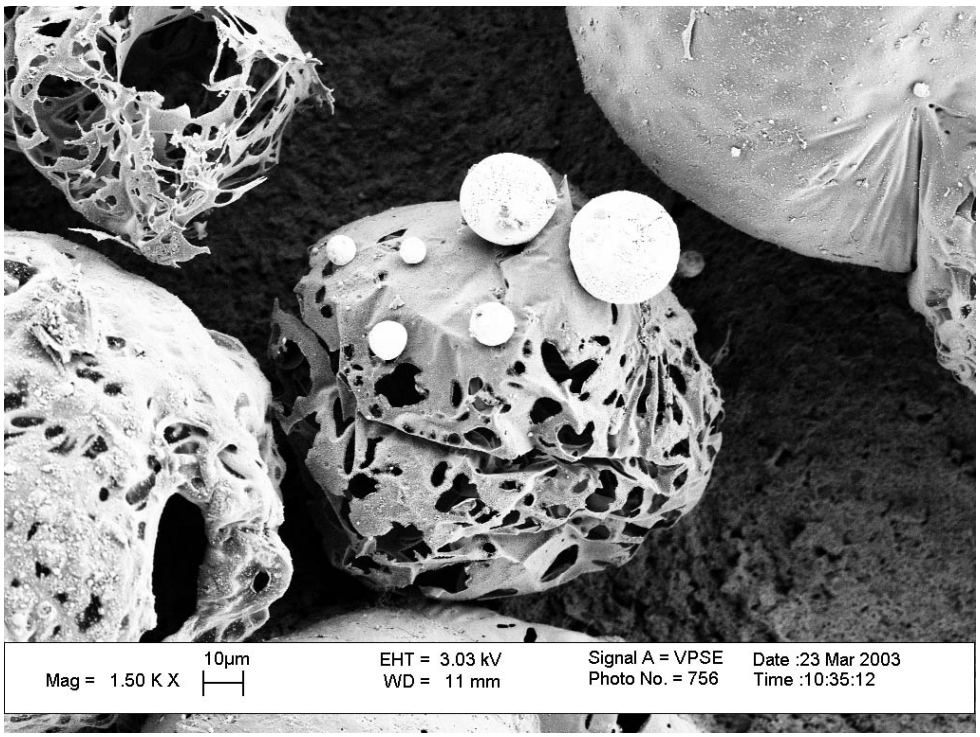

Figure C.9. High-resolution field emission SEM images of NBFZ chars

Agglomeration and coalescence

Illinois #6, 2 atm.
O/C: 160%

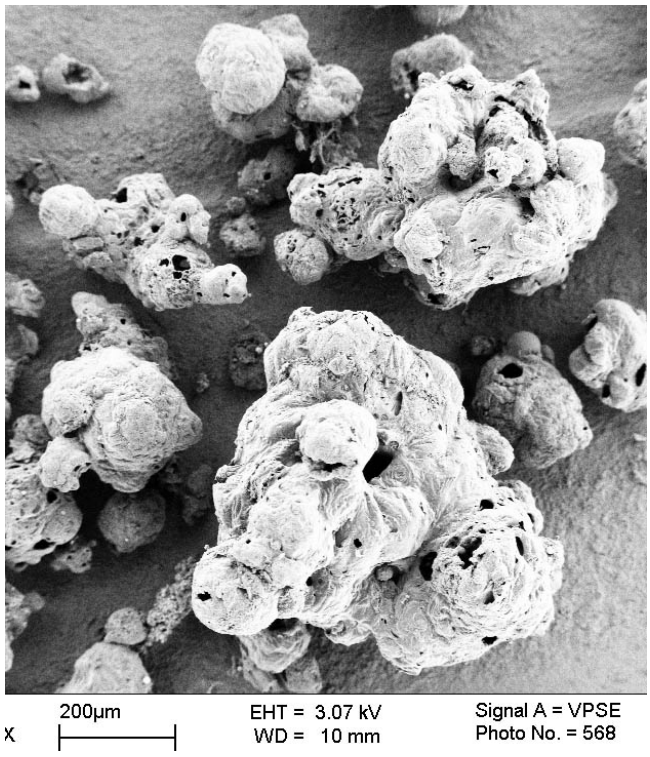

Figure C.10. High-resolution field emission SEM images of NBFZ chars

Illinois #6, 10 atm.
O/C: 40%

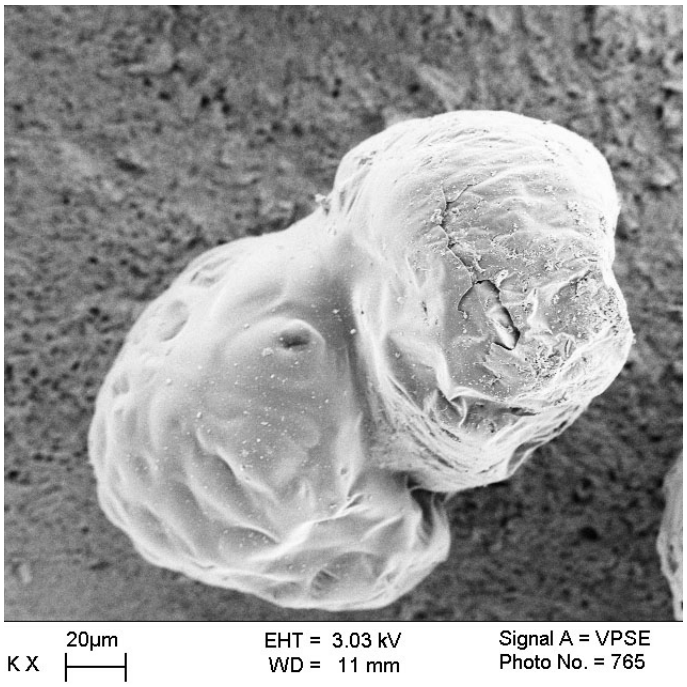

Figure C.11. High-resolution field emission SEM images of NBFZ chars

Illinois #6, 20 atm., O/C 257%

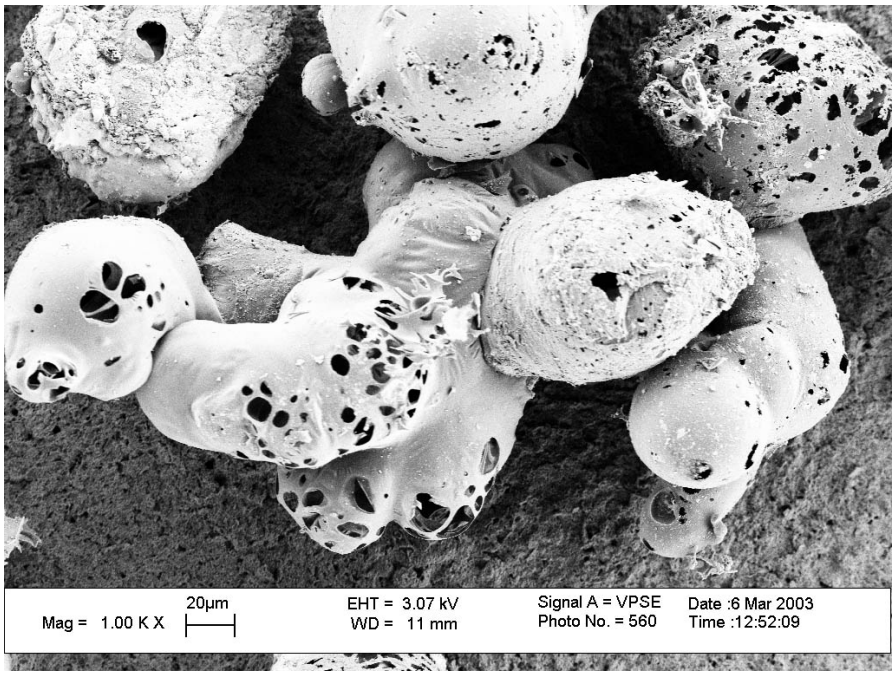

Figure C.12. High-resolution field emission SEM images of NBFZ chars

PRB Coal Char

10 bar, O/Coal 200% 30 bar, O/Coal 154%

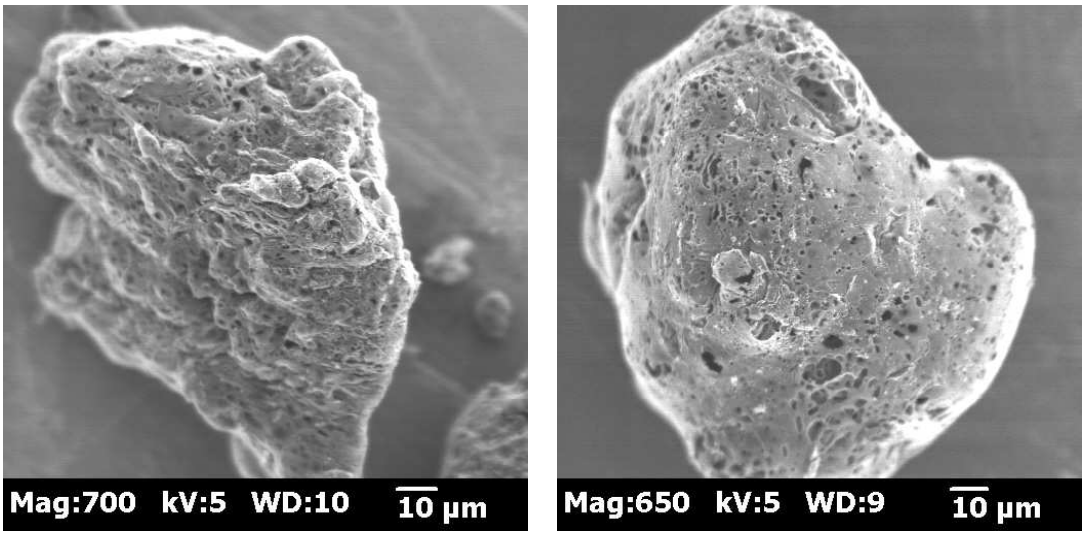

Figure C.13. High-resolution field emission SEM images of NBFZ chars

C.2.4 Swelling Factors

The swelling behavior of the near burner flame zone chars was investigated by measuring particle density for both the raw coals and the chars. The volumes of particle beds were measured in a graduated cylinder for a series of increasing sample masses and the bulk densities (particles plus interparticle voids) determined from the slopes of the best fit linear relations. Assuming similar interparticle void fraction for the chars and coals, the swelling factors were computed from a particle mass and volume balance as:

$$d/d_0 = (\rho/\rho_0)^{-1/3}(m/m_0)^{-1/3} \qquad (C.2)$$

where d/d_0 is the normalized particle size, char diameter divided by raw coal diameter.

For conditions where char oxidation is negligible, these normalized particle sizes can be interpreted as swelling factors, ω, whereas for higher O/C ratios they represent the net effect of swelling during devolatilization and size reduction during char oxidation.

The results are shown in Figure C.14. The PRB coal (top panel) shows all d/d_0 values starting at near until and decreasing with increasing mass loss. The low values at high mass loss are very likely due to diameter reduction from char oxidation in this highly reactive coal. There is no evidence of swelling at pressure consisting with the very low fluidity seen on the SEM images.

The Pittsburgh and Illinois coals show swelling factors as high as 1.4 or 1.5 for the 10 and 20 atm samples with some evidence of lower values at both 2 atm and 30 atm. This again is consistent with the apparent fluidity trends in the micrographs. The Pittsburgh chars shows some decreases in d/d_0 with increasing mass loss, which may indicate some influence of char oxidation.

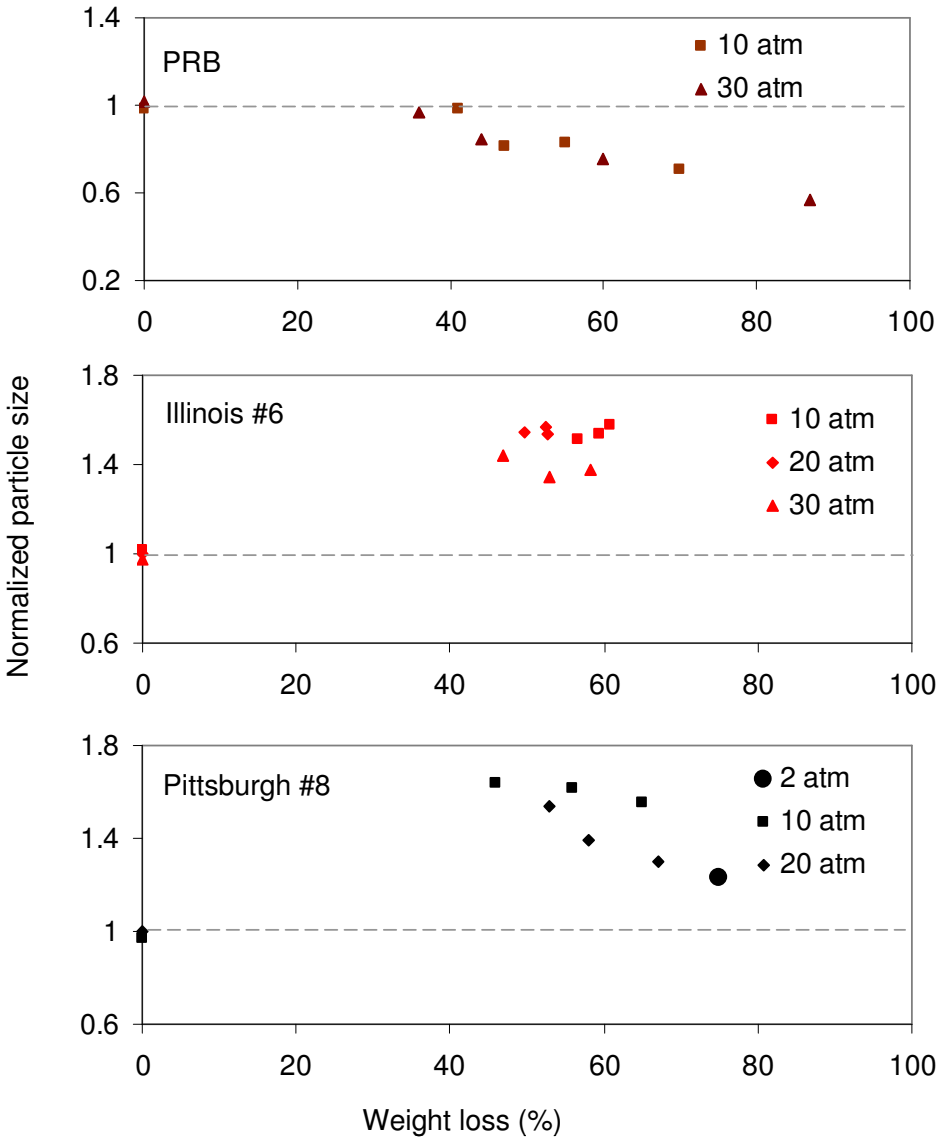

Figure C.14. Normalized char particle sizes, d/d_0, for PRB, Illinois #6 and Pittsburgh #8 coals at different operating pressures.

Overall, the values of d/d_0 in the 40-60% mass loss range are reasonably interpreted as swelling factors and are summarized and compared to atmospheric data in Figure C.15. This figure plots swelling factors from the present study along with standard values used in CBK based on similar measurements made on chars generated at atmospheric-pressure

in the Sandia flow reactor. The comparison shows significantly higher swelling factors for the bituminous coals under the higher pressure and lower heating rate conditions found in the P-RDFR. Overall, these results are similar in trend to several experimental data sets [5-7] that reported increased swelling factors at elevated pressure.

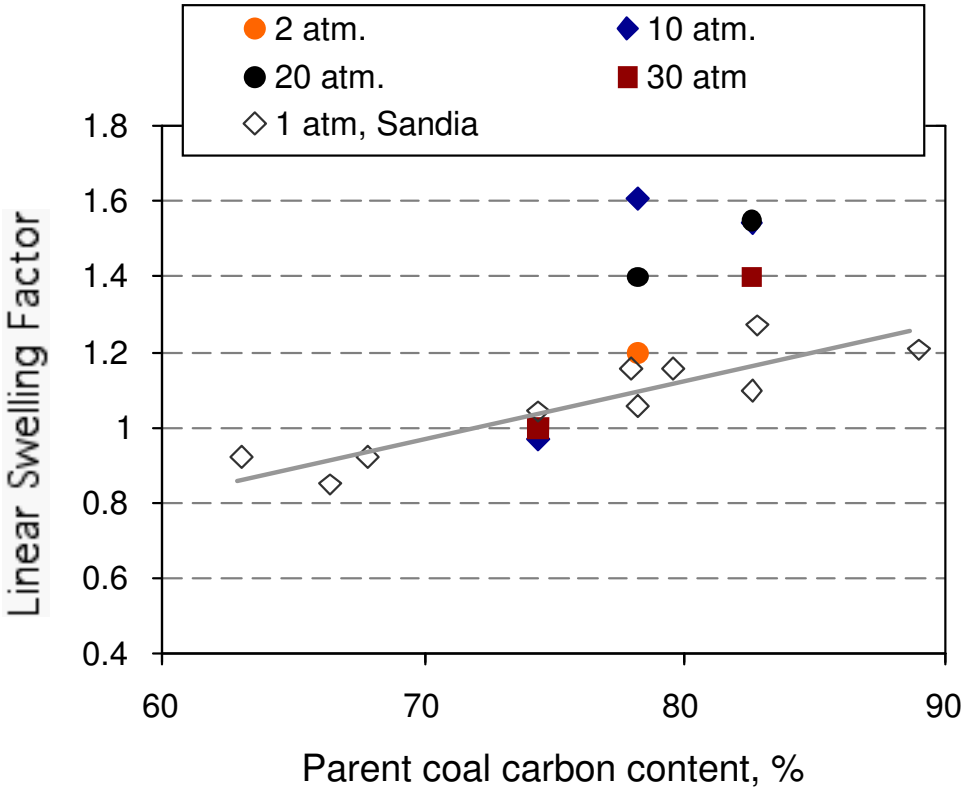

Figure C.15. Swelling factors for PRB, Illinois #6 and Pittsburgh #8 coals at both atmospheric pressure (literature data as open diamonds and grey correlation line) and elevated pressure (this study).

C.3 Characterization of HPBO Chars

C.3.1 Surface Area and Porosity Characterization

Pittsburgh Chars

Figure C.16 shows the isotherms of all Pittsburgh coal char samples superimposed on one plot. According to Brunauer the physisorption isotherms of gases on solids are grouped into six classes [types] of solid behavior and character. The isotherms shown on Figure C16 exhibit mostly type II isotherm behavior. The inflection point known as “knee” occurs near the completion of the adsorbed monolayer.

The isotherms on Figure C.16 show that Pittsburgh chars oxidized at different pressures have similar pore size distributions. The ‘knee’ part at the relative pressure range less than 0.1 provides information about the sample microporosity. Since the size of the isotherm ‘knee’ is similar in char samples oxidized at 10, 20 and 30 atm the amount of

micropores in those samples is quite similar. However the 'knee' of the isotherm of the sample char oxidized at 2 atm is approximately two times smaller in the relative pressure range of P/Po<0.1, which tells us that there is less microporosity in this char sample than the other Pittsburgh samples oxidized under higher pressures.

The mesoporosity of the char samples is determined from an isotherm total porosity value at relative pressure P/Po = 0.95 minus DR micropore volume value. Similarly with micropore distribution of Pittsburgh coal char samples the isotherms of samples oxidized at 10, 20 and 30 atmospheres have similar slopes and therefore also have similar mesoporosities available in their samples. The slope of the sample oxidized under 2 atm is approximately twice smaller compared to the ones oxidized under high-pressure conditions. Therefore the 2 atm sample has twice less mesopores available in the char compared to char samples oxidized under greater pressure conditions.

The isotherm partial pressure region above 0.95 provides the information about the sample macroporosity. The macroporosity of the sample is determined from the total porosity value of the isotherm at P/Po = 0.99 minus the total porosity value at P/Po = 0.95. The far right end of the isotherm [P/Po>0.95] shows that the samples oxidized under elevated pressure condition have more macropores available compared to the sample oxidized under 2 atm pressure condition. One must be cautious when trying to interpret the isotherm results near the saturation point [around P/Po = 0.99] of a nitrogen isotherm. The state of the nitrogen close to saturation pressure is unknown and could lead the researchers to faulty conclusions due to the various uptakes of nitrogen with similar nature samples between different experiments.

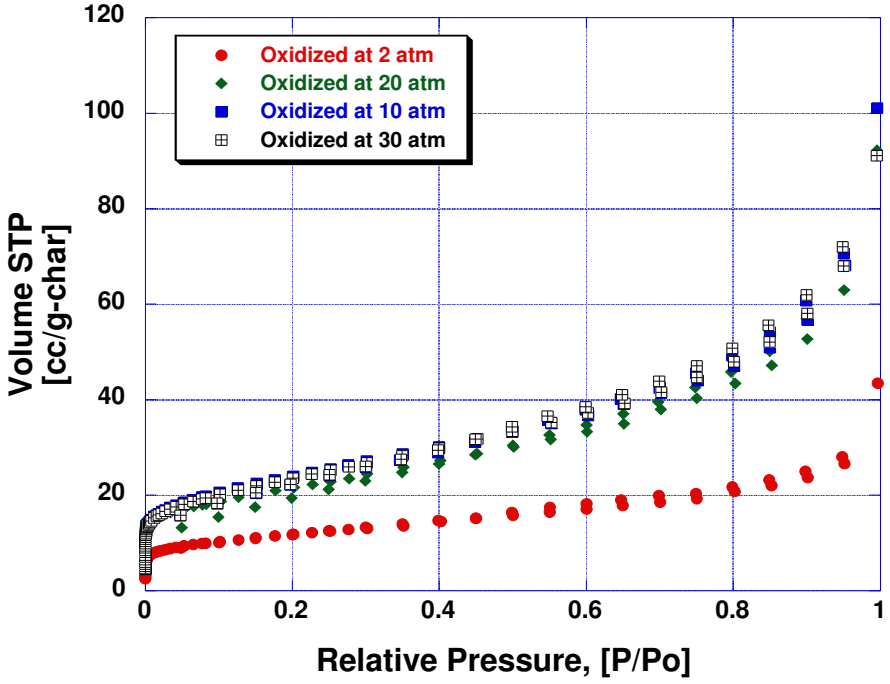

Figure C.16 Pittsburgh coal char nitrogen adsorption isotherms oxidized under different elevated pressure conditions.

The Brunauer, Emmet and Teller (BET) model is one of the most commonly used and best known model for adsorption theories used for characterizing adsorbent surface areas. The BET theory and experimental isotherms agree well in the region of relative pressures 0.05<P/Po<0.3. The BET surface areas of the Pittsburgh coal char oxidized at various pressure conditions are presented in Table C.6.

Table C.6. BET surface areas of the Pittsburgh coal char oxidized at various pressure conditions.

Sample	Oxidation Pressure [atm]	BET Surface Area [m^2/g-char]	LOI Loss-On-Ignition [wt%]	BET Surface Area [m^2/g-carbon]
Pitts. 206	2	40.4	63	63.7
Pitts. 223	10	84.1	40.4	207
Pitts. 218	20	74.8	44.3	167.8
Pitts. 224	30	83.1	44.1	187.4

The contribution of the mineral part of the coal char to the total porosity and surface area has been extensively investigated elsewhere[2] and was not the focus of the current investigation. The BET surface area of the mineral part is reported to be approximately 0.8 m^2/g independent of the coal mineral part origin and whether the coal ash is class F (mostly from bituminous coals) or class C (mostly from sub-bituminous coals).

The surface area and porosity of the coal char mostly comes from the carbon portion of the char sample, therefore it is customary to represent the BET surface area as value per gram of carbon (see Table C.7 results). Simple TGA experiments are performed to measure the amount of carbon in each Pittsburgh coal char sample and the results are provided in Tables C.6 and C.7.

Dubinin-Radushkevich (DR) model was applied in order to determine quantitatively the micropore volume present in Pittsburgh coal samples oxidized at various pressure conditions. Table C.7 shows DR microporosity values for the coal char samples investigated in this research. The results have been calculated on the basis of carbon content of the char. The porosity of the mineral portion of the char is taken to be zero.

Table C.7. DR microporosity, meso- and macroporosity of the Pittsburgh coal chars combusted at various pressures.

Sample	LOI [wt%]	DR Microp. Vol. [cc/g-carbon]	Mesopore Vol. [cc/g-carbon]	Macropore Vol. [cc/g-carbon]
Pitts. 206	63.0	0.025	0.041	0.041
Pitts. 223	40.4	0.078	0.183	0.126
Pitts. 218	44.3	0.061	0.159	0.102
Pitts. 224	44.1	0.071	0.167	0.081

As qualitatively already seen from the isotherms of the Pittsburgh char samples the amount of micropores in the samples oxidized under 10, 20 and 30 atm is similar and therefore the oxidation has been independent of the pressure value. The results in Table C.7 quantitatively confirm the observation above that DR micropore volume is similar in the Pittsburgh coal char samples oxidized under 10 atm and above. DR micropore volume of the sample oxidized under 2 atm is slightly lower than the micropore volume of the samples oxidized higher pressures.

Density Functional Distribution (DFT) analysis together with DR analysis are commonly applied models to investigate microporosity of the samples. The results of the DFT analysis of the Pittsburgh coal char samples oxidized at various pressure conditions are presented in Figure C.17.

Together with the DR analysis DFT analysis shows total micropore volumes available in the samples. In addition DFT analysis provides the information what pore sizes are to grow under different experimental conditions. As seen on Figure C.17, at elevated pressure conditions the pores to grow are pore sizes approximately 8 and 18 Angstroms. No pressure effect on the coal char sample has been observed at higher than 10 atm pressure condition. This confirms the results discussed above in the body text.

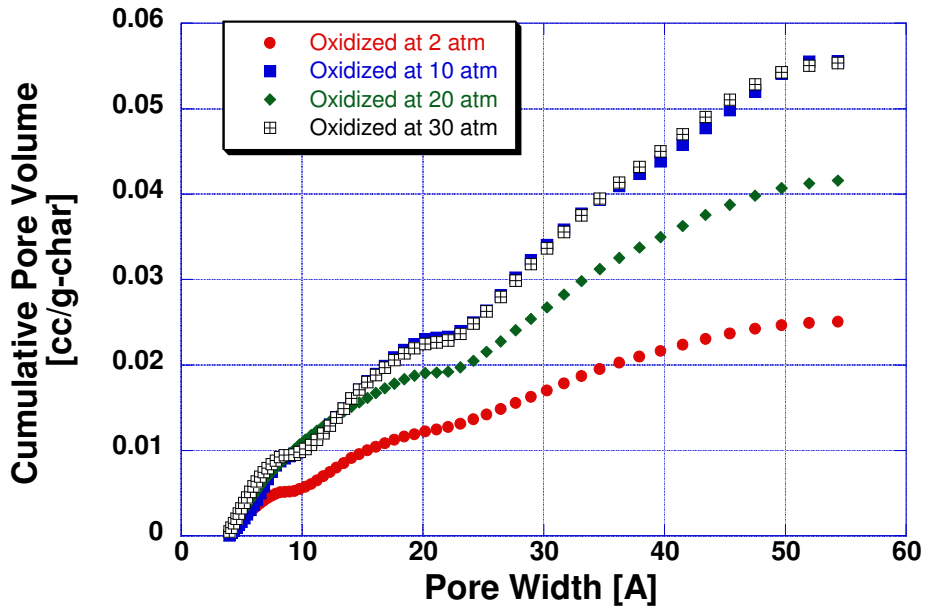

Figure C.17. DFT analysis of Pittsburgh coal char samples oxidized under various pressure conditions.

Illinois and Powder River Basin Chars

From the 11 samples from the PRB data sheet and the 13 samples from Illinois data sheet provided, two pairs of samples of each were chosen for surface area and porosity analysis. PRB samples 264 and PRB 270 are chosen from sub-bituminous char list and samples Illinois 298 and Illinois 292 are chosen from the bituminous char list. One of the samples in those pairs is oxidized under 20 atm pressurized condition while the other sample has been oxidized at 2 atm pressure. Figure C.18 shows both nitrogen isotherms of Powder River Basin and Illinois coal char samples calculated on the bases of carbon in the char. The amount of carbon in char samples was not measured at Brown, instead it was taken from the data sheet provided with the samples. For the sample PRB 264 oxidized under 2 atm the amount of carbon is taken to be 80 wt% and for the PRB 270 sample LOI is taken to be 69 wt% (Table C.8). The Illinois 292 sample has 29.8% carbon, while Illinois 298 sample has 50.2% carbon in its char. The uptake of the mineral part of a char is taken to be 0 cc per gram of mineral, which is a suitable approximation based on our years of experience with commercial and laboratory ash samples.

The isotherms shown in Figure C.18 exhibit mostly type II isotherm behavior. The isotherms obtained with the PRB and ILL char samples oxidized under 20 atm condition have clearly higher nitrogen uptake compared to the same samples oxidized at 2 atm condition. The inflection point occurs near the completion of the adsorbed monolayer and the ‘knee’ is deeper for the samples oxidized under 20 atm. Therefore more micropores are created under 20 atm pressure independent of the origin of the char; bituminous or sub-bituminous respectively.

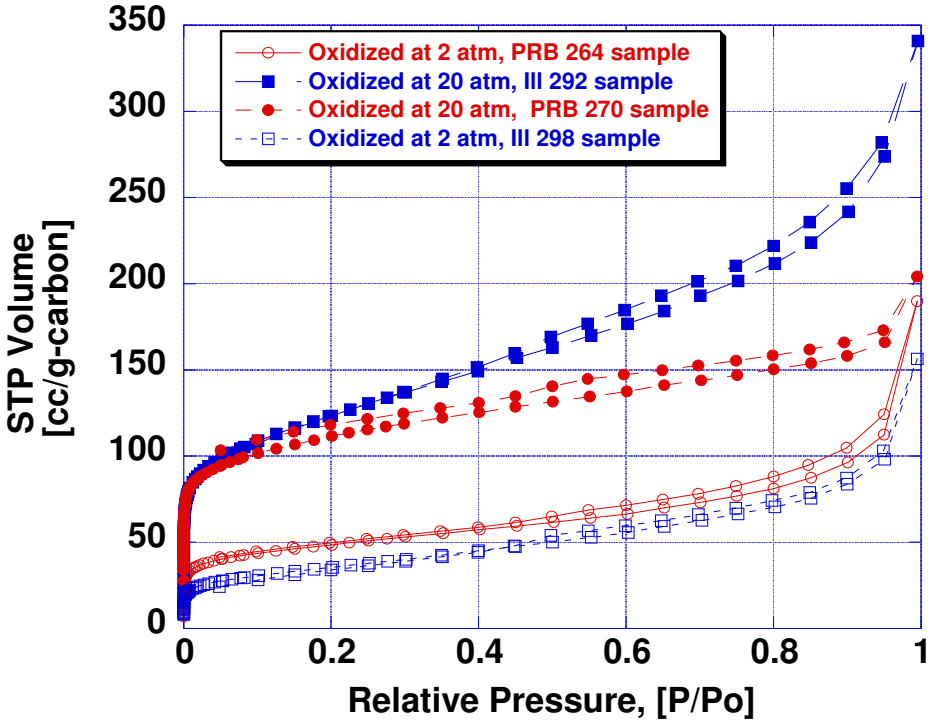

Figure C.18. PRB and Illinois char nitrogen adsorption isotherms oxidized under different elevated pressure conditions.

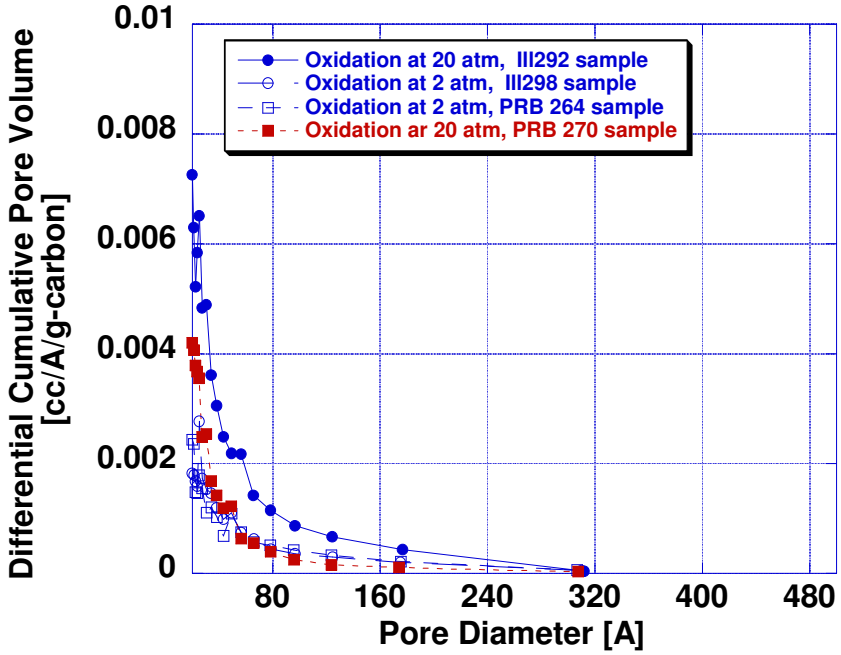

Figure C.19. BJH analysis results of PRB and Illinois char nitrogen adsorption isotherms oxidized under different elevated pressure conditions.

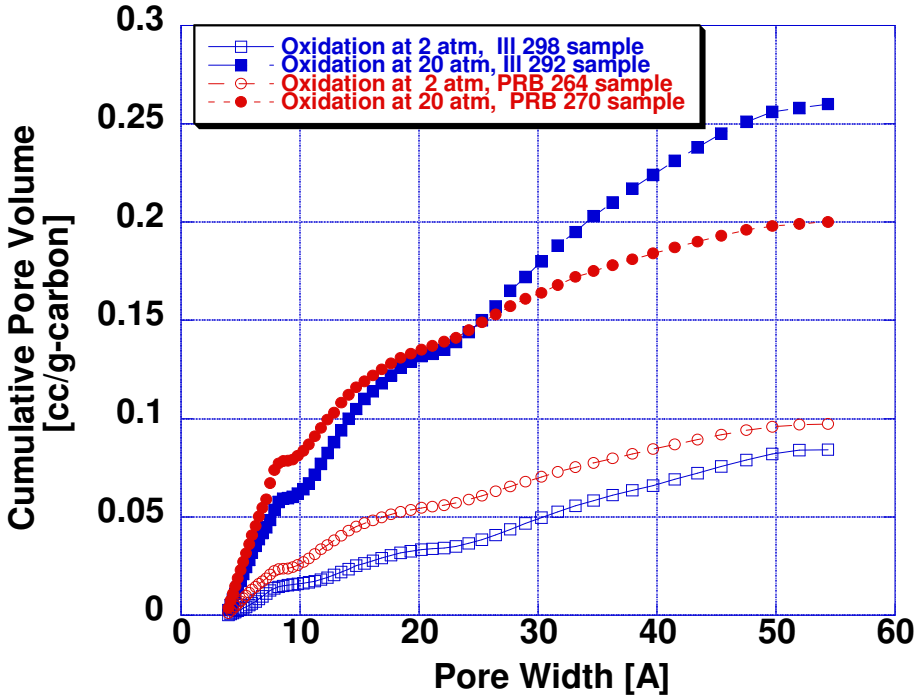

Figure C.20. DFT analysis of Illinois and PRB coal char samples oxidized under 20 and 2 atm pressure conditions.

Similar slopes of PRB char isotherms at relative pressure region 0.1<P/Po<0.95 shows that the amount of mesopores in both samples oxidized at different pressure is quite the same. The amount of mesopores of the Illinois char samples is slightly greater at relative pressure region of 0.1<P/Po<0.95 for the 20 atm sample compared with the 2 atm Illinois char isotherm (see Figure C.18). The results above are confirmed with the results of BJH analysis (Figure C.19); relatively more mespores are developed in Illinois char at 20 atm pressure than at 20 atm pressure PRB char sample.

The BET surface area results of PRB and Illinois coal char sample are presented in Table C.8. The PRB sample has originally relatively high surface area before the char combustion process, which is common characteristic for sub-bituminous coal char samples. Clearly at 20 atm pressure the surface area is being doubled compared to the surface area available in 2 atm samples for both types of chars. The higher surface area of the 20 atm char samples comes mostly from higher micro- and mesoporosity available in those samples (see results in Table C.8). Both micro- and mesopores are being created in both chars PRB and Illinois during 20 atm combustion. According to isotherm interpretation and BJH analysis results however in Illinois coal char sample more mesopores are being created only under 20 atm pressure (see Table C.9 and Figure C.19).

Table C.8. BET surface areas of the PRB and Illinois coal char oxidized at various pressure conditions.

Sample	Oxidation Pressure [atm]	BET Surface Area [m^2/g-char]	LOI Loss-On-Ignition [%]	BET Surface Area [m^2/g-carbon]
PRB 264	2	130.1	80	162.4
PRB 270	20	251.3	69	363.8
Ill 298	2	62.3	50.2	123.3
Ill 292	20	125.7	29.8	419.9

Table C.9. DR microporosity, meso- and macroporosity of the PRB and Illinois coal char samples oxidized in various pressure conditions.

Sample	LOI wt%	DR Microp. Vol. [cc/g-carbon]	Mesopore Vol. [cc/g-carbon]	Macropore Vol. [cc/g-carbon]
PRB 264	80	0.0318	0.1085	0.1199
PRB 270	69	0.150	0.107	0.0587
Ill 298	50.2	0.0435	0.1084	0.09
Ill 292	29.8	0.159	0.265	0.103

The results of the DFT analysis of PRB and Illinois char samples (Figure C.20) agree well with DR analysis results. Clearly, more micropores are created under 20 atm oxidation pressure condition in both char ILL and PRB samples. The pores to develop under high pressure oxidation conditions are the pores with size of 8 and 18 Angstroms and this result is independent of the char origin; either bituminous or sub-bituminous coal char.

C.3.2 Carbon Morphology by SEM

Pittsburgh Chars

The SEM images of Pittsburgh coal char samples are presented on Figures C.21-C.32. Figures C.21 and C.22 show the images of the Pittsburgh coal char activated under 2 atm pressure condition. The carbon char particles exhibit irregular shape and structure. Some of them are fractions and some of them are like sphere looking particles with lots of holes covering their surfaces. Most particles are highly porous and have skeletal form. This kind of particle form suggests that the carbon particles have gone through softened state

during the combustion in high pressure. The large blow-holes seen on the images are the result of the devolatilization and softening of the coal char particle during the combustion. The char particle sizes range from a sub-micron level up to 100 micron in size. The average size of the particles seen on Figure C.21 is about 50 to 100 microns. Some of the char particles are in their late stage of burn off and have only the skeletons left from complete char structure. The char particles on SEM images are more porous compared with the mineral particles present in the char. Most of the mineral particles are intact and are seen as solid few micron size spheres containing hardly any porosity. Figure C.22 shows the magnified image of the same Pittsburgh char 218 sample as presented on Figure C.21. As seen, the surface of the char particles is highly porous with pore sizes approximately 1000 Angstroms and below (macropores). The complete surface of the particle around 1000 Angstroms holes are covered with smaller opening sizes of 100 Angstroms and below (mesopores). The existence of micropores (pores below 20 Angstroms) requires TEM imaging.

Figures C.22-C.24 show the energy dispersive spectroscopy (EDS) SEM images of Pittsburgh 206 char sample. The solid sphere 50 micron size particle (Figure C.22) on top of the 120 micron holly skeleton carbon particle has mainly iron atoms. There are plenty solid intact spheres (mineral particles) sitting on top of the iron particle. In addition, there is a significant amount of approximately 1 micron size mineral particles embedded in larger unburned carbon particles. Figure C.23 shows approximately 35 micron size mineral particle (mostly Fe, S, O atoms) fused on big carbon particle. The surface structure of this mineral particle was distinctive for all other mineral particle present in this char exhibiting Fe, S, O atom specs with EDS. It seems that the mineral particle has either already cracked or it would have cracked if the oxidation under 2 atm pressure would have proceeded to completion. Most particles and their fractions exhibit carbon specs with EDS and presented on Figure C.24. The blowhole in the carbon particle tells that the particle is in the early stage of the burn off.

Figures C.25-C.27 show Pittsburgh 223 char sample SEM images. This sample is oxidized under slightly higher oxidation pressure condition than Pittsburgh 206 sample. Pittsburgh 223 sample has been prepared under 10 atm pressure. The SEM image presented on Figure C.25 tells quite similar story than similar image for Pittsburgh 206 char. Most of the carbon particles are in the size range of 50 to 100 microns. Some of them are at earlier, some of them at later stage of burn off. There seems to be more pieces of fractions of carbon particles (Figure C.27) present in Pittsburgh 223 sample compared with Pittsburgh 206 char sample SEM images. However no effort has been made to perform quantitative analysis out from these SEM images to define the amount of fractioned carbon particles versus whole shape particles (early burn-off stage particles). SEM images on Figures C.29-C.32 present Pittsburgh char samples of 218 and 224 oxidized under 20 and 30 atm pressure condition respectively. In both samples the amount of the fractioned carbon particles versus intact carbon particles is easily noticed with SEM imaging compared to Pittsburgh samples oxidized under significantly lower pressure condition. This reveals that pressure has a tendency to produce skeletal particles with higher surface area, as confirmed by the BET analysis.

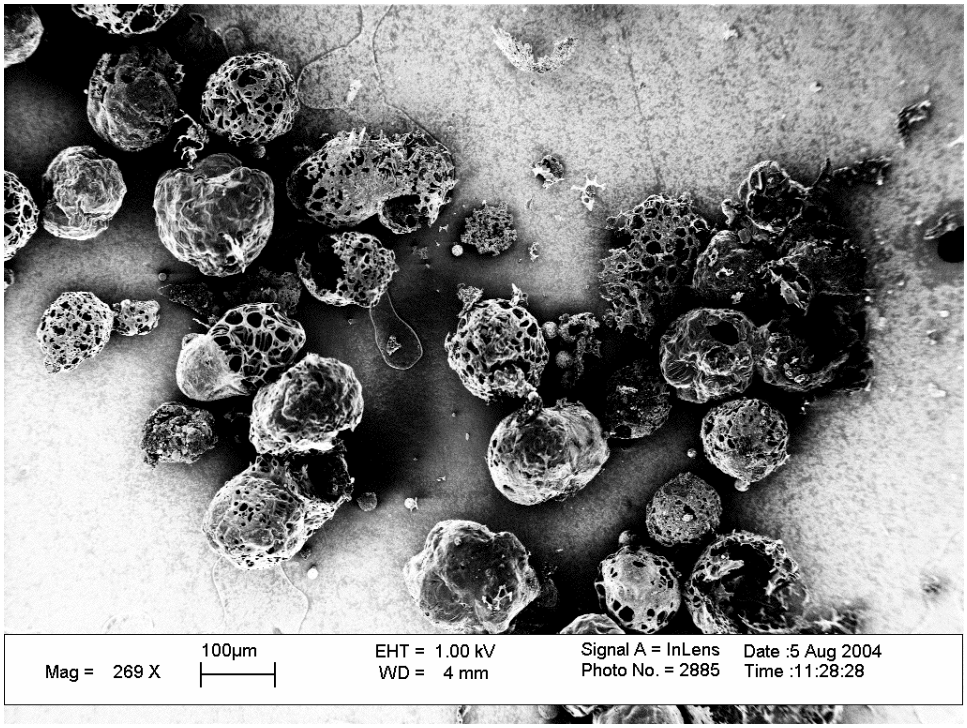

Figure C.21. Scanning Electron Microscopy image of Pittsburgh 206 (bituminous) char sample oxidized under 2 atm oxidation pressure.

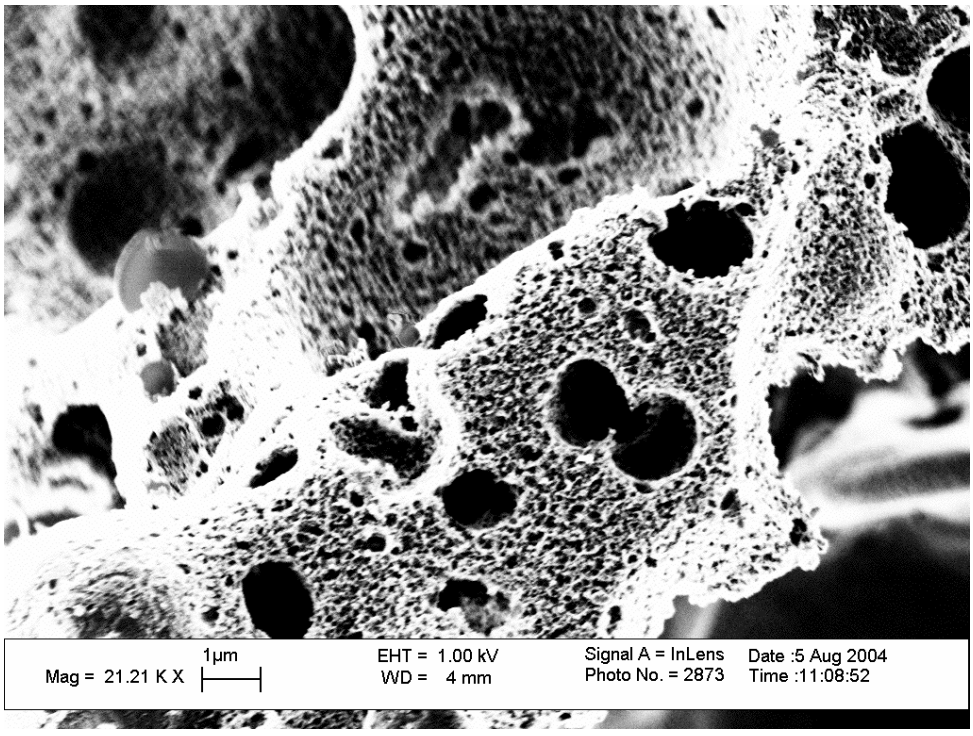

Figure C.22. Magnified Scanning Electron Microscopy image of Pittsburgh 206 sample oxidized under 2 atm oxidation pressure.

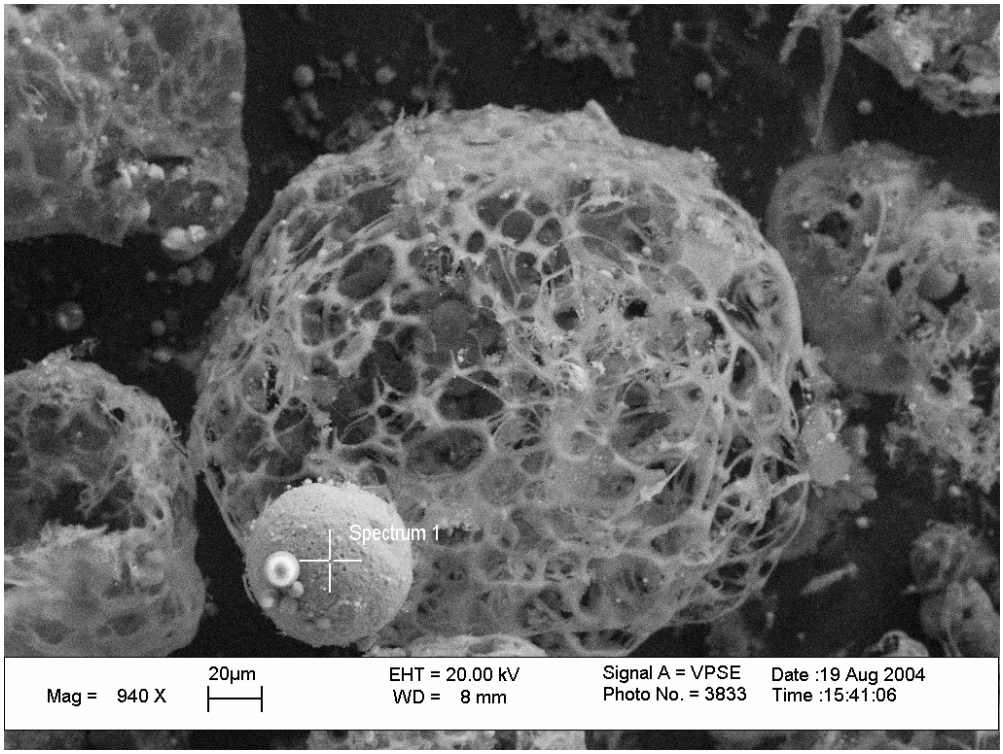

Figure C.23. EDS Scanning Electron Microscopy image of Pittsburgh 206 sample oxidized under 2 atm oxidation pressure conditions. Iron particle of a size of 40 micron on top of 100 micron carbon skeleton.

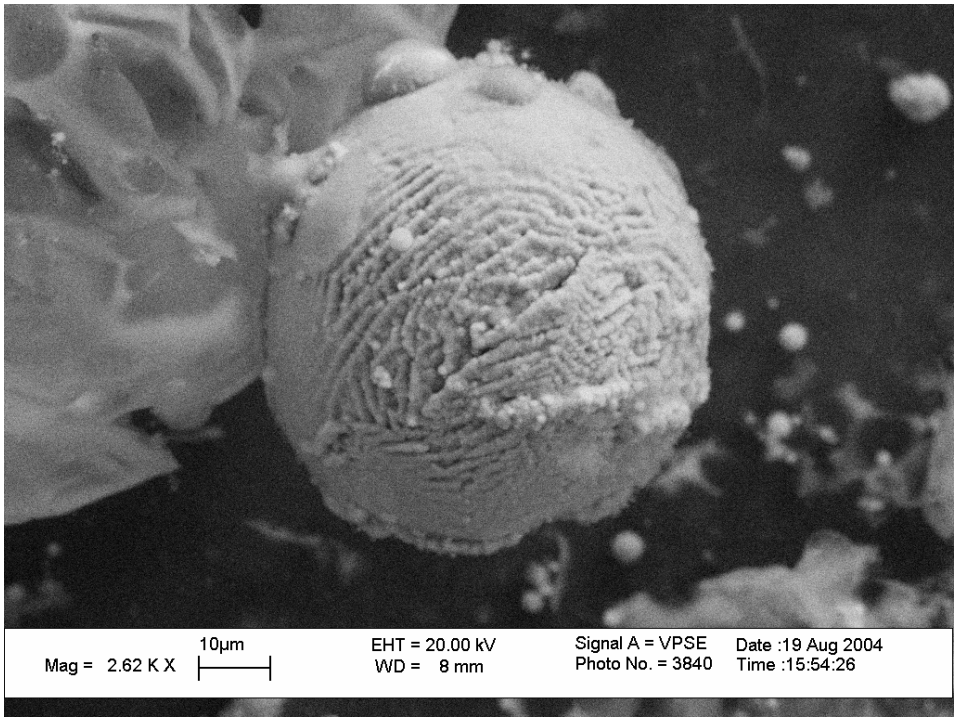

Figure C.24. EDS Scanning Electron Microscopy image of Pittsburgh 206 sample oxidized under 2 atm oxidation pressure conditions. Mineral particle [Fe, S, O] of a size of 40 micron on top of 100 micron carbon skeleton.

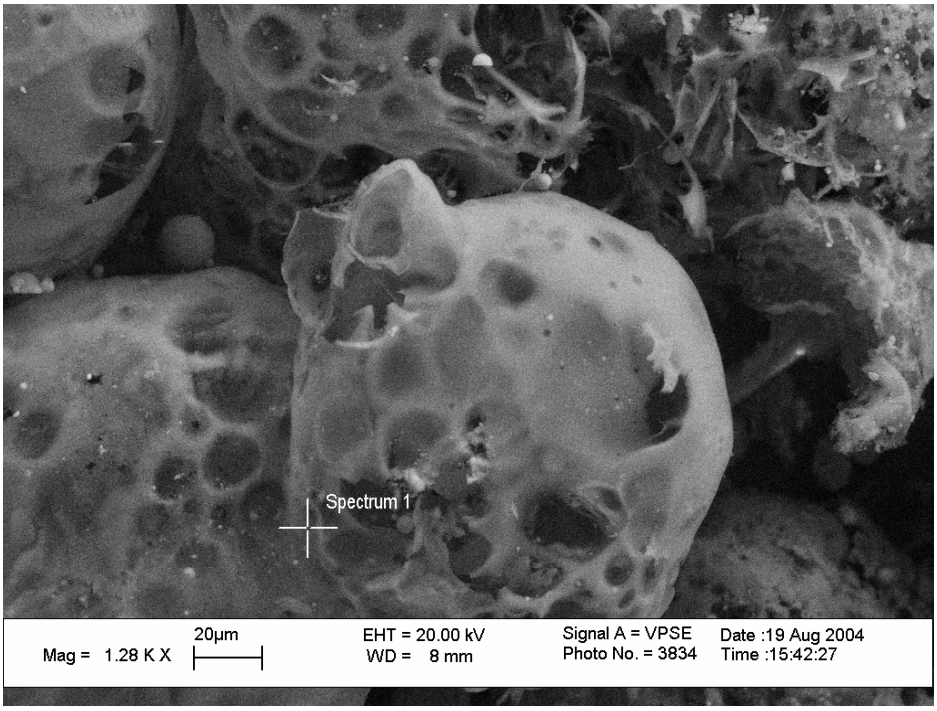

Figure C.25. EDS Scanning Electron Microscopy image of Pittsburgh 206 sample oxidized under 2 atm oxidation pressure conditions. Carbon particles and their fractions and a blow-hole formation in the carbon particle.

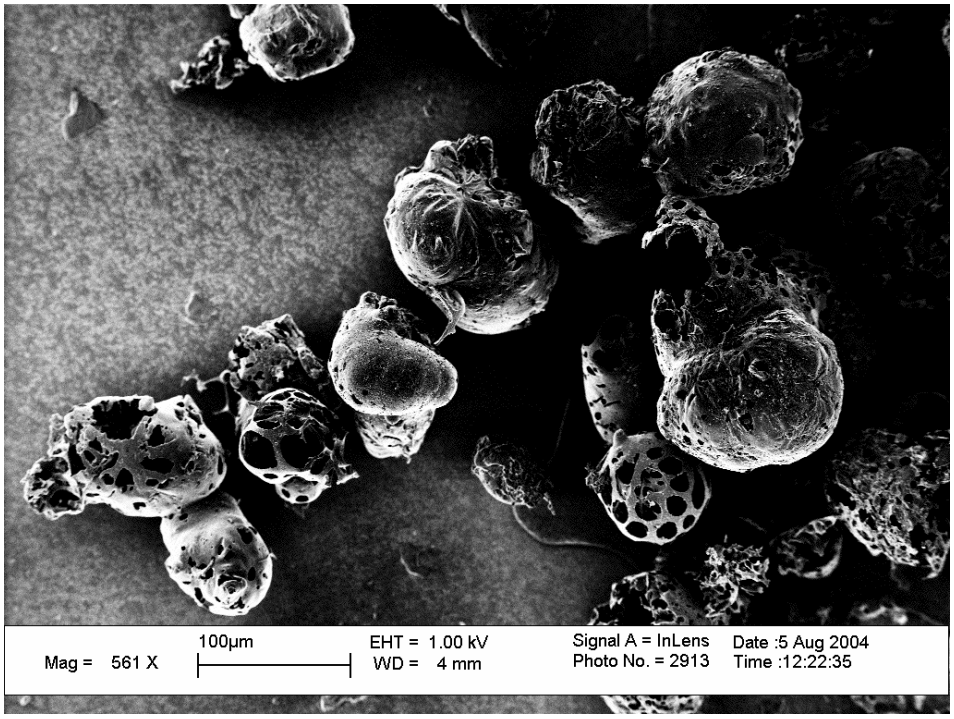

Figure C.26. Scanning Electron Microscopy image of Pittsburgh 223 sample oxidized under 10 atm oxidation pressure.

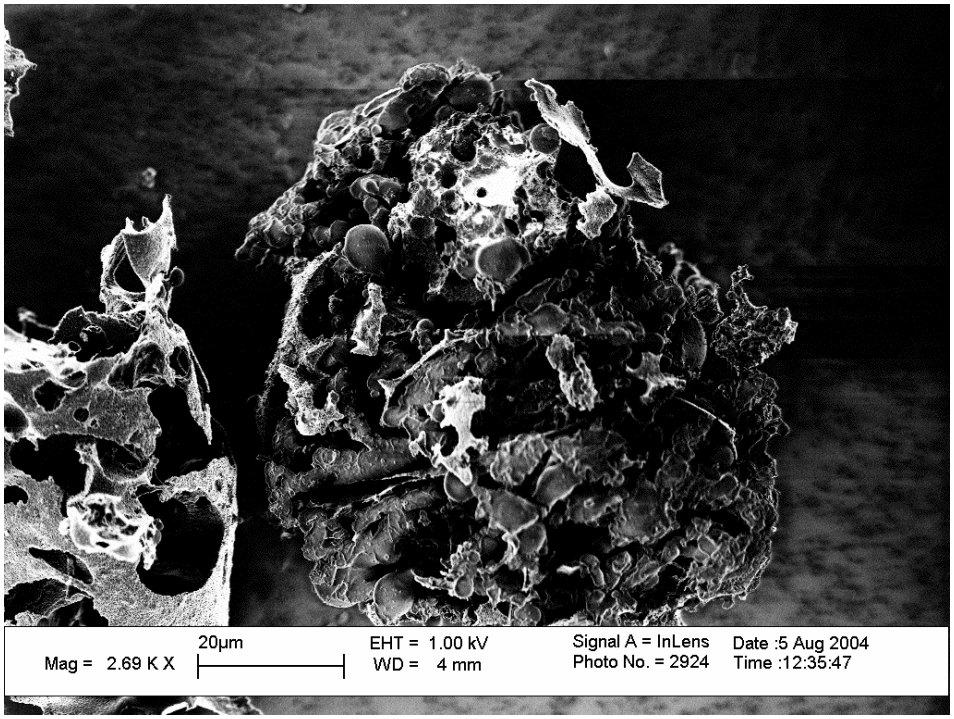

Figure C.27. Magnified Scanning Electron Microscopy image of Pittsburgh 223 sample oxidized under 10 atm oxidation pressure conditions.

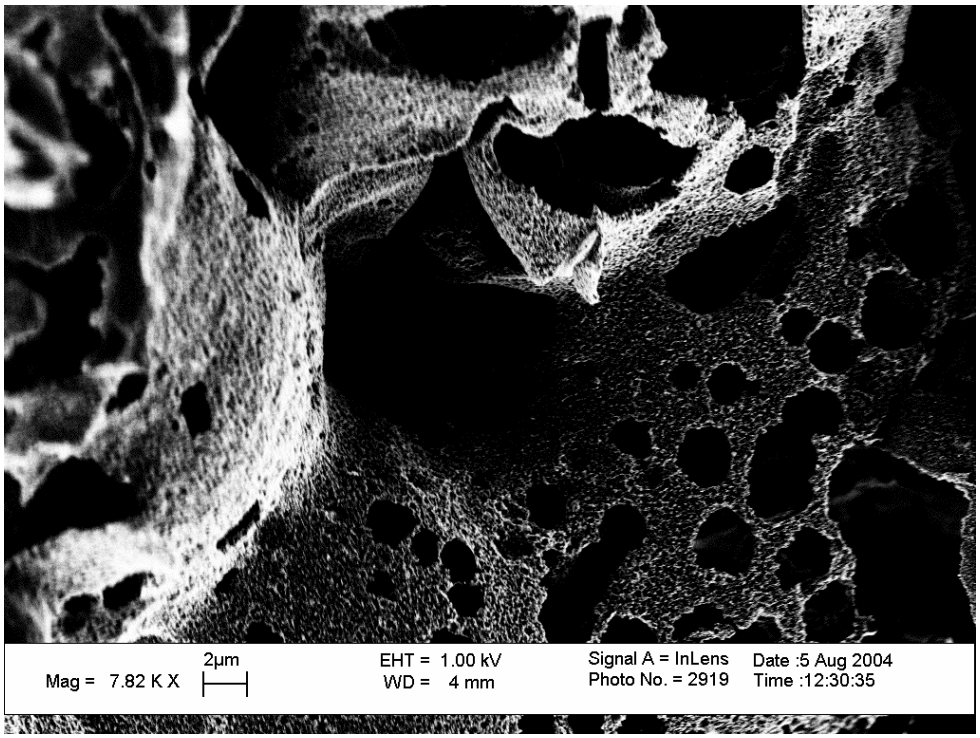

Figure C.28. A magnified Scanning Electron Microscopy image of Pittsburgh 223 sample oxidized under 10 atm oxidation pressure.

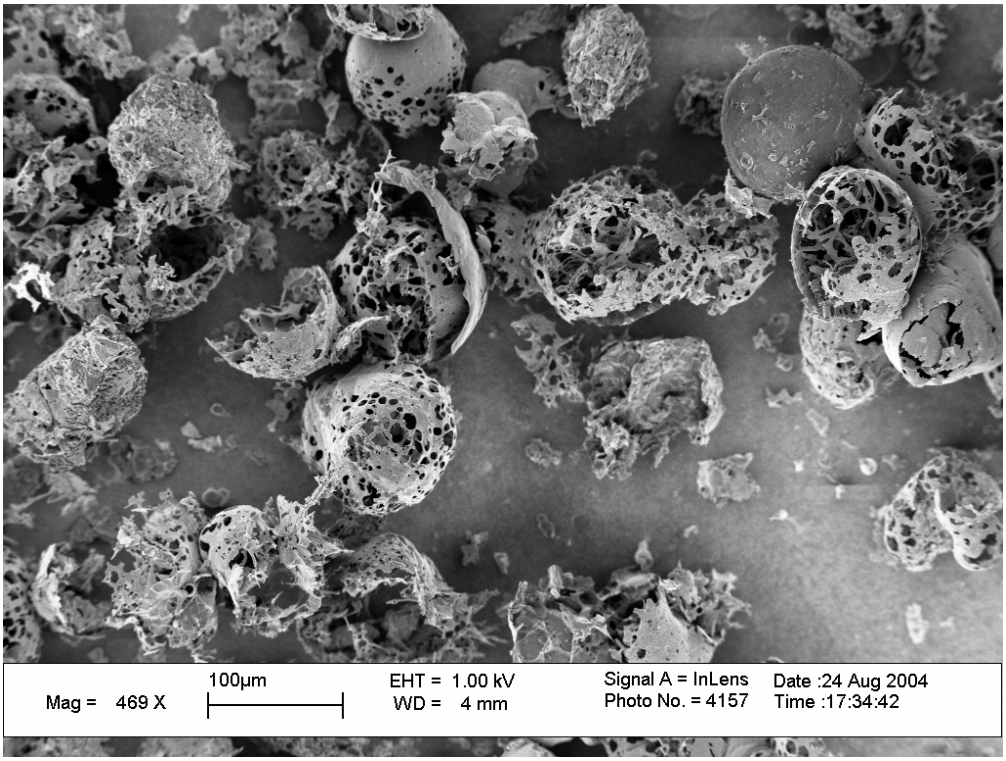

Figure C.29. A Scanning Electron Microscopy image of Pittsburgh 218 sample oxidized at 20 atm pressure.

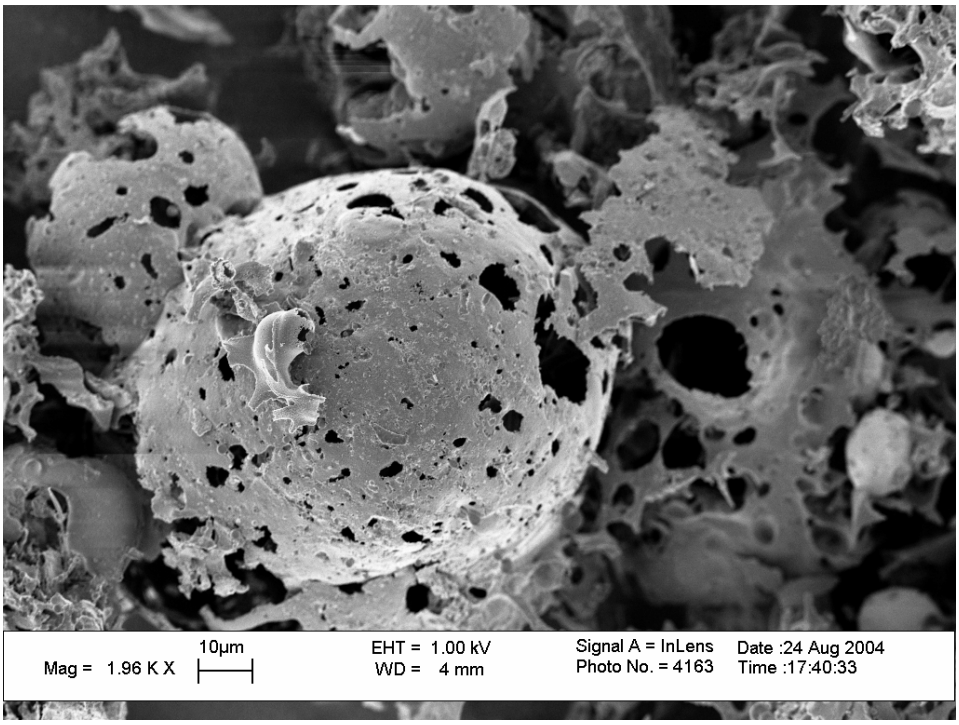

Figure C.30. A magnified Scanning Electron Microscopy image of Pittsburgh 218 sample oxidized at 20 atm pressure.

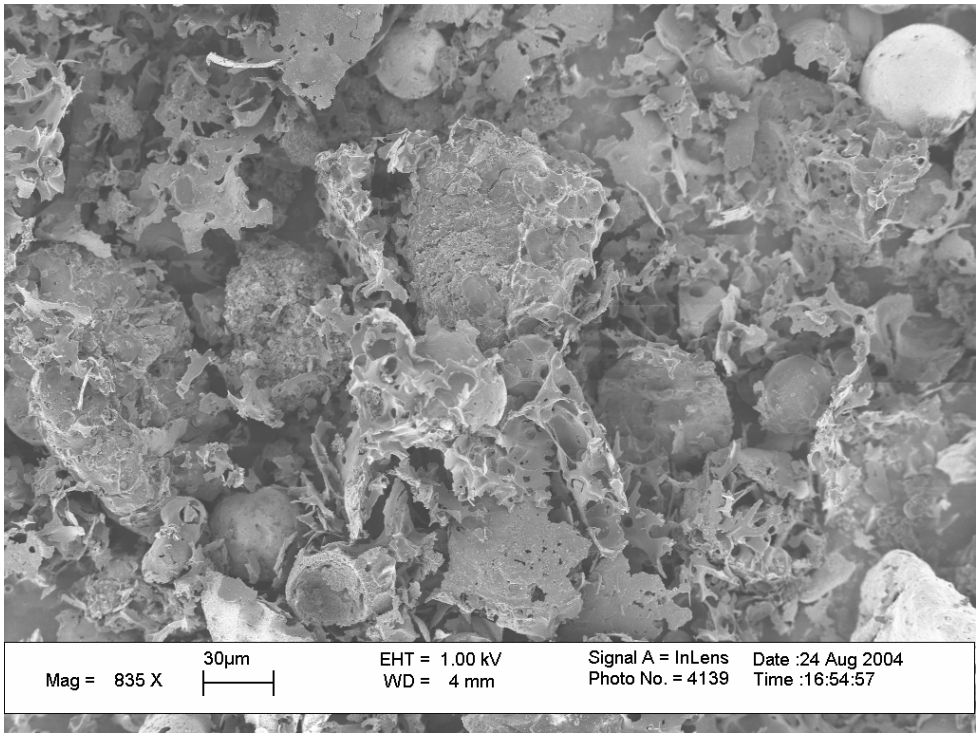

Figure C.31. A Scanning Electron Microscopy image of Pittsburgh 224 sample oxidized at 30 atm pressure.

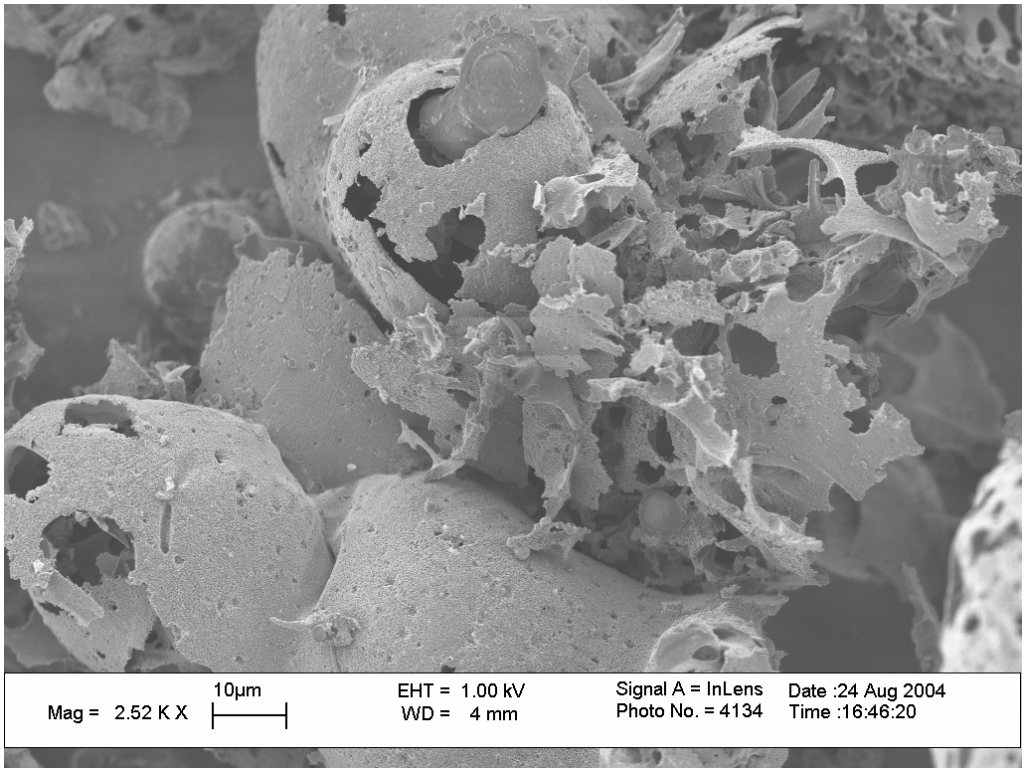

Figure C.32. A magnified Scanning Electron Microscopy image of Pittsburgh 224 sample oxidized at 30 atm pressure.

Powder River Basin and Illinois Chars

SEM images of PRB and Illinois char samples activated under 2 and 20 atmosphere oxidation conditions are shown on Figures C.33-C42. Both PRB char samples, PRB 270 and PRB 264 have slightly unlike char structure compared with the bituminous Pittsburgh char particle images discussed before. On the SEM image in Figure C.33, a layout of PRB char particles is shown. The particles seem to be in a size range from 30 up to 90 micron. They appear to be intact and kept their integrity in combustion process. In previous studies [Külaots] it has also seen that sub-bituminous char samples tend to save their structure during the combustion process even at the late stages of burn off. A slightly closer image of the PRB 264 char particle is shown in Figures C.34 and C.35. The particle in Figure C.34 seems to have more disordered structure compared with the particles shown in Figure C.35. The particles are also highly porous and therefore provide significant surface area as seen from BET analysis results of PRB char samples.

Quite a similar picture is seen when PRB char sample 270 (PRB 270) SEM images are taken (Figures C.36 and C.37). There seems to be no effect of the pressure observing the images by eye. However, as seen from the BET analysis, the surface area has nearly doubled at 20 pressure oxidation pressure. The micropores that have been created are inside of this whole chunk looking particles and are not seen under SEM.

Figures C.38-C.40 show SEM images of Illinois char [bituminous] sample 298 prepared under 2 atm pressure. The SEM images are quite similar compared to SEM images obtained with Pittsburgh char. The char particles look like skeletons with relatively big blow-holes.

Illinois char sample 292 SEM images are presented on Figures C.41 and C.41. The sample is prepared under 20 atm pressure. Clearly more particles have collapsed due to the high pressure; the similar effect has seen with Pittsburgh char samples oxidized under high pressure (Figure C.31 and C.32).

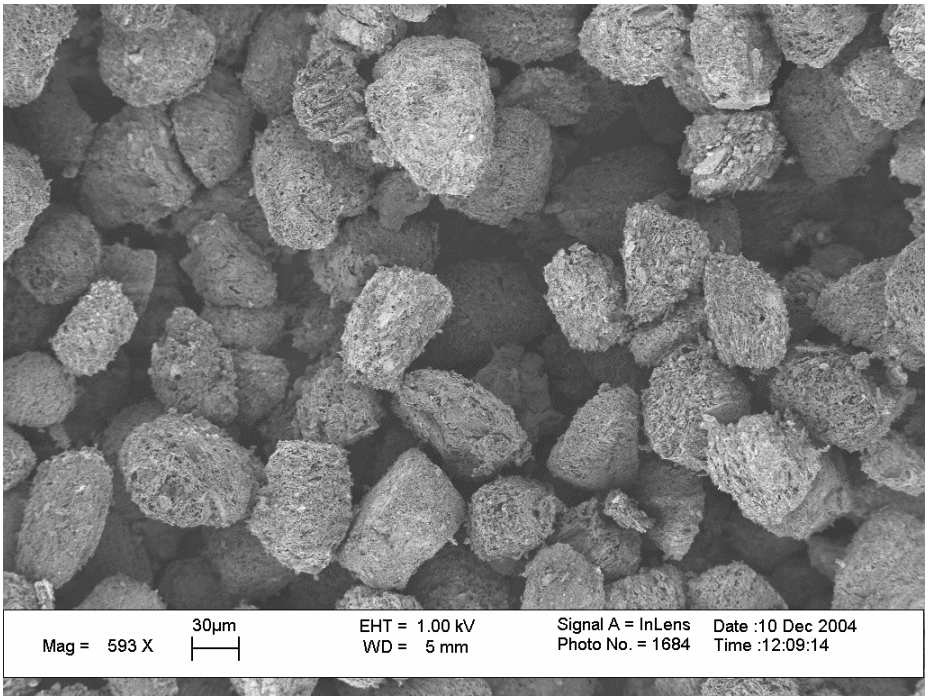

Figure C.33. Scanning Electron Microscopy image of Powder River Basin 264 [sub-bituminous] sample oxidized at 2 atm pressure.

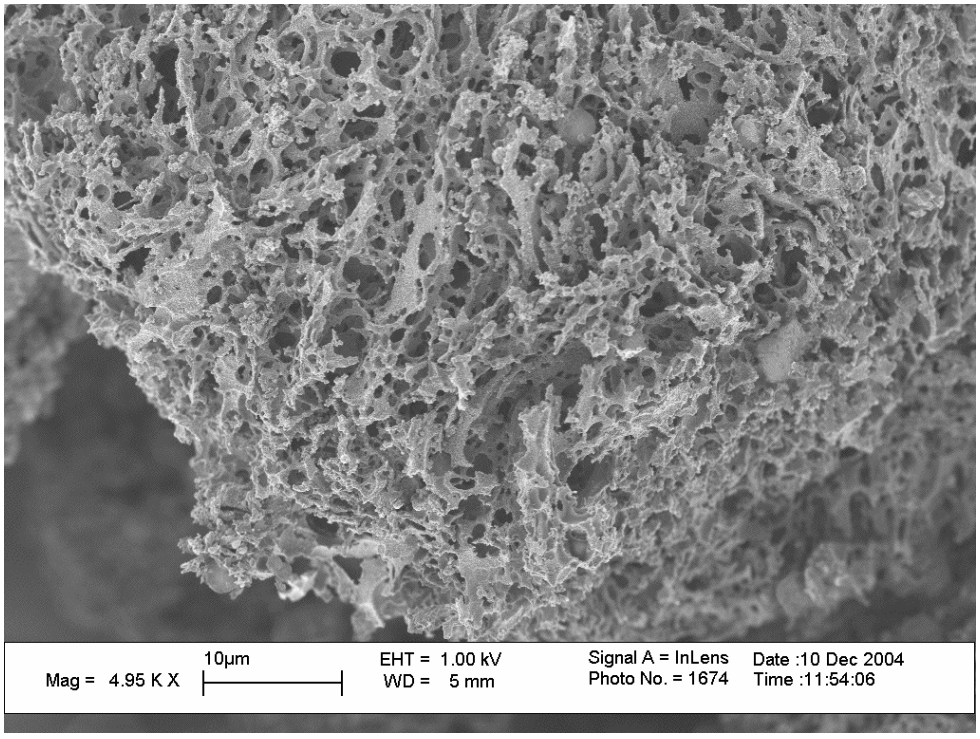

Figure C.34. A magnified Scanning Electron Microscopy image of Powder River Basin 264 char particle oxidized at 2 atm pressure. Somewhat disordered char structure.

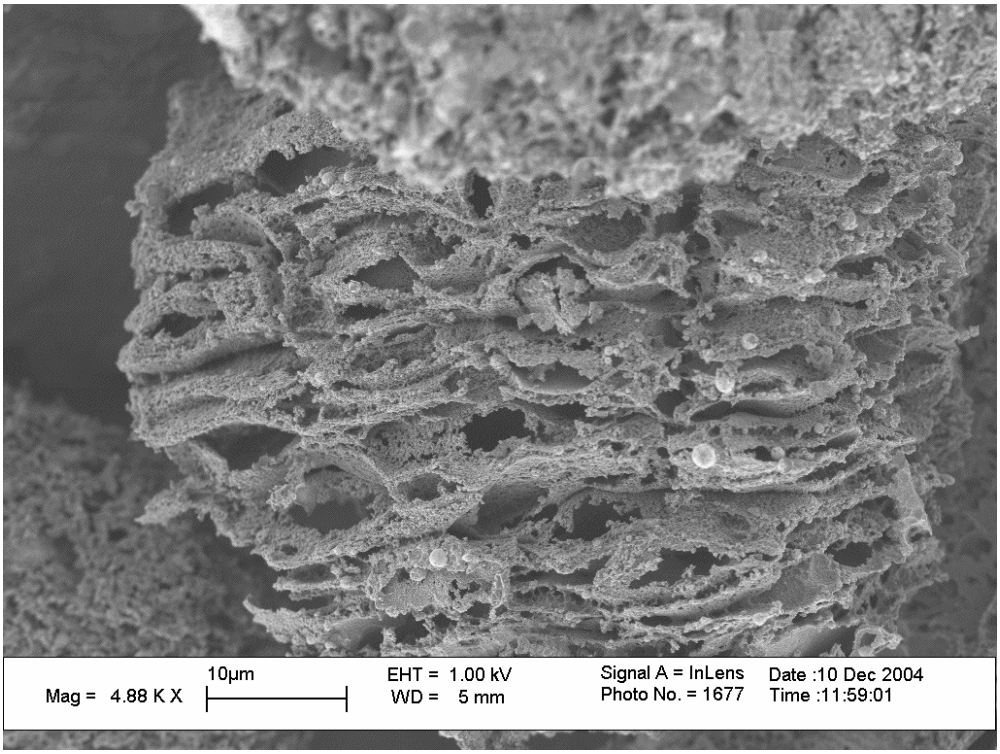

Figure C.35. A magnified Scanning Electron Microscopy image of Powder River Basin 264 char particle oxidized at 2 atm pressure.

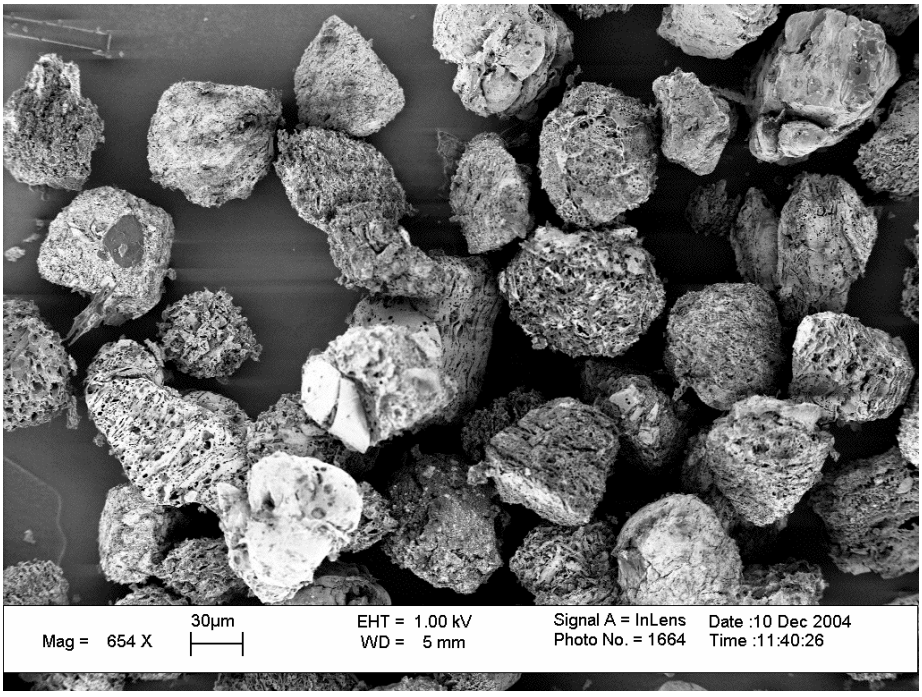

Figure C.36. A Scanning Electron Microscopy image of Powder River Basin 270 sample oxidized at 20 atm pressure.

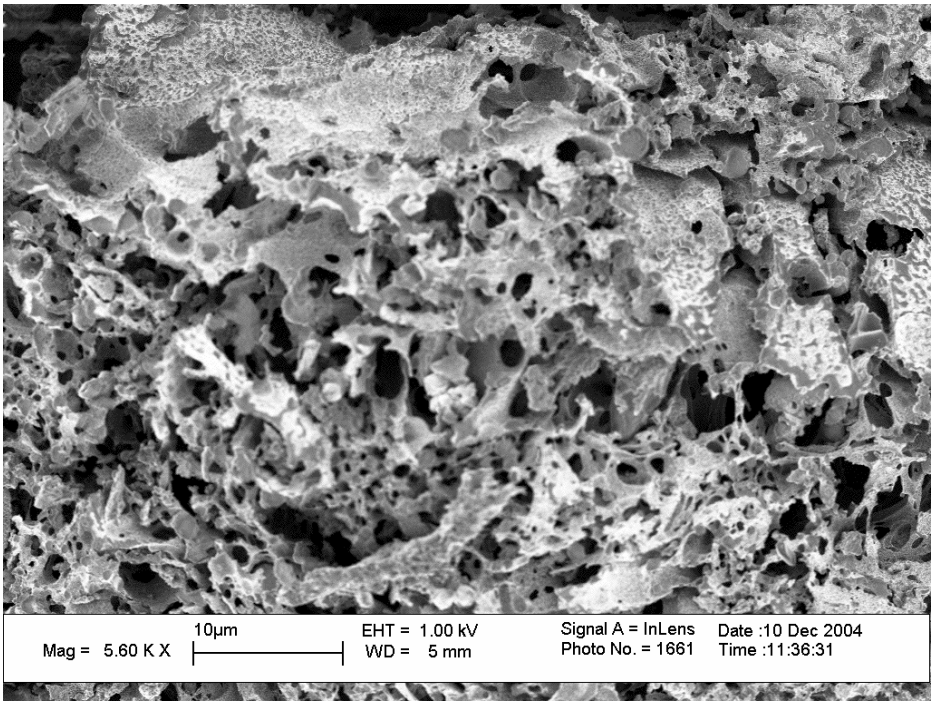

Figure C.37. A magnified Scanning Electron Microscopy image of Powder River Basin 270 char particle oxidized under 20 atm pressure.

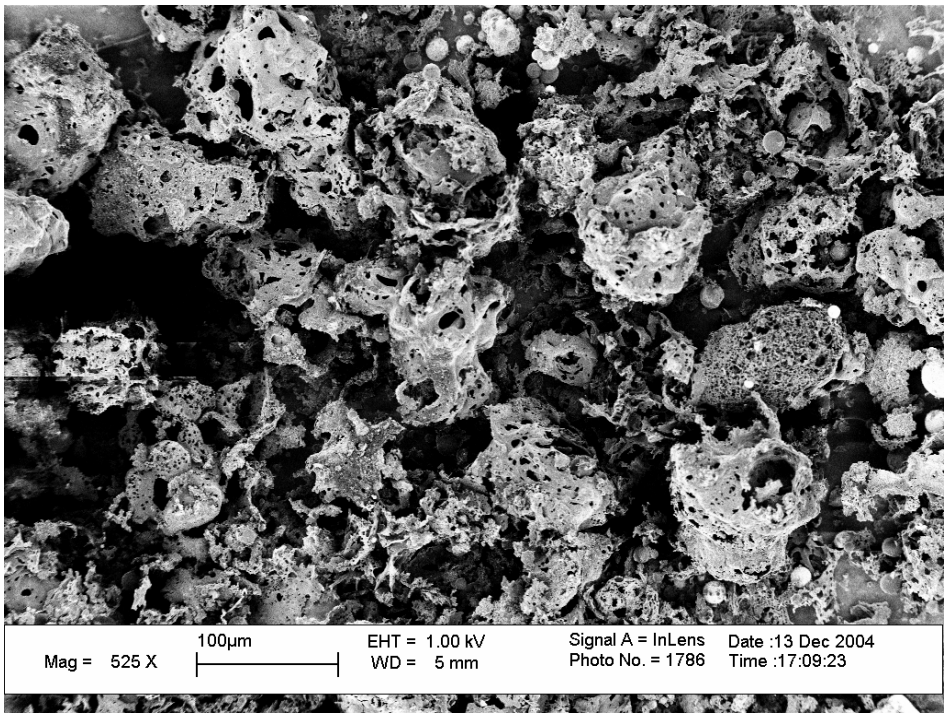

Figure C.38. A Scanning Electron Microscopy image of Illinois 298 [bituminous] char particles oxidized under 2 atm pressure.

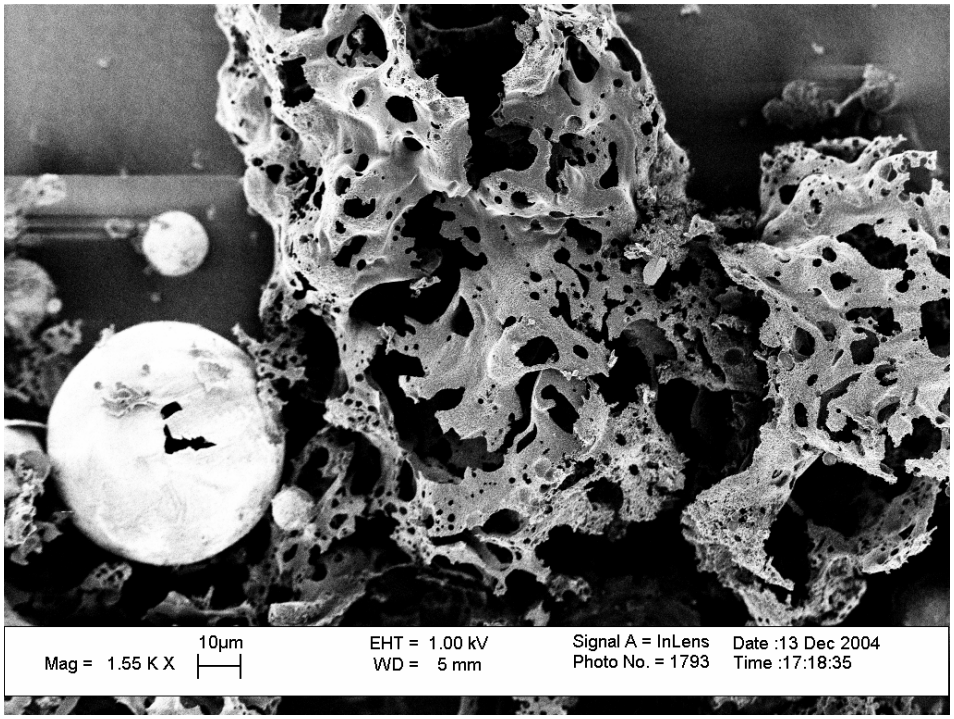

Figure C.39. Magnified SEM image of Illinois 298 char particles [mineral particle on left and carbon particles on right side of the image] oxidized under 2 atm pressure.

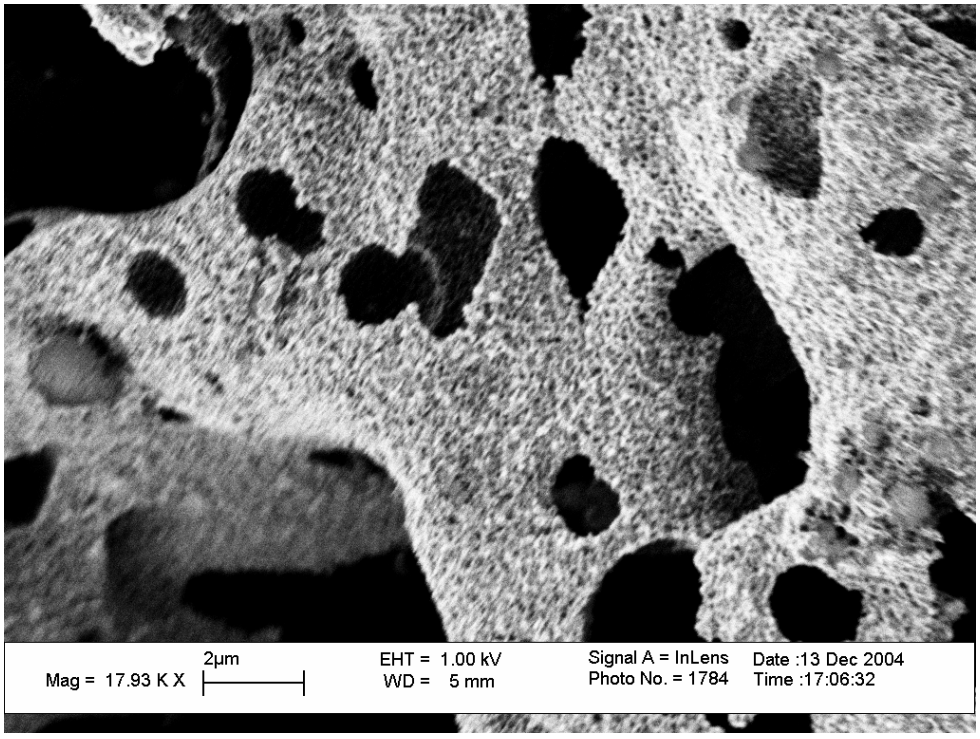

Figure C.40. A magnified Scanning Electron Microscopy image of Illinois 298 char particle surface, sample oxidized under 2 atm pressure. 1 to 2 micron size holes on the surface of the char particle.

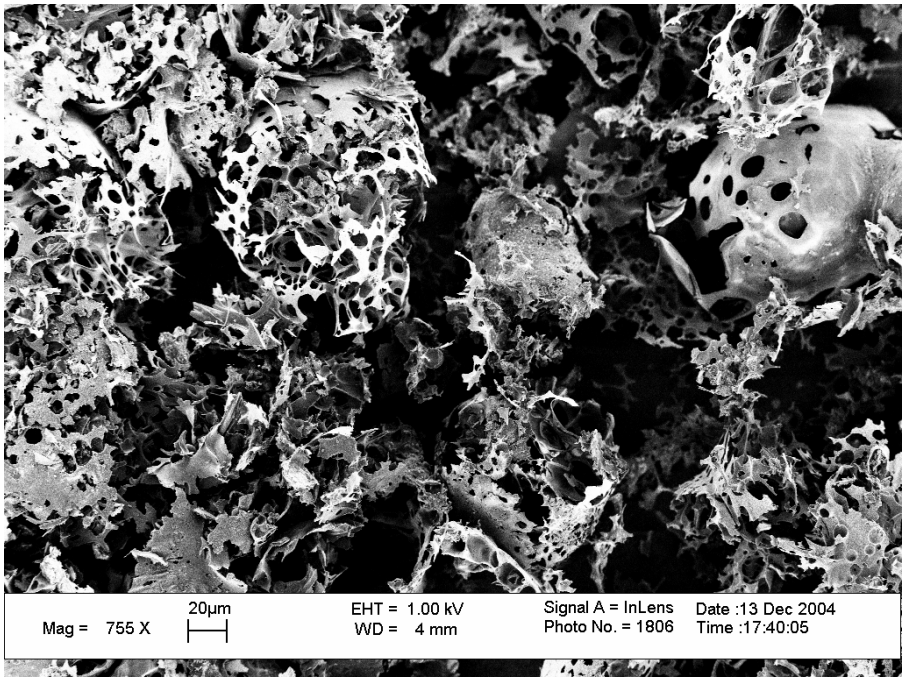

Figure C.41. A Scanning Electron Microscopy image of Illinois 292 char particles oxidized under 20 atm pressure. A majority of the particles have disintegrated.

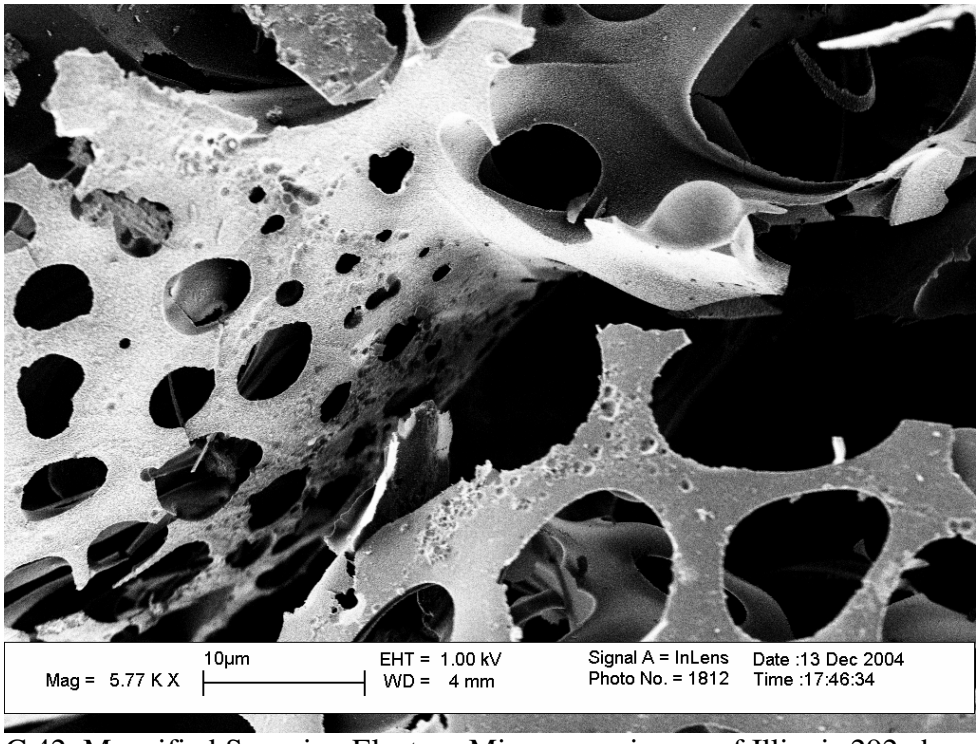

Figure C.42. Magnified Scanning Electron Microscopy image of Illinois 292 char particle surface, sample oxidized at 20 atm pressure.

C.4 Evaluation of Power-Law Kinetics for Char Oxidation

This chapter is a comparative evaluation of power law kinetics (used in CBK8), relative to more complex rate laws such as that used in CBK/E, in an attempt to identify the best approach for high pressure conditions expected in advanced combustors and gasifyers.

The simple stoichiometry of the carbon/oxygen reaction, $C + O_2 \rightarrow CO / CO_2$, belies a complex kinetic behavior, which has to date prevented a consensus on the kinetic parameters or even the proper form of the rate expression. Identifying the most appropriate rate form remains an important practical goal, since in the long term it will allow more meaningful correlation and unification of the data needed to design furnaces and burner systems.

This session focuses initially on low-temperature studies (< 1000 K) where the kinetic data are much more suitable to detailed analysis, and on near-atmospheric studies (P_{ox} >0.01 bar), which are of greatest technological relevance. This literature contains many reports of fractional orders (see Figure C.43), a fact that suggests complex kinetics. The Figure C.43 data includes a large and significant cluster of high fractional reaction orders, but also credible reports of low order [1,2], and a robust kinetic law must be capable of predicting both. Most of the studies in Figure C.43 employ relatively narrow ranges of oxygen pressure (factors of 3-10) and the reported orders that are best interpreted as local values, $n_{loc} = dlnR/dlnP$, that are slopes of some governing kinetic law whose functional form is not directly revealed. One of several exceptions in the literature is the study of Suuberg et al. who measured combustion rates from 0.005 - 1 bar oxygen partial pressure from 573-673 K for a phenol-formaldehyde resin char (see Figure C.44). These authors find that the rates followed a power-law form: $R = k\, P_{ox}^{\,n}$, where n is constant at 0.62 over the entire range of oxygen pressure (see Figure C.44A). Similar behavior has been observed in a recent study motivated by technological interest in high-pressure combustion and gasification [5,6] (see Figure C.44B).

This "persistent" power-law behavior is inconsistent with simple theories of adsorption and desorption on homogeneous (i.e. single site type) surfaces, which give the Langmuir law:

$$R = k_{des} k_{ads} P_{ox} / (k_{des} + k_{ads} P_{ox}) \qquad \text{(C.3)}$$

This form requires the reaction to be first order, zeroth order, or in a transition zone between the two. Logarithmic differentiation of Equation C.3 yields the local reaction order implicit in the Langmuir law:

$$n_{local} = dlnR/dlnP = 1 / [1 + (k_{ads} P_{ox} / k_{des})] \qquad \text{(C.4)}$$

Defining the transition region as $0.2 < n_{local} < 0.8$, its width by Equation C.4 is always a factor of 16 in oxygen pressure regardless of the specific values of k_{ads} and k_{des}.

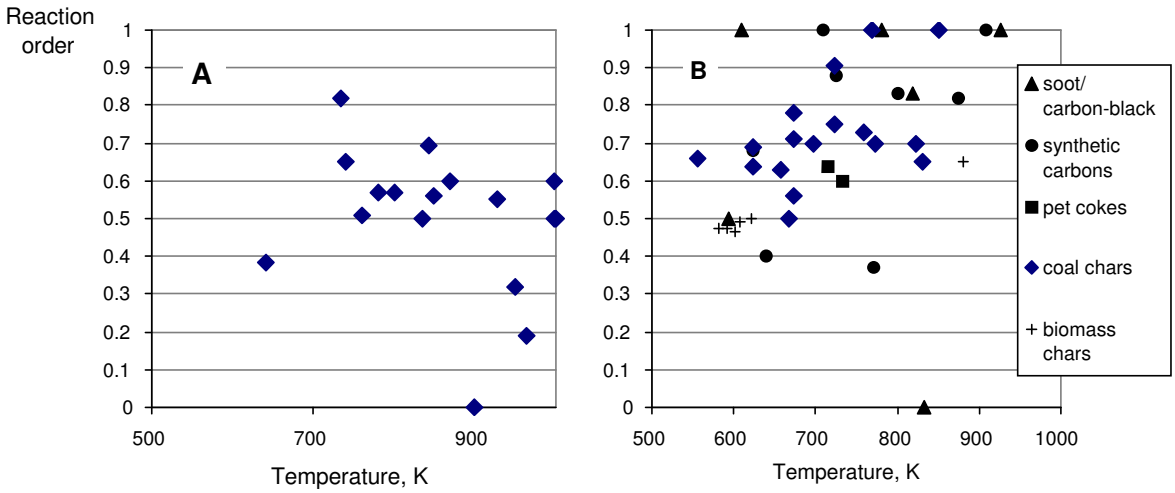

Figure C.43. Summary of measured reaction orders reported in the literature for carbon oxidation at $T < 1000$ K, $P_{ox} > 0.01$ bar. **A:** graphitic carbons, **B:** non-graphitic carbons. The coal char data in this figure was taken from a previous compilation [3].

Experimental verification of this transition is conspicuously absent in the low-temperature carbon oxidation literature. The power law behavior reported by Suuberg et al. [4] over a factor of 200 in oxygen pressure is particularly incompatible with the simple Langmuir form (see Figure C.44). Further since measured activation energies for transient desorption are typically much greater than those for adsorption, this form requires zeroth order in the low-temperature, high-pressure limit, which is incompatible with the majority of the low-temperature data in Figure C.43. The power-law form may be an attractive alternative, but without a fundamental basis its use in combustion models will remain empirical and ultimately controversial.

The present chapter addresses the mechanistic origin of power-law kinetics by drawing from the fundamental literature on heterogeneous (real) surfaces. We will show that global power-law kinetics is a natural consequence of the already well-established heterogeneity of real carbon surfaces [7-10], whether the heterogeneity is intrinsic or induced. The chapter then compares the specific heterogeneous surface model of Haynes[11] to several example datasets and the results used to discuss the main features of the carbon oxidation database in the intrinsic regime at $T < 1000$ K and $P_{ox} > 0.01$ bar.

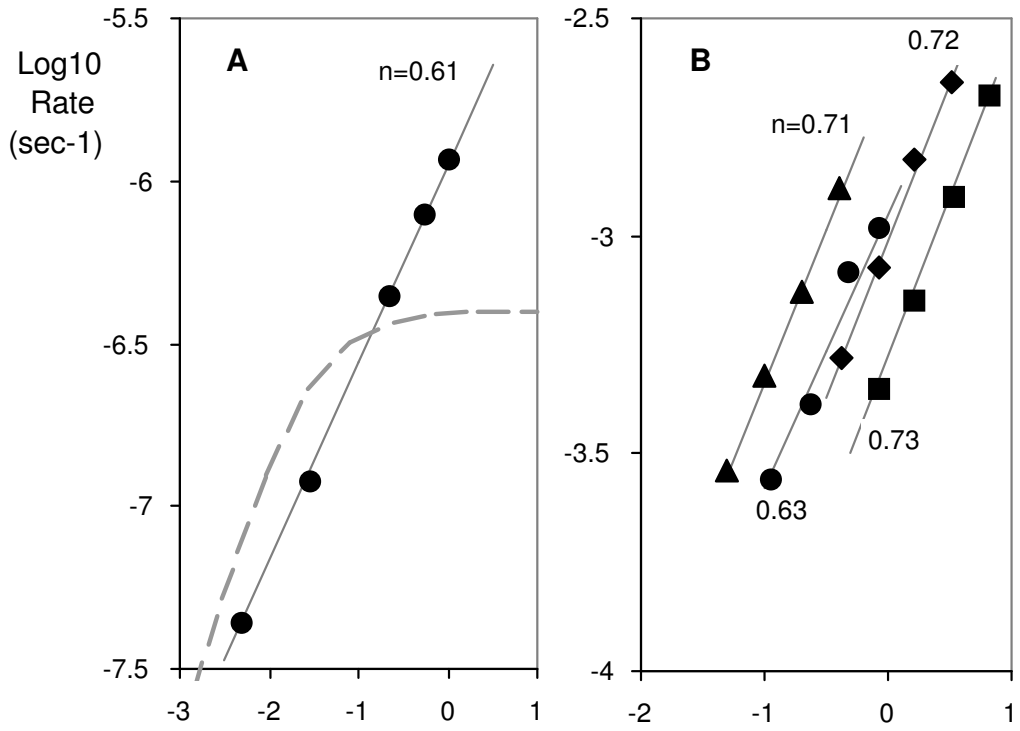

Figure C.44. Global pressure dependence of low-temperature carbon oxidation kinetics on non-graphitic chars in the data of **A:** Suuberg et al. [4] for a phenol-formaldehyde resin char, and **B:** Madsen et al.[5] (see also Hecker et al.[6]) for high pressure oxidation of Pittsburgh seam bituminous coal char at various temperatures (triangles: 823 K, circles: 773, diamonds: 748K, squares: 723 K). The straight lines are empirical power-law fits with the best-fit exponent for each curve shown on the graph. The dashed curve shows the single-site Langmuir form, which always undergoes a transition from global first to zeroth order over a factor of 16 in oxygen pressure.

C.4.1 Simple Treatments of Turnover Kinetics on Heterogeneous Surfaces

This section explores the effects of surface heterogeneity on the global kinetics of a general heterogeneous reaction using simple theories of intrinsic and induced heterogeneity.

Intrinsic Heterogeneity

Almost all solid surfaces exhibit site-to-site variations in turnover rates that reflect intrinsic local variations in bonding, composition, or surface nanotopology[12]. This intrinsic heterogeneity appears most notably as variations in activation energies for adsorption, surface reaction, and/or desorption. The simplest model of intrinsic

heterogeneity assumes Langmuir kinetics on parallel, independent reaction sites with a distribution of activation energies. For illustration we consider the effect of a distribution of the desorption energies only, and write the total rate as:

$$R_{global} = \int f(E_{des})R(E_{des})dE_{des} \qquad \text{(C.5)}$$

where R_{global} is the overall rate of gasification, $f(E_{des})$ is the site density distribution, and R is given by Equation C.3 where k_{des} depends on E_{des}, and k_{ads} is a simple rate constant. Figure C.45 shows the pressure dependence predicted by Equation C.5 for Gaussian distributions of E_{des} with various values of the standard deviation, $\sigma_{E\text{-}des}$. As the distribution breadth, $\sigma_{E\text{-}des}$, increases from 0 (the uniform surface) to 80 kJ/mol, the pressure dependence shifts gradually from the Langmuir-type to a linear $logR_{global}$-$logP$ relation. At $\sigma_{E\text{-}des}$ = 20 kJ/mol the R_{gobal}-P relation is adequately approximated by a power law function over about three orders of magnitude in pressure, while at $\sigma_{E\text{-}des}$ = 80 kJ/mol the behavior is indistinguishable from power law kinetics over the entire range of calculation. Whether power-law behavior is observed in practice depends critically on the breadth of the energy distribution, $\sigma_{E\text{-}des}$ for the solid surface in question.

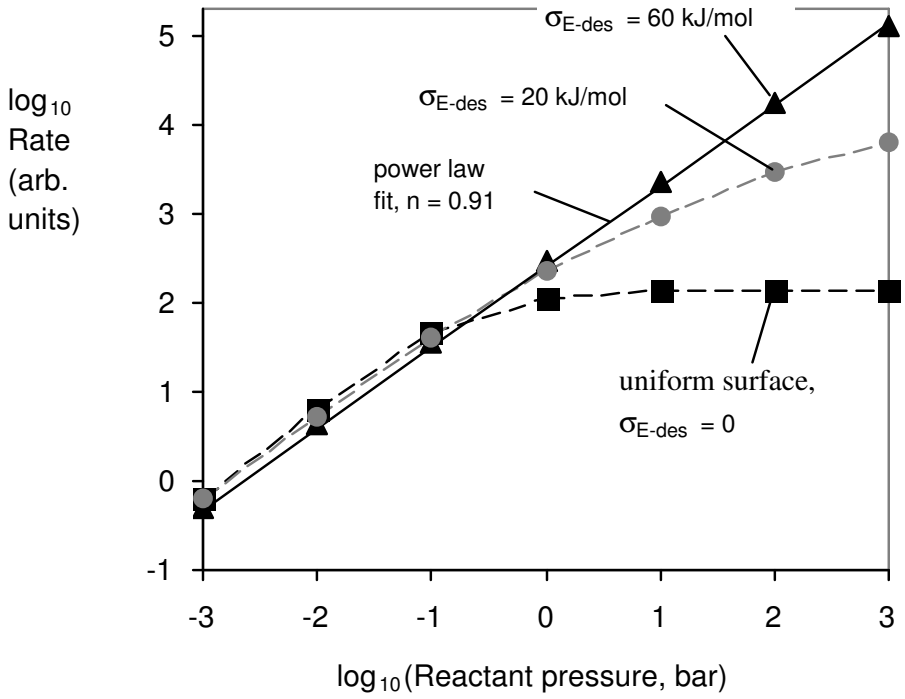

Figure C.45. Behavior of the global reaction rate predicted by simple treatment of generic solid surfaces possessing *intrinsic* site heterogeneity. As the breadth of the desorption activation energy distribution, $\sigma_{E\text{-}des}$, increases, the global behavior gradually shifts from Langmuirian kinetics with its surface-saturated asymptote to a linear $logR_{global}$ vs. $logP$ relationship indicating power-law kinetics.

Induced Heterogeneity

A second form of surface heterogeneity is not intrinsic to the solid phase, but occurs when adsorbed species influence the energetics of surface reactions. Chemisorbed species can alter solid surface properties through electron donation or withdrawal, or can interact with neighboring adsorbed species in either a cooperative or competitive fashion. Chemisorption on one site can either inhibit adsorption on neighboring sites by stearic exclusion or can enhance adsorption on those sites by adsorbate-adsorbate attractive forces [12]. In each case the result is an activation energy for adsorption and/or desorption that varies with surface coverage, θ.

A very simple model describing this induced heterogeneity allows both adsorption and desorption activation energies to vary with coverage according to:

$$E_{ads} = E^o_{ads} + \alpha\theta \; ; \qquad E_{des} = E^o_{des} - \beta\theta \qquad \text{(C.6)}$$

where α and β are parameters. Equating the rates of adsorption and desorption at steady state yields:

$$R_{global} = A_{ads}\, e^{-((E_{o,ads} + \alpha\theta)/RT)} P_{ox}(1-\theta) = A_{des} e^{-((E_{o,des} - \beta\theta)/RT)}\theta \qquad \text{(C.7)}$$

which defines a complete model that for a given set of conditions can be solved numerically for coverage, θ, and then global rate. At α=β=0 this model reduces to the one-site Langmuir form, while Figure C.46 shows that large values of α and/or β give a global behavior that is essentially indistinguishable from power-law kinetics. The global behavior is quite similar to that for intrinsic heterogeneity in Figure C.45, though the mathematical formulations are rather different, Eq. 3 being a statistical relation.

Figure C.46.
Behavior of the global reaction rate predicted by simple treatment of generic solid surfaces possessing *induced* heterogeneity. Parameters α, β describe the coverage-dependence of adsorption and desorption activities energies respectively. As they increase, the global behavior gradually shifts from Langmuirian kinetics to a linear $logR_{global}$ *vs.* *logP* relationship indicating power-law kinetics.

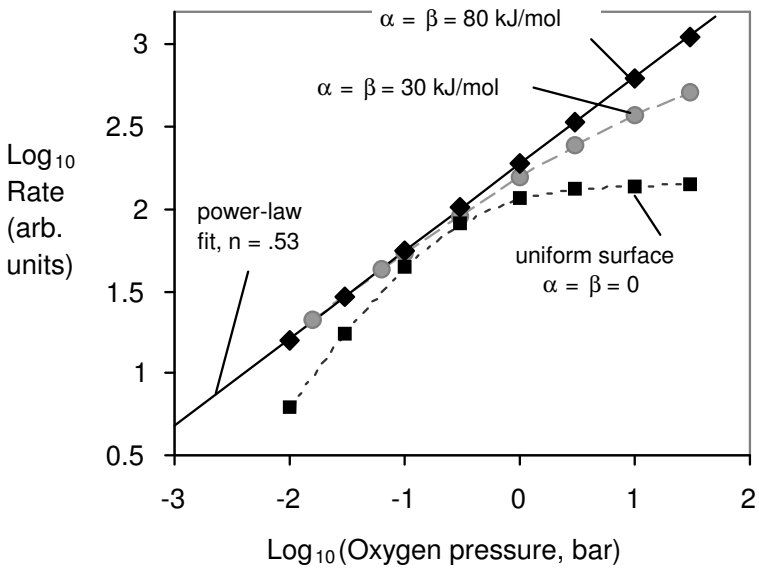

The origin of this power-law behavior imbedded in Equation C.7 can be understood as follows. Adsorption slows sharply as coverage increases, and desorption slows sharply as coverage decreases, so the steady-state coverage, which represents a competition between adsorption and desorption rates, does not easily reach either limiting case (desorption control at $\theta=1$, or adsorption control at $\theta=0$). Rather, the coverage remains at intermediate values over wide ranges of pressure, and the reaction occurs in a stable regime of mixed adsorption/desorption control that yields n^{th}-order kinetics.

C.4.2 Surface Heterogeneity in Carbon Oxidation

The Turnover Model of Haynes

Here we consider a specific formulation for carbon oxidation that has been developed by Haynes and co-workers [10,13] from transient measurements of adsorption and desorption for Spherocarb. This work culminated recently in a turnover model [11] based on the following reaction sequence:

1. $C + O_2 \rightarrow C(O) + CO$
2. $C(O) \rightarrow CO$ (C.8)
3. $C(O) + O_2 \rightarrow C(O) + CO/CO_2$

The Haynes turnover model contains explicit descriptions of site heterogeneity and has been shown to provide a good prediction of Spherocarb burning rates at 2.7 Pa from 873-1073 K[11]. Here we use a pseudo-steady version of this model to explore carbon oxidation kinetic behavior over wide pressure ranges. The key equations in the Haynes turnover model used here are:

$$R_{ads} = A_{ads}\, e^{(-E_{ads}/RT)}\, P_{ox}\, (1-\theta) \tag{C.9}$$

where θ is the fraction coverage and A_{ads} comes from gas kinetic theory as:

$$A_{ads} = S / (2\pi M_{O2} RT)^{1/2} \tag{C.10}$$

The activation energy, E_{ads}, is coverage-dependent according to

$$E_{ads} = a + b\, ln(N) \tag{C.11}$$

where N is the total number of oxides and a and b are parameters. Experimentally determined parameters for Spherocarb are: a = 165 and b = 10.38 for N in mol/kg-carbon and E_{ads} in kJ/mol [11]. The desorption rate is obtained by integration over a distribution of sites of varying desorption activation energy:

$$R_{des} = \int A_{des}\, e^{(-E_{des}/RT)} q(E_{des})\, f(E_{des})\, dE_{des} \qquad \text{(C.12)}$$

where A_{des} is 10^{14} sec^{-1} and the site density $f(E_{des})$ distribution has been determined for Spherocarb by TPD experiments with variable isothermal soak time. The present version adopts a Gaussian form for the distribution, as also assumed in the work of Du et al.[8], with baseline parameters from the Spherocarb studies: mean E_{des} = 300 kJ/mol and σ_{des} = 60 kJ/mol.

At pseudo-steady-state, $R_{ads} = R_{des}$ since the gas-complex reaction step propagates the complex, and the overall gasification rate is:

$$R_{global} = R_{des} + R_{g\text{-}c} \qquad \text{(C.13)}$$

The gas/complex reaction step underlying $R_{g\text{-}c}$ (step 3) is not as well understood as steps 1 and 2. There is evidence of its importance at 2.7 Pa and 870-1080 K, but a reliable assessment of its role in traditional char combustion kinetic experiments at and above atmospheric pressure awaits further experimental data. The present study therefore focuses on the role of heterogeneity in reaction steps 1 and 2, where detailed quantitative treatments of site energy distributions are available from TPD experiments [10]. A minor modification was made to the original Haynes formulation [11] by introducing a total site number as a parameter to facilitate the examination of widely diverse carbon surfaces. A value of 0.85 mol/gm was used for the disordered carbons in this study (a value near the maximum experimental coverage in transient chemisorption data for Spherocarb[11]), while for graphite the parameter was adjusted to fit the data of Tyler as described later.

Figure C.47 shows the Haynes model predictions with the previously determined numerical values for Spherocarb. The steady-state global kinetics follow fractional power-law kinetics (n = 0.78) over the entire numerical range — at least six orders of magnitude in oxygen pressure. In agreement with the previous simple heterogeneous surface model, this model of carbon oxidation predicts persistent n^{th}-order behavior to be a natural consequence of a broad distribution of activation energies. Figure C.47 also shows a series of cases in which the E_a distribution for desorption is artificially narrowed in steps to examine behavior. At half the original breadth (σ = 30 kJ/mol) the persistent n^{th}-order behavior remains, but when the heterogeneity is essentially removed (σ = 0.1 kJ/mol), curvature in the $logR_{global}$ - $logP_{ox}$ space appears. Only when both the desorption and adsorption heterogeneity are effectively removed (σ = 0.1 kJ/mol, b = 0 in Eq. 9) does the model collapse to the simple Langmuir law with its distinct transition from first to zeroth order. The actual distribution breadth for Spherocarb is 60 kJ/mol, and a similar TPD profile has been reported for a low-rank coal char[14], so based on these results persistent power-law behavior would be expected for both of these disordered carbons.

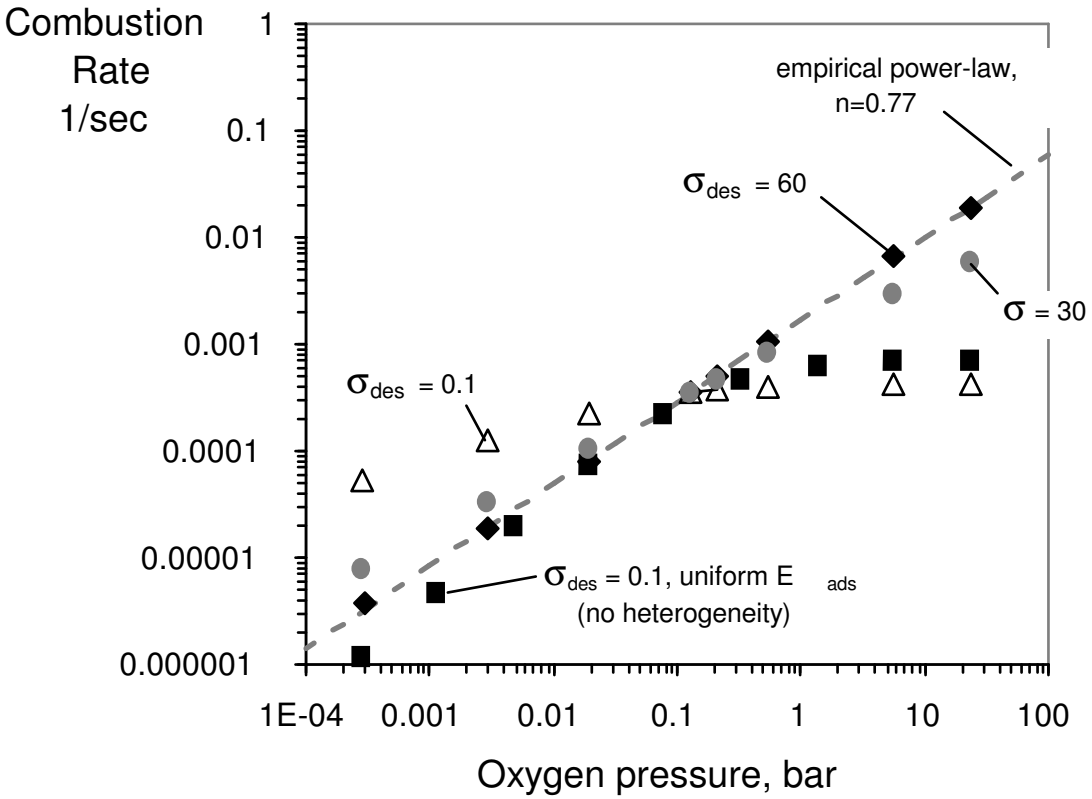

Figure C.47. Oxygen pressure dependence predicted by a pseudo-steady version of the Haynes turnover model[11]. Using the original reported parameters for Spherocarb (σ_{des} = 60 kJ/mol) the predictions follow a global power-law form (n=0.78) over at least 6 orders of magnitude in oxygen pressure. Additional curves give predictions with the original breadth of the desorption activation energy distribution artificially reduced from 60 to 30 to 0.1 kJ/mol. Note the mean desorption activation energy was adjusted to hold the absolute rate fixed at an oxygen pressure of 0.1 bar. The black squares show the Langmuirian behavior only when both adsorption and desorption distributions are narrowed to effectively zero breadth.

Partitioning of $f(E_{des})$ into Three Site Classes

Figure C.48 provides more insight into the origin of the persistent power-law behavior. For each value of E_{des} in the distribution, adsorption and desorption rates can be equated and the resulting local value of coverage, $\theta(E_{des})$, can be used to define three site classes: adsorption limited sites with $\theta \cong 0$, desorption-limited sites with $\theta \cong 1$, and transitional sites with fractional coverage. For this analytical form we define a parameter $E_{0.5}$ as the desorption activation energy on those sites that are exactly half covered $(\theta=0.5)$ at pseudo-steady-state, obtained by solving:

$$A_{ads}\, e^{(-E_{ads}/RT)}\, P_{ox}\, (1-\theta) \;=\; A_{des}\, e^{(-E_{des}/RT)}\, \theta \qquad \text{(C.14)}$$

for E_{des} when θ is 0.5 (see Figure C.48). It can be shown that θ goes from 0.1 to 0.9 over $\Delta E = 4.4RT$ or so the transition zone is conservatively defined as $E_{0.5}$ +/- $3RT$. The contribution

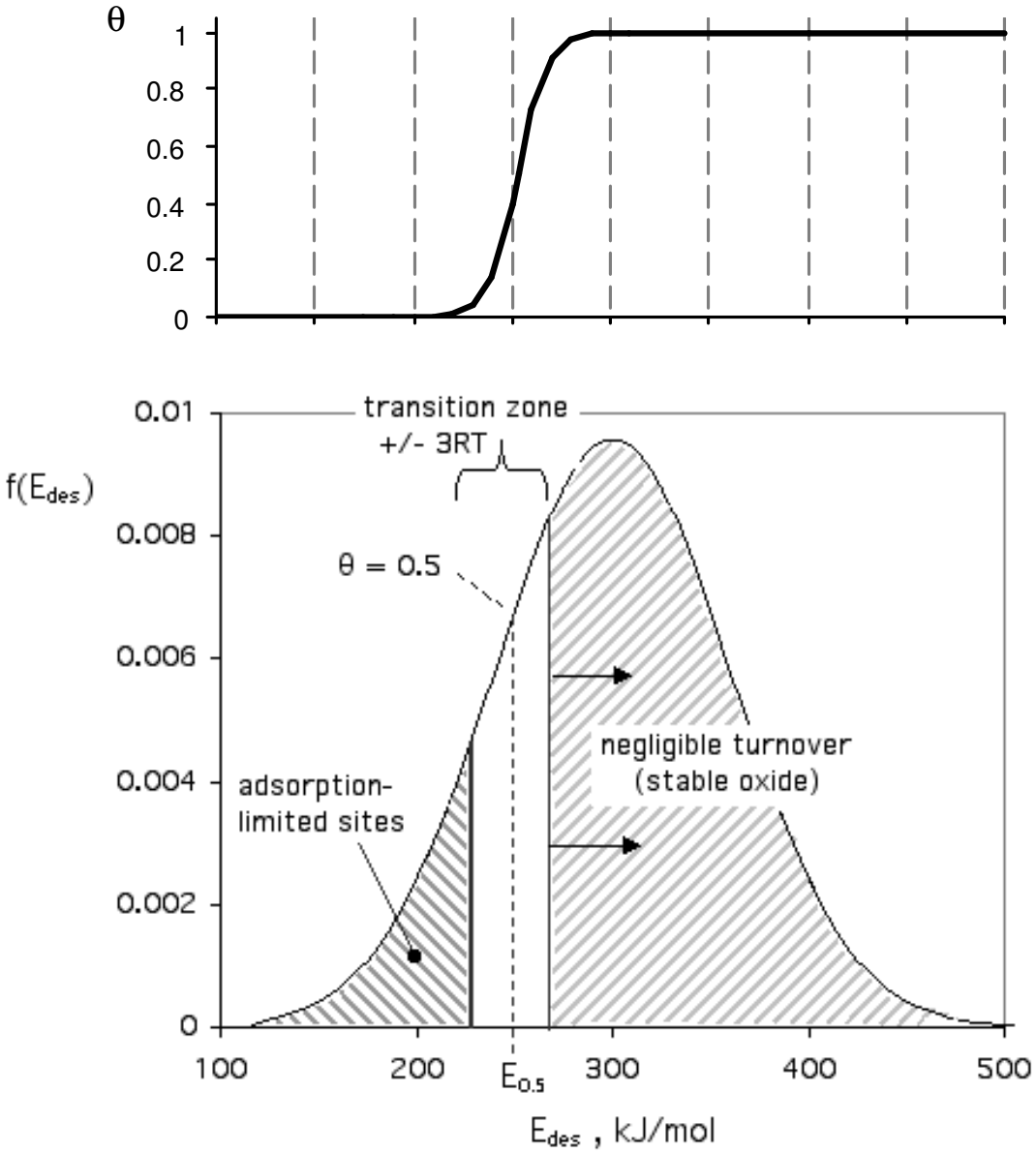

Figure C.48. Distribution of desorption activation energies originally reported for Spherocarb [11]. The distribution curve is labeled to show the various site populations for an example set of conditions (873 K, 0.1 bar O_2). Under these conditions the sites with 50% coverage have desorption activation energies of 253 kJ/mol ($E_{0.5}$ = 253 kJ/mol). The top panel shows coverage, θ, as a function of E_{des}.

to steady gasification from all sites with E above $E_{0.5} + 3RT$ is negligible, and these constitute the abundant stable oxides observed during low-temperature gasification experiments.

The global gasification reaction is thus dominated by two contributions: a first-order contribution on the bare sites in the low-E_{des} tail and a zeroth order contribution on covered sites that is attenuated rapidly as E_{des} increases due to rapidly decreasing reactivity as the stable oxide regime is approached and entered. In practice the fraction of these covered sites that significantly contributes is often small and the result is high fractional order, as observed experimentally (Figure C.43). Finally, since the threshold value, $E_{0.5}$, changes only slowly with oxygen pressure, this physical picture remains unaltered over wide pressure ranges, and persistent fractional order is observed, again in agreement with experiments (Figure C.44).

Derivation of an Approximate Analytical Expression for n_{global}

Since the stable oxide does not turn over at a significant rate, there are two components to steady gasification: (1) first-order adsorption-limited reaction on bare sites with $E < E_{0.5} - 3RT$, and (2) mixed-order reaction on partially covered sites in the transition zone: $E_{0.5} - 3RT < E < E_{0.5} + 3RT$. In the limit of large σ_{des}, the transition zone becomes small relative to the total distribution breadth and can be adequately described as a step function in coverage from 0 to 1 at the threshold value of $E_{0.5}$. This overestimates the rate in the transition zone for both site types, but the errors approximately cancel when the expression is differentiated for reaction order, whose value depends largely on the relative contribution of the two site types to the overall rate. In this limit there are only bare sites $(E < E_{0.5})$ and covered sites $(E > E_{0.5})$ yielding the following two contributions to the overall rate:

$$R_1 = A_{ads} e^{(-E_{ads}/RT)} P_{ox} \int_0^{E0.5} f(E_{des}) \, dE_{des} \qquad \text{(C.15)}$$

$$R_0 = \int_{E0.5}^{\infty} f(E_{des}) \, A_{des} e^{(-E_{des}/RT)} dE_{des} \qquad \text{(C.16)}$$

where R_1 is the first-order component on bare sites and R_0 the zeroth order component on the covered sites and the global rate is

$$R_{global} = R_1 + R_0 \qquad \text{(C.17)}$$

Differentiation of Equation C.17 together with Equations C.15 and C.16 yields, after some algebraic manipulation,

$$\frac{d \ln R_{global}}{d \ln P_{ox}} \equiv n_{global} = \frac{R_1}{R_1 + R_0} - \frac{R_0}{R_1 + R_0} \left(\frac{P_{ox}}{RT} \right) \frac{dE_{ads}}{dP_{ox}} \qquad \text{(C.18)}$$

The second term containing dE_{ads}/dP_{ox} is difficult to simplify but is small under most practical conditions. Ignoring this term, Equations C.15, C.16, and C.18 can be taken together give a working relation for the reaction order. This relation can be greatly simplified by recognizing that the local desorption rate: $A_{des}e^{(-E_{des}/RT)}$ is equal to the local adsorption rate, $A_{ads}e^{(-E_{ads}/RT)}P_{ox}$, at $E_{0.5}$, yielding:

$$n_{global} \approx \frac{1}{1 + (1/A_{<0.5}) \int_{E0.5}^{\infty} f(E_{des})\, e^{((E_{0.5} - E_{des})/RT)} dE_{des}} \qquad \text{(C.19)}$$

Where $A_{<0.5}$ is the area of the E_{des} distribution below $E_{0.5}$. An even simpler form can be written for very broad distributions where $f(E_{des})$ changes slowly compared to $e^{((E_{0.5}-E_{des})/RT)}$. In this case $f(E_{des})$ is approximated as $f(E_{0.5})$ and simple integration yields

$$n_{global} \approx \frac{1}{1 + RTf(E_{0.5})/A_{<0.5}} \qquad \text{(C.20)}$$

where $f(E_{0.5})$ is the height of the distribution at $E_{0.5}$. For the parameters used to generate Figure C.48: $f(E_{0.5})$ = 0.0065 mol/kJ, $A_{<0.5}$ = 0.22, T = 873 K, and Eq. 18 yields n_{global} = 0.82 in good agreement with Eq. 17 (n_{global} = 0.81) and in reasonable agreement with the full theory (n_{global} = 0.78), which requires numerical solution of Equations C.9-C.12 and fitting of the resultant R_{global} - P_{ox} relation with a power law expression.

Application to the Carbon Oxidation Database at T < 1000 K, P > 0.01 Bar

The previous sections demonstrate that surface heterogeneity, whether intrinsic or induced, is capable of explaining the long-standing paradox of power-law kinetics in carbon oxidation. The particular formulation of Haynes [11] is a promising candidate for application to the carbon oxidation database, but the model requires extensive surface characterization, which to date has only been carried out on the model carbon, Spherocarb. The philosophy, however, behind these detailed surface studies on model carbons has always been to identify the correct kinetic *framework,* which can then be extended to other chars in the form of a parameterized engineering model.

The goal of this section therefore is to explore the ability of the Haynes model framework to describe typical data on a range of carbons from the oxidation kinetic database. There is only limited experimental guidance on how best to parameterize the model. Important model parameters most likely to vary from one carbon to the next are the mean and standard deviation of E_{des} and the parameters a and b in Equation C.11 that govern adsorption kinetics. The experiments of Lear[14] show similar temperature programmed desorption spectra for Spherocarb and Loy Yang coal char, with somewhat larger differences in transient chemisorption kinetics. We therefore attempt here to describe the disordered carbon data of Suuberg [4] and Madsen [5] by starting with the Spherocarb parameters and making small adjustments to the adsorption and, if necessary, desorption energy distributions to match the overall rate and pressure dependence.

Figure C.49A compares Haynes model predictions to the Figure C.44A data of Suuberg et al.[4] taken over a factor of 200 in partial pressure. The final parameter set is identical to that for Spherocarb except the parameter "a" in Equation C.11 was reduced from 165 kJ/mol to 152 kJ/mol and the desorption distribution breadth, σ_{des}, decreased from 60 kJ/mol to 45 kJ/mol. Figure C.49B shows the results of similar fits to the coal char data of Madsen et al.[5].

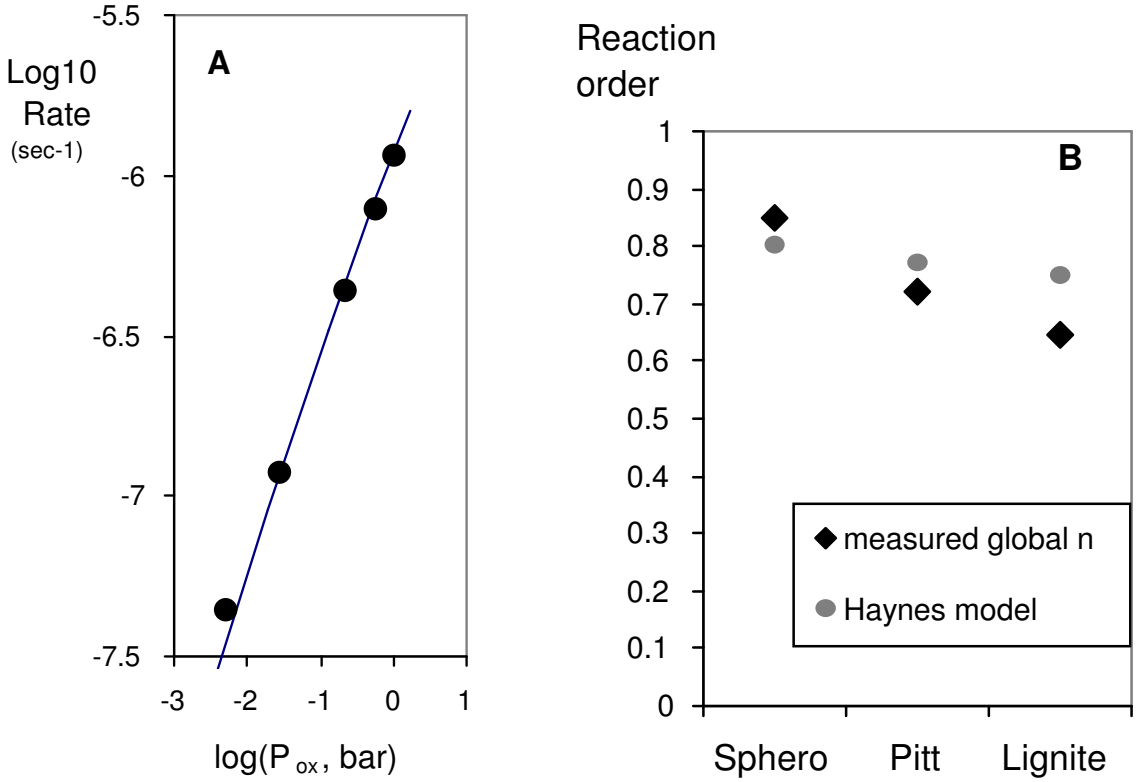

Figure C.49 Example application of the Haynes model framework to the oxidation kinetics of polymer and coal chars. **A.** The persistent power-law behavior observed by Suuberg et al.[4] on a polymer char is well described by the Haynes model with a = 139 kJ/mol in Eq. 9 and σ_{des} = 45 kJ/mol. **B.** Extension to coal char data of Madsen[5], (see also Hecker et al.[6]) by variation in "a" from 153 to 118 kJ/mol. All other parameters are identical to those determined experimentally for Spherocarb[11].

These chars have global kinetic parameters that are similar to those for Spherocarb, though the absolute rates differ greatly. In this case adjustments were made only to parameter "a" (Equation C11) yielding 153 kJ/mol (Spherocarb), 142 kJ/mol (Pitt. coal), and 118 kJ/mol (lignite). All other parameters remain identical to those determined experimentally for Spherocarb. The model successfully predicts slight decreases in global order and activation energy as reactivity increases in the series Spherocarb < Pittsburgh #8 < Lignite char. The fit is not perfect, but the comparison is very encouraging, since only one parameter was adjusted ("a" in Equation C.11) to fit in

essence three data features: the absolute rate, n_{global}, and the pressure dependence of n_{global}. The Haynes model with only small perturbations to the experimental Spherocarb parameters is clearly capable of describing typical low temperature char oxidation data at and above atmospheric pressure.

Another useful modeling target is the graphite data of Tyler et al. [1], who published a particularly thorough study of the reaction order over a wide pressure range (see Figure C.50). The reported reaction orders vary *gradually* with oxygen pressure in a manner that is intermediate between the power-law and Langmuir limiting cases. Lear [14] found that the TPD distribution on Graphon, a highly annealed carbon black, has a similar mean E_{des} to disordered carbon, but is significantly narrower ($\sigma_{E\text{-}des}$ = 35 kJ/mol vs. 60 kJ/mol for Spherocarb and 65 kJ/mol for Loy Yang coal char[14]). Lear also showed that oxygen chemisorption on Graphon is about 10% of that on Spherocarb, per unit mass of carbon. Therefore we attempted here to fit the Tyler global kinetic data starting with the Spherocarb parameters and varying the distribution width, σ_{des}, and the number of active sites per unit mass.

Figure C.50 shows the result. The Haynes model can predict the Tyler et al. reaction orders and their gradual shift with pressure. The same parameters give a good prediction of the global activation energy, (258 kJ/mol vs. 268 kJ/mol measured), and an exact match (by design) to the absolute rate. Here two parameters ($\sigma_{E\text{-}des}$ and $N_{Graphon}/N_{Spherocarb}$) were adjusted to fit four data features: n, the pressure dependence of n, E, and the absolute rate, R. The final parameters were $\sigma_{E\text{-}des}$ = 17 kJ/mol and 0.033 mol-active-sites/kg. The active site number is a factor of 30 below the disordered carbon Spherocarb, which is not unreasonable, while the distribution breadth is significantly smaller than for the disordered chars, as expected. The narrower distribution is responsible for the weak pressure dependence of order (the distribution is not broad enough for full n^{th}-order kinetics) and the generally low orders, which arise from contraction of the low-E_{des} tail, giving a smaller value of $A_{<0.5}$ in Eq. 18 and thus fewer adsorption-limited sites). This fit offers an attractive explanation for the generally lower orders for graphitic carbons relative to disordered carbons in Figure C.43 — it is a natural consequence of reduced heterogeneity in these low-defect-density materials.

Conclusions

A sufficient explanation for the long-standing paradox of persistent, high fractional order in the carbon/oxygen reaction is surface heterogeneity. Simple models of surface heterogeneity, whether intrinsic or induced, predict power-law behavior over wide ranges of partial pressure if the breadth of the activation energy distribution for adsorption and/or desorption is large. The available measurements of desorption activation energy distributions show more than enough breadth for this power-law behavior to be generally expected for non-graphitic carbons, in accordance with experimental observations.

The heterogeneous surface model of Haynes is a promising framework for describing the major features in the low-temperature carbon oxidation database. The Haynes model

with minor perturbations to the original parameters determined experimentally for Spherocarb is capable of describing the rates, reaction orders, and pressure dependence of reaction order for several literature datasets on polymer and coal chars, along with the known existence of stable oxide. The Haynes model is also capable of predicting the lower orders and the gradual change in reaction order with pressure for graphitized carbon black, a behavior that is intermediate between power-law and Langmuirian kinetics. The model predicts these features as the direct consequence of the narrower distribution of site energies for the more homogeneous highly annealed carbon forms.

It is impractical to carry out the detailed surface characterization to fully define heterogeneous surface models for each carbon material of technological interest. Such models do provide, however, much needed theoretical underpinning for the commonly used power-law kinetic form, and the Haynes formulation in particular offers a new framework for the development of robust parameterized engineering models for practical application. More work is needed on the oxide oxidation step, *O_2 + C(O) -> products* before a comprehensive model is available for application to the literature database. This reaction step is likely to be significant at the lowest temperatures of interest, where its kinetics will be superimposed on the power law behavior described here. The oxide oxidation step is likely complex, but is nominally first order in O_2, and its influence may thus provide an explanation for the significant number of unity and near unity orders seen in the literature compilation of Figure C.43.

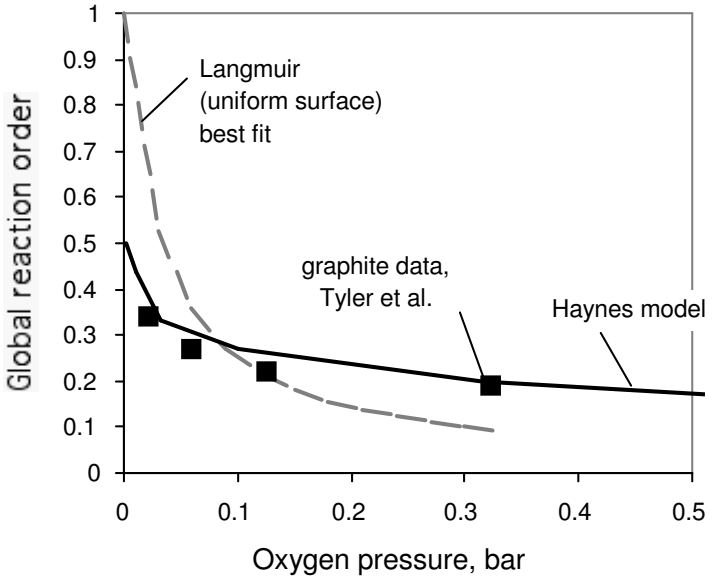

Figure C.50. Graphite oxidation data of Tyler et al. [1] showing reaction order that varies gradually with pressure (closed diamonds), a behavior that is transitional between the single-site Langmuir form (dashed grey curve) and power-law kinetics. The solid curve gives the predictions from the Haynes model with σ_{des} = 18 kJ/mol, and an active site number ratio ($N_{Graphon}$ / $N_{Spherocarb}$ of 1/30). All other parameters were the same as determined experimentally for Spherocarb [11].

C.5 Char Burnout Predictions for HPBO Combustion Tests

C.5.1 CBK/E vs. a Char Oxidation Sub-Model for FLUENT

CBK/E was used to interpret the measured extents of char oxidation from the HPBO test series. Actually, all reactivity parameters for the three coals in this project were previously specified to match the extents of char burnout reported in the NBFZ test series which, depending on the pressure, range from 26% to 58% for Pittsburgh #8; 73% to 81% for Illinois #6; and 92% for PRB. So the HPBO evaluations directly assess CBK/E's predictive capabilities because no parameter adjustments are involved.

C.5.2 Overview of CBK/E

CBK is a kinetics package that describes char oxidation under conditions relevant to pulverized fuel. firing. It has been developed by Hurt and co-workers both at Sandia National Laboratories, Livermore and currently, at Brown University. Detailed publications on the earlier versions of CBK are available (Hurt et al. 1996 & 1998; Sun and Hurt 1997), and the technical basis for the rate expression in CBK/E has been described by Hurt and Calo (2001). The mechanism describes the rate of burning, the char particle temperature, and the changes in the particle diameter as combustion proceeds, given a gas temperature, radiative exchange temperature, and oxygen partial pressure. It is specially designed for carbon burnout applications, because it treats the late stages of char combustion in detail.

Within the theory, char reactivity is a dynamic function of heat treatment severity, based on a distributed activation energy model of thermal annealing. The thermal annealing mechanism acts to destroy active oxidation sites during heat-up and devolatilization, and throughout combustion. The annealing kinetics are so fast that the maximum temperature often determines the extent of reduction of the intrinsic reactivity. The theory uses mass-specific intrinsic kinetics, and earlier versions emphasized the statistical variability of intrinsic char oxidation reactivity. There is a standard model of the reaction/diffusion process within porous char particles, and the "one-film" description of the boundary layer processes which accounts for bulk (Stefan) flow and continuum diffusion but ignores all chemistry in the gas phase. The code also includes a model of the effect of ash inhibition in the late stages of combustion. Together, these mechanisms act to significantly reduce char conversion rates during the later stages of combustion, in accord with observations of very long reaction times for conversion of the last few percentage points of the char mass.

The transport rate of O_2 to the char surface is determined by bulk diffusion through an external boundary layer, in series with pore diffusion through an ash layer that forms over the char surface during the later stages, in series with pore diffusion through the pore system of the carbonaceous char core. These transport mechanisms must balance the consumption of O_2 in the chemical mechanism for oxidation, which was previously represented with an nth-order global rate expression. Now a three-step quasi-global surface reaction mechanism has been incorporated. The interplay among the transport

and chemical reaction mechanisms automatically determines whether burning rates are governed by the chemical kinetics (Zone I), internal pore diffusion (Zone II), or external film diffusion (Zone III). Under typical p. f. firing conditions, this intrinsic formulation quickly shifts from Zone I during the ignition stage to Zone III during quasi-steady combustion at the hottest particle temperatures. As the particle burns, the core of remaining combustible material shrinks, so the burning regime can shift back into Zone I, in which O_2 completely penetrates the internal pore structure and both external film and intraparticle diffusion resistances are negligible.

The intrinsic formulation also allows more accurate extrapolation of the primary high temperature data on which CBK is based to lower temperatures. Although CBK is not specifically designed for predictions far outside the pc-combustion regime, it has been found to yield useful predictions at temperatures as low as 500°C and is reasonably consistent with TGA data. As an option, the theory contains fuel-general correlations for each of the reactivity parameters, so that predictions can be made knowing only the proximate and ultimate analyses of the parent coal.

CBK/E includes all the same transport-related and annealing mechanisms, including single-film char combustion, intraparticle reaction/diffusion, thermal annealing, and ash inhibition. The new three-step intrinsic kinetics resolves the problems in the reaction order for conventional char oxidation kinetics. They are based on the following reactions:

$$\begin{aligned} &1.\ C + O_2 \rightarrow 2C(O) \\ &2.\ C(O) + O_2 \rightarrow CO_2 + C(O) \\ &3.\ C(O) \rightarrow CO \end{aligned} \tag{C.21}$$

The corresponding rate laws for each step are:

$$\begin{aligned} R_1 &= k_1 P_{O_2} (1-\theta) \\ R_2 &= k_2 P_{O_2} \theta \\ R_3 &= k_3 \theta. \end{aligned} \tag{C.22}$$

where θ represents the fraction of sites occupied by the adsorbed oxygen complex, P_{O_2} is the O_2 partial pressure on the carbon surface, and k_1, k_2 and k_3 denote the rate constants for Step 1, Step 2 and Step 3 in Equation C.21, respectively.

These laws can be combined to yield the steady-state expression for the overall oxidation rate and primary CO/CO_2 ratio, which are:

$$r_{gas} = \frac{k_1 k_2 P_{O_2}^2 + k_1 k_3 P_{O_2}}{k_1 P_{O_2} + k_3 / 2} \tag{C.23}$$

$$\frac{CO}{CO_2} = \frac{k_3}{k_2 P_{O_2}} \tag{C.24}$$

An effectiveness factor is required when oxygen transport through the pores becomes a rate controlling mechanism at high particle temperatures. Due to the complexity of the rate law, an analytical solution for the effectiveness factor is not available, so a generalized modulus approach was incorporated into CBK/E (Hong 2000).

In addition to the new intrinsic kinetics, CBK/E also incorporates the following new correlation for coal swelling ratio (Benfell 2001), in which the operating pressure is involved:

$$\begin{aligned} Sw &= Sw_1^{\,0.7143+2.857P_T} && (0.1 \le P_T \le 0.8) \\ &= Sw_1^{\,3.5-0.625P_T} && (0.8 \le P_T \le 4.0) \end{aligned} \qquad \text{(C.25)}$$

where P_T is the total pressure in MPa and Sw_1 represents the swelling ratio at atmospheric pressure, which is evaluated from

$$\begin{aligned} Sw_1 &= 8.67 - 0.0833C_{daf} && (89 \le C_{daf} \le 92) \\ &= -0.0458 + 0.01459C_{daf} && (72 \le C_{daf} < 89) \\ &= 1.0 && (C_{daf} < 72) \end{aligned} \qquad \text{(C.26)}$$

where C_{daf} denotes the DAF carbon content of the parent coal.

All the rate parameters are specified by correlations with the parent coal properties, except for A_{30}, which is denoted as the initial char oxidation reactivity (Niksa et al. 2003). Default values for this parameter are inversely proportional to the fuel's carbon content on a daf-basis. For high rank coals with daf carbon contents above 80 %, the magnitudes of A_{30} for oxidation at atmospheric pressure is only slightly greater than the values for elevated pressures, so that the differences are within the scatter in the assignments for elevated pressure. However, the magnitude of A_{30} for low rank coal oxidation at high pressures is lower than for atmospheric pressures, although most of the cases with low-rank coals were found to be too close to the film diffusion limit for accurate determination of A_{30}. Default values are assigned from

$$\log_{10}(A_{30}) = 12.22 - 0.0535C_{daf} \qquad \text{(C.27)}$$

where C_{daf} denotes the carbon content (%) on a DAF basis.

It is also important to realize that the correlation in Equation 10 can only depict the overall tendency in the initial reactivity for different coal samples, not the sample-to-sample variability. We currently do not know which of the many potential aspects of the composition and morphology of coal and char actually determine the initial char oxidation reactivity. Until the essential nature of this rank dependence has been resolved, models such as CBK/E should be regarded as powerful tools for extrapolating across a wide domain of operating conditions, given sufficient measurements on the burnout of every coal of interest to specify the initial reactivity parameter. In general, a one-point calibration for every sample with either an extent of burnout or loss-on-ignition

measurement for the latest stages of combustion is sufficient to predict char oxidation across a wide domain of operating conditions.

C.5.3 HPBO Database

As originally proposed to DOE, the test program at SRI was subdivided into two coordinated series: (1) the NBFZ series and the HPBO series. NBFZ tests characterized the process chemistry during the first 200 ms for a broad range of stoichiometric ratio (S. R.), while HPBO tests imposed much longer residence times to monitor the latest stages of char burnout at elevated pressure. The flow and thermal conditions within the radiant furnace for NBFZ tests are extremely complex, and could only be assigned with 2-D CFD simulations that incorporated numerous reaction sub-models. To avoid the expense of a second series of CFD simulations for the radiant section of the test facility, all HPBO tests were supposed to be run at the same inlet conditions as NBFZ tests (for which CFD was already available), with additional heated reactor sections downstream to provide the extended residence times.

However, one of the primary objectives of the HPBO test series was the preparation of chars during the latest stages of burnout, to guide the development of flyash formation models for elevated pressures by Prof. Helble at UConn and the development of char oxidation mechanisms by Prof Hurt at Brown. Toward this end, HPBO tests at 0.2 MPa were added for all three coals in this project, even though this pressure was omitted from the NBFZ test series. In addition, HPBO tests with PRB were run at 2.0 MPa, not at the pressure of 1.0 MPa used in the NBFZ tests. HPBO tests with Pit. #8 covered the original NBFZ test domain, as well as many other cases with different suspension loadings and inlet O_2 levels (to achieve very high extents of char burnout).

NEA was able to compensate for some, but not all, of these variations with scaling laws for variable inlet O_2 levels and pressures, as explained in below. Consequently, we could interpret all HPBO tests with Ill. #6 and all but one test with PRP. But it was not possible to repeat the CFD simulations needed to assign the char combustion conditions for various coal suspension loadings, so numerous runs with Pit. #8 had to be excluded.

Qualified Datasets

The entire HPBO database is collected in Table C.10. Each test is described with a coal type; run number assigned by SRI International; pressure; furnace length; and residence time. The furnace length of the radiant section is 15.5 cm, as used for all

Table C.10. HPBO Database.

Run No.	P (atm)	Furnace Length (cm)	Res. Time (ms)	Coal Feed Rate (g/min)	Coal Susp'n Loading (Wt %)	O_2 Conc. (Wt %)	O_2/Coal (Wt. %)	Wt. Loss (%AR)	Retained Ash (Wt%)	Primary Char Yield (Wt%)[a]	C Yield In Char (Wt%)[b]	C-Content of Char (%)[c]	Ash Content of Char (%)[d]	O_2 at exit of (Wt%)
Pittsburgh #8														
180	**2**	**120**	**2676**	**0.74**	**7.6**	**23.5**	**309**	**89.0**	**64**	**11**	**4.0**	**26.0**	**72.8**	**6.9**
183	2	88	1956	0.66	6.8	19.1	282	91.0	66	9.0	1.1	8.5	90.9	4.0
197	2	56	1244	0.62	6.4	20.3	319	89.4	59	10.6	4.5	29.6	69.1	6.5
198	2	15.5	344	0.68	7.0	19.8	282	82.8	43	17.2	17.0	68.6	30.4	6.0
199	2	15.5	172	1.44	7.5	19.8	264	74.9	64	25.1	24.1	67.8	31.4	6.2
200	**2**	**15.5**	**115**	**2.25**	**7.9**	**22.9**	**290**	**72.2**	**90**	**27.8**	**23.3**	**59.1**	**40.0**	**8.6**
206	2	15.5	86	2.83	7.4	20.3	275	64.9	63	35.1	38.2	76.7	22.1	9.0
226	**2**	**88**	**1977**	**0.75**	**7.6**	**20.3**	**266**	**90.0**	**42**	**10.0**	**6.6**	**46.3**	**51.6**	**4.0**
173	**10**	**120**	**4000**	**1.72**	**5.4**	**19.5**	**365**	**96.7**	**20**	**3.3**	**1.3**	**26.6**	**72.9**	**7.5**
190	**10**	**89**	**2967**	**1.52**	**4.7**	**17.0**	**361**	**88.9**	**67**	**11.1**	**3.8**	**24.4**	**75.1**	**6.7**
204	**10**	**15.5**	**129**	**5.97**	**4.7**	**20.0**	**431**	**86.4**	**33**	**13.6**	**13.3**	**13.3**	**30.0**	**11.0**
207	10	15.5	129	9.75	7.6	22.8	300	74.5	70	25.5	23.4	64.8	34.1	8.8
208	10	15.5	172	7.86	8.2	17.8	217	68.2	69	31.8	32.5	72.0	26.9	5.7
209	10	15.5	258	5.14	8.0	19.9	247	77.8	84	22.2	16.7	52.8	46.4	5.5
210	10	15.5	517	2.53	7.9	21.6	275	78.1	53	21.9	21.6	69.2	29.6	8.1
221	10	56	1867	2.52	8.0	24.2	303	88.2	68	11.8	4.9	29.1	70.4	7.3
223	10	89	2967	2.53	7.9	21.4	271	89.4	36	10.6	8.6	57.4	41.6	5.6
169	**20**	**120**	**4000**	**1.76**	**2.72**	**14.6**	**538**	**92.0**	**49**	**8.0**	**2.8**	**24.6**	**74.9**	**8.7**
191	**20**	**89**	**2967**	**1.59**	**2.45**	**13.4**	**548**	**91.6**	**67**	**8.4**	**0.2**	**1.6**	**98.3**	**7.9**
205	**20**	**15.5**	**517**	**1.63**	**2.51**	**16.1**	**643**	**93.7**	**49**	**6.3**	**0.4**	**4.2**	**95.4**	**10.6**
211	20	15.5	517	3.29	5.07	14.0	276	81.6	57	18.4	Na	Na	Na	4.8
212	20	15.5	259	6.39	4.92	16.1	326	81.7	42	18.3	na	na	na	7.7
213	20	15.5	259	6.17	4.73	9.9	209	68.0	75	32.0	34.3	71.2	27.2	3.1
214	20	15.5	518	3.24	4.97	14.2	286	81.1	66	18.9	15.1	56.3	42.9	5.2
218	**20**	**56**	**1867**	**1.55**	**2.32**	**5.53**	**239**	**82.7**	**66**	**17.3**	**12.8**	**52.3**	**46.9**	**1.0**
225	**20**	**89**	**2967**	**1.52**	**2.28**	**5.54**	**243**	**87.7**	**48**	**12.3**	**9.0**	**51.5**	**47.8**	**1.0**
193	**30**	**89**	**2967**	**1.61**	**1.63**	**8.26**	**506**	**93.1**	**55**	**6.9**	**0.1**	**1.0**	**98.9**	**4.6**
194	**30**	**56**	**1867**	**1.65**	**1.67**	**9.38**	**562**	**90.6**	**73**	**9.4**	**0.3**	**2.4**	**95.7**	**5.6**
215	30	15.5	517	5.04	5.14	10.7	208	75.0	88	25.0	19.6	55.3	43.6	2.2
217	**30**	**56**	**1867**	**1.53**	**1.52**	**3.44**	**226**	**82.9**	**47**	**17.1**	**15.8**	**65.0**	**34.2**	**0.7**
224	**30**	**89**	**2967**	**1.50**	**1.50**	**3.32**	**222**	**80.2**	**55**	**19.8**	**18.2**	**64.6**	**34.3**	**0.6**

Table C.10, Cont'd. HPBO Database.

Run No.	Pressure (atm)	Furnace Length (cm)	Res. Time (ms)	Coal Feed Rate (g/min)	Coal Susp'n Loading (Wt %)	O_2 Conc. (Wt %)	O_2/Coal (Wt. %)	Wt. Loss (%AR)	Retained Ash (Wt%)	Primary Char Yield (Wt%)[a]	C Yield In Char (Wt%)[b]	Carbon Content of Char (%)[d]	Ash Content of Char (%)[e]	O_2 content At exit of Flowtube (Wt%)
Illinois #6														
298	**2**	**15.5**	**172**	**1.73**	**8.27**	**25.7**	**311**	**90.8**	**25.9**	**9.2**	**7.44**	**50.2**	**49.1**	**10.3**
297	**2**	**15.5**	**344**	**0.87**	**9.01**	**23.9**	**265**	**89.6**	**25.2**	**10.4**	**9.55**	**56.9**	**42.3**	**7.07**
290	**2**	**56**	**622**	**1.73**	**8.01**	**20.9**	**261**	**90.4**	**49.1**	**9.6**	**1.51**	**9.8**	**89.5**	**4.90**
288	**2**	**56**	**1244**	**0.86**	**8.30**	**23.3**	**281**	**87.9**	**44.4**	**12.1**	**6.60**	**33.6**	**63.7**	**7.61**
296	**2**	**88**	**1600**	**1.06**	**8.94**	**24.3**	**272**	**91.1**	**48.0**	**8.9**	**0.81**	**5.6**	**93.9**	**6.4**
286	**2**	**88**	**1956**	**0.87**	**8.37**	**21.2**	**254**	**91.1**	**50.1**	**8.9**	**0.27**	**1.9**	**97.9**	**4.5**
287	**2**	**88**	**1956**	**0.88**	**8.69**	**25.9**	**298**	**92.9**	**36.1**	**7.1**	**1.11**	**9.7**	**89.2**	**9.8**
299	**20**	**15.5**	**517**	**1.50**	**2.17**	**5.22**	**241**	**78.5**	**43.7**	**21.5**	**22.0**	**63.3**	**35.5**	**1.9**
292	**20**	**56**	**1244**	**2.25**	**2.18**	**5.94**	**273**	**86.3**	**54.6**	**13.7**	**6.6**	**29.8**	**69.4**	**1.8**
291	**20**	**56**	**1867**	**1.50**	**2.17**	**5.51**	**254**	**89.3**	**54.3**	**10.7**	**2.01**	**11.6**	**88.0**	**1.3**
295	**20**	**88**	**2400**	**1.83**	**2.22**	**5.44**	**245**	**87.6**	**67.8**	**12.4**	**0.88**	**4.4**	**95.4**	**1.0**
294	**20**	**88**	**2933**	**1.50**	**2.16**	**5.72**	**264**	**93.1**	**39.6**	**6.9**	**0.03**	**0.23**	**99.6**	**1.4**
285	**20**	**88**	**2933**	**1.47**	**2.00**	**15.48**	**774**	**91.8**	**47.0**	**8.2**	**0.06**	**0.45**	**99.5**	**11.4**
PRB Subbituminous														
264	**2**	**15.5**	**115**	**2.49**	**9.62**	**19.1**	**198**	**83.4**	**64**	**16.6**	**18.9**	**80**	**19.3**	**2.8**
265	**2**	**15.5**	**172**	**1.67**	**8.7**	**17.4**	**199**	**86.5**	**60**	**13.5**	**14.9**	**77**	**22.3**	**2.0**
266	2	15.5	344	0.83	9.7	23.1	237	97.3	20	2.7	2.4	62	37	3.3
272	**2**	**56**	**622**	**1.66**	**8.2**	**17.8**	**218**	**96.4**	**34**	**3.6**	**2.6**	**51**	**47**	**1.5**
271	**2**	**56**	**1244**	**0.83**	**7.9**	**17.4**	**220**	**98.4**	**24**	**1.6**	**0.5**	**21**	**78**	**1.3**
273	**2**	**88**	**1956**	**0.83**	**8.3**	**19.5**	**235**	**98.6**	**26**	**1.4**	**0.1**	**7**	**93**	**2.1**
267	**20**	**15.5**	**517**	**1.5**	**2.15**	**5.0**	**232**	**81.2**	**83**	**18.8**	**20.3**	**76**	**22**	**1.5**
270	**20**	**56**	**1244**	**2.25**	**2.2**	**4.5**	**204**	**90.8**	**54**	**9.2**	**9.0**	**69**	**29**	**0.4**
269	**20**	**56**	**1867**	**1.5**	**2.18**	**4.16**	**191**	**94.6**	**46**	**5.4**	**4.2**	**55**	**43**	**0.2**
275	**20**	**88**	**2933**	**1.5**	**2.25**	**8.0**	**355**	**94.2**	**75**	**5.8**	**2.6**	**32**	**65**	**3.4**
276	**20**	**88**	**2933**	**1.5**	**2.17**	**17.1**	**790**	**98.1**	**37**	**1.9**	**0.02**	**0.9**	**99**	**12.5**

[a]Primary char yield on an as-received basis. Equals total char weight divided by total coal sample weight. [b]Percent of carbon in coal sample retained in char. [c]Percent of char that is carbon and [d]percent of char that is ash from Huffman analysis.

NBFZ tests. Longer lengths consist of modular units heated uniformly to 1400°C by Kanthal heating elements attached to the same radiant section. Residence times in Table C.10 are nominal values based on the inlet flow rate and reactor cross section. These values do not account for the lower gas densities at the elevated flame temperatures, and are therefore several times longer than the actual residence times. Better estimates are presented below. Table C.10 also reports coal feed rates; nominal suspension loadings (which do not account for segregation of most particles into wall layers); the inlet O_2 concentrations; and mass ratios of O_2/coal. The reported measurements comprise values for the following variables at the reactor exit, after cold gas quenching: weight loss on an as-received basis; the percentage of coal ash recovered with char particles; char yields on an as-received basis (100-Wt. Loss); char combustibles yield, which is one minus the extent of coal burnout; carbon and ash contents of char; and the residual O_2 concentration.

Runs accepted for detailed interpretation appear in boldface type in Table C.10. The determining factor to exclude tests was the suspension loading. Consequently, all runs with Pit. #8 at 1.0, 2.0, and 3.0 MPa that had much higher loadings that those in the corresponding NBFZ tests were excluded. In addition, most runs at 0.2 MPa were excluded because no CFD was available for this pressure, and these cases are included for illustrative purposes only. In contrast, all the loadings imposed with Illinois #6 and PRB were close enough to those in the corresponding NBFZ tests, so only one run was excluded from these datasets.

The primary conversion index is the burnout expressed on the basis of the combustibles in the whole coal, X_{COAL}, which is obtained by subtracting the values in the twelfth column of Table C.10 from unity. This index is related to the more conventional extent of char burnout as follows:

$$X_{COAL} = W^{\infty} + Y_{CHAR} X_{CHAR} \qquad \text{(C.28)}$$

Extents of char burnout predicted by CBK/E will be combined with ultimate volatiles yields to assign extents of coal burnout for direct comparison with the measured values.

C.5.4 Assigning HPBO Operating Conditions

The extent of coal burnout from each qualified HPBO test will be compared with a prediction from CBK/E. Each CBK/E simulation requires the parent coal properties and particle size, thermal histories for gas and ambient (wall) temperatures, plus an O_2 concentration history. Since the testing deliberately emphasized cases with extended residence times to achieve very high extents of burnout, we will approximate several aspects of the reaction system which are deemed to be less important for the final stages of burnout, as follows: First, devolatilization is omitted from the simulations, and replaced by a time lag for heat-up and a measured ultimate weight loss for each coal and pressure. This procedure introduces no uncertainty, but circumvents serious numerical stability issues for cases with the highest inlet O_2 concentrations. Second, the complex and diverse gas temperature field within the radiant section is represented with a single

mean gas temperature history specified as that assigned for the boundary layer in NEA's CNPP simulations of the corresponding NBFZ test. Third, the reactor sections downstream of the radiant section are modeled as isothermal plug flow reactors at 1400°C. Fourth, the wall temperature history, to evaluate radiant fluxes from the burning char particles, is uniform throughout the entire system at 1400°C. Fifth, the O_2 concentration history is assigned for the boundary layer in NEA's CNPP simulations of the corresponding NBFZ test, with additional adjustments for different inlet O_2 levels. Many additional aspects and consequences of these approximations will be explained in succeeding sections.

Assigning Thermal Histories

The gas and wall temperature profiles downstream of the radiant section really are near-isothermal, because these section operate uniformly at 1400°C and the inlet temperature of the gas stream is close to this value in most runs. All the complexity is within the radiant section. The CFD simulations of the NBFZ tests revealed two primary flow paths through the radiant section, a very hot wall layer with most of the particles and a cooler central core carrying a very dilute particle suspension. Since only a single gas thermal history can be imposed in a CBK/E simulation, we use that for the denser suspension in the wall layer.

NEA's CNPP analysis was used to assign the structure of the wall layer flows for all NBFZ tests. A case for a near-stoichiometric test with Pittsburgh #8 appears in Figure C.51. In counterclockwise order from the upper left, the four panels of this figure display the variation in gas temperature and S.R. values for the gas phase only; the mass fractions of O_2 and CO; the extent of burnout of char and soot; and the mass concentrations of the major N-species. The S.R. values do not include the combustibles in either soot or char and therefore indicate the oxidation potential for the gas phase chemistry. Each parameter is plotted versus the mean residence time. For this particular test, devolatilization is completed within 134 ms, and
the flow leaves the reactor at 158 ms.

The gas temperature increases gradually and approaches a maximum of 1540°C at 105 ms, then decreases to 1150°C at the exit of the reactor. The S.R. value for the gas phase begins at infinity (because no fuel vapor is present at the inlet), then falls quickly while volatiles are released into the flow, making it less oxidizing. But it does not ever cross the threshold for reducing conditions despite the abundant yield of volatiles from this coal, because a very large portion of volatiles are converted into soot, which does not factor into the S.R. value for the gas phase. Significant amounts of volatiles are released when the gas temperature is roughly 1300°C, based on the decay in the O_2 concentration. The O_2 concentration is depleted at about 120 ms. Char competes very effectively with the gaseous fuel compounds for the available O_2 at the beginning, due to the very rapid burning rates of the smallest char particles in the PSD. The char ignites even in the first reactor of the CSTR-series, where the gas temperature is 870°C. An ultimate char burnout of 67.1% is achieved at 110 ms when O_2 is depleted.

In this case there is a lag of about 70 ms before significant volatiles combustion, while the particles are heated to the threshold temperature for ignition. Also note that char ignites even before volatiles, and burns along with volatiles until nearly all the O_2 has been consumed. Since the devolatilization stage will not be resolved in the CBK/E simulations, we will impose a lag to account for the heating time. In the assigned gas temperature history for this case, a lag for devolatilization of 50 ms would be followed by a temperature ramp from 1185°C to the maximum of 1550°C in 60 ms. Thereafter, the gas temperature would gradually relax to 1400°C after an additional 25 ms, and remain isothermal for all succeeding residence time. The gas temperature continues to cool in the NBFZ simulations because no isothermal reactor modules were included in the analysis.

Wall temperature histories are uniform at 1400°C, which is the calculated normal operating temperature of the inner flow tube in the radiant section, and the actual operating temperatures of all succeeding reactor modules in the tests.

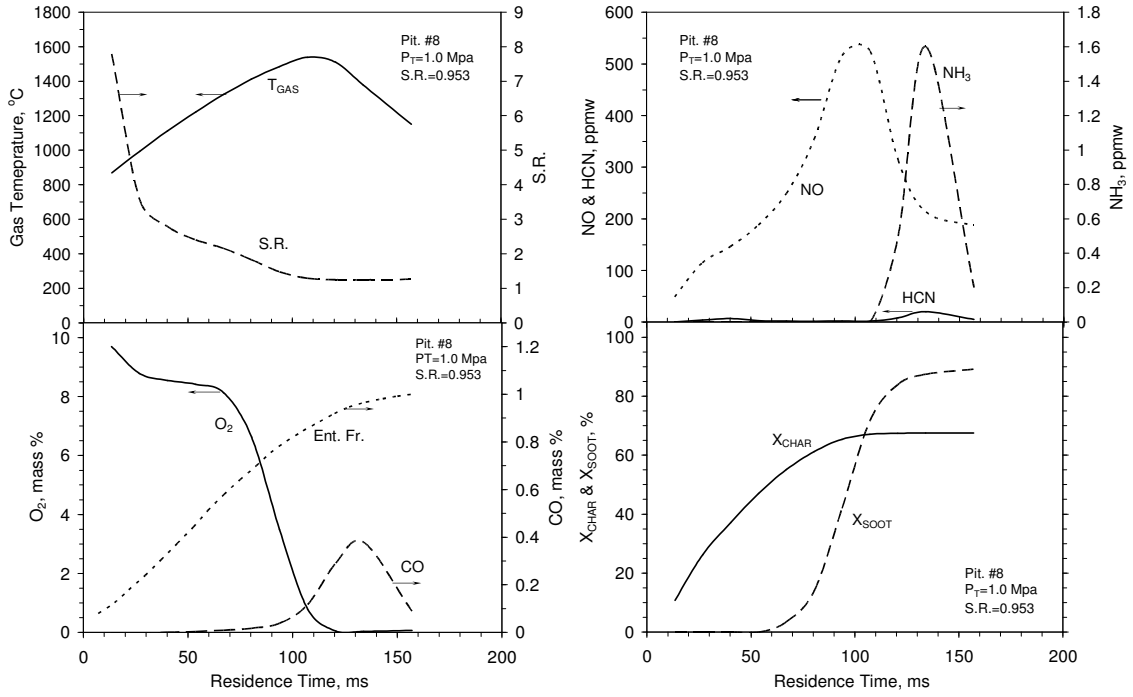

Figure C.51. Structure of the boundary layer of the baseline Run 51C for a Pit. #8 flame at 1.0 MPa showing, in counterclockwise order from the upper left, the operating conditions, major species, char and soot burnout, and N-species.

Assigning O_2 Concentrations Histories

The key feature in the O_2 concentration history in Figure C.51 is the steep decay during simultaneous combustion of volatiles and char. Magnitudes of the decay were taken

directly from the NBFZ simulations; for the example in Figure C.51, a value of 7.3% was assigned. For cases in which the inlet O_2 level, O_2/coal ratio, or pressure was different from the closest NBFZ conditions, the raw reduction in the O_2 concentration was re-scaled. To complete the concentration history, the assigned value at the outlet of the radiant section is gradually relaxed to the measured value in the flue gas from the test. Usually the difference between these respective outlet values was well below 0.5 % because most char burned in the radiant section.

Scalings for Variable Operating Conditions

Coal suspension loadings are primary influences on the partitioning of the inlet coal flow into wall layer and core flows within the radiant section. This behavior could have been characterized with CFD simulations, but not within the original scope of this project. So we do not know how to re-scale the operating conditions in the radiant section for variations in the suspension loading. But information was recorded to re-scale the magnitude of O_2 consumption in the radiant section for variations in pressure and the inlet O_2 concentration. We propose that the change in the O_2 concentration within the radiant section is inversely proportional to both pressure and to the inlet O_2 level, so that

$$\Delta y_{O_2}(p_2) = \left(\frac{p_1}{p_2}\right) \frac{\left(\frac{O_2}{Coal}\right)_{p_1}}{\left(\frac{O_2}{Coal}\right)_{p_2}} \left(\frac{F_{Coal}(p_2)}{F_{Coal}(p_1)}\right) \Delta y_{O_2}(p_1) \qquad \text{(C.29)}$$

where Δy_{O2} is the change in the O_2 mass fraction; subscripts 1 and 2 denote baseline and new conditions, respectively; and the dependences on pressure, p, mass ratio of O_2 to coal, and the coal feed rate, F_{Coal}, are explicit. This expression gives estimates that are quantitatively consistent with the measured flue gas O_2 levels for wide ranges of inlet O_2 concentrations.

Thermal histories for the wall layer flows in the NBFZ tests were available for all HPBO cases at 1.0, 2.0, and 3.0 MPa, except for the PRB tests at 2.0 MPa. The estimate for the PRB test was made by first comparing the near-stoichiometric cases at 1.0 MPa for Pittsburgh #8 and PRB, which showed temperatures higher by 40 – 100°C with PRB during the initial stages, but nearly the same temperatures after 70 ms. Consequently, the thermal history for Pittsburgh #8 was increased by up to 45°C to estimate the initial thermal history for PRB at 2.0 MPa, then the original history was applied for times after 90 ms.

In a similar way, thermal histories for tests at 0.2 MPa (for which no CFD was available) were estimated by first comparing cases at 1.0 and 2.0 MPa to determine that thermal histories were hotter by roughly 135°C for this reduction in pressure. The thermal history for Pittsburgh #8 at 0.2 MPa was assigned by reducing the calculated history for 1.0 MPa by this amount. Comparable reductions were applied to the other coals, except that the histories for PRB and Illinois #6 were kept 50 and 75°C cooler than the comparable cases with Pittsburgh #8, consistent with their calculated thermal histories at 1.0 MPa for near-stoichiometric conditions.

The nominal residence times in Table C.10 are re-scaled for the uniform operating temperature of 1400°C in the extended reactor modules as follows:

$$\tau = (\tau_0 - 0.10)\frac{273}{1673} + 0.10 \qquad \text{(C.30)}$$

where τ_0 is the tabulated residence time. The factor of 0.1 appears because the nominal residence time in the radiant section is roughly 100 ms for all cases.

Assigned HPBO Operating Conditions

The assigned changes in the O_2 mass fractions for the qualified database are collected in Table C.11. The run numbers listed in each row have similar operating conditions, so that one CBK/E simulation was applied to all these cases. Only the residence times when the extent of coal burnout was evaluated differ among these tests in our evaluation. The assigned O_2 consumptions decrease for progressively higher pressures, and are usually similar for all cases at the same pressure with a specified coal.

Table C.11. Assigned O_2 consumption for the qualified HPBO database.

Coal	P, MPa	Runs	Inlet O_2	Δy_{O2}
Pit. #8	0.2	200,226,180	0.180	0.130
	1.0	204,190,173	0.180	0.090
	2.0	218,225	0.055	0.045
		205,191,169	0.146	0.048
	3.0	217,224	0.033	0.023
		194,193	0.083	0.033
Ill. #6	0.2	290,286	0.210	0.163
		298,287,288,296,287	0.246	0.160
	2.0	299,292,291,295,294	0.056	0.042
		285	0.155	0.041
PRB	0.2	264,265,272,271,273	0.180	0.130
	2.0	267,270,269	0.045	0.035
		275	0.080	0.035
		276	0.171	0.033

The assigned histories for gas temperature and O_2 concentration appear in Figure C.52. These cases show the operating conditions for the highest inlet O_2 mass fraction at each pressure. Gas temperatures within the radiant section become much hotter than the 1400°C isothermal sections downstream for 0.2 and 1.0 MPa, but not for the higher test pressure. This is another consequence of high gas densities at higher pressures, which increases the sensible enthalpy requirements for gas heating accordingly. The O_2 mass fraction histories decay at similar rates at 0.2 and 1.0 MPa, but the O_2 consumption is much lower at 1.0 MPa, as expected. These concentrations decay on the much slower time scales for gas heating at the higher test pressures. The assigned operating conditions

for the other inlet O_2 mass fractions and for the other coals exhibit these same tendencies, but for the different O_2 consumptions indicated in Table C.11.

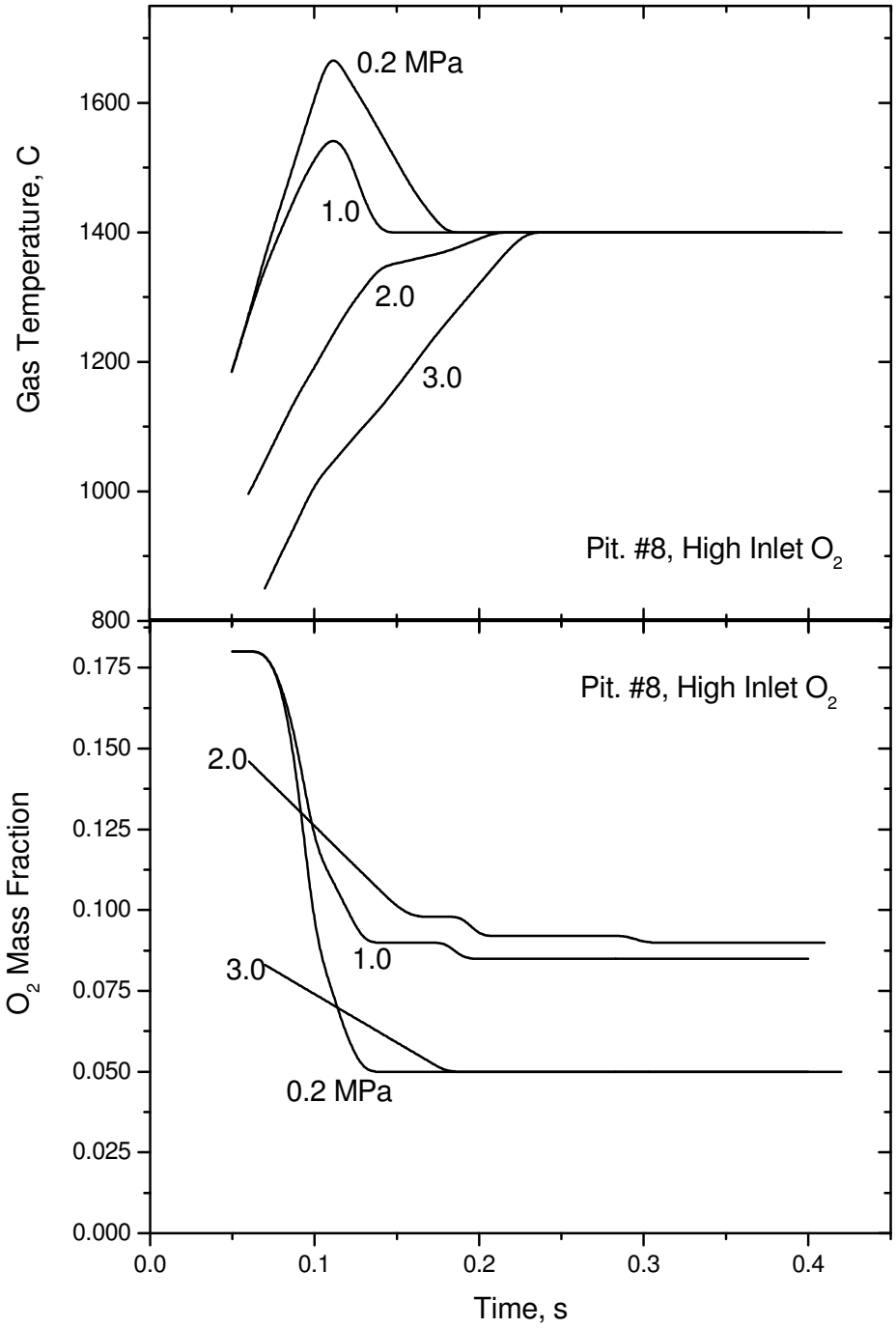

Figure C.53. Assigned histories for gas temperature (top) and O_2 mass fraction (bottom) for tests with Pit. #8 at high inlet O_2 mass fractions.

The ultimate weight losses were 52.9, 52.4, and 47.6 DAF wt. % for Pit. #8, Ill. #6, and PRB, respectively, based on the measured values from the NBFZ tests with the smallest O_2 levels. These values were applied to all test pressures, which is probably a slight underestimation for 0.2 MPa, but not for the other cases.

C.5.5 Interpreting HPBO Conversion Data

The operating conditions were implemented in CBK/E simulations using PC Coal Lab® without further adjustments. The initial char oxidation reactivities were set to the values assigned to interpret char conversion during the NBFZ tests, which were 1.31 $x10^7$ s^{-1} for Pittsburgh #8; 8.96$x10^7$ s^{-1} for Illinois #6; and 9.19$x10^7$ s^{-1} for PRB. Hence, no model parameters were adjusted to improve the fit in any of the HPBO test evaluations.

The predicted extents of coal burnout are compared to measured values in Table C.12. The test runs are grouped according to coal type, pressure, then inlet O_2 concentration. Within each group, they are arranged in order of increasing residence time, which were evaluated with eq. 13 to account for the impact of gas heating. Residence times range from 100 to over 700 ms, which are shorter by a factor of 6 than the cold-flow values in Table C.10. The predicted extents of char burnout obtained directly from the CBK/E simulations appear in the last column. These values were converted to extents of coal burnout with Equation C.28 and the ultimate volatiles yields for direct comparison with the measured values. The tests cover the last quarter of burnout for all three coals, which corresponds to roughly the last 50 to 60% of char burnout. These ranges complement the extents of char burnout recorded in the NBFZ tests, and illustrate the behavior during the later stages of burnout, as originally intended.

The measured conversions generally increase for progressively longer times, except for the tests with Pittsburgh #8 at the highest inlet O_2 at 2.0 MPa and at the lowest inlet O_2 at 3.0 MPa, and with Illinois #6 at the highest inlet O_2 at 0.2 MPa. The parity plot in Figure 2-3 illustrates the accuracy for each coal individually. The data for Pittsburgh #8 cover the broadest range of coal burnout, for which the predictions are uniformly accurate throughout. The worst discrepancy is for the data at 3.0 MPa that did not exhibit the correct dependence on residence time. The extents of burnout for the Illinois #6 are overpredicted by up to 7 % for extents of burnout under 90%, but there are only two measured values in this range. The worst performance is for PRB for extents of burnout under 90 %, which is not surprising because no NBFZ CFD simulations were available for either pressure in these HPBO tests. Even so, the predictions for the last 10 % of coal conversion are reasonably accurate for PRB and for both other coals. Considering that none of the reactivity parameters in CBK/E were adjusted, and that the thermal and O_2 concentration histories were estimated rather than simulated with CFD, the performance in Figure C.53 is satisfactory.

Table C.12. Evaluation of predicted coal burnout for all qualified HPBO tests.

Run No.	P, MPa	Inlet O_2	τ, s	X_{COAL}		X_{CHAR}
				Measured	Predicted	Predicted
Pittsburgh #8						
200	0.2	0.180	0.10	0.767	0.830	0.635
226			0.41	0.934	0.899	0.785
180			0.52	0.960	0.924	0.839
204	1.0	0.180	0.11	0.867	0.839	0.655
190			0.57	0.962	0.983	0.963
173			0.74	0.987	0.990	0.979
218	2.0	0.055	0.39	0.872	0.856	0.695
225			0.74	0.910	0.921	0.831
205	2.0	0.146	0.17	0.996	0.909	0.805
191			0.57	0.998	0.996	0.991
169			0.74	0.972	0.999	0.998
217	3.0	0.033	0.39	0.842	0.813	0.604
224			0.57	0.818	0.901	0.789
194	3.0	0.083	0.29	0.997	0.941	0.873
193			0.57	0.999	0.994	0.987
Illinois #6						
290	0.2	0.210	0.19	0.985	0.982	0.962
286			0.40	0.997	0.991	0.991
298	0.2	0.246	0.12	0.926	0.957	0.910
297			0.14	0.904	0.976	0.949
288			0.29	0.934	0.992	0.984
296			0.35	0.992	0.995	0.989
287			0.40	0.989	0.996	0.992
299	2.0	0.056	0.17	0.780	0.863	0.713
292			0.29	0.934	0.959	0.913
291			0.39	0.980	0.978	0.954
295			0.48	0.991	0.983	0.964
294			0.56	0.999	0.987	0.973
285	2.0	0.155	0.56	0.998	1.000	1.000
Wyodak PRB						
264	0.2	0.180	0.10	0.811	0.981	0.961
265			0.11	0.851	0.987	0.973
272			0.19	0.974	0.986	0.971
271			0.29	0.995	0.984	0.987
273			0.40	0.999	0.998	0.996
267	2.0	0.045	0.17	0.797	0.707	0.437
270			0.29	0.910	0.867	0.721
269			0.39	0.958	0.938	0.880
275	2.0	0.080	0.56	0.974	0.999	0.999
276	2.0	0.171	0.56	0.999	0.999	0.999

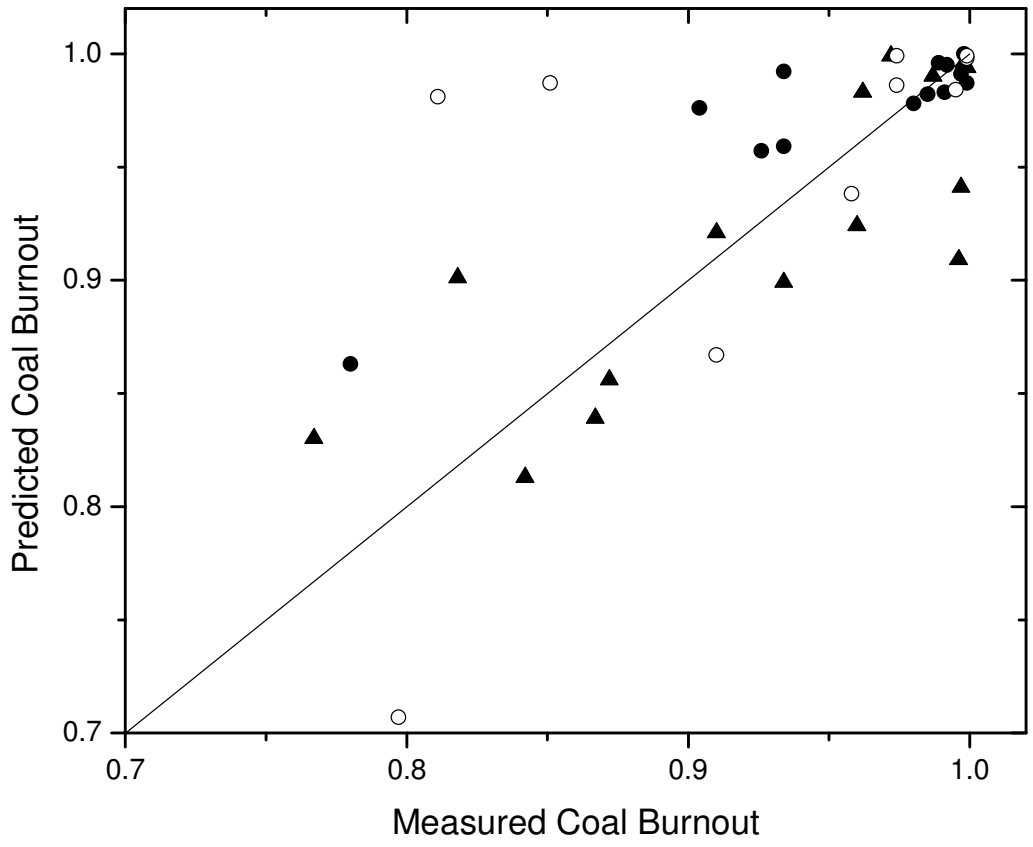

Figure C.53. Parity plot to evaluate extents of coal burnout in HPBO tests with Pit. #8 (▲), Ill. #6 (●) and Wyodak PRB (O).

Based on the satisfactory performance over the full range of conditions in the HPBO database, it is worth examining the dynamics of burnout as a function of pressure. Figure C.54 shows the particle and char burnout histories from CBKE for the tests with Pit. #8 at the highest inlet O_2 concentrations for each pressure. Each particle thermal history exhibits two initial surges before it relaxes to an ultimate temperature of 1400°C. The first surge is due to ignition under the very high inlet O_2 concentrations, which abruptly diminishes as O_2 is depleted by simultaneous volatiles combustion and char oxidation. The second surge is associated with the increasing gas temperatures in Figure C.54 over the same time period. Ultimately, these surges also dissipate, because too little char remains to sustain the necessary heat release rate. Note that the second surge dissipates as soon as the char burning rate relaxes to some saturation limit for each of the different pressures, around the time where the extent of char burnout approaches 80 % for the higher test pressures. This near-extinction phenomenon is associated with a transition in the burning mechanism, either back to kinetic control (Zone I) or to ash layer transport control during the latest stages.

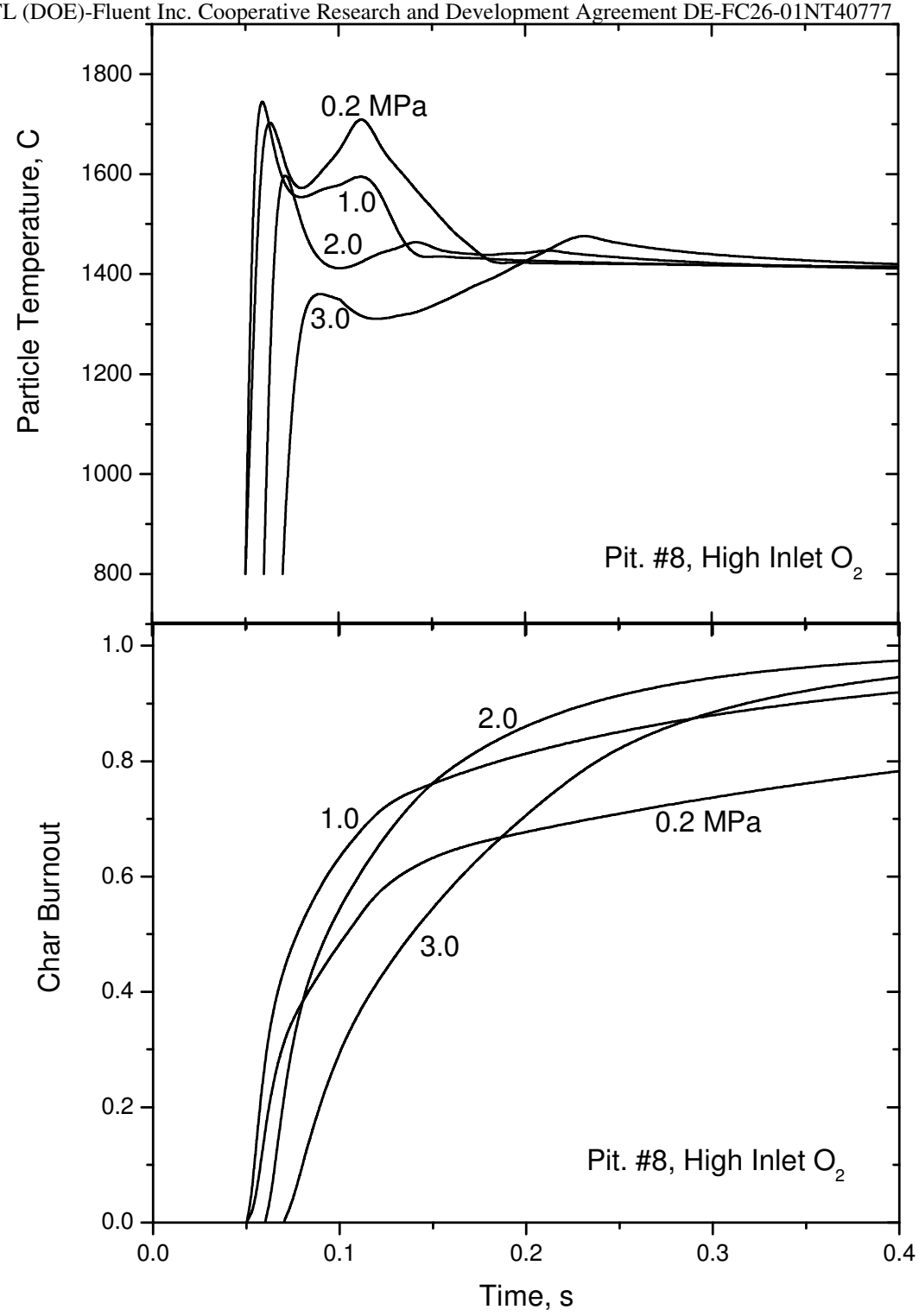

Figure C.54. Predicted histories for particle temperature (top) and char burnout (bottom) for tests with Pit. #8 at high inlet O_2 mass fractions.

The predicted char burnout histories exhibit a complex dependence on pressure because the inlet O_2 mass fractions for 2.0 and 3.0 MPa were significantly lower than for the lower test pressures. The clearest indication of the impact of pressure is evident in a comparison of burnout histories for 0.2 and 1.0 MPa, because these cases have the same inlet O_2 mass fraction of 0.180. As expected, chars burnout much faster at the higher pressure, because the O_2 partial pressure is higher at the higher pressure. Since the inlet O_2 mass fraction at 2.0 MPa is only slightly lower, at 0.146, chars burn even faster at this pressure (because the O_2 partial pressure is again higher). The increase in pressure to 3.0 MPa is almost compensated for by the reduction in inlet O_2 mass fraction (to 0.083). But chars burn slower at 3.0 MPa because the gas temperatures (cf. Figure C.52), hence, particle temperatures, are cooler throughout.

To assist in the interpretation of char characterization data from the HPBO tests, the maximum predicted char particle temperatures are compiled in Table C.13. The maximum particle temperatures vary with pressure as well as inlet O_2 level. The maximum is hotter at 1.0 MPa despite hotter gas temperatures at 0.2 MPa because the O_2 partial pressure is much higher. But for higher pressures, the cooler gas temperatures partially compensate for the higher O_2 pressures. For similar operating conditions, PRB generates the hottest chars because it burns fastest, followed by the next-fastest burning char, Illinois #6, followed by Pittsburgh #8.

Table C.13. Predicted maximum char particle temperatures.

Run No.	P, MPa	Loading, wt. %	y_{O2}	T_{MAX},°C
Pittsburgh #8				
180	0.2	7.0	0.200	1982
190	1.0	4.7	0.180	2020
225	2.0	2.4	0.055	1708
169			0.146	1870
224	3.0	1.5	0.034	1719
193			0.083	1749
Illinois #6				
286	0.2	8.4	0.210	2160
287		8.7	0.246	2230
294	2.0	2.2	0.056	1500
285		2.0	0.155	1930
Wyodak PRB				
271-273	0.2	8.0	0.180	2419
270	2.0	2.2	0.044	1745
275			0.080	1859
276			0.171	2269

The tabulated cases are for the longest residence times in each test series. Maximum temperatures for shorter residence times are the same because all the tabulated maximum

values were achieved within the radiant section near the onset of char oxidation, roughly 55-100 ms after injection. Since the particle temperatures relaxed to the assumed ultimate gas temperature of 1400°C at much longer residence times, the tabulated values are the hottest exposure temperatures for char, but at a point when very little flyash had been released into the free stream.

C.5.6 Assigning Global Rates for Char Burnout from CBK/E

Based on CBK/E's satisfactory performance in the previous section with HPBO data and in NEA's Fourth Interim Report with NBFZ data, FLUENT users may wish to be able to incorporate this mechanism into their CFD simulations. As noted previously, Prof. Hurt oversaw the incorporation of CBK8 directly into FLUENT. In this section, we briefly survey NEA's alternative approach.

According to CBK/E, char oxidation rates are actually determined by multi-step surface reaction kinetics mediated by numerous physical processes, including annealing and film and intraparticle transport rates. Notwithstanding these complexities, nominal char conversion rates can always be evaluated simply as the consumption rates of char on a mass basis as functions of time. The consumption rates can be evaluated from CBK/E simulations as easily as they are evaluated from measured char conversion histories. Nominal oxidation rates determined this way correctly indicate the magnitude of the overall char consumption rate. But this is the extent of all that is simple in the specification of nominal char oxidation rates.

The real challenge in specifying nominal oxidation rates arises because almost none of the factors that actually determine oxidation rates are uniform throughout any practical combustion process. The O_2 concentration and particle temperature swing through wide ranges while particle size and char density vary continuously. Annealing compounds the temperature dependences in the oxidation kinetics. So the simple rate law one uses to specify nominal oxidation rates must be robust enough to depict these concentration and temperature dependences, as well as the consequences of the physical structure evolution. Contrast this situation with that for nominal devolatilization rates, where even a SFOR could represent the nominal rates from FLASHCHAIN® within useful quantitative tolerances.

We have never seen a rate law for oxidation in the literature that can depict the predictions from CBK/E. Usually nth-order power laws are used, in which the O_2 concentration is raised to some fractional power, which is usually close to one-half. The temperature dependence is expressed by the activation energy parameter in a rate constant of Arrhenius form. Such an expression is adequate for the initial oxidation reactivity, but cannot resolve the independent influences of intrinsic chemistry, transport, pore evolution, and deactivation, so they cannot possibly remain accurate over broad domains of the operating conditions. Since broad ranges of all the operating conditions are traversed in every practical furnace environment, nth-order rate laws, alone, are simply inadequate.

Whereas an nth-order global rate law is inadequate for simulations in pulverized-fuel furnaces, a modest expansion restores its practical utility. Under the best circumstances – which almost never arise in practice – the parameters can be assigned from a database compiled for the same operating conditions as the practical application. In practice, however, the CFD practitioner is usually left to determine how the kinetic parameters should be adjusted to extrapolate from a calibration domain to the operating domain, and for different coal samples. He or she can compile a database, consult an expert, or use NEA's PC Coal Lab® to extrapolate.

To represent char gasification by CO_2, PC Coal Lab® uses a single, nth-order reaction (SNOR) modified for structural evolution effects, as follows:

$$R_{O_2} = \vartheta \cdot R^0_{O_2} = \vartheta \cdot A_{O_2} \cdot \exp(-E_{O_2} / RT) P^{n_{O_2}}_{O_2,S} \qquad \text{(C.31)}$$

where $R^0_{O_2}$ is the surface reaction rate not subject to annealing and physical evolution effects; ϑ is a factor to account for annealing and physical evolution effects to be defined further; A_{O_2}, E_{O_2} and n_{O_2} are the pre-exponential factor, activation energy and reaction order for char oxidation; and $P_{O_2,S}$ is the instantaneous O_2 partial pressure (in atm) on the particle surface. Factoring the oxidation rate into separate contributions for the primary concentration and temperature dependences in $R^0_{O_2}$ and for the annealing and physical evolution effects in ϑ is a convenient way to expand the domain of applicability of the rate expression. ϑ represents the joint impact of the main inhibitory mechanisms that decelerate the char oxidation rate with conversion, including annealing and char density changes. ϑ will be expressed as a fifth-order polynomial regression.
This rate expression is implemented with explicit account for film transport, but without any effectiveness factors. Since it is evaluated with conditions at the particle external surface in PC Coal Lab®, the rate law should only be implemented in other calculations, such as CFD, with the same explicit resolution of film transport; however, no effectiveness factors are required.

In the rate law, all parameters are adjustable constants that change with pressure, gas composition, temperature history and coal type, due to the inherent limitations. It is important to realize that their magnitudes have no mechanistic significance whatsoever, because such simple reaction rate expressions cannot possibly represent the numerous mechanisms that, in actuality, govern the kinetics of char oxidation.

The parameters A_{O_2}, E_{O_2} and n_{O_2} are usually assigned from laboratory test data. Instead, we use PC Coal Lab® to synthesize simulation "data" that can subsequently be analyzed for rate parameters just like one would analyze test measurements. The goal is to specify rate parameters for the modified SNOR that are able to accurately describe the oxidation rate over a complete combustion history as, for example, across a p. f. fired furnace. Consequently, it is important that the ambient conditions in PC Coal Lab® to obtain a combustion history for the parameter assignments are as similar as possible to the ambient conditions in the application of interest. The procedure first evaluates the rate

for a baseline extent of char conversion, then at a different temperatures and different surface O_2 partial pressures. A, E and n are assigned from the CBK/E-based rates by rearrangements of the modified SNOR expression.

To specify a global rate law for char oxidation, we first specify the ambient conditions of interest, then use CBK/E to predict the extents of char conversion and the oxidation rates throughout a complete oxidation history. From the predicted oxidation history, first evaluate the reaction rates $R^0_{O_2}(1)$, $R^0_{O_2}(2)$ and $R^0_{O_2}(3)$ and the surface O_2 partial pressures ($P_{O_2,S1}$, $P_{O_2,S2}$ and $P_{O_2,S3}$) and particle temperatures (T_1, T_2, T_3) at char conversion levels of 0.5, 40 and 80 %, respectively, using CBK/E. Equation C.31 can then be re-arranged into

$$\ln(R^0_{O_2}) = \ln(A_{O_2}) + \frac{E_{O_2}}{RT} + n_{O_2} \ln(P_{O_2,S}) \qquad \text{(C.32)}$$

Equation C.32 specifies a third-order system of linear equations whose coefficients are based on the evaluated oxidation rates $R^0_{O_2}(1)$, $R^0_{O_2}(2)$ and $R^0_{O_2}(3)$, and the corresponding O_2 surface partial pressures $P_{O_2,S1}$, $P_{O_2,S2}$ and $P_{O_2,S3}$ and particle temperatures T_1, T_2, T_3. The values of A_{O_2}, E_{O_2}, and n_{O_2} are obtained as the solution to the system of linear equations.

The fifth-order polynomial correlation for the decay in the reaction rate with conversion is written as:

$$\vartheta = a_0 + a_1 X + a_2 X^2 + a_3 X^3 + a_4 X^4 + a_5 X^5 \qquad \text{(C.33)}$$

where X is extent of char conversion and a_i ($i = 0$ to 5) denotes the regression coefficients. These coefficients are evaluated by fitting the product of the annealing factor and char density factor evaluated directly from the baseline CBK/E simulation. To improve the accuracy, two separate correlations are specified for extents of char conversion above and below 10 %.

The test case for this comparison is based on typical pulverized-fuel. firing conditions for an Eastern high-volatile bituminous coal. This test represents pulverized-fuel combustion under 8% O_2 with uniform gas and wall temperatures of 1325 to 1725°C, respectively. The performance of the method is illustrated in Figure C.55. The surface partial pressure of O_2 changes continuously throughout combustion as the rate limiting mechanism shifts from film diffusion, to pore diffusion, to the surface reaction kinetics. The char conversion history based on the modified SNOR-assignment is compared to the original CBK/E predictions in the upper panel of Figure C.55. Notwithstanding the wide variations in the O_2 concentration, the agreement is close throughout the entire combustion history. The lower panel demonstrates the performance for an extrapolation for the same coal to 10 % less O_2. Even though the modified SNOR parameters determined for the baseline case were used in the simulation, the predicted char conversion history is very close to the CBK/E-based history. The very minor discrepancies would be inconsequential in most design studies. Hence, the oxidation rate

parameters assigned with PC Coal Lab® accurately depict the CBK/E-based oxidation rate throughout a complete combustion history, and also handle modest extrapolations from the operating conditions used to assign the parameters. FLUENT users simply incorporate the equivalent SNOR with a user-defined function and use the parameters specified with PC Coal Lab®.

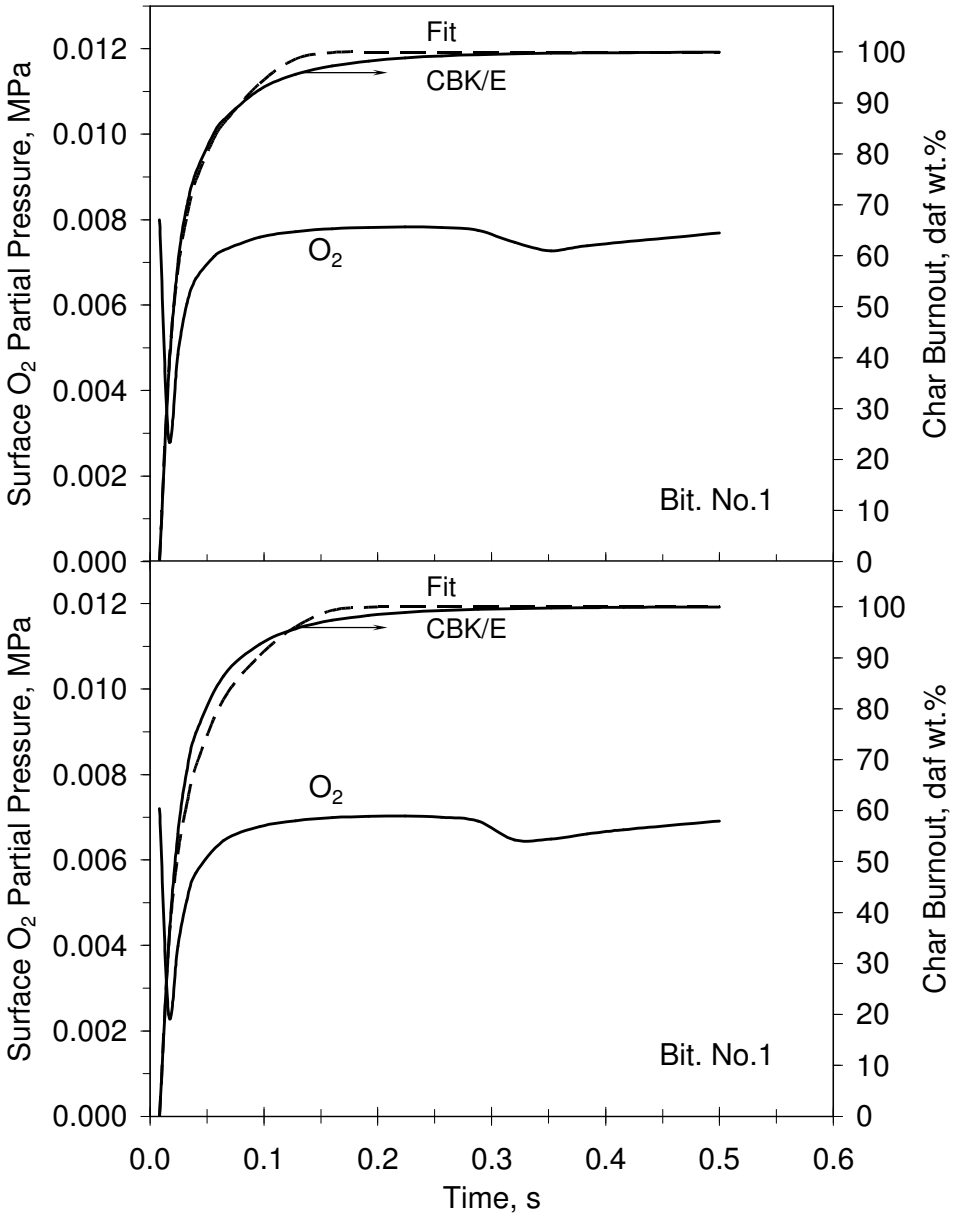

Figure C.55. Comparison of predicted char conversion histories from CBK/E (solid curves) and the modified SNOR rate assignments (dashed curves) for typical p. f. firing conditions (top panel) and a case with 10 % less O_2 (bottom panel).

HIGH PRESSURE COAL COMBUSTION KINETICS PROJECT
Appendix D – Submodels for flyash and fumes

D.1. Preliminary ash formation modeling calculation

To assess the effect of excluded mineral matter on ash particle formation, and to determine whether differences in the fraction of mineral matter present as excluded minerals would be detectable in an experimental measurement of the overall ash particle size distribution generated during combustion, simulations were conducted in which the amount of excluded mineral matter was varied systematically from 1% to 90% number percent of the total mineral matter present in the coal. The mineral size and composition distributions were taken to be identical for both the excluded and included minerals. As discussed later in this report, included and excluded mineral distributions often differ considerably. These calculations are therefore not meant to simulate the behavior of an actual coal sample, but rather to provide a parametric evaluation of the influence of the excluded fraction on the ash particle distribution. An ash content of 7.4 weight percent was used in these calculations, with the coal properties taken to be those of a Kentucky bituminous coal. Note that this was not one of the coals examined in the experimental portion of this project, but again, that is not significant. This coal was simply selected as a representative bituminous coal and used for parametric analysis as previously discussed. These Coal properties used in these calculations are shown in Table D.1.

Stoichiometric Ratio:	1.2
Coal:	Bituminous
T gas:	1538°C
Swelling Index:	1, 1.1, 2
Proximate (wt%, as received)	
Fixed Carbon	56.5
Volatile Matter	33.8
Ash	7.4
Moisture	33.8
Mineral Composition (%vol)	
Quartz	12.6
Kaolinite	26.2
Illite	15.3
Miscellaneous Silicates	30.0
Pyrite	3.4
Others	14.5
Mineral Size Distribution (%vol)	
2 µm	18.4
4 µm	28.2
8 µm	18.4
16 µm	18.1
30 µm	6.8
60 µm	5.7
80 µm	3.9

Table D-1. Coal characteristics and combustion conditions used in initial model calculations to determine effect of extent of excluded mineral fraction of ash particle size distributions.

The calculations were conducted under conditions of full coalescence. The particle size distribution and composition of the coal mineral matter and the proximate analysis of the coal are also shown in Table D.1.
The effect of coal particle swelling (believed from the outset ot be an important parameter affecting char fragmentation) was also considered by examining a non-swelling coal and two representative swelling coals (with assumed swelling indexes of 1.1 and 1.9). The swelling index is a measure of the propensity of a coal to swell upon heating. The model treats the swelling index as a diameter-based increase in char particle size. Corresponding ASTM standard free swelling indexes (FSI) based on ASTM standard D 720-91 for these diameter based values are 1, 2 and 9, respectively as shown in Table D.2.

ASTM Free Swelling Index	Diameter ratio
1	1.0
2	1.1
3	1.2
4	1.3
5	1.4
6	1.5
7	1.6
8	1.8
9	1.9

Table D-2 ASTM Free Swelling Index and correspondent swelling diameter ratio.

D.1.1. Results of Parametric Calculations

For a fixed swelling index, as the amount of excluded mineral matter in the coal increased, the fraction of ash particles present in the smallest size range (2 and 4 μm) increased (Figure D.1). This is reflective of the decrease in coalescence associated with the reduction in the amount of included minerals. Increased fragmentation of excluded minerals may also be contributing, although the amount of reactive minerals present in this particular coal (i.e. pyrite) is relatively small (3.4% by volume). Figures D.2 and D.3 show that the same trend was obtained independent of swelling index.

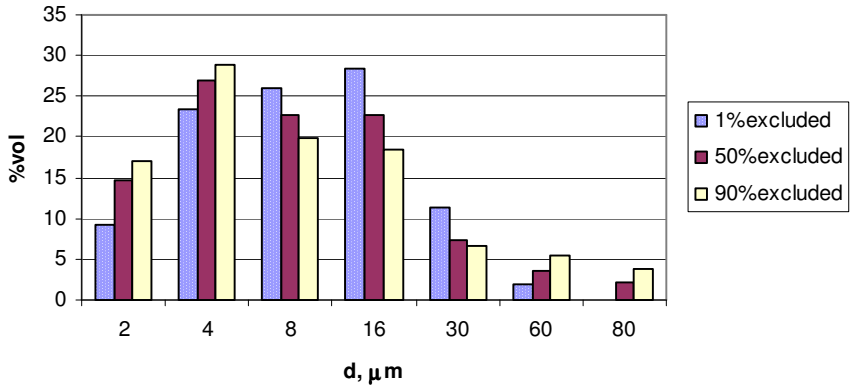

Figure D-1 Ash size distribution for a coal with SI = 1.1, at different excluded % (number basis).

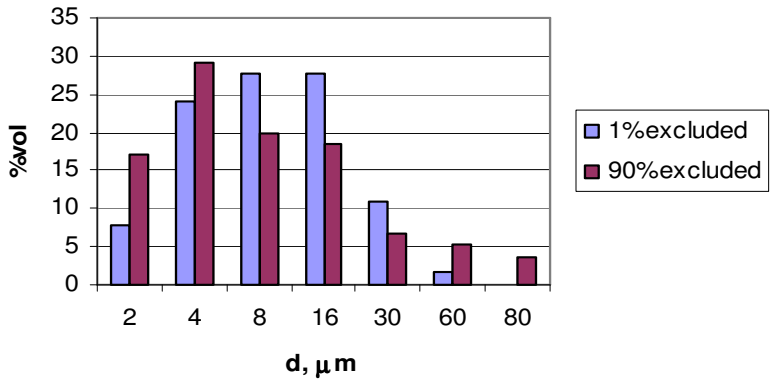

Figure D-2. Ash size distribution for a non-swelling coal (SI = 1.0), at different % excluded (number basis).

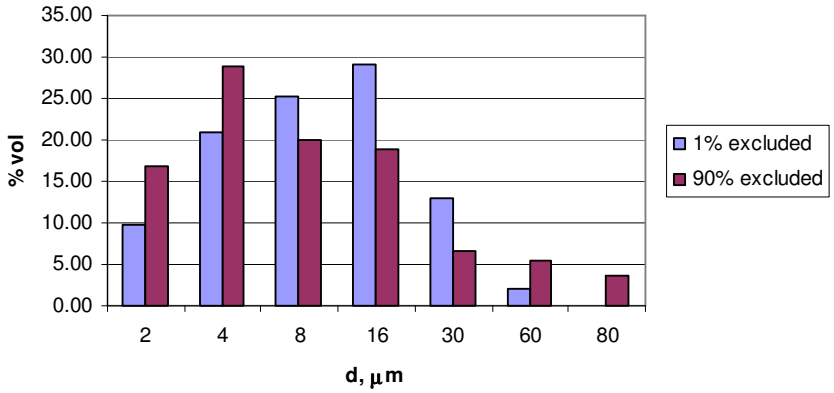

Figure D-3 Ash particle size distribution for a swelling coal (SI = 1.9), at different % excluded (number basis).

When comparing the composition distributions of the resulting ash particles, changes are observed as shown in Figure D.4. The aluminosilicate category (SiAl) represents aluminosilicate derived ash particles that have no third element (for example, Ca or K) present at concentrations higher than 6%. The percentage of the ash particles in this category decreases as the amount of excluded minerals increases. This is again associated with the reduction in the coalescence of included minerals (and is in part a consequence of the binning of ash particles into broad compositional categories). Coalescence with the dominant aluminosilicate minerals such as kaolinite will reduce the concentration of iron and calcium in individual particles, resulting in them being classified as SiAl aluminosilicates. An increase in silicates (Si), potassium aluminosilicates (SiAlK) and iron aluminosilicates (SiAlFe) is also noted as the amount of included minerals decreases. As expected, the ash particle composition distribution is therefore becoming more reflective of the initial mineral composition distribution as the fraction of excluded minerals in the coal increases.

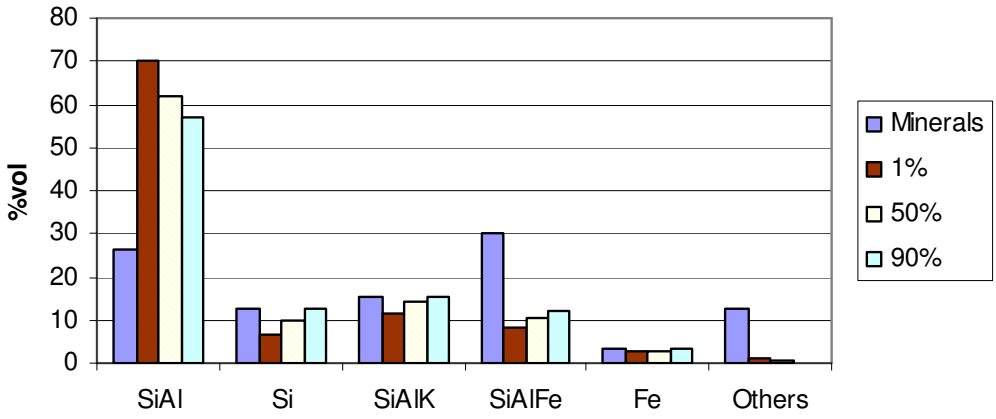

Figure D-4 Ash composition for a swelling coal (SI = 1.1), at different % excluded (number basis).

Note: "Miscellaneous silicate" minerals were included as SiAlFe. "Others" include miscellaneous carbonates, phosphates and sulfates; siderite and calcite.

When comparing the concentrations of specific ash particle types with the parent minerals (i.e., comparing illite with the SiAlK in the ash), it is clear that at higher concentrations of excluded mineral matter, the amount in the ash remains relatively constant. At an excluded mineral matter concentration of 50% the change becomes insignificant. Significant interaction between iron and aluminosilicates was observed, but this was only slightly influenced by the amount of excluded minerals.

With a higher swelling index, coal fragmentation increases, leading to the formation of a larger number of small ash particles (Figure D.5). Ash particles in the smaller size range (2μm) increase from 6.7 to 8.6% for the case where most of the mineral matter is included. As would be expected, little change is seen when 90% of the mineral matter is excluded. There is also a decrease in the 4 μm range, as the swelling index increases. The amount of ash appearing in each of the other size ranges remains approximately constant.

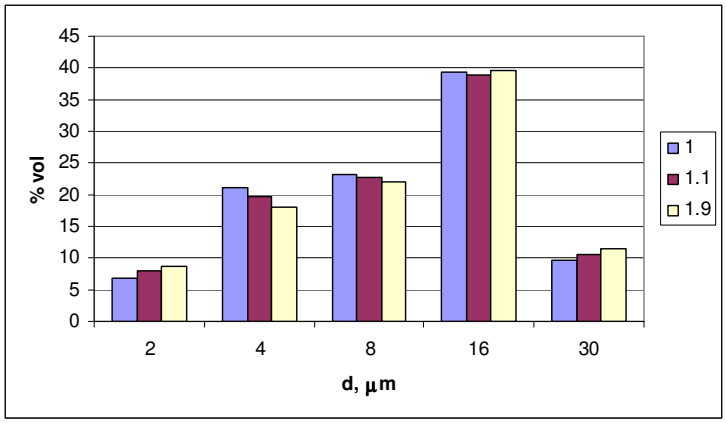

Figure D-5 A comparison of the calculated ash particle size distributions for different swelling indexes. Excluded mineral matter is 1% of the total in each case.

This study varies the amount of excluded minerals, considering the same mineral distribution for both excluded and included minerals. The actual amount of excluded mineral matter varies in a wide range from 0.03 to 0.73 according to different studies (Gupta et al., 1998; McLenan, et al., 2000; Smith et al., 1993; Wigley et al., 1997; Yan, 2000; Yan et al., 2002). Among the former studies, the smaller fraction of excluded minerals has been reported by Wigley et al. 1997. Examination of the analytical procedure used by different studies, however, indicated that different definitions of the excluded fraction were used. McLenan et al., 2000 and Yan et al., 2002 defined a mineral as excluded if less than 50% of the surroundings of that mineral were carbon. Wigley et al., 1997 used a more stringent threshold of 10%, resulting in consistently lower predicted values for the extent of excluded mineral matter. The definition of excluded minerals is an important parameter in the effort to address ash formation, as the association with organic coal would result in reaching higher temperatures leading to different ash formation pathways.

D.1.2. Effect of Coal Particle Size Distributions

Different Rosin-Rammler Distribution Parameters

In order to account for the broader coal particle size distribution used in the experimental tasks of this project, preliminary calculation of the effect of differences on coal particle

size distribution on the fly ash composition and size distributions was conducted. First a baseline bituminous coal having a coal particle size distribution fitting the Rosin-Rammler distribution function with parameters b=0.17 and n =0.7 was considered. Mineralogy was taken to be that of the Elkhorn Hazard bituminous coal, again as a parametric study. Perturbations about this baseline coal particle size distribution were then considered as indicated in Table D.3. The coal particle size distributions associated with each of these cases are shown in Figure D.6.

Case ID and description	B	n
RR1 – Baseline	0.17	0.7
RR2 – Fine	0.40	0.7
RR3 - Coarse	0.08	0.7

Table D-3 Rosin-Rammler distribution parameters for different coal size distribution cases.

Using these size distributions as input, ash particle size and composition distributions were calculated under conditions of full mineral coalescence only (Table D.4). Changes among the ash composition calculated for the three coal size distributions were not significant.

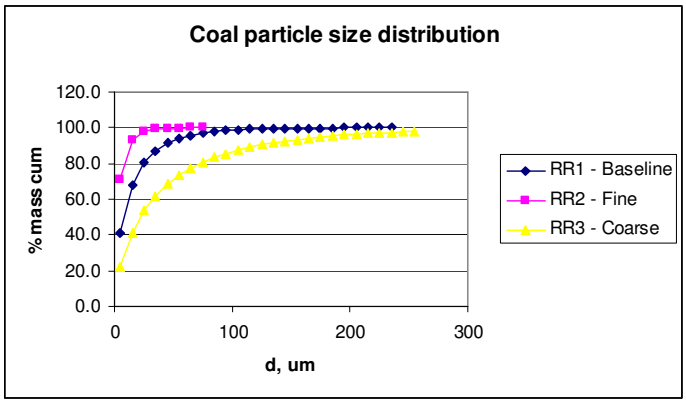

Figure D-6. Coal particle size distributions examined for effect on ash formation.

	RR 1- Baseline	RR 2 – Fine	RR 3 – Coarse
SiAl	66.7	65.3	68.2
SiAlK	12.6	12.8	11.6
SiAlFe	8.4	9.3	7.9
Si	9.4	9.6	9.2
Others	2.9	3.0	3.1

Table D-4 Ash particle composition distributions calculated under conditions of particle coalescence. Results presented as percent by volume.

Ash particle formation calculations were also run under conditions where specific (artificially generated) mineral compositions were considered. The cases considered were all mixed aluminosilicates, all illite, all pyrite and all quartz. Calculations were then preformed for each mineral type, using each of the baseline, fine and coarse coal particle size distributions to look for any effects of coal particle size distribution function on the ash distribution. In each calculation, the mineral particle size distribution was held constant.

Changes in the fly ash particle size distribution with changing coal particle size distribution were relatively small as shown in Figures D.7 and D..8, except for the case of mixed AlSi. For these minerals, there were more ash particles noted in the 30 μm bin using the coarse coal particle size distribution as compared to the fine coal particle size distribution. This phenomenon is expected because aluminosilicates coalesce readily at combustion temperatures to form larger ash particles. The same trend was observed for illite.

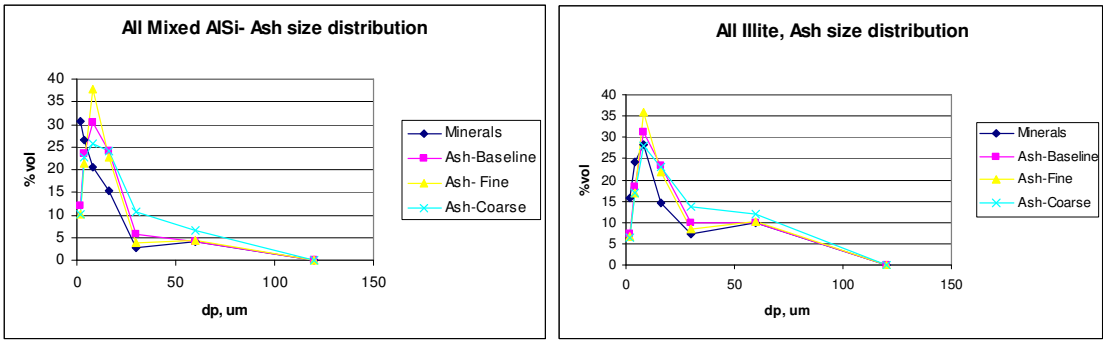

Figure D-7 Predicted fly ash particle size distribution in % vol, when mixed AlSi (left) and illite (right) are the only minerals considered in the calculation.

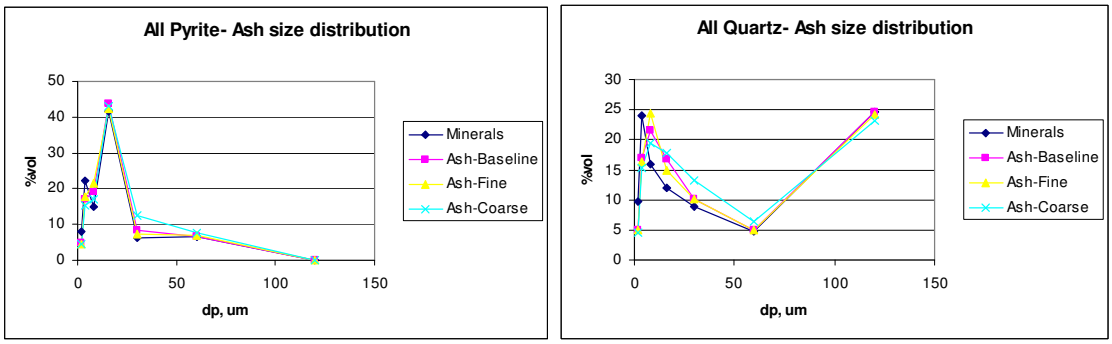

Figure D-8 Predicted fly ash particle size distribution in % vol, when just pyrite (left) and quartz (right) are present in the mineral composition.

These preliminary results showed that variations in Rosin Rammler distribution parameters did not lead to large changes in ash size and composition, except when AlSi or illite were present as the major compound in the mineral matter. These results therefore suggest that differences in coal particle size distribution will not greatly effect the resulting ash particle size distribution for ranges typically encountered, all else being equal, *unless* the coal mineralogy is dominated by included aluminosilicates *and* coalescence is dominant over char fragmentation as an ash formation mechanism.

Different Coal Size Range Distributions

Following the idea to evaluate the effect of different coal size distributions on the calculated fly ash particle composition and size distributions, another parametric study allowing for different but narrow coal particle size ranges was conducted. As the coal combustion experiments conducted at SRI used a broader size cut of coal than was originally planned (75-105 µm vs. 75-90 µm), the following coal particle size distributions were considered in tehse calculations:

- Distribution 76/108: coal size distribution corresponds to a normal distribution between 76 and 108 µm.
- Distribution 76/92: normal distribution between 76 and 92 µm.
- Distribution 92/108: normal distribution between 92 and 108 µm.
- Distribution 44/52: normal distribution between 44 and 52 µm.

The latter case was examined to determine the extent of the changes in ash particle size that would result from a significantly smaller coal particle size cut.
In each of these calculations, we considered a baseline coal with proximate and ultimate analysis corresponding to Elkhorn Hazard. This coal was chosen because CCSEM data were available from previous studies (calculations were conducted before CCSEM analysis of program coals was completed), and because it was expected to present a “typical” bituminous coal for study. Combustion was conducted under fuel lean conditions at a stoichiometric ratio of 1.2 in all cases. The ash content of the coal was 7.59 mass percent.

Ash particle formation calculations were run under full mineral coalescence conditions. The results of these calculations are presented in Tables D.5 and D.6 and Figure D.9.

		D. 44/52	D. 76/108	D. 76/92	D. 92/108
D, µm	Minerals, % vol	Ash, % vol	Ash, % vol	Ash, % vol	Ash, % vol
2	18.3	8.0	5.7	5.9	5.3
4	27.0	16.3	17.4	18.2	16.1
8	19.3	19.0	13.8	13.2	14.8
16	18.9	39.8	22.4	28.0	13.7
30	7.1	7.1	31.0	25.0	40.5
60	5.3	5.8	5.6	5.7	5.5
80	4.1	4.0	4.1	4.1	4.1

Table D-5 Calculated ash particle size distributions resulting from combustion of coal with different coal particle size distributions.

	D. 44/52	D. 76/108	D. 76/92	D. 92/108
Composition	Ash, % vol	Ash, % vol	Ash, % vol	Ash, % vol
SiAl	68.4	71.2	70.0	72.8
Si	9.2	8.3	8.7	7.8
SiAlK	11.5	10.6	11.3	9.6
SiAlFe	7.7	6.8	6.7	7.2
Fe	2.0	1.9	1.9	1.9
Others	1.2	1.2	1.4	0.8

Table D-6 Calculated ash particle composition (major classes) resulting from combustion of bituminous coal with different coal particle size distributions.

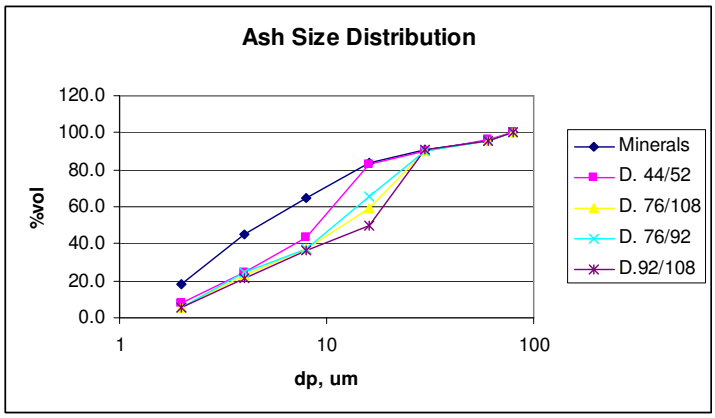

Figure D-9 Cumulative ash size distributions for different coal distributions.

As the results of these calculations indicate, there were no major differences in the ash particle composition distribution resulting from changes in coal particle size among the 76/108, 76/92 and 92/108 μm size distributions. Slight differences in ash particle size are observed, with the largest difference corresponding to the 16 and 30 μm average size ash particles. The 92/108 coal distribution shows the largest size fraction of ash in the 30 μm bin, suggesting increased coalescence for minerals contained within the largest coal particles. Similarly, the 76/92 distribution exhibits the smallest extent of mineral coalescence. Comparing these three distributions with the 44/52 μm distribution, the relative constancy of the fraction of ash in the largest size bins (60 and 80 μm) suggests that minerals in these ranges correspond to excluded minerals for this specific coal. These calculations were conducted under the assumption that all of the minerals were included. Excluded minerals would tend to smoth out these minor differences observed with changes in coal particle size.

D.2. CCSEM ANALYSIS OF COALS

D.2.1. Pittsburgh #8 Bituminous Coal

Mineral composition data obtained from CCSEM analysis of the Pittsburgh bituminous coal sample used in experimental work at SRI are shown in Figures D-10 and D-11 and Tables D-7 and D-8. Figure D-10 shows the mineral composition detected by CCSEM, corresponding to 25 weight percent of the coal. In this sample, there was an unexpectedly large amount of pyrrhotite (46.3% of the minerals), which, together with K-Al-silicates (13.6%w) constituted the main components of the sample. The unusually high percentage of pyrrhotite suggests partial oxidation of the pyrite contained within the coal. The pyrrhotite and pyrite minerals were mainly excluded (92.8 and 91.1%), while just 51.1% of the K-Al-silicates were excluded.

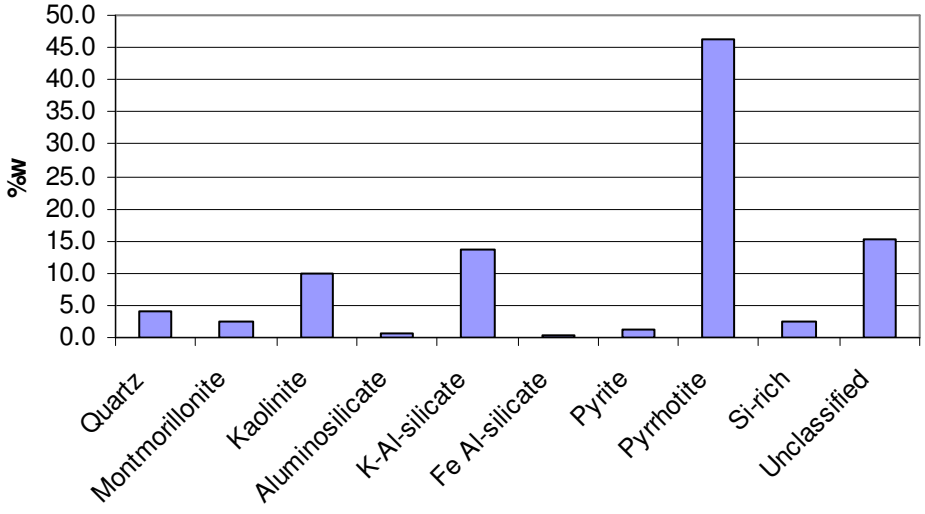

Figure D-10 Mineral composition of the Pittsburgh bituminous coal sample used in the experimental effort in this project.

The mineral size distribution (Figure D-11 and Table D-7) shows a large amount of large mineral particles (>46μm) present in this coal. The size range 4.6 – 10 μm was dominated by K-Al-silicate and kaolinite, minerals that in addition to pyrrhotite were also present in the 22-46 μm size range. The larger particles were mainly pyrrhotite. The K-Al-silicates were distributed through all the size ranges. Table D-8 shows the oxide form of the minerals that was calculated from the CCSEM data.

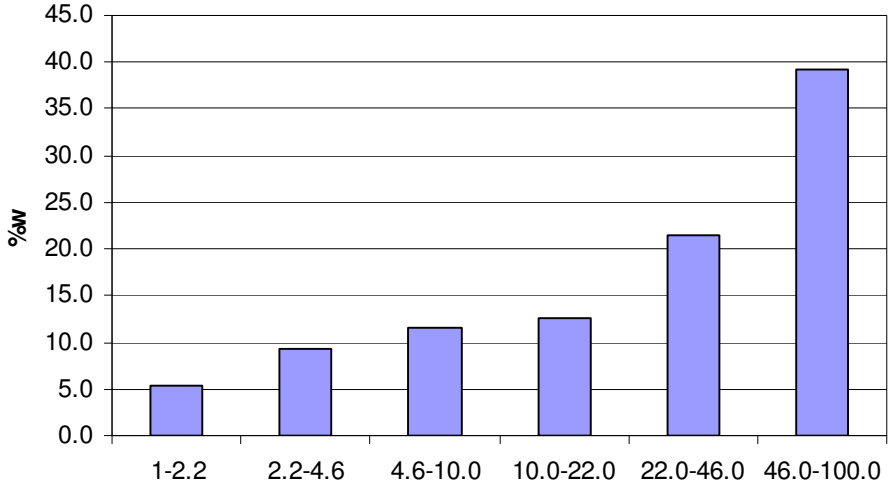

Figure D-11 Mineral particle size distribution of the Pittsburgh sample.

	1-2.2μm	2.2-4.6 μm	4.6-10.0μm	10.0-22.0μm	22.0-46.0μm	46.0-100.0μm	Total, %w
Quartz	4.9	19.5	24.4	17.1	12.2	22.0	4.1
Calcite	0.0	0.0	0.0	10.0	20.0	70.0	1
Kaolinite	7.1	18.4	23.5	23.5	9.2	18.4	9.8
Montmorillonite	7.7	15.4	15.4	11.5	15.4	30.8	2.6
K Al-silicate	5.1	17.6	17.6	18.4	16.9	23.5	13.6
Fe Al-silicate	0.0	0.0	50.0	0.0	50.0	0.0	0.2
Ca-Al-silicate	0.0	0.0	0.0	0.0	0.0	50.0	0.2
Aluminosilicate	0.0	0.0	0.0	16.7	16.7	50.0	0.6
Mixed Al-silicate	0.0	0.0	33.3	33.3	16.7	16.7	0.6
Pyrite	0.0	0.0	9.1	9.1	45.5	36.4	1.1
Pyrrhotite	0.4	1.7	4.5	8.0	27.9	57.5	46.3
Oxidized Pyrrho	0.0	9.1	18.2	0.0	45.5	27.3	1.1
Gypsum/Al-Silic	37.5	25.0	0.0	0.0	12.5	25.0	0.8
Si-rich	7.7	7.7	15.4	15.4	11.5	42.3	2.6
Ca-rich	0.0	0.0	0.0	0.0	100.0	0.0	0.1
Unclassified	19.1	16.4	15.8	13.8	16.4	18.4	15.2

Table D-7 Mineral particle size distribution and composition of the Pittsburgh sample.

	Pittsburgh
SiO_2	0.29
Al_2O_3	0.13
Fe_2O_3	0.18
TiO_2	0.00
P_2O_5	0.01
CaO	0.01
MgO	0.00
Na_2O	0.00
K_2O	0.02
SO_3	0.36

Table D-8 Calculated oxide composition obtained from CCSEM analysis of Pittsburgh sample (mass fraction as oxide)

The high percentage of pyrrhotite identified in this sample was not expected, so additional analyses were conducted in an attempt to verify the high iron percentage and high overall ash content of the sample. ASTM standard D3174-93 was followed in these tests. The results for two Pittsburgh samples, one sent in September 2002 and one in November 2002, were 13.2 weight percent and 11.3 weight percent ash content respectively. Since these ash values were considerably lower than those identified by CCSEM, the CCSEM analysis was repeated on a second sample.

The results of the CCSEM analysis of the second Pittsburgh #8 sample did not show major differences from the results of the initial CCSEM sample. Size differed slightly, with smaller amounts of large minerals and large excluded minerals observed in this sample (Figure D-12). Nevertheless, the overall amount of excluded minerals was about the same: 70 - 71 %w. Pyrrhotite and K-Al-Silicate continued to dominate the sample (Figure D-13). As the mineral content was detected as 25% by weight versus 9.44% from the Penn State database and 11.3% following ASTM D3174-93 conducted in our laboratory, an ash chemical analysis was also done in order to compare these results with those derived from the CCSEM analysis.

According to the ash chemical composition analysis done by an external laboratory, the mineral content determined by ASTM D3174 was 12.3 weight percent, which corresponds to the value determined in our in-house analysis. These values differ from the level calculated from the CCSEM analysis of the coal minerals reported previously (25.6%). A comparison of the chemical composition resulting from bulk ash analysis and calculated from the CCSEM mineral analysis is reported in Table D-9.

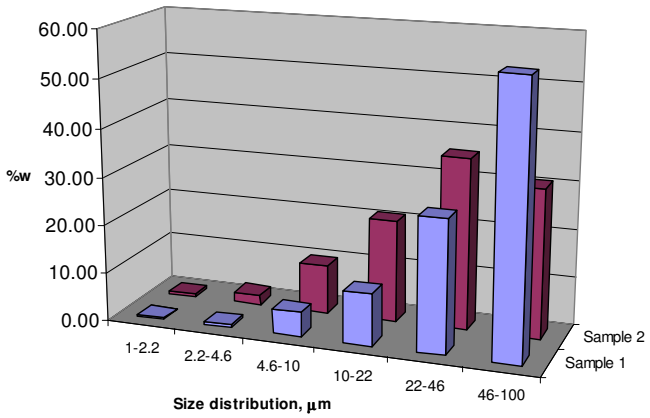

Figure D-12 Particle size distribution for excluded minerals – Pittsburgh #8 coal. Sample 1 corresponds to the results received October 2002. Sample 2 corresponds to the results received in March 2003.

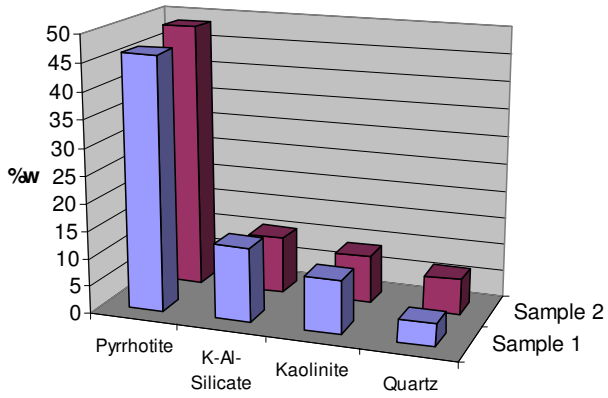

Figure D-13 Mineral composition distribution. Sample 1 corresponds to initial sample. Sample 2 corresponds to the results received in March 03

Compound	Calculated from CCSEM results	ASTM D3682 results
SiO_2	43	31
Al_2O_3	17	16
Fe_2O_3	32	47
TiO_2	0.6	0.6
P_2O_5	1	0.3
CaO	4	3
MgO	0.6	0.5
Na_2O	0.6	0.5
K_2O	2	2

Table D-9 Comparison of the results from CCSEM and ASTM D3682 for Pittsburgh #8

D.2.2. Illinois Bituminous Coal

The CCSEM results for the Illinois coal sample as mineral composition and mineral size distributions are shown in Figure D-14, D-15, Tables D-10 and D-11. The mineral content of the coal reported by CCSEM was 13.91 %wt. This amount is in agreement with the proximate analysis for ash content of this coal (13.39%). Table D-10 shows the detailed mineral particle size distribution of the major minerals present in these samples. Table D-11 presents the oxide form of the minerals that was calculated from the CCSEM data. This information can be compared with the ASTM ash analysis.

In the Illinois sample, there is an unexpectedly large amount of pyrrhotite (66.9%w of the minerals), which, together with calcite (9.0%w) and quartz (6.1%w) constitute the main components of the sample. The pyrrhotite and calcite in the Illinois sample are mainly excluded minerals (79.2% and 87.5%w).

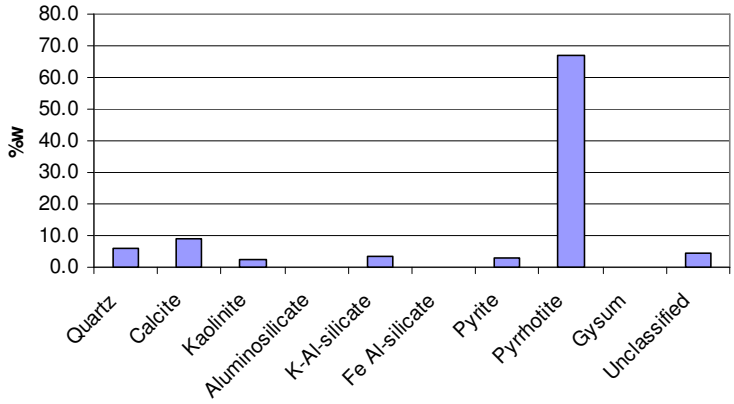

Figure D-14 Mineral composition of the Illinois sample.

As shown in Figure D-15, there is a high percentage of large minerals (>22μm) present in this coal. According to the detailed mineral data shown in Table D-10, all size ranges are dominated by pyrrhotite, a mineral that, in addition to calcite, is also present as a major component in the larger particles.

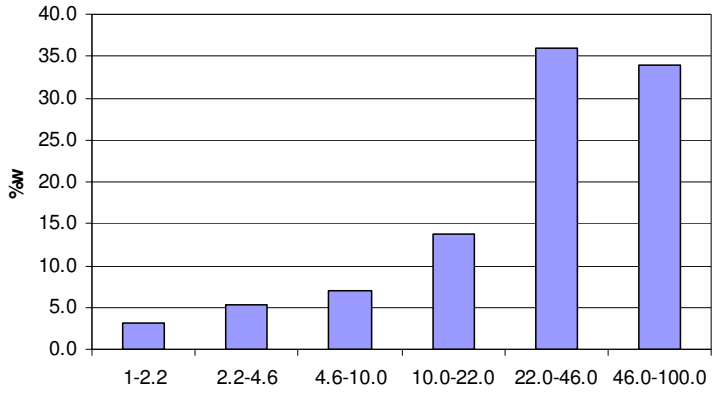

Figure D-15 Mineral particle size distribution of the Illinois sample.

	1-2.2 µm	2.2-4.6 µm	4.6-10.0µm	10.0-22.0µm	22.0-46.0µm	46.0-100.0µm	Total, %w
Quartz	18.0	31.1	27.9	19.7	0.0	1.6	6.1
Calcite	0.0	0.0	0.0	1.1	33.3	65.6	9.0
Kaolinite	12.5	16.7	16.7	18.8	4.2	31.3	2.4
Montmorillonite	10.0	20.0	10.0	20.0	30.0	10.0	1.0
K Al-silicate	14.7	20.6	17.6	19.1	19.1	8.8	3.4
Fe Al-silicate	0.0	0.0	0.0	50.0	50.0	0.0	0.2
Na-Al-silicate	0.0	0.0	0.0	0.0	0.0	0.0	0.1
Aluminosilicate	0.0	0.0	25.0	25.0	25.0	25.0	0.2
Mixed Al-silicate	0.0	16.7	16.7	16.7	0.0	33.3	0.6
Ca Silicate	0.0	0.0	0.0	0.0	0.0	50.0	0.2
Pyrite	0.0	0.0	0.0	3.6	46.4	50.0	2.8
Pyrrhotite	0.6	1.5	4.9	14.3	43.8	34.8	66.9
Oxidized Pyrrho	0.0	0.0	25.0	56.3	18.8	0.0	0.8
Gypsum	0.0	0.0	0.0	0.0	0.0	0.0	0.1
Apatite	0.0	0.0	0.0	0.0	10.0	90.0	1.0
Si-rich	14.3	42.9	14.3	0.0	14.3	14.3	0.7
Unclassified	16.3	16.3	11.6	16.3	18.6	18.6	4.3

Table D-10 Mineral particle size distribution and composition of the Illinois sample.

	Illinois
SiO_2	0.14
Al_2O_3	0.03
Fe_2O_3	0.25
TiO_2	0.00
P_2O_5	0.00
CaO	0.07
MgO	0.00
Na_2O	0.00
K_2O	0.01
SO_3	0.48

Table D-11 Calculated composition, CCSEM analysis of Illinois sample (mass fraction as oxide)

D.2.3. Wyodak Anderson PRB Subbituminous Coal

The data for the PRB coal sample are shown in Figures D-16 and D-17 and Tables D-12 and D-13. Figure D-16 shows the mineral composition detected by CCSEM, which constituted 3.99%w for PRB, which is close to the reported proximate analysis (5.01%). Figure D-17 shows the reported mineral size distributions. Table D-12 shows the detailed mineral particle size distribution of the major minerals present in these samples. Table D-13 presents the oxide form of the minerals that was calculated from the CCSEM data. For this coal sample, the major components are quartz (27.1%w), kaolinite (20.5%w), Cal Al-P (12.2%w) and unclassified ones (13.3%w). There is a small amount of pyrrhotite (6.4%w), but mainly as excluded minerals (95%).

The major amount of minerals is concentrated between 4.6 and 46μm (Figure D-16). All the size ranges up to 22 μm are dominated by quartz, kaolinite and CaAlP. In particles larger than 22μm, kaolinite, quartz, pyrrhotite, gypsum/aluminosilicates and unclassified minerals are the major components.

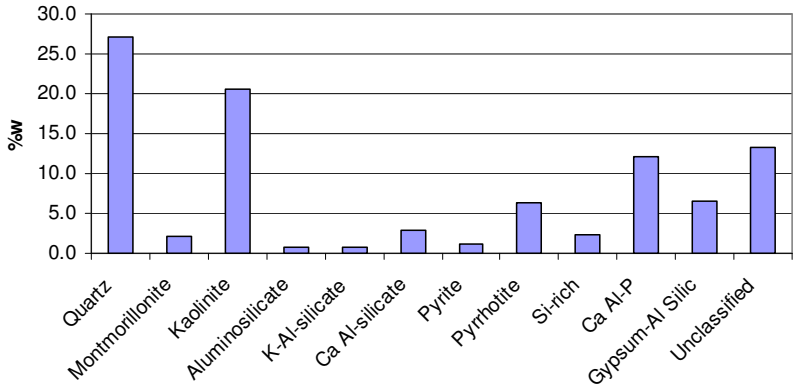

Figure D-16Mineral composition of the PRB sample

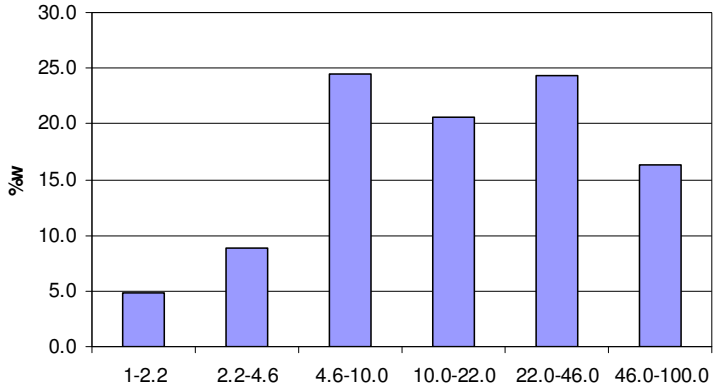

Figure D-17 Mineral particle size distribution of the PRB sample

	1-2.2µm	2.2-4.6 µm	4.6-10.0µm	10.0-22.0µm	22.0-46.0µm	46.0-100.0µm	Total, %w
Quartz	8.9	15.1	27.3	18.5	16.2	13.7	27.1
Iron oxide	12.5	12.5	12.5	0.0	62.5	0.0	0.8
Rutile	0.0	40.0	40.0	0.0	20.0	0.0	0.5
Dolomite	0.0	0.0	100.0	0.0	0.0	0.0	0.2
Kaolinite	3.4	12.2	18.0	28.8	26.8	9.8	20.5
Montmorillonite	4.5	0.0	4.5	27.3	40.9	22.7	2.2
K Al-silicate	12.5	25.0	0.0	0.0	25.0	37.5	0.8
Ca-Al-silicate	0.0	3.6	14.3	21.4	32.1	28.6	2.8
Aluminosilicate	0.0	0.0	0.0	0.0	37.5	50.0	0.8
Mixed Al-silicate	0.0	0.0	0.0	0.0	0.0	100.0	0.2
Fe Silicate	0.0	83.3	16.7	0.0	0.0	0.0	0.3
Ca Silicate	0.0	0.0	25.0	25.0	40.0	10.0	1.0
Pyrite	0.0	0.0	0.0	0.0	27.3	72.7	1.1
Pyrrhotite	4.7	0.0	4.7	10.9	47.7	32.0	6.4
Oxidized Pyrrho	0.0	0.0	0.0	0.0	100.0	0.0	0.3
Gypsum	0.0	0.0	100.0	0.0	0.0	0.0	0.1
Barite	0.0	100.0	0.0	0.0	0.0	0.0	0.1
Apatite	0.0	0.0	0.0	0.0	0.0	100.0	0.2
Ca Al-P	6.6	9.0	36.1	33.6	9.8	4.9	12.2
Gypsum/Al-Silic	0.0	0.0	24.6	10.8	40.0	24.6	6.5
Si-rich	0.0	0.0	16.7	25.0	25.0	29.2	2.4
Unclassified	2.3	1.5	38.3	15.8	23.3	18.0	13.3

Table D-12 Mineral particle size distribution and composition of the PRB sample

	PRB
SiO_2	0.54
Al_2O_3	0.18
Fe_2O_3	0.04
TiO_2	0.01
P_2O_5	0.05
CaO	0.07
MgO	0.01
Na_2O	0.00
K_2O	0.00
SO_3	0.09

Table D-13Calculated oxide composition obtained from CCSEM analysis of PRB sample (mass fraction as oxide)

D.2.4. Excluded and Included Minerals

As excluded and included minerals may follow different ash formation pathwyas, an analysis of the different mineral types considering particle size and composition distributions was done, based on the CCSEM results. Figure D-18 displays the mineral particle size distribution (psd) of the excluded minerals for each coal. For the Illinois and Pittsburgh 8 bituminous coals, more than 80% of the excluded minerals are larger than 22 μm. For the PRB coal, the excluded minerals are slightly smaller in size; here, only 63% of the excluded mineral matter is greater than 22 μm. The main component for excluded minerals in Illinois and Pittsburgh #8 coals is pyrrhotite. For the PRB coal, the excluded minerals are mainly kaolinite and quartz.

Figure D-19 shows the particle size distribution for the *included* minerals, i.e. those associated with the carbon of the coal. The mode of the PRB coal mineral distribution lies in the 4.6 – 10 μm size range, whereas it is slightly smaller for the Pittsburgh #8 coal (2.2 – 4.6 μm) and larger for the Illinois 6 coal (22-46 μm). This suggests that mineral coalescence may be more limited during combustion of the Illinois coal than during combustion of the other two program coals.

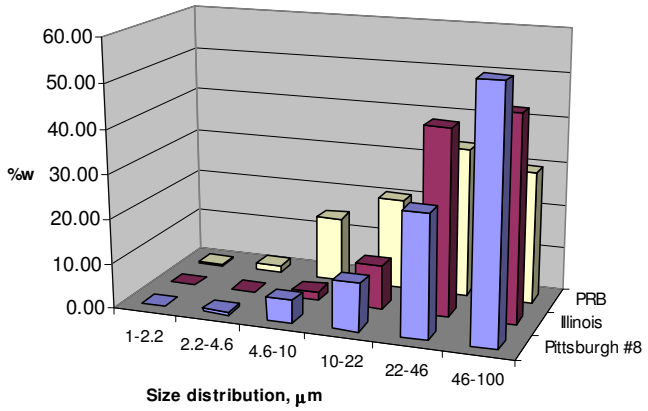

Figure D-18 Particle size distributions for excluded minerals.

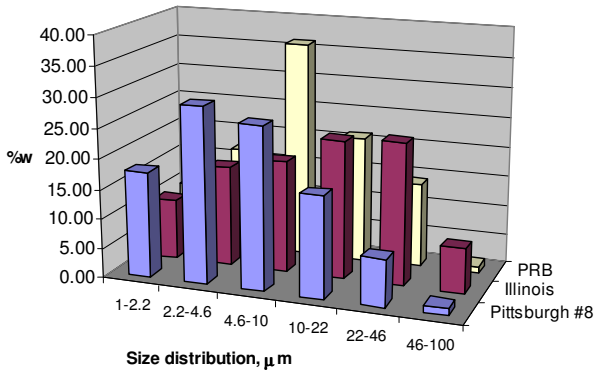

Figure D-19 Particle size distributions for included minerals.

The size of the included minerals is important in the different transformations of the ash, but the composition of these ranges is relevant as well. Figures D-20 to D-22 show the composition of included minerals for the different mineral size groupings extracted from the CCSEM analysis for the three coals. As seen in the figures, for the Illinois and PRB coals, the smallest mineral size ranges (1-2.2 µm and 2.2-4.6 µm) are dominated by quartz. For the Pittsburgh #8 bituminous coal, kaolinite and illite (K-Al-silicates) are the main minerals identified at sizes less than 10 µm. In the 4.6-22 µm size range, the Illinois coal is dominated by pyrrhotite and quartz; pyrrhotite also dominates the two larger particle ranges (22-46 and 46-100 µm). Quartz and kaolinite are the main components of the included minerals for the PRB coal for minerals larger than 4.6 µm. For Pittsburgh #8, pyrrhotite and illite are the main components of particles in the range between 10-22 µm, and only illite is important in the composition of the largest minerals.

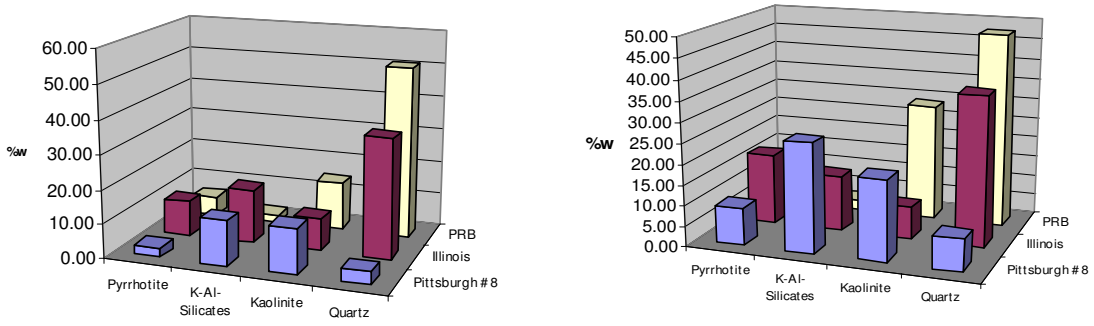

(A) (B)

Figure D-20Mineral composition for included minerals in the size ranges: (A) 1-2.2 µm (B) 2.2-4.6 µm.

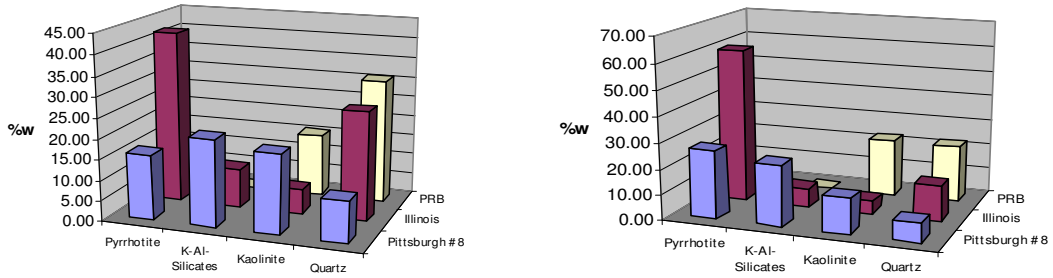

(A) (B)

Figure D-21Mineral composition for included minerals in the size ranges: (A) 4.6-10 µm (B) 10-22 µm.

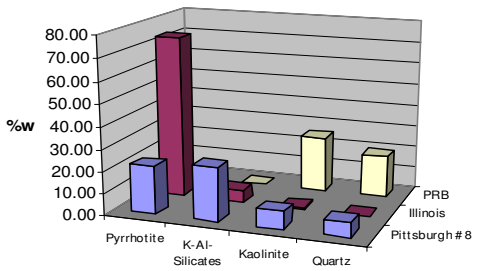

(A)

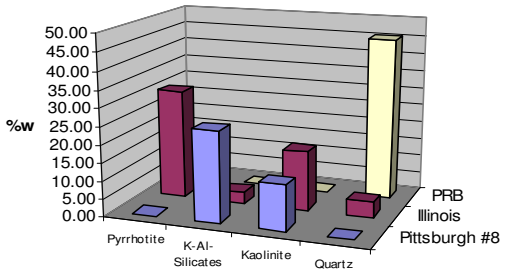

(B)

Figure D-22Mineral composition for included minerals in the size ranges: (A) 22-46 µm (B) 46-100 µm.

D.3. CHAR CHARACTERIZATION (Near-burner Flame Zone Experiments)

D.3.1. FE-SEM and Cross-Section

Some FE-SEM micrographs are shown in Figures D-23 through D-26 for the three different coals analyzed. The two bituminous coals (Pittsburgh #8 and Illinois) showed high swelling at higher pressures (Kulaots et al., 2005). The largest change was observed from atmospheric pressure to 10 atm, remaining constant after this pressure. Particles with thin walls or cenospheres were predominant in those samples.

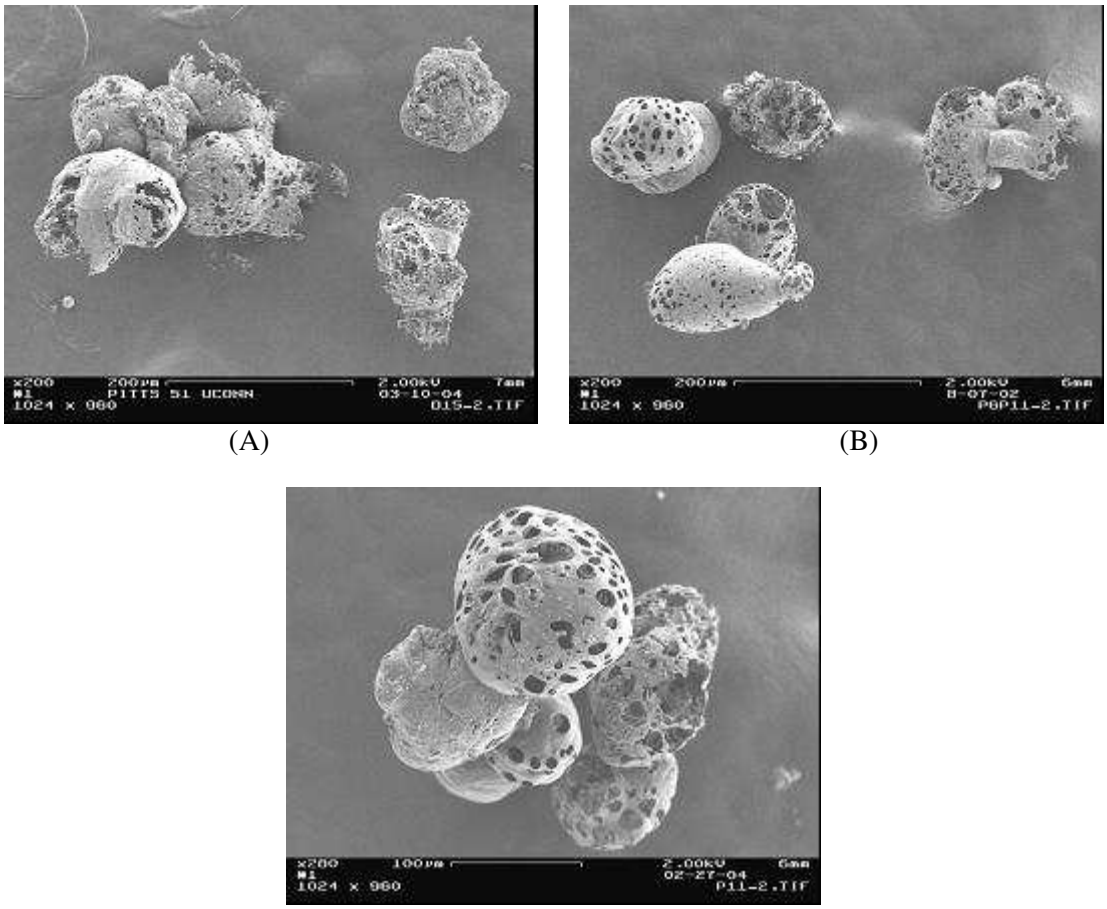

(A) (B)

(C)

Figure D-23 Pittsburgh #8 char micrographs at different pressures: (A) 10 atm (B) 20 atm and (C) 30 atm

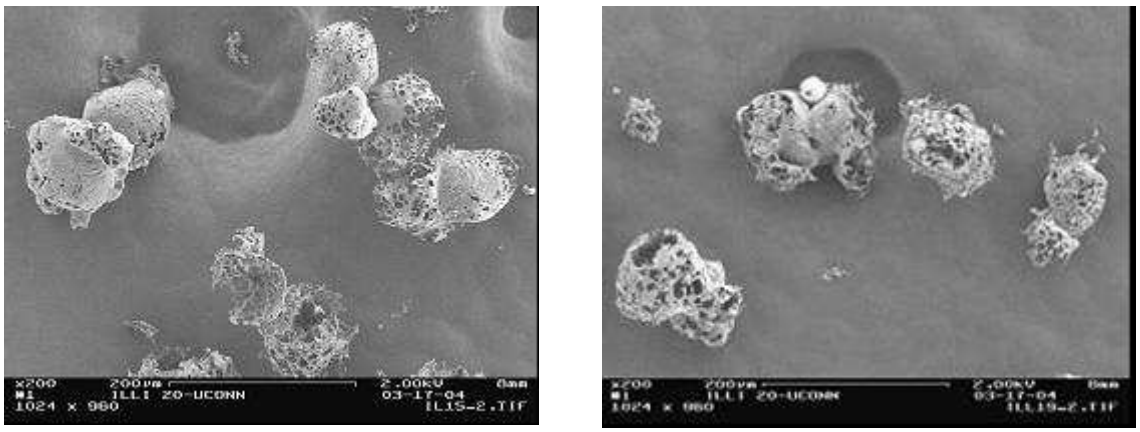

(A) (B)

Figure D-24 Illinois char micrographs at different pressures: (A) 10 atm (B) 20 atm

Figure D-25 confirms the non-swelling characteristics of PRB at higher pressures observed by Brown University (Kulaots et al., 2005). Figure D-26 shows another PRB porous structure at higher burnout where it is possible to observe the ash particles at the edges of the char structure. Table D-14 summarizes the operating conditions of the samples analyzed for this part.

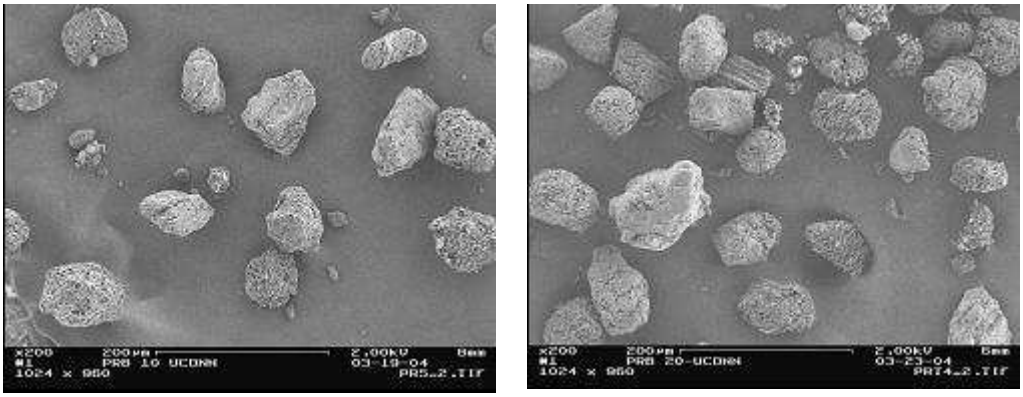

(A) (B)

Figure D-25 PRB char micrographs at different pressures: (A) 10 atm (B) 20 atm

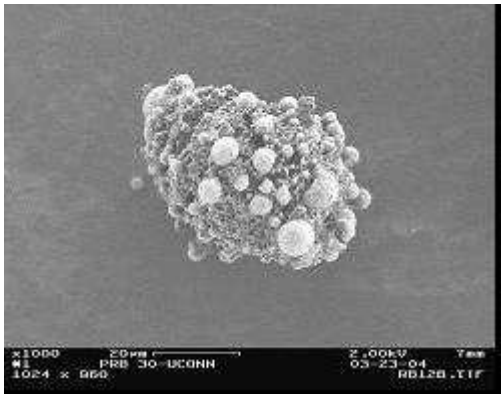

Figure D-26 PRB char at 30 atm

ID #	Pressure, atm	Oxygen/Coal ratio (%)	Carbon content of char, %wt [a]	Ash content of char, %wt [a]	Wt Loss (%)
Pitts-51	10	193.2	70.4	30.7	74.3
Pitts-58	20	204.4	74.5	23.5	62.3
Pitts-68	30	210	-	-	62.3
ILL-82	10	234	52.1	47.0	80
ILL-99	20	245	-	-	77
PRB-13	10	200	77.7	15.9	70
PRB-19	20	275	68.8	26.2	85
PRB-28	30	220	66.0	24.3	87

[a] wt % according to Huffman analysis (SRI Communication)

Table D-14. Operating conditions of the NBFZ samples analyzed by SEM.

D.3.2. Methodology

Characterization of the char particles was done by Scanning Electron Microscopy for whole and cross-sectioned char particles. The methodology proposed by Wu, 2000 using Field Emission Electron Microscopy (FE-SEM) was followed in this study, which permits examination of the internal structures of the chars. A Leo/Zeiss DSM982 Gemini FE-SEM was used to characterize the char samples at different voltages at a working distance of 6 mm. Samples were dispersed on a double-side carbon tape and mounted on an SEM stub for analysis. Higher voltages (20kV) permitted the study of internal structures. Shown in Figure D-27 are two example micrographs of the same particles, one obtained at 2 kV and the other at 20 kV. While the higher accelerating voltage provides more detail of the underlying wall structure, the macroporous and cenospheric nature of the particles is apparent in both images.

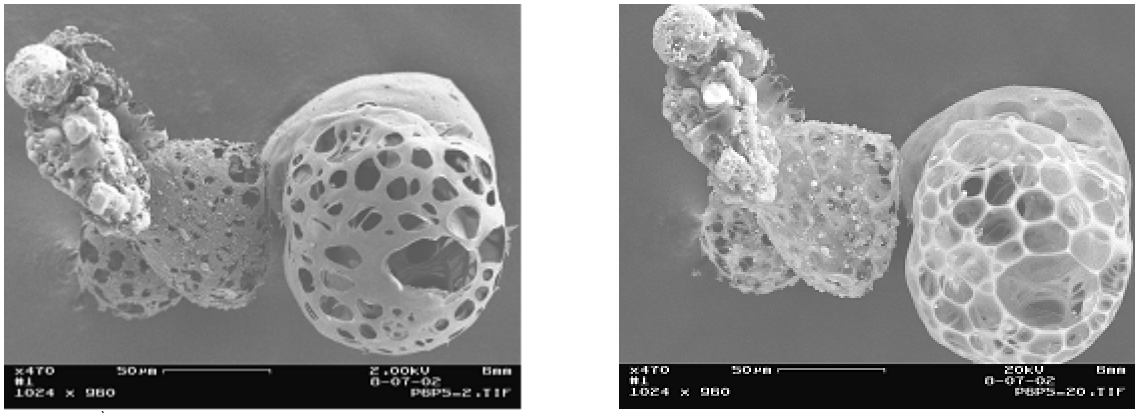

Figure D-27 Chars from sample Pittsburgh #8 at 20 atm. Left image collected at 2 kV accelerating voltage; right image collected at 20 kV accelerating voltage.

Two different types of char particles were observed, one identified as cenospheric and the other one as a solid structure. Cenospheric char particles have a thin wall thickness (<10 µm) and a pseudo-spherical shape. Solid chars have a thicker wall thickness (>10 µm) and angular shapes. Figure D-28 shows an Illinois #6 cenospheric char particle produced at 20 atm pressure and imaged at 2 kV and at 20 kV. The right micrograph permits observation of the hollow structure of this particle. Figure D-29 shows a solid Pittsburgh #8 char particle produced at 20 atm. This solid char particle does not present holes in its internal structure at either accelerating voltage.

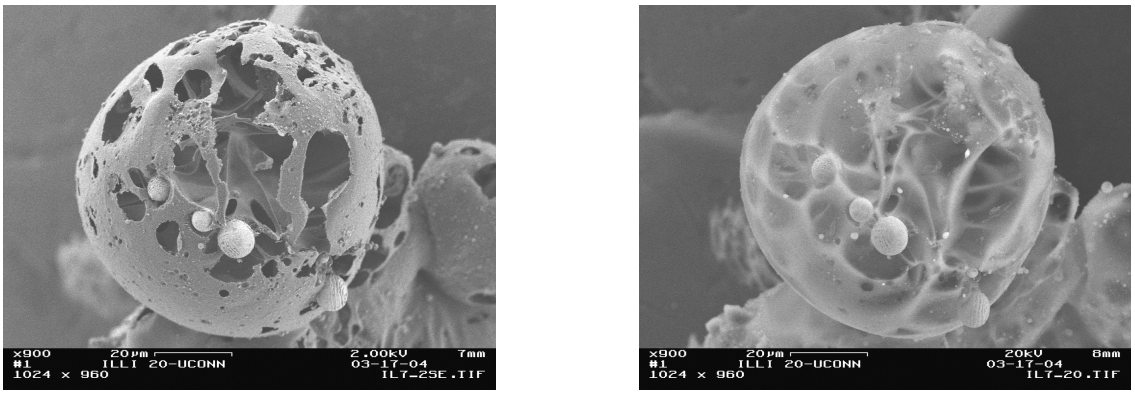

Figure D-28 Type No. 1 - Cenospheric Char under FE-SEM a. 2 kV b. 20 kV

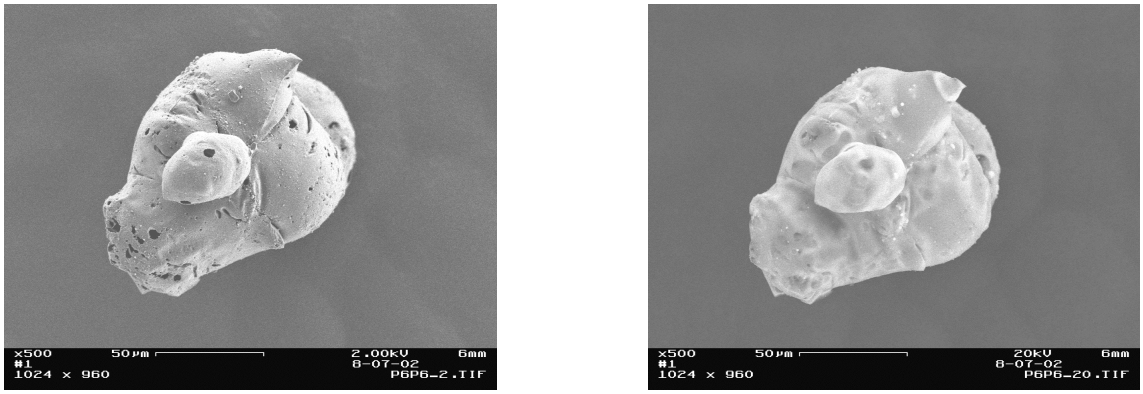

Figure D-29 Type No. 2 - Solid Char under FE-SEM a. 2 kV b. 20 kV

Cross sections of the char particles were also prepared to permit a more detailed examination of the pore structure. To prepare cross-sectioned samples, char particles were embedded in mounting Epoxy Resin EPO-TEK, ground at 800 mesh, and then polished with aluminum oxide. Mounted polished samples were then coated with a gold-palladium layer and analyzed on an Amray 1200 Scanning Electron Microscope. Images were taken at 20 kV and at a working distance of 15mm. The image analysis software MicroGop 2000 was used in a semi-automatic mode to count classified char particles from the different FE-SEM micrographs. The minimum number of particles counted was 160 for each pressure condition.

D.3.3. Results and Discussion

Cross-sectioned samples of char particles were also prepared as discussed above to permit a more detailed examination of internal char structures. The difference in the shell thickness of the different types of chars can be observed in Figure D-30. This micrograph of a Pittsburgh #8 char shows both char types: a cenospheric type of char with a wall thickness of less than 10 µm and a solid char where this wall does not present itself clearly. An optical micrograph for a cenospheric char can be seen in Figure D-31. It corresponds to a cross sectional preparation of Illinois at 20 atm and it is also possible to recognize the thin wall.

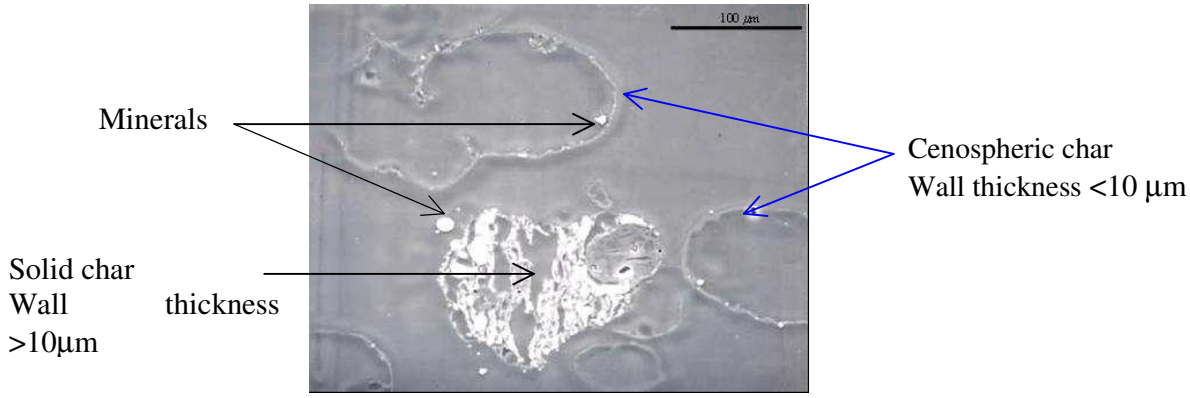

Figure D-30 SEM of cross sectioned Pittsburgh char generated at 10 atm.

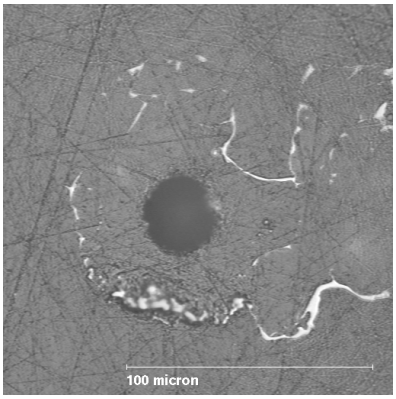

Figure D-31 Cross Section Illinois char generated at 20 atm.

Results of the char classification for the bituminous coals, Pittsburgh #8 and Illinois are shown in Figure D-32. For Pittsburgh #8, a maximum in the number of cenospheric char particles formed was observed at 10 atm. The amount of these particles decreases from 89% of the total particles at 10 atm to 66% at 30 atm. For Illinois #6 coal, the change in char structure with pressure for the three pressures studied was not significant.

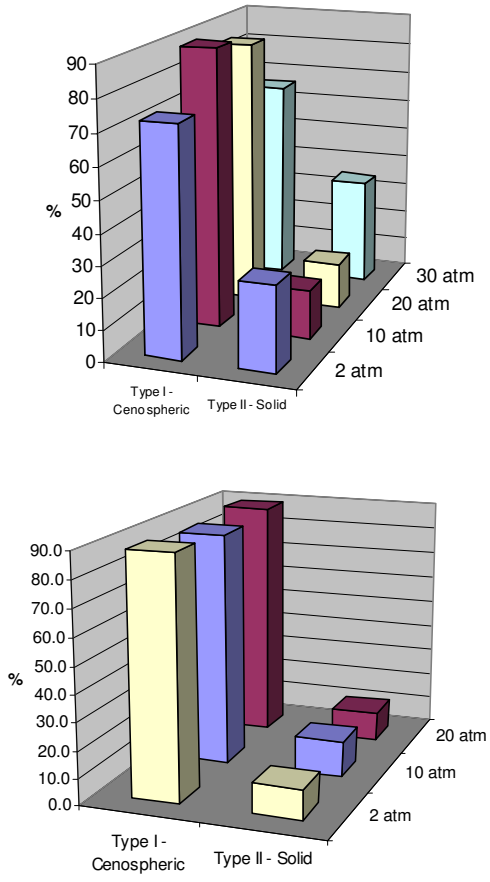

Figure D-32 Char distributions for a. Pittsburgh and b. Illinois bituminous coals. (a) top; (b) bottom.

The results for Pittsburgh #8 in this study differ from the work presented for an Australian bituminous coal by Wu et al., 2000. Their study concluded that over the range of pressures tested (1-15 atm), an increase in operating pressure would increase swelling and therefore increase the formation of cenospheric char particles. The work presented here, examining higher pressure up to 30 atm and a Pittsburgh bituminous coal, concludes that a maximum in the amount of cenospheric particles is reached at 10 atm for this coal, whereas little difference with pressure is seen for the Illinois coal. This suggests that there may be a limit where pressure does not favor the formation of these cenospheric particles.

The results for Illinois #6 may be explained as a function of the amount of the maceral vitrinite present in the coal. Table D-15 contains maceral information for the two bituminous coals. Vitrinite is a maceral that has been associated with the formation of cenospheric chars (Wall et al., 2002, Bailey et al., 1990, Wu, 2000). It is derived from the wall cells of plants and is rich in oxygen (Speight, 1983). The vitrinite content is particularly high for Illinois #6 coal (90.2% vol) and it may be responsible for the fact that the formation of cenospheric chars was unaffected by pressure up to 20 atm.

	Pittsburgh #8	**Illinois**
Vitrinite, %vol	79.4	90.2
Liptinite, % vol	6.9	3.0
Inertinite, %vol	13.7	6.8

Table D-15 Maceral information for Pittsburgh #8 and Illinois coals

The char particle size distribution of the two types of chars using the FE-SEM micrographs for Pittsburgh #8 is also shown in Figure D-33. The cenospheric type of char particles swells the most at 10 atm, presenting a larger char particle size distribution compared to 2 atm pressure. These results were also corroborated by measuring the swelling ratio of the char sample, using density measurements for char and coal particles. The largest swelling index was also observed at 10 atm and had a value of 1.6 on a diameter basis (Kulaots et al., 2005). For 30 atm, the swelling index measured was 1.4, compared to 1.2 for the char sample at 2 atm pressure.

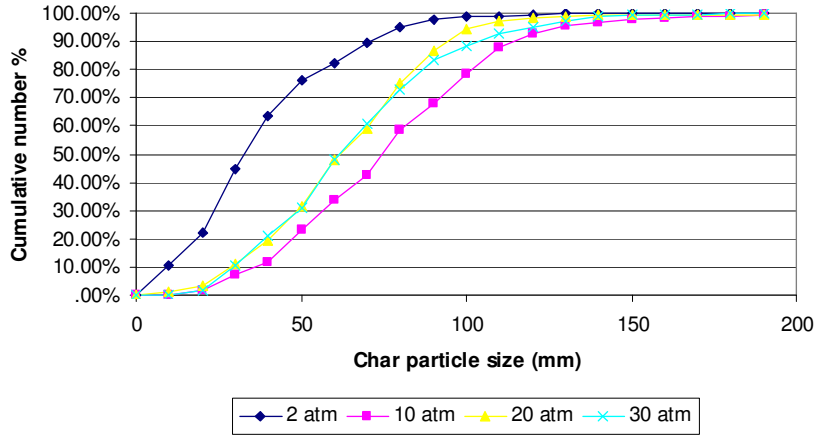

Figure D-33 Char particle size distribution for Pittsburgh #8 bituminous coal.

An effort to correlate the type of chars produced by pyrolysis at different pressures, taking into account the operating pressure and maceral composition of the parent coal, was made. The first correlation was proposed by Wu, 2000 as a function of vitrinite content and operating pressure as n_cenosp = 0.60P + 0.53V + 37 where n_cenosp is the number of cenospheric char particles, P is the operating pressure in atm and V is the vitrinite content in %volume. While this correlated with the data of the Australian coal studied by Wu et al. 2000, there was no linear correlation with pressure observed in our study. The following correlation is therefore proposed in this work for bituminous coals. The correlation included the data presented for the Australian coal (Wu et al., 2000) and the data for this study (Pittsburgh #8 and Illinois) and has an R^2 value of 0.93:

$$C = 34.92 + 1.76\,P - 0.07\,P2 + 0.51\,V$$

where C is the percentage of cenospheric chars, P is the operating pressure in atm and V is the vitrinite content in %vol.

D.3.4. Mercury Porosimetry

Char porosity is also an important parameter in understanding ash formation under pressurized conditions. Mercury porosimetry analyses of selected NBFZ char samples were conducted. A coal sample and three char samples (10, 20 and 30 atm) from Pittsburgh #8 parent coal were analyzed, as well as a sample from the PRB and two NBFZ chars of PRB at 10 and 20 atm. A Quantachrome Poremaster Mercury Porosimeter 33/60 was used in order to get data on mercury porosimetry. Figures D-34 and D-35 show the pore size distribution for Pittsburgh #8 and PRB samples respectively.

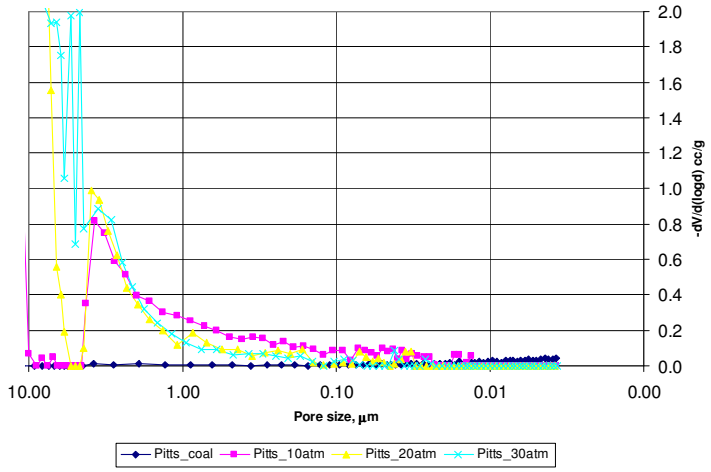

Figure D-34 Pore size distributions for Pittsburgh #8 coal and chars.

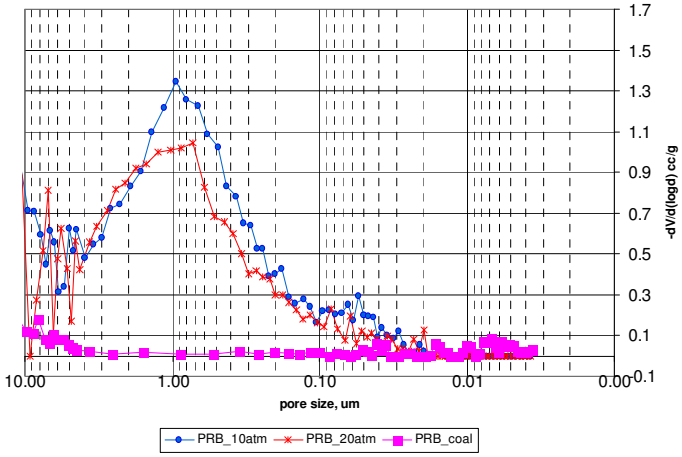

Figure D-35 Pore size distributions for PRB coal and chars.

Note that the differentiation between interparticle and intraparticle porosity was difficult for these samples because it is possible to find intraparticle pores as well as interparticle spacing of approximately the same size. Consequently, it was assumed that the intraparticle porosity classification cover the range 5 - 5000 nm as reported by Tomeczek and Gil, 1997 was appropriate here. The same three different pore size groups analyzed by Tomeczek and Gil, 1997 and 2003 were analyzed. The results for these groups of Pittsburgh #8 coal and chars are shown in Figure D-36 and Figure D-37 contains the results for the PRB coal and chars

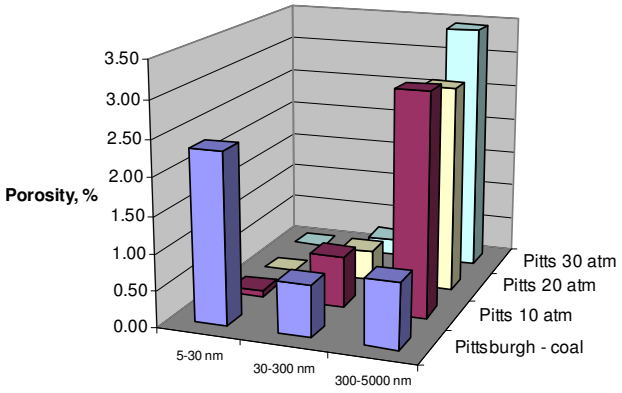

Figure D-36 Pore size group distributions for Pittsburgh #8 coal and chars.

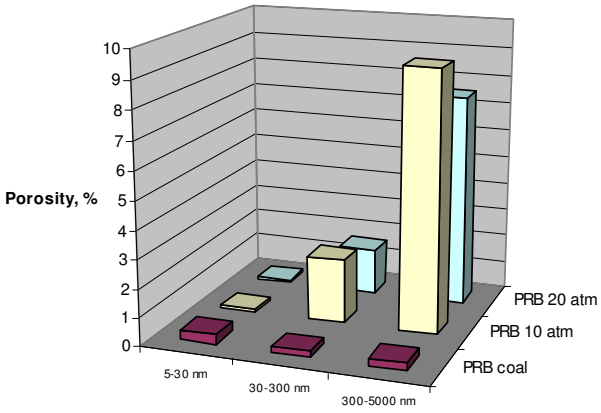

Figure D-37 Pore size group distributions for PRB coal and chars.

D.4. ASH FORMATION EXPERIMENTS: CASCADE IMPACTOR TESTS

D.4.1. Experimental Set-up and Cut-off Size Range Calculations

The first step was to evaluate the operation of the existing impactor at high pressures. The dimensions of the impactor and the cyclone pre-separator under consideration for these experiments are shown in Figures D-38 and D-39. An Al-foil substrate was placed in each stage in order to collect the segregated ash. Alternative stage substrates were greased with high-vacuum grease, allowing SEM to be done in selected, non-greased ones. Grease is used in order to avoid particle bounce (Reist, 1993).

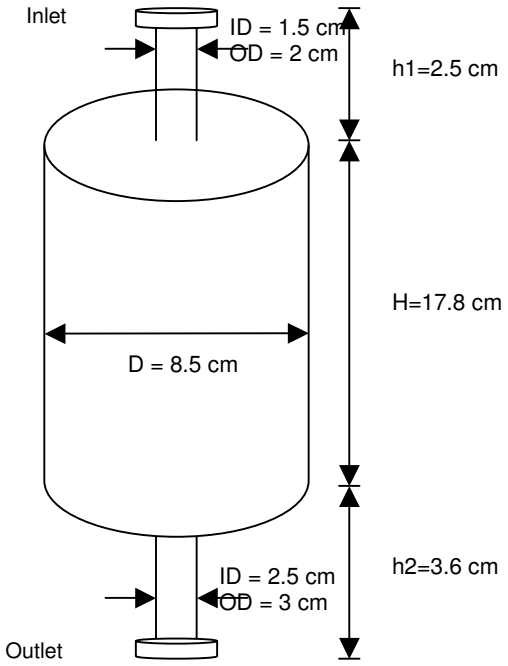

Figure D-38 Low pressure impactor (figure not to scale).

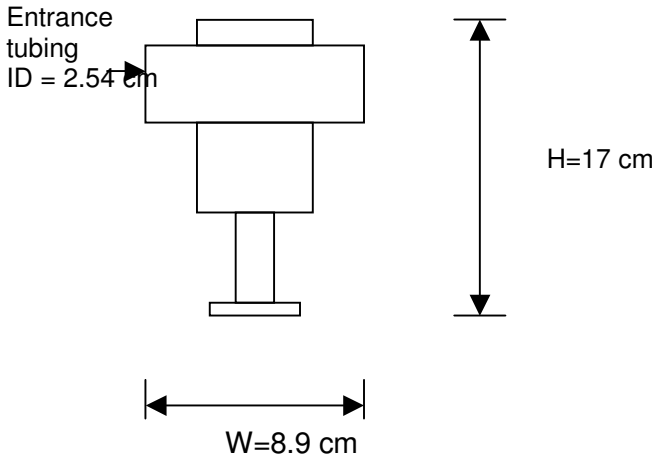

Figure D-39 Pre-separator cyclone of the low pressure impactor (figure not to scale).

During testing of the low pressure impactor and the pre-separator cyclone, it was found that the seals at the inlet to the cyclone leaked at elevated pressure, resulting in the cyclone not being usable for the HPBO experiments. The impactor, however, did not leak at pressures up to 170 psi. Higher pressure clamps were installed that allowed the operation to at least 10 bar.

The calculated ash particle size cuts (Table D-16) were done considering pressure drop in the impactor measured by SRI at 2 and 10 atm. Following these pressure drop measurements, 10% of the pressure drop was assumed for 20 and 30 atm operating pressure. It was also assumed that upstream pressure increased linearly with operating pressure. The flowrates considered were 13, 40, 70 and 110 slpm for 2, 10, 20 and 30 atm experiments respectively. The cut-off diameters corresponded to the particle size that could be collected with 50% efficiency. These results indicated that it was possible to use this impactor at high pressures obtaining a reasonable separation of ash in the size range 40 to 1.5 μm

Stage	2 atm	10 atm	20 atm	30 atm
11	30.46	37.84	39.72	38.04
10	14.78	19.06	20.12	19.41
9	7.57	9.83	10.38	10.01
8	3.98	5.23	5.52	5.33
7	2.00	2.62	2.77	2.67
6	1.13	1.51	1.59	1.53
5	0.78	1.05	1.12	1.08
4	0.58	0.79	0.84	0.81
3	0.61	-	-	-
2	-	-	-	-
1	-	-	-	-

Table D-16 Cut-off diameters for impactor, μm

Table entries containing a – in the cell represent conditions where calculations indicated there would be an increase in size, a likely reflection of using an impactor designed to operate at low pressures at elevated pressure. The hole ("jet") pattern in the lower stages was designed such that it would not provide any additional separation under elevated pressure conditions. Preliminary SEM characterization of ash samples generated in HPBO experiments was done in order to determine if it would be possible to identify only ash in the samples (complete burnout tests). Examples of these SEM micrographs for PRB at 2 atm pressure are shown in Figures D-40 and D-41 and show no presence of char residue.

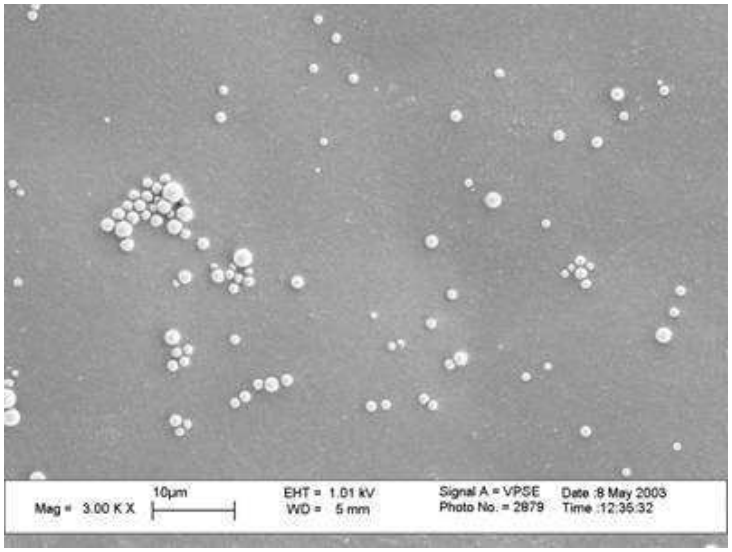

Figure D-40 SEM of PRB #139 ash – Stage 7.

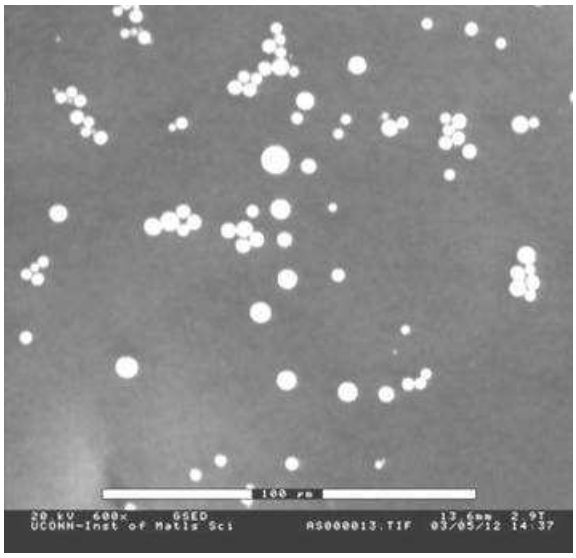

Figure D-41 SEM of PRB #139 ash – Stage 11.

D.4.2. Particle Size Distribution of Impactor Experiments vs. CCSEM Results

Particle size distribution results collected ash generated from combustion of the three coals at different pressure conditions can be found in the SRI section of the report for this project (Eckstrom et al. 2005). A comparison between these results and the ones obtained by CCSEM of the ash samples from HPBO experiments was done for Pittsburgh #8.

Figures D-42 to D-45 show the cumulative mass percentage comparison for particles less than 40 microns for the different pressures. These results include stage 0 (corresponding to a quartz paper filter located after the impactor) to stage 11 of the impactor. The conditions for these experiments are summarized in Table D-17. As observed in Figure D-42 and D-45, the impactor and the CCSEM results for 10 and 30 atm are in reasonably good agreement. In all cases, the impactor samples report a finer ash particle size distribution. At 20 atm, the distributions show the greatest difference between the two measurements. This may be due to a high Carbon content of this sample for the CCSEM analysis.

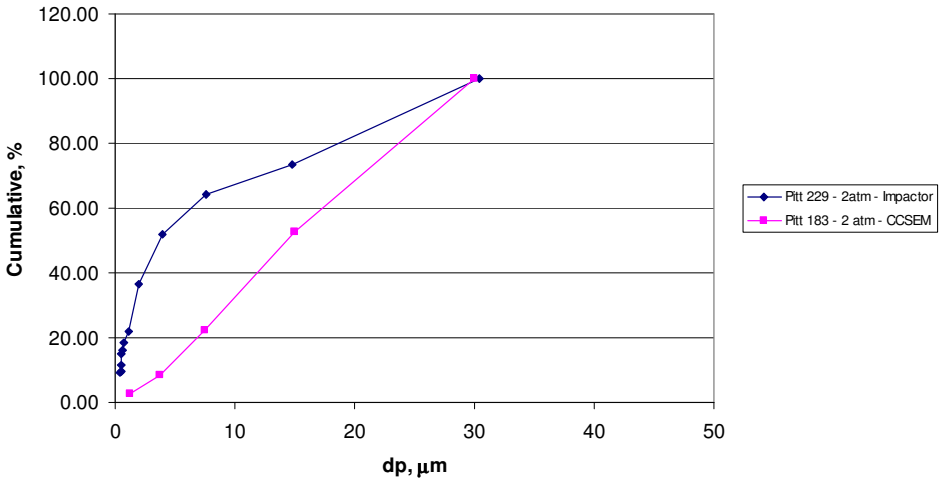

Figure D-42 CCSEM results versus Impactor results at 2 atm pressure for HPBO experiments.

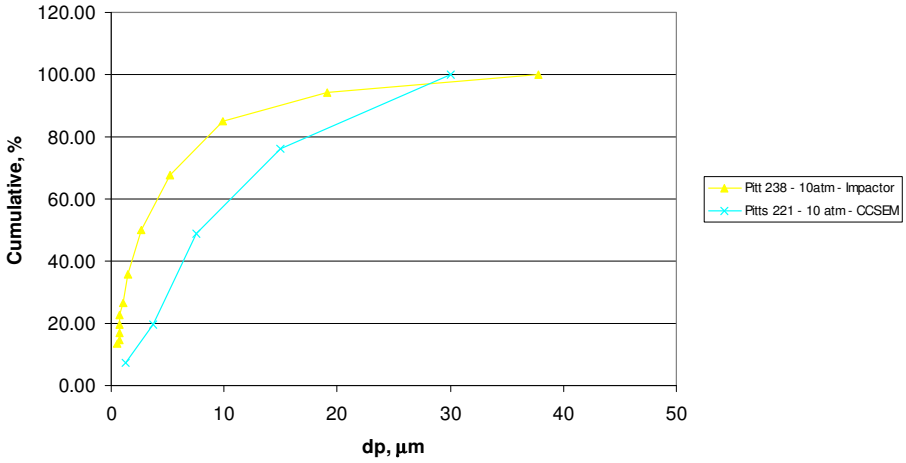

Figure D-43 CCSEM results versus Impactor results at 10 atm pressure for HPBO experiments.

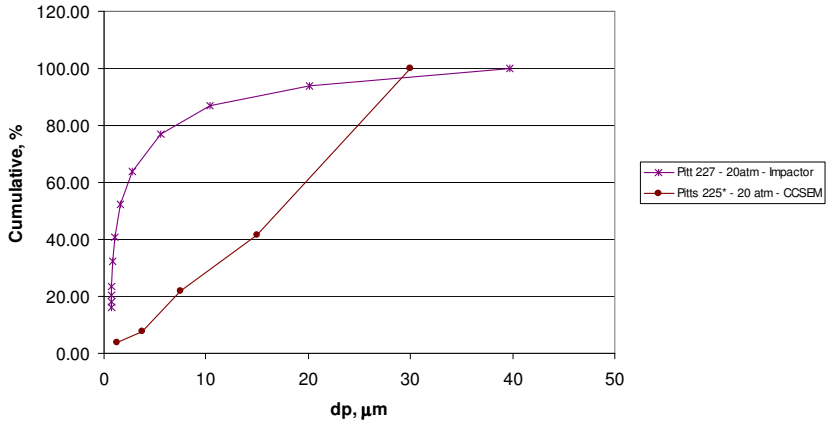

Figure D-44 CCSEM results versus Impactor results at 20 atm pressure for HPBO experiments.

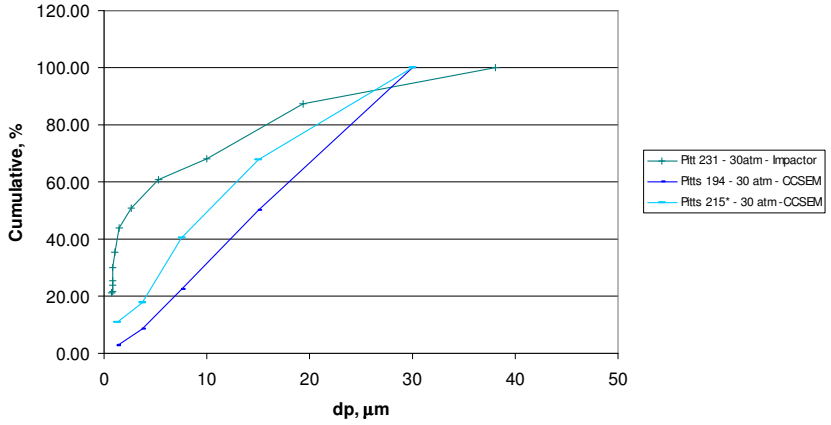

Figure D-45 CCSEM results versus Impactor results at 30 atm pressure for HPBO experiments.

	Pressure, atm	Coal susp loading, %wt	O2 conc, %wt	Furnace length, cm	Res. Time (ms)	Ash content of solid, %
Pitts 183 - 2 atm - CCSEM	2	6.8	26.0	88	1956	90.9
Pitts 229 - 2atm - Impactor	2	7.8	31.2	89	1977	
Pitts 221 - 10 atm - CCSEM	10	8.0	26.0	56	1867	70.4
Pitts 238 - 10atm - Impactor	10	5.3	21.0	89	2967	
Pitts 225* - 20 atm - CCSEM	20	2.28	7.4	89	2967	47.8
Pitts 227 - 20atm - Impactor	20	2.3	9.2	89	2967	
Pitts 194 - 30 atm - CCSEM	30	1.67	12.5	56	1867	95.7
Pitts 231 - 30atm - Impactor	30	1.68	10.0	89	2967	
Pitts 215* - 30 atm -CCSEM	30	5.14	15.7	15.5	517	43.6

Table D-17 Conditions for the tests for Pittsburgh #8 of the CCSEM and Impactor samples analyzed. * High carbon samples

The cumulative ash particle size distributions for the impactor samples for Pittsburgh #8 at pressures of 2, 10, 20 atm is shown in Figure D-46. The finer size distribution for the impactor agrees with the CCSEM results and it is obtained at 10 atm, as a result of a high number of swollen char particles that allow formation of finer ash particles, not allowing for the coalescence of those. The larger particle size distribution among the ones analyzed is obtained at the condition closest to atmospheric pressure (2 atm).

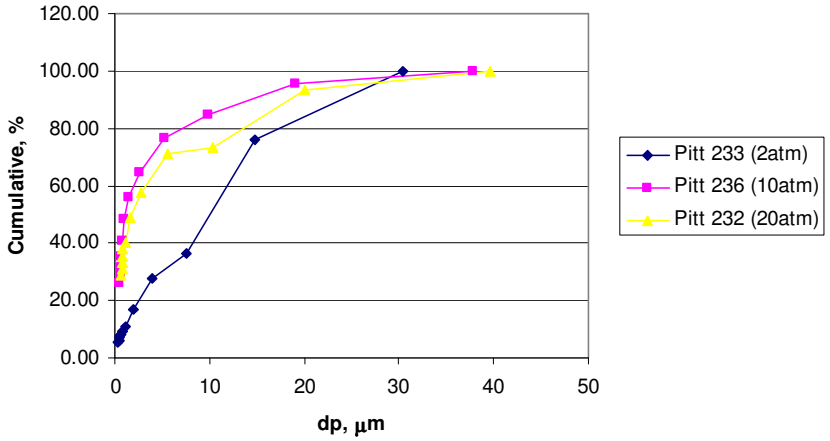

Figure D-46 Impactor results at different pressures for Pittsburgh #8.

As a general note, to obtain more accurate size distribution from using an impactor in the pressurized reactor, it would be recommended that the impactor be calibrated under pressurized conditions with monodisperse spheres, and that pressure drop between stages be measured. It was also noted that there was more particle deposition on the walls of the reactor and inlet to the impactor, potentially complicating interpretation of these results. Comparisons with CCSEM should therefore be considered relative (for pressure effect trends) rather than absolute.

D.5. ASH CHARACTERIZATION (HIGH-PRESSURE BURNOUT EXPERIMENTS)

D.5.1. Preliminary SEM Characterization

Two micrographs of Pittsburgh #8 particles obtained at 2 atmospheres pressure are shown in Figures D-47 and D-48. The formation of small molten ash particles on the rims of the pore structures strongly suggests that char fragmentation in the late stages of burnout will affect the ash particle size distribution at the smallest particle sizes. Micrographs of the same coal at 10 atmospheres pressure are shown in Figures D-49 and D-50. Ash particles are clearly evident at the edges of the char structures.

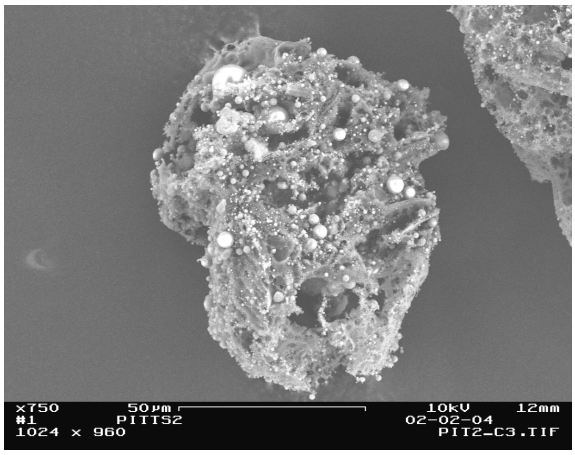

Figure D-47 Char from sample Pittsburgh #8 at 2 atm

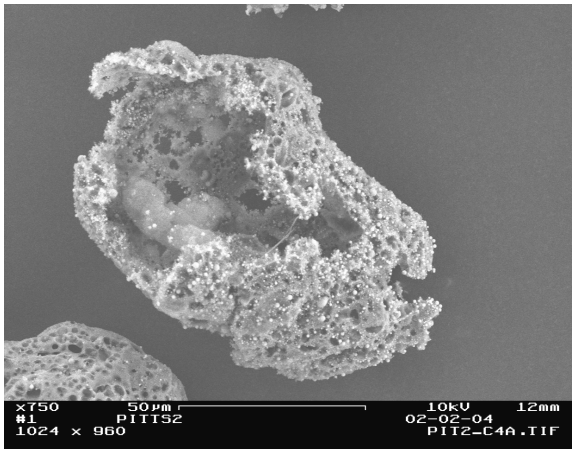

Figure D-48 Char from sample Pittsburgh #8 at 2 atm.

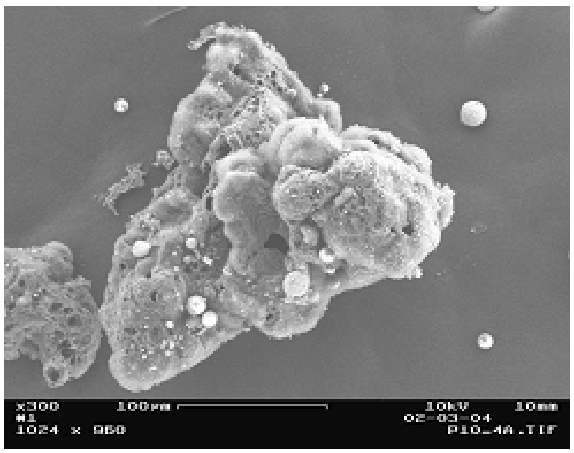

Figure D-49 Char particle generated in HPBO experiment of Pittsburgh #8 at 10 atmosphere pressure.

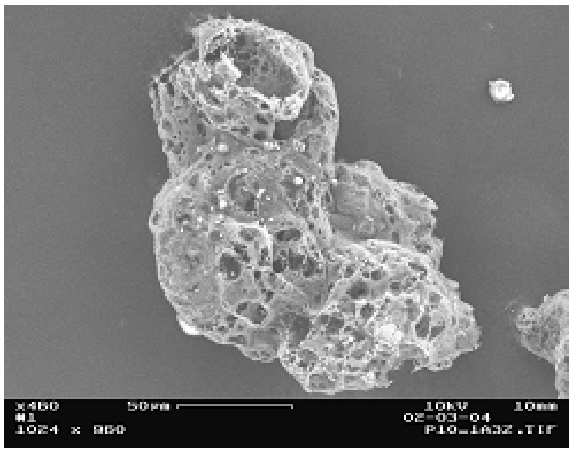

Figure D-50 Char particle generated in HPBO experiment of Pittsburgh #8 at 10 atmosphere pressure.

D.5.2. CCSEM Analysis

Computer Controlled Scanning Electron Microscopy analysis was done for selected HPBO samples from Pittsburgh #8. The operating conditions for these samples is summarized in Table D-18.

Table D-18 Operating conditions of HPBO samples analyzed by CCSEM.

Sample ID	Pressure (atm.)	%C in Sample	Stoichiometric Ratio
183	2	8.5	1.29
221	10	29.1	1.24
225	20	51.5	1.20
194	30	2.4	2.72
215	30	55.3	1.04

Results of the cumulative ash particle size distributions extracted from the CCSEM data indicate a smaller ash particle size distribution, and hence a maximum in the formation of fine ash particles, at a pressure of 10 atmospheres as shown in Figure D-51. These data must be examined as a function of char burnout, however, and in conjunction with data from the impactor experiments, as the levels of carbon vary considerably from sample to sample. Comparison of the two samples obtained at 30 atm pressure, one at an SR of 2.72 (sample #194) yielding an ash sample with 2.4% carbon (SRI data), and one at an SR of 1.04 (#215) yielding a sample with 55.3% carbon (SRI data), suggest an increase in ash particle size with increasing burnout, indicative of mineral / ash particle coalescence in the late stages of burnout. This trend in size correlating with pressure is consistent with the maximum value in the swelling index occurring for this coal at 10 atm pressure, and also

with the maximum extent of cenospheric char formation as measured by microscopy at this pressure and as reported earlier in this report.

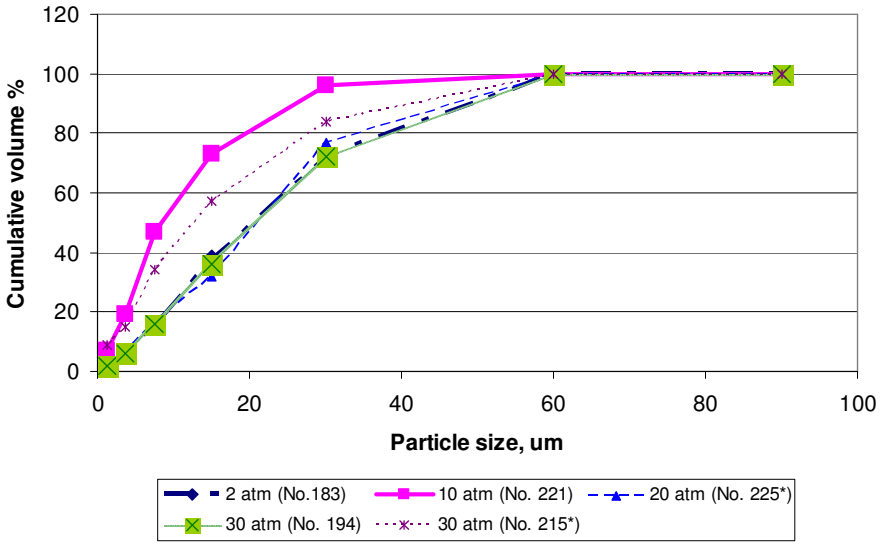

Figure D-51 Particle size distribution of ash from Pittsburgh #8 coal HPBO samples.

In examining trends in ash particle composition as a function of pressure from these CCSEM results, the following classification was used: composition X Y Z, with X representing the predominant component, Y being the second element and present in at least 10% concentrations, and Z being the third element listed and present in concentrations greater than 6%.

Figure D-52 shows volume percentage results for Al versus Si for ash generated from combustion of Pittsburgh #8 coal at different pressures. There is a small peak at SiO_2 mineral coordinates (Si 88.2, Al 4.8) that may correspond to unreacted quartz from the parent coal (5.2 vol%). This peak had a maximum at 20 atm (4.4 vol%) and a minimum at 2 atm pressure (1 vol%), suggesting that with an increase in pressure, there is a maximum for the amount of unreacted quartz. Comparing only those ash samples that were associated with low carbon content (#183, 221 and 194), the maximum occurs at 10 atm (3.8 vol%).

In the same figure, the larger peaks are seen to correspond to aluminosilicate (Si 58.8, Al 33.6) and result from interaction of the illite (17.5 vol%) and miscellaneous silicates (19 vol %) present in the parent coal. For the samples with low carbon content (less than 9%), an increase in pressure leads to reduced formation of mixed aluminosilicates in the ash. The largest value of mixed aluminosilicates is observed in the sample generated at a pressure of 2 atm (46.9 vol%) and drops to 37.5 vol% at 30 atm pressure. Si Al K has a maximum at 30 atm pressure, suggesting that illite transformations are less extensive at this pressure. Comparing the two samples at 30 atm suggests that these illite transformations through coalescence occur at later stages of burnout, decreasing from 9.6

vol% of the ash in the 55.3% carbon content sample to 4.3 vol% in the 2.4% carbon content sample.

Other peaks observed in the sample at intermediate compositions of Si and Al are due to possible interactions of illite and miscellaneous aluminosilicates with Ca, Fe, S and Na. As pressure increases, there appears to be less extensive formation of Si Al Fe and Si Al S compounds and greater formation of Si Al Ca and Fe Si Al.

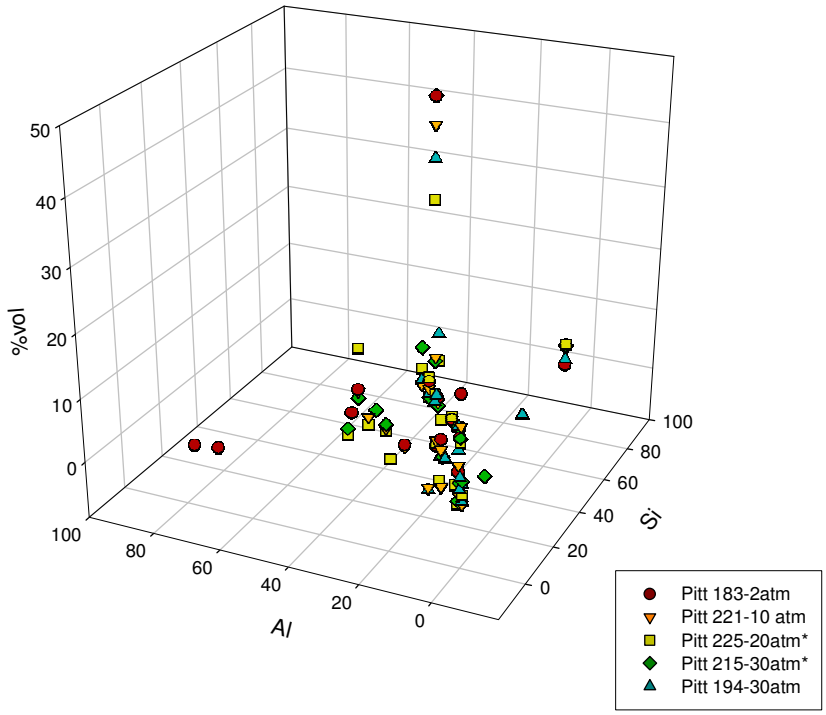

Figure D-52 Si versus Al CCSEM results Pittsburgh #8.

Note: * indicates ash samples with high carbon content.

Figure D-53 shows K versus Si results in the ash samples analyzed by CCSEM. There are several intermediate compositions of silicates and aluminosilicates that contain potassium. At intermediate stages of burnout, (samples #225 and 215) the concentration of Al Si K increases. For the samples with high carbon burnout (samples #183, 221 and 194), as pressure increases, there is also an increase in the concentration of Si Al K (Si 48, K 7.5).

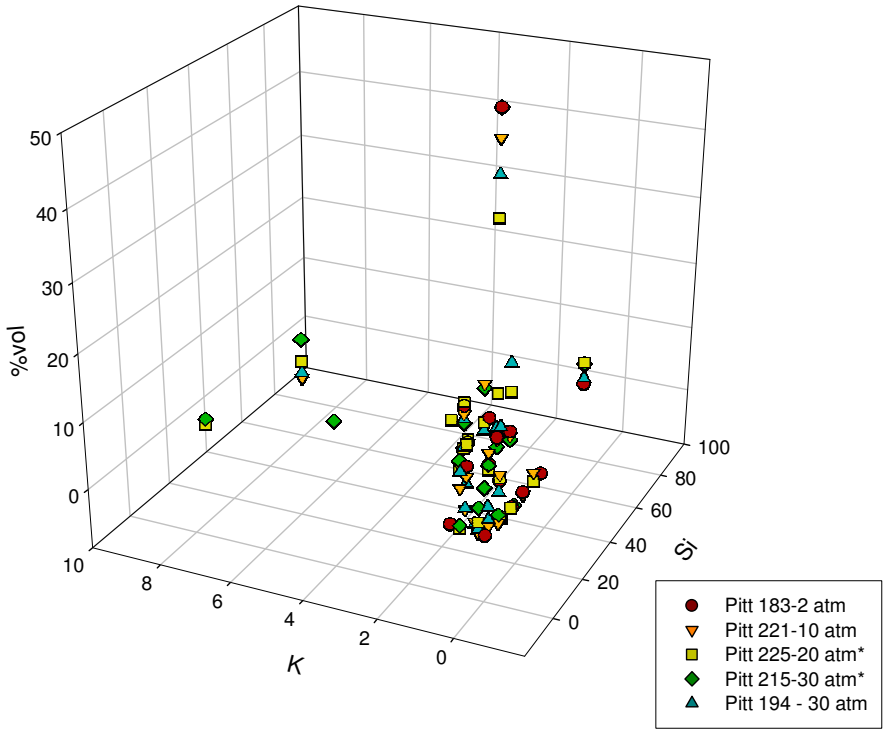

Figure D-53 Si versus K CCSEM results Pittsburgh #8.

Note: * indicates ash samples with high carbon content.

Figure D-54 shows volume percentage results for Si versus Ca. There is a peak in compounds where Ca is the main component (Si 1.2, Ca 89.6). These compounds can be explained by the presence of calcite (1.1% vol) and gypsum/silicates (1% vol) in the parent coal. As pressure increases, the concentration of Ca rich ash decreases. The maximum value is 17.5 vol% at 2 atm versus 4.8 vol% at 30 atm. The aluminosilicates seem to interact with Ca, forming higher amounts of Si Al Ca (Si 49.6 Ca 11) as the pressure increases. The trend of this particular composition can be also observed in Figure D-55. Taking into consideration samples with high burnout, the formation of ash that is primarily Si (Si 88.2, Ca 1) decreases as pressure increases (see major peaks in Figure D-54).

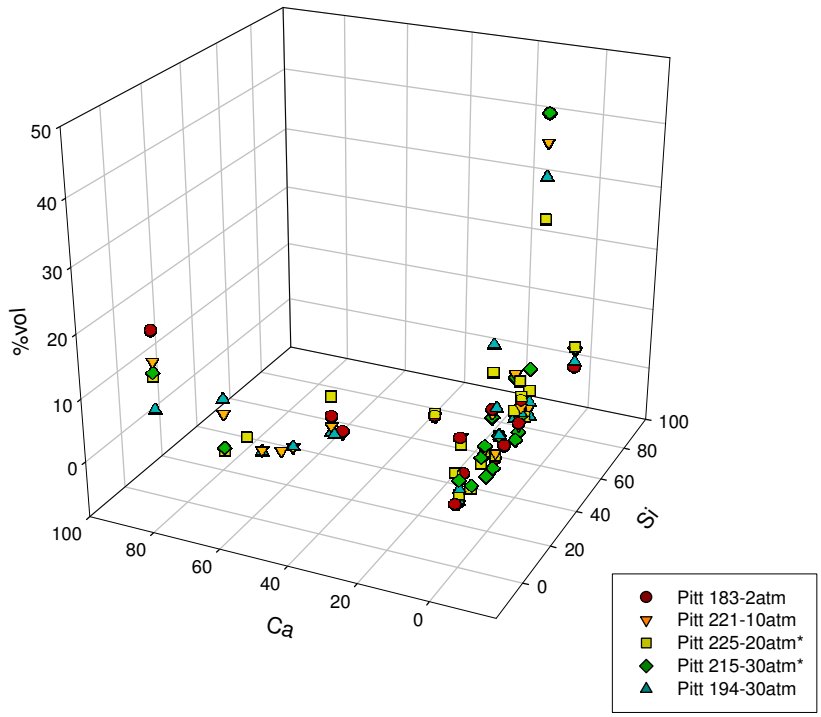

Figure D-54 Si versus Ca CCSEM results Pittsburgh #8.

Note: * indicates ash samples with high carbon content.

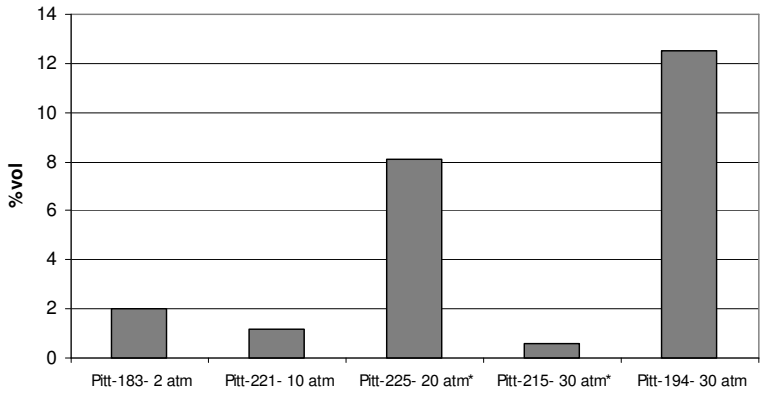

Figure D-55 Si Al Ca formation at different pressures. Pittsburgh #8.

This tendency can also be observed in Figure D-56 where Si versus Fe results are shown. In this figure, iron oxide can be observed at (Si 1.7, Fe 93.7). This peak represents iron-rich ash particles derived from pyrite and pyrrhotite present in the parent coal (47.4 vol%). This peak has a maximum at 2 atm. This indicates that there is more coalescence of iron occurring at higher pressures, mainly forming Fe Si Al and Ca S Fe. This last species is likely formed by interactions of calcium with pyrrhotite. It is also interesting that no iron

dominant ash particles appear in samples with a low percentage of burnout. In those samples, the main ash composition observed was Si Al Fe.

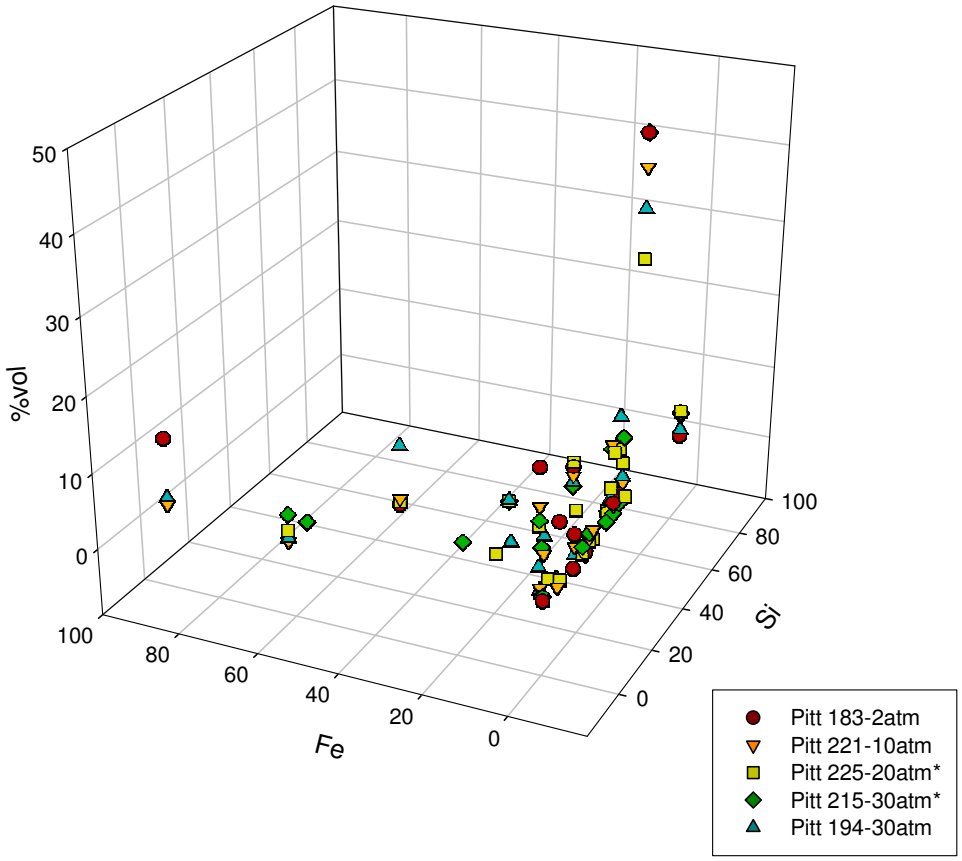

Figure D-56 Si versus Fe CCSEM results Pittsburgh #8.

Note: * indicates ash samples with high carbon content

Examining the distribution for specific chemical compositions, Figure D-57 shows cumulative Si size distributions for the coal (quartz) and for ash samples generated at pressures of 10, 20 and 30 atm at SRI. There is a finer size distribution at 10 atm compared to the quartz present in the parent coal. For samples with higher amounts of carbon (Pittsburgh #225 and Pittsburgh #215), there is a finer size distribution at 30 atm. These results suggest possible fragmentation of the Si minerals at higher pressures. Size ranges less than 20 µm increased, especially 0.3-2.5 µm.

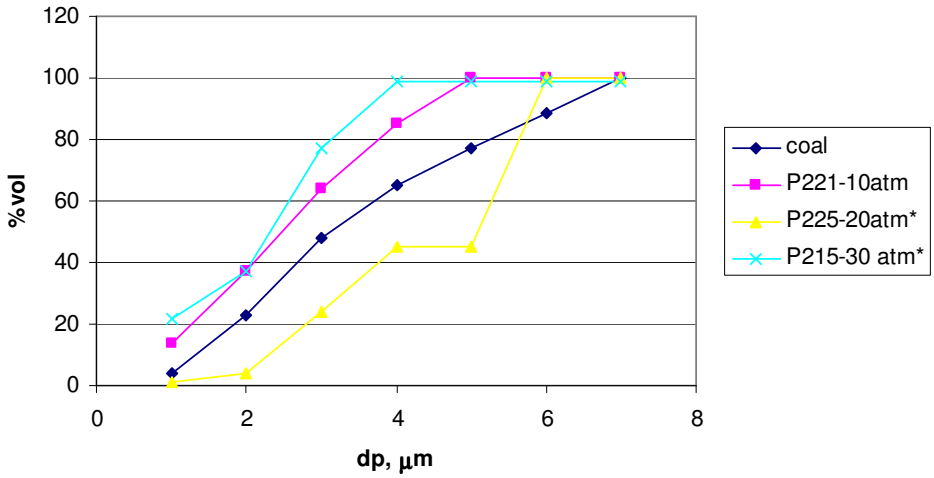

Figure D-57 Cumulative size distribution for silica oxide for Pittsburgh #8.

* Samples with high carbon content.

Figure D-58 shows cumulative potassium aluminosilicate size distributions for two of the samples of Pittsburgh #8 at 10 and 30 atm. These two operating pressures were chosen as the specific composition was the same for both conditions (around 4%vol of the ash analyzed). A finer size distribution for the two operating conditions was observed at 10 atm, suggesting that illite transformations were less extensive at higher pressures.

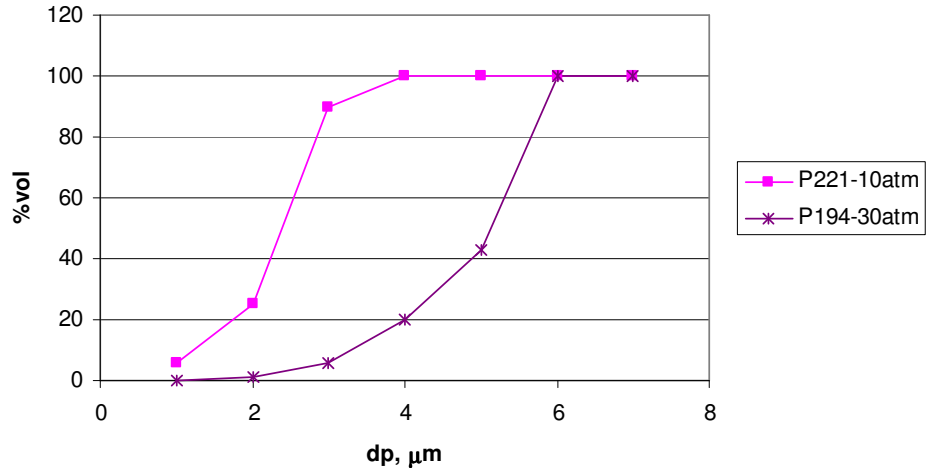

Figure D-58 Cumulative size distributions for potassium alumino-silicates for Pittsburgh #8.

The possibility of conducting additional CCSEM analysis of the impactor samples was considered; however, it was determined that the limitation in mass on individual stages would hamper this analysis. Optical microscopy of some of the samples for Pittsburgh #8 was done in order to identify the presence of carbonaceous material in some of the samples.

Addressing the issue of why ash seems to be liberated earlier during combustion than expected, additional analysis of data from the HPBO experiments was conducted. The following terms were defined for this analysis:

"Carbon Burnout"	= 100 - "Carbon content of the solid collected in the centripeter"
"Retained Ash"	= "Ash content of the solid collected" / "Ash in the coal that was fed" * 100%
"Ash Free"	= 100 - "Retained Ash". It also includes all the other ash liberated, possibly collected in the walls and filter, plus ash losses.

Figure D-59 shows "Ash Free" vs. "Carbon Burnout" results for HPBO experiments for Pittsburgh with argon as a carrier gas at different pressures. Ash is mainly released at more than 70% burnout. The maximum "Ash Free" occurs at 10 atm for these experiments.

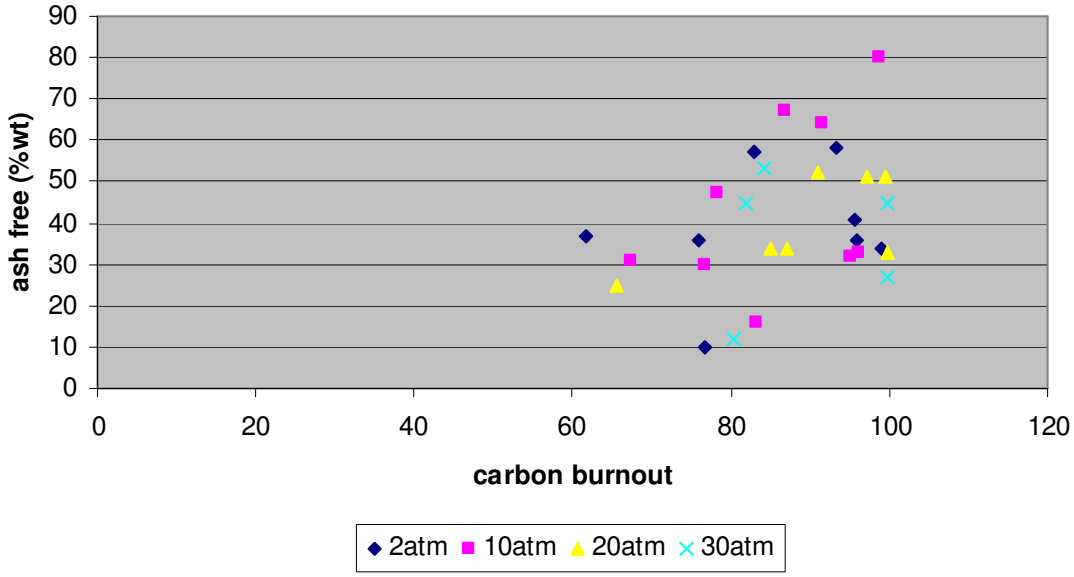

Figure D-59 HPBO experiments for Pittsburgh #8

These results agree with Wu et al., 1999's findings at atmospheric pressure. Their study showed the expected trend of increasing ash release with extent of burnout. At 54% burnout, there were only 11% liberated ash particles. This percentage of free ash particles increases to 80% at 87% carbon burnout.

Analyzing the ash particle size distribution, a maximum in the finest ash size particle distribution was observed at 10 atm for Pittsburgh #8 experiments. Figure D-60 shows the overall ash particle size distribution from the CCSEM analysis of Pittsburgh #8 ash at different pressures. The size ranges between 0.3 and 20 µm had their maximum at 10 atm. The pathways that lead to the formation of these size range particles, were therefore favored at these experimental conditions. As discussed in the section of this report on char

characterization, cenospheric type of chars were also more abundant at 10 atm, showing that char fragmentation of these thin wall structures was an important ash formation pathway for these fine particles (Wu et al., 2000). The other possible pathway, vaporization, is not expected to be significant, as it only accounts for 1% of the total inorganic content transformations.

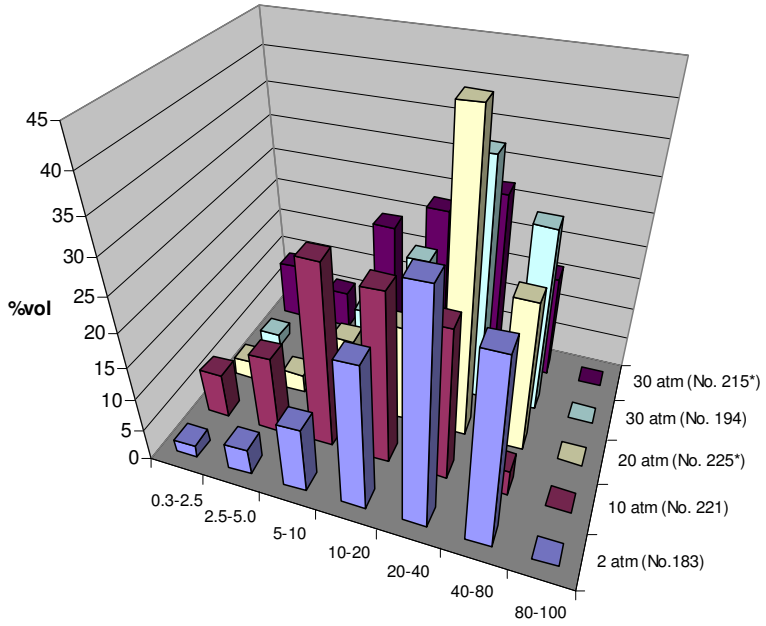

Figure D-60 Ash particle size distributions at different pressures for Pittsburgh #8.

D.5.3. Analysis of Mercury Retention in Solid Residue

Contributing to the analysis of mercury retention for Pittsburgh #8 in solid residue, analysis of the BET surface measurements provided by Brown University was done. Table D-19 summarizes the data available for these samples.

With increasing pressure (see samples # 206, 218, 223 and 224), a decrease in LOI was observed. Data showed higher mercury retention at higher pressures (10, 20 and 30 atm) compared to 2 atm data, which has a higher LOI value. It should be noted that residence time may be contributing to mercury retention behavior. Here, the high pressure samples (10, 20 and 30 atm) had longer residence times than those collected at 2 atm, possibly acting as a counter effect to the higher levels of carbon in the shorter residence time samples.

Sample	P (atm)	Residence time (msec)	O_2/Coal (Wt%)	Char Yield (Wt% AR)	Hg in Char (ng/g)	Retained Hg (Wt%)	BET S.A. (m^2/gchar)	Loss-on-ignition (LOI) %	Carbon based BET S.A. (m^2/gchar)	Mesoporosity (cc/g-char)	Macroporosity (cc/g-char)	C yield in solid sample [b] (Wt %)
Virgin Coal	--	--	--	--	355	--						
Pitt-56	10	400	29.8	39.2	51.4	5.7						
Pitt-77	30	400	19.8	60.3	13.5	2.3						
Pitt-206	2	86	275	35.1	89.8	8.9	40.4	63.0	63.7	0.0256	0.0260	38.2
Pitt-223	10	2967	271	10.6	262	7.8	84.1	40.4	207.0	0.0740	0.0510	8.6
Pitt-218	20	1867	239	17.3	311	15.2	74.8 [a]	44.3	167.8	0.0700	0.0453	12.8
Pitt-224	30	2967	222	19.8	212	11.8	83.1	44.1	187.5	0.0740	0.0360	18.2

Table D-19 Pittsburgh #8 samples – Hg retention information

Another factor to be considered is the carbon based BET surface area. This factor is almost three times higher for higher pressures (10, 20 and 30 atm) when compared to the sample at 2 atm. The higher surface area at higher pressure may also contribute qualitatively to increased mercury retention in these samples. These are qualitative trends only, however, and merit detailed examination, but are outside the scope of the present effort.

It is interesting to note that the carbon BET surface area agrees qualitatively with the swelling factor results at different pressures. For this type of coal, there was a maximum in the carbon-based BET surface area (207 m^2/g carbon) at a pressure of 10 atm. In addition, the swelling factor for this coal also shows a maximum value (1.6) at this pressure.

D.6. ASH FORMATION MODEL

D.6.1. Agglomerates of Particles

As micrographs of char particles at high pressures show the formation of agglomerates specially for Illinois bituminous coal, a calculation that addresses the effect of agglomeration on the ash particle formation was also done. A program that randomly generates dimers, trimers and larger combinations of coal particles by randomly selecting and combining particles taken from the original coal particle size distribution (Pittsburgh #8), was written. For example, to generate dimers, the program randomly selects two coal particles from the original coal particle size distribution and joins them, assuming they form one particle with the corresponding equivalent diameter. The same is done for trimers, tetramers and so on. With this approach, we generated agglomerated coal particle size distributions to match the distributions observed in the SEM micrographs (Tables D-20) and used them as input to the ash formation model to generate ash particle size distributions for Pittsburgh #8. There is a slight reduction of 4 and 8 μm ash particles and a

slight increase of 30 and 60 μm ash particles formed for the char distribution observed at 10 and 20 atm.

	10 atm	20 atm
Single particles	15.6 %	11.2 %
Dimers	28.9 %	23.0 %
Trimers	26.7 %	28.3 %
Tetramers	17.8 %	23.6 %
Pentamers	11 %	10.3 %
Sextamers	0 %	3.5 %
Total particles counted	180	339

Table D-20 Char agglomerate distribution for Pittsburgh #8.

D.6.2. Algorithm

The framework of the modified algorithm is shown in Figure D-61.

With the initial information, the mineral redistribution into the coal particles is performed and the two possibilities of having or not having the detailed mineral information for excluded minerals by CCSEM are considered. If the mineral information is available, the Monte Carlo method will be used to distribute only the included minerals. Otherwise, the mineral distribution will follow the approach by Charon et al., 1990. The algorithm treats included and excluded transformations separately as shown in Figure D-61 and takes coalescence, char fragmentation, mineral reactions transformations and excluded mineral fragmentation into consideration.

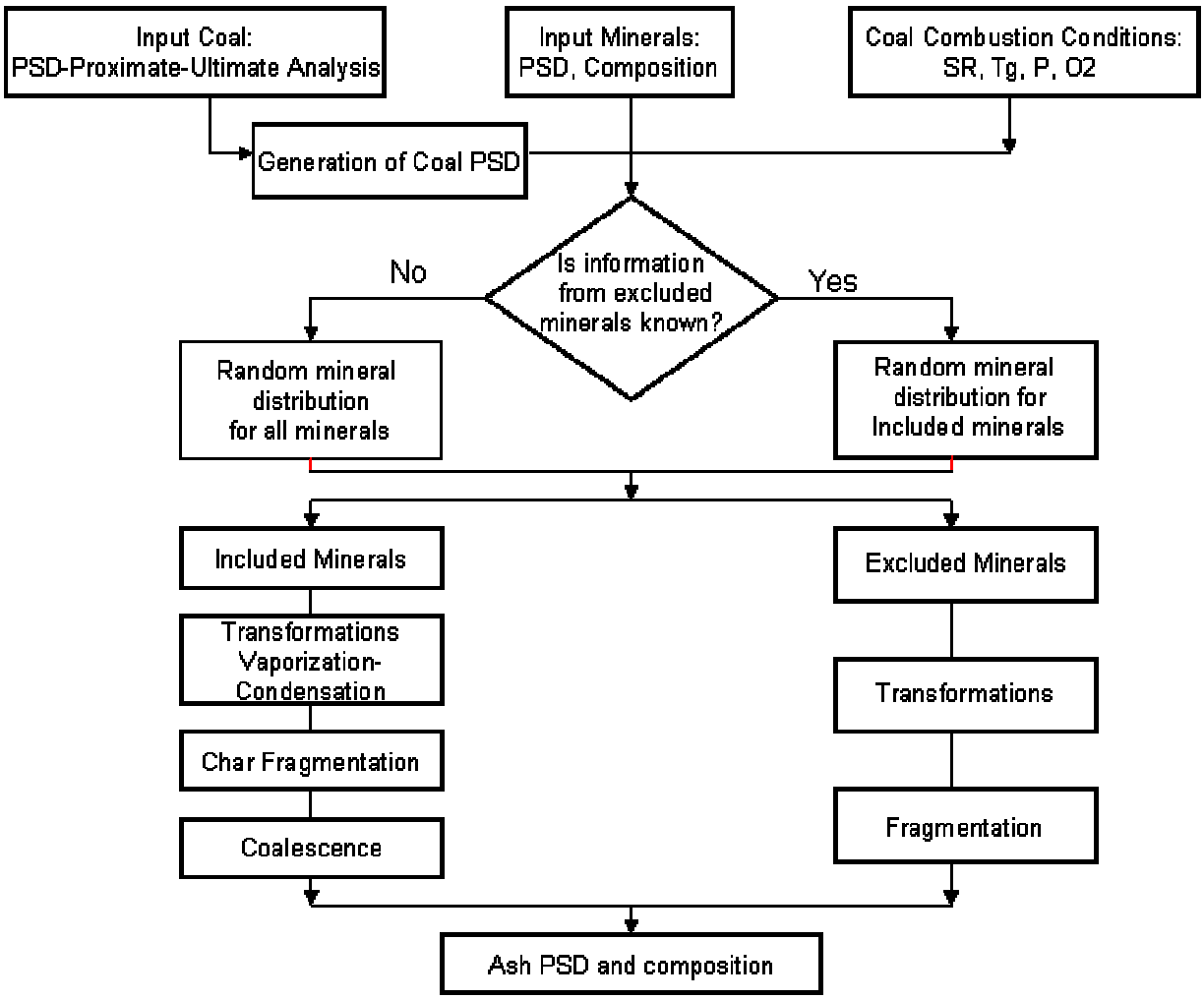

Figure D-61 Algorithm for ash formation

D. APPENDIX A

This appendix contains summary of CCSEM results for the coals and chars analyzed during the project.

Pittsburgh #8 bituminous coal

```
SAMPLE DESCRIPTION    > Pitts Coal
SUBMITTER             > Kurt Eylands
ICC # AND FUND #      > 46970938
RUN DATE AND TIME     >  10  4 2002   9:42

SUMMARY OF PARAMETERS

PERCENT EPOXY USED                          =        71.3
TOTAL MINERAL AREA ANALYZED AT  800.0 MAG   =      4158.3
NORMALIZED AREA ANALYZED AT  800.0 MAG      =    608698.6
MINERAL AREA ANALYZED  250.0 MAG            =     67957.8
NORMALIZED AREA ANALYZED  250.0 MAG         =    917781.3
TOTAL MINERAL AREA ANALYZED AT   50.0 MAG   =   1828569.0
NUMBER OF FRAMES AT  800.0 MAG              =          39
NUMBER OF FRAMES AT  250.0 MAG              =          43
NUMBER OF FRAMES AT   50.0 MAG              =          23
TOTAL MINERAL WGHT % ON A COAL BASIS        =      25.233
TOTAL NUMBER OF POINTS ANALYZED             =        3610
NUMBER OF POINTS UNDER THRESHOLD            =         116

WEIGHT PERCENT ON A MINERAL BASIS
                  1.0    2.2    4.6   10.0   22.0   46.0
                   TO     TO     TO     TO     TO     TO TOTALS
                  2.2    4.6   10.0   22.0   46.0  100.0        % EXCLUDED

QUARTZ             .2     .8    1.0     .7     .5     .9    4.1   45.9
IRON OXIDE         .0     .0     .0     .0     .0     .0     .0     .0
PERICLASE          .0     .0     .0     .0     .0     .0     .0     .0
RUTILE             .0     .0     .0     .0     .0     .0     .0     .0
ALUMINA            .0     .0     .0     .0     .0     .0     .0     .0
CALCITE            .0     .0     .0     .1     .2     .7     .9   99.2
DOLOMITE           .0     .0     .0     .0     .0     .0     .1   53.4
ANKERITE           .0     .0     .0     .0     .0     .0     .0     .0
KAOLINITE          .7    1.8    2.3    2.3     .9    1.8    9.8   49.6
MONTMORILLONITE    .2     .4     .4     .3     .4     .8    2.6   50.9
K AL SILICATE      .7    2.4    2.4    2.5    2.3    3.2   13.6   51.1
FE AL SILICATE     .0     .0     .1     .0     .1     .0     .2   45.7
CA AL SILICATE     .0     .0     .0     .0     .0     .1     .2   50.0
NA AL SILICATE     .0     .0     .0     .0     .0     .0     .0  100.0
ALUMINOSILICATE    .0     .0     .0     .1     .1     .3     .6   74.6
MIXED AL SILICA    .0     .0     .2     .2     .1     .1     .6   70.6
FE SILICATE        .0     .0     .0     .0     .0     .0     .0     .0
CA SILICATE        .0     .0     .0     .0     .0     .0     .0     .0
CA ALUMINATE       .0     .0     .0     .0     .0     .0     .0     .0
PYRITE             .0     .0     .1     .1     .5     .4    1.1   92.8
PYRRHOTITE         .2     .8    2.1    3.7   12.9   26.6   46.3   91.1
OXIDIZED PYRRHO    .0     .1     .2     .0     .5     .3    1.1   87.7
GYPSUM             .0     .0     .0     .0     .0     .0     .0     .0
BARITE             .0     .0     .0     .0     .0     .0     .0     .0
APATITE            .0     .0     .0     .0     .0     .0     .0   70.4
CA AL P            .0     .0     .0     .0     .0     .0     .0     .0
```

KCL	.0	.0	.0	.0	.0	.0	.0	.0
GYPSUM/BARITE	.0	.0	.0	.0	.0	.0	.0	.0
GYPSUM/AL SILIC	.3	.2	.0	.0	.1	.2	.8	36.9
SI RICH	.2	.2	.4	.4	.3	1.1	2.6	60.2
CA RICH	.0	.0	.0	.0	.1	.0	.1	93.0
CA SI RICH	.0	.0	.0	.0	.0	.0	.0	.0
UNCLASSIFIED	2.9	2.5	2.4	2.1	2.5	2.8	15.2	43.7
TOTALS	5.5	9.3	11.9	12.4	21.4	39.4	100.0	

SAMPLE DESCRIPTION > Pitts Coal
SUBMITTER > Kurt Eylands
ICC # AND FUND # > 46970938
RUN DATE AND TIME > 10 4 2002 9:42

Percent excluded as a function of particle size and phase.

	1.0 TO 2.2	2.2 TO 4.6	4.6 TO 10.0	10.0 TO 22.0	22.0 TO 46.0	46.0 TO 100.0
QUARTZ	3.2	13.9	18.8	46.4	67.7	100.0
IRON OXIDE	.0	.0	.0	.0	.0	.0
PERICLASE	.0	.0	.0	.0	.0	.0
RUTILE	.0	.0	.0	.0	.0	.0
ALUMINA	.0	.0	.0	.0	.0	.0
CALCITE	.0	.0	.0	100.0	100.0	100.0
DOLOMITE	.0	.0	.0	.0	66.7	.0
ANKERITE	.0	.0	.0	.0	.0	.0
KAOLINITE	.0	4.0	32.2	69.4	78.8	97.4
MONTMORILLONITE	4.9	.0	38.8	39.5	66.8	94.9
K AL SILICATE	1.2	3.3	28.6	52.5	74.9	97.1
FE AL SILICATE	.0	.0	19.5	.0	100.0	.0
CA AL SILICATE	.0	.0	64.9	.0	.0	100.0
NA AL SILICATE	.0	.0	100.0	.0	.0	.0
ALUMINOSILICATE	34.4	.0	38.4	.0	100.0	100.0
MIXED AL SILICA	.0	.0	29.7	69.7	100.0	100.0
FE SILICATE	.0	.0	.0	.0	.0	.0
CA SILICATE	.0	.0	.0	.0	.0	.0
CA ALUMINATE	.0	.0	.0	.0	.0	.0
PYRITE	.0	.0	53.9	100.0	95.3	100.0
PYRRHOTITE	28.2	.0	39.0	63.8	96.0	100.0
OXIDIZED PYRRHO	.0	.0	78.6	.0	100.0	100.0
GYPSUM	.0	.0	.0	.0	.0	.0
BARITE	.0	.0	.0	.0	.0	.0
APATITE	.0	.0	51.2	.0	100.0	.0
CA AL P	.0	.0	.0	.0	.0	.0
KCL	.0	.0	.0	.0	.0	.0
GYPSUM/BARITE	.0	.0	.0	.0	.0	.0
GYPSUM/AL SILIC	.0	23.1	58.1	.0	74.0	100.0
SI RICH	.0	.0	13.5	40.5	73.4	100.0
CA RICH	.0	.0	.0	.0	100.0	.0
CA SI RICH	.0	.0	.0	.0	.0	.0
UNCLASSIFIED	2.6	7.0	25.8	61.1	74.9	93.4

SAMPLE DESCRIPTION > Pitts Coal
SUBMITTER > Kurt Eylands
ICC # AND FUND # > 46970938
RUN DATE AND TIME > 10 4 2002 9:42

Average phase composition.
(Percent Relative X ray Intensity)

	SI	AL	FE	TI	P	CA	MG	NA	K	S	BA	CL
QUARTZ	93.3	1.5	.8	.3	.4	.4	.1	.1	.5	2.0	.3	.3
IRON OXIDE	.0	.0	.0	.0	.0	.0	.0	.0	.0	.0	.0	.0
PERICLASE	.0	.0	.0	.0	.0	.0	.0	.0	.0	.0	.0	.0
RUTILE	.0	.0	.0	.0	.0	.0	.0	.0	.0	.0	.0	.0
ALUMINA	.0	.0	.0	.0	.0	.0	.0	.0	.0	.0	.0	.0
CALCITE	.3	.2	3.0	.1	.1	94.5	.4	.1	.2	.8	.2	.2
DOLOMITE	1.7	1.3	1.4	.5	.4	62.7	24.5	.5	.5	3.1	.3	3.0
ANKERITE	.0	.0	.0	.0	.0	.0	.0	.0	.0	.0	.0	.0
KAOLINITE	53.3	38.4	1.3	.3	.3	.3	.2	.3	1.3	3.3	.5	.4
MONTMORILLONITE	54.9	33.1	1.9	.4	.5	.3	.4	.3	2.7	4.4	.6	.6
K AL SILICATE	50.2	29.3	2.4	.4	.7	.5	.7	.5	9.6	4.5	.7	.5
FE AL SILICATE	43.9	29.9	15.2	.1	.3	.3	3.9	.3	1.8	2.8	.9	.5
CA AL SILICATE	37.6	27.1	1.8	.1	6.0	21.5	.7	.1	2.6	1.8	.4	.2
NA AL SILICATE	50.8	36.7	2.1	.4	.0	.0	.1	5.9	3.5	.4	.0	.0
ALUMINOSILICATE	64.5	23.4	1.4	.7	.5	.6	.5	.3	2.9	4.2	.3	.6
MIXED AL SILICA	47.8	30.6	5.3	.6	1.5	1.7	.8	.5	7.5	2.4	.9	.4
FE SILICATE	.0	.0	.0	.0	.0	.0	.0	.0	.0	.0	.0	.0
CA SILICATE	66.8	.2	1.0	.0	.8	28.7	1.4	.0	.3	.3	.0	.4
CA ALUMINATE	.0	.0	.0	.0	.0	.0	.0	.0	.0	.0	.0	.0
PYRITE	1.8	1.6	29.9	.7	.5	.8	.3	1.1	.2	61.3	.6	1.2
PYRRHOTITE	.6	.4	47.3	.0	.1	.1	.1	.4	.1	50.6	.1	.1
OXIDIZED PYRRHO	.6	.6	60.7	.1	.1	.2	.2	.8	.3	35.6	.3	.5
GYPSUM	.0	.0	.0	.0	.0	.0	.0	.0	.0	.0	.0	.0
BARITE	.0	.0	.0	.0	.0	.0	.0	.0	.0	.0	.0	.0
APATITE	1.6	1.4	3.4	.1	24.8	65.2	.3	.6	.3	1.6	.2	.4
CA AL P	.0	.0	.0	.0	.0	.0	.0	.0	.0	.0	.0	.0
KCL	.0	.0	.0	.0	.0	.0	.0	.0	.0	.0	.0	.0
GYPSUM/BARITE	.0	.0	.0	.0	.0	.0	.0	.0	.0	.0	.0	.0
GYPSUM/AL SILIC	32.0	20.9	2.7	.6	1.2	19.0	1.3	.5	3.5	15.5	1.4	1.3
SI RICH	73.2	10.6	2.3	.6	.8	1.0	.4	.4	2.9	6.3	.8	.7
CA RICH	5.0	4.4	4.5	.5	.3	72.5	.4	.1	.7	10.0	1.1	.7
CA SI RICH	.0	.0	.0	.0	.0	.0	.0	.0	.0	.0	.0	.0
UNCLASSIFIED	40.3	22.0	5.4	1.1	1.7	2.8	.9	.6	5.4	16.9	1.4	1.5

Illinois bituminous coal

```
SAMPLE DESCRIPTION    > Illinois No.6 Coal
SUBMITTER             > Kurt Eylands
ICC # AND FUND #      > 46970940
RUN DATE AND TIME     >  10  8 2002  11: 4

SUMMARY OF PARAMETERS
PERCENT EPOXY USED                          =        71.0
TOTAL MINERAL AREA ANALYZED AT  800.0 MAG   =      3108.4
NORMALIZED AREA ANALYZED AT  800.0 MAG      =    270037.1
MINERAL AREA ANALYZED  250.0 MAG            =     57801.8
NORMALIZED AREA ANALYZED  250.0 MAG         =    510798.5
TOTAL MINERAL AREA ANALYZED AT   50.0 MAG   =   1541909.0
NUMBER OF FRAMES AT  800.0 MAG              =         100
NUMBER OF FRAMES AT  250.0 MAG              =         100
NUMBER OF FRAMES AT   50.0 MAG              =          35
TOTAL MINERAL WGHT % ON A COAL BASIS        =      13.911
TOTAL NUMBER OF POINTS ANALYZED             =        2962
NUMBER OF POINTS UNDER THRESHOLD            =          21

WEIGHT PERCENT ON A MINERAL BASIS
                   1.0    2.2    4.6   10.0   22.0   46.0
                    TO     TO     TO     TO     TO     TO TOTALS
                   2.2    4.6   10.0   22.0   46.0  100.0        % EXCLUDED

QUARTZ             1.1    1.9    1.7    1.2     .0     .1    6.1    7.6
IRON OXIDE          .0     .0     .0     .0     .0     .0     .1   85.3
PERICLASE           .0     .0     .0     .0     .0     .0     .0     .0
RUTILE              .0     .0     .0     .0     .0     .0     .0     .0
ALUMINA             .0     .0     .0     .0     .0     .0     .0     .0
CALCITE             .0     .0     .0     .1    3.0    5.9    9.0   87.5
DOLOMITE            .0     .0     .0     .0     .0     .0     .0   71.1
ANKERITE            .0     .0     .0     .0     .0     .0     .0     .0
KAOLINITE           .3     .4     .4     .5     .1     .8    2.4   24.1
MONTMORILLONITE     .1     .2     .1     .2     .3     .1    1.0   29.3
K AL SILICATE       .5     .7     .6     .7     .7     .3    3.4   19.9
FE AL SILICATE      .0     .0     .0     .1     .1     .0     .2   12.6
CA AL SILICATE      .0     .0     .0     .0     .0     .0     .0     .0
NA AL SILICATE      .0     .0     .0     .0     .0     .0     .1     .0
ALUMINOSILICATE     .0     .0     .1     .1     .1     .1     .2   40.6
MIXED AL SILICA     .0     .1     .1     .1     .0     .2     .6   22.9
FE SILICATE         .0     .0     .0     .0     .0     .0     .0     .0
CA SILICATE         .0     .0     .0     .0     .0     .1     .2   87.4
CA ALUMINATE        .0     .0     .0     .0     .0     .0     .0     .0
PYRITE              .0     .0     .0     .1    1.3    1.4    2.8   78.6
PYRRHOTITE          .4    1.0    3.3    9.6   29.3   23.3   66.9   79.2
OXIDIZED PYRRHO     .0     .0     .2     .5     .2     .0     .8   90.1
GYPSUM              .0     .0     .0     .0     .0     .0     .1   96.1
BARITE              .0     .0     .0     .0     .0     .0     .0     .0
APATITE             .0     .0     .0     .0     .1     .9    1.0   94.5
CA AL P             .0     .0     .0     .0     .0     .0     .0     .0
KCL                 .0     .0     .0     .0     .0     .0     .0     .0
GYPSUM/BARITE       .0     .0     .0     .0     .0     .0     .0     .0
GYPSUM/AL SILIC     .0     .0     .0     .0     .0     .0     .0   23.8
SI RICH             .1     .3     .1     .0     .1     .1     .7   12.5
CA RICH             .0     .0     .0     .0     .0     .0     .0     .0
CA SI RICH          .0     .0     .0     .0     .0     .0     .0     .0
UNCLASSIFIED        .7     .7     .5     .7     .8     .8    4.3   35.9
TOTALS             3.4    5.3    7.1   13.9   36.2   34.0  100.0
```

SAMPLE DESCRIPTION > Illinois No.6 Coal
SUBMITTER > Kurt Eylands
ICC # AND FUND # > 46970940
RUN DATE AND TIME > 10 8 2002 11: 4

Percent excluded as a function of particle size and phase.

	1.0 TO 2.2	2.2 TO 4.6	4.6 TO 10.0	10.0 TO 22.0	22.0 TO 46.0	46.0 TO 100.0
QUARTZ	1.3	1.5	10.0	20.4	.0	.0
IRON OXIDE	62.9	.0	.0	.0	100.0	.0
PERICLASE	.0	.0	.0	.0	.0	.0
RUTILE	.0	.0	.0	.0	.0	.0
ALUMINA	.0	.0	.0	.0	.0	.0
CALCITE	.0	.0	.0	100.0	85.5	88.7
DOLOMITE	.0	.0	.0	.0	100.0	.0
ANKERITE	.0	.0	.0	.0	.0	.0
KAOLINITE	.0	.0	12.6	17.8	61.3	49.0
MONTMORILLONITE	.0	20.8	.0	19.8	46.6	100.0
K AL SILICATE	1.6	.0	7.7	22.3	41.3	75.8
FE AL SILICATE	.0	.0	43.5	.0	42.1	.0
CA AL SILICATE	.0	.0	.0	.0	.0	.0
NA AL SILICATE	.0	.0	.0	.0	.0	.0
ALUMINOSILICATE	.0	.0	32.4	.0	33.6	100.0
MIXED AL SILICA	.0	.0	.0	.0	.0	68.2
FE SILICATE	.0	.0	.0	.0	.0	.0
CA SILICATE	.0	.0	.0	.0	.0	100.0
CA ALUMINATE	.0	.0	.0	.0	.0	.0
PYRITE	.0	.0	.0	.0	72.2	92.1
PYRRHOTITE	19.8	11.0	26.6	55.9	81.8	97.0
OXIDIZED PYRRHO	.0	.0	76.5	100.0	81.4	.0
GYPSUM	.0	.0	.0	100.0	100.0	.0
BARITE	.0	.0	.0	.0	.0	.0
APATITE	.0	.0	.0	.0	30.9	100.0
CA AL P	.0	.0	.0	.0	.0	.0
KCL	.0	.0	.0	.0	.0	.0
GYPSUM/BARITE	.0	.0	.0	.0	.0	.0
GYPSUM/AL SILIC	.0	.0	100.0	.0	.0	.0
SI RICH	.0	.0	.0	.0	20.8	100.0
CA RICH	.0	.0	.0	.0	.0	.0
CA SI RICH	.0	.0	.0	.0	.0	.0
UNCLASSIFIED	.7	.0	7.4	35.2	71.5	75.8

SAMPLE DESCRIPTION > Illinois No.6 Coal
SUBMITTER > Kurt Eylands
ICC # AND FUND # > 46970940
RUN DATE AND TIME > 10 8 2002 11: 4

Average phase composition.
(Percent Relative X ray Intensity)

	SI	AL	FE	TI	P	CA	MG	NA	K	S	BA	CL
QUARTZ	94.7	1.2	.7	.1	.4	.1	.1	.1	.3	1.8	.3	.2
IRON OXIDE	1.3	1.9	94.0	.1	.1	.1	.2	.1	.0	1.8	.0	.2
PERICLASE	.0	.0	.0	.0	.0	.0	.0	.0	.0	.0	.0	.0
RUTILE	.7	.5	1.7	93.6	.1	.0	.2	.0	.0	.0	3.2	.0
ALUMINA	.0	.0	.0	.0	.0	.0	.0	.0	.0	.0	.0	.0

CALCITE	.1	.1	1.4	.1	.1	96.9	.4	.1	.1	.3	.3	.1
DOLOMITE	.2	.0	10.7	.0	.0	64.6	24.1	.1	.0	.0	.0	.3
ANKERITE	.3	.3	35.1	.0	.2	47.9	12.0	.0	.3	4.0	.0	.0
KAOLINITE	54.8	39.3	1.2	.1	.2	.2	.2	.2	1.2	2.1	.3	.2
MONTMORILLONITE	57.0	33.2	2.2	.3	.3	.2	.4	.3	2.8	2.6	.3	.2
K AL SILICATE	52.5	28.0	2.9	.5	.2	.3	.9	.6	10.1	3.3	.5	.2
FE AL SILICATE	45.6	25.5	17.2	.5	.2	.2	5.0	.4	2.7	2.4	.1	.2
CA AL SILICATE	51.4	39.0	.2	.0	.5	5.4	.1	.1	.0	3.3	.0	.0
NA AL SILICATE	66.6	19.7	1.8	.1	.2	.2	.3	8.6	1.4	1.0	.1	.1
ALUMINOSILICATE	67.1	22.1	2.8	1.1	.3	.4	.6	.5	3.7	.8	.4	.1
MIXED AL SILICA	51.9	26.5	6.3	1.7	.3	.5	1.5	.7	7.7	2.3	.4	.2
FE SILICATE	.0	.0	.0	.0	.0	.0	.0	.0	.0	.0	.0	.0
CA SILICATE	53.2	1.0	2.4	.1	.5	39.7	1.3	.3	.3	.6	.3	.2
CA ALUMINATE	.0	.0	.0	.0	.0	.0	.0	.0	.0	.0	.0	.0
PYRITE	1.6	1.1	30.9	.5	.2	.6	.2	.8	.5	62.1	.6	.9
PYRRHOTITE	.4	.2	47.4	.0	.0	.1	.1	.5	.1	51.0	.0	.1
OXIDIZED PYRRHO	.8	.3	62.2	.1	.1	.2	.1	.9	.2	34.5	.3	.3
GYPSUM	1.2	1.3	1.0	.0	.3	62.0	.7	.4	.5	30.7	.0	2.0
BARITE	.0	.0	.0	.0	.0	.0	.0	.0	.0	.0	.0	.0
APATITE	.2	.1	.3	.1	27.3	71.0	.1	.2	.1	.4	.1	.1
CA AL P	.0	.0	.0	.0	.0	.0	.0	.0	.0	.0	.0	.0
KCL	.0	.0	.0	.0	.0	.0	.0	.0	.0	.0	.0	.0
GYPSUM/BARITE	.0	.0	.0	.0	.0	.0	.0	.0	.0	.0	.0	.0
GYPSUM/AL SILIC	39.2	15.7	4.3	.2	.2	15.2	.9	2.2	4.6	17.2	.1	.1
SI RICH	74.5	11.0	2.4	.2	.4	.3	.6	.5	4.2	5.3	.3	.3
CA RICH	.0	.0	.0	.0	.0	.0	.0	.0	.0	.0	.0	.0
CA SI RICH	.0	.0	.0	.0	.0	.0	.0	.0	.0	.0	.0	.0
UNCLASSIFIED	46.0	16.5	8.0	.9	1.1	1.8	1.5	.8	6.9	15.1	.6	.7

PRB sub- bituminous coal

```
SAMPLE DESCRIPTION    > PRB Coal
SUBMITTER             > Kurt Eylands
ICC # AND FUND #      > 46970939
RUN DATE AND TIME     >  10  8 2002   7:54

SUMMARY OF PARAMETERS
PERCENT EPOXY USED                          =        76.8
TOTAL MINERAL AREA ANALYZED AT  800.0 MAG   =      1091.4
NORMALIZED AREA ANALYZED AT  800.0 MAG      =    273637.7
MINERAL AREA ANALYZED  250.0 MAG            =     35585.5
NORMALIZED AREA ANALYZED  250.0 MAG         =    898490.0
TOTAL MINERAL AREA ANALYZED AT   50.0 MAG   =    770686.8
NUMBER OF FRAMES AT  800.0 MAG              =          99
NUMBER OF FRAMES AT  250.0 MAG              =         100
NUMBER OF FRAMES AT   50.0 MAG              =         100
TOTAL MINERAL WGHT % ON A COAL BASIS        =       3.987
TOTAL NUMBER OF POINTS ANALYZED             =        1721
NUMBER OF POINTS UNDER THRESHOLD            =         153

WEIGHT PERCENT ON A MINERAL BASIS
                   1.0    2.2    4.6   10.0   22.0   46.0
                    TO     TO     TO     TO     TO     TO TOTALS
                   2.2    4.6   10.0   22.0   46.0  100.0        % EXCLUDED

QUARTZ             2.4    4.1    7.4    5.0    4.4    3.7   27.1   44.4
IRON OXIDE          .1     .1     .1     .0     .5     .0     .8   83.3
PERICLASE           .0     .0     .0     .0     .0     .0     .0     .0
RUTILE              .0     .2     .2     .0     .1     .0     .5   28.2
ALUMINA             .0     .0     .0     .0     .0     .0     .0     .0
CALCITE             .0     .0     .0     .0     .0     .0     .0     .0
DOLOMITE            .0     .0     .2     .0     .0     .0     .2     .0
ANKERITE            .0     .0     .0     .0     .0     .0     .0     .0
KAOLINITE           .7    2.5    3.7    5.9    5.5    2.0   20.5   53.4
MONTMORILLONITE     .1     .0     .1     .6     .9     .5    2.2   81.8
K AL SILICATE       .1     .2     .0     .0     .2     .3     .8   57.5
FE AL SILICATE      .0     .0     .1     .0     .0     .0     .1     .0
CA AL SILICATE      .0     .1     .4     .6     .9     .8    2.8   55.6
NA AL SILICATE      .0     .0     .0     .0     .0     .0     .0     .0
ALUMINOSILICATE     .0     .0     .0     .0     .3     .4     .8   90.2
MIXED AL SILICA     .0     .0     .0     .0     .0     .2     .2     .0
FE SILICATE         .0     .3     .1     .0     .0     .0     .3  100.0
CA SILICATE         .0     .0     .3     .3     .4     .1    1.0   47.4
CA ALUMINATE        .0     .0     .0     .0     .0     .0     .0     .0
PYRITE              .0     .0     .0     .0     .3     .8    1.1  100.0
PYRRHOTITE          .3     .0     .3     .7    3.1    2.1    6.4   95.0
OXIDIZED PYRRHO     .0     .0     .0     .0     .3     .0     .3  100.0
GYPSUM              .0     .0     .1     .0     .0     .0     .1   30.1
BARITE              .0     .1     .0     .0     .0     .0     .1     .0
APATITE             .0     .0     .0     .0     .0     .2     .2  100.0
CA AL P             .8    1.1    4.4    4.1    1.2     .6   12.2   30.5
KCL                 .0     .0     .0     .0     .0     .0     .0     .0
GYPSUM/BARITE       .0     .0     .0     .0     .0     .0     .0     .0
GYPSUM/AL SILIC     .0     .0    1.6     .7    2.6    1.6    6.5   60.6
SI RICH             .0     .0     .4     .6     .6     .7    2.4   57.6
CA RICH             .0     .0     .0     .0     .0     .0     .0  100.0
CA SI RICH          .0     .0     .1     .0     .1     .0     .1   42.5
UNCLASSIFIED        .3     .2    5.1    2.1    3.1    2.4   13.3   57.6
 TOTALS            5.0    9.0   24.6   20.5   24.4   16.5  100.0
```

SAMPLE DESCRIPTION > PRB Coal
SUBMITTER > Kurt Eylands
ICC # AND FUND # > 46970939
RUN DATE AND TIME > 10 8 2002 7:54

Percent excluded as a function of particle size and phase.

	1.0 TO 2.2	2.2 TO 4.6	4.6 TO 10.0	10.0 TO 22.0	22.0 TO 46.0	46.0 TO 100.0
QUARTZ	1.2	7.5	30.5	56.5	71.3	93.5
IRON OXIDE	.0	100.0	58.5	.0	100.0	.0
PERICLASE	.0	.0	.0	.0	.0	.0
RUTILE	.0	.0	23.2	.0	100.0	.0
ALUMINA	.0	.0	.0	.0	.0	.0
CALCITE	.0	.0	.0	.0	.0	.0
DOLOMITE	.0	.0	.0	.0	.0	.0
ANKERITE	.0	.0	.0	.0	.0	.0
KAOLINITE	4.1	8.5	29.7	62.8	69.8	100.0
MONTMORILLONITE	.0	.0	49.7	71.6	92.7	100.0
K AL SILICATE	.0	.0	.0	.0	100.0	100.0
FE AL SILICATE	.0	.0	.0	.0	.0	.0
CA AL SILICATE	.0	.0	39.6	.0	72.7	88.9
NA AL SILICATE	.0	.0	.0	.0	.0	.0
ALUMINOSILICATE	.0	.0	.0	.0	89.8	100.0
MIXED AL SILICA	.0	.0	.0	.0	.0	.0
FE SILICATE	.0	100.0	100.0	.0	.0	.0
CA SILICATE	.0	.0	65.8	.0	49.9	100.0
CA ALUMINATE	.0	.0	.0	.0	.0	.0
PYRITE	.0	.0	.0	.0	100.0	100.0
PYRRHOTITE	12.1	.0	100.0	100.0	97.6	100.0
OXIDIZED PYRRHO	.0	.0	100.0	.0	100.0	.0
GYPSUM	.0	.0	30.1	.0	.0	.0
BARITE	.0	.0	.0	.0	.0	.0
APATITE	.0	.0	.0	.0	.0	100.0
CA AL P	.0	.0	21.5	32.0	68.4	100.0
KCL	.0	.0	.0	.0	.0	.0
GYPSUM/BARITE	.0	.0	.0	.0	.0	.0
GYPSUM/AL SILIC	.0	.0	43.3	15.7	58.2	100.0
SI RICH	.0	.0	10.1	46.1	55.1	100.0
CA RICH	.0	.0	.0	.0	100.0	.0
CA SI RICH	.0	.0	.0	.0	100.0	.0
UNCLASSIFIED	12.1	.0	36.2	71.2	60.2	100.0

SAMPLE DESCRIPTION > PRB Coal
SUBMITTER > Kurt Eylands
ICC # AND FUND # > 46970939
RUN DATE AND TIME > 10 8 2002 7:54

Average phase composition.
(Percent Relative X ray Intensity)

	SI	AL	FE	TI	P	CA	MG	NA	K	S	BA	CL
QUARTZ	95.6	.5	.5	.3	.4	1.1	.2	.2	.2	.6	.3	.2
IRON OXIDE	.3	.3	95.7	.1	.1	.9	.2	.7	.2	1.0	.1	.6
PERICLASE	.0	.0	.0	.0	.0	.0	.0	.0	.0	.0	.0	.0
RUTILE	1.6	1.6	1.5	89.1	.2	3.8	.6	.1	.1	.5	.8	.1

ALUMINA	.0	.0	.0	.0	.0	.0	.0	.0	.0	.0	.0	.0
CALCITE	.5	.3	.9	.4	.5	95.5	.6	.0	.4	.1	.0	.8
DOLOMITE	.4	4.2	1.6	.5	.0	70.1	11.6	2.2	1.8	7.2	.0	.5
ANKERITE	.0	.0	.0	.0	.0	.0	.0	.0	.0	.0	.0	.0
KAOLINITE	55.2	41.6	.6	.2	.3	.7	.1	.1	.3	.4	.4	.1
MONTMORILLONITE	58.5	30.6	1.9	1.0	.3	2.2	.5	.2	2.1	1.9	.6	.2
K AL SILICATE	54.7	29.2	2.2	1.0	.2	1.4	.6	.2	8.6	1.0	.7	.3
FE AL SILICATE	51.4	30.9	6.4	.2	.2	2.2	5.5	1.1	1.5	.6	.0	.2
CA AL SILICATE	47.2	32.3	1.5	.9	1.7	9.8	1.0	.4	1.1	2.9	.9	.3
NA AL SILICATE	.0	.0	.0	.0	.0	.0	.0	.0	.0	.0	.0	.0
ALUMINOSILICATE	64.6	23.6	2.1	.8	.4	1.7	.5	.3	2.1	3.0	.6	.3
MIXED AL SILICA	45.6	29.3	4.3	1.2	.2	8.0	1.3	.7	4.2	3.5	1.7	.1
FE SILICATE	42.2	2.4	48.8	4.9	.5	.4	.1	.5	.1	.1	.1	.0
CA SILICATE	67.8	1.2	1.6	1.3	1.4	18.6	1.5	.6	.7	2.4	2.4	.6
CA ALUMINATE	.0	.0	.0	.0	.0	.0	.0	.0	.0	.0	.0	.0
PYRITE	.3	1.0	35.1	.3	.1	2.7	.8	1.2	.2	57.3	.7	.3
PYRRHOTITE	.2	.4	47.5	.1	.1	1.0	.3	.5	.1	49.5	.2	.1
OXIDIZED PYRRHO	1.2	.3	67.4	.3	.1	.6	.7	1.3	.2	27.4	.4	.2
GYPSUM	.5	3.7	.2	.1	.8	51.0	3.3	1.0	2.0	35.9	1.1	.4
BARITE	.6	.6	.1	3.3	.0	3.6	.8	.5	.3	20.0	70.0	.2
APATITE	.1	.1	.0	.3	26.0	73.2	.0	.0	.0	.1	.3	.0
CA AL P	.5	36.1	1.0	.4	22.8	27.4	.9	.4	.4	1.6	8.2	.3
KCL	.0	.0	.0	.0	.0	.0	.0	.0	.0	.0	.0	.0
GYPSUM/BARITE	.0	.0	.0	.0	.0	.0	.0	.0	.0	.0	.0	.0
GYPSUM/AL SILIC	42.4	19.5	2.6	1.7	.8	14.3	1.8	.7	1.7	12.2	1.5	.5
SI RICH	73.1	9.9	2.1	1.1	.6	4.7	1.5	.3	1.5	4.1	.8	.3
CA RICH	.0	2.0	.0	.0	2.2	68.9	10.5	4.0	2.0	4.0	6.3	.0
CA SI RICH	54.0	1.7	5.9	3.7	.4	28.9	.9	.6	.3	2.8	.9	.0
UNCLASSIFIED	16.5	14.7	5.5	3.9	7.3	26.5	3.5	1.5	1.5	12.1	6.5	.7

Pittsburgh #8 – char sample # 183

```
Pittsburgh 183 - 2 atm
TOTAL Volume FACTOR:  0.17791E+07

AVERAGE SPECIES COMPOSITION
  #   SPECIES      C   O  Na  Mg  Al  Si   P   S  Cl  K   Ca  Ti   V  Cr  Mn  Fe
Ni  Cu  Zn   X    Vol %
-------------------------------------------------------------------------------
------------------------
  44  Fe  -  -     0.  0.  0.  1.  1.  2.  0.  2.  0.  0.  1.  0.  0.  0.  0. 92.
0.  0.  0.  0.  10.8
 244  Ca  -  -     0.  0.  0.  0.  1.  1.  0.  1.  1.  0. 92.  0.  0.  0.  0.  1.
0.  0.  0.  0.  17.6
  19  Si  -  -     0.  0.  1.  0.  5. 89.  0.  0.  0.  1.  1.  0.  0.  0.  0.  1.
0.  0.  0.  0.   1.0
 183  Si Al  -     0.  0.  0.  0. 32. 63.  0.  0.  0.  2.  1.  0.  0.  0.  0.  2.
0.  0.  0.  0.  46.9
  27  Al Si  -     0.  0.  0.  0. 52. 44.  0.  0.  0.  1.  1.  0.  0.  0.  0.  1.
0.  0.  0.  0.   2.5
   5  Al S   -     0.  0.  0.  0. 70.  2.  0. 25.  0.  1.  1.  0.  0.  0.  0.  1.
0.  0.  1.  0.   0.8
  32  Si Al Fe     0.  0.  0.  0. 30. 53.  0.  0.  0.  2.  1.  0.  0.  0.  0. 12.
0.  1.  0.  0.   5.2
  10  Fe Si Al     0.  0.  1.  0. 18. 29.  0.  0.  0.  0.  0.  0.  0.  0.  0. 52.
0.  0.  0.  0.   1.0
  23  Al Si Fe     0.  0.  0.  1. 48. 35.  0.  0.  0.  0.  2.  1.  0.  0.  0. 11.
0.  0.  0.  0.   0.6
  11  Ca Si Al     0.  0.  1.  0. 19. 27.  0.  4.  0.  2. 43.  0.  0.  0.  0.  1.
0.  1.  1.  0.   3.8
   4  Si Ca Al     0.  0.  0.  0. 25. 44.  0.  0.  0.  1. 28.  0.  0.  0.  0.  1.
0.  0.  0.  0.   0.7
  17  Si Al Ca     0.  0.  0.  1. 32. 51.  0.  0.  0.  1. 12.  1.  0.  0.  0.  2.
0.  0.  0.  0.   2.0
   1  Zn Si Mg     0.  0.  0. 12.  6. 14. 11.  0.  4.  0.  4.  2.  3.  9.  4.  0.
0.  0. 31.  0.   0.6
   1  Al Cl S      0.  0.  0.  1. 77.  0.  0.  9. 11.  0.  1.  0.  0.  0.  0.  0.
0.  0.  0.  0.   1.0
 102       ALL  CATEGORIES  WITH  VOLUME  %  LESS  THAN  1.0  COMBINED  IN  ONE
5.7
-------------------------------------------------------------------------------
------------------------
 723  TOTALS -     0.  0.  0.  1. 23. 39.  0.  1.  0.  1. 20.  0.  0.  0.  0. 13.
0.  0.  0.  0.  100.0


Volume DISTRIBUTION
SPECIES        Volume %   0.3-  2.5  2.5-  5.0  5.0- 10.0 10.0- 20.0 20.0- 40.0
40.0- 80.0 80.0-100.0
-------------------------------------------------------------------------------
-----------
 Fe  -  -        10.8          0.        1.        6.       27.       15.       51.
0.
 Ca  -  -        17.6          5.        9.       23.       25.       39.        0.
0.
 Si Al  -        46.9          0.        1.        7.       17.       29.       45.
0.
 Al Si  -         2.5          0.        9.       15.       23.       53.        0.
0.
 Si Al Fe         5.2          0.        6.       12.       17.       41.       24.
0.
```

```
 Fe Si Al         1.0          0.        0.       10.       77.       13.        0.
0.
 Ca Si Al         3.8          0.        1.        5.        1.       93.        0.
0.
 Si Al Ca         2.0          4.        3.       15.       41.       36.        0.
0.
 OTHERS -        10.2          6.       10.        9.       33.       42.        0.
0.
-------------------------------------------------------------------------------
-----------
TOTALS -        100.0          2.        4.       10.       22.       34.       28.
0.

NUMBER DENSITY DISTRIBUTION
SPECIES      NUMBER    0.3-  2.5   2.5-  5.0   5.0- 10.0  10.0- 20.0  20.0- 40.0
40.0- 80.0  80.0-100.0
-------------------------------------------------------------------------------
----------------
 Fe  -  -        44      3  92.8   5   3.1   4   2.5  26   1.3   4   0.2   2   0.1
0   0.0
 Ca  -  -       244     44  94.3  91   3.9  36   1.5  60   0.2  13   0.0   0   0.0
0   0.0
 Si  -  -        19      1  85.0   7  11.9   1   1.7  10   1.4   0   0.0   0   0.0
0   0.0
 Si Al  -       183      8  86.3  31   6.7  23   5.0  88   1.5  24   0.4   9   0.2
0   0.0
 Al Si  -        27      1  75.9  11  16.7   4   6.1   7   0.9   4   0.5   0   0.0
0   0.0
 Si Al Fe        32      1  74.4  13  19.3   3   4.5  10   1.2   4   0.5   1   0.1
0   0.0
 Fe Si Al        10      0   0.0   0   0.0   1  58.1   8  37.2   1   4.7   0   0.0
0   0.0
 Al Si Fe        23      1  72.2  18  26.0   1   1.4   3   0.3   0   0.0   0   0.0
0   0.0
 Ca Si Al        11      0   0.0   2  43.9   2  43.9   1   1.8   6  10.5   0   0.0
0   0.0
 Si Al Ca        17      1  86.6   3   5.2   4   6.9   7   1.0   2   0.3   0   0.0
0   0.0
 Al Si Ca        10      1  87.5   6  10.5   1   1.7   2   0.3   0   0.0   0   0.0
0   0.0
---------        103    CATEGORIES WITH # OF PARTICLES LESS THAN 10 COMBINED INTO
ONE
-------------------------------------------------------------------------------
----------------
TOTALS -        723     79  92.1 221   5.2  92   2.1 249   0.5  70   0.1  12   0.0
0   0.0
```

Pittsburgh #8 – char sample # 221

```
Pittsburg 221 - 10 atm

TOTAL Volume FACTOR:  0.64530E+06

AVERAGE SPECIES COMPOSITION
  #   SPECIES      C   O  Na  Mg  Al  Si   P   S  Cl  K   Ca  Ti   V  Cr  Mn  Fe
Ni  Cu  Zn   X    Vol %
-------------------------------------------------------------------------------
------------------------
  57  Ca  -  -     0.  0.  0.  0.  1.  1.  0.  3.  1.  0. 89.  0.  0.  0.  0.  2.
0.  0.  1.  0.  12.5
  29  Si  -  -     0.  0.  1.  1.  6. 82.  0.  2.  0.  2.  1.  0.  0.  0.  0.  1.
0.  1.  1.  0.   4.7
   6  Fe  -  -     0.  0.  1.  0.  2.  2.  0.  1.  0.  0.  0.  1.  0.  0.  0. 93.
0.  0.  0.  0.   1.8
 204  Si Al  -     0.  0.  1.  1. 35. 55.  0.  1.  0.  2.  1.  0.  0.  0.  0.  1.
0.  1.  1.  0.  41.6
  13  Al Si  -     0.  0.  2.  1. 46. 41.  0.  2.  1.  1.  1.  0.  0.  0.  0.  1.
1.  1.  1.  0.   2.0
  28  Ca S   -     0.  0.  1.  0.  0.  1.  0. 15.  0.  0. 80.  0.  0.  0.  0.  1.
0.  0.  0.  0.   6.4
  16  Si Al S      0.  0.  1.  1. 25. 41.  0. 13.  4.  2.  3.  2.  1.  0.  1.  1.
0.  5.  1.  0.   8.9
   2  Al Si S      0.  0.  6.  3. 30. 24.  0. 15.  0.  0. 10.  4.  0.  0.  1.  5.
0.  2.  0.  0.   0.8
  30  Si Al Fe     0.  0.  1.  1. 32. 49.  0.  2.  0.  2.  1.  1.  0.  0.  0.  9.
0.  0.  0.  0.   4.1
   5  Fe Si Al     0.  0.  0.  2. 20. 28.  0.  6.  1.  2.  1.  2.  0.  0.  0. 34.
0.  2.  1.  0.   1.7
   8  Al Si Ca     0.  0.  0.  3. 39. 28.  0.  3.  1.  2. 13.  3.  0.  0.  1.  2.
2.  2.  2.  0.   0.6
   9  Ca Si Al     0.  0.  0.  1. 17. 24.  1.  4.  1.  1. 46.  0.  1.  0.  0.  3.
0.  1.  0.  0.   1.5
  15  Si Al Ca     0.  0.  2.  1. 30. 45.  0.  1.  1.  2. 12.  2.  0.  0.  0.  2.
0.  1.  0.  0.   1.0
   4  Si Ca Al     0.  0.  0.  2. 20. 40.  0.  3.  1.  2. 25.  0.  0.  0.  0.  6.
0.  0.  0.  0.   0.6
   3  Ca Al Si     0.  0.  0.  1. 25. 22.  1.  5.  1.  0. 43.  1.  1.  0.  0.  0.
0.  1.  0.  0.   0.5
   1  Ca S  Al     0.  0.  0.  0. 11.  4.  0. 12.  0.  0. 68.  0.  0.  1.  0.  4.
0.  0.  0.  0.   0.7
   1  Al Si Zn     0.  0.  0.  0. 34. 25.  0.  7.  0.  0. 13.  0.  2.  0.  2.  0.
0.  3. 14.  0.   1.4
  21  Si Al K      0.  0.  1.  1. 35. 52.  0.  1.  0.  7.  0.  0.  0.  0.  0.  1.
0.  0.  0.  0.   3.5
   2  Si Al Ni     0.  0.  0.  0. 27. 38.  0.  6.  0.  2.  2.  1.  2.  0.  1.  2.
10.  0.  7.  0.   0.5
   1  Ca P  Al     0.  0.  3.  0.  9.  8. 24.  0.  0.  0. 55.  0.  0.  0.  0.  0.
0.  0.  0.  0.   0.5
  54       ALL  CATEGORIES  WITH  VOLUME  %  LESS  THAN  1.0  COMBINED  IN  ONE
4.4
-------------------------------------------------------------------------------
------------------------
 509  TOTALS -     0.  0.  1.  1. 24. 39.  0.  4.  1.  2. 20.  1.  0.  0.  0.  5.
0.  1.  1.  0.  100.0
```

Volume DISTRIBUTION

SPECIES	Volume %	0.3- 2.5	2.5- 5.0	5.0- 10.0	10.0- 20.0	20.0- 40.0	40.0- 80.0	80.0-100.0
Ca - -	12.5	5.	11.	43.	25.	17.	0.	0.
Si - -	4.7	14.	23.	27.	21.	16.	0.	0.
Fe - -	1.8	0.	3.	24.	16.	57.	0.	0.
Si Al -	41.6	7.	13.	36.	25.	19.	0.	0.
Al Si -	2.0	16.	6.	27.	30.	21.	0.	0.
Ca S -	6.4	1.	10.	21.	17.	51.	0.	0.
Si Al S	8.9	0.	0.	7.	31.	22.	41.	0.
Si Al Fe	4.1	27.	12.	9.	39.	12.	0.	0.
Fe Si Al	1.7	2.	0.	0.	13.	85.	0.	0.
Ca Si Al	1.5	0.	10.	44.	46.	0.	0.	0.
Si Al Ca	1.0	18.	26.	0.	56.	0.	0.	0.
Al Si Zn	1.4	0.	0.	0.	0.	100.	0.	0.
Si Al K	3.5	6.	19.	65.	11.	0.	0.	0.
OTHERS -	8.9	15.	15.	8.	38.	24.	0.	0.
TOTALS -	100.0	7.	12.	28.	26.	23.	4.	0.

NUMBER DENSITY DISTRIBUTION

SPECIES	NUMBER	0.3- 2.5	2.5- 5.0	5.0- 10.0	10.0- 20.0	20.0- 40.0	40.0- 80.0	80.0-100.0
Ca - -	57	4 77.4	16 11.3	15 10.6	18 0.6	4 0.1	0 0.0	0 0.0
Si - -	29	9 94.2	13 4.9	2 0.8	4 0.1	1 0.0	0 0.0	0 0.0
Si Al -	204	31 88.4	69 7.2	40 4.1	53 0.3	11 0.1	0 0.0	0 0.0
Al Si -	13	5 96.4	3 2.1	2 1.4	2 0.1	1 0.0	0 0.0	0 0.0
Ca S -	28	2 76.9	10 14.0	6 8.4	8 0.5	2 0.1	0 0.0	0 0.0
Si Al S	16	0 0.0	0 0.0	1 57.7	12 33.8	2 5.6	1 2.8	0 0.0
Si Al Fe	30	12 97.8	6 1.8	1 0.3	9 0.1	2 0.0	0 0.0	0 0.0
Si Al Ca	15	8 98.2	4 1.8	0 0.0	3 0.1	0 0.0	0 0.0	0 0.0
Si Al K	21	5 91.3	9 6.0	4 2.7	3 0.1	0 0.0	0 0.0	0 0.0
---	96							
CATEGORIES WITH # OF PARTICLES LESS THAN 10 COMBINED INTO ONE								
TOTALS -	509	109 92.6	153 4.7	78 2.4	137 0.2	31 0.0	1 0.0	0 0.0

Pittsburgh #8 – char sample # 225

```
Pittsburgh 225 - 20 atm
TOTAL Volume FACTOR:  0.89373E+06

AVERAGE SPECIES COMPOSITION
  #   SPECIES      C   O  Na  Mg  Al  Si   P   S  Cl  K   Ca  Ti   V  Cr  Mn  Fe
Ni  Cu  Zn   X    Vol %
-------------------------------------------------------------------------------
------------------------
  73  Ca  -  -     0.  0.  1.  1.  2.  2.  1.  3.  0.  0. 86.  0.  0.  0.  0.  1.
0.  1.  0.  0.  10.1
  18  Si  -  -     0.  0.  2.  0.  4. 80.  0.  5.  0.  0.  1.  2.  0.  0.  0.  2.
1.  1.  1.  0.   4.3  192  Si Al  -     0.  0.  1.  1. 36. 54.  0.  1.  0.  2.
1.  0.  0.  0.  0.  2.  0.  1.  0.  0.  30.8
  27  Al Si  -     0.  0.  0.  0. 49. 42.  0.  2.  0.  2.  0.  0.  1.  0.  0.  0.
1.  2.  0.  0.   7.3
   6  Fe S   -     0.  0.  0.  0.  0.  4.  2. 36.  1.  0.  3.  0.  2.  0.  0. 49.
1.  2.  0.  0.   2.1
   3  Ca S   -     0.  0.  4.  0.  3.  3.  0. 22.  0.  2. 61.  1.  0.  0.  0.  0.
2.  3.  0.  0.   0.5
   7  Fe Si Al     0.  0.  1.  1. 19. 28.  0.  2.  0.  0.  2.  0.  1.  0.  0. 45.
0.  1.  1.  0.   1.3
  39  Si Al Fe     0.  0.  2.  1. 27. 42.  1.  4.  1.  2.  2.  1.  1.  0.  0. 12.
0.  2.  1.  0.   5.5
   5  Si Fe Al     0.  0.  1.  0. 19. 35.  2.  4.  0.  2. 10.  1.  1.  0.  0. 20.
2.  2.  2.  0.   0.5
  17  Si Al Na     0.  0.  9.  2. 26. 49.  1.  2.  0.  4.  1.  2.  0.  1.  1.  0.
1.  1.  0.  0.   1.6
  17  Si Al Cu     0.  0.  4.  1. 22. 40.  1.  2.  4.  2.  5.  1.  1.  0.  1.  4.
0.  9.  4.  0.   8.1
   4  Al Si Cu     0.  0.  2.  3. 41. 30.  1.  5.  1.  1.  2.  0.  0.  1.  0.  0.
2. 10.  0.  0.   2.5
   9  Ca Si Al     0.  0.  0.  0. 12. 19.  2.  2.  0.  0. 53.  1.  0.  0.  0.  2.
3.  1.  4.  0.   6.4
   5  Si Ca Al     0.  0.  0.  0. 18. 45.  1.  3.  0.  4. 23.  0.  0.  0.  1.  1.
2.  3.  0.  0.   1.1
  17  Al Si Ca     0.  0.  0.  1. 38. 35.  1.  0.  1.  0. 20.  0.  0.  0.  0.  1.
0.  1.  1.  0.   1.8
  19  Si Al Ca     0.  0.  1.  3. 33. 42.  2.  1.  1.  3. 12.  0.  0.  0.  0.  0.
1.  1.  1.  0.   1.9
  15  Si Al S      0.  0.  2.  1. 27. 49.  1.  8.  1.  2.  2.  1.  0.  0.  1.  1.
0.  1.  2.  0.   2.7
  19  Si Al K      0.  0.  1.  1. 24. 43.  4.  5.  2.  8.  1.  2.  2.  0.  0.  3.
2.  1.  1.  0.   4.5
   8  Si Al Ti     0.  0.  1.  5. 22. 31.  0.  7.  2.  1.  0. 12.  4.  1.  0.  6.
0.  5.  4.  0.    0.5    1  Al Fe S       0.  0.  3.  0. 24. 14.  0. 15.  3.  0.
7.  0.  2.  2.  1. 16.  3.  0.  9.  0.   0.6    1  Al Zn Ni      0.  0.  0.  0.
23.  8.  0.  0.  0.  4.  3.  0.  3.  0.  3.  0. 18. 16. 22.  0.   0.6    1  Cu S
Na     0.  0. 11.  7.  4.  7.  8. 16.  5.  0.  1.  4.  0.  1.  0.  2.  8. 26.  0.
0.   0.7    1  Ca Al S       0.  0.  2.  0. 10.  9.  0.  9.  0.  0. 66.  2.  0.
0.  1.  0.  0.  0.  0.  0.   1.2   85   ALL CATEGORIES WITH VOLUME % LESS THAN
1.0 COMBINED IN ONE                                  2.9
-------------------------------------------------------------------------------
------------------------
 589  TOTALS -     0.  0.  1.  1. 25. 39.  1.  4.  1.  2. 16.  1.  0.  0.  0.  5.
1.  2.  1.  0.  100.0


Volume DISTRIBUTION
```

```
SPECIES        Volume %    0.3-  2.5  2.5-  5.0  5.0- 10.0 10.0- 20.0 20.0- 40.0
40.0- 80.0 80.0-100.0
-------------------------------------------------------------------------------
-----------
 Ca  -  -        10.1          0.        6.       21.       28.       45.        0.
0.
 Si  -  -         4.3          1.        3.       20.       21.        0.       55.
0.  Si Al  -       30.8          6.        4.       14.       16.       45.       15.
0.
 Al Si  -         7.3          1.        2.        5.       10.       12.       70.
0.  Fe S   -        2.1          3.        0.        0.       21.       77.        0.
0.  Fe Si Al        1.3          2.        0.        8.       43.       47.        0.
0.
 Si Al Fe         5.5          2.        4.        5.        2.       87.        0.
0.  Si Al Na        1.6          4.        5.       28.       20.       43.        0.
0.  Si Al Cu        8.1          1.        0.        0.        5.       40.       53.
0.
 Al Si Cu         2.5          0.        0.        0.        0.      100.        0.
0.  Ca Si Al        6.4          0.        0.        1.        2.       31.       65.
0.
 Si Ca Al         1.1          0.        8.        0.        0.       92.        0.
0.
 Al Si Ca         1.8          4.        1.       13.        4.       77.        0.
0.
 Si Al Ca         1.9          5.        2.       22.       33.       37.        0.
0.  Si Al S         2.7          0.        1.        7.       42.       50.        0.
0.  Si Al K         4.5          4.        2.       15.        4.       22.       53.
0.  Ca Al S         1.2          0.        0.        0.        0.      100.        0.
0.  OTHERS -        6.9          3.        5.       13.       27.       51.        0.
0.
-------------------------------------------------------------------------------
-----------
TOTALS -       100.0          3.        3.       11.       15.       45.       23.
0.
NUMBER DENSITY DISTRIBUTION
SPECIES      NUMBER    0.3-  2.5   2.5-  5.0   5.0- 10.0  10.0- 20.0  20.0- 40.0
40.0- 80.0  80.0-100.0
-------------------------------------------------------------------------------
----------------
 Ca  -  -       73      2  38.8  27  35.0  17  22.0  21   3.3   6   0.9   0   0.0
0   0.0
 Si  -  -       18      1  58.0   5  19.3   5  19.3   6   2.8   0   0.0   1   0.5
0   0.0  Si Al  -      192     37  84.6  57   8.7  37   5.6  36   0.7  23   0.4
2   0.0   0   0.0
 Al Si  -       27     10  93.8   5   3.1   4   2.5   5   0.4   2   0.2   1   0.1
0   0.0  Si Al Fe       39     17  95.1   9   3.4   3   1.1   1   0.0   9   0.4
0   0.0   0   0.0  Si Al Na       17      6  93.2   3   3.1   3   3.1   3   0.4
2   0.2   0   0.0   0   0.0  Si Al Cu       17      7  97.3   1   0.9   1   0.9
2   0.2   5   0.6   1   0.1   0   0.0  Al Si Ca       17     12  98.2   1   0.5
2   1.1   1   0.1   1   0.1   0   0.0   0   0.0
 Si Al Ca       19      8  94.8   3   2.4   3   2.4   3   0.3   2   0.2   0   0.0
0   0.0  Si Al S        15      2  90.0   1   3.0   1   3.0   8   2.9   3   1.1
0   0.0   0   0.0  Si Al K        19      6  90.5   4   4.0   5   5.0   2   0.2
1   0.1   1   0.1   0   0.0 ---------      136   CATEGORIES WITH # OF PARTICLES
LESS THAN 10 COMBINED INTO ONE
-------------------------------------------------------------------------------
----------------
TOTALS -      589    162  90.5 138   5.1  93   3.5 111   0.5  77   0.3   8   0.0
0   0.0
```

Pittsburgh #8 – char sample # 194

```
Pittsburgh 194 - 30 atm
TOTAL Volume FACTOR:  0.20907E+07

AVERAGE SPECIES COMPOSITION
  #   SPECIES      C   O  Na  Mg  Al  Si   P   S  Cl  K   Ca  Ti   V  Cr  Mn  Fe
Ni  Cu  Zn   X    Vol %
-------------------------------------------------------------------------------
------------------------
  25  Si  -  -     0.  0.  0.  0.  5. 91.  0.  0.  0.  0.  2.  0.  0.  0.  0.  1.
0.  0.  0.  0.   1.8
  72  Ca  -  -     0.  0.  1.  0.  1.  2.  0.  6.  0.  0. 87.  0.  0.  0.  0.  1.
1.  0.  0.  0.   4.7
  39  Fe  -  -     0.  0.  1.  1.  1.  1.  0.  0.  0.  0.  1.  0.  0.  0.  0. 94.
0.  1.  1.  0.   2.8
 252  Si Al  -     0.  0.  0.  0. 31. 62.  0.  0.  0.  2.  1.  1.  0.  0.  0.  1.
0.  0.  0.  0.  37.5
 140  Ca S   -     0.  0.  0.  0.  1.  1.  0. 19.  0.  0. 74.  0.  0.  0.  0.  2.
1.  0.  0.  0.   8.8
   2  Fe S   -     0.  0.  1.  0.  0.  0.  0. 27.  0.  0.  0.  0.  0.  0.  0. 72.
0.  0.  0.  0.   1.1
  13  Ca S  Si     0.  0.  0.  1.  5.  9.  0. 21.  0.  1. 53.  1.  1.  0.  1.  2.
0.  1.  3.  0.   0.7
  69  Si Al Ca     0.  0.  1.  1. 27. 48.  0.  4.  1.  2. 12.  1.  0.  0.  0.  2.
0.  0.  1.  0.  12.4
  12  Ca Si Al     0.  0.  1.  3. 16. 21.  2.  7.  1.  2. 41.  0.  0.  0.  0.  3.
1.  1.  1.  0.   0.5
  18  Si Al K      0.  0.  0.  0. 35. 54.  0.  0.  0.  7.  1.  1.  0.  0.  0.  2.
0.  0.  0.  0.   4.3
   6  Si Fe Al     0.  0.  1.  0. 19. 42.  0.  1.  0.  2.  5.  1.  0.  0.  0. 28.
0.  1.  0.  0.   0.6
  28  Si Al Fe     0.  0.  0.  1. 29. 48.  0.  1.  1.  3.  3.  1.  0.  0.  0. 13.
0.  1.  0.  0.   3.1
  22  Fe Si Al     0.  0.  1.  1. 17. 22.  0.  1.  0.  0.  1.  0.  0.  0.  0. 55.
1.  0.  0.  0.   8.9
  17  Ca S  Al     0.  0.  0.  1. 12.  7.  0. 23.  1.  1. 50.  1.  0.  0.  0.  2.
1.  0.  2.  0.   0.5
  44  Ca S  Fe     0.  0.  1.  0.  8.  8.  3. 25.  0.  0. 39.  1.  0.  1.  2. 10.
1.  0.  0.  0.   5.0
   1  Si Al Cu     0.  0.  0.  0. 25. 43.  0.  8.  4.  1.  5.  1.  0.  0.  0.  5.
0.  8.  0.  0.   1.0
   6  Si Al S      0.  0.  2.  1. 25. 50.  0. 10.  1.  2.  4.  0.  0.  0.  0.  2.
1.  1.  1.  0.   1.2
   1  Si S  Cu     0.  0.  0.  4.  5. 48.  0. 12.  6.  2.  2.  0.  3.  0.  1.  5.
0. 11.  0.  0.   0.5
 138       ALL  CATEGORIES  WITH  VOLUME  %  LESS  THAN  1.0  COMBINED  IN  ONE
4.4
-------------------------------------------------------------------------------
------------------------
 905  TOTALS -     0.  0.  1.  1. 21. 40.  0.  5.  0.  2. 17.  1.  0.  0.  0. 11.
0.  1.  0.  0.  100.0
```

```
Volume DISTRIBUTION
SPECIES        Volume %    0.3-  2.5  2.5-  5.0  5.0- 10.0 10.0- 20.0 20.0- 40.0
40.0- 80.0 80.0-100.0
-------------------------------------------------------------------------------
-----------
 Si  -  -         1.8          6.        1.       18.       39.       36.        0.
0.
 Ca  -  -         4.7          6.        7.       31.       35.       20.        0.
0.
 Fe  -  -         2.8          3.        5.       14.       17.       61.        0.
0.
 Si Al  -        37.5          1.        2.        9.       23.       43.       21.
0.  Ca S   -        8.8          4.       12.       28.       11.       12.       32.
0.  Fe S   -        1.1          0.        0.        0.        0.      100.        0.
0.  Si Al Ca       12.4          0.        2.        2.       18.       30.       48.
0.  Si Al K         4.3          0.        1.        5.       14.       23.       57.
0.  Si Al Fe        3.1          0.        5.        4.       28.       63.        0.
0.
 Fe Si Al         8.9          0.        1.        1.        8.       36.       54.
0.  Ca S  Fe        5.0          2.        9.        4.        0.        0.       84.
0.  Si Al S         1.2          0.        0.        0.        6.       94.        0.
0.  OTHERS -        8.5          6.       10.       13.       30.       42.        0.
0.
-------------------------------------------------------------------------------
-----------
TOTALS -       100.0          2.        4.       10.       20.       36.       28.
0.
NUMBER DENSITY DISTRIBUTION
SPECIES      NUMBER    0.3-  2.5   2.5-  5.0   5.0- 10.0  10.0- 20.0  20.0- 40.0
40.0- 80.0  80.0-100.0
-------------------------------------------------------------------------------
----------------
 Si  -  -       25      7  97.2   2   1.0   3   1.4  11   0.4   2   0.1   0   0.0
0   0.0
 Ca  -  -       72      8  86.0  22   8.1  14   5.2  25   0.6   3   0.1   0   0.0
0   0.0
 Fe  -  -       39     17  97.5   9   1.8   3   0.6   7   0.1   3   0.0   0   0.0
0   0.0  Si Al  -      252     17  85.9  39   6.8  31   5.4 121   1.5  41   0.5
3   0.0   0   0.0  Ca S   -      140     16  82.2  71  12.5  28   4.9  19   0.2
5   0.1   1   0.0   0   0.0  Ca S  Si       13      2  87.7   7  10.5   1   1.5
2   0.2   1   0.1   0   0.0   0   0.0  Si Al Ca       69      9  93.2  12   4.3
4   1.4  31   0.8  11   0.3   2   0.0   0   0.0
 Al Si Ca       10      4  97.3   3   2.5   0   0.0   3   0.2   0   0.0   0   0.0
0   0.0
 Ca Si Al       12      1  78.0   3   8.0   5  13.4   3   0.6   0   0.0   0   0.0
0   0.0  Si Al K        18      2  91.0   3   4.7   2   3.1   7   0.8   3   0.3
1   0.1   0   0.0  Si Al Fe       28      1  72.3   9  22.3   1   2.5  11   1.9
6   1.0   0   0.0   0   0.0
 Fe Si Al       22      2  90.6   4   6.2   1   1.6   6   0.7   7   0.8   2   0.2
0   0.0  Ca S  Al       17      1  70.4   9  21.7   3   7.2   4   0.7   0   0.0
0   0.0   0   0.0  Ca S  Fe       44      9  88.8  28   9.5   5   1.7   1   0.0
0   0.0   1   0.0   0   0.0 ---------       144   CATEGORIES WITH # OF PARTICLES
LESS THAN 10 COMBINED INTO ONE
-------------------------------------------------------------------------------
----------------
TOTALS -      905    142  91.2 256   5.6 115   2.5 285   0.4  97   0.1  10   0.0
0   0.0
```

Pittsburgh #8 – char sample # 215

Pittsburgh 215 - 30 atm*

TOTAL Volume FACTOR: 0.35309E+06

AVERAGE SPECIES COMPOSITION

#	SPECIES		C	O	Na	Mg	Al	Si	P	S	Cl	K	Ca	Ti	V	Cr	Mn	Fe	Ni	Cu	Zn	X	Vol %
24	Ca	- -	0.	0.	0.	0.	0.	0.	0.	4.	1.	0.	89.	0.	0.	0.	1.	2.	0.	0.	0.	0.	10.7
17	Si	- -	0.	0.	0.	0.	5.	91.	0.	0.	0.	1.	0.	0.	0.	0.	0.	1.	1.	0.	0.	0.	4.5
8	Fe S	-	0.	0.	0.	0.	0.	1.	0.	38.	0.	0.	0.	0.	0.	0.	0.	59.	0.	0.	0.	0.	4.2
90	Si Al	-	0.	0.	1.	1.	33.	57.	0.	1.	0.	3.	1.	0.	1.	0.	0.	1.	0.	1.	1.	0.	46.3
8	Al Si	-	0.	0.	1.	0.	48.	45.	0.	0.	0.	2.	0.	0.	1.	0.	0.	1.	0.	0.	1.	0.	1.0
2	Ca S	-	0.	0.	0.	0.	3.	2.	0.	33.	0.	0.	52.	2.	2.	0.	1.	0.	1.	3.	0.	0.	0.9
7	Si Al S		0.	0.	0.	0.	31.	44.	0.	10.	0.	4.	1.	1.	0.	0.	1.	3.	1.	1.	1.	0.	6.3
1	Al Si S		0.	0.	1.	1.	41.	38.	0.	6.	4.	2.	0.	0.	3.	0.	0.	0.	0.	2.	0.	0.	1.5
3	Fe S Si		0.	0.	0.	0.	4.	8.	1.	23.	3.	0.	0.	0.	0.	0.	0.	61.	0.	0.	0.	0.	1.7
1	S Fe Si		0.	0.	0.	0.	1.	17.	0.	47.	0.	0.	0.	2.	0.	0.	0.	26.	0.	4.	2.	0.	0.5
17	Si Al K		0.	0.	0.	2.	35.	49.	0.	2.	0.	8.	0.	0.	0.	0.	0.	1.	0.	0.	1.	0.	9.6
3	Al Si K		0.	0.	4.	1.	43.	34.	0.	4.	1.	8.	1.	0.	0.	0.	0.	1.	0.	1.	0.	0.	2.4
2	Si Fe Al		0.	0.	0.	1.	14.	43.	0.	7.	0.	3.	0.	0.	0.	0.	1.	27.	0.	2.	2.	0.	0.5
14	Si Al Fe		0.	0.	4.	1.	29.	38.	0.	3.	1.	4.	1.	1.	0.	0.	0.	16.	2.	0.	0.	0.	2.5
3	Si Al Ca		0.	0.	0.	2.	26.	62.	0.	0.	1.	1.	7.	0.	0.	0.	0.	0.	0.	0.	0.	0.	0.6
1	Si Al Ni		0.	0.	5.	3.	20.	44.	0.	5.	2.	0.	5.	0.	3.	0.	0.	2.	10.	0.	0.	0.	2.3
1	S Si Zn		0.	0.	0.	0.	14.	21.	0.	23.	4.	1.	0.	1.	0.	0.	9.	8.	0.	2.	17.	0.	0.5
48	ALL CATEGORIES WITH VOLUME % LESS THAN 1.0 COMBINED IN ONE																						3.7
250	TOTALS	-	0.	0.	1.	1.	26.	43.	0.	5.	1.	3.	11.	0.	1.	0.	0.	6.	1.	1.	1.	0.	100.0

Volume DISTRIBUTION

SPECIES	Volume %	0.3- 2.5	2.5- 5.0	5.0- 10.0	10.0- 20.0	20.0- 40.0	40.0- 80.0	80.0-100.0
Ca - -	10.7	4.	6.	37.	26.	27.	0.	0.
Si - -	4.5	22.	15.	40.	22.	0.	0.	0.
Fe S -	4.2	1.	0.	25.	20.	54.	0.	0.
Si Al -	46.3	8.	4.	9.	25.	24.	30.	0.
Si Al S	6.3	0.	3.	0.	26.	71.	0.	0.
Al Si S	1.5	0.	0.	0.	0.	100.	0.	0.
Fe S Si	1.7	0.	0.	0.	38.	62.	0.	0.
Si Al K	9.6	9.	6.	59.	2.	23.	0.	0.
Al Si K	2.4	59.	0.	0.	0.	41.	0.	0.
Si Al Ni	2.3	0.	0.	0.	0.	0.	100.	0.
Si Al Fe	2.5	14.	8.	68.	10.	0.	0.	0.
OTHERS -	7.9	12.	27.	8.	48.	5.	0.	0.
TOTALS -	100.0	9.	6.	19.	23.	27.	16.	0.

NUMBER DENSITY DISTRIBUTION

SPECIES	NUMBER	0.3- 2.5	2.5- 5.0	5.0- 10.0	10.0- 20.0	20.0- 40.0	40.0- 80.0	80.0-100.0
Ca - -	24	2 85.9	6 6.2	7 7.2	8 0.6	1 0.1	0 0.0	0 0.0
Si - -	17	3 91.8	6 4.4	5 3.7	3 0.2	0 0.0	0 0.0	0 0.0
Si Al -	90	20 96.2	23 2.7	7 0.8	32 0.3	6 0.1	2 0.0	0 0.0
Si Al K	17	6 96.8	3 1.2	5 1.9	1 0.0	2 0.1	0 0.0	0 0.0
Si Al Fe	14	8 98.5	3 0.9	2 0.6	1 0.0	0 0.0	0 0.0	0 0.0
---------	88	CATEGORIES WITH # OF PARTICLES LESS THAN 10 COMBINED INTO ONE						
TOTALS -	250	74 96.9	62 1.9	30 0.9	64 0.2	17 0.0	3 0.0	0 0.0

HIGH PRESSURE COAL COMBUSTION KINETICS PROJECT

Appendix E – Deployment of Sub-Models in Design Codes and Process Design Analysis

E.1 DEPLOYMENT OF SUBMODELS IN DESIGN CODES

E.1.1 Installation of the Aspen Plus PC Coal Lab module

The following files are distributed with the PC Coal Lab module for Aspen Plus.

File Name	Description
PCCoalLab.apm	Module deploying PC Coal Lab in Aspen Plus.
PCCOV3b.exe	PC Coal Lab executable. This is a restricted version of the PC Coal Lab program. The user should contact Niksa Energy Associates to obtain a fully functional version of the program.
FBCOEFS.dat	Input file for PC Coal Lab
FLCOEFS.dat	Input file for PC Coal Lab
FLCOEF2.dat	Input file for PC Coal Lab
PCCoalLab_loc_dll.opt	Text file for Aspen Plus Linker options, provides the complete path to the usrpcc.dll file.
PCCL.ocr	pcCoalLab module file
PCCL.ocx	pcCoalLab module file
Usrpcc.dll	pcCoalLab module file
delFiles.exe	File manipulation program for the PC Coal Lab output files.

PC Coal Lab requires five input files to run. Three of these files are distributed with the PC Coal Lab module. The remaining two files are generated from the input entered through the Aspen Plus forms. The future versions of PC Coal Lab must, therefore, strictly follow the same format for reading the input data from the files coalpc.dat and testplan.dat. In this implementation, part of the input for PC Coal Lab is provided through the standard input forms in Aspen Plus and part of the input is provided through the configured variables through Aspen Plus.

Installation step are as follows:

Step 1. Move the files “pccl.ocr” and “pccl.ocx” to the GUI/forms folder of your Aspen Plus Installation.

Step 2. Run “ApwnSetup.exe” from the GUI/xeq folder of your Aspen Plus installation. This will open the following box.

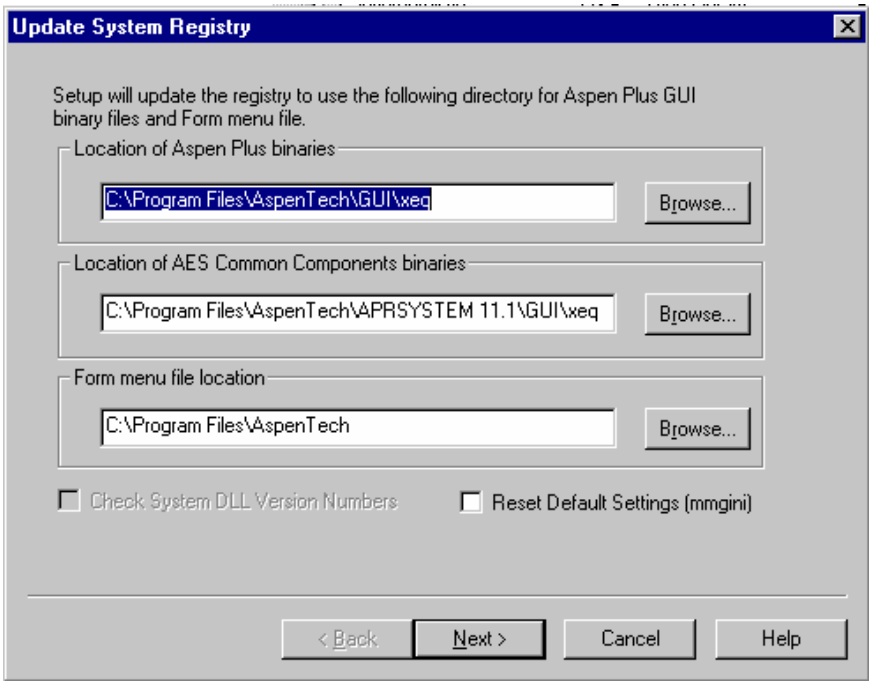

Make sure that path to these folders are correct. Normally, these will be properly set at the time of Aspen Plus installation. Then click on **Next**.

Step 3. On the "Register Forms" window, first de-select all, then scroll down all the way down and select PCCL.ocx. Also select "Update Data Browser Menu," as shown in the figure below.

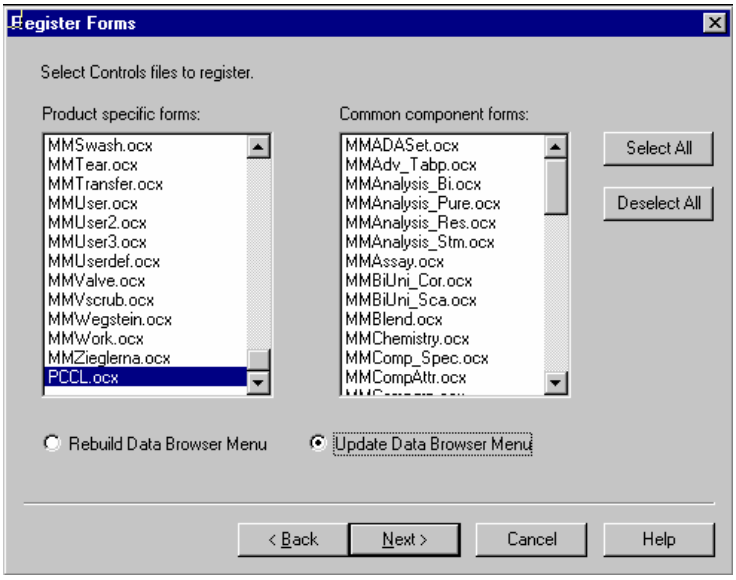

Now click on next.

Step 4. This opens the "Register PlotWizard" window. Deselect all and then click on finish.

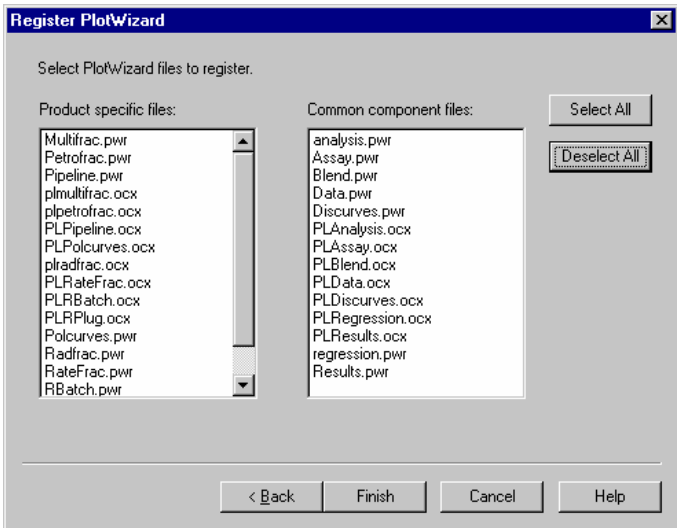

This may issue some error or warning messages. You may either ignore those or download the file "WAApwnSetup.bat" from support.aspentech.com to resolve these issues. Please refer to Solution ID: 107422 in Aspen Technology's Knowledge Base, for additional information.

Step 5. Place the following files in your working folder:

1. Pccov3b.exe
2. Fbcoefs.dat
3. Flcoefs.dat
4. Flcoef2.dat
5. DelFiles.exe
6. Pccoallab_loc_dll.opt.

Step 6. Place the following two files either in your working directory or in your Aspen Plus installation sub-folder e.g., xeq folder.

1. PcCoalLab.apm
2. Usrpcc.dll.

Step 7. Edit the file Pccoallab_loc_dll.opt and specify the correct path to the usrpcc.dll file on your system.

This completes the installation of the pcCoalLab module on your system. You are now ready to use the pcCoalLab module under Aspen Plus.

E.1.2 Using the Aspen Plus PC Coal Lab Module

The use of PC Coal Lab module in Aspen Plus requires that the user is familiar with both PC Coal Lab and Aspen Plus. Therefore, it is assumed that the user is able to run these

two packages. The implementation of PC Coal Lab in Aspen Plus was carried out with the following two objectives:

1. The use of PC Coal Lab as a stand-alone block from Aspen Plus.
2. The use of PC Coal Lab as an integrated block in Aspen Plus.

The stand-alone version provides the ultimate results generated by PC Coal Lab, which are loaded into appropriate forms in Aspen Plus simulation. The results for the secondary pyrolysis of tar, however, are not loaded into aspen plus and the user is directed to view these results by accessing the output file.

The use as an integrated block may need further development as appropriate model were needed for the gas phase reactions of the gases and the tar produced by the primary pyrolysis of coal. In the absence of such models, the usefulness of such an integrated block may be very limited. The implementation of PC Coal Lab is performed in a way that the block has only one inlet and one outlet. More inlet streams, should, therefore be manipulated so that only a single stream is fed to the block.

E.1.3 Use of PC Coal Lab as a Stand-alone Block

This section describes how to set up an Aspen Plus simulation to run PC Coal Lab module as a stand-alone block. Step-by-step procedure is outlined below.

1. Start a new simulation by opening Aspen Plus and selecting General with Metric Units.
2. Open Aspen Plus and place a PCCL block from the pcCoalLab tab as shown in the figure below. If the pcCoalLab library is not shown, then activate it by selecting **Library | Reference** and checking pcCoalLab, as shown.

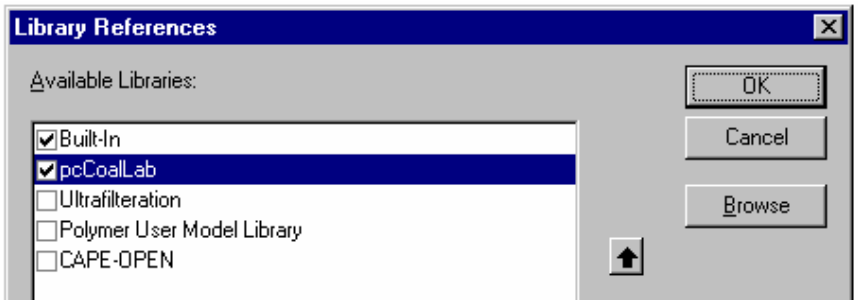

pcCoalLab library now should be available as shown below.

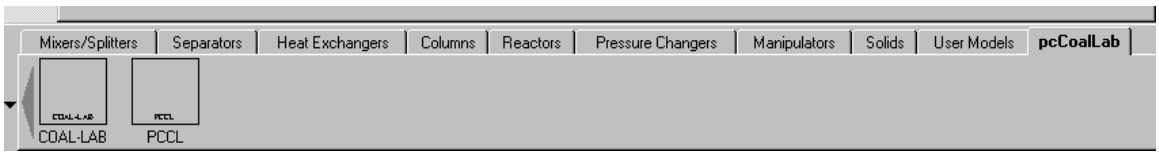

3. Connect an input and an output stream to the block, as shown in the figure.

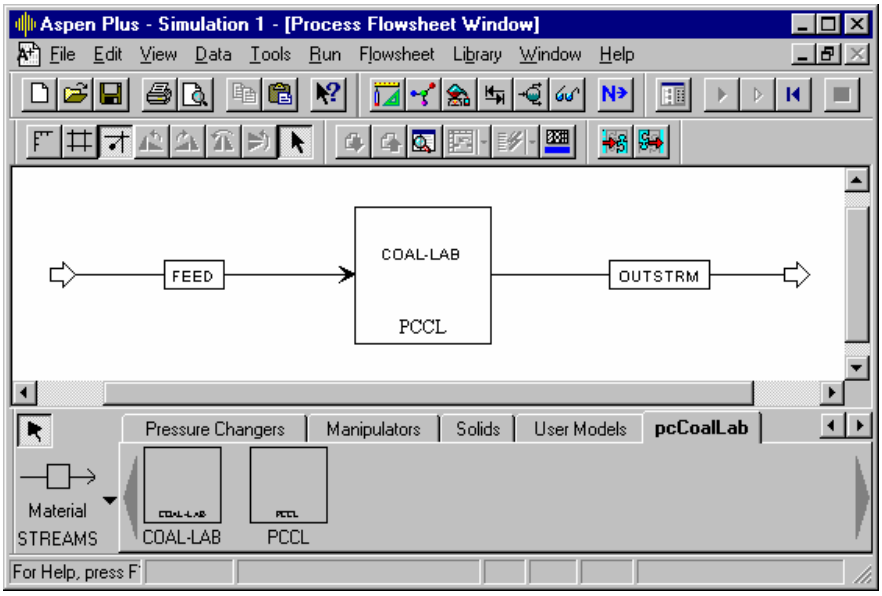

4. Start the data browser and set the global parameters as shown.

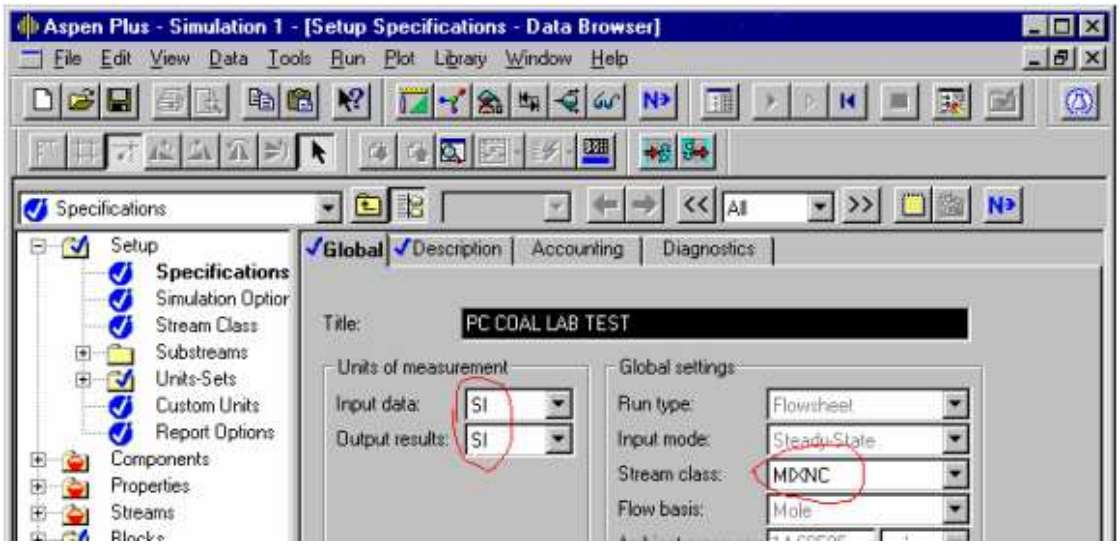

Make sure that Stream Class is selected to MIXNC and the units of measures are SI.

5. In the next step, set up the components to involved in the simulations. First, add sixteen gaseous components as show in the figure below:

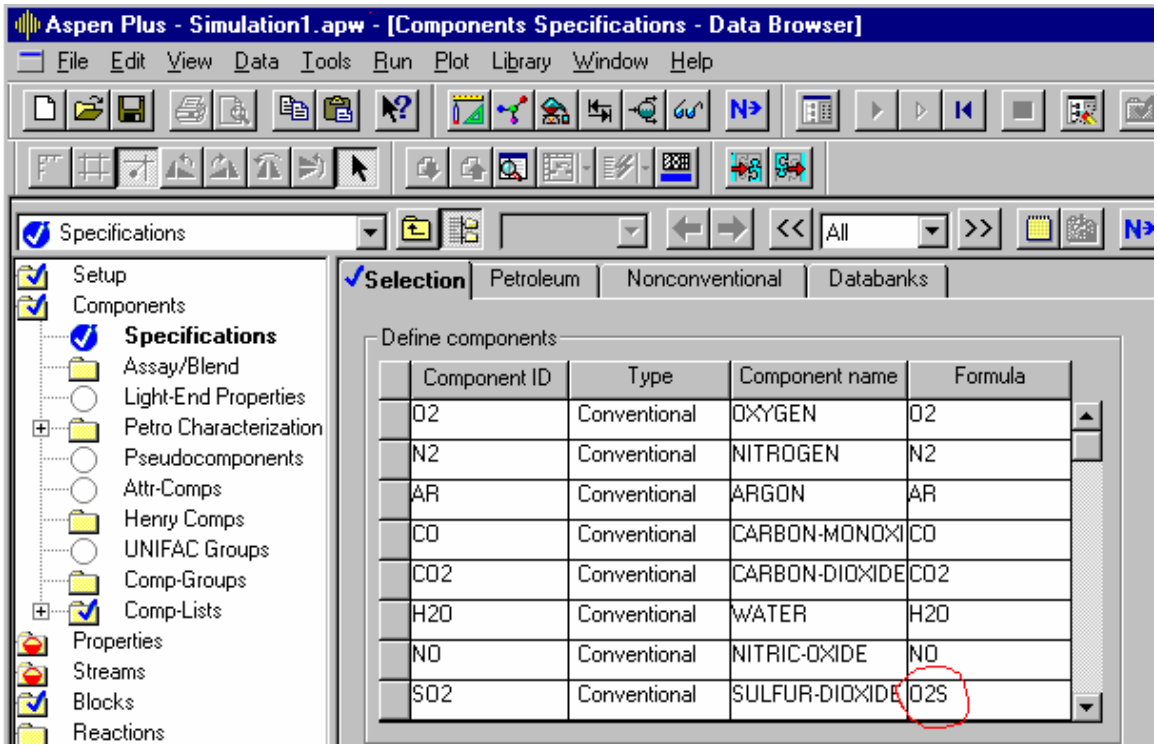

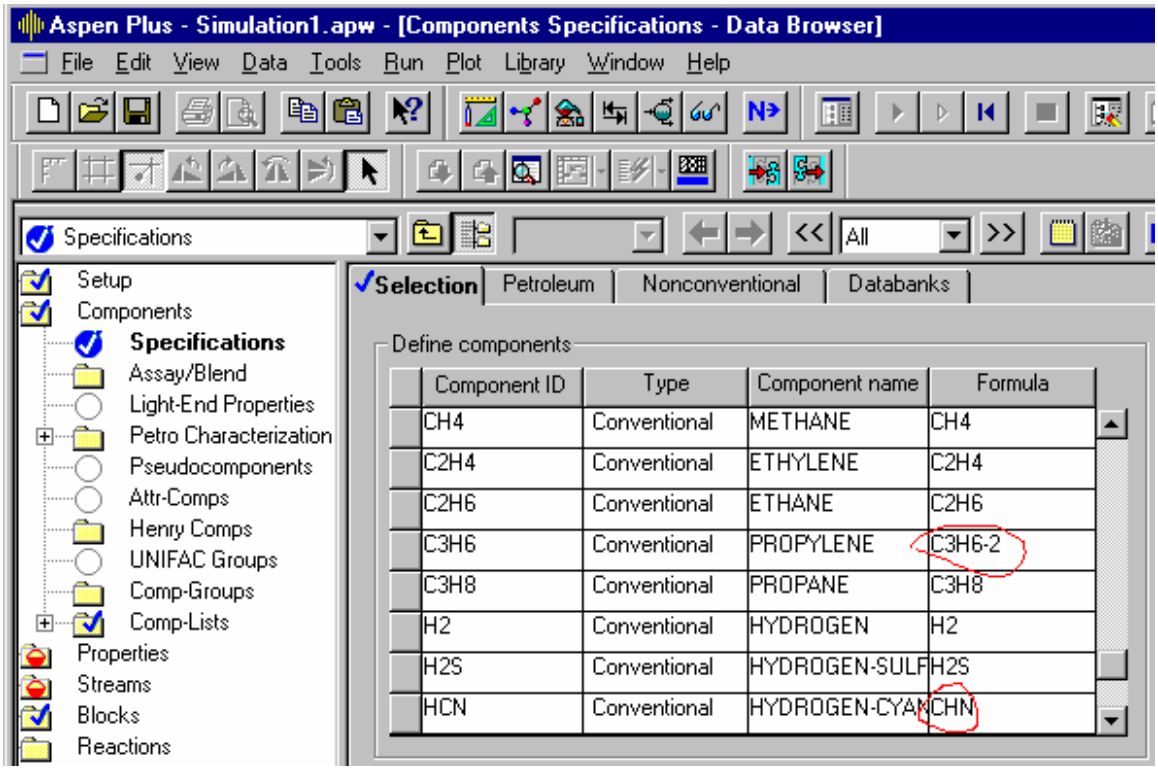

Please note the formulas for C_3H_6, SO_2 and HCN as used in Aspen Plus.

6. In the next step, add the non-conventional components Coal, Tar, Char and Ash as shown below:

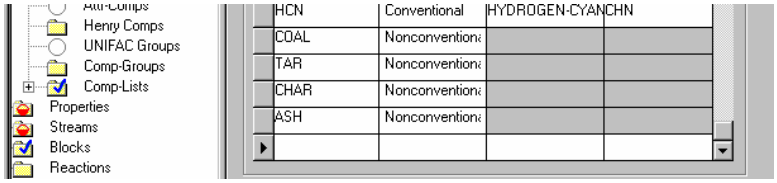

7. Set up the properties, we can select ideal gas or another method, as PC Coal Lab does not perform any calculations that are affected by the selection of the property estimation method. However, we select PR-BM method to account for deviation from ideal behavior, if needed.

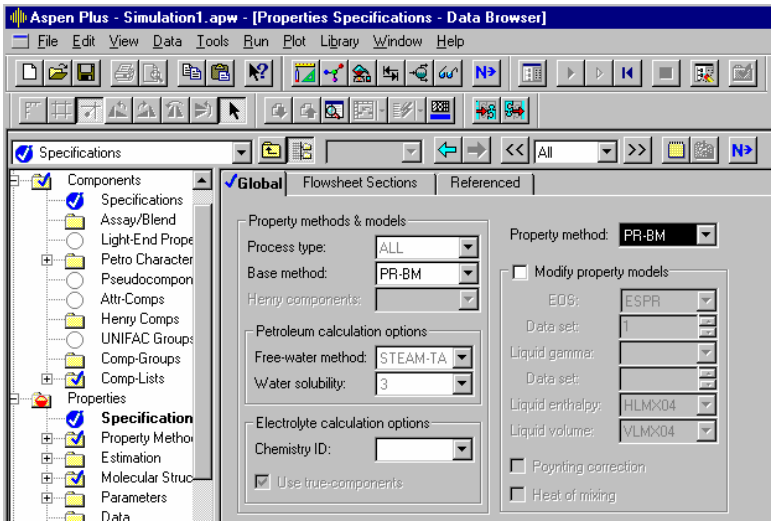

8. Set up the property methods for the non-conventional components as shown in the next four figures:

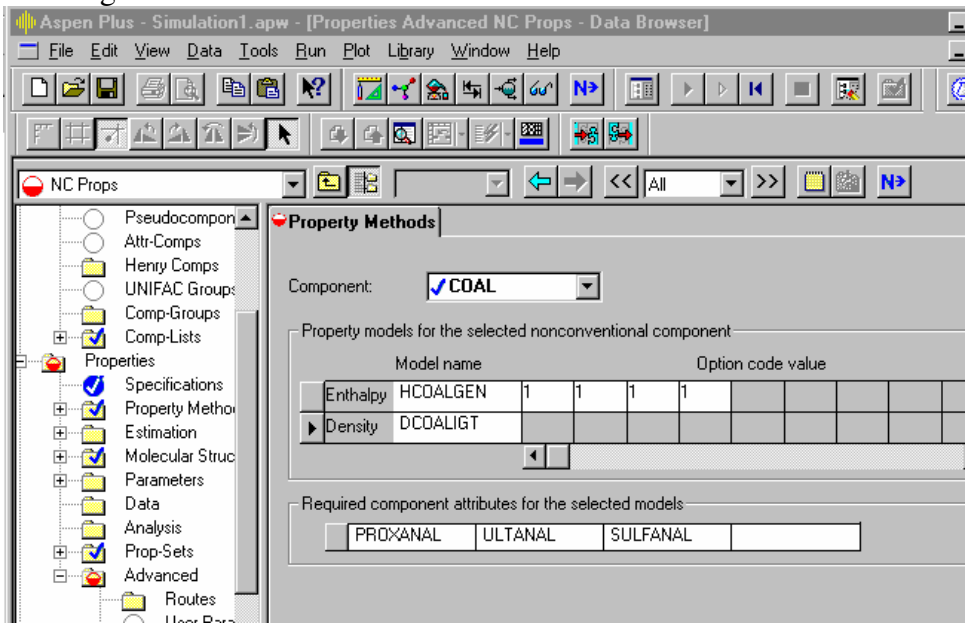

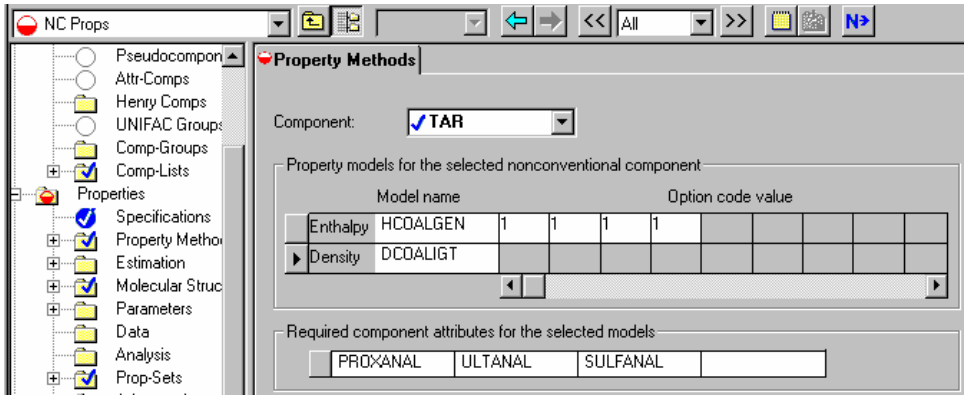

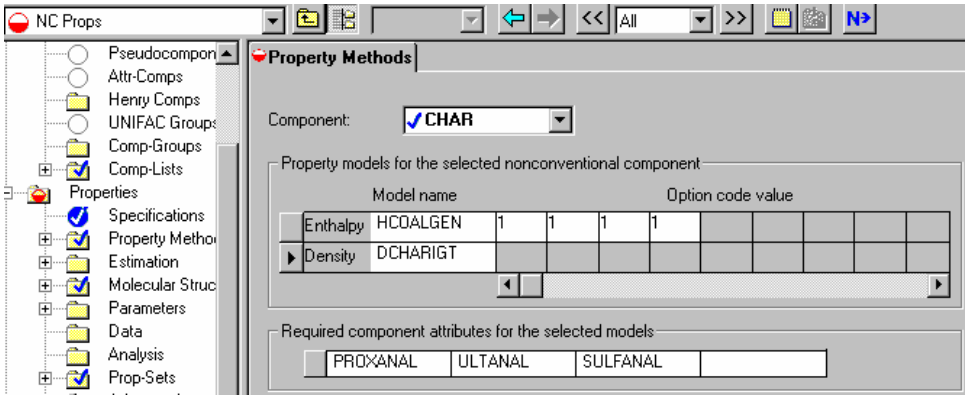

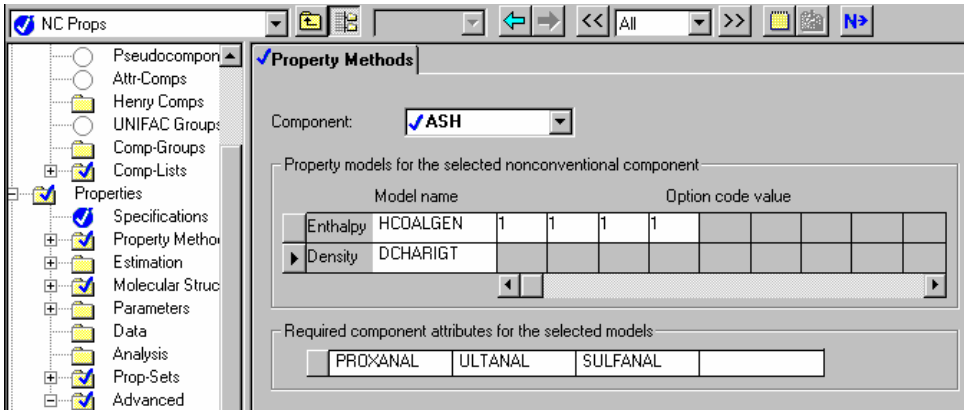

These properties selection indicates that the proximate analysis, ultimate analysis and sulfur analysis attributes for these non-conventional components may be needed.

9. Set up the stream specifications, starting with the mixed stream. The mixed stream here specifies the carrier gas for the coal particles in PC Coal Lab simulations. PC Coal Lab does not require the flow rate of the carrier gas. Thus, for the case when the carrier gas is composed of inert species, a flow rate of zero may be specified. For the case when we have oxidizing environment, mole fraction of oxygen is specified in this form. However, the flow rate of the stream MUST be NON-ZERO and should be specified as a small value e.g., 1.0e-8. The next two figures show these two cases.

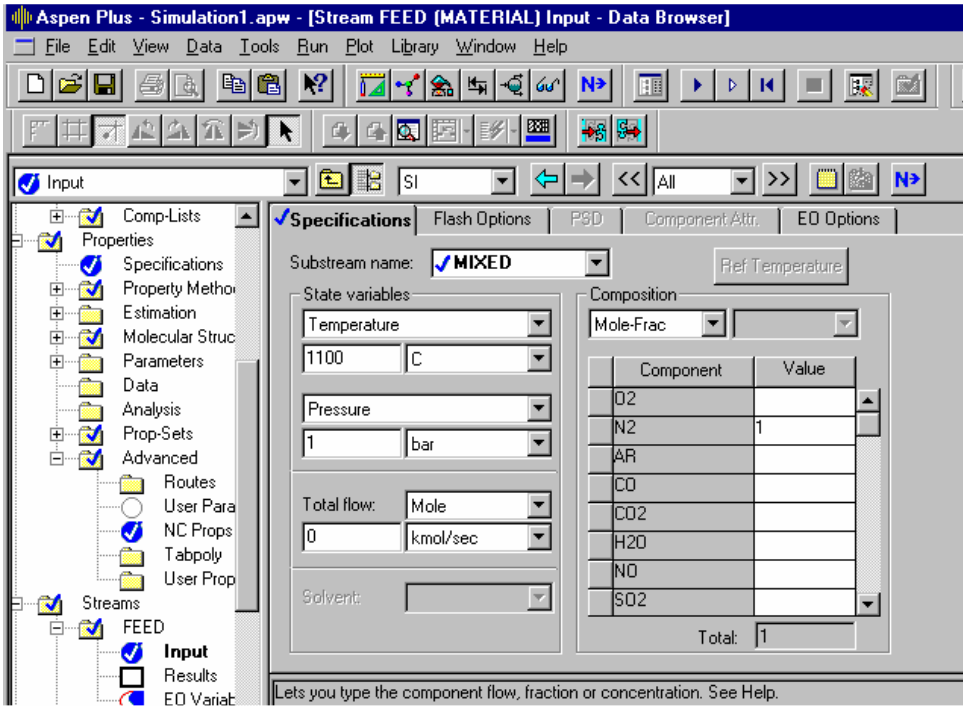

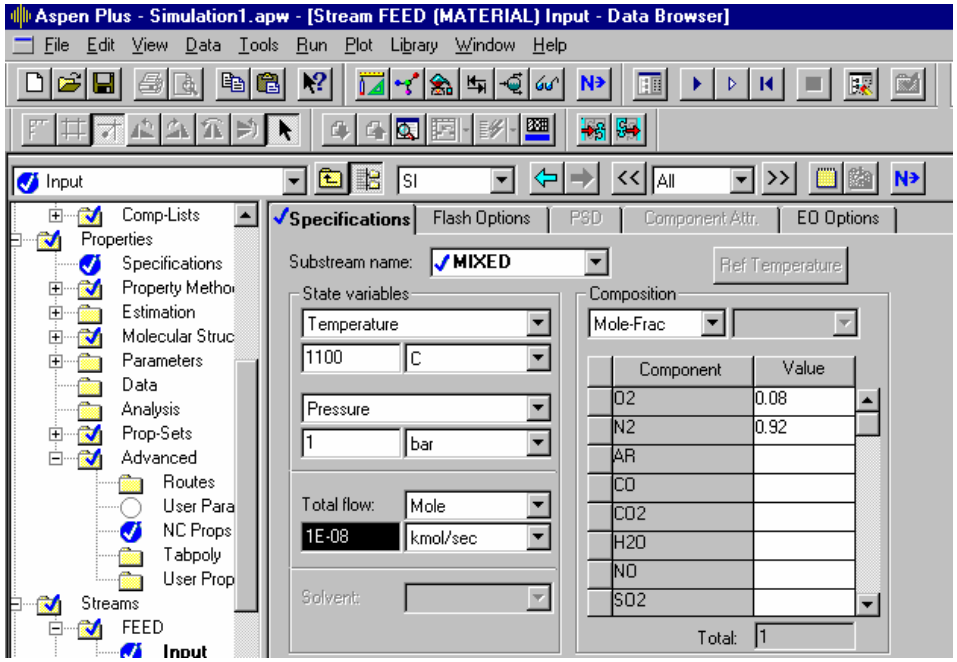

10. Set up the input stream specification for the non-conventional component coal, shown in the figure below:

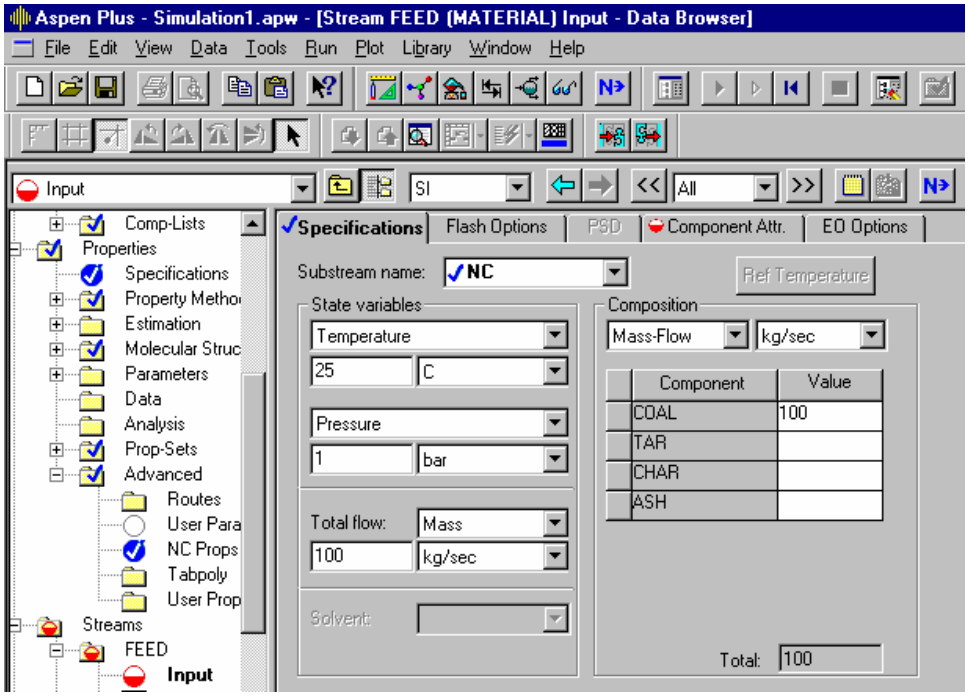

The temperature of this stream corresponds to the injection temperature of the coal particles. We have specified a flow rate of 100 kg/sec, but any positive value will work for the stand-alone run of PC Coal Lab through the Aspen Plus user block. Since this value is not required for PC Coal Lab calculations.

11. Specify the component attributes for coal as shown in the figures below.

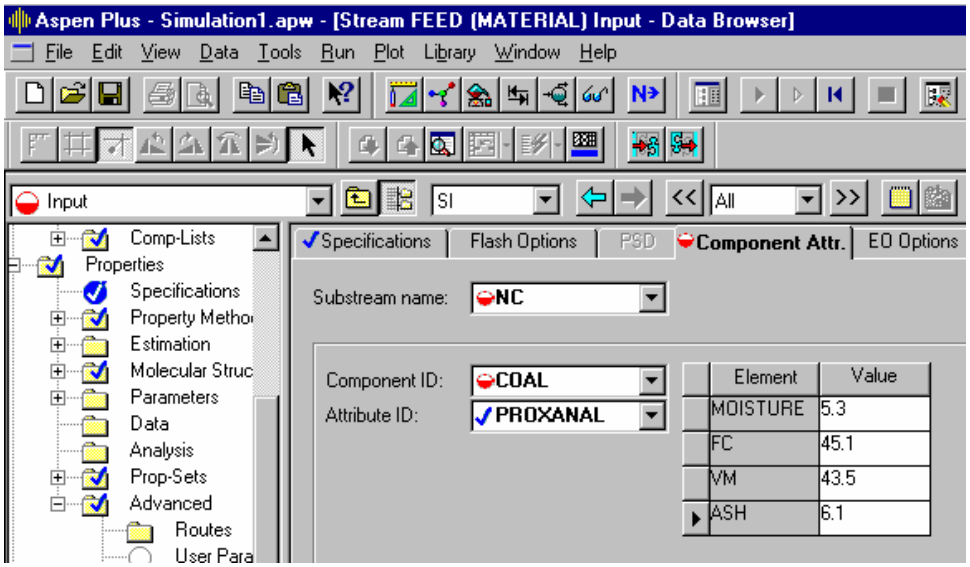

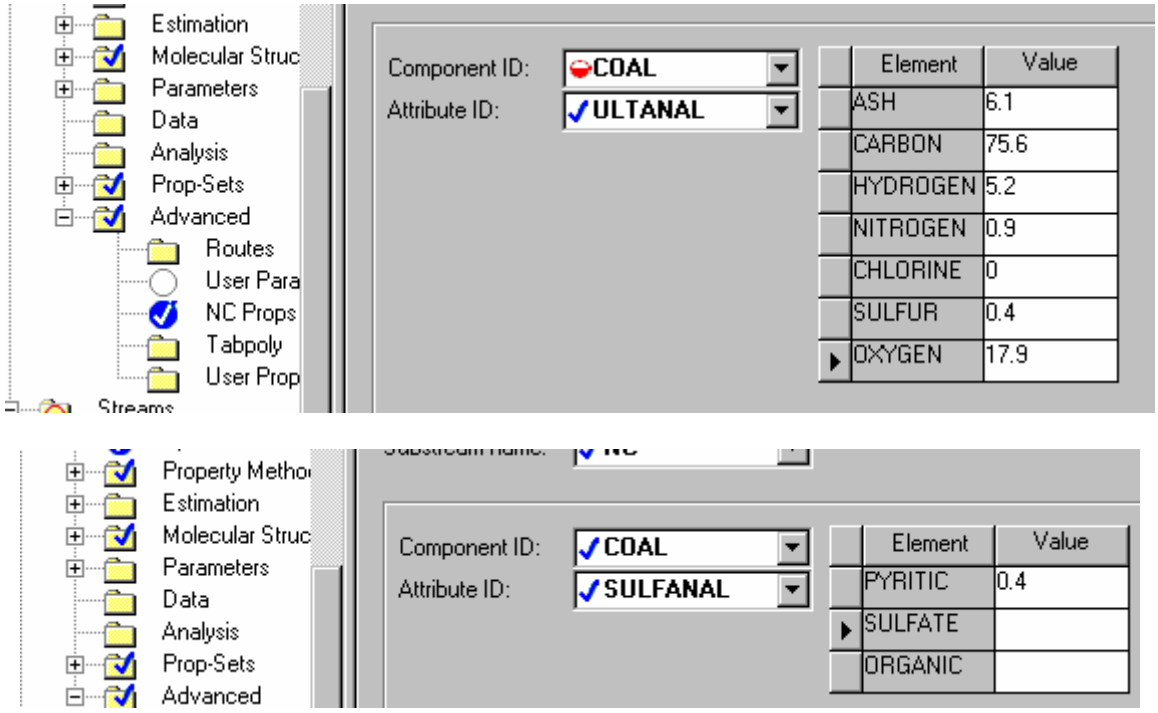

The sum of pyretic, sulfate, and organic sulfur must be equal to the value specified under ultimate analysis of coal. The selection, however, is immaterial for PC Coal Lab simulations.

12. In the final step for setting up the simulation, specify the remaining input conditions required for PC Coal Lab. The user must be familiar with the codes used for generating the input files for a PC Coal Lab simulation. Please refer to **Chapter 4** of the "**User Guide and Tutorial for PC Coal Lab Version 2.2,**" for guidance for the selection of appropriate codes for setting up the simulation parameters. These values are specified under the configured variables tab for the BLOCKS | block-name set-up form. The input values are shown below.

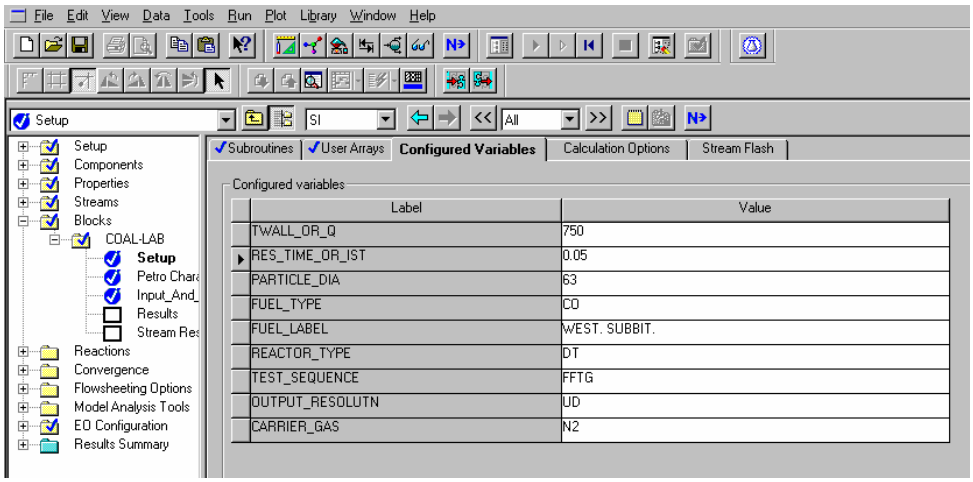

Alternatively, these values may be specified on the **input tab** and **Operating Conditions** tab of the **Input_And_Results** forms under **BLOCKS | block-name** (Coal-Lab in this test problem). The following figures show the values used in this test problem.

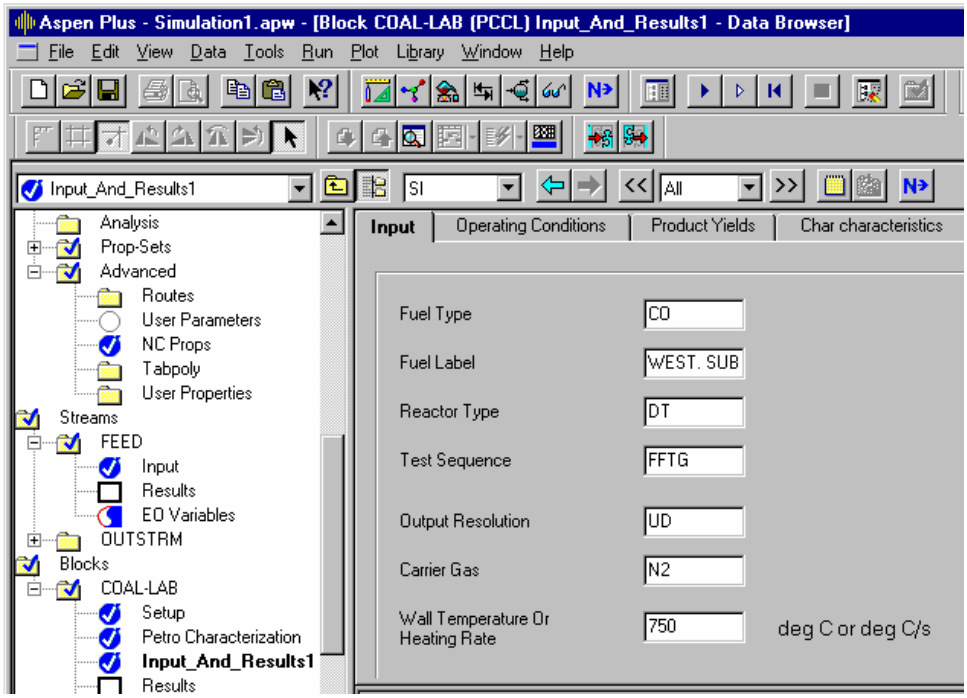

It is again pointed out that the input required for PC Coal Lab is partly provided through the Aspen Plus input forms. This includes the operating conditions for the carrier stream. The solid stream i.e., coal particle stream operating conditions. The species involved in the simulation are specified through the specification form under components. The codes for the simulation parameters, particle diameter, furnace temperature and carrier gas are entered either through the configured variables form or through the Input_And_Results form of the block. The configured variables form provides for all the values needed for the simulation, whereas there is some overlap between the two tabs under the Input_And_Results. However, changing a value on one form will reflect the change on the other form. It is preferred to use the configured variables form since it is list all the input variables. On the Operating Conditions tab, changes may only be made to the fields, which are white and not grayed out. The white fields are the input fields.

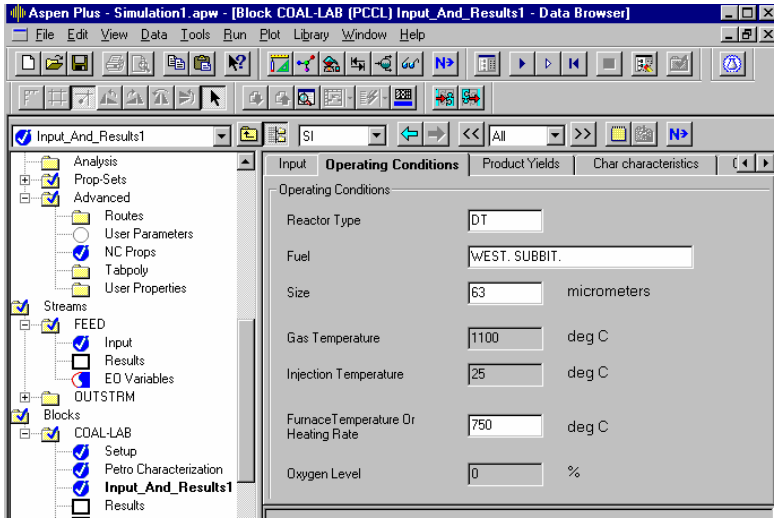

13. However, before we run the simulation, provide the link to the file, which contains the customized pcCoalLab module for Aspen Plus. To do this, enter the name of the file containing the complete path to the usrpcc.dll file under RUN | Settings | Linker Options, as shown below and then click apply and then OK.

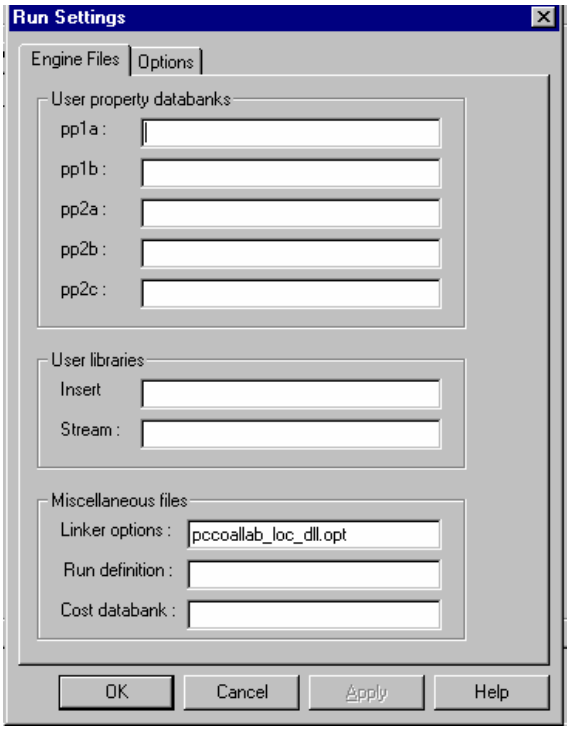

The file "**pccoallab_loc_dll.opt**" is shown below and is included with the distribution of the pcCoalLab module. The sample is shown below. The user must edit this file to reflect the correct path on his or her system.

pccoallab_Loc_DLL.opt

```
1 d:\simulations_2002\aspenPlus\pccl\usrpcc.dll
```

14. Run the simulation. The simulation should complete with some warning messages. These messages are due to mass imbalance. However, we can ignore these messages as stand-alone implementation does use the mass flows of the in-stream and the out-streams.

15. View the results. The results are available under the respective tabs of the Input_And_Results form of the block (Coal-Lab in the test problem). The results are as follows:

Ultimate Product Yields

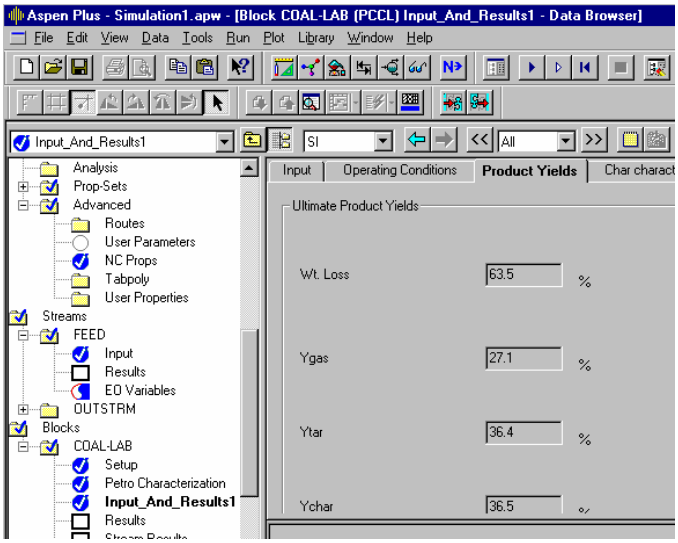

Ultimate Char Characteristics

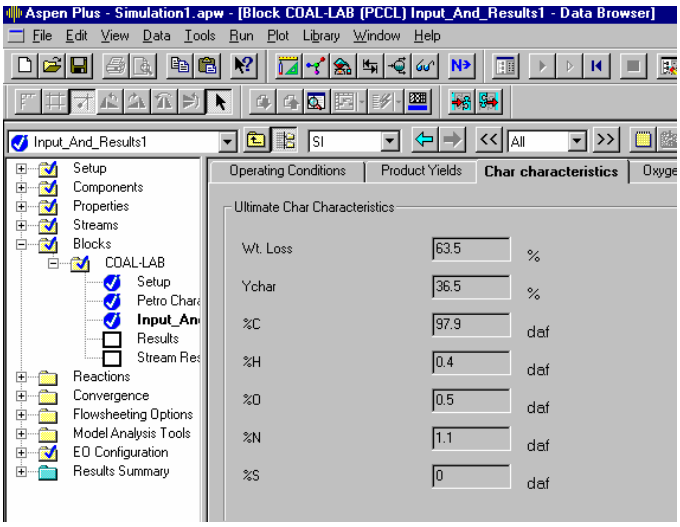

Ultimate Tar Characteristics

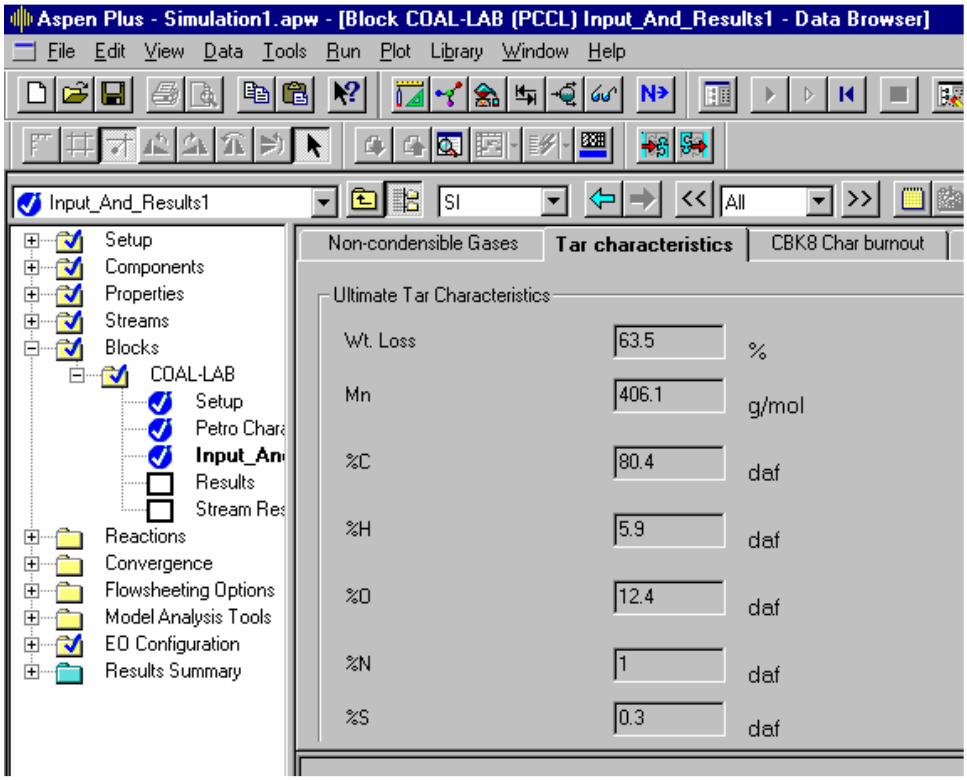

Non-condensible Gases distribution

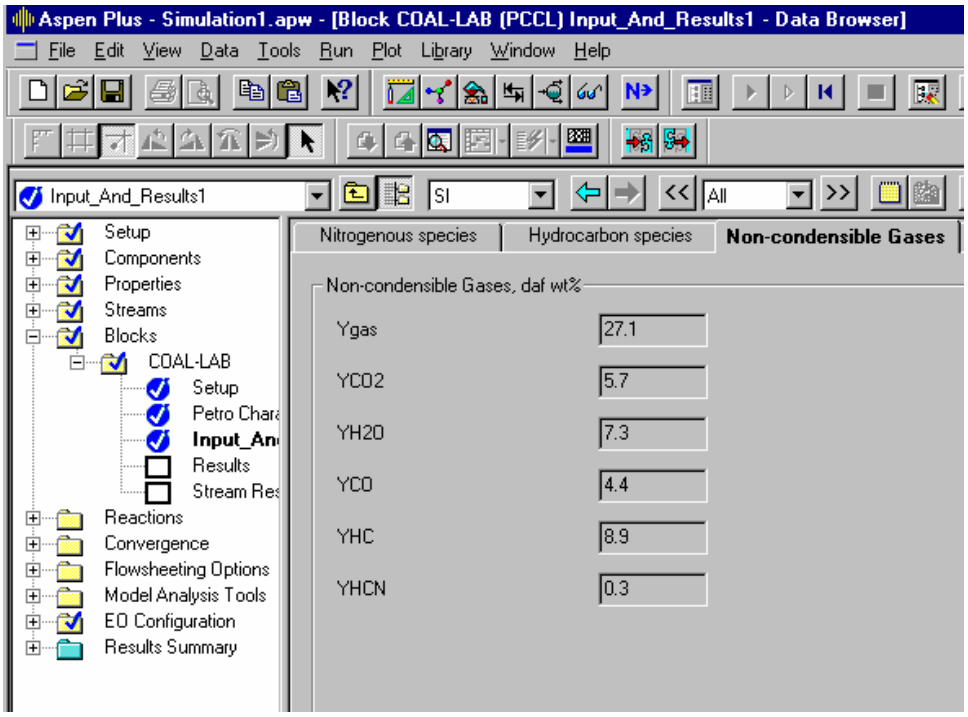

Hydrocarbon species distribution

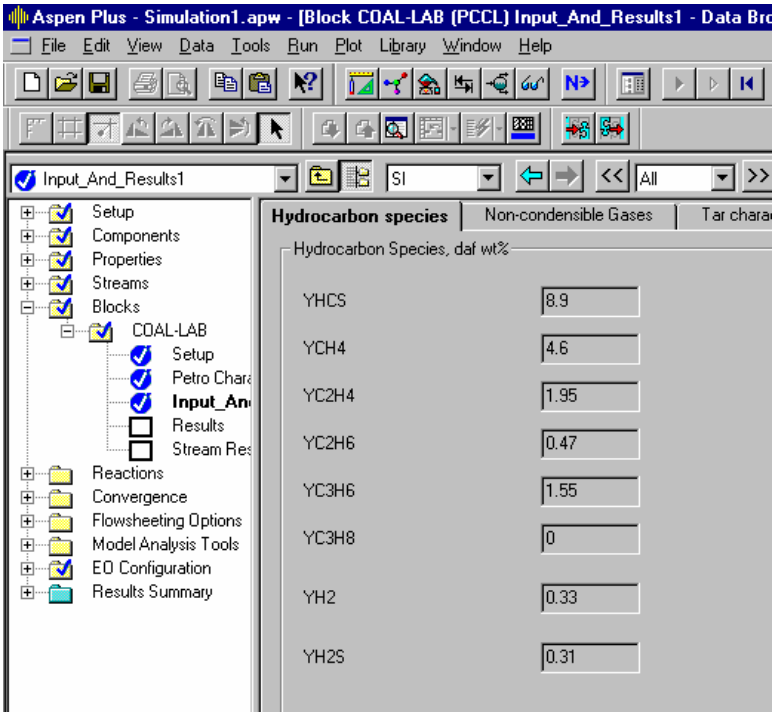

Oxygen species distribution

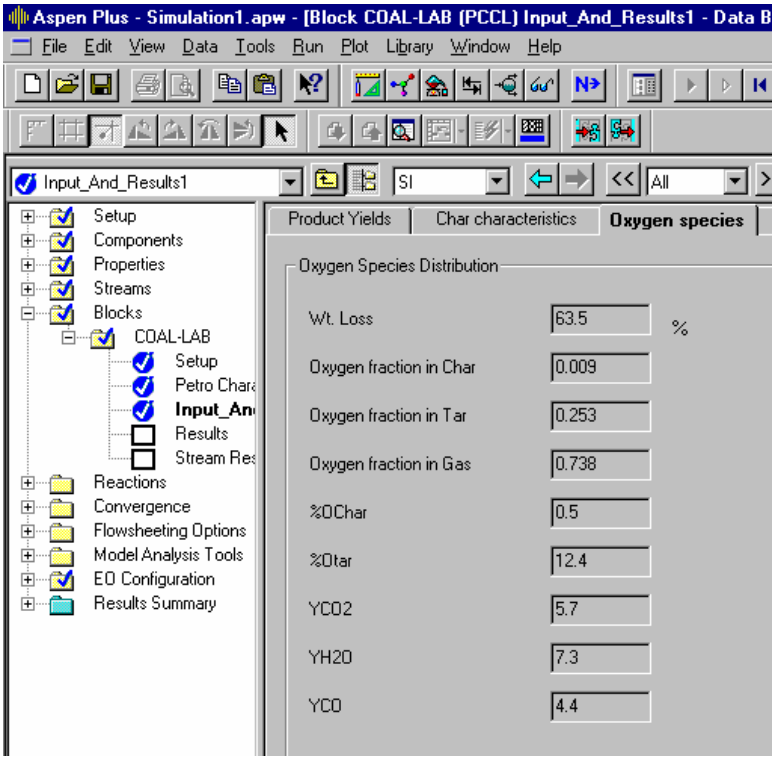

Nitrogen species distribution

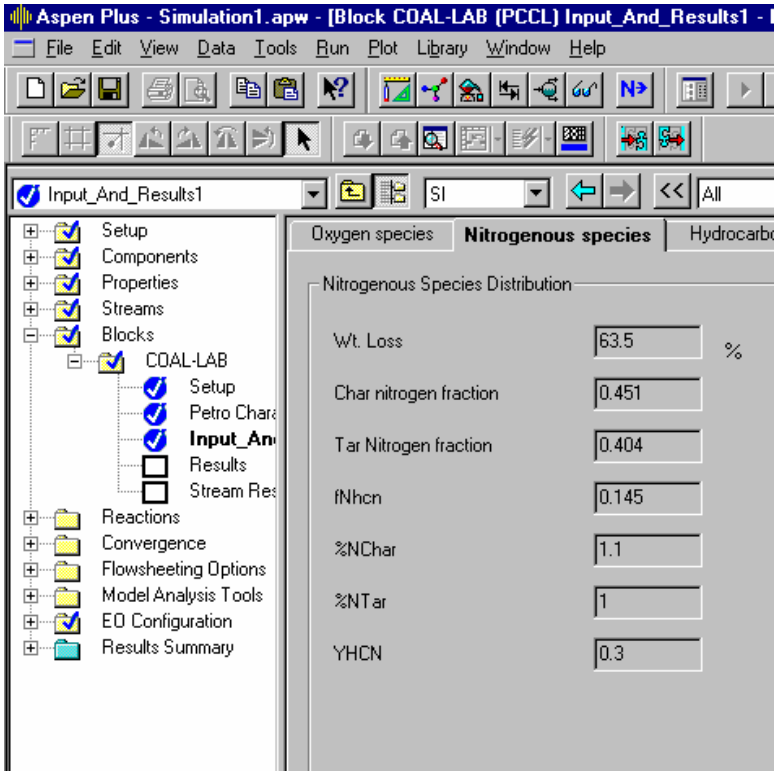

CBK8 Char Burnout Characteristics

These results are relevant in the presence of oxygen.

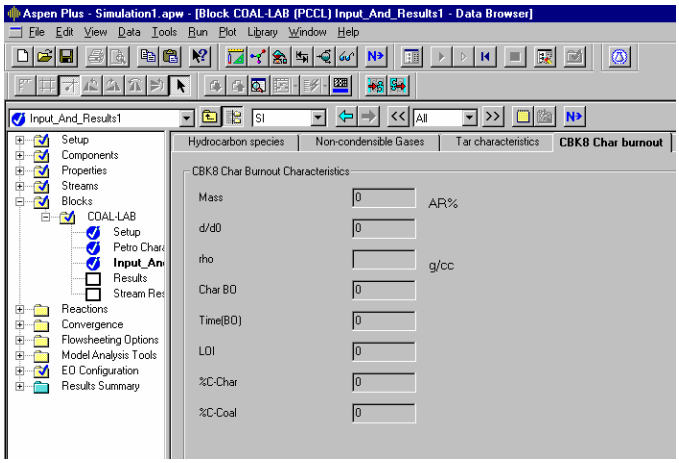

SNLL Char Burnout Characteristics

These results are relevant in the presence of oxygen.

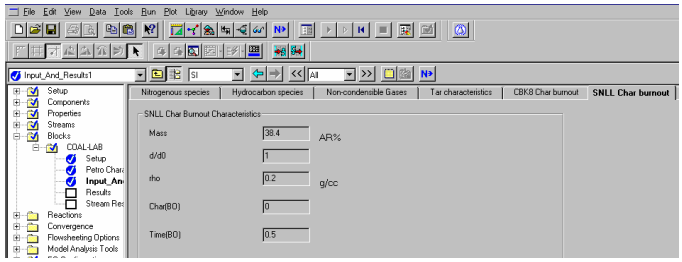

Rate parameters

This tab provides the parameters for Arrhenius type rate expression for the evolution of various products. These parameters can be used as input for customizing the coal devolatilization models in the commercial CFD packages such as FLUENT.

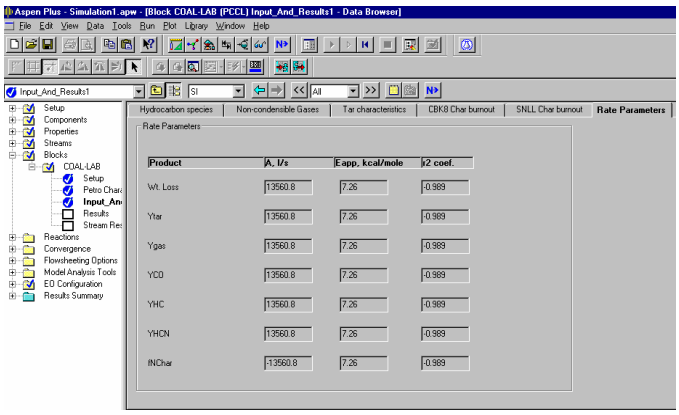

In this case, the rate parameters for different products show the same values. This anomaly was pointed out to Niksa Energy Associates and a modified executable was sent to us. However, the new PC Coal Lab executable still does not seem to provide the correct values. It is therefore suggested that a fully functional code be used for looking into these values.

Secondary Pyrolysis of Tar

To view the results for the secondary pyrolysis of tar, the user should open the file "**spuyc1t1.rpt**" with any text editor.

All other files generated by PC Coal Lab are deleted from within the user model. If the user is interested in looking at the dynamic output file, PC Coal Lab could be run outside the Aspen Plus.

E.1.4 Use of PC Coal Lab as an Integrated Block

The use of PC Coal Lab as an integrated block with other unit operations blocks from Aspen may be a useful tool for design purposes involving coal combustion systems. However, for this implementation to be a useful tool, additional information is needed, such as:

1. How to treat tar and the gases produced?
2. Should we assume that under availability of proper quantity of oxygen, all hydrocarbon gases ultimately react to form CO_2 and H_2O?
3. Do we make similar assumption for tar? Do we assume that all Nitrogen in Char goes to form NO or implement further nitrogen species kinetics for the prediction of nitrogen pollutants?
4. In cases where sufficient quantity of oxygen is not available, what reaction schemes should be considered?

The developer of the PC Coal Lab software should consider these guidelines and implement appropriate sub-models in the next release of the software. Once implemented, it would also be appropriate to compare the results of the new implementation with the Aspen Plus built-in models. The implementation of PC Coal Lab using an executable required that we write the input files using the data provided

through the Aspen Plus interface, and to read the output files generated by PC Coal Lab. This makes the implementation very inefficient. All future versions of PC Coal Lab must adhere to the format standards for the input and output files as specified in its user's manual (version 2.2). If changes are made to those formats, the Aspen Plus pcCoalLab module will only work after corresponding modifications are made in the pcCoalLab block.

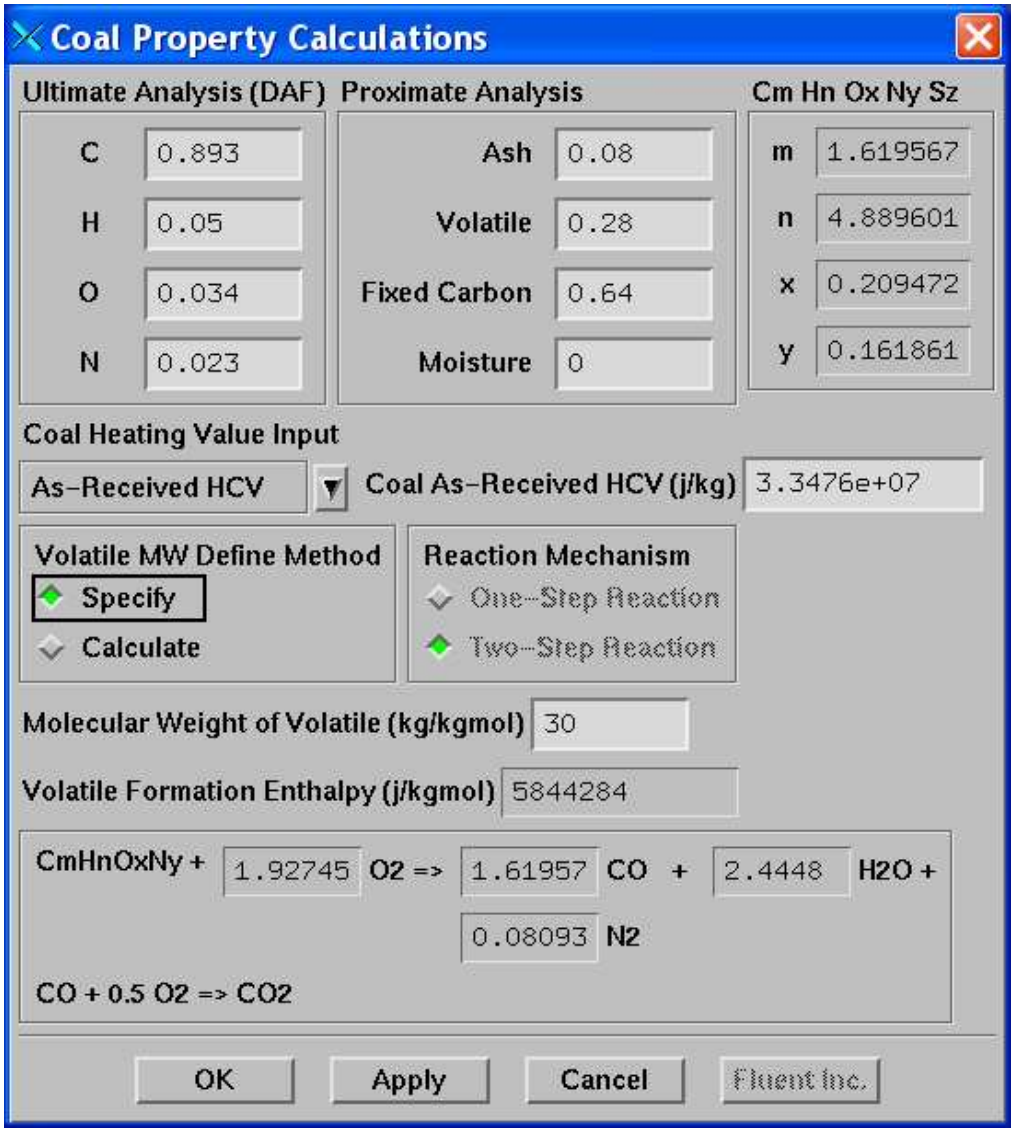

E.2 Coupling PC Coal and FLUENT

The coal properties (proximate and ultimate analysis) are supplied to FLUENT through a new developed interface (see Figure E.1).

Figure E.1. FLUENT coal properties interface

The CFD parameters required to set up the case are calculated from the coal properties. These include the heat of formation of the volatile and stioichiometry of the gas phase reaction. An user defined function have been developed to extract the required data from the preliminary CFD runs and generated and input file for PC Coal Lab (see Fig E.2). The information sent to the interface from FLUENT specifies all the necessary conditions for a devolatilization simulation. As seen in Fig. E.2, this comprises a Rosin-Rammler particle size distribution (PSD); the coal's proximate analysis on an as-received basis; the temperature history, expressed as discrete values of time, in s, and temperature, in Kelvins. ultimate analysis on a dry-ash-free (daf) basis; the pressure in Pa; and a particle The PSD is specified by minimum and maximum sizes, a mean size, the spread parameter (or exponent n), and the number of size increments. All sizes are in meters. The proximate and ultimate analyses are expressed in mass fractions on their respective bases. The particle temperature history should contain at least 10 discrete values, but no more than 40.

In principle, one could assign thermal histories for the various sizes in the PSD, and evaluate the devolatilization characteristics for all size increments. This approach is suitable for dilute suspensions, as normally used in drop-tube tests and other small-scale experiments. However, for applications simulations, devolatilization always occurs in very dense suspensions immediately downstream of fuel injectors and burners. In such situations, bulk two-phase heat transfer determines the fuel's thermal history, and we generally find that variations in the radial position within the suspension are much more important than size variations. At this point, the interface treats the thermal history in part_history.dat as a suitably defined average for the suspension as a whole. Accordingly, only a single set of devolatilization characteristics is reported, and the PSD is not implemented in the calculations.

Moreover, this thermal history must be of the following form:

$$\Theta = 1 - \exp(-t / \tau) \qquad \text{(E.1)}$$

where $\Theta = (T(t)-T_0)/(T_{MAX}-T_0)$; T_0 is the initial or minimum temperature, T_{MAX} is the ultimate or maximum temperature; and τ is the time constant in s. The mass-averaged mean temperature histories of coal suspensions near fuel injectors usually abide by this form, although other forms could be implemented, as necessary.

PC Coal Lab® requires a proximate and ultimate analysis for the fuel, plus a thermal history and pressure for the devolatilization simulation. The interface imposes a simulation based on the form of the thermal history shown in Fig. E.2, which is called the "heated wire grid simulation."

```
Rosin Rammler Parameters

min dia  max dia  mean dia  spread_parameter  number_of_inj

 1.00e-06   1.00e-03  1.00e-04   1.00e+00   1.00e+01

Proximate Analysis

VM     FC     MOIST     ASH

0.600  0.350  0.000  0.050

Ultimate Analysis

C      H      O      N      S

0.870  0.100  0.003  0.007  0.020


Operating Pressure (Pa)

 101325.00

Particle Temperature History


Time (s)  Temperature (K)

0.000e+00  3.4e+02
1.104e-01  4.2e+02
2.209e-01  4.8e+02
3.313e-01  5.1e+02
4.418e-01  5.6e+02
5.522e-01  6.2e+02
6.627e-01  6.8e+02
7.731e-01  7.1e+02
8.836e-01  7.5e+02
9.940e-01  7.9e+02
1.104e+00  8.3e+02
1.215e+00  8.5e+02
1.325e+00  8.4e+02
1.436e+00  8.6e+02
1.546e+00  8.9e+02
1.657e+00  9.0e+02
1.767e+00  9.0e+02
1.878e+00  9.1e+02
1.988e+00  9.1e+02
2.098e+00  9.2e+02
```

Figure E.2. Sample version of part_history.dat.

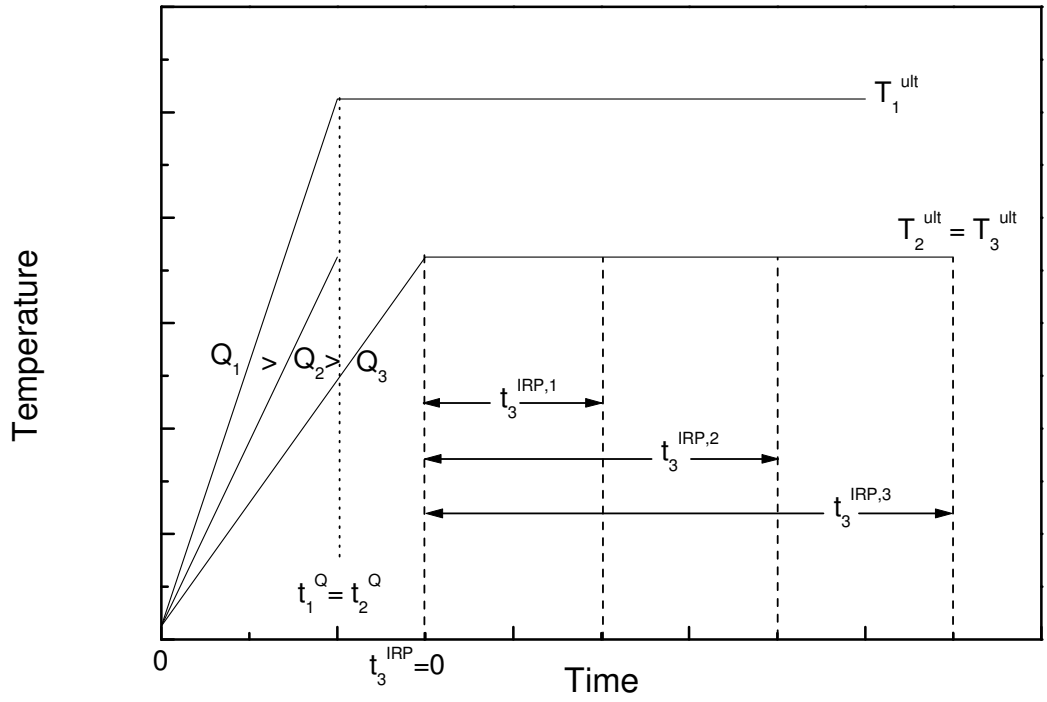

Figure E.3. Three thermal histories for wire-grid simulations.

PC Coal Lab's wire grid simulator imposes strictly uniform heating rates from a specified initial temperature to the ultimate reaction temperature. Users also specify the duration of the isothermal reaction period as the elapsed time after the coal reached the ultimate temperature. These input values appear in Fig. E.3 for three thermal histories that have progressively slower heating rates. The heating rate is uniform in all cases but at different magnitudes. The initial coal temperature is the same. History No. 1 has the fastest heating rate, Q_1, and also the hottest ultimate reaction temperature, T_1^{ult}. The heating rate in History No. 2 is faster than that in History No. 3; i. e., $Q_2>Q_3$. But their ultimate temperatures are the same; i. e., $T_2^{ult} = T_3^{ult}$.

Whereas heating rates and ultimate temperatures for these thermal histories are straightforward, the definitions of reaction times are potentially confusing, because only the time beyond the end of the heating period is specified as an input variable. The total reaction time is the sum of the heating period, t^Q, and the isothermal reaction period, t^{IRP}. The isothermal reaction period extends from the end of the heating period, not the beginning of the test. Accordingly, Histories Nos. 1 and 2 have the same heating periods, but there is no isothermal reaction period for History No. 2 because it ends as soon as the fuel is brought to the ultimate temperature. Fig. E.3 shows three isothermal reaction periods for History No. 3. They all begin at the end of the heating period, which is labeled as $t_3^{IRP} = 0$. Each successive period is extended by the same time increment.

It may seem odd to apply the angular thermal history in Fig. E.3 to the exponential thermal history from FLUENT. Provided that the heating rate is specified appropriately,

this approximation is inconsequential. But the assignment of devolatilization rate parameters is slightly more robust with this thermal history than an exponential one.

The first step is to evaluate the time constant in the thermal history in part_history.dat. As seen in Fig. E.4, this is a simple graphical operation in the plane of ln(1-Θ) vs. t.

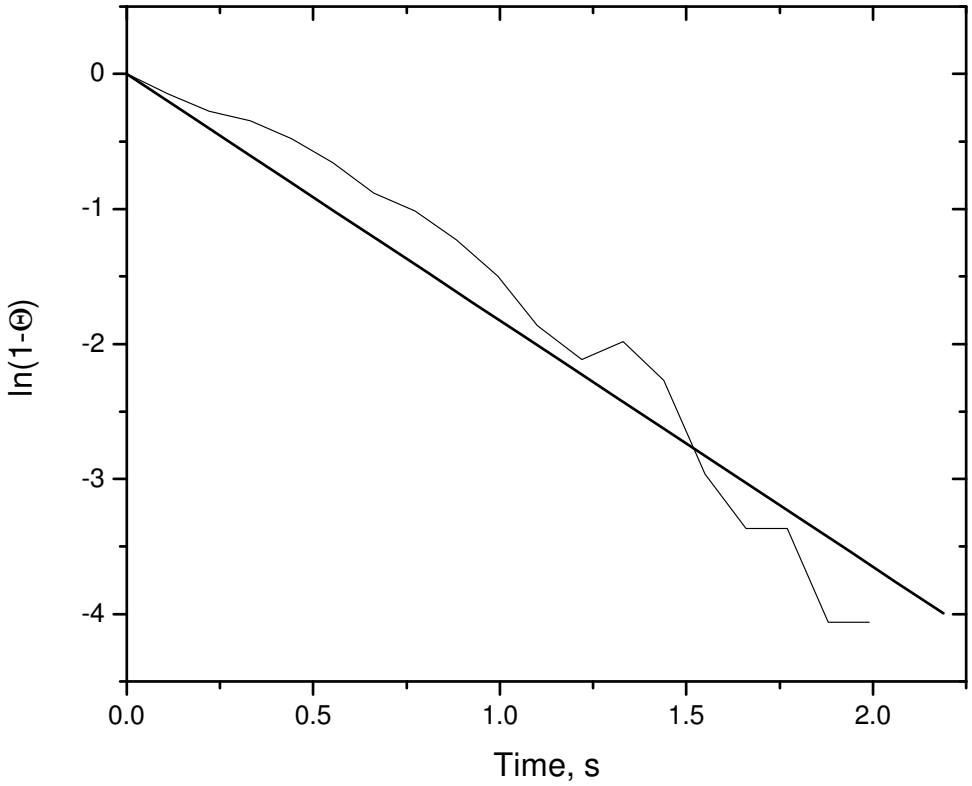

Figure E.4. Assignment of the thermal time constant in eq. E.1.

In this example, the time constant is just under 0.5s. We next assign an equivalent uniform heating rate for all 350 ≤T, °C ≤ T(2τ). The heating rate for all temperatures below 350°C is inconsequential, because the onset temperature for devolatilization is always much hotter. So we assign the uniform heating rate for the wire grid simulation from the portion of the FLUENT thermal history that extends from roughly 350°C to the temperature when the time is twice the thermal time constant. In most applications, the upper temperature limit will be hot enough to cover most of the devolatilization process. For this example, the assigned heating rate is just under 400°C/s.

We next complete the thermal history for the PC Coal Lab® simulation as shown in Fig. E.5. The assigned heating rate is used to specify the thermal history from the initial temperature up to the time when the temperature reaches T_{MAX} which, in this case, occurs at 1.46s. Thereafter, the temperature is uniform at T_{MAX} for the duration of the heating cycle specified in part-history.dat which, in this case, is 2.098s.

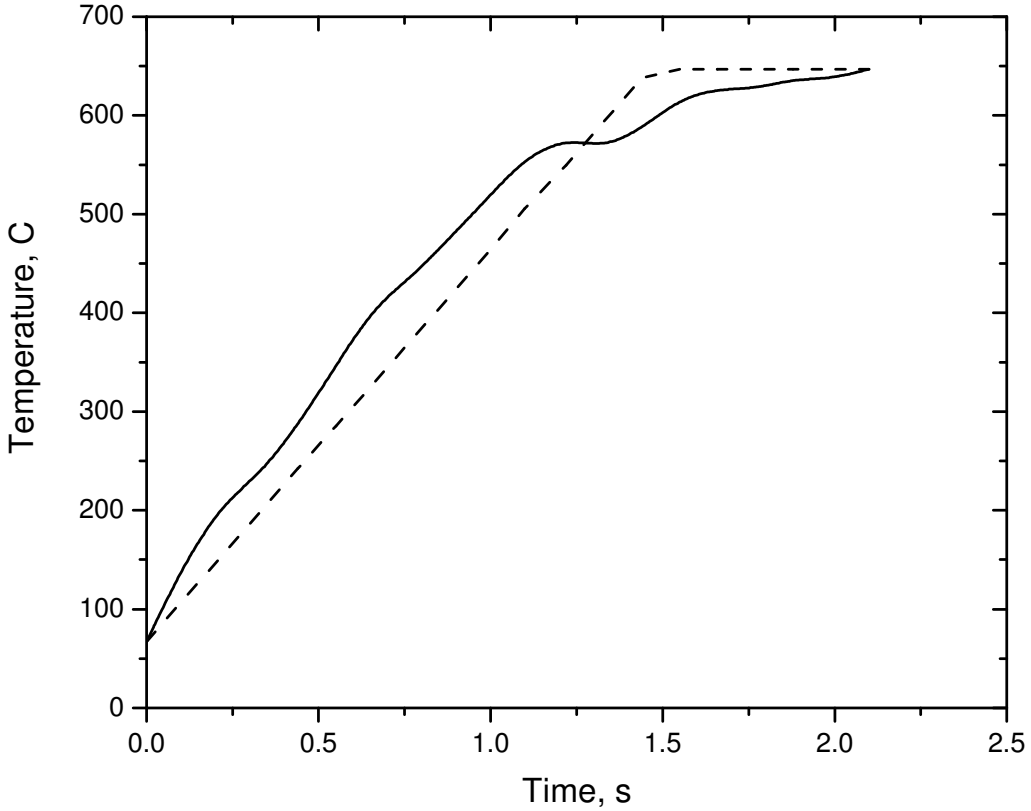

Figure E.5. Thermal histories from FLUENT (solid curve) and for PC Coal Lab® (dashed curve).

The input files for PC Coal Lab® automatically written by the interface from the input specifications appear in Fig. E.6. The Coalpc.dat file begins with the label "CO" to denote a case with coal, then contains a 40-character label, followed by the 4-element proximate analysis and the 5-element ultimate analysis. The reason that the coal properties do not match those in part-history.dat is that the interface is currently restricted to a single Pit. #8 hv bituminous coal for demonstration purposes only under this DoE project. A fully functional version of the interface would write the fuel properties in part_history.dat into Coalpc.dat.

The testplan.dat file begins with a block of 5 rows that specify the operating conditions. Each row begins with a numerical index that is followed by a code for wire grid simulations. After 2 obscure reporting flags, the line continues with the composition of

the ambient gas, the initial sample temperature, the ultimate sample temperature, the heating rate, O_2 mole fraction, pressure, isothermal reaction period, and a particle size. Temperatures are in °C and the pressure is in MPa.

```
CO FLUENT SAMPLE                                    2.0 35.0   0.0   5.0 87.0
10.0  0.3  0.7  2.0N

       1 WG FFTG UD N2    67.  647.   397.   0.0  0.10   0.639 100.0
       2 WG FFTG UD N2    67.  647.   397.   0.0  0.10   0.639   0.0
       3 WG FFTG UD N2    67.  647.   397.   0.0  0.10   0.639   0.0
       4 WG FFTG UD N2    67.  647.   397.   0.0  0.10   0.639   0.0
       5 WG FFTG UD N2    67.  647.   397.   0.0  0.10   0.639   0.0
      NNNNNNNYYNN
      YNN
      YNNNNNNNNN
```

Figure E.6 Coalpc.dat (upper) and Testplan.dat (lower) for the PC Coal Lab® simulation.

The four succeeding rows contain the same information except that the particle size is zero. These entries indicate that only a single set of operating conditions will be simulated. The next three rows indicate which output reports will be prepared and which quantities will be analyzed for reaction rates, as explained in the PC Coal Lab® Users Guide and Tutorial.

CFD Input Values From PC Coal Lab®

The CFD data specifications are reported in FluFace.out, which appears in Fig. E.7. This file first reports the coal properties and operating conditions in the devolatilization simulation. It then gives the ultimate weight loss and a single, first-order devolatilization rate, in DAF wt. % and DAF wt. %/s, respectively. The elemental compositions of char and volatiles are reported next, followed by the standard heat of volatiles combustion and the volatile-N percentage.

```
                    WIRE GRID SIMULATION WITH PC COAL LAB

                              CFD INPUT PARAMETERS

COAL CHARACTERISTICS:

           Ultimate, daf wt.%        Proximate, as rec wt.%
                %C 83.3                   Moisture   1.8
                %H  5.4                   Vol. Mat. 34.2
                %O  8.6                        Ash  10.1
                %N  1.4                    Fixed C  53.9
                %S  1.3

OPERATING CONDITIONS:

          Coal at   67. C is heated in N2 with 0 % O2 to
           647. C at    397.0 C/s, then held for .639E+00 s.
          The ambient pressure is   0.10 MPa.



Wt. Loss = 33.4 daf wt.%
    Rate = 0.146E+06exp(-17.44kcal/mole/RT)(33.4-V(t)) daf wt.%/s

            Y,wt.%    %C    %H    %O    %N    %S    %Ash

Char         68.8    77.6   3.0   2.9   1.4   0.4  14.7
Volatiles    29.4    68.1   9.1  18.9   1.0   2.9


DelH-Vol = 2584. cal/g-Vol
   Vol-N = 24.4 % Coal-N
```

Figure E.7. The FluFace.out file.

Future Development

Any of the quantities predicted by PC Coal Lab® could be included on the output report prepared by the interface. The predicted product distributions include the yields of CO, CO_2, H_2O, H_2, HCN, H_2S, CH_4, C_2H_4, C_2H_6, C_3H_6, C_3H_8, tar and char. Distributions of secondary pyrolysis products, including yields for C_2H_2 and soot, are also predicted. Evolution rates for any of these species or groups of species may be assigned. More complex global rate expressions, such as the competing, 2-step model or distributed activation energy model, could also be analyzed. These capabilities have already been extended to any form of biomass, pet coke, or black liquor.

PC Coal Lab® also contains specialized versions of the Carbon Burnout Kinetics (CBK) model for char oxidation by O_2 and for char gasification by H_2O, CO_2, CO, and H_2. These mechanisms have also been analyzed to automatically prepare global rate expressions that reproduce the simulation results with the full mechanism, so the capabilities demonstrated here for devolatilization could be immediately extended to cover char conversion via combustion and gasification.

E.3 Sub-Models Incorporated into FLUENT

The CBK model is presented in this session in the form of an equation for the simple case of an ash-free char, the table gives recommended values for the input parameters and/or rank dependent correlations for these inputs. The input values and the simplifications in this scheme are based on some years of experience with the application of CBK6, CBK8, and CBK/E, as well as the results of the present project focused on evaluation of models suitable for high pressure operation.

Instantaneous burning rate, R:

$$R = A_o e^{(-E/RT_p)}(P_{ox}^{n})(\pi/6)d^3 \rho\, \eta\, (A/A_o)$$

Effectiveness factor, η

$$\eta = (1/\phi)[\coth(3\phi) - (1/3\phi)]$$

Thiele modulus, ϕ

$$\phi = (d/6)\left[(n+1)A_o(A/A_o)\rho(P_{ox}/RT)^{(n-1)}/(2D_{eff})\right]^{1/2}$$

Effective Diffusivity, D_{eff}

$$D_{eff} = D\theta/(\tau/f)$$

Annealing factor, (A/A_o)

$$(A/A_o) = \Sigma\, F_E\, \Delta E_d \quad \text{(sum over all active site classes in } E_d\text{)}$$

$$\ln(F_E)_{t+\Delta t} = \ln(F_E)_t - A_D e^{(-E_D/RT_p)}\Delta t \quad \text{(one equation for each } E_d \text{ class)}$$

Product ratio at particle surface (for heat balance)

$$N_{CO}/N_{CO2} = A_c e^{(-E_c/RT)}$$

Initial char particle density, ρ_o

$$\rho_o = \rho_{coal}(1 - \text{fractional volatile loss})\omega^{-3}$$

Partially reacted char particle density, ρ

$$\rho = \rho_o(m/m_o)^{\alpha}$$

Initial char particle diameter, d_o

$$d_o = d_{coal}\,\omega$$

Partially reacted char particle diameter, d

$$d = d_o\,(m/m_o)^{+1/3}(\rho/\rho_o)^{-1/3}$$

Table E.1. Recommended Parameter Values

Parameter	Recommended value	Comments
A_o, pre-exponential factor (initial value, before	input, varies greatly with coal type. For estimates use	This is the main char reactivity parameter in CBK

annealing)	Correlation 1 below	
E, intrinsic activation energy	35 kcal/mol recommended	
n, intrinsic reaction order	0.5 recommended	
D, O_2 molecular diffusivity		Estimated in CFD codes
τ/f, internal mass transport parameter (tortuosity / feeder-pore-fraction)	6.0, recommended value	
Initial $F_E(E_d)$, annealing model distribution	$\ln[F_E(E_d)]$ is standard Gaussian with mean 2.8 (ln kcal/mol) and standard deviation 0.46 (in ln kcal/mol).	
A_D, annealing model parameter	$8.863 \cdot 10^7$ recommended	A_D, annealing model parameter
Ac, product ratio parameter	200, recommended	
Ec, product ratio parameter	9 kcal/mol, recommended	
m/m_o, partially reacted char mass/initial char mass		
ω, swelling factor	model input. Use correlation 2 if data unavailable	Defined as initial char diameter / initial coal particle diameter
α, mode of burning parameter	0.2 recommended	

Correlation 1: Intrinsic reactivity, A_o

$\log_{10}(A_o) = 14.97 - 0.0764$(wt-% elemental carbon, daf in parent coal)

Correlation 2: Swelling factor (based on wt-% elemental carbon in parent coal)

For wt-% C > 92: $\omega = 1.0$

For wt-% C < 92 and > 89: $\omega = 8.6667 - 0.083333 *$ wt-% C

For wt-% C < 89: $\omega = -0.045834 + 0.014587 *$ wt-% C

* for elevated pressure operation, swelling factors for bituminous coals should be elevated to 1.45 unless experimental data are available for the coal in question.

The Char burnout Kinetics model had been implemented into FLUENT following the stand-alone version of CBK8. The graphical user interface of the CBK model is shown in Figure E.8.

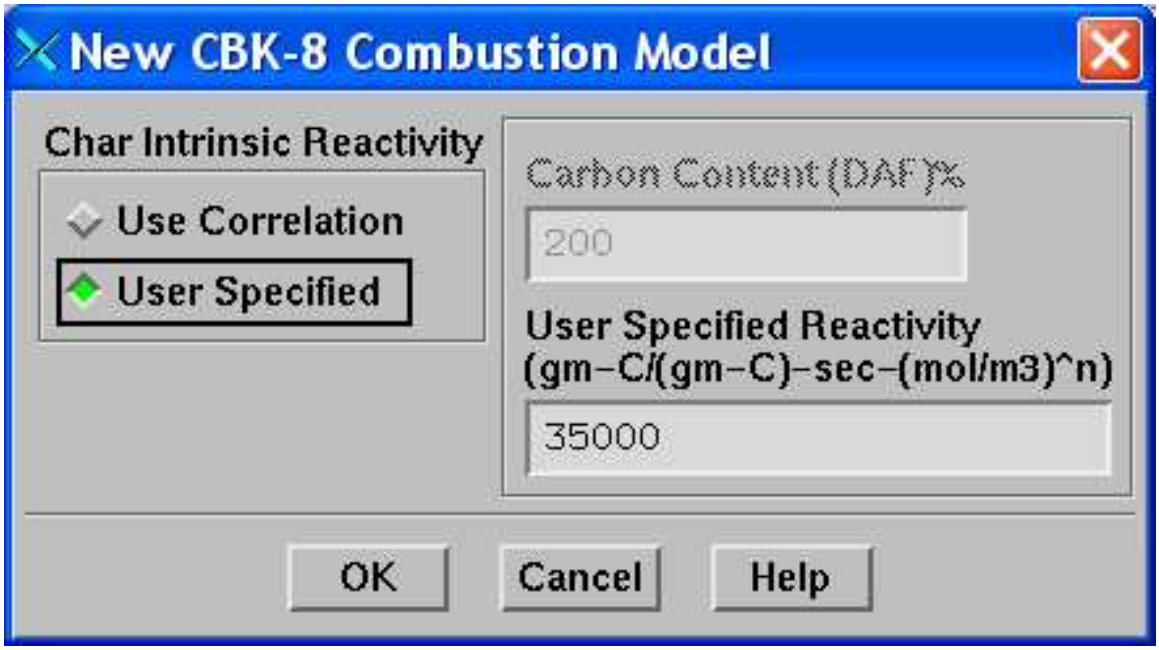

Figure E.8. CBK FLUENT GUI

The main two parameters that the CFD user has to supply are the char intrinsic reactivity and the swelling factor. The swelling factor is specified together with the other coal particle properties. There are two options to input the char intrinsic reactivity:

- estimate that from a correlations based on the carbon content, in this case the user will supply the Carbon content as DAF.
- specify directly the char reactivity.

The recommended values reported in the table have been used for all the other inputs.

E.4 Process Design Analysis

E.4.1 Description of Vision 21 Plant Layout

The integrated power plant shown in **Error! Reference source not found.** consists mainly of a partial gasification module (PGM), a pressurized pulverized coal and char combustor with steam generation and high-temperature air heating (PPCC), a solid oxide fuel cell (SOFC) unit, a topping combustor, an air compressor, an advanced gas turbine, a supercritical steam turbine, and a heat recovery steam generator (HRSG). The plant uses coal as the only fuel, air as the oxidizer, and steam as reactant for gasification. Net electrical generation of this reference plant is 796 MW.

The PGM is operated to provide high overall carbon conversion, thus maximizing the gas turbine/SOFC to steam turbine power ratio. However, for fuels like coal, it is difficult to completely gasify the solid particles at a certain desired bed temperature. Therefore, the PPCC (a secondary combustion module) is required to serve as the final fuel-processing step and to maximize the carbon utilization for the entire plant.

The majority (90%) of the coal fired in the plant is introduced to the PGM with the balance (10%) fired in the PPCC unit. Compressed air and a portion of the low pressure (LP) steam turbine reheat inlet flow are fed into the PGM, which is a pressurized circulating fluidized-bed gasifier operating at a temperature of 1800°F (982°C). In the PGM, coal particles undergo devolatilization to form volatiles and char particles. The coal volatiles and the gasification products form the syngas that contains H_2, which is used in the SOFC to generate electricity.

The solids and syngas from the PGM are then cooled in a syngas cooler before entering the high-temperature syngas filter. The unburned char particles, separated by the filter, are introduced to the PPCC unit along with small amount of pulverized coal that is used as the support fuel to help ignite the char particles. The syngas exiting from the filter enters a syngas desulfurization unit where H_2S and other sulfur-containing species are eliminated. The clean syngas goes to a solid oxide fuel cell where the H_2 in the syngas reacts with the O_2 in the air (from the air heater inside the PPCC unit) to generate electricity and heat. The products from the fuel cell and the remaining syngas are further burned in the topping combustor with the compressed air. The air provided to the topping combustor by the gas turbine compressor is a mixture of two streams: 1) preheated air from the PPCC and 2) air directly from the compressor exhaust. The split between these two streams is regulated to control the exit temperature of the topping combustor. The products from the topping combustor are sent to the advanced gas turbine to generate electricity. The exhaust gas from the gas turbine then enters a heat recovery steam generator (HRSG) before exiting to the stack.

The water from the steam turbine condenser is pumped to a supercritical pressure and heated in the low temperature section of the HRSG. The supercritical water is then vaporized inside the water walls of the PPCC unit and then superheated to 1300°F (704°C) in the high-temperature section of the HRSG before entering the high-pressure (HP) stage of the steam turbine. The steam turbine incorporates two steam reheat stages: an intermediate pressure (IP) and a low pressure (LP). Both the IP and LP reheaters are located inside the HRSG. Part of the IP reheat inlet steam is sent to the PGM to gasify the char particles. Feedwater is added to the system, downstream of the condenser, to make up for the steam used for the gasification.

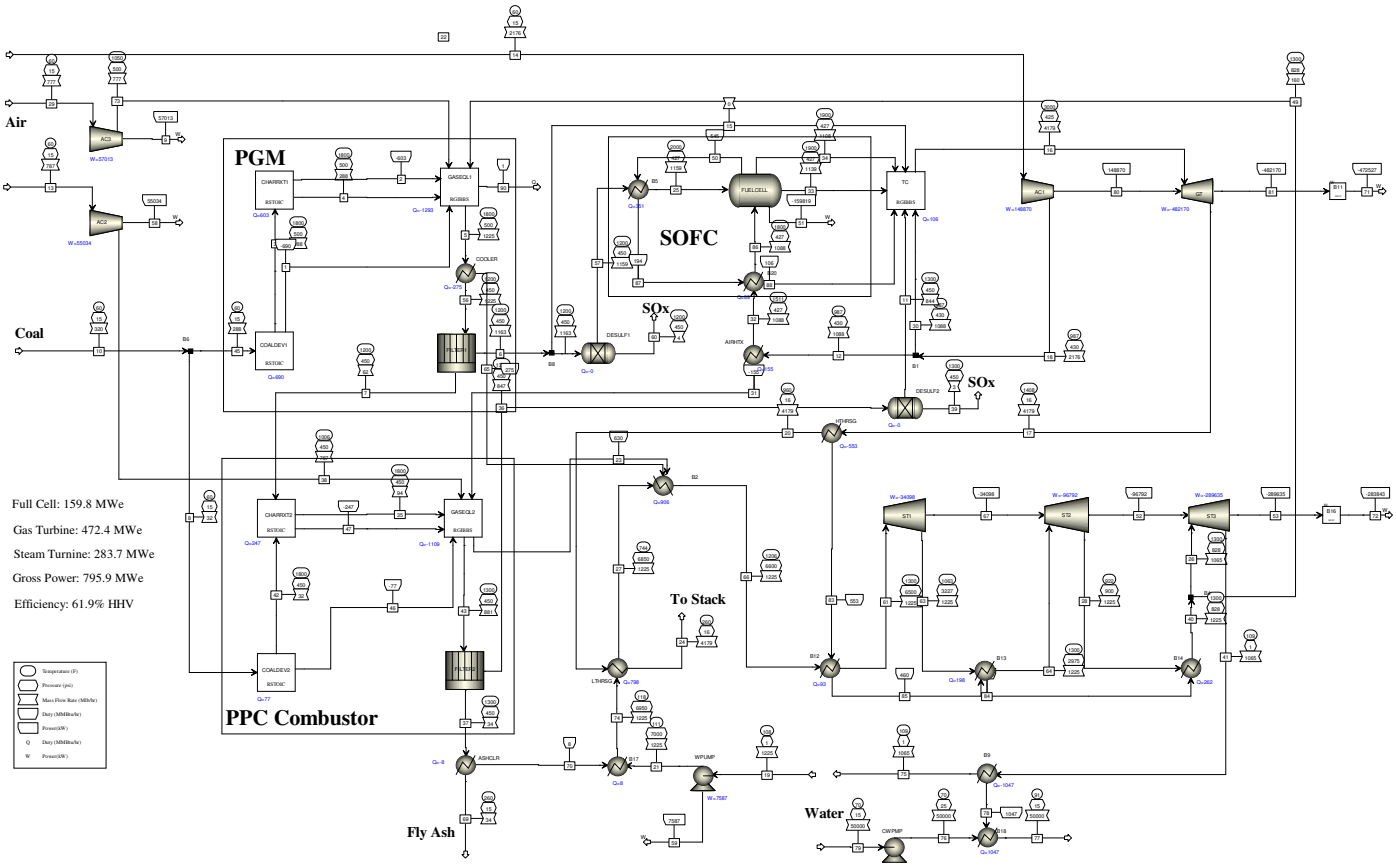

Figure E.9. Aspen Flow Sheet of the Vision 21 Power Plant

E.4.2 Critical Components in the Vision 21 Plant

The overall plant schematic highlights the integration of all the modules, which form the fundamental building blocks of the conceptual Vision 21 plant. The components that require further development and are critical to the success of the entire plant include PGM, syngas cooler, syngas and flue gas filters, SOFC, topping combustor, steam and gas turbines, HRSG, and PPCC. Special attentions must be paid to the design and development of these components. The specifications of these components are discussed in this section. The design considerations of the PPCC unit, which will be designed as part of the HPCCK project, are also presented.

Partial Gasification Module (PGM)

The partial gasifier serves as the initial fuel-processing unit, converting the fuel feedstock into a fuel gas (syngas) and a solid char. The unique aspect of the process is that it utilizes a pressurized circulating fluidized bed partial gasification unit and does not attempt to consume the coal in a single step. To convert all the coal to syngas in a single

unit requires extremely high temperatures [2500°F (1371°C) to 2800°F (1538°C)] to melt and vaporize the coal, but has the negative effect of driving all coal ash contaminants into the syngas. Since these contaminants are corrosive to power generating equipment such as gas turbines, the syngas must be cooled to a low temperature to enable a series of chemical processes to clean the syngas. Foster Wheeler's process operates at a much lower temperature [1800°F (982°C)] to control/minimize the release of contaminants and to eliminate/minimize the need for expensive, complicated syngas heat exchangers and chemical cleanup systems, typical of high-temperature gasification. By performing the gasification in a circulating fluidized bed, a significant amount of syngas is produced despite the reduced temperature. Furthermore, the circulating bed can be easily scaled-up to large size plants and can accommodate a wide range of fuels.

The PGM does not contain any heat transferring area, which facilitates the reactor design. Since the operating temperature is limited to minimize the release of corrosive contaminants inside the fuel, it is impractical/uneconomic to design for a 100% carbon conversion. The optimal carbon conversion is determined by the reactivity of the fuel fired. Based on Foster Wheeler's analysis and experimental tests, a carbon conversion of up to 80% is achievable when firing a high volatile bituminous coal such as used in this study. For coals with a low percentage of moisture (such as the coal used in this study), steam is generally added to the PGM to increase the yield of H_2 in the syngas. H_2 is the species that is later consumed in the fuel cell to generate electricity. The amount of steam introduced to the PGM needs to be optimized; excessive steam injection results in too high a loss of latent heat of water vapor in the flue gas and a reduced PGM bed temperature. The PGM operates at 500 psia (3.45 MPa).

Syngas Cooler

The purpose of the syngas cooler is to cool the syngas and char to a temperature where downstream processing (char removal, desulfurization) can be performed. Since the FW PGM operates at relatively low temperature, only a convective section of the syngas cooler is required, as opposed to high-temperature gasifiers, which require both radiant and convective sections. In the syngas cooler, the syngas and char are cooled from 1800ºF (982°C) to 1200ºF (649°C) by supercritical steam, which flows in the counterflow direction and is heated from 982ºF (528°C) to 1206ºF (652°C). Required overall thermal duty of the unit is 275 MM Btu/hr (80.6 MW) with a logarithmic mean temperature difference (LMTD) of 375ºF (208°C) for the reference 796 Mwe plant. Critical issues determining the syngas cooler layout, orientation, and syngas location (i.e. tubeside or shellside) are the avoidance of tube pluggage, erosion, and fouling of the syngas solids. In general, the adverse effects of syngas solids can be mitigated by a vertical design in which syngas flows vertically downward within the tubes. However, such a design must be properly baffled on the shellside to avoid steamside thermal and flow maldistribution, which can cause structural fatigue (i.e. of the tubesheet) and to avoid flow induced vibrations. Proper material selection is essential for materials contacting the syngas to avoid erosion (i.e. from the char/ash) and corrosion (i.e. from the H_2S). FW has designed and tested syngas coolers as part of the High Performance Power System (HIPPS) program and its gasification fluidized bed combined cycle (GFBBC) program.

High-Temperature Syngas And Flue Gas Barrier Filters and Desulfurization Units

High-temperature barrier filters and desulfurization units are used to remove solids and SOx from the gas streams of the syngas after exiting the syngas cooler and the flue gas after exiting the PPCC. The high-temperature syngas barrier filter removes the particulates from the syngas stream. The main components of the syngas are CO_2, N_2, CO, H_2, CH_4, and H_2O. After the particle-laden syngas is cooled to a temperature of 1200°F (649°C) by the syngas cooler, it is split into two separate streams by the barrier filter: one containing the gas mixture only and the other containing ash and unburned char particles. The syngas leaving the barrier filter is fed into a desulfurization unit to remove H_2S and other sulfur-containing species prior to entering the SOFC. Presently, all sulfur removal systems are limited to operating temperatures below 1000°F (538°C). However, as part of the Vision 21 program, gas stream purification is identified as a high priority task, and advancements in this area will enable the desulfurization unit to be operated at a high temperature up to 1200°F (649°C).

The high-temperature flue gas barrier filter removes the particulates from the flue gas stream. Particle-laden flue gas exiting the PPCC at 1300°F (704°C) is split into two separate streams by the barrier filter: one containing the gas mixture only and the other containing fly ash. The flue gas leaving the barrier filter is fed into a desulfurization unit to remove H_2S and other sulfur-containing species prior to entering the topping combustor.

High-temperature barrier filters have been tested at Foster Wheeler. Better designs of the filter are expected to increase the filter efficiency and reduce the pressure drop.

Solid Oxide Fuel Cell (SOFC)

After the sulfur species are removed from the syngas, the syngas is sent to the fuel cell where 159.8 MW of electricity is generated. The SOFC technology is best suited for this cycle because of the high operating temperatures of the air and the fuel gas. The SOFC is designed to operate at 2000°F (1093°C) and is outfitted with solid-state ceramic components, which allow it to operate up to a temperature of 2300°F (1260°C). The syngas generated in the PGM is well suited for fuel cell operation since H_2 is one of the main chemical components after steam is added. As H_2 is consumed in the fuel cell, the water gas shift reaction produces additional H_2, thereby creating a stable and thermodynamically replenishing fuel supply. The CH_4 in the fuel gas can also be readily converted through a steam reforming process to produce additional H_2. Although at high temperature, chemical equilibrium does not favor the formation of H_2, by proper selection of chemical residence time, the increased chemical reaction kinetics are used to maximize the formation of H_2. Furthermore at high temperature, the heat of reaction of H_2 and O_2 is increased, resulting in greater electricity generation. To operate the fuel cell at a high temperature, the heat generated through the oxidation of H_2 by O_2 is used to heat the syngas and air. This requires a special design of the fuel cell unit such that the heat released in the fuel cell is transferred to the syngas and air, which serve as cooling agents of the SOFC. In this study, 50% of the energy input to the fuel cell is taken to be converted to electricity and thus the corresponding electric output is 159.8 MW. The

SOFC represents one of the essential enabling technologies defined in the Vision 21 program.

Topping Combustor and Advanced Gas Turbine System

The 1900°F (1038°C) exhaust gas from the fuel cell is combusted in the topping combustor. The oxidizer supply for the topping combustor is derived from three sources: 1) the remaining oxygen in the fuel cell exhaust, 2) excess oxygen in the PPCC flue gas, and 3) air from the compressor outlet. The combustible components in the SOFC and PPCC exhausts are fully combusted to raise the temperature of the mixed flue gas prior to expansion through the gas turbine. Gas turbine entrance temperature is limited to 3000°F (1649°C) by introducing part of the air compressor exhaust to the topping combustor. A turbine mechanical efficiency of 92% and a generator electrical efficiency of 98% are applied to generate 621.2 MW of electricity.

The advanced gas turbine system (ATS) represents one of the critical enabling technologies within the Vision 21 program. The ATS program has made significant improvements in the overall performance of gas turbines, and the reference cycle is designed to incorporate further advancements in ATS technology.

Supercritical Steam Turbine and Heat Recovery Steam Generator

The conceptual Vision 21 plant arrangement employs an ultra-supercritical pressure, double reheat steam cycle operating at 6500 psia/1300°F/1300°F/1300°F (44.8 MPa/704°C/704°C/704°C). Turbine mechanical efficiencies of 91% (HP), 87% (IP), and 92% (LP) and a generator electrical efficiency of 98% are applied to generate 283.7 MW of electricity.

The Heat Recovery Steam Generator (HRSG) for the Vision 21 Plant contains two sections. The high-temperature section contains the HP superheater, IP reheater, and LP reheater to raise the steam temperatures to 1300°F (704°C). Since the HP superheater, IP reheater, and LP reheater sections all generate steam at the same outlet temperature, they need to be arranged in parallel or as a series of alternating bank subsections (Figure E9 shows them only schematically and is not meant to portray physical layout). The HRSG high-temperature section has a total thermal duty of 553 MM Btu/hr (162 MW), an inlet flue gas temperature of 1408°F (764°C), and an outlet flue gas temperature of 960°F (516°C). The HRSG low-temperature section contains an economizer, which preheats the water from the ash cooler from 118°F (48°C) to 717°F (381°C). Total thermal duty of the economizer is 798 MM Btu/hr (234 MW) with an LMTD of 188°F (104°C). Flue gas exits the HRSG low-temperature section to the stack at 260°F (127°C).

Pressurized Pulverized Coal Combustor (PPCC)

The pressurized pulverized coal (PC) combustor technology has been identified as an enabling technology within the Vision 21 advanced combustion systems program. The PC combustor designed herein performs both steam generation and air heating duties.

The solid char that is generated in the PGM gasifier is fired in the pressurized PC combustion furnace. Hot char enters the furnace at 1200°F (649°C) after being cooled in a syngas/char cooler. To aid in combustion initiation and stabilization, 10% of the raw coal fed to the plant is burned with the char in the furnace to achieve a 99.5% char burnout. Air pressurized to 450 psia (3.10 MPa) and 1006°F (541°C) is introduced into the furnace as the fuel oxidizer. Flue gas exits the PPCC at 1300°F (704°C) with 3.0% O_2 and is sent to a filter where the fly ash is separated from the gas.

High-pressure supercritical water [1.22 MM lb/hr (154 kg/sec)] enters the furnace waterwalls (from the HRSG economizer) at 6850 psia (47.2 MPa) and 717°F (381°C) and exits at 982°F (528°C) to the syngas/char cooler. Air [1.09 MM lb/hr (137 kg/sec)] from the gas turbine air compressor [430 psia (2.96 MPa)] is heated in the PPCC from 987°F (531°C) to 1509°F (821°C) and is sent to the fuel cell. Thermal duty of the furnace is 785 MM Btu/hr (230 MW) consisting of 154 MM Btu/hr (45 MW) of air heating and 631 MM Btu/hr (185 MW) of water/steam heating.

E.4.3 System Analysis and Results

The Aspen Plus computer program was used to perform the analysis for the conceptual Vision 21 power plant shown in Figure E9. Fig presents the flow sheet with labels for all units and streams. Note that the PGM was modeled as a combination of three Aspen standard reactors: a reactor for coal devolatilization, a reactor for char gasification and a reactor for chemical equilibrium. Likewise, the PPCC was also modeled as a combination of three standard reactors. The SOFC was modeled using a custom User2 model in which 85% of the H_2 in the syngas stream reacted with O_2 in the air stream and 50% of the heat of the reaction was converted to electricity. The balance of the heat generated was absorbed by the syngas and air entering the fuel cell. Due to the limitation of the User2 model, two heaters were added in the flow sheet to model the SOFC unit. The syngas desulfurization unit was simplified as an Aspen component separator that separates sulfur-containing species (S, SO_2, SO_3 and H_2S) from other species in the syngas produced in the PGM. Likewise, the PPCC flue gas desulfurization unit was also modeled as a component separator. The simplified separators did not account for the energy required for the desulfurization. Mass and energy balances were performed for each unit in the system. The operating conditions for the overall plant were determined to achieve the Vision 21 goal plant efficiency. The modeled operating conditions for major components in the system are given in this section along with the properties of individual streams calculated from the Aspen model.

Operating Conditions

The Vision 21 plant modeled is an air-blown system that consumes 320,000 lb/hr (40.3 Kg/sec) of high-volatile bituminous coal. The heat input (HHV) to the system is 1287 MW or 4397 MMBtu/hr. The gross power output is 795.9 MWe. The overall plant efficiency is 61.9%. Note that since the desulfurization units consume certain amounts of power, the actual plant efficiency is slightly lower. Table E.2 lists the coal analysis data.

Table E.3 lists the operating conditions of the major components in the Vision 21 power plant. The unit names in the parentheses are the names shown in the Aspen flow sheet.

Table E.2 - Coal Analysis Data

Component	Basis	1.1.1.1 Weight %
Proximate Analysis		
Moisture	As Received	1.50
Fixed Carbon	As Received	54.59
Volatile Matters	As Received	33.33
Ash	As Received	10.58
Total		100.00
Ultimate Analysis		
C	Dry	75.90
H	Dry	5.22
O	Dry	4.98
N	Dry	1.65
S	Dry	1.51
Ash	Dry	10.74
Total	Dry	100.00
HHV (Btu/lb)	As Received	13,742

Table E.3 - Operating Conditions of Individual Components in the Vision 21 Plant

Component	Fluid	Connection	Node No.	Temp. F	Press. psia	Flow Rate M lb/hr	Heat Duty MM Btu/hr	Elec. Gen MW	Other	Eff. %
PGM	Fluid Bed	Interior	1	1800	500				Carbon Conv.	80.0%
(COALDEV1,	Coal	Inlet	2	60	15	288				
CHARRXT1,	Air	Inlet	3	1050	500	777				
GASEQL1)	Steam	Inlet	4	1300	828	160				
	Syngas+Char	Outlet	5	1800	500	1225				
Syngas/Char	Syngas+Char	Inlet	5	1800	500	1225				
Cooler	Syngas+Char	Outlet	6	1200	450	1225				
(COOLER)	Steam	Inlet	7	982	6700	1224				
	Steam	Outlet	8	1206	6600	1224				
	Steam (Heat Added)	Internal	9				-275			
Syngas Filter	Syngas+Char	Inlet	6	1200	450	1225				
(FILTER1)	Syngas	Outlet	10	1200	450	1163				
	Char	Outlet	11	1200	450	62				
Syngas Desulf.	Syngas	Inlet	10	1200	450	1163				
Unit	Syngas	Outlet	12	1200	450	1159				
(DESULF1)	SOx	Outlet	13	1200	450	4				
PPCC	Comb. Air	Inlet	14	1006	450	787				
Combustor/										
Boiler	Preheat Air	Inlet	15	987	430	1088				
(COALDEV2,	Preheat Air	Outlet	16	1509	427	1088				
CHARRXT2,	Air (Heat Added)	Internal	17				154			
GASEQL2)	Water	Inlet	18	717	6850	1224				
	Steam	Outlet	7	982	6700	1224				
	Steam (Heat Added)	Internal	20				631		Char Burnout	99.5%
	Flue Gas + Ash	Outlet	19	1300	450	881				
	Coal	Inlet	21	60	15	32				
	Char	Inlet	11	1200	450	62				
PPCC Flue Gas	Flue Gas + Ash	Inlet	19	1300	450	881				
Filter	Flue Gas	Outlet	22	1300	450	847				
(FILTER2)	Ash	Outlet	23	1300	450	34				
Flue Gas	Flue Gas	Inlet	22	1300	450	847				
Desulf. Unit	Flue Gas	Outlet	24	1300	450	844				
(DEFULF2)	SOx	Outlet	25	1300	450	3				
SOFC	Syngas	Inlet	12	1200	450	1159				
(FUELCELL)	Flue Gas	Inlet	24	1300	450	844				
	Fuel Cell	Internal	26	2000	427			159.8	H_2 Conversion	85.0%

	Syngas (Energy Added)	Internal	26				51			
	Flue Gas (Energy Added)	Internal	26				89			
	Fuel Cell Gas	Outlet	27	1900	427	2247				
Topping Comb. (TC)	Flue Gas	Inlet	24	1300	450	844				
	Fuel Cell Gas	Inlet	27	1900	427	2247				
	Air	Inlet	28	987	430	1088				
	Flue Gas	Outlet	29	3000	425	4179				
Gas Turbine (GT)	Flue Gas	Inlet	29	3000	425	4179				
	Flue Gas	Outlet	30	1408	16	4179				
	Turbine	Internal	31						Mechanical	92.0%
	Generator	Internal	32					621.2	Electrical	98.0%
Steam Turbine (ST1, ST2, ST3)	HP Steam	Inlet	33	1300	6500	1224				
	HP Steam	Outlet	34	1063	3227	1224				
	IP Steam	Inlet	35	1300	2975	1224				
	IP Steam	Outlet	36	922	900	1224				
	LP Steam	Inlet	37	1300	828	1064				
	LP Steam	Outlet	38	109	1	1064				
	HP Turbine	Internal	39						Mechanical	91.0%
	IP Turbine	Internal	40						Mechanical	87.0%
	LP Turbine	Internal	41						Mechanical	92.0%
	Generator	Internal	42					283.7	Electrical	98.0%
Compressor (AC1, AC2, AC3)	Air	Inlet	43	60	15	3740				
	1st Air	Outlet	44	987	430	2176				
	2nd Air	Outlet	14	1006	450	787				
	3rd Air	Outlet	3	1050	500	777				
	Compressor	Internal	45					-260.8		
HRSG (HTHRSG, LTHRSG)	Fluegas	Inlet	30	1408	16	4179				
	Fluegas	Outlet	51	260	16	4179				
	Water	Inlet	46	118	6950	1224				
	Water	Outlet	18	717	6850	1224				
	Water Heat Added (Econ)	Internal	47				798			
	LP Steam	Inlet	36	922	900	1224				
	LP Steam	Outlet	37	1300	828	1064				
	LP Steam Heat Added (Reheater)	Internal	48				262			
	IP Steam	Inlet	34	1063	3227	1224				
	IP Steam	Outlet	35	1300	2975	1224				
	IP Steam Heat Added (Reheater)	Internal	49				198			
	HP Steam	Inlet	8	1206	6600	1224				
	HP Steam	Inlet	33	1300	6500	1224				
	HP Steam Heat Added (Superheater)	Internal	50				93			
Feedwater Pump (WPUMP)	Water	Inlet	52	108	1	1224				
	Water	Outlet	53	111	7000	1224				
	Pump	Internal	54					-7.6	Pump	99.0%
Cooling Water Pump (CWPMP)	Water	Inlet	55	70	15	50000				
	Water	Outlet	56	70	25	50000				
	Pump	Internal	57					-0.4	Pump	99.0%
Condenser	Steam	Inlet	38	109	1	1064				
	Water	Outlet	58	109	1	1064				
	Cooling Water	Inlet	56	70	25	50000				
	Cooling Water	Outlet	60	91	15	50000				
	Steam (Heat Added)	Internal	59				-1047			
Ash Cooler (ASHCLR)	Ash	Inlet	23	1300	450	34				
	Ash	Outlet	61	260	15	34				
	Water	Inlet	53	111	7000	1224				
	Water	Outlet	46	118	6950	1224				
	Water (Heat Added)	Internal	62				8			
Cycle	Net Power Output	Total						796.0		
Cycle Efficiency	Coal Energy Added (HHV)	Total	63				4397.4		Cycle	61.9%

Properties of Streams

Table E.4 lists all streams on the Aspen Plus flow sheet. The stream number listed in the table corresponds to the same stream number listed in the flow sheet. The tabulated properties of a stream include stream location, temperature, pressure, flow rates, enthalpies, vapor fraction, mole fractions of species in the gas phase and the mass fraction of species in the solid phase. These stream numbers also correspond to the labeled locations in Figure E.9.

Table E.4 - Streams in the Aspen Plus Model of the Vision 21 Plant

Stream Number	2	3	4	5
Stream Location	coal to PGM	air to PGM	steam to PGM	syngas from PGM
Temperature (F)	60.0	1050.5	1299.8	1800.0
Pressure (psia)	14.7	500.0	828.0	500.0
Total Mass Flow (M lb/hr)	288.0	777.0	160.0	1,225.0
Total Enthalpy (MM Btu/hr)	-33.2	191.2	-830.1	-672.6
Vapor Fraction		1	1	1
Gas Mass Flow (M lb/hr)	0.0	777.0	160.0	1,163.1
Gas Enthalpy (MM Btu/hr)		191.2	-830.1	-713.2
Mole Fraction				
C	0.000	0.000	0.000	0.000
S	0.000	0.000	0.000	0.000
H2	0.000	0.000	0.000	0.225
N2	0.000	0.790	0.000	0.408
O2	0.000	0.210	0.000	0.000
CO	0.000	0.000	0.000	0.240
CO2	0.000	0.000	0.000	0.048
H2O	0.000	0.000	1.000	0.071
CH4	0.000	0.000	0.000	0.007
NH3	0.000	0.000	0.000	0.000
NO	0.000	0.000	0.000	0.000
SO2	0.000	0.000	0.000	0.000
H2S	0.000	0.000	0.000	0.002
SO3	0.000	0.000	0.000	0.000
Solid Mass Flow (M lb/hr)	288.00	0.00	0.00	61.91
Solid Enthalpy (MM Btu/hr)	-33.21			40.68
Solid Mass Fraction				
Coal	1.000	0.000	0.000	0.000
Char	0.000	0.000	0.000	0.508
Ash	0.000	0.000	0.000	0.492

Table E.4 (Continued)

Stream Number	6	7	8	10
Stream Location	syngas to syngas filter	steam to syngas cooler	steam from syngas cooler	syngas from syngas filter
Temperature (F)	1200.0	981.8	1205.6	1200.0
Pressure (psia)	450.0	6700.0	6600.0	450.0
Total Mass Flow (M lb/hr)	1,225.0	1,224.3	1,224.3	1,163.1
Total Enthalpy (MM Btu/hr)	-948.1	-6,850.1	-6,574.6	-975.1
Vapor Fraction	1	1	1	1
Gas Mass Flow (M lb/hr)	1,163.1	1,224.3	1,224.3	1,163.1
Gas Enthalpy (MM Btu/hr)	-975.1	-6,850.1	-6,574.6	-975.1
Mole Fraction				
C	0.000	0.000	0.000	0.000
S	0.000	0.000	0.000	0.000
H2	0.225	0.000	0.000	0.225
N2	0.408	0.000	0.000	0.408
O2	0.000	0.000	0.000	0.000
CO	0.240	0.000	0.000	0.240
CO2	0.048	0.000	0.000	0.048
H2O	0.071	1.000	1.000	0.071
CH4	0.007	0.000	0.000	0.007
NH3	0.000	0.000	0.000	0.000
NO	0.000	0.000	0.000	0.000
SO2	0.000	0.000	0.000	0.000
H2S	0.002	0.000	0.000	0.002
SO3	0.000	0.000	0.000	0.000
	0.000	0.000	0.000	0.000
Solid Mass Flow (M lb/hr)	61.91	0.00	0.00	0.00
Solid Enthalpy (MM Btu/hr)	27.07			
Solid Mass Fraction				
Coal	0.000	0.000	0.000	0.000
Char	0.508	0.000	0.000	0.000
Ash	0.492	0.000	0.000	0.000

Table E.4 (Continued)

Stream Number	11	12	13	14
Stream Location	char/ash to PPCC	syngas to fuel cell	SOx from syngas Desulf.	air to PPCC
Temperature (F)	1200.0	1200.0	1200.0	1006.2
Pressure (psia)	450.0	450.0	450.0	450.0
Total Mass Flow (M lb/hr)	61.9	1,159.4	3.7	787.4
Total Enthalpy (MM Btu/hr)	27.1	-975.3	0.2	184.5
Vapor Fraction		1	1	1
Gas Mass Flow (M lb/hr)	0.0	1,159.4	3.7	787.4
Gas Enthalpy (MM Btu/hr)		-975.3	0.2	184.5
Mole Fraction				
C	0.000	0.000	0.000	0.000
S	0.000	0.000	0.000	0.000
H2	0.000	0.225	0.000	0.000
N2	0.000	0.408	0.000	0.790
O2	0.000	0.000	0.000	0.210
CO	0.000	0.240	0.000	0.000
CO2	0.000	0.048	0.000	0.000
H2O	0.000	0.071	0.000	0.000
CH4	0.000	0.007	0.000	0.000
NH3	0.000	0.000	0.000	0.000
NO	0.000	0.000	0.000	0.000
SO2	0.000	0.000	0.000	0.000
H2S	0.000	0.000	1.000	0.000
SO3	0.000	0.000	0.000	0.000
	0.000	0.000	0.000	0.000
Solid Mass Flow (M lb/hr)	61.91	0.00	0.00	0.00
Solid Enthalpy (MM Btu/hr)	27.07			
Solid Mass Fraction				
Coal	0.000	0.000	0.000	0.000
Char	0.508	0.000	0.000	0.000
Ash	0.492	0.000	0.000	0.000

Table E.4 (Continued)

Stream Number	15	16	18	19
Stream Location	air to air heater	air from air heater	water to PPCC	flue/ash to flue gas filter
Temperature (F)	987.4	1508.8	717.4	1300.0
Pressure (psia)	430.0	427.0	6850.0	450.0
Total Mass Flow (M lb/hr)	1,087.5	1,087.5	1,224.3	881.3
Total Enthalpy (MM Btu/hr)	249.3	403.7	-7,481.2	-577.7
Vapor Fraction	1	1	1	1
Gas Mass Flow (M lb/hr)	1,087.5	1,087.5	1,224.3	847.2
Gas Enthalpy (MM Btu/hr)	249.3	403.7	-7,481.2	-580.4
Mole Fraction				
C	0.000	0.000	0.000	0.000
S	0.000	0.000	0.000	0.000
H2	0.000	0.000	0.000	0.000
N2	0.790	0.790	0.000	0.776
O2	0.210	0.210	0.000	0.030
CO	0.000	0.000	0.000	0.000
CO2	0.000	0.000	0.000	0.159
H2O	0.000	0.000	1.000	0.033
CH4	0.000	0.000	0.000	0.000
NH3	0.000	0.000	0.000	0.000
NO	0.000	0.000	0.000	0.000
SO2	0.000	0.000	0.000	0.000
H2S	0.000	0.000	0.000	0.000
SO3	0.000	0.000	0.000	0.001
	0.000	0.000	0.000	0.000
Solid Mass Flow (M lb/hr)	0.00	0.00	0.00	34.10
Solid Enthalpy (MM Btu/hr)				2.69
Solid Mass Fraction				
Coal	0.000	0.000	0.000	0.000
Char	0.000	0.000	0.000	0.007
Ash	0.000	0.000	0.000	0.993

Table E.4 (Continued)

Stream Number	21	22	23	24
Stream Location	coal to PPCC	flue to flue gas desulf	ash to ash cooler	flue gas to TC
Temperature (F)		1300.0		1300.0
Pressure (psia)	14.7	450.0		450.0
Total Mass Flow (M lb/hr)	32.0	847.2	34.1	844.2
Total Enthalpy (MM Btu/hr)	-3.7	-580.4	2.7	-574.8
Vapor Fraction		1		1
Gas Mass Flow (M lb/hr)	0.0	847.2	0.0	844.2
Gas Enthalpy (MM Btu/hr)	0.0	-580.4		-574.8
Mole Fraction				
C	0.000	0.000	0.000	0.000
S	0.000	0.000	0.000	0.000
H2	0.000	0.000	0.000	0.000
N2	0.000	0.776	0.000	0.777
O2	0.000	0.030	0.000	0.030
CO	0.000	0.000	0.000	0.000
CO2	0.000	0.159	0.000	0.160
H2O	0.000	0.033	0.000	0.033
CH4	0.000	0.000	0.000	0.000
NH3	0.000	0.000	0.000	0.000
NO	0.000	0.000	0.000	0.000
SO2	0.000	0.000	0.000	0.000
H2S	0.000	0.000	0.000	0.000
SO3	0.000	0.001	0.000	0.000
	0.000	0.000	0.000	0.000
Solid Mass Flow (M lb/hr)	32.00	0.00	34.10	0.00
Solid Enthalpy (MM Btu/hr)	-3.69		2.69	
Solid Mass Fraction				
Coal	1.000	0.000	0.000	0.000
Char	0.000	0.000	0.007	0.000
Ash	0.000	0.000	0.993	0.000

Table E.4 (Continued)

Stream Number	25	27	28	29
Stream Location	SOx from flue gas desulf.	flue gas from fuel cell	air to TC	flue gas to GT
Temperature (F)	1300.0	1900.0	987.4	2999.9
Pressure (psia)	450.0	427.0	430.0	425.0
Total Mass Flow (M lb/hr)	3.0	2,246.9	1,087.5	4,178.6
Total Enthalpy (MM Btu/hr)	-5.6	-1,222.1	249.3	-1,442.5
Vapor Fraction	1	1	1	1
Gas Mass Flow (M lb/hr)	3.0	2,246.9	1,087.5	4,178.6
Gas Enthalpy (MM Btu/hr)	-5.6	-1,222.1	249.3	-1,442.5
Mole Fraction				
C	0.000	0.000	0.000	0.000
S	0.000	0.000	0.000	0.000
H2	0.000	0.042	0.000	0.000
N2	0.000	0.505	0.790	0.714
O2	0.000	0.000	0.210	0.025
CO	0.000	0.297	0.000	0.000
CO2	0.000	0.059	0.000	0.139
H2O	0.000	0.088	0.000	0.120
CH4	0.000	0.009	0.000	0.000
NH3	0.000	0.000	0.000	0.000
NO	0.000	0.000	0.000	0.002
SO2	0.308	0.000	0.000	0.000
H2S	0.000	0.000	0.000	0.000
SO3	0.692	0.000	0.000	0.000
	0.000	0.000	0.000	0.000
Solid Mass Flow (M lb/hr)	0.00	0.00	0.00	0.00
Solid Enthalpy (MM Btu/hr)				
Solid Mass Fraction				
Coal	0.000	0.000	0.000	0.000
Char	0.000	0.000	0.000	0.000
Ash	0.000	0.000	0.000	0.000

Table E.4 (Continued)

Stream Number	30	33	34	35
Stream Location	exhaust from GT	steam to HP ST	steam from HP ST	steam to IP ST
Temperature (F)	1407.5	1300.0	1063.0	1300.0
Pressure (psia)	16.1	6500.0	3227.0	2975.0
Total Mass Flow (M lb/hr)	4,178.6	1,224.3	1,224.3	1,224.3
Total Enthalpy (MM Btu/hr)	-3,595.2	-6,481.5	-6,597.8	-6,400.1
Vapor Fraction	1	1	1	1
Gas Mass Flow (M lb/hr)	4,178.6	1,224.3	1,224.3	1,224.3
Gas Enthalpy (MM Btu/hr)	-3,595.2	-6,481.5	-6,597.8	-6,400.1
Mole Fraction				
C	0.000	0.000	0.000	0.000
S	0.000	0.000	0.000	0.000
H2	0.000	0.000	0.000	0.000
N2	0.714	0.000	0.000	0.000
O2	0.025	0.000	0.000	0.000
CO	0.000	0.000	0.000	0.000
CO2	0.139	0.000	0.000	0.000
H2O	0.120	1.000	1.000	1.000
CH4	0.000	0.000	0.000	0.000
NH3	0.000	0.000	0.000	0.000
NO	0.002	0.000	0.000	0.000
SO2	0.000	0.000	0.000	0.000
H2S	0.000	0.000	0.000	0.000
SO3	0.000	0.000	0.000	0.000
	0.000	0.000	0.000	0.000
Solid Mass Flow (M lb/hr)	0.00	0.00	0.00	0.00
Solid Enthalpy (MM Btu/hr)				
Solid Mass Fraction				
Coal	0.000	0.000	0.000	0.000
Char	0.000	0.000	0.000	0.000
Ash	0.000	0.000	0.000	0.000

Table E.4 (Continued)

Stream Number	36	37	38	43
Stream Location	steam from IP ST	steam to LP ST	exhaust from LP ST	air to compressor
Temperature (F)	921.5	1299.8	108.8	60.0
Pressure (psia)	900.0	828.0	1.2	14.7
Total Mass Flow (M lb/hr)	1,224.3	1,064.3	1,064.3	3,739.4
Total Enthalpy (MM Btu/hr)	-6,614.0	-5,521.9	-6,179.7	-15.8
Vapor Fraction	1	1	0.953	1
Gas Mass Flow (M lb/hr)	1,224.3	1,064.3	1,064.3	3,739.4
Gas Enthalpy (MM Btu/hr)	-6,614.0	-5,521.9	-6,179.7	-15.8
Mole Fraction				0
C	0.000	0.000	0.000	0.000
S	0.000	0.000	0.000	0.000
H2	0.000	0.000	0.000	0.000
N2	0.000	0.000	0.000	0.790
O2	0.000	0.000	0.000	0.210
CO	0.000	0.000	0.000	0.000
CO2	0.000	0.000	0.000	0.000
H2O	1.000	1.000	1.000	0.000
CH4	0.000	0.000	0.000	0.000
NH3	0.000	0.000	0.000	0.000
NO	0.000	0.000	0.000	0.000
SO2	0.000	0.000	0.000	0.000
H2S	0.000	0.000	0.000	0.000
SO3	0.000	0.000	0.000	0.000
	0.000	0.000	0.000	0.000
Solid Mass Flow (M lb/hr)	0.00	0.00	0.00	0.00
Solid Enthalpy (MM Btu/hr)				
Solid Mass Fraction				
Coal	0.000	0.000	0.000	0.000
Char	0.000	0.000	0.000	0.000
Ash	0.000	0.000	0.000	0.000

Table E.4 (Continued)

Stream Number	44	46	51	52
Stream Location	air from compressor	water to HRSG	flue gas to stack	water to feedwater pump
Temperature (F)	987.4	118.4	260.0	108.0
Pressure (psia)	430.0	6950.0	16.4	1.2
Total Mass Flow (M lb/hr)	2,175.0	1,224.3	4,178.6	1,224.3
Total Enthalpy (MM Btu/hr)	498.6	-8,279.1	-4,945.8	-8,313.5
Vapor Fraction	1	0	1	0
Gas Mass Flow (M lb/hr)	2,175.0	1,224.3	4,178.6	1,224.3
Gas Enthalpy (MM Btu/hr)	498.6	-8,279.1	-4,945.8	-8,313.5
Mole Fraction				
C	0.000	0.000	0.000	0.000
S	0.000	0.000	0.000	0.000
H2	0.000	0.000	0.000	0.000
N2	0.790	0.000	0.714	0.000
O2	0.210	0.000	0.025	0.000
CO	0.000	0.000	0.000	0.000
CO2	0.000	0.000	0.139	0.000
H2O	0.000	1.000	0.120	1.000
CH4	0.000	0.000	0.000	0.000
NH3	0.000	0.000	0.000	0.000
NO	0.000	0.000	0.002	0.000
SO2	0.000	0.000	0.000	0.000
H2S	0.000	0.000	0.000	0.000
SO3	0.000	0.000	0.000	0.000
	0.000	0.000	0.000	0.000
Solid Mass Flow (M lb/hr)	0.00	0.00	0.00	0.00
Solid Enthalpy (MM Btu/hr)				
Solid Mass Fraction				
Coal	0.000	0.000	0.000	0.000
Char	0.000	0.000	0.000	0.000
Ash	0.000	0.000	0.000	0.000

Table E.4 (Continued)

Stream Number	53	55	56	58
Stream Location	water after feedwater pump	water to cooling water pump	water after cooling water pump	water after condenser
Temperature (F)	111.2	70.0	70.0	108.8
Pressure (psia)	7000.0	14.7	24.7	1.2
Total Mass Flow (M lb/hr)	1,224.3	50,000.0	50,000.0	1,064.3
Total Enthalpy (MM Btu/hr)	-8,287.6	-341,402.3	-341,400.8	-7,226.2
Vapor Fraction	0	0	0	0
Gas Mass Flow (M lb/hr)	1,224.3	50,000.0	50,000.0	1,064.3
Gas Enthalpy (MM Btu/hr)	-8,287.6	-341,402.3	-341,400.8	-7,226.2
Mole Fraction				
C	0.000	0.000	0.000	0.000
S	0.000	0.000	0.000	0.000
H2	0.000	0.000	0.000	0.000
N2	0.000	0.000	0.000	0.000
O2	0.000	0.000	0.000	0.000
CO	0.000	0.000	0.000	0.000
CO2	0.000	0.000	0.000	0.000
H2O	1.000	1.000	1.000	1.000
CH4	0.000	0.000	0.000	0.000
NH3	0.000	0.000	0.000	0.000
NO	0.000	0.000	0.000	0.000
SO2	0.000	0.000	0.000	0.000
H2S	0.000	0.000	0.000	0.000
SO3	0.000	0.000	0.000	0.000
	0.000	0.000	0.000	0.000
Solid Mass Flow (M lb/hr)	0.00	0.00	0.00	0.00
Solid Enthalpy (MM Btu/hr)				
Solid Mass Fraction				
Coal	0.000	0.000	0.000	0.000
Char	0.000	0.000	0.000	0.000
Ash	0.000	0.000	0.000	0.000

Table E.4 (Continued)

Stream Number	60	61	63	64
Stream Location	cooling water out	ash from ash cooler	coal from stock	steam from LP reheater
Temperature (F)	91.0			1299.8
Pressure (psia)	14.7	14.7	14.7	828.0
Total Mass Flow (M lb/hr)	50,000.0	34.1	320.0	1,224.3
Total Enthalpy (MM Btu/hr)	-340,354.2	-5.8	-36.9	-6,352.0
Vapor Fraction	0			1
Gas Mass Flow (M lb/hr)	50,000.0	0.0	0.0	1,224.3
Gas Enthalpy (MM Btu/hr)	-340,354.2			-6,352.0
Mole Fraction				
C	0.000	0.000	0.000	0.000
S	0.000	0.000	0.000	0.000
H2	0.000	0.000	0.000	0.000
N2	0.000	0.000	0.000	0.000
O2	0.000	0.000	0.000	0.000
CO	0.000	0.000	0.000	0.000
CO2	0.000	0.000	0.000	0.000
H2O	1.000	0.000	0.000	1.000
CH4	0.000	0.000	0.000	0.000
NH3	0.000	0.000	0.000	0.000
NO	0.000	0.000	0.000	0.000
SO2	0.000	0.000	0.000	0.000
H2S	0.000	0.000	0.000	0.000
SO3	0.000	0.000	0.000	0.000
	0.000	0.000	0.000	0.000
Solid Mass Flow (M lb/hr)	0.00	34.10	320.00	0.00
Solid Enthalpy (MM Btu/hr)		-5.79	-36.91	
Solid Mass Fraction				
Coal	0.000	0.000	1.000	0.000
Char	0.000	0.007	0.000	0.000
Ash	0.000	0.993	0.000	0.000

E.4.4 Modification for ASPEN-FLUENT Modeling

To allow for FLUENT modeling of the PPCC within the ASPEN model, the Vision 21 plant ASPEN model was modified such that the PPCC model is consistent with the FLUENT CFD model. PPCC module blocks, COALDEV2, CHARRXT2, and GASEQL2 were combined into two modules, HP-PC and HUA. HP-PC represents the combustor furnace, which was modeled in FLUENT. HUA represents the air heater portion of the combustor (which was not included in the FLUENT CFD model). In addition improved model convergence was achieved by eliminating the syngas and air preheaters before the fuel cell by changing the fuel cell parameters to allow the cold inlet streams to be heated within the fuel cell. The revised ASPEN run flow sheet is presented in Figure E.10. The performance conditions are virtually identical to the previous ASPEN run (see Figure).

Figure E.10 – Revised Aspen Flow Sheet of the Vision 21 Power Plant (For ASPEN-FLUENT Modeling)

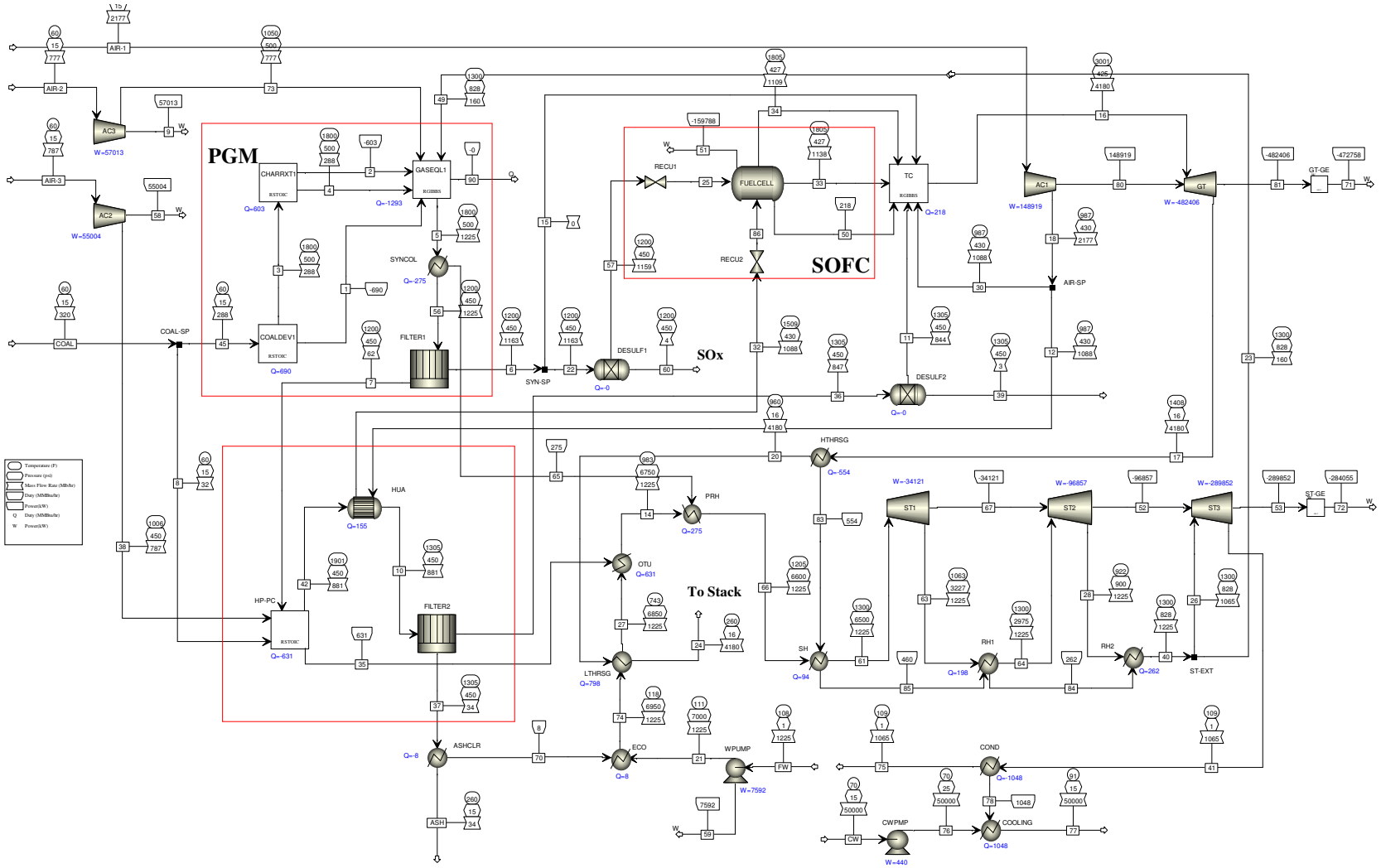

E.5 FLUENT-Aspen Coupled simulation

The software, as originally developed, did not have any provision for non-conventional components such as coal. Thus, in the simulation involving pulverized coal, the pulverized fuel was replaced with equivalent gaseous fuel. The current version has addressed this issue and the functionality to handle non-conventional component is now available.

The Foster Wheeler Vision 21 power plant design has a Partial Gasification module (PGM) and a pressurized pulverized combustion (PPC) module. The PPC module receives char and ash from the PGM and 10% of the raw coal. It was decided to replace only the PPC module with a fluent block. To make the PPC module, that originally had a series of reactors, compatible some changes were made in the Aspen flowsheet. The heat stream between the two software utilities could only be transferred through a user defined function (udf). The flowsheet also needed additional modifications to accommodate the primary, secondary, and tertiary air streams as well as separate inlet/outlet ports for each solid streams. In order to reduce the number of these ports and the corresponding modifications needed to split the streams coming from the PGM, the fluent case file was modified and a mass-weighted-average particle size diameter was used for coal, char, and ash. In view of these difficulties and other issues encountered in running the coupled aspen-fluent simulation, it was not possible to complete the full coupled simulation by the end of the project. Some suggestion have been generated for the further development of the Controller:

- The user friendliness of the Controller should be improved, the Controller is not as user friendly as commercial software like FLUENT or Aspen. As an example, if a user makes a mistake, the controller simply does not work and does not give any error message. During the testing, the only way to overcome this difficulty was to start over.
- The procedure of treating a non-conventional component in Aspen Plus is not compatible with fluent. Aspen Plus, though allows non-conventional components such as coal and char. It coverts these components into conventional components such as C, S, H, N, and O which take part in the decomposition/reactions. FLUENT, on the other hand, can handle coal and char as such and provides a superior treatment of these compounds. As a results, mapping issues between Aspen Plus and FLUENT arise.
- The User's Manual lacks sufficient information and examples that would allow a common user to come up to speed and use the controller efficiently. At present it has only two examples. These examples show only basic steps to make Aspen Plus run with a fluent block.
- The controller also requires use of schemes, which is considerably more complex than a typical Aspen Plus user can handle.

E.6 Pressurized Pulverized Coal Combustor Design and Analysis

E.6.1 Initial FLUENT Modeling

Based on preliminary FLUENT modeling (number of burners and burner locations were varied), a furnace design of the Pressurized Pulverized Coal Combustor (PPCC) was created with eight opposed burners, six OFA ports, and dimensions of 20' (6.1 m) x 20' (6.1 m) x 72' (21.9 m) (W x D x H). The PPCC consists of a rectangular combustion furnace enclosed in a cylindrical vessel as shown in Figure E.11. The cylindrical vessel is designed to contain the high-pressure combustion gases [450 psia (3.10 MPa)]. The rectangular combustion furnace, which houses the furnace water walls and air heater, has a negligible pressure across its walls due to the hydraulic inter-connection between the interior and exterior of the PPCC furnace. The model contains 101,950 cells and is shown in Figure E.12. To reduce NOx formation, the burner separates the secondary air into two zones: a low velocity inner zone and a high velocity swirled outer zone. Over-fire air ports are provided for combustion staging to further reduce NOx production.

FLUENT Sub-Models

The following fluent sub-models were utilized:

Turbulence:	standard two-equation k-ε model.
Radiation:	discrete ordinate
Species Transport:	non-premixed combustion (pdf)
Gaseous radiation emissivity:	domain based
Char devolatilization:	two competing rates
Char oxidation:	kinetics/diffusion limited with low pressure Pittsburgh 8 data (Sandia)
NOx:	FLUENT fuel+ thermal

Boundary Conditions

Boundary conditions are based on the Vision 21 Plant Concept Specification. A schematic of the Vision 21 Plant is presented in **Error! Reference source not found.**. The Vision 21 plant PPCC requirements are shown in Table E.5. The input data required by FLUENT include fuel analysis, coal/char particle size distribution (mass percentage for each size bin), waterwall temperatures, and the velocities, flow rates and temperatures of primary and secondary air streams.

The waterwalls of the furnace are assumed to be gray and diffusive. A uniform emissivity of 0.7 was applied to the walls. Average wall temperature was assumed to be 1000ºF (538ºC).

The coal devolatilization kinetic properties were obtained from Steve Niksa at SRI for Pittsburgh 8 and 30 atm. as follows:

y1= 0.38; A1= 1.4e05; E1= 17.6 kcal/mole
y2= 1.00; A2= 3.2e06; E2= 30.0 kcal/mole

Furnace Model Results

FLUENT 6.1.18 was run until the results reached an approximate steady state. The predicted heat absorption of the design predicted by FLUENT is 624 MM Btu/hr (182.8 MW), which is close to the 631 MM Btu/hr (184.9 MW) requirement.

Figure E. is a plot of the flue gas velocity magnitude in a vertical plane through a burner column. Figure E. presents a plot of gas temperature distribution. The heat flux at the furnace water wall is shown in Figure E.. The residence time of the solid particles (coal, char, and ash) are plotted in Figure E.3 along with residence times for a typical atmospheric furnace. Particle residence time for the PPCC is approximately 40 seconds at the outlet. This is substantial greater than the typical 2-5 second residence time of a atmospheric boiler due to the much lower volumetric flow rate of the PPCC produced by the pressure of 30 atm.

E.6.2 Revised FLUENT Modeling

A revised PPCC design was made to produce a more compact design by reducing the particle residence time. Compared to the initial design, the revised PPCC design has significantly less volume (less than half) while maintaining approximately the same waterwall surface area (a full division wall was added). The revised design reduces substantially the particle residence time (by over a factor of two) and thereby creates a more economic design. The revised PPCC has eight opposed burners, eight opposed OFA ports, and dimensions of 6’ (1.8 m) x 14’ (4.3 m) x 100’ (30.5 m) (WxDxH). The model contains 142,104 cells (symmetric ½ of the furnace was modeled) and is shown in Figure E.. The model was run using the same FLUENT models described in Section E6.1. Figure E.4 is a plot of the flue gas temperature in a vertical plane through a burner column.

By making this revised design more compact concerns were raised about flame impingement on furnace walls and flame instabilities, consequently it was judged that a more suitable design for the PPCC would be a down-fired cylindrical design rather than a wall-fired rectangular design.

Figure E. 11 – Rectangular PPCC Design

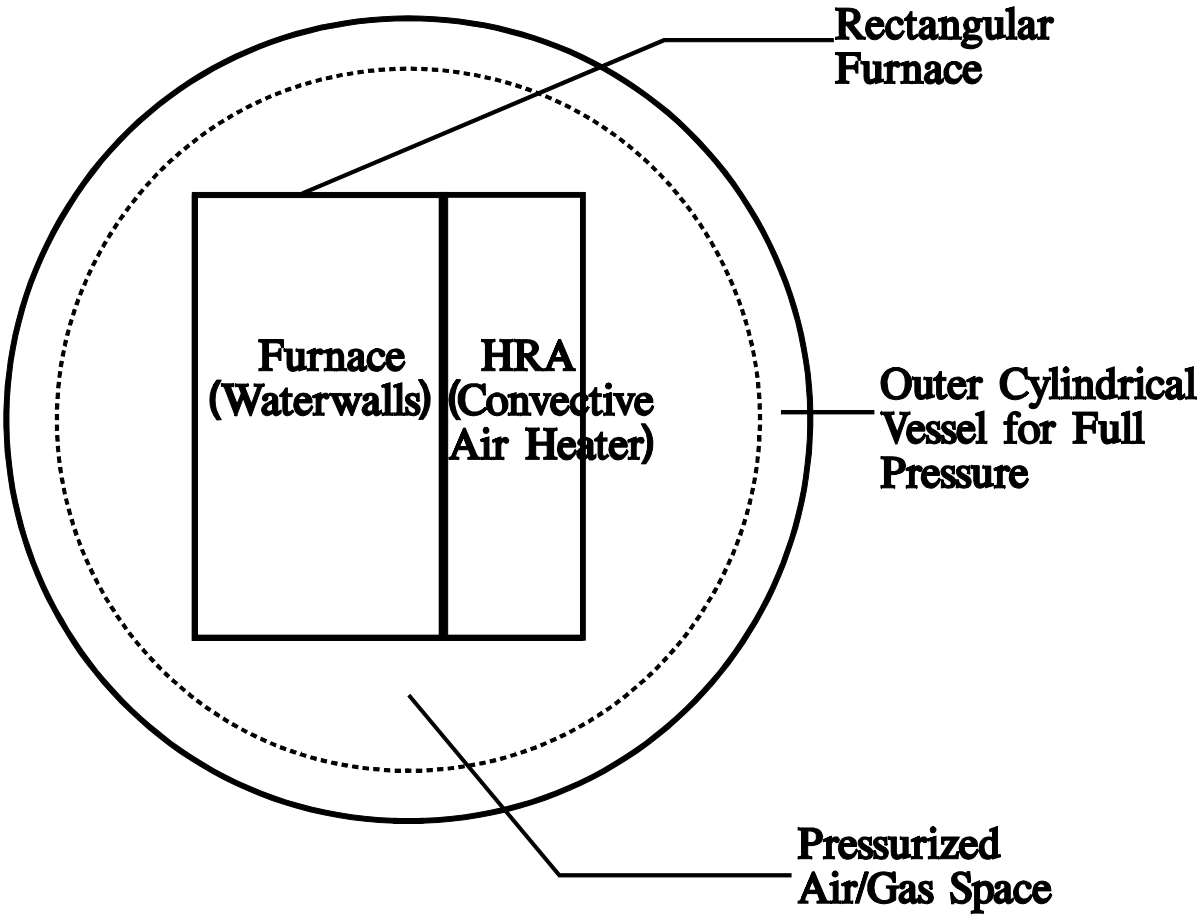

Figure E.12 – PPCC Furnace Model: Initial Design

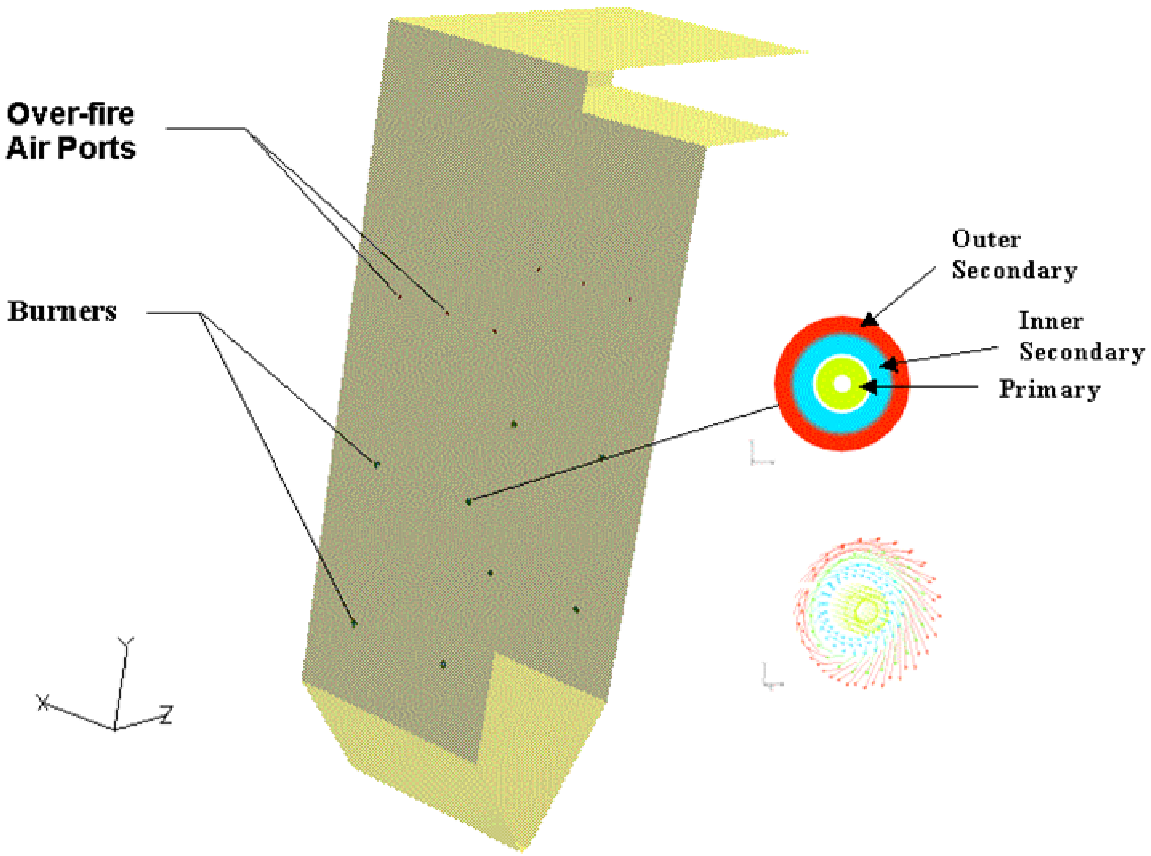

Dimensions: 20' x 20' x 72' (W x D x H)

Table E.5 – PPCC Performance Specification

	Pressure (psia)	Temperature (F)	Flow Rate (lb/hr)	Heat Duty (MM Btu/hr)	Other
Furnace					
Primary Air Inlet	450	200	201,672		
Secondary Air Inlet	450	1100	403,344		
Overfire Air Inlet	450	1100	201,672		
Total Combustion Air			806,688		
Coal Inlet	450	60	32,000		
Char Inlet	450	1200	31,500		
Ash Inlet	450	1200	30,410		
Total Solid Inlet			93,910		burnout > 99.5%
Flue Gas + Ash Outlet		1905	900,598		O2 = 3.0%
Water Inlet	6850	717	1,224,000		
Steam Outlet	6700	982	1,224,000	631	
HRA					
Preheat Air Inlet	430	987	1,088,000		
Preheat Air Outlet		1509	1,088,000	154	
Flue Gas + Ash Outlet		1300	900,598		

Figure E.13 – Gas Velocity: Initial PPCC Design

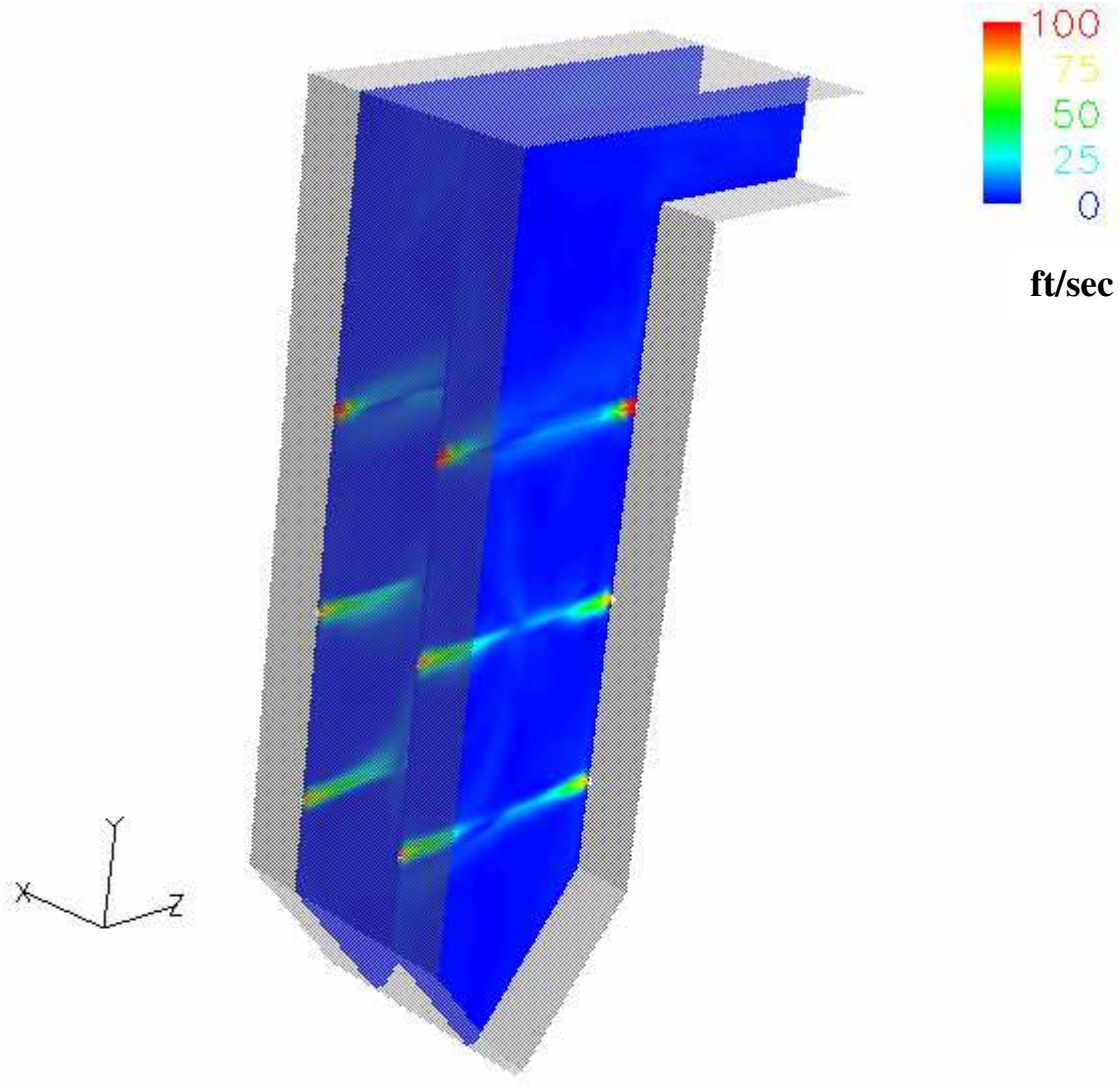

Figure E.14 - Gas Temperature: Initial PPCC Design

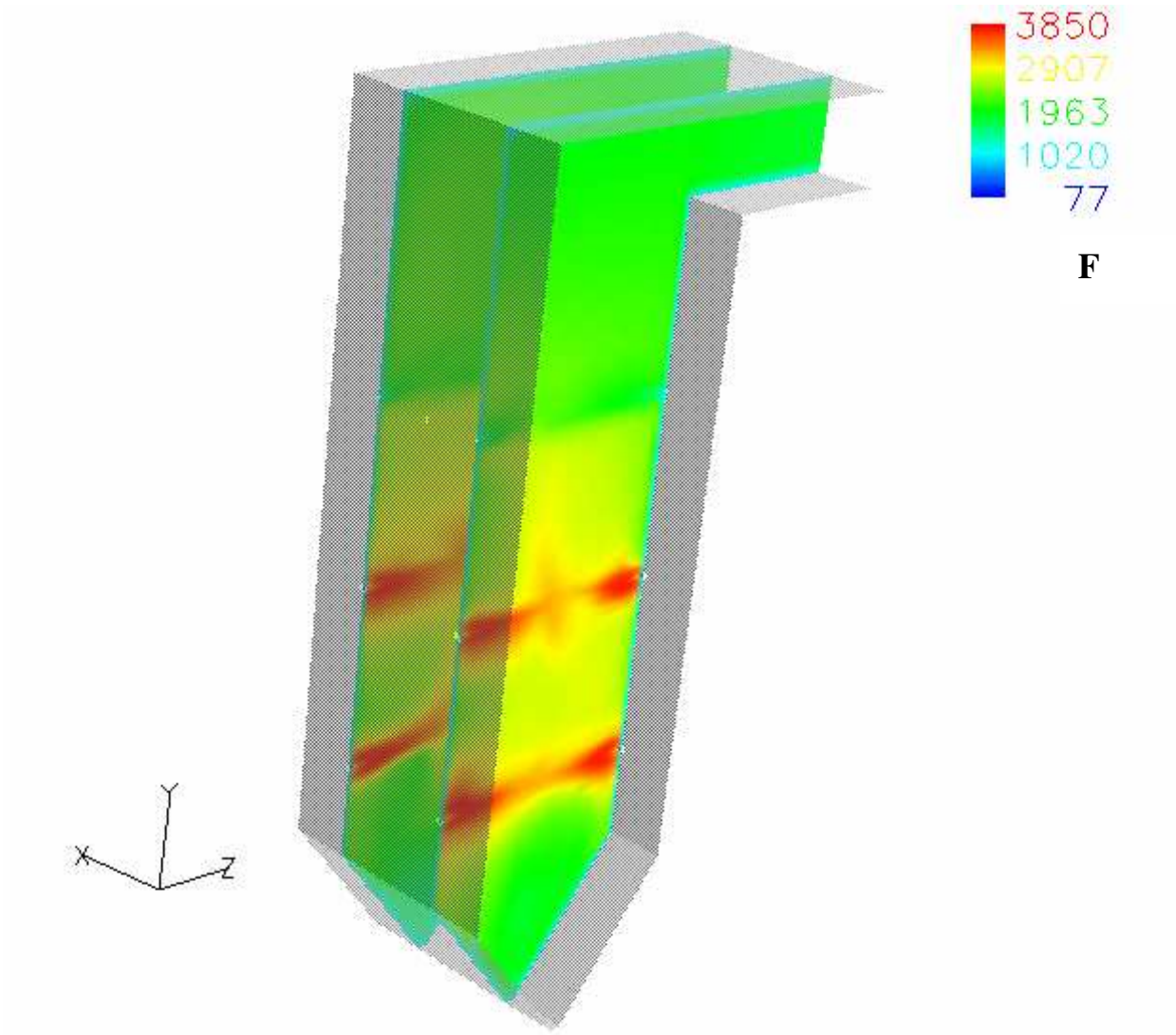

Figure E.15 – Wall Heat Flux: Initial PPCC Design

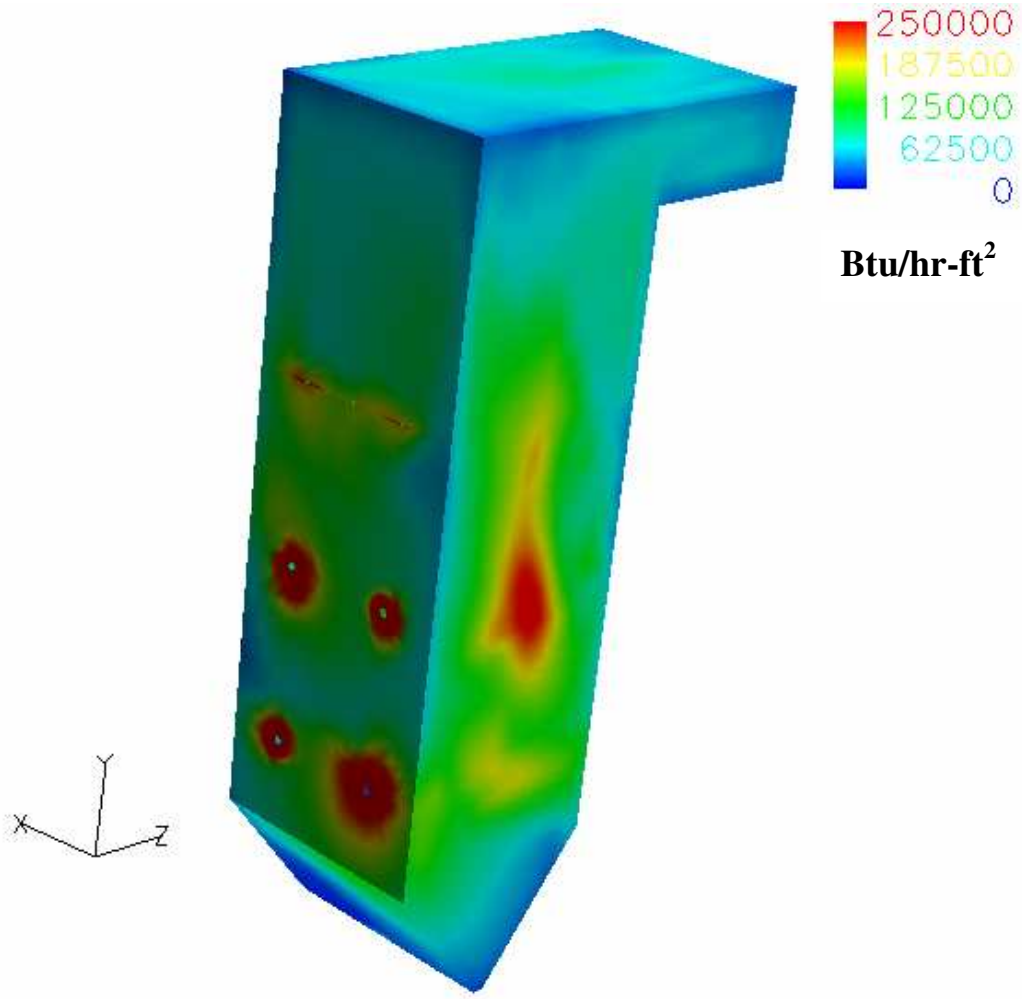

Figure E.36 – Particle Residence Time: Initial PPCC Design

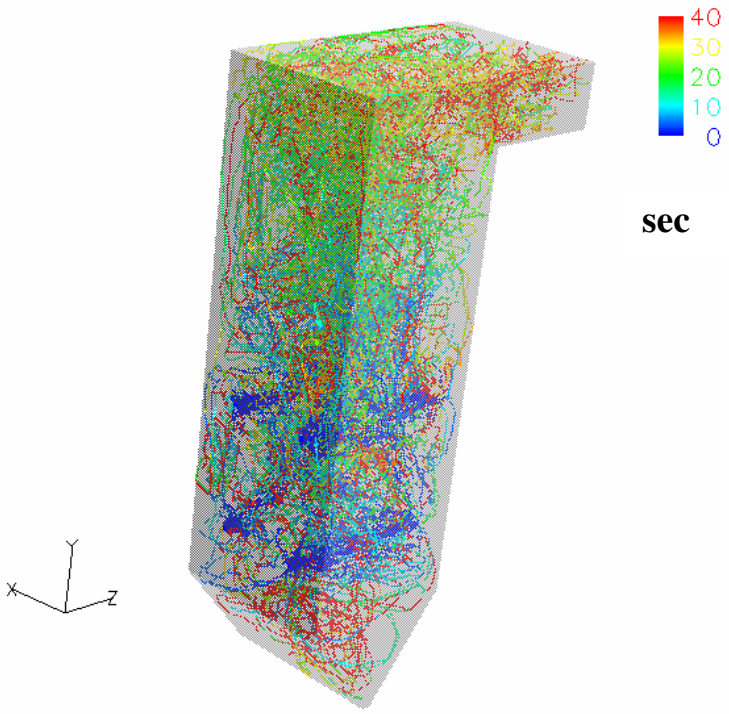

30 atm Furnace (PPCC)

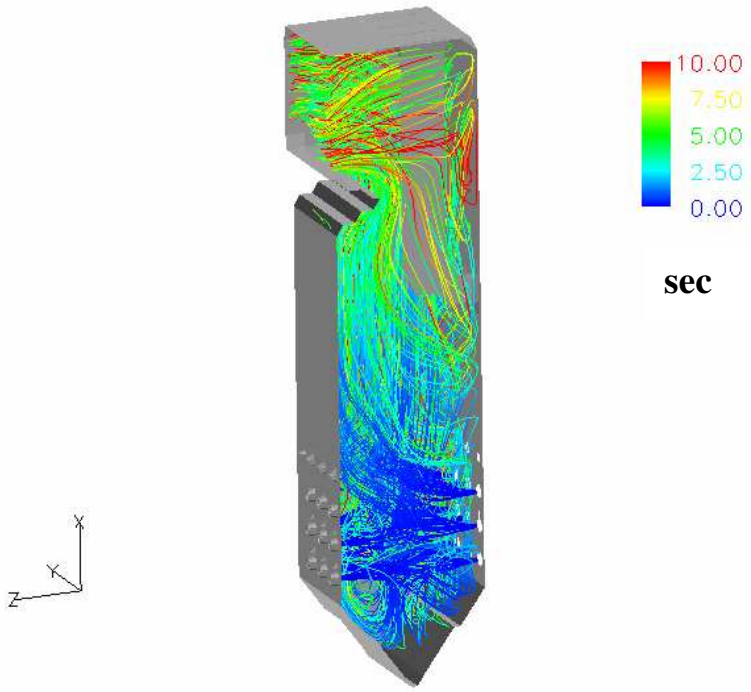

1 atm Furnace

Figure E.17 – PPCC Model: Revised Design
(FLUENT Model is one symmetric half in the width direction)

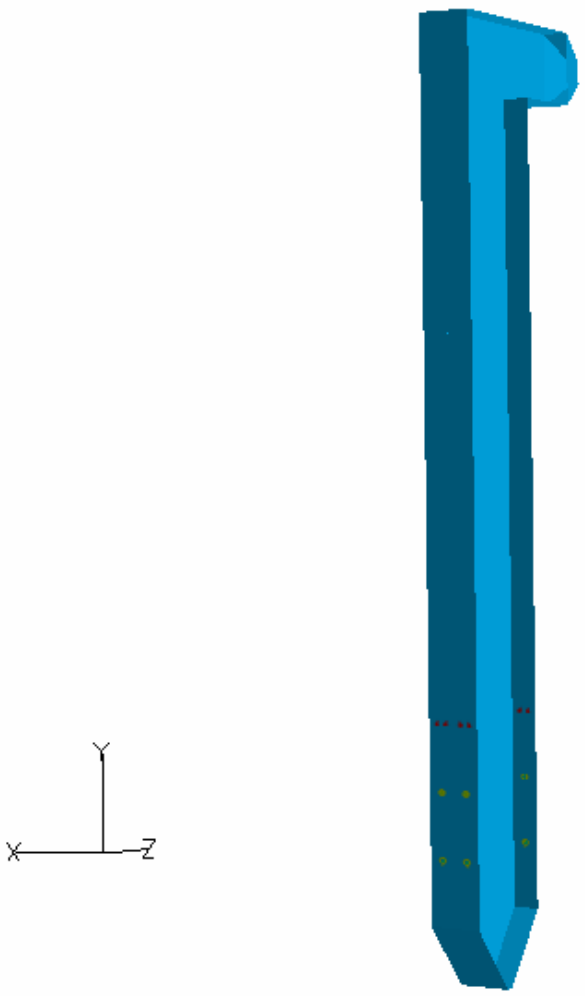

Figure E.4 – Gas Temperature: Revised PPCC Design

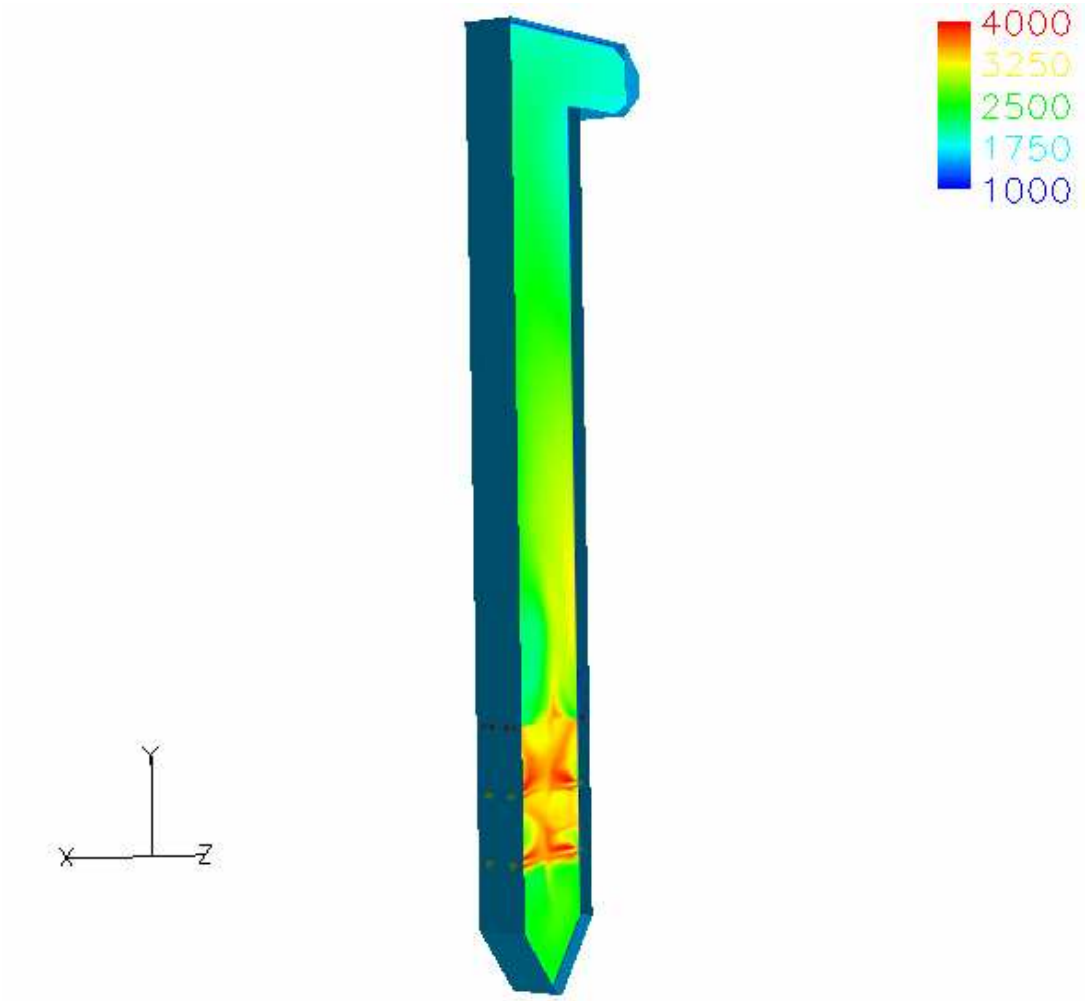

E.6.3 Final FLUENT Model

Figure E.5Figure E.19 is a plot of the flue gas velocity magnitude in a vertical plane through a diametral slice. OFA penetration is small due to injecting the OFA through a ring rather than through discrete ports. Injecting the OFA through a discrete number (e.g. 6 or 8) of ports would improve penetration (due to larger hydraulic diameter) and mixing and increase particle burnout. Figure E.20 presents a plot of gas temperature in a diametral slice. The maximum flue gas temperature is approximately 4300°F (2371ºC) and occurs in the near burner region. The mole fraction of O_2 is presented in figure E21. Total excess air is 17% with –8% stoichiometric air injected at the burner and the remaining 25% injected through the OFA ports. Average O_2 at the model outlet is 3.29%. Figure E.22 presents the coal volatile mole fraction and shows that nearly all of the volatiles are consumed by approximately 45' (13.7 m) from the burner.

The heat flux at the furnace water wall is shown in Figure E.23. The maximum heat flux is approximately 320,000 Btu/hr-ft^2 (1.009 MW/m^2) and occurs approximately 20' (6.1 m) from the burner. The total heat absorbed by the furnace walls before the furnace exit is 632 MM Btu/hr hr (185.2 MW) (average heat flux is approximately 95,000 Btu/hr-ft^2 (0.30 MW/m^2)).

The residence time of the solid particles (coal, char, and ash) are plotted in figure E.24. Particle residence time is approximately 10-12 seconds at the outlet. This is substantial greater than the typical 2 second residence time of a atmospheric boiler due to the much lower volumetric flow rate produced by the pressure of 30 atm. The masses of the 70-micron coal particles and the 175-micron coal particles are plotted in Figure E.25 and E.26, respectively, with the dark blue color representing the residual ash (when the particles are totally burned out). Figure E.25 and E.26 show that all of the coal particles are completely burned before the furnace exit. The masses of the 70-micron coal particles and the 175-micron char particles are plotted in figure E.27 and E.28, respectively, with the dark blue color representing the residual ash. Figure E.28 shows that some of the larger char particles are not completely burned at the exit of the furnace, causing unburned carbon in the fly ash. Total burnout of all particle sizes is 98.4%.

Fuel NOx was calculated by applying a user defined scalar routine supplied by SRI. The resultant NO concentration is presented in Figure E.29. NO concentration at the furnace outlet is 373 ppm. A case was run with no over-fire air and the resultant NO concentration at the furnace outlet was 387 ppm. Assuming the UDF NOx model is correct, this indicates that introducing over-fire air after the devolatilization zone has little effect on reducing NOx in a high pressure coal combustion.

Figure E.5 – Gas Velocity: Final Model

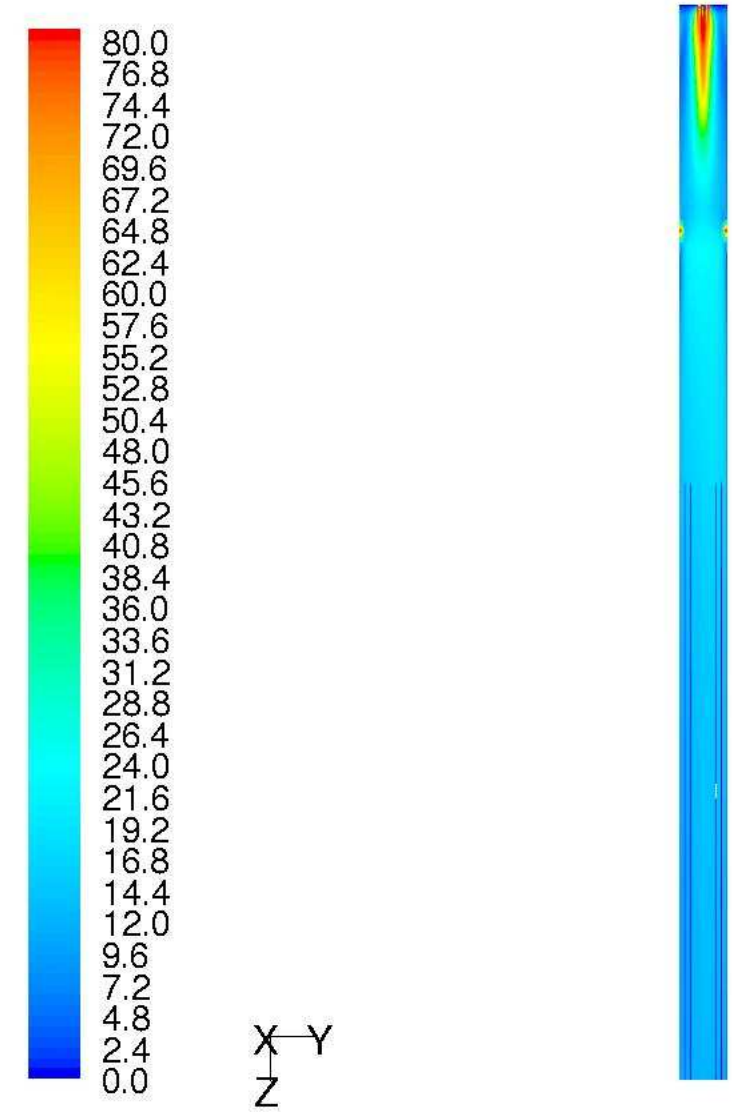

Contours of Velocity Magnitude (ft/s) Nov 16, 2004
FLUENT 6.2 (3d, segregated, spe, ske)

Figure E.20 – Gas Temperature: Final Model

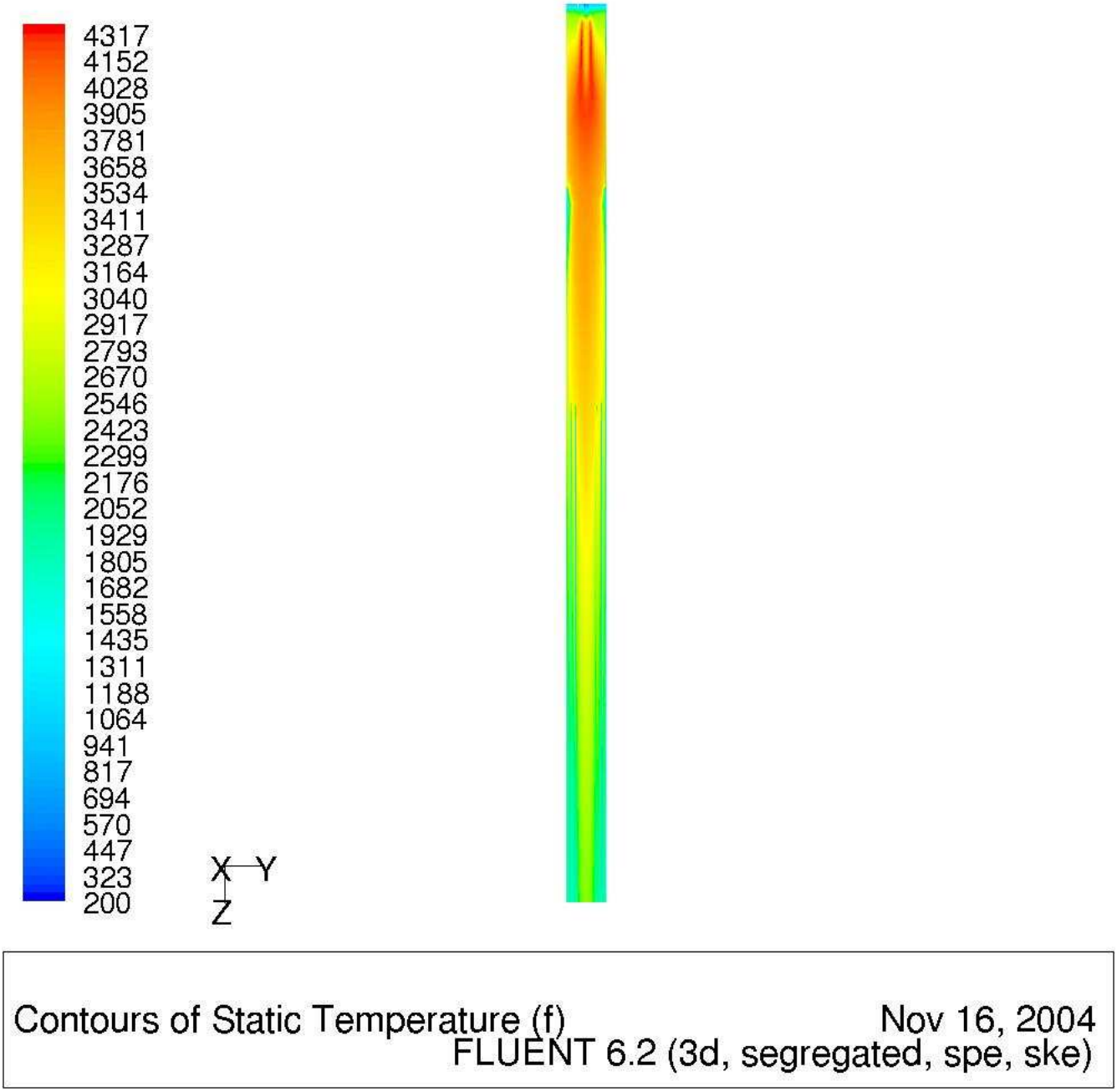

Figure E.21 – O_2 Mole Fraction: Final Model

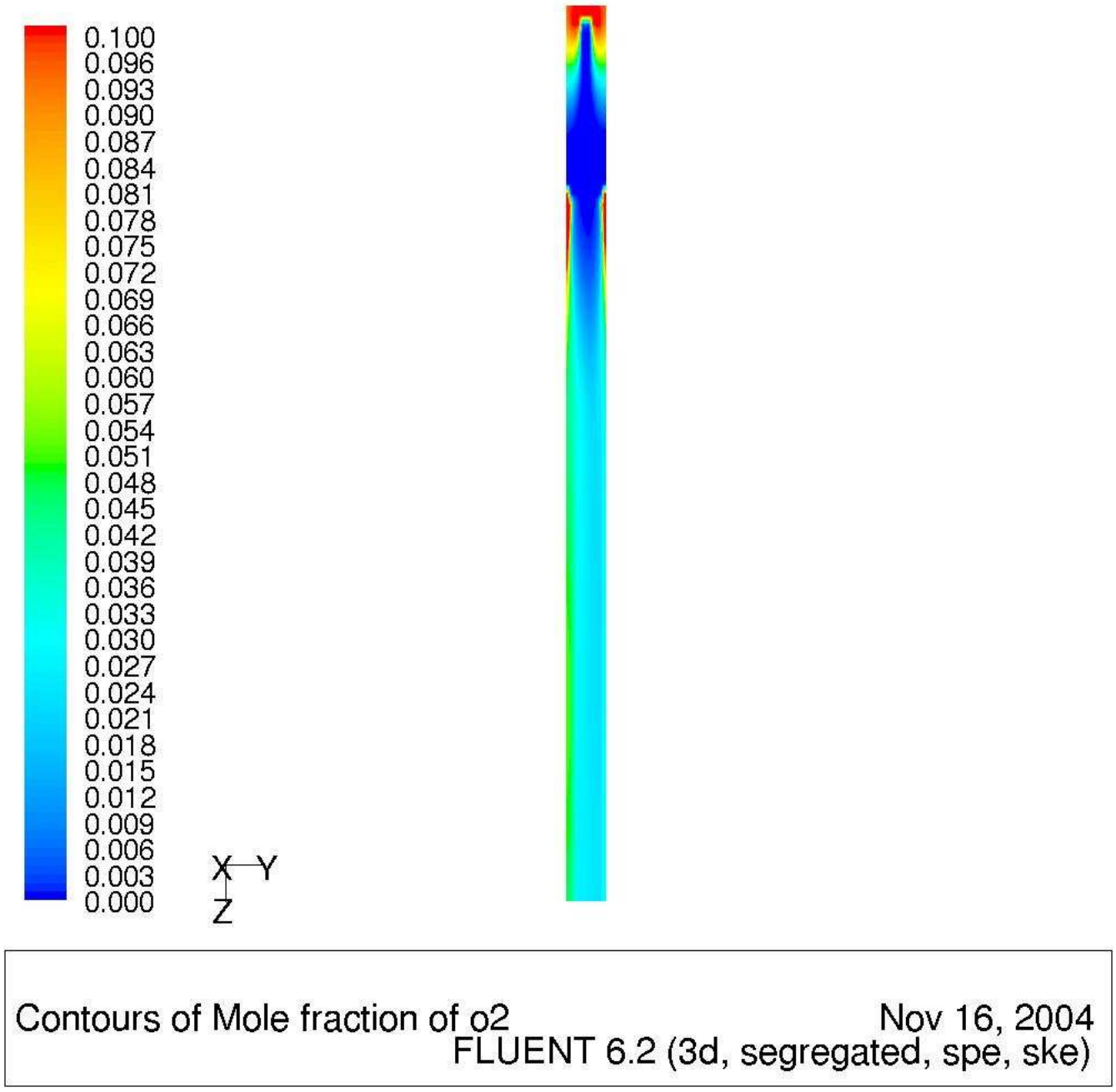

Figure E.22 – Coal Volatile Mole Fraction: Final Model

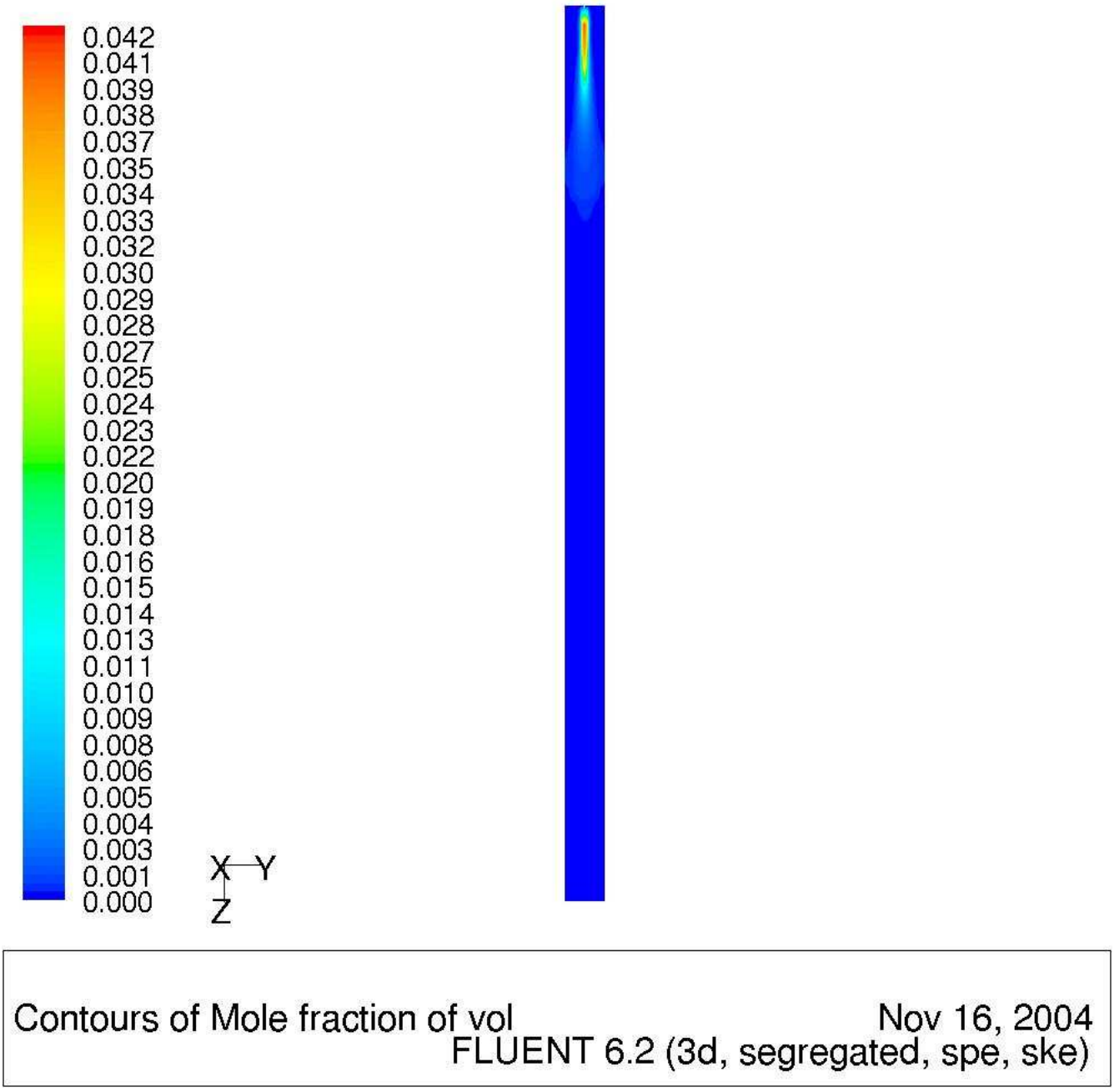

Figure E.23– Wall Surface Heat Flux: Final Model

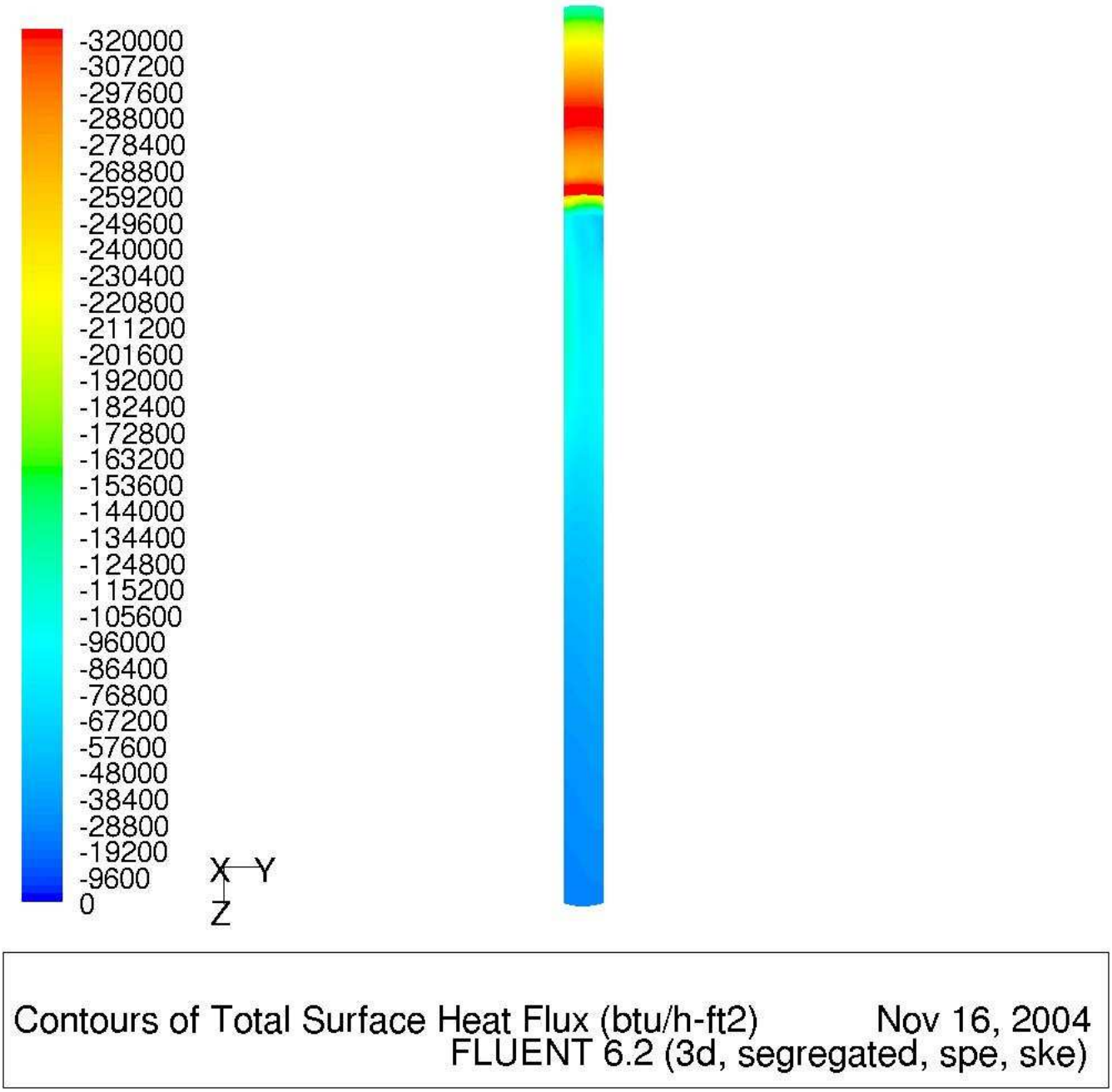

Figure E.24 – Particle Residence Time: Final Model

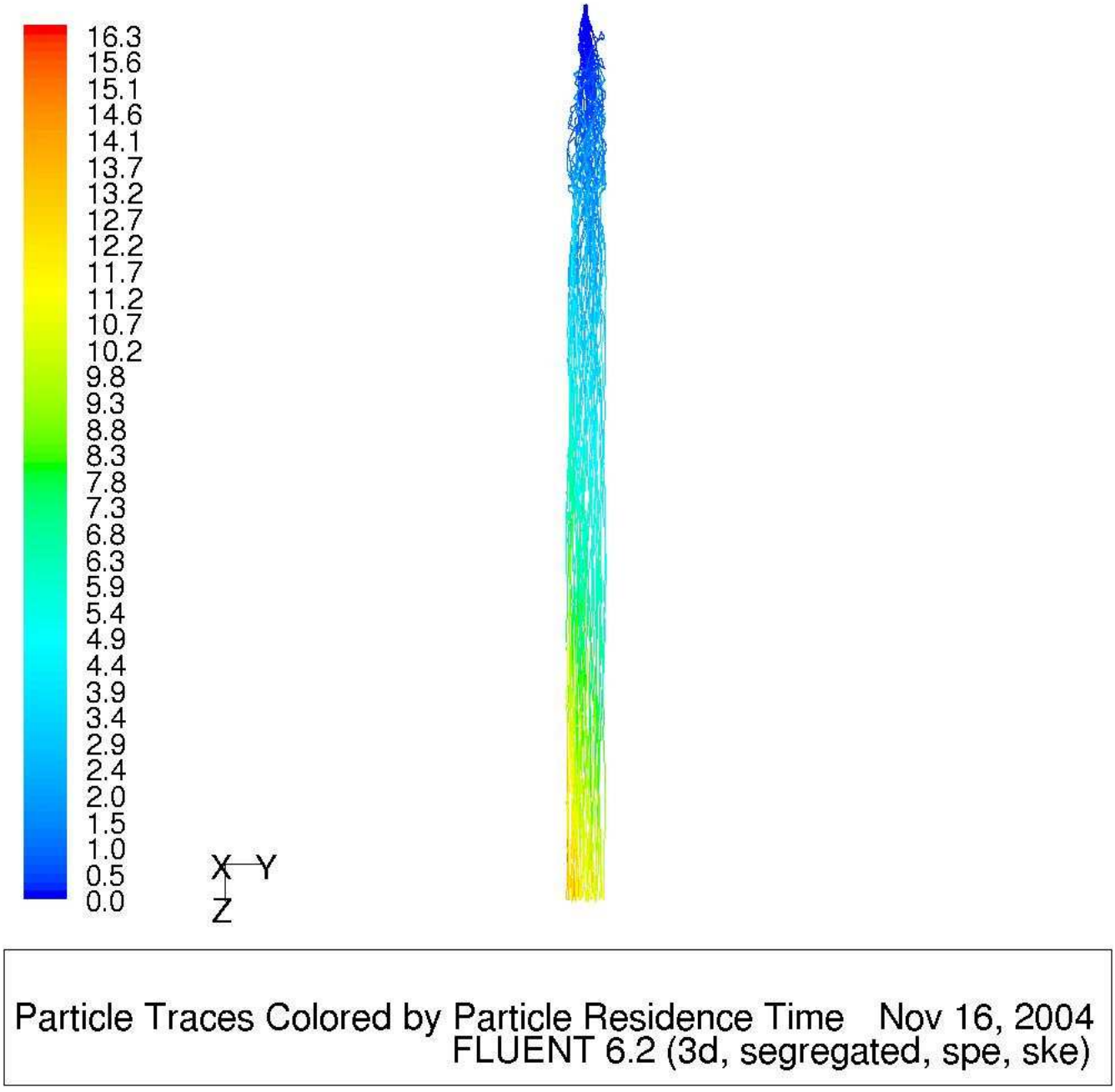

Figure E25 – Mass of Coal Particles (70 micron): Final Model

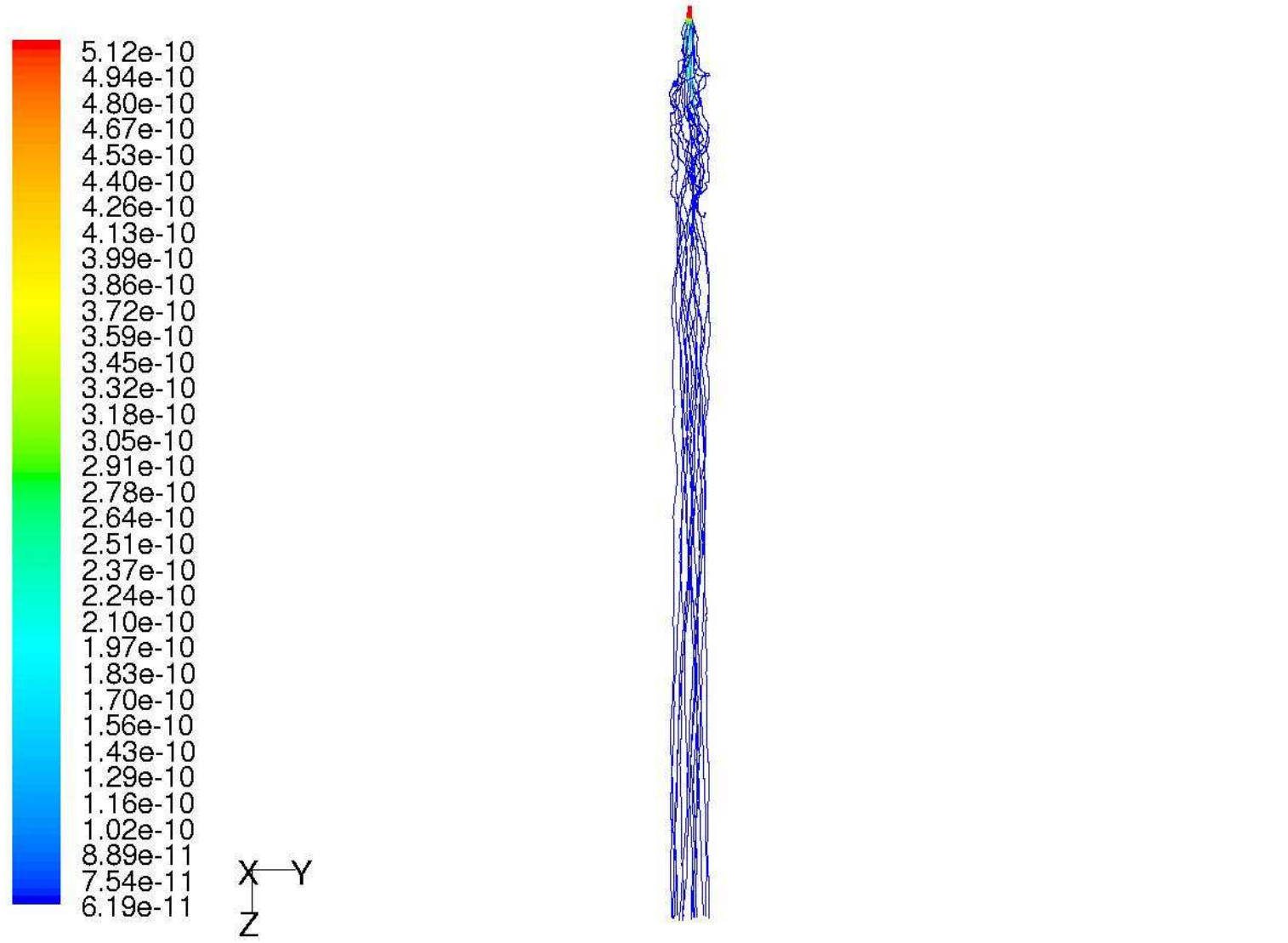

Figure E.26 – Mass of Coal Particles (175 micron): Final Model

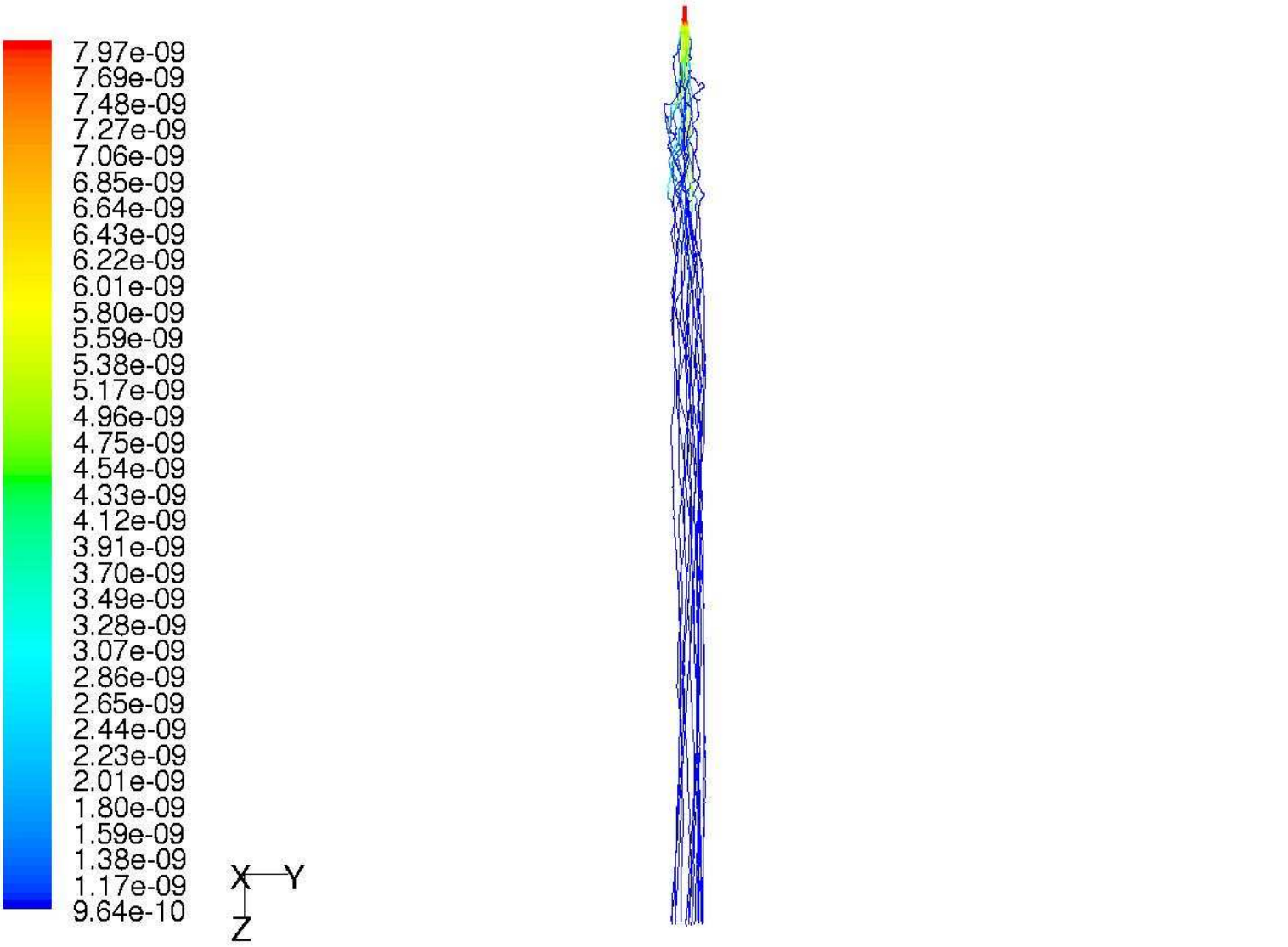

Figure E.27 – Mass of Char Particles (70 micron): Final Model

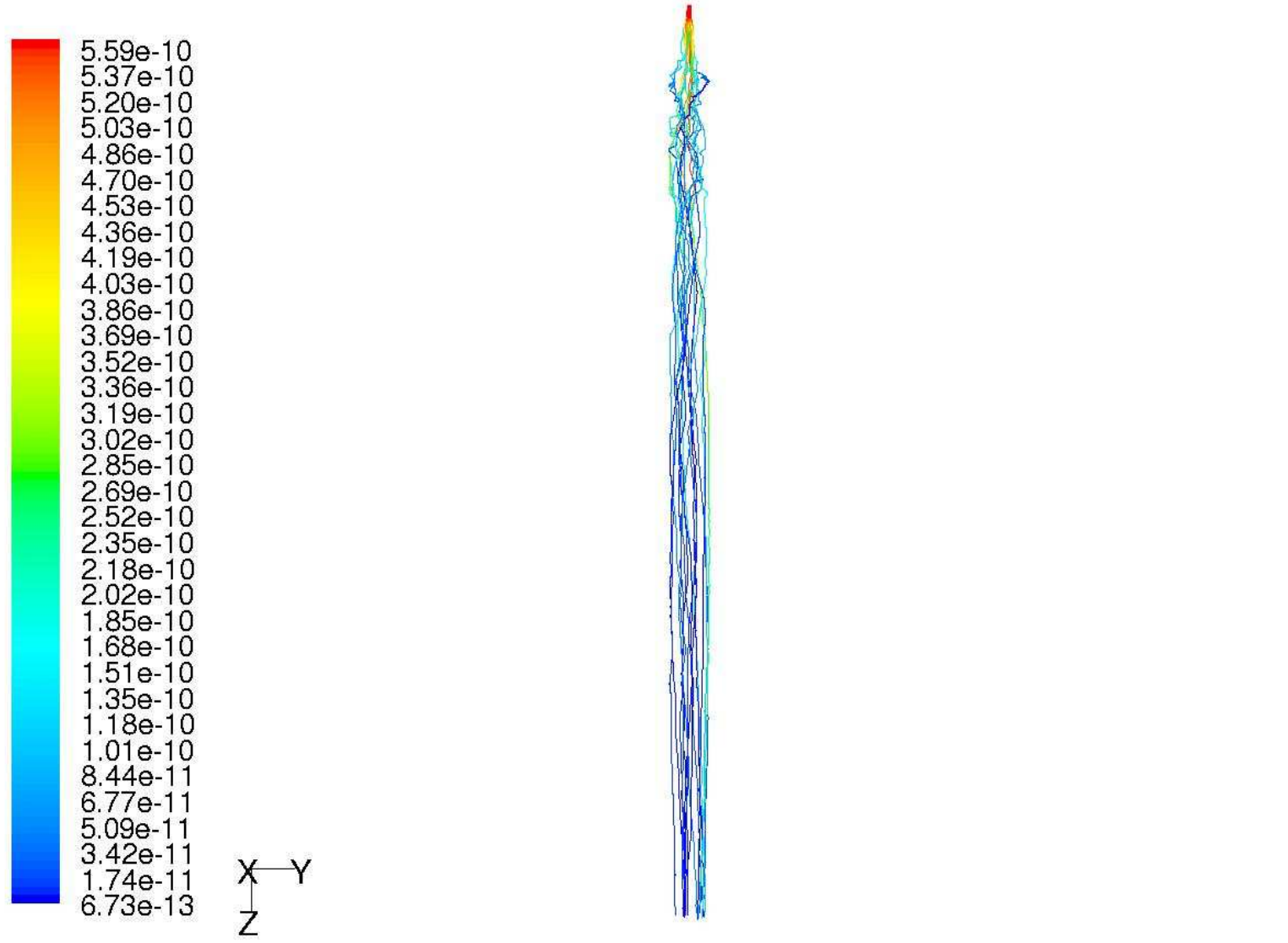

Figure E.28 – Mass of Char Particles (175 micron): Final Model

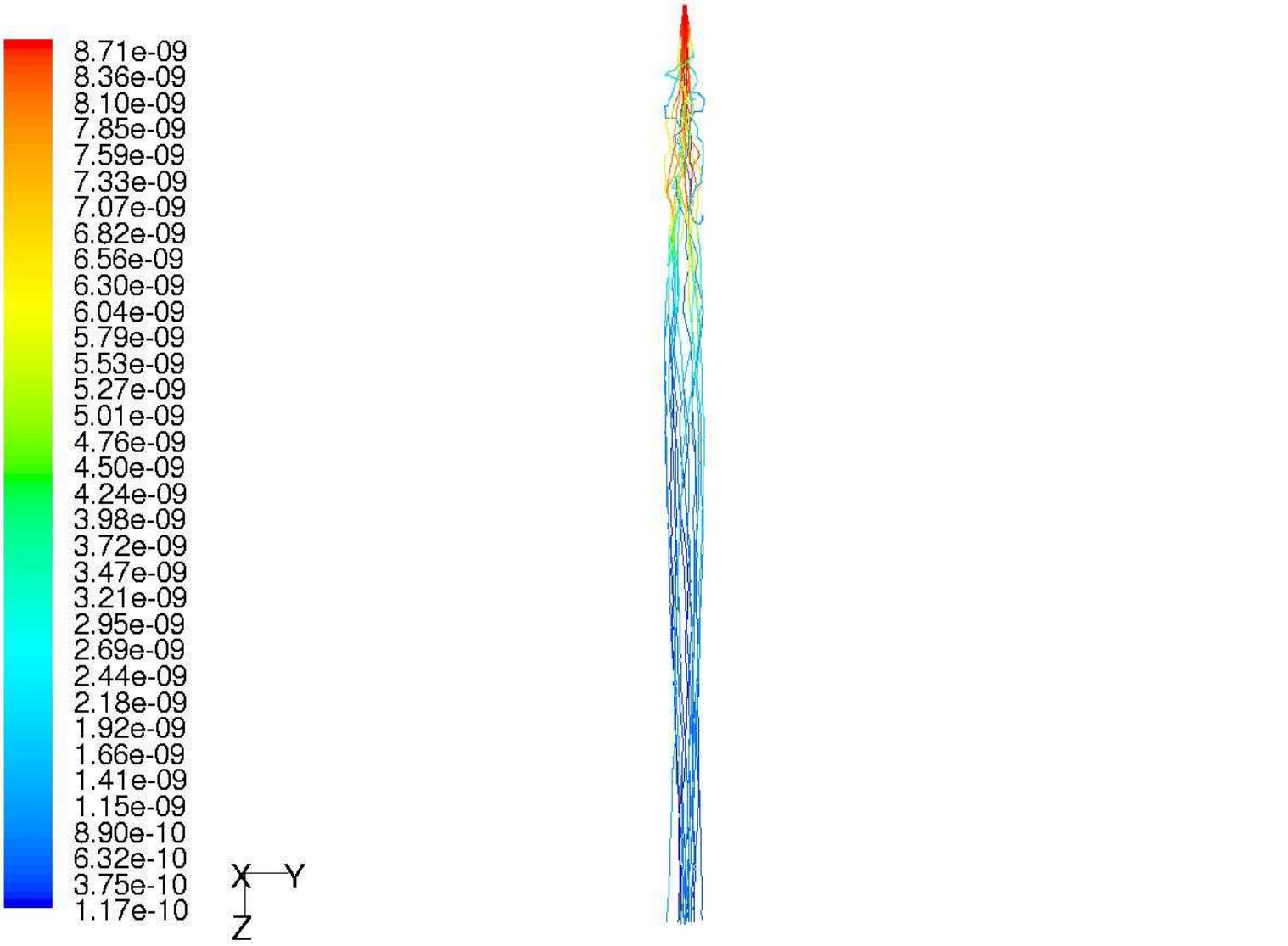

Figure E.29 – NO Concentration (ppm): Final Model

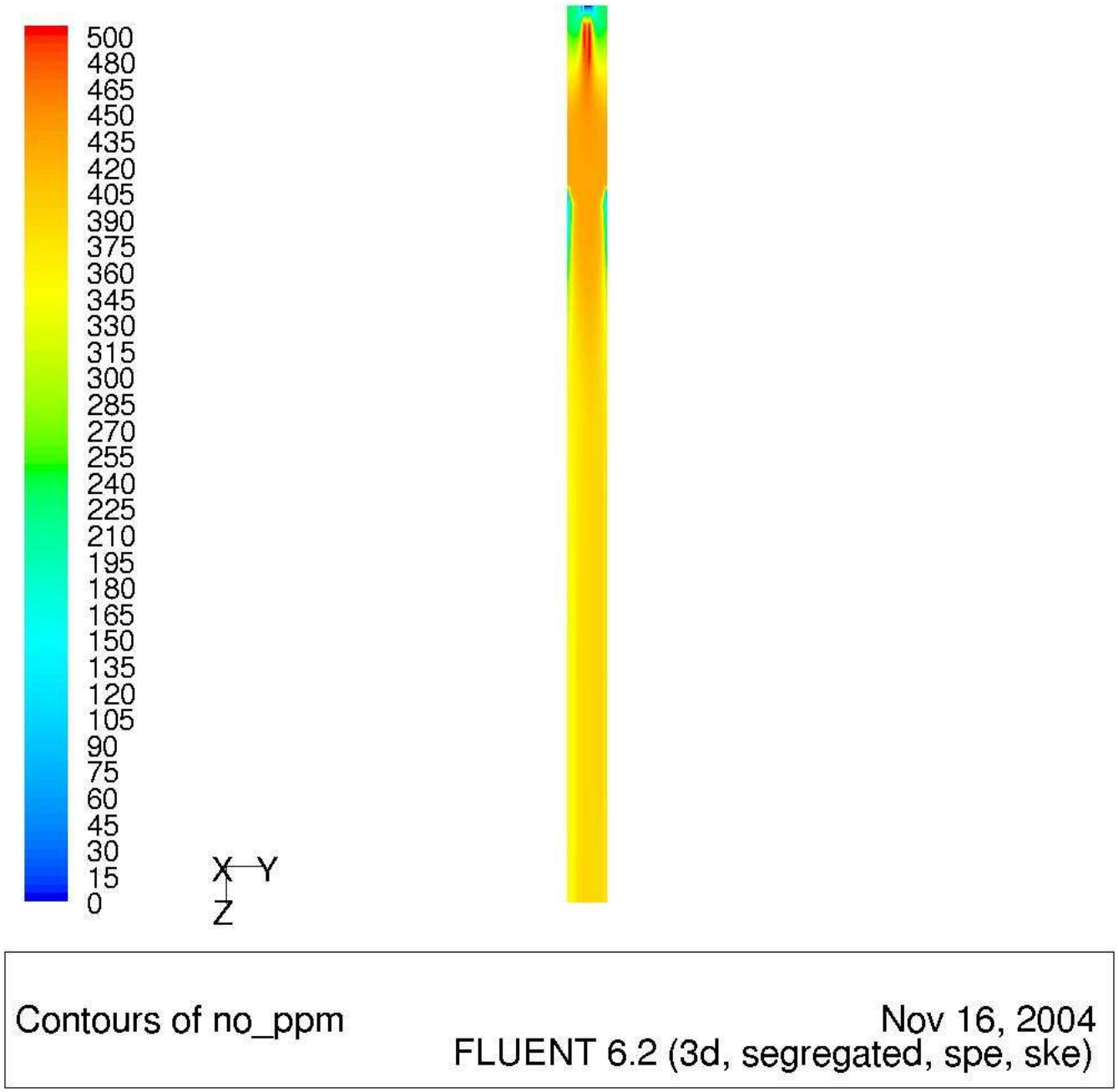

E.6.4 Air Heater

The PPCC includes a combustion furnace and a convective air heater. HEATEX was used to determine the air heater convective tube bank design. HEATEX is a Foster Wheeler general-purpose program for thermal/hydraulic analysis of tube banks. The program performs heat transfer calculations on a local basis by dividing the tube bundle into a number of small heat transfer elements.

Flue gas exits the furnace at approximately 1905ºF (1041^{o}C) and flows over the air heater tube bundle where it heats the air from the gas turbine air compressor from 987^{o}F (531^{o}C) to 1509^{o}F (821^{o}C) and sends the hot air to the fuel cell.

The air heater design is summarized in Table E.6. The air heater tube bundle consists of 10' (3.0 m) long 2.5" (63.5 mm) OD bare tubes in a 69 tubes wide by 42 tubes deep in-line pattern. The tubeside air flows in three parallel rows (to meet pressure drop limits) and makes 14 passes before exiting. Maximum tube wall operating temperature is approximately 1600ºF (871ºC), which requires the use of Incoloy 800HT material. More detailed structural evaluation, which is beyond the scope of the current study, is required to confirm the tube material and wall thickness.

The air heater performance is summarized in Table E.7. Although the use of finned tubes could increase the outside heat transfer coefficient (and reduced the number of tubes), it would increase the maximum metal temperature and require significantly more expensive tube materials. Furthermore, the use of finned tubes is somewhat limited due to the ash environment.

Table E.6 – PPCC Air Heater Design

Tube Length	ft	10.0
Bundle Depth	ft	12.3
Bundle Width	ft	20.1
No. of Tubes Deep		42
No. of Tubes Wide		69
Total Number of Tubes		2,898
No. of Tubes Carrying Air		207
Tube Outside Diameter	in	2.500
Tube Thickness	in	0.35
Longitudinal Pitch	in	3.5
Transverse Pitch	in	3.5
Tube Material		Incoloy 800HT
Total Surface Area	ft2	18,967

Table E.7 – PPCC Air Heater Performance

Tubeside		
Fluid		Air
Inlet Pressure	psia	430
Flow Rate	lb/hr	1,088,000
Inlet Temperature	F	987
Outlet Temperature	F	1509
Frictional Pressure Loss	psi	39
Shellside		
Fluid		Flue Gas
Inlet Pressure	psia	450
Flow Rate	lb/hr	900,598
Inlet Temperature	F	1905
Outlet Temperature	F	1300
Frictional Pressure Loss	in H2O	1.25
Heat Transfer Coefficient		
Inside	Btu/hr-ft2-F	178
Outside	Btu/hr-ft2-F	31.5
Overall	Btu/hr-ft2-F	22.6
Surface Area	ft2	18,967
Mean Temperature Difference	F	360
Heat Transfer	MM Btu/hr	154